Victor Petuya
Charles Pinto
Erwin-Christian Lovasz   *Editors*

New Advances in Mechanisms, Transmissions and Applications

Proceedings of the Second Conference MeTrApp 2013

Springer

Mechanisms and Machine Science

Volume 17

Victor Petuya · Charles Pinto
Erwin-Christian Lovasz
Editors

New Advances in Mechanisms, Transmissions and Applications

Proceedings of the Second Conference
MeTrApp 2013

Springer

Editors
Victor Petuya
Mechanical Engineering Department
University of the Basque Country
Bilbao
Spain

Erwin-Christian Lovasz
Mechanical Engineering Faculty
Politehnica University of Timisoara
Timisoara
Romania

Charles Pinto
Mechanical Engineering Department
University of the Basque Country
Bilbao
Spain

Preface

The Second Conference on Mechanisms, Transmissions and Applications, MeTrApp 2013, has been organized by the Department of Mechanical Engineering of the University of the Basque Country, and has been held in the Bizkaia Aretoa building in the city of Bilbao, Spain, during the period 2–4 October 2013. This conference constitutes the consolidation of the new born MeTrApp conference, which was held for the first time in Timisoara.

The International Federation for the Promotion of the Mechanism and Machine Science, IFToMM, has several technical committees, two of them being the Technical Committee on Linkages and Mechanical Controls and the Technical Committee on Micromachines. One of the main efforts of these two committees is directed to promoting the interaction among university professors and researchers, engineers that work in industry and postgraduate students, with the purpose of testing hypothesis and sharing knowledge in the field of Machine Theory. In this sense, this Conference constitutes the most suitable atmosphere to achieve this target.

The contents of this conference are brought together in this book formed by a collection of 50 peer-reviewed papers, dealing with important and up-to-date topics in the field of mechanisms and robotics. The main areas covered in this conference are mechanism and machine design, mechanical transmissions, automotive applications, biomechanical applications, parallel mechanisms, walking mechanisms, and computational and experimental methods.

A significant number of authors have contributed to the success of this conference. The research papers included in this book are a compilation of relevant results developed by active research groups from many universities and institutions all over the world such as: Canada, Germany, Japan, Italy, France, Poland, Romania, Russia, Turkey, and Spain.

We are grateful to the authors for their contributions and to all reviewers for their critical and valuable recommendations. Also, we want to thank IFToMM, the Spanish Association of Mechanical Engineering and the MeTrApp 2013 International Scientific Committee for their cooperation and support. A special recognition is also due to all members of the Local

Organizing Committee for their continuous work during the preparation of the meeting.

Finally, we kindly appreciate the work done by the staff of Springer in assisting to prepare this book.

Prof. Alfonso Hernández
Conference Chairman

Contents

Automotive Applications

Mechanical Transmissions

Biomechanical Applications

Walking Mechanisms

Mechanism and Machine Design

Parallel Mechanisms

Computational and Experimental Methods

Kinetostatic Benchmark of Rear Suspension Systems for Motorcycle

A. Noriega, D.A. Mántaras, and D. Blanco

University of Oviedo, Spain
noriegaalvaro@uniovi.es

Abstract. This paper provides a benchmark for motorcycle rear suspension systems. The main goal is to determine whether any of the suspension systems provides clear advantages over the others when seeking for a previously defined progressive wheel rate. A kinetostatic formulation of the mechanism is therefore presented. In this formulation, kinematics is based on groups of elements, while statics is based on the principle of virtual work. This formulation has been proved to be efficient and robust. It allows for building objective functions which are especially suitable for evolutionary algorithm optimization. Results show that there are no significant differences between the four types of analysed suspensions.

Keywords: motorcycle, rear suspension, dimensional synthesis, progressiveness, groups of elements.

1   Introduction

The main function of the suspension of a vehicle is to maximize comfort by reducing vertical acceleration of the passenger seat. Furthermore, the suspension system should maximize tyre-road contact to ensure traction and braking. To achieve these goals and, in addition, offer an improved driving feeling, the rear suspension of the motorcycle should have a progressive wheel rate. Therefore, roughness of the road can be adequately filtered while, simultaneously, large vertical displacements under heavy braking or traction are avoided.

A non-progressive behaviour shall be obtained by connecting a spring (with K stiffness constant) and a viscous damper (with a C damping constant) directly to the swing-arm. If a non-linear behaviour is desired, it shall be obtained using tie rods, with K and C values remaining constant. In motorcycles, tie rod systems are usually planar mechanisms (four-bar linkage) which are placed between the rear wheel swing-arm and the rear spring-damper to achieve a non-linear wheel rate.

Different configurations of tie rod systems have been introduced by the major motorcycle manufacturers during the past 30 years.

Almost all of these systems are variations of the four-bar linkage. The most common types can be classified according to the different possibilities of joints for the two ends of the spring-damper, as the lower one can be jointed to the tie rod or

to the rocker, and the upper one can be hinged to the frame or to the swing-arm. Fig. 1 shows schemes of the tie rod systems analysed in this paper which are among the most common types.
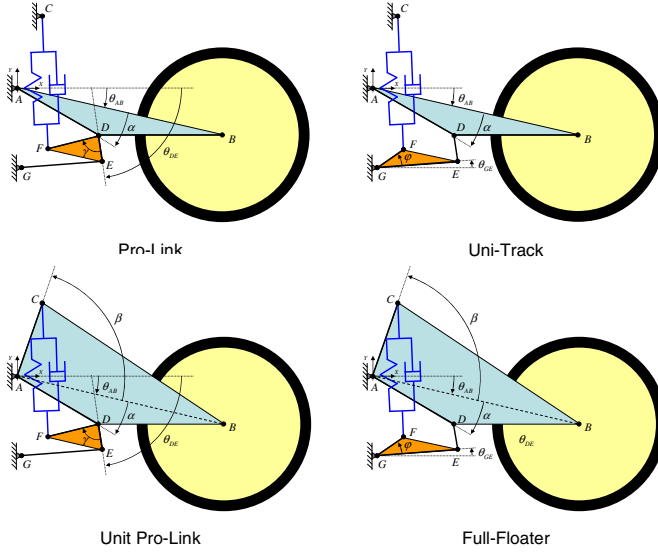
Fig. 1 Kinematic schemes for the tie rod systems

Foale [3] has indicated that all these systems are very similar to each other, in spite of the affirmations of the manufacturers. This work will explore whether this assertion is truthful through comparison of the ability of each system for achieving pre-defined wheel rate.

2   Kinetostatic Dimensional Synthesis

In order to obtain a proper comparison among the four types of suspensions in-cluded in this study, a group of fixed geometric parameters shall be defined. This group includes:

- Values of X and Y coordinates for point A: $x_A = 0$ mm, $y_A = 0$ mm

  This point indicates the position where the swing-arm is jointed to the frame, and it has been used as the origin of the coordinate system.
- Value of X coordinate for point G: $x_G = 0$ mm

  This point indicates the position where the rocker is jointed to the frame.
- The length of the swing-arm: $L_{AB} = 500$ mm
- Minimum length of the spring-damper: $L_{sd\_min} = 210$ mm
- Maximum length of the spring-damper: $L_{sd\_max} = 260$ mm

- Limits for the displacement along Y axis for the rear wheel: $y_B \in \begin{bmatrix} -100 & 20 \end{bmatrix}$

The remaining lengths, angles, stiffness and preloads defined for each suspension system evaluated in this work have been considered as variables in the dimensional synthesis problems. These parameters are depending on the characteristics of each single type of suspension.

In order to simplify the problem and eliminate the influence of the damper, movement of the suspension has been considered quasi-static. Furthermore, neither the mass nor the inertia of moving parts have been considered in the dimensional synthesis problems.

Taking these considerations into account, modelling of each suspension system has the objective of determining length variation of the spring-damper for a given Y coordinate variation of the rear wheel axle, under certain values of the geometric and load parameters.

Castillo et al. [1] had proposed the use of closed loop equations for modelling the Pro-Link suspension kinematic. Nevertheless, it is not clear how they deal with those cases where the mechanism cannot be disassembled. Fernández de Bustos et al. [2] had modelled the kinematics by means of finite elements, so that mentioned problem is avoided.

Problem modelling must be robust and contemplate the most appropriate way of dealing with situations where the mechanism cannot be assembled. This way on, it will be possible to obtain surjective and monotonous functions for the synthesis problems. In addition, modelling has to provide an unambiguous definition for the configuration of the mechanism, which will be maintained throughout the movement. For this purpose, a kinematic modelling based on groups of elements has been used in this work. This model has been previously described in [4], and additionally used for modelling suspensions in synthesis problems [5]. The geometry of each single link can be defined through lengths and/or angles. Therefore, bounds can be easily established for these geometric parameters in the dimensional synthesis problem. Moreover, to obtain a full definition, the assembly mode for certain groups must be introduced as constants of the mechanism. The nomenclature that has been used in this work is as follows:

L_{ij} : Distance between points i and j

θ_{ij} : Angle between the *ij* vector and the X positive axis. Counter-clockwise is assumed to be positive

$\alpha, \beta, \gamma, ...$: Angle between two vectors belonging to the same rigid body. Counter-clockwise is assumed to be positive

Desired progressiveness curve is defined in Eq. (1) based on practical knowledge and previous experiences.

$$F_{y_B-desired} = 0.1025 \cdot y_B^2 + 27.3457 \cdot y_B + 2412,1 \tag{1}$$

2.1   Parametric Formulation of Kinematics

Formulation of kinematics for considered suspension types has been defined following the sequential procedure described in [5]. The steps of this procedure are:

1. Calculate the θ_{AB} angle from y_B and L_{AB} using the arcsine function.
2. Calculate the θ_{AD} angle from θ_{AB} and α. Additionally, when modelling the Unit Pro-Link or the Full-Floater suspensions, calculate the θ_{AC} angle from θ_{AB} and β. In both cases the consideration of the swing-arm as a rigid body has been applied.
3. Calculate the coordinates for the D point. Additionally, calculate the coordinates for the C point when modelling the Unit Pro-Link or the Full-Floater suspensions.
4. Calculate the coordinates for the E point as a function of the positions of points D and G, by solving the RRR group according to [2] and indicating the assembly mode. It has to be remarked that this group suitability for assembling depends on actual positions and dimensions. Mentioned solving procedure takes into account all possible options and provides a value for the *assembly error* parameter. If assembly error equals 0, the group can be assembled. Otherwise, if assembly error is above 0, then the RRR group cannot be assembled.
5. Once the coordinates for the D, E and G points are already known, and using the arctangent function, calculate the θ_{DE} angle for the Pro-link and the Unit Pro-Link suspensions, or the θ_{GE} angle for the Uni-Track and the Full-Floater ones.
6. Calculate the coordinates of the F point using the coordinates of point D (cases of the Pro-link and the Unit Pro-Link suspensions) or the coordinates of point G (when modelling the Uni-Track or the Full-Floater)
7. Once the coordinates for the C and F points are known, calculate the L_{sd} length of the spring-damper.

Each suspension system has its own geometric parameters. These parameters have been grouped in the **p** vector. According to this, the Pro-Link suspension geometric parameters are:

$$\mathbf{p} = \begin{bmatrix} x_C & y_C & y_G & \alpha & L_{AD} & L_{DE} & L_{EG} & \gamma & L_{DF} \end{bmatrix}$$

While the Uni-Track ones are:

$$\mathbf{p} = \begin{bmatrix} x_C & y_C & y_G & \alpha & L_{AD} & L_{DE} & L_{EG} & \varphi & L_{FG} \end{bmatrix}$$

And in the case of the Unit Pro-Link:

$$\mathbf{p} = \begin{bmatrix} y_G & \beta & L_{AC} & \alpha & L_{AD} & L_{DE} & L_{EG} & \gamma & L_{DF} \end{bmatrix}$$

Finally, the parameters of the Full-Floater suspension are:

$$\mathbf{p} = \begin{bmatrix} y_G & \beta & L_{AC} & \alpha & L_{AD} & L_{DE} & L_{EG} & \varphi & L_{FG} \end{bmatrix}$$

2.2   Parametric Formulation of Statics

Formulation of kinematics from section 2.1 allows for determining the value of L_{sd}. The error related to the assembly of the DEG dyad can be also determined using the y_B value and the geometric parameters in $\mathbf{p}$ for each single type of suspension.

$\mathbf{y}_B$ and $\mathbf{L}_{sd}$ have been defined as the n-component vectors constructed from y_B and L_{sd} values for each j-th evenly spaced position in the $\begin{bmatrix} -100 & 20 \end{bmatrix}$ range, given $j = 1,...,n$. Eq. (2) shows the expression that has been obtained for F_{y_B-mech} applying the principle of virtual work for $j = 2,...,n$ and neglecting the force at the damper.

$$\mathbf{F}_{y_B-mech}(j) = \frac{\left(K \cdot \left(\mathbf{L}_{sd}(j) - \mathbf{L}_{sd}(1) \right) - F_{preload} \right) \cdot \left(\mathbf{L}_{sd}(j) - \mathbf{L}_{sd}(j-1) \right)}{\mathbf{y}_B(j) - \mathbf{y}_B(j-1)} \tag{2}$$

2.3   Formal Approach for the Optimization Problem

The variables that have been considered as unknown for the optimization problem have been grouped in vector $\mathbf{v}$, defined as follows:

$$\mathbf{v} = \begin{bmatrix} \mathbf{p} & K & F_{preload} \end{bmatrix}$$

Therefore, this problem has been formulated as:

"Determining the values for the components in $\mathbf{v}$, that make the value for the vertical force in the wheel (F_{y_B-mech}) as close as possible to a desired value ($F_{y_B-desired}$)". Two additional constraints have been imposed for this problem: firstly, vertical displacement in the wheel must fulfil the working range of the spring-damper; secondly, the mechanism does not get locked in an intermediate position.

The so defined optimization problem can be formulated as Eq. (3).

$$\min \sum_{j=2}^{n} \left(\mathbf{F}_{y_B-desired} \left(\mathbf{y}_B(j) \right) - \mathbf{F}_{y_B-mech} \left(\mathbf{y}_B(j), \mathbf{v} \right) \right)^2$$

with

$$L_{sd\_max} = \mathbf{L}_{sd}(1)$$
$$L_{sd\_min} = \mathbf{L}_{sd}(n) \tag{3}$$
$$\sum_{j=1}^{n} error_j = 0$$

being $$\mathbf{y}_B(j) = \frac{-100 \cdot (n-j) + 20 \cdot (j-1)}{n-1}$$

The $error_j$ value represents assembly error for the DEG dyad in the position j. It must be remarked that this error is not calculated for the first point in the wheel rate curve, as $F_{y_B - mech}$ is calculated through increments.

2.4   Solving the Optimization Problem

Four synthesis problems have been therefore posed independently, one for each type of suspension. All of them share a series of characteristics:

- They are minimization problems with equality constraint.
- They have eleven continuous type variables
- The derivatives of the objective functions with respect to the variables are not available
- They have low computational costs
- Neither the number of optima nor their possible values are known.
- Though an approximation to the optimum solution is not available, it is relatively simple to set bounds based on practical considerations

Once these characteristics have been analysed, the evolution strategy DDM-ES has been finally selected for the optimization problem. This election is based on the ability of the DDM-ES strategy for natively working with bounded and continuous variables, an also for its good performance when working with multimodal functions [6]. After this, solutions are refined with the SQP method.

Nevertheless, this algorithm does not admit constraints. Therefore, the original problem has been transformed into a new unconstrained optimization problem. The formulation of this new problem is reflected on Eq. (4).

$$
\min \sum_{j=2}^{n} \left(\mathbf{F}_{y_B - desired} \left(\mathbf{y}_B \left(j \right) \right) - \mathbf{F}_{y_B - mech} \left(\mathbf{y}_B \left(j \right), \mathbf{v} \right) \right)^2 + \ldots
$$

$$
\ldots + \omega_1 \cdot \left(L_{sd\_max} - \mathbf{L}_{sd} \left(1 \right) \right)^2 + \omega_2 \cdot \left(L_{sd\_min} - \mathbf{L}_{sd} \left(n \right) \right)^2 + \omega_2 \cdot \sum_{j=1}^{n} error_j^2
$$

(4)

In this equation ω_1 and ω_2 are used for weighting possible failures on the extreme lengths of the damper. ω_3, on the other hand, is used for weighting the relative effect of error assembly.

3   Results

Formulations of the synthesis problems for the suspension systems have been programmed using MATLAB. These problems have later been solved, considering variable limits as shown in Table 1.

Table 1 Bounds for the variables

Variable	Min	Max	Variable	Min	Max
$x_C \, (mm)$	-30	100	$y_C \, (mm)$	30	100
$y_G \, (mm)$	-150	-50	$\beta \, (rad)$	$\pi/10$	$\pi/2$
$L_{AC} \, (mm)$	50	200	$\alpha \, (rad)$	$-\pi/10$	0
$L_{AD} \, (mm)$	50	200	$L_{DE} \, (mm)$	50	200
$L_{EG} \, (mm)$	50	200	$\gamma \, (rad)$	$-\pi/3$	0
$L_{DF} \, (mm)$	50	200	$\varphi \, (rad)$	$-\pi/10$	$\pi/10$
$L_{FG} \, (mm)$	50	200	$K \, (N/mm)$	10	200
$F_{preload} \, (N)$	0	1000			

Weights have been fixed as: $\omega_1 = \omega_2 = \omega_3 = 10^6$. Population size for the DDM-ES has been fixed to a 500 value, while the number of generations has been fixed to a 40 value. Fig. 2 shows the desired and optima wheel rate curves for each single suspension system.
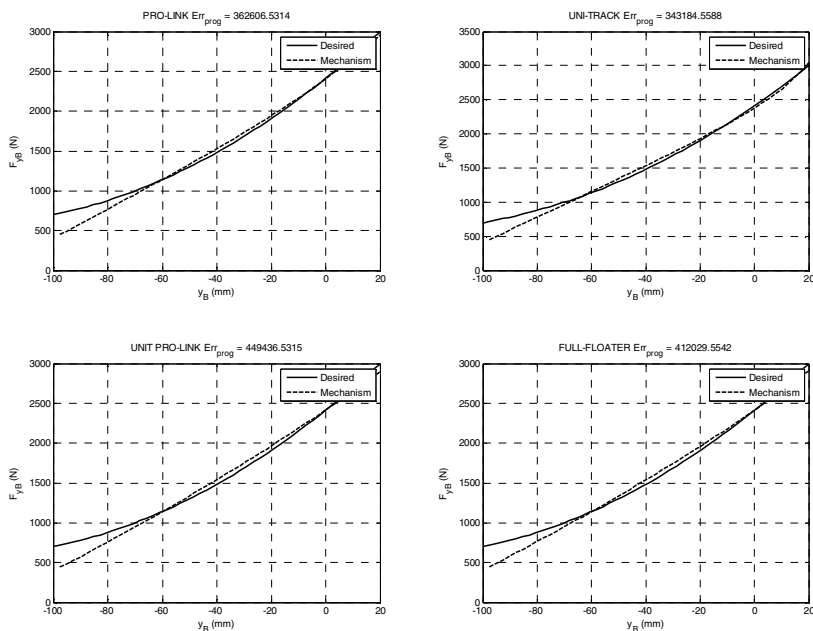
Fig. 2 Desired and optima wheel rate curves for each single suspension system

For the evaluated suspension systems, optimal solutions show a zero assembly error in all positions. Likewise, in the four cases, error related to the achievement of maximum and minimum damper lengths shows values below 0.2 mm.

Computational time for solving each optimization problem has been as follows: Pro-Link suspension: 27.43 s, Uni-Track suspension: 27.79 s, Unit Pro-Link suspension: 28.66 s, Full-Floater suspension: 28.41 s.

4   Conclusions

Firstly, a brand new kinetostatic formulation has been proposed. This formulation, based on groups of elements and the principle of virtual work, allows for defining a robust and efficient objective function. Secondly, a comparative among different types of motorcycle rear suspensions systems is presented. This comparative provides a promising approach to an integral synthesis of mechanisms (structural + dimensional). Thirdly, results reveal that none of the suspension systems studied is qualitatively superior to the others under a kinetostatic criterion. This statement agrees with Foale conclusions. Finally, it can be established that all the analysed mechanism are only capable for accurately fulfilling the final 2/3 of the desired wheel rate curve.

References

1. Castillo, J.J., Giner, P., Simón, A., Cabrera, J.A.: Optimal design of motorcycle rear suspension systems using genetic algorithms. In: Mechanisms and Machine Science 7, New Trends in Mechanism and Machine Science, Theory and Applications in Engineering, pp. 181–189. Springer (2012)
2. Fernández de Bustos, I., Aguirrebeitia, J., Avilés, R., López, D.: Optimización dimensional de mecanismos incluyendo objetivos de velocidad. In: Proceedings of XVIII Congreso Nacional de Ingeniería Mecánica (CNIM 2010), Ciudad Real, Spain (2010)
3. Foale, T.: Motocicletas, Comportamiento dinámico y diseño de chasis. Ed. Tony Foale Designs (2003)
4. Noriega, A., Cadenas, M., Fernández, R.: Position problems in Assur's groups with revolute pairs. In: Mechanisms and Machine Science 7, New trends in Mechanism and Machine Science, Theory and Applications in Engineering, pp. 141–148. Springer (2012)
5. Noriega, A., Moreda, Y., Sierra, J.-M.: Síntesis cineto-estática de una suspensión delantera alternativa para una motocicleta. In: Proceedings of XIX Congreso Nacional de Ingeniería Mecánica (CNIM 2012), Castellón, Spain (2012)
6. Noriega, A., et al.: An efficient optimization method to obtain the set of most promising minima in multimodal problems. Int. J. for Simulation and Multidisciplinary Optimization 3-4, 424–431 (2009)

Interconnected Suspension System on Sport Motorcycles

C. Moreno-Ramírez[1], P. García-Fernández[2], A. de-Juan[2],
and M. Tomas-Rodríguez[1]

[1] City University London, U.K.
`{ciromoreno,Maria.Tomas-Rodriguez.1}@city.ac.uk`
[2] Universidad de Cantabria, Spain
`{pablo.garcia,ana.dejuan}@unican.es`

Abstract. The dynamical response of an interconnected suspension system on a standard sport motorcycle is investigated. The paper contains the geometrical analysis of the interconnection system, an explanation of the mathematical model of the motorcycle under study and the results for bump simulations under straight running conditions. The analysis is done by using the state space representation of the motorcycle model which had been obtained by taking advance of VehicleSim software. Optimization processes are performed in order to find the best values of interconnection coefficients. Finally the work concludes that a better performance in terms of suspension precision and comfort can be achieved by an interconnected suspension system on this kind of motorcycle.

Keywords: Motorcycle, modelling, dynamics, suspension, VehicleSim.

1   Introduction

Interconnected suspension has been widely used on car industry and referenced on the literature [6]. The first mass production car with front to rear mechanical interconnected suspension was the 1948 Citroën 2CV. Nowadays most of the marketed cars are equipped with antiroll bars. Several companies carry on research on semi-active/passive connected suspension obtaining good results.

However, in the motorcycle field these systems are not as extended as in the car industry. Some proposal has been placed in the last years being the Creuat system [10] one of the most significant example. Also there exist a couple of bicycle demonstrators for this concept. These are the case of the Toptrail Interconnected Suspension Bicycle Project developed by Adrian Griffiths [12] or the Robert Rae's bicycle design [11].

In all the cases the interconnection is presented as a way to uncouple the different bicycle/motorcycle modes involved in the suspension motion. Being these modes *pitch* and *bounce,* with an interconnected suspension system their stiffness and damping can be set independently.

In this work we focus on the suspension performance and how an interconnected system can improve it. For this goal we consider four variables as performance indicators. The precision of the suspension will be studied through the distance of the wheels to the road after a bump. The comfort will be defined through the motorcycle's pitch variation and the total acceleration perceived by the rider.

By means of a high fidelity motorcycle model and dynamics simulation we will be able to understand how the different suspension settings will affect the behaviour of the vehicle, to finally propose a suitable configuration for the interconnected system that would allow better performance in terms of precision and comfort for the motorbike model under study.

2   Interconnected Suspension Systems

A simple interconnection mechanism is shown in Fig.1. It consists in the classical front and rear suspension systems of a sport motorbike which are connected through a spring/damper unit. In this scheme two levers systems are used to represent the physical connection between the central unit and the wheels. In a first approach the geometrical relation between the wheels displacements and the spring/damper compression provided by these levers will be considered as constant. In a real motorcycle, different mechanisms can be design in order to meet these constant relations.
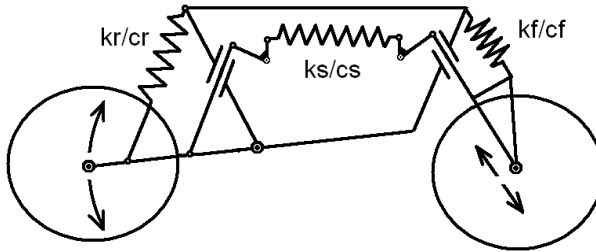
Fig. 1 Interconnected suspension system scheme. *ki* represent the stiffness coefficients. *ci* represent the damping coefficients.

Being *cdf* the geometrical relation between front fork compression and the front tip of the interconnection spring/damper and c*dr* the geometrical relation between rear swinging-arm rotation and the rear tip of the interconnection spring/damper, the total force and moment exerted by the spring system on each wheel can be written as in Eq. (1) and Eq. (2). Both of them will depend on the front fork compression (Z) and the swinging arm angle (θ).

$$F_s = -(kf + cdf^2 \cdot ks) \cdot Z - (cdf \cdot cdr \cdot ks) \cdot \theta \qquad (1)$$

$$M_s = -(cdf \cdot cdr \cdot ks) \cdot Z - (kr + cdr^2 \cdot ks) \cdot \theta \qquad (2)$$

As we consider constant geometrical relation we can extend these expressions to the damper force and moment in Eq. (3) and Eq. (4).

$$F_d = -(cf + cdf^2 \cdot cs) \cdot \dot{Z} - (cdf \cdot cdr \cdot cs) \cdot \dot{\theta} \qquad (3)$$

$$M_d = -(cdf \cdot cdr \cdot cs) \cdot \dot{Z} - (cr + cdr^2 \cdot cs) \cdot \dot{\theta} \qquad (4)$$

Finally these expressions can be simplified as follow:

$$F_s = -FK \cdot Z - SK \cdot \theta \qquad (5)$$

$$M_s = -SK \cdot Z - RK \cdot \theta \qquad (6)$$

$$F_d = -FC \cdot \dot{Z} - SC \cdot \dot{\theta} \qquad (7)$$

$$M_d = -SC \cdot \dot{Z} - RC \cdot \dot{\theta} \qquad (8)$$

FK and *FC* are the front suspension constants, *RK* and *RC* the rear suspension constants and *SK* and *SC* the interconnection constants.

3   Mathematical Modelling

The mathematical model used for this study is a modification of an existing model of a Suzuki GSX-R1000. This model has been widely used in the past for several contributions in the field of motorcycle dynamics and stability analysis (see [2, 3, 4, 5]). It consists of seven bodies: rear wheel, swinging arm, main frame (comprising rider's lower body, engine and chassis), rider's upper-body, steering frame, telescopic fork suspension and front wheel assembly. It involves three translational and three rotational freedoms of the main frame, a steering freedom associated with the rotation of the front frame relative to the main frame and spinning freedoms of the road wheels. The road tires are treated as wide, flexible in compression and the migration of both contact points as the machine rolls, pitches and steers is tracked dynamically. The tyre's forces and moments are generated from the tyre's camber angle relative to the road, the normal load and the combined slip using Magic Formulae models [1,7]. For a detailed description of the complete model the reader is referred to [9].

It has been developed using VehicleSim, which is a set of LISP macros enabling the description of mechanical multi-body systems. The outputs from VehicleSim are a simulation program based on "C" language with the implementation of the equations of motion and a Matlab file containing the model's linear state-space equations. VehicleSim commands are used to describe the components of the motorcycle multi-body system in a parent-child relationship according to their physical constraints and joints. Once the VehicleSim code generates the simulation program, this is capable of computing general motions corresponding to specified initial conditions and external forcing inputs.

Some modifications had to be done to the model. The rear suspension forces are redefined to behave linearly and the interconnection forces have been introduce following the Eq. (5) to Eq. (8). We considered *cdf*=1 (dimensionless) and

cdr=0.549 m (horizontal projection of the swinging arm length). In order to reduce the computational time, all the degrees of freedom related with the out-of-plane motion have been removed since they will not be involved in the dynamics under study. The aerodynamic forces have not been considered in this first approach to keep a clearer view of the interconnected suspension effects. Finally the wheel inputs method has been modified in order to keep linear requirement.

Once the model has been programmed we take advantage of VehicleSim to obtain the linear state space which will describe it. With this state space model we can perform the bump simulations for the different forward speeds varying the stiffness and damping on the interconnection spring/damper unit. The bump simulation will be performed through a 10mm step input on the front wheel and a similar time delayed input on the rear wheel, where the delay depends on the speed.

4   Results

The two most important features of a sport motorcycle suspension system are to provide precision for the wheels to follow the road profile and to keep a certain comfort for the rider under road perturbation. For the linear model under study, we will measure the precision of the suspensions through the maximum separation of the wheels contact point to the road surface after a step input. While the comfort will be measured through the maximum acceleration and pitch angle experienced by the rider.

The forces of the front and the rear suspension are described by the Eq. (5) to the Eq. (8). So the connection force and moment are defined by the stiffness and damping coefficient *SK* and *SC*. We call 'efficiency on each variable' to the normalized difference between the maximum value achieved by the variable after a step input with (SK≠0 or SC≠0) and without (SK=0 and SC=0) interconnection forces between suspensions. It is defined by Eq. (9) as follows:

$$Eff(x) = 100 \cdot \big(mv_0(x) - mv_c(x)\big)/mv_0(x) \qquad (9)$$

x is the variable under study. It can be the acceleration (*acc*), pitch (*ptc*), front (*fwz*) and rear (*rwz*) wheels vertical displacements from the road. $mv_0(x)$ is the maximum value achieved by the variable with non-connected suspensions and $mv_C(x)$ is the maximum value achieved by the variable with connected suspensions. *Eff* will be expressed as a percentage and will be positive if the connection arrangement provides a reduction on the variable's value.

We have run bump simulations for a range of forward speeds going from 10 to 80 m/s in which the stiffness and damping coefficient of the equivalent interconnection spring/damper unit were varied. With the results we can map the efficiency on the comfort and precision variables. For all the cases we can see that the variation on the damping coefficient (*SC*) strongly modifies the response of all the four variables. However, the variation on the stiffness coefficient (*SK*) only affects their behaviour in a very lightly way. Fig.2 shows the efficiency on all the variables for the different values of stiffness and damping coefficient at a forward speed of 50m/s.
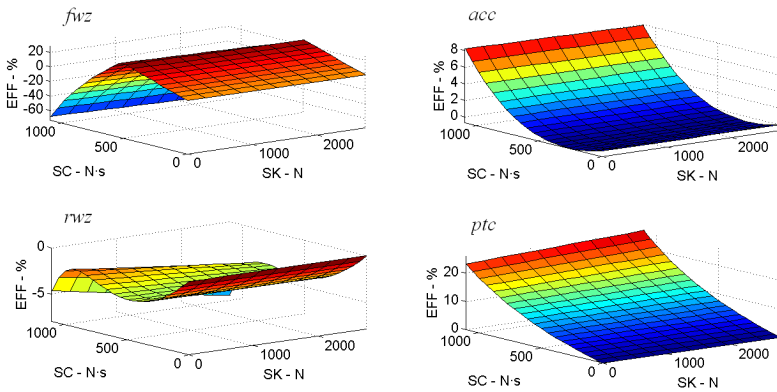
Fig. 2 Mapping of the efficiency on the comfort and precision variables for the different values of *SK* and *SC* for a 10mm step input at 50m/s

In the light of these results we can set the stiffness coefficient as zero. This will allow us to simplify the present study and, as well, a possible design of a future interconnection mechanism. Under this consideration and in order to get a clearer view of the interconnected suspension performance, we can map the efficiencies varying the damping coefficient and the forward speed for *SK*=0N. In Fig.3 it is shown the mapping for all the four variables. It can be seen how the efficiency on pitch is improved for all the speed range by increasing the damping. For speeds under 15m/s there exist a limit on *SC*=700N·s from where the efficiency starts to decrease. For the rider's acceleration higher values of damping results in negative values of efficiency for speeds less than 10m/s. Between 10m/s and 30m/s the damping improve the efficiency and above this speed the maximum rider's accelerations tends to stay more or less unaffected by the interconnection damping.
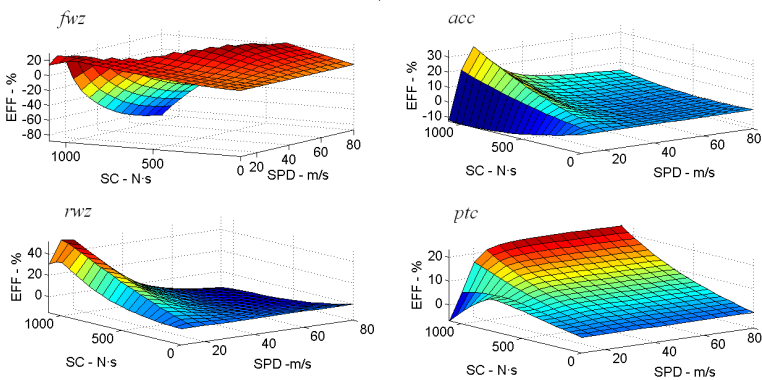
Fig. 3 Mapping of the efficiency on the comfort and precision variables for the different values of *SC* and the forward speed for a 10mm step input

Fig.3 also shows that the increase of damping will improve the response of the front wheel in all the range of speeds until a certain limit that vary for each speed. After this limit the efficiency decays drastically. However, for the rear wheel, the efficiency is increased with the damping only until 40m/s. After this speed, the efficiency becomes negative for all the values of damping. This can be a handicap for the design of the interconnection system and will impose a compromise solution.

In order to find the best value for the damping coefficient we performed a multi-target optimization process taking advantage of the Matlab's optimization toolbox. Considering the behaviour of all the precision and comfort efficiencies we defined a target function to be maximized for the different forward speeds:

$$target = c_f \cdot E_f + c_r \cdot E_r \qquad (10)$$

E_f and E_r are the efficiencies on the front and rear wheels displacement respectively whilst c_f and c_r are their weighs.

With this target function we are looking for the best precision in front and rear wheels while keeping an acceptable level of comfort. The front wheel behaviour has main relevance on the handling and the stability of the motorcycle. If we are able to get a significant improvement on the front wheel behaviour, a small reduction in the rear wheel precision would be acceptable. Following this approach we found that c_f=0.76 and c_r=0.24 will allow us to find a solution for which the maximum reduction of efficiency on the rear wheel is less than 10% whilst the front wheel improves its precision up to 27%.
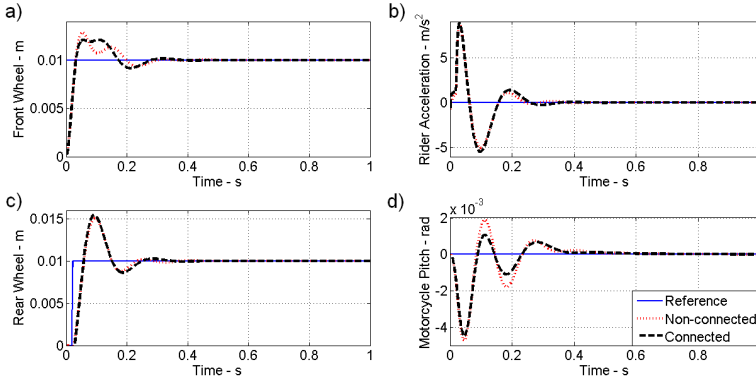
Fig. 4 Front wheel (a), rear wheel (c), rider's acceleration (b) and motorcycle pitch (d) response to a step input of 10mm at 70 m/s for the optimal interconnection damping coefficient at this speed SC =416.6 N·s

We found the maximum of Eq. (10) for speeds going from 10m/s to 80m/s obtaining 15 different values of *SC*. Then we found the efficiency on the precision and comfort variables for each of these values along all the speed range. Fig.4 shows the response to a step input of 10mm at 70m/s for the optimal interconnection damping coefficient *SC*=416.6N·s, which was found for the maximization of

Eq.(10) at 70m/s. We consider this as one of the most suitable values for a constant interconnection damping coefficient, since it keeps the reduction on the rear wheel precision less than 10% and allows a good efficiency on the front wheel for a wide range of speeds between 35 and 80 m/s. The comfort is improved in general with the exception of the acceleration at very low speeds. This results can be observed in Fig.5-a.

A different approach consists in using a speed variable damper. Nowadays several sport motorbikes include this technology for their steering dampers. Fig.5-b shows the efficiencies for a system applying the optimal damping coefficient at each speed. In comparison with Fig.5-a, it presents an important increase in the efficiencies on the front and the rear wheels at low-medium speeds while the comfort is reduced in this range. Considering that at low speeds the energy transmitted from the wheels to the rider is much lower, this reduction in comfort can be acceptable. The efficiency on front wheel at high speeds is also improved whilst on rear wheel remains practically unaffected.
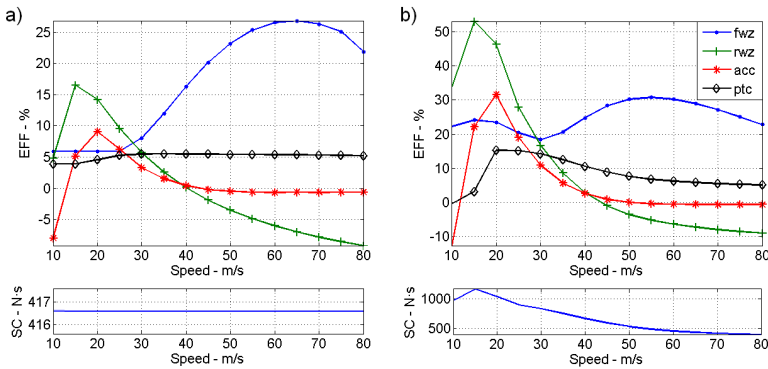
Fig. 5 a) Efficiencies for constant SC= 416.6 N·s. b) Efficiencies for speed optimal values of SC.

5   Conclusions and Further Work

This work presents the potential benefits in terms of comfort and precision that an interconnected suspension system could introduce in a sport motorbike if adequately implemented. For the motorbike model under study we have concluded that satisfactory results are achieved by the connection of the front and rear suspension only by means of a simple damper unit. When the coefficient of this damper is constant, a good level of performance is achieved. However, a speed varying damper will allow better performances, mostly for low and medium speeds.

The results shown in here are related to a linear model in which only small perturbation can be considered. Once the interconnection has been proved to be effective in the linear model, the next step will be to reproduce similar results for

the nonlinear model of the same motorcycle. If these results are satisfactory, then a complete stability analysis, similar to that in [8], will be carried out to ensure that this kind of systems do not compromise the safety of the motorcycle.

The final goal is to design a real interconnection mechanism for the motorcycle under study.

References

1. De Vries, E.J.H., Pacejka, H.B.: Motorcycle tyre measurements and models. Veh. Syst. Dyn. 29, 280–298 (1998)
2. Evangelou, S., Limebeer, D.J.N.: Mechanical Steering Compensators for High-Performance Motorcycles. J. Appl. Mech. 74, 15 (2007)
3. Evangelou, S., Limebeer, D.J.N., Sharp, R.S., Smith, M.C.: Control of motorcycle steering instabilities. IEEE Control Systems 26(5), 78–88 (2006)
4. Evangelou, S., Limebeer, D.J.N., Tomas Rodriguez, M.: Influence of Road Camber on Motorcycle Stability. Journal of Applied Mechanics 75(6) (2008)
5. Limebeer, D.J.N., Sharp, R.S.: Bicycles, motorcycles, and models. IEEE Control Systems 26(5), 34–61 (2006)
6. Newton, K., Steeds, W., Garret, T.K.: The motor vehicle, 12th edn. Butterworth-Heinemann (1997)
7. Pacejka, H.B.: Tire and Vehicle Dynamics, 2nd revised edn. SAE International (2005)
8. Ramirez, C.M., Tomas-Rodriguez, M., Evangelou, S.A.: Dynamical analysis of a duo-lever suspension system. In: 2012 UKACC International Conference on Control (CONTROL), pp. 1106–1111 (2012)
9. Sharp, R.S., Evangelou, S., Limebeer, D.J.N.: Advances in the Modelling of Motorcycle Dynamics. Multibody System Dynamics 12(3), 251–283 (2004)
10. Creuat Suspension Technology (April 2013), `http://www.creuat.com`
11. RaerDesign (April 2013), `http://www.raerdesign.com`
12. The TopTrail Interconnected Suspension Bicycle Project (April 2013), `http://www.toptrail.co.uk`

Simulation Tool for Motorbike Prototype Design

P. García-Fernández[1], J. Gutierrez de Quevedo[1], C. Moreno-Ramírez [2], and A. Fernández del Rincón[1]

[1] Universidad de Cantabria, Spain
 {garciafp,fernandra}@unican.es,
 jesus.gutierrez-de-quevedo@alumnos.unican.es
[2] City University London, U.K.
 ciromoreno@city.ac.uk

Abstract. This paper shows the development of a motorcycle simulation tool built at the University of Cantabria (UC) whose main aim is to support design tasks for future teams that will take part in the interuniversity competition MotoStudent. The tool has been implemented in a commercial multi-body software (MBS) in order to extend the model in a near future. Besides, the tool makes use of customized menu and user interfaces to have easy and quick use by non-especially trained engineers in MBS. The tool has been evaluated by comparison with a widely proved model and used to improve the UC 2010 prototype planar dynamics.

Keywords: Multibody system, motorbike, simulation model, machine dynamics.

1 Introduction

This work is motivated by Motostudent competition. This is a challenge among university teams around the world about the design and develop of a racing motorcycle prototype on a given technical and economic constraints. In the first edition of this competition the University of Cantabria presented a team lead by the Mechanical Engineer Group.

In the design process the students made use of several CAD tools. One of these tools was software for multibody dynamic simulation (MBS). But it could not take advantage of all the power of this tool because developing of advanced models and virtual test implied more time than available.

According to this difficulty it was decided to build a general motorbike model in MSC ADAMS® that would be extended along future. The main aim of this model is to be used by the Motostudent teams of the UC as optimization tool of their prototype. Moreover, the model development can be by itself a didactic resource and, maybe in the future, a research line.

Bearing this aim in mind, the requirements established for this model were: fully parametric, substructure format for suspension types, pre-defined manoeuvres, scalable. This is fulfilled by using this general commercial software. Model variables can be parameterized and manage from a single table. Furthermore, the creation of user interface to introduce data and to manage postprocess graphics in a simple and quick way is also possible. Parts of the model can be treated as submodel and combined with the model as one unit. These characteristics made the model suitable to use by the competition team as an efficient tool to quickly build the virtual prototype and perform usual tests in order to set up the prototype without to be expertise in multibody simulation software. Additionally, the use of general software makes the opportunity of improving model capabilities depending on the required necessities in a future.

2 Model Outline

The motorbike is modelled with nine rigid bodies including the ground. The chassis, motor and pilot are considered as one single body although their mass properties are specified independently. The front suspension is a telescopic fork type. The rear suspension is modelled as a swing-arm type with direct connection to shock absorber. Consequently the model has 11 degrees of freedom (DOF) which are shown in Fig. 1.

The variables are fully parameterized. The Fig. 2a and 2b summarizes the geometrical parameters considered in the model definition. Also the mass properties of bodies are parameterized with respect to centres of mass (CoM).
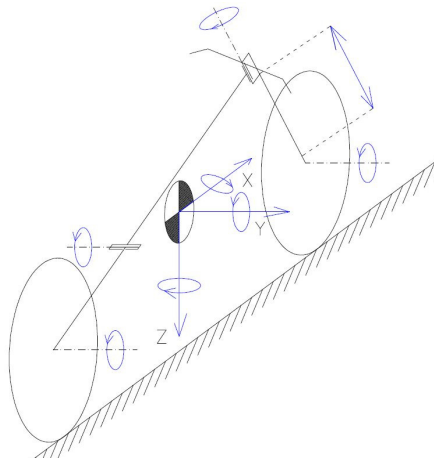
Fig. 1 Model DOF

The motorcycle model uses a Magic Formula tire model specific for motorbikes which is applicable up to 60 degrees of camber angle and rather smooth roads up to frequencies of 8 Hz [5].
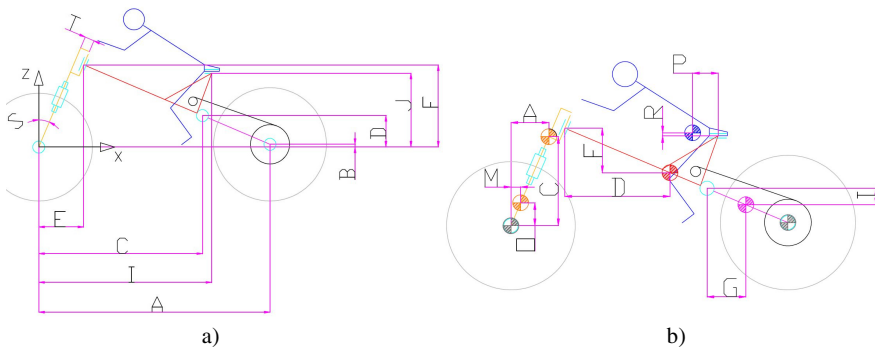
Fig. 2 a) Model geometry parameters, b) Position of bodies CoM

The equivalent motor torque is applied directly in the rear wheel and the reaction torque over the chassis. The chain force is applied both at centre of rear wheel and in the centre of motor pinion. Its direction always matches with the tight side of roller chain.

The brake system is modelled as a disk type both in front and rear wheels. The braking torque is applied upon the wheel and the reaction torque upon the fork of the swing-arm.

3   Interface and Pre-defined Manoeuvres

In order to reduce the time to carry out the virtual tests to a particular motorbike model, both configuration and handling manoeuvres parameters have been established through one specific menu and some user interfaces. The interfaces collect the necessary data to define the manoeuvre and active the more significant outputs measurements for post-process task.

The menu is arranged following a typical sequence test [1]. The first command loads the general parametric model. The second one allows selecting either 2D or 3D model. In the first case, the movement is bounded to a plane blocking the steering joint and setting a planar constraint. The viewpoint is set normal to motion plane and the required number of mass body data will be decreased. The three next menu commands set the stiffness and damping curves of suspensions, the geometrical parameters and the mass properties of bodies respectively. The next command is related to the definition of test manoeuvres. Up to now three tests have been defined. All of them are related with in-plane motorcycle dynamics: acceleration, braking and comfort in riding over rather smooth road.

3.1   Acceleration and Braking Tests

The default road is the flat type, but through the button "road" you can choose the other road definition file. In the same way is possible to choose the type (PAC_MC default) [5] and parameters of each tire. Finally, the curve torque-time needs to be defined. The rest of buttons allow activating the measurements of standard output variables in this type of test.

   Two braking types can be selected. In the first one the user specifies the preferred deceleration from an initial speed and the share braking force between wheels. In the other case, the user can set individually constant braking force in each wheel.

3.2   Comfort Test

This test analyses mainly the accelerations suffered by the pilot and the suspension behaviour in a running straight ahead manoeuvre over a relatively uneven road. Besides the road and tire model files selection, a constant speed must be set. Fig. 3 shows the braking and comfort test interfaces.
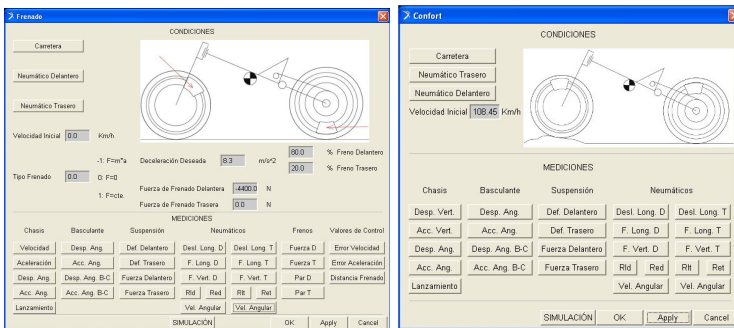
Fig. 3 Braking and comfort test interfaces

4   Model Assessment

An existing model developed in VehicleSim® environment, which has been widely used in the pass for several authors [2, 4], is used to assess the results provided by the model developed in this work.

   The motorcycle data belongs to a Suzuki GSX-R 1000 K4 and have been obtained by reverse engineering at the Imperial College of London. More details about the VehicleSim® (VS) model can be found in [4]. In both models tire forces calculation are based in the *Pacekjka Magic Formula* [3]. Slight differences

between Pacekjka's formulas have been worked out by appropriate parameter value setting. The comparative test is based in the three planar manoeuvres previously presented.

Acceleration test reaches a constant value of 6 m/s^2 starting at rest. In order to reproduce the same test conditions in both models the motor torque is applied in VS model through a PID controller. The equivalent time-torque curve is then applied in the ADAMS$^®$ model. Fig. 4a shows the time-torque curve and Fig. 4b shows the result acceleration in both models. In red the ADAMS$^®$ model an in blue the VS model.

a)   b)
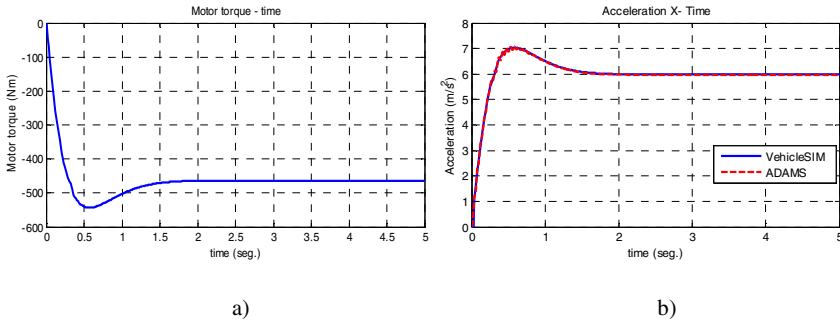
Fig. 4 a) Torque curve; b) Chassis CoM longitudinal acceleration

Steady state results agree in both models. ADAMS$^®$ model transitory response presents little oscillations around the curve obtained by the VS model. It can be proved that the normal forces match whereas the longitudinal friction force does not. This is because tire models consider different relaxation strategy to deal with the transitory states.

The braking test begins from 30 m/s speed and a braking torque is applied to the front wheel according the curve shown in Fig. 5a to get 8 m/s^2 deceleration. The chassis pitch and normal forces in tires are quite similar as can be seen in Fig. 5b and 5c respectively.

In the last comparison test, a harmonic surface road is defined. It has 0.1 meter amplitude and a 4 m wavelength. The motorbike speed is 20 m/s, therefore the tire model works below its 8 Hz limit. Neither join friction nor aerodynamic resistance is considered in this test.

Chassis pitch results are similar in both models. The main differences appear in longitudinal tire forces, Fig. 6a as consequence of distinct relaxation formulas between the tire models. Regarding normal forces, it can be seen in Fig. 6b that are practically equals.

The tests show that the results obtained by ADAMS$^®$ model are similar in accuracy than those of VS model.

a)

b)   c)
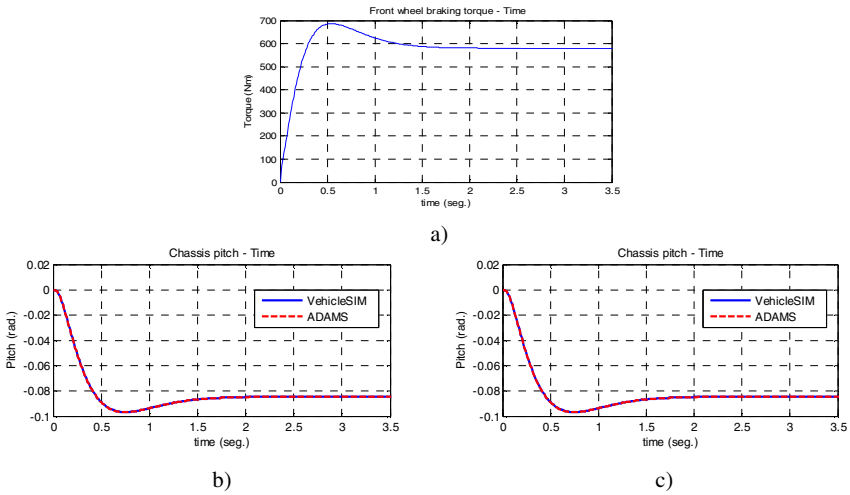
Fig. 5 a) Curve braking torque; b) Chassis pitch; c) Tires normal forces in braking valida-
tion test
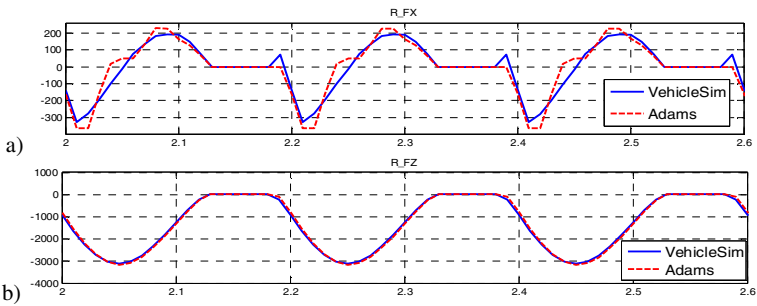
Fig. 6 a) Rear tire longitudinal forces; b) Rear tire normal forces in comfort validation test

5   Application Example

The developed simulation tool is used to study the planar dynamics of the racing
motorbike prototype that took part in the 2010 edition of interuniversity challenge
MotoStudent. This is done to obtain both forces in chassis and rear swing arm and
to set guidelines for a design improvement.

The mass properties of bodies were obtained from the CAD model. The spring
and dampers curves were provided by the respective manufacturers. The model
has been tested in the three defined manoeuvres. The acceleration test considers a
increasing motor torque up to 400 Nm. The braking test establishes 1g decelera-
tion and the comfort test considers a harmonic surface of 0.1m amplitude, 4 m
wavelength and a motorbike constant speed 74 Km/h. Figs. 7-8 shows respectively
acceleration, braking and comfort results both in chassis pitch and tire normal
forces.

a) Acceleration test   b) Braking test   c) Comfort test
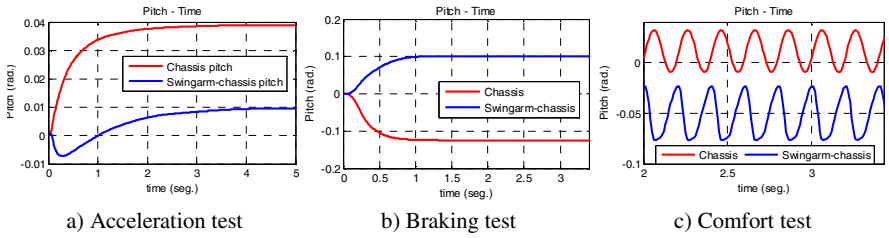
Fig. 7 Chassis pitch and relative swingarm-chassis angle in motorbike prototype tests

a) Acceleration test   b) Braking test   c) Comfort test
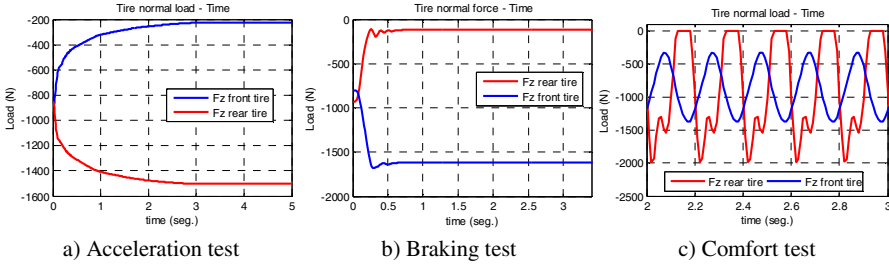
Fig. 8 Tires normal forces in motorbike prototype tests
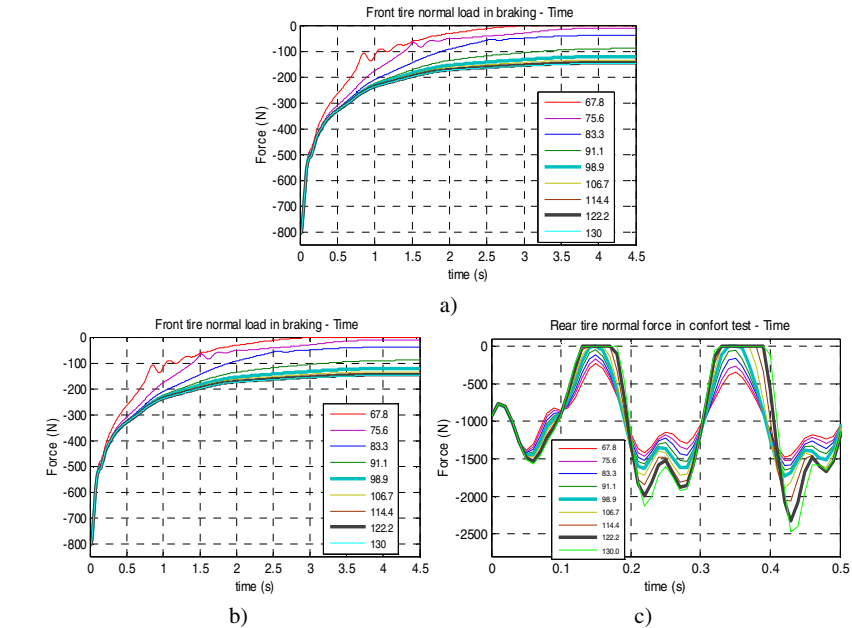
Fig. 9 a) Rear tire force in accel., b) Front tire load in braking, c) Rear tire force in comfort test

Acceleration and braking tests show a high load transfer. It could be recommended lower CoM, however the longitudinal pilot position is correct because current weight share is 50/50. The comfort test shows lack of contact in rear wheel. It is proposed a simple optimization of tire rear force taking as variable the rear shock connecting point position with swingarm. Fig. 9 shows the rear tire normal force in the three tests.

According this study the recommended shock connection point position is 98.9 mm from the pivot swingarm in the direction connecting this point with the centre rear wheel (the original value was 122.2 mm). This is trade off to get a better behaviour in uneven road without being detrimental to the braking and acceleration ones.

6   Conclusions

A friendly simulation tool has been developed mainly as support for future UC teams that may take part in MotoStudent competition. Currently, the tool has only implemented planar dynamic manoeuvres but in the near future it will be complemented with standard cornering manoeuvres.

Tool assessment has been based in comparative tests with a proved model developed in VehicleSim® used by others researches. The steady state results differ less than 1%. In the transitory states the differences between both models are slightly greater. These differences are mainly because of the distinct relaxation models that are used in the tire model. Therefore, the results obtained from the ADAMS® model can be considered of similar accuracy than those obtained from the VS model.

The tool utility has been proved through an improvement study over the race motorbike prototype presented in the 2010 edition of aforementioned interuniversity competition.

References

1. Berritta, R., Biral, F., Garbin, S.: Evaluation of motorcycle handling with multibody modelling and simulation. In: 6th International Conference on High Tech Engines and Cars, May 25-26 (2000)
2. Evangelou, S., Limebeer, D.J.N., Tomas Rodriguez, M.: Influence of Road Camber on Motorcycle Stability. Journal of Applied Mechanics 75(6) (2008)
3. Pacejka, H.B.: Tire and vehicle dynamics. BH (2006)
4. Sharp, R.S., Evangelou, S., Limebeer, D.J.N.: Advances in the Modelling of Motorcycle Dynamics. Multibody System Dynamics 12(3), 251–283 (2004)
5. TNO Automotive. Tyre models user manual; Using the MF-MCTyre model (May 2002)

Modelling and Control of a Semi-active Suspension System

A. Colina[1], G. Lerma[1], I. Cabanes[1], and I. Iglesias[2]

[1] Department of Automatic Control and System Engineering,
  University of the Basque Country, Spain
  `itziar.cabanes@ehu.es`
[2] Industry and Transport Division, Vehicle Dynamics Group,
  Tecnalia Research & Innovation, Spain
  `inaki.iglesias@tecnalia.com`

Abstract. The suspension system is composed of several deformable elements such as springs and dampers, which connect the car body to wheels and absorb vibrations generated by road irregularities. The main purpose of suspension system is to isolate the vehicle body from disturbances in order to keep wheels in contact with the road surface to contribute to road holding, and in order to maximize passenger ride comfort. This paper describes a semi-active suspension system of 2 degrees of freedom (2DOF), typically referred to as a quarter car model. To design a suspension control system that improve ride comfort, dynamic modelling of semi-active suspension was developed. Control strategies were implemented for these semi-active suspension systems using MATLAB® and Simulink® software. The results show that the semi-active suspension system controlled by a logical strategy minimizes vertical acceleration experienced by passengers, compared to passive suspension system.

Keywords: semi-active suspension, quarter car model, ride comfort, classical control.

1   Introduction

In recent years, researches in the field of automotive vehicles are focused on improving driving safety and passenger comfort. These two parameters are mainly influenced by the design of the suspension system. The suspension system works between vehicle chassis and wheels, and its main goal is to reduce motion of the vehicle body called sprung mass. The design of a good suspension system is focused on the isolation of the disturbances coming from road irregularities, cornering and breaking, in order to maximize passenger ride comfort and keep wheels in contact with the road surface to contribute to road holding.

A good ride comfort requires a soft suspension, however, this suspension system produces excessive roll during cornering and pitch during breaking, and

therefore can be uncomfortable for passengers. While a stiffer suspension improves the phenomena of roll and pitch, ride comfort is reduced. As suspension design is a compromise between these two goals, this problem can be solved with an adaptive suspension system that changes the suspension parameters depending of the features of the terrain or the vehicle driving manoeuvres.

Suspension systems are classified by the control system in passive, semi-active and active. Passive suspension systems consist of conventional springs and dampers, whose properties are fixed, and there is no external energy source in the system. Semi-active suspension systems, generally, consist of controllable dampers and passive springs without requiring large power sources, so the control system is not destabilized [1]. Different types of semi-active dampers have been investigated, the most representative are: magnetorheological dampers, whose response varies with the magnetic field applied [1], electrorheological dampers, whose response varies with the electric field applied [11], pneumatics dampers, generally used in buses and lorries [3], and dry friction dampers, highly non-linear and based on the friction between surfaces in contact [8]. Finally, active suspension systems have the capabilities to adjust themselves continuously to changing road conditions, so that mechanical elements (springs and dampers) are replaced by actuators that can generate forces according to a control algorithm [7, 10, 16, 18]. Moreover, semi-active and active suspensions can reduce the resonance peak and the amplitude of movement of the sprung mass in most of the frequency range [19].

To study the behaviour of suspension systems, different vehicle models have been used. The most used model is the quarter car model [1, 16], because it takes into account the most important features of suspension system preserving the simplicity of the model. It is a model of two degrees of freedom (2DOF) which considers the vertical dynamics of a single wheel. The half vehicle model is four degrees of freedom model (4DOF) which generally represents the pitch motion [4]. And the full vehicle model is a model of seven degrees of freedom (7DOF) that consists of a sprung mass that is connected to four unsprung masses, and represents the pitch, roll and yaw movements of the vehicle body [7, 10, 18].

Regarding the control, it is a multi-objective and non-linear problem for which classical and modern methodologies, based on a mathematical model of the system, have been developed [9, 15].

Due to its simplicity, classical control strategies for semi-active suspension have been implemented: PID [16] and Logical Control Strategies [15]. These last Control Strategies are oriented to improve in a simple way the comfort, so its goal is to minimize the vertical acceleration of the sprung mass. The most common logical control strategies oriented to comfort are the 2-States Skyhook Control, Skyhook Linear Control, Acceleration Driven Damper Control (ADD), Power Driven Damper Control (PDD), Skyhook-Add Control and Skyhook-PDD Control.

Modern control strategies for semi-active suspension are more difficult to implement with higher computational cost: Adaptive Control [17], Optimal Control [6], Predictive Control [5] and Robust Control [7]. Adaptive Control automatically adjusts its characteristics to operate optimally in a changing environment, reducing disturbances and vibration of the vehicle at specified levels. The use of

Optimal Control is recommended when the system behaviour has uncertainties. Predictive Control is used in complex, multivariable or unstable dynamic system; it is based on the use of an optimized model for predicting system behaviour and future control signal. The Robust Control considers the uncertainties in the mathematical modelling in order to become independent the system of disturbances.

In this paper a quarter car model is used to analyse the ride performance behaviour. The purpose of this paper is to compare the different logical control strategies for semi-active suspension system based on a quarter car model, due to its simplicity, in order to maximize passenger ride comfort. In order to detail this approach, the rest of the paper is structured as follows. In section 2, the suspension system modelling is detailed; section 3 presents the control strategies; in section 4 a discussion of simulation results is presented. Finally, the most important ideas are summarized.

2   Suspension System Modelling

In this paper, a quarter car model with two degrees of freedom (2DOF) is considered (Fig.1), because this model represents most of the features of the full vehicle model while preserving the simplicity of the model.
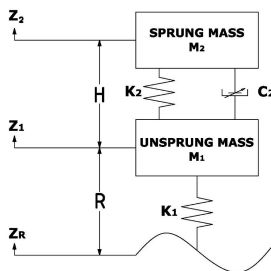
Fig. 1 Quarter car model with semi-active suspension

The vehicle chassis is modelled as a rigid body of mass M_2, and unsprung mass, represented by M_1. The suspension system consists of a spring of stiffness K_2, and a damper with a variable damping C_2. The wheel is modelled as a single spring with a stiffness constant K_1.

This model is described by the following system of second order ordinary differential equations:

$$\ddot{Z}_2 M_2 = -M_2 g - K_2(Z_2 - Z_1 - H) - C_2(\dot{Z}_2 - \dot{Z}_1) \tag{1}$$

$$\ddot{Z}_1 M_1 = -M_1 g - K_1(Z_1 - Z_R - R) - K_2(Z_1 - Z_2 + H) - C_2(\dot{Z}_1 - \dot{Z}_2)$$

Where Z_2 is the sprung mass vertical displacement, Z_1 is the unsprung mass vertical displacement and Z_R is road profile acting as the disturbance. Gravity is represented by g. H and R are two parameters that represent initial conditions.

Furthermore, in order to make sure that the suspension system is working properly, certain functional limit values must be defined, so that it cannot be extended or compressed more than a certain predetermined amount. For this purpose, two bump stop limits have been modelled. Moreover, the system distinguishes the motion of the damper between rebound travel and jounce travel.

3   Control Strategies

The control objective of this paper is oriented to comfort performance. To evaluate passenger comfort, the approach considered to determine the performance of the suspension system is the acceleration of the sprung mass. So the control objective consists in minimizing the vertical acceleration of sprung mass with the most simple control strategies. The different logical control strategies mentioned above are implemented in a quarter car model. Then, analysing the results, the best control strategy will be determined.

The following logical control strategies have in common that change the damping factor of the damper (C_2) according to the chassis velocity ($\dot{Z}_2$), the chassis acceleration ($\ddot{Z}_2$), the suspension deflection position ($Z_{def} = Z_2 - Z_1$) and/or the suspension deflection velocity ($\dot{Z}_{def} = \dot{Z}_2 - \dot{Z}_1$), depending on the algorithm. Moreover, all of them use only two sensors. Control strategies that will be implemented are shown in Table 1.

Table 1 Logical Control Strategies

Controller	Control Law	Other Authors
SH2-States	$C_2 = \begin{cases} C_{min} & if \ \dot{Z}_2 \dot{Z}_{def} \leq 0 \\ C_{max} & if \ \dot{Z}_2 \dot{Z}_{def} > 0 \end{cases}$	[2]
SH Linear	$C_2 = \begin{cases} C_{min} & if \ \dot{Z}_2 \dot{Z}_{def} \leq 0 \\ sat_{C_2 \in [C_{min}; C_{max}]} \left(\dfrac{\alpha C_{max} \ddot{Z}_{def} + (1-\alpha) C_{max} \ddot{Z}_2}{\dot{Z}_{def}} \right) & if \ \dot{Z}_2 \dot{Z}_{def} > 0 \end{cases}$	[13]
ADD	$C_2 = \begin{cases} C_{min} & if \ \ddot{Z}_2 \dot{Z}_{def} \leq 0 \\ C_{max} & if \ \ddot{Z}_2 \dot{Z}_{def} > 0 \end{cases}$	[14]
PDD	$C_2 = \begin{cases} C_{min} & if \ k Z_{def} \dot{Z}_{def} + C_{min} \dot{Z}_{def} \geq 0 \\ C_{max} & if \ k Z_{def} \dot{Z}_{def} + C_{max} \dot{Z}_{def} < 0 \\ \dfrac{C_{min} + C_{max}}{2} & if \ Z_{def} \neq 0 \ and \ \dot{Z}_{def} = 0 \\ -\dfrac{k Z_{def}}{\dot{Z}_{def}} & otherwise \end{cases}$	[12]

Table 1 (*continued*)

SH-ADD	$\begin{cases} if \;\; f > f_c \;\;\; then \;\;\; ADD \\ \;\; if \;\; f < f_c \;\;\; then \;\;\; SH \end{cases}$
SH-PDD	$\begin{cases} if \;\; f > f_c \;\;\; then \;\;\; PDD \\ \;\; if \;\; f < f_c \;\;\; then \;\;\; SH \end{cases}$

Where f_c is the cut-off frequency. In this paper, it is considered that f_c has a value of 3 Hz.

4   Simulation and Results

In order to simulate the control strategies mentioned above, the general Sine Sweep test (ISO7401) is considered. This input represents variations of the road irregularities amplitude at high and low frequencies, from 0.1 to 12 Hz, allowing to analyse how the controller responds to both effects. Moreover, this test covers different types of roads with different frequency disturbances from typical low frequency speed bumps, to high frequency Belgian blocks pavement.

Table 2 shows the parameters used for simulation tests, which are based on a Fiat Punto.

Table 2 Parameter Values for Simulation tests

Parameters	*Value*	*Parameters*	*Value*
Sprung mass (M_2)	284.325 kg	Suspension Stiffness (K_2)	58,860 N/m
Unsprung mass (M_1)	41.8125 kg	Extended Damping (C_2)	8,181.8 Ns/m
Tire Stiffness (K_1)	210,000 N/m	Compression Damping (C_2)	4,090.88 Ns/m
Tire Radius (R)	0.33 m	Jounce Travel	0.06 m
		Rebound Travel	0.075 m

Fig. 2 shows road profile and the simulations results of the vertical acceleration of sprung mass for passive suspension system and for each Control strategies: SH 2-States, SH Linear, ADD, PDD, Mixed SH-ADD and Mixed SH-PDD, respectively.

Fig. 3 shows a comparison between the above strategies (Table 1).

The problem of the on/off control algorithms is the chattering phenomenon, which consist in a very fast change of the controlled variable in the nearest of the change position. In the simulations, this phenomenon appeared in the SH, ADD and SH-PDD strategies. In the ADD this problem is more relevant because the oscillations are bigger and faster, but in the SH-PDD is an allowable phenomenon because it only appeared in a small range of frequencies, more specifically at low frequencies.
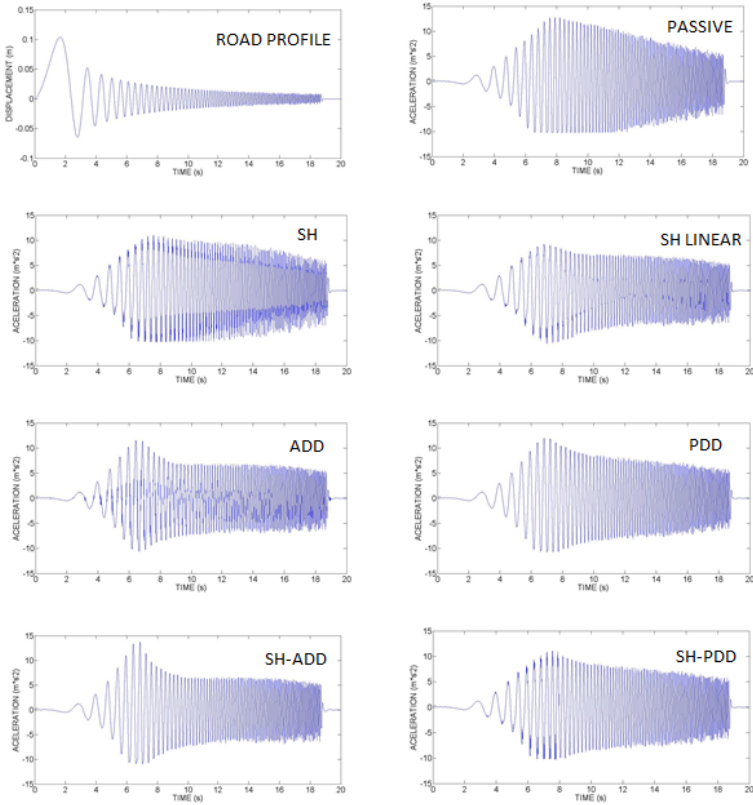
Fig. 2 Road profile and vertical acceleration of sprung mass for each control strategy
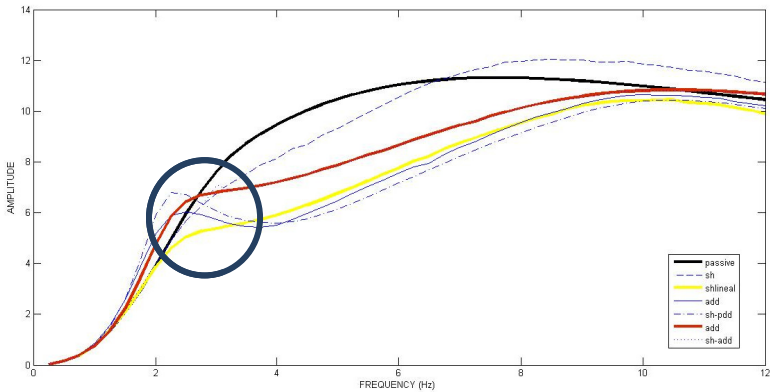
Fig. 3 Comparison between all strategies

On the other hand, in Fig.3 it can be emphasized that at 3 Hz frequency the SH algorithm is intersected by the ADD algorithm, so that is the reason why 3Hz is the cut off frequency (f_c) in the mixed algorithm, SH-ADD. As a result, the best control strategy in order to improve ride comfort is the Skyhook Linear Control. However, this control has the disadvantage that it is difficult to control a linear damper because it is necessary to have a continuous damper. Another control strategy that provides a good result is the Mixed SH-PDD strategy, where a frequency selector has been developed to avoid the problems of chattering from the Savaresi's frequency selector. The problem is that this control needs also a linear damper and it does not improve the Skyhook Linear Control results. In order to implement an on/off control algorithm that can be implemented with discontinues damper, the Mixed SH-ADD Control has been adjusted to avoid the chattering problem that this model showed introducing a relay in the logical algorithm conditions. The relay deteriorates the attenuation but avoid the high frequency accelerations.

5   Conclusions

Different logical control strategies have been implemented in order to improve ride comfort with a semi-active suspension system. The results indicate that semi-active suspension with Mixed Skyhook-ADD Control is the best on/off suspension control. It is a simple control that avoids the problem of chattering by the use of relays. This control uses the good behaviour of Skyhook Control at low frequencies, and good dynamic response of the algorithm ADD at mid and high frequencies, where shows a better response that a continues algorithm like Skyhook Linear Control. If the damper is continuous, the best suspension control is the Skyhook Linear Control, although at high frequencies it is exceeded by the ADD strategy.

Future work will be performed to improve passenger ride comfort by implementing an active suspension control system. This improvement will be accomplished through the utilization of force actuators.

References

1. Aguilera, L.A., Padilla, O.I., González-Palacios, M.A., González-Galván, E.J.: Simulación de una suspensión semi-activa us,o amortiguador magnetoreológico. In: Memorias del XIII Congreso Intern. de la SOMIM y Congreso Intern. de Metal Mecánica, México (2007)
2. Ahmadian, M., Song, X., Southward, S.: No-jerk skyhook control methods for semiactive suspensions. Transactions of the ASME 126, 580–584 (2004)

3. Biral, F., Grott, M., Oboe, R., Makei, C., Vincenti, E.: Modelling, control and design of heavy duty suspension systems. In: 10th IEEE International Workshop on Advanced Motion Control, pp. 771–776 (2008)
4. Can, W., Weirui, W.: Chaotic Behaviors of Half Car Model Excited by the Road Surface Profile. In: 2009 1st International Conference on Information Science and Engineering (ICISE), Nanjing, China, December 18-20, pp. 3752–3755 (2009)
5. Canale, M., Milanese, M., Ahmad, Z., Matta, E.: An improved semiactive suspension control strategy using predictive techniques. In: International Conference on Information and Communication Technologies: From Theory to Applications (2004)
6. Chen, J., Guo, W., Feng, W., Chen, H., Dong, F.: Research of semi-active suspension self adjust sky/ground-hook hybrid control simulation. In: International Conference Suspension Self- on Electric Information and Control Engineering (2011)
7. Creed, B., Kahawatte, N., Varnhagen, S.: Design of an LQR Control Strategy for Implementation on a Vehicular Active Suspension System. In: MAE 272, vol. II (2010)
8. Guglielmino, E., Edge, K.: A controlled friction damper for vehicle applications. Control Engineering Practice 12(4), 431–443 (2004)
9. Hurel, J., Mandow, A., García, A.: Los Sistemas de Suspensión Activa y Semiactiva, Una Revista Iberoamericana de Automática e Informática Industrial, pp. 121–132 (2013)
10. Ikenaga, S., Lewis, F.L., Campos, J., Davis, L.: Active Suspension Control of Ground Vehicle based on a Full-Vehicle Model. In: Proceedings of American Control Conference, vol. 6, pp. 4019–4024 (2000)
11. Lou, Z., Ervin, R., Filisko, F.: A preliminary parametric study of electrorheological dampers. Transaction. ASME Journal Fluids Engineering 116(3), 570–576 (1994)
12. Morselli, R., Zanasi, R.: Control of a port hamiltonian systems by dissipative devices and its application to improve the semi-active suspension behavior. Mechatronics 18(7), 364–369 (2008)
13. Sammier, D., Sename, O., Dugard, L.: Skyhook and H^∞ control of active vehicle suspensions: some practical aspects. Vehicle Systems Dynamics 39(4), 279–308 (2003)
14. Savaresi, S., Siciliani, E., Bittanti, S.: Acceleration driven damper (ADD): an optimal control algorithm for comfort oriented semi-active suspensions. ASME Transactions: Journal of Dynamic Systems Measurements and Control 127(2), 218–229 (2005b)
15. Savaresi, S.M., Poussot-Vassal, C., Spelta, C., Sename, O., Dugard, L.: Semi-Active Suspension Control Design for Vehicles. Elsevier (2010)
16. Senthil-kumar, M.: Development of Active Suspension System for Automobiles using PID Controller. In: Proceedings of the World Congress on Engineering 2008, WCE 2008, London, U.K., July 2-4, vol. II (2008)
17. Venugopal, R., Beine, M., Ruekgauer, A.: Real-time simulation of adaptive suspension control using dSPACE control development tools. International Journal of Vehicle Design 29(1-2), 128–138 (2002)
18. Wang, J., Wilson, D., Xu, W., Crolla, D.: Active Suspension Control to Improve Vehicle Ride and Steady-State Handling. In: 44th IEEE Conference on Decision and Control and the European Control Conference, Seville, Spain, December 12-15 (2005)
19. Yagiz, N., Yuksek, I.: Sliding mode control of active suspensions for a full vehicle model. International Journal of Vehicle Design 26(2), 264–276 (2001)

Topological Synthesis of a Novel Parallel Mechanism for Vehicle Rear Suspensions

F. Malvezzi[1] and T.A.H. Coelho[2]

[1] Maua Institute of Technology, Brazil
  `fernando.malvezzi@maua.br`
[2] University of São Paulo, Brazil
  `tarchess@usp.br`

Abstract. This work deals with the topological synthesis of a novel parallel mechanism to be employed in vehicle rear suspensions to improve the overall stability. The approach followed here considers the design of an active rear suspension, with three degrees of freedom, able to adjust the camber, toe and roll angles simultaneously. By applying two distinct methods to perform the topological synthesis, several architecture candidates are generated that satisfy the design specifications. Then, the synthesized candidates are ranked according to some proposed indexes and the most promising topology is selected. In order to evaluate the capability of the parallel mechanism to improve the vehicle dynamic behaviour, numerical simulations are conducted to compare it with a similar vehicle equipped with a conventional suspension system. The obtained results have shown that, in double lane change maneuvers, the novel parallel mechanism is able to reduce not only the yaw rate but also the roll angle.

Keywords: Parallel mechanism, Mechanism synthesis, Automotive suspension, Vehicle dynamics.

1   Introduction

The suspension systems are extremely important for comfort, stability and handling of the vehicle. In order to contribute for the stability control of passenger cars, many technologies have been used, such as active camber control [1], active rear steer, active front steer, active anti-roll bar and active wheel drive and active brake [2]. Currently there is a trend towards the integration of two or more technologies for stability control [3, 4]. Despite the fact that parallel mechanisms have been applied in flight simulators, robotic manipulators and machine tools, they are not currently employed in vehicle suspensions.

This work deals with the topological synthesis of a novel parallel mechanism to be employed in vehicle rear suspensions to improve the overall stability. The approach followed here considers the design of an active rear suspension, with three degrees of freedom, able to adjust the camber, toe and roll angles simultaneously.

In section 2, by applying two distinct methods to perform the topological synthesis, several architecture candidates are generated that satisfy the design specifications. Then, in section 3, the synthesized candidates are ranked according to some proposed indexes and the most promising topology is selected. In order to evaluate the capability of the parallel mechanism to improve the vehicle dynamic behaviour (section 4), numerical simulations are conducted to compare it with a similar vehicle equipped with a conventional suspension system.

2   The Generation of Candidate Topologies

In order to be applied in suspension system, this parallel mechanism must have three independent motions to satisfy the design specifications: two motions for setting the camber and toe angles and one passive movement to permit vertical movement of the wheel (wheel travel), which also can be an active movement in order to provide anti-roll control. Two topological synthesis methods are applied: the method of the addition of a passive limb and the alternative method.

The method of addition of a passive limb [5]

The method of addition of a passive limb considers that the platform motion is constrained by a passive limb connected to it. The passive limb must be carefully chosen in such a way that the mobility (M) and type of available motions for the end-effector correspond to the desired ones. Moreover, partial connectivities of remaining m active limbs must be equal to the space dimension where the mechanism is supposed to function (λ).
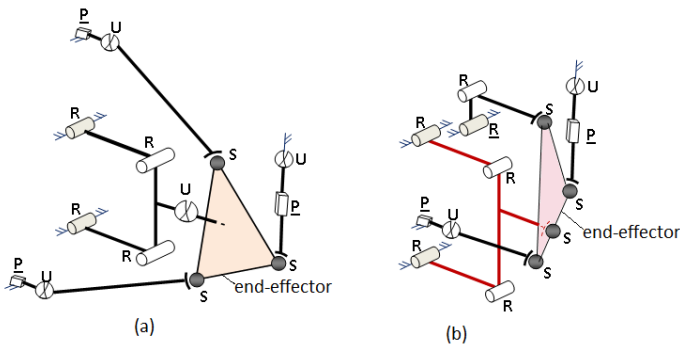
Fig. 1 Mechanisms: (a) 2PUS +UPS+ PaU; (b) RRS + PUS +UPS + PaS

Two different architectures are generated by applying this method. One of them has a PaU passive limb, two PUS active limbs and an active limb UPS, to control the roll angle (see Fig. 1a). When the car does not perform evasive maneuvers or cornering, the prismatic actuator of the limb UPS does not exert force on the sprung mass and the wheel travel is influenced only by the action of the spring and

the damper. The end-effector movements are two rotations and the displacement along the vertical axis. To satisfy the design specifications, it is necessary the actuation of the actuators to maintain the camber and toe angles during the wheel travel, causing energy consumption.

Another possible architecture, generated by the same method, is built with a PaS passive limb, an active limb RRS, for setting the camber angle, an active limb, PUS, for setting the toe angle and another active limb, UPS, to control the roll angle. When the car does not perform evasive maneuvers or cornering, the prismatic actuator of the limb UPS does not exert force on the sprung mass and the wheel travel is influenced only by the action of the spring and the damper. Because the lengths of all bars are the same, it is not necessary the actuation of the actuators to maintain the camber and toe angles during wheel travel. Another advantage of this mechanism is the complete uncoupling with respect to the movements to toe change, camber change and wheel travel.

Alternative Method [6]

To apply the alternative method, first it is generated a mechanism with a passive limb, 2PUS + UPS + PRSSR showed in Fig. 2a.
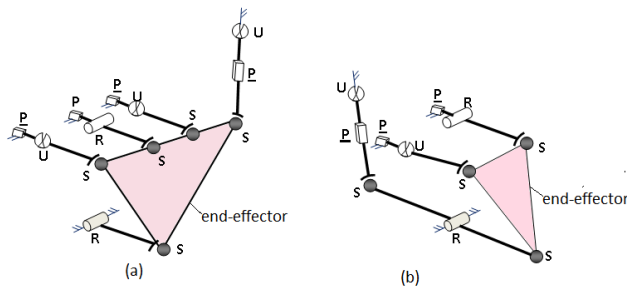
Fig. 2 Mechanisms: (a) 2PUS + UPS + PRSSR; (b) PUS + PRS + UPSRS

Then, one of the active limbs is eliminated and the passive limb becomes an active limb as shown in Fig. 2b. Because the lengths of the all bars are the same, it is not necessary the actuation of the actuators to maintain the camber and toe angles during wheel travel.

3   The Ranking and the Selection of a Topology

After applying methods to perform topological synthesis, the architecture candidates need to be ranked in order to choose the most promising one. To achieve this goal, we propose three merit indexes. The first index evaluates the level of complexity of the considered topology [7]. To compute this index, it is previously necessary to calculate the number of components (links and joints) in the mechanical structure. Then, the candidates receive a grade from 1 to 5. Table 1 shows the structural complexity index (SCI) for each topology.

Table 1 Structural complexity index

Mechanism	Number of components			Structural complexity index
	links	joints	total	SCI
2PUS + UPS + PaU	11	14	25	1
RRS + PUS + UPS +PaS	11	14	25	1
2PUS + UPS + PRSSR	11	14	25	1
PUS + PRS + UPSRS	9	11	20	5

The second index evaluates the presence of joints that might reduce the mechanism workspace. These joints, such as universal and spherical ones, are characterized by reduced stroke angles. After calculating the number of universal and spherical joints in the mechanical structure, candidates also receive a grade from 1 to 5. Table 2 shows the joint stroke index (JSI) for each topology.

Table 2 Joint stroke index

Mechanism	Number of Universal or Spherics joints			Joint stroke index
	U	S	total	JSI
2PUS + UPS + PaU	4	3	7	2,5
RRS + PUS + UPS +PaS	2	4	6	5
2PUS + UPS + PRSSR	3	5	8	1
PUS + PRS + UPSRS	2	4	6	5

The third index, called the uncoupling index (UI), is equal to 5 when the end-effector movements to achieve toe variation, camber variation and wheel travel are totally independent, such as the mechanism RRS + PUS + UPS + PaS. On the other hand, the movements of the mechanism 2PUS + UPS + PaU are totally coupled, so the UI is 1. For the mechanisms 2PUS + UPS + PRSSR and PUS + PRSSR + UPS, the UI is 3 because the movements to toe and camber variation are coupled but these movements are independent of the wheel travel.

Table 3 Mechanism performance comparison

Mechanism	SCI	UI	JSI	Global index
2PUS + UPS + PaU	1	1	2,5	4,5
RRS + PUS + UPS +PaS	1	5	5	11
2PUS + UPS + PRSSR	1	3	1	5
PUS + PRS + UPSRS	5	3	5	13

Table 3 shows the global index, defined by the sum of the three indexes SCI, UI and JSI. Consequently, the first ranked topology is the PUS + PRS + UPSRS that reached a global index of 13. Fig. 3 shows that the action on the body roll angle is achieved by the force exerted by the actuator 1 on the sprung mass (body). On the other hand, when the car does not perform evasive maneuvers or cornering, the actuator 1 does not exert force on the sprung mass and the wheel travel (passive movement) is influenced only by the action of the spring and the damper. In addition, the camber angle is changed by the simultaneous movement of the actuators 2 and 3, while the toe angle is modified by the actuator 3.
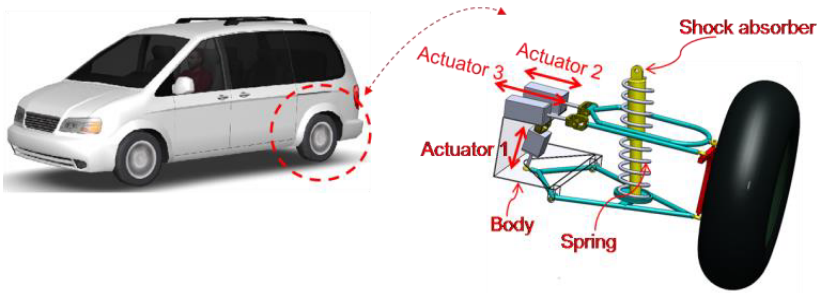
Fig. 3 CAD Model of PUS + PRS + UPSRS

4   Simulations and Results

In order to evaluate the potential of the mechanism to improve vehicle stability, a co-simulation, implemented in *MATLAB/Simulink* and *CarSim* softwares, was performed to compare the dynamic behavior of two vehicles. One vehicle is equipped with a conventional suspension and another vehicle, similar to the first one but equipped with the parallel mechanism, is able to adjust roll, toe and camber angles simultaneously.

In the case of the second vehicle, the mechanism actuation depends on the following vehicle variables: wheel steering angle, vehicle velocity, lateral acceleration, and yaw rate, which are calculated by *CarSim* and exported to *Matlab/Simulink* model. On the other hand, the camber and toe angles and the auxiliary roll moment, applied by the mechanism on the chassis, are determined by the *MATLAB/Simulink* model and exported to *CarSim*.

By changing the camber angle, it is possible to generate an additional lateral force on the rear wheels. In order to achieve this feature, the wheels are tilted by the parallel mechanism to the cornering side in accordance with the lateral acceleration of the vehicle. The setting of the toe angle aims to improve handling, which is obtained by steering the rear wheels as linear functions of the steering wheel angle and the longitudinal speed. The action of the auxiliary roll moment has two goals, namely, to reduce the roll angle of the sprung mass during cornering and contribute to the stability control.

The vehicle parameters correspond to a D-Class Minivan car, with 2037 kg and engine power of 150 kW. Table 4 shows the characteristics of the simulated vehicles.

Table 4 Characteristics of the simulated vehicles

Vehicle	Front suspension	Rear suspension
Original	Independent, with anti-roll bar	Independent, with anti-roll bar
RTC	Independent, with active anti-roll bar	Independent, without anti-roll bar

The double lane change maneuver was chosen to simulate the dynamic behavior of the vehicles. In addition, the car velocity was set in 70 km/h. Fig 4 shows the path of the vehicle equipped with conventional suspension (original) and the modified vehicle with the parallel mechanism (RTC).
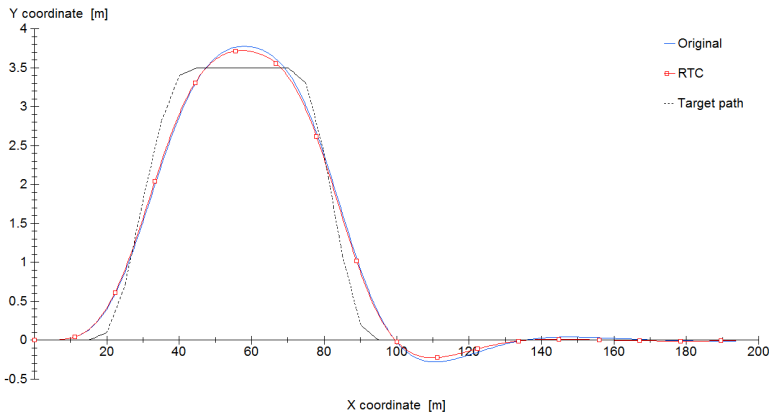
Fig. 4 Path of the vehicles at double lane change maneuver

With respect to the roll angle, the second vehicle (RTC) demonstrated lower oscillation of the sprung mass in a comparison with the first (original), as shown in Fig. 5.
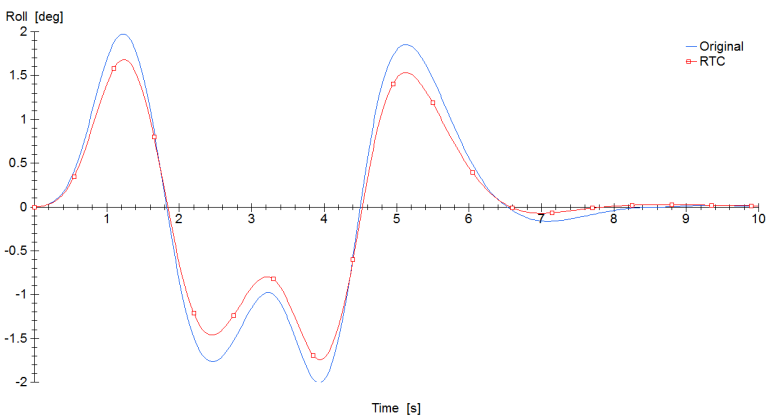
Fig. 5 Roll angle of the vehicle equipped with conventional suspension (original) and of the modified vehicle with the parallel mechanism (RTC), during a double lane change maneuver

According to Fig. 6, the modified vehicle (RTC) reached lower values of the yaw rate than the original vehicle.
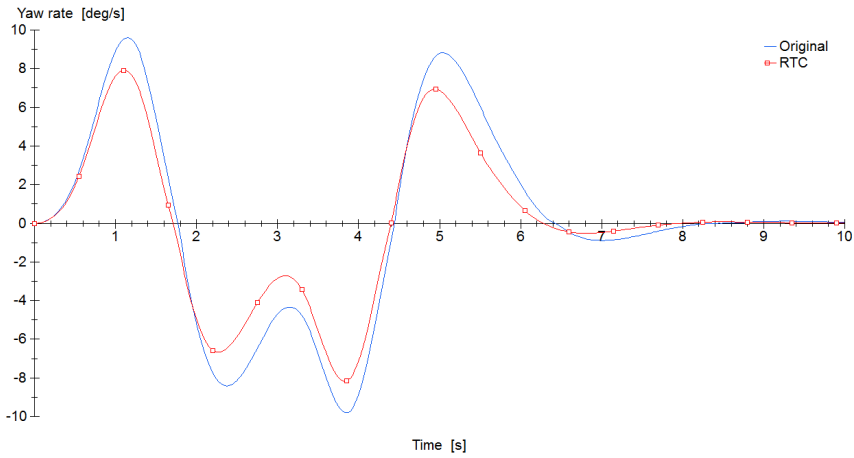
Fig. 6 Yaw rate of the vehicle equipped with conventional suspension (original) and of the modified vehicle with the parallel mechanism (RTC), during a double lane change maneuver

Fig. 7 shows that the values of lateral acceleration are similar for the two vehicles. Table 5 lists the peaks of the roll angle, yaw rate and lateral acceleration of the vehicles during double lane change maneuver.
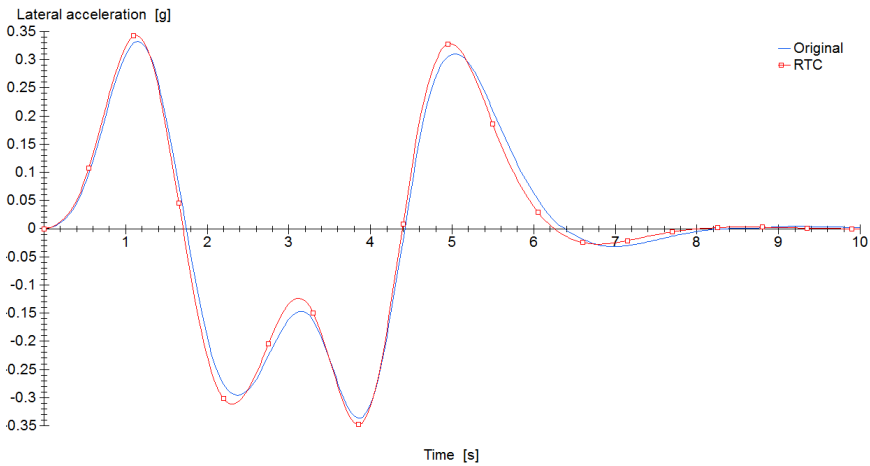
Fig. 7 Lateral acceleration of the vehicle equipped with conventional suspension (original) and of the modified vehicle with the parallel mechanism (RTC), during a double lane change maneuver

The vehicle equipped with the parallel mechanism (RTC) demonstrated advantages over the one with conventional suspension (original), during the chosen maneuver. The lower values of body roll angle transmit to the driver greater security and lower values of yaw rate facilitate the vehicle control.

Table 5 Results at Double lane change maneuver

Vehicle	Roll [deg]		Yaw Rate [deg/s]		ay [g]	
	Max.	Min.	Max.	Min.	Max.	Min.
Original	1.97	-2.00	9.61	-9.79	0.33	-0.34
RTC	1.68	-1.74	7.91	-8.17	0.34	-0.35

5   Conclusions

This work presented the topological synthesis of a novel parallel mechanism to be employed in vehicle rear suspensions to improve the overall stability. Basically, the goal was to determine a 3-dof architecture, able to adjust the camber, toe and roll angles simultaneously. After applying methods to perform topological synthesis, the architecture candidates were ranked in accordance with some proposed indexes. The effect of the most promising topology in a vehicle rear suspension was evaluated through numerical simulations. The obtained results revealed a superior behaviour of the synthesized mechanism in a comparison with a similar vehicle equipped with a conventional suspension system.

References

1. Park, S.J., Sohn, J.H.: Effects of camber angle control of front suspension on vehicle dynamics behaviors. Journal of Mechanical Science and Technology, 307–313 (2012)
2. Shibahata, Y.: Progress and future direction of Chassis control technology. Annual Reviews in Control, 8 (2005)
3. Scalzi, S.: Integrated control of active steering and electronic differentials in four wheel drive and steering vehicle. Ph.D. Dissertation on Sensorial and Learning Systems – Eletronic Engineering Departament, University of Rome tor Vergata, Rome, 142 p. (2009)
4. Rengaraj, C., Crolla, D.: Integrated chassis control to improve vehicle handling dynamics performance. SAE International 2011-01-0958, 11 p. (2011)
5. Brogårdh, T.: PKM Research - Important Issues, as seen from a Product Development Perspective at ABB Robotics. In: Proceedings on "Fundamental Issues and Future Research Directions for Parallel Mechanisms and Manipulators", Quebec City, pp. 68–82 (2002)
6. Hess-Coelho, T.A.: An alternative procedure for type synthesis of paralell mechanisms. In: 12th IFTOMM World Congress, Besançon (2007)
7. Hess-Coelho, T.A.: Topological Synthesis of a Parallel Wrist Mechanism. Transactions of the ASME J. Mech. Des. 128(1), 230–235 (2006)

Vibration Model of a POM Chain Conveyor for the Automobile Industry

A.F. Cubero[1] and M. Artés[2]

[1] Industry, Siemens S.A., Spain
   `alejandro.fernandez@siemens.com`
[2] Department of Mechanics, UNED, Spain
   `martes@ind.uned.es`

Abstract. The aim of the present paper is to set up a first approach of a Vibration Model of a POM Conveyor System, commonly used nowadays in Automobile Industry to transport vehicles and workers together as Final Assembly Lines, composed by extremely long length Polymer Chain. Although these conveyor systems offer a successfully behaviour in terms of reliability, endurance and load capacity, sometimes but rarely appears a swing-effect in the middle and the end of the chain conveyor when a worker walks or gets into the beginning of it. This undesired vibration provokes, as well as an uncomfortable and anti-ergonomic situation for the worker, a loss of quality of the manufactured product, in this case, automobiles. Once the main objective is the study of the swing effect under a dynamic point of view, starting by setting a vibration model based on differential equations, and later, by the use of computer software, to set up a simplified dynamical model to analyse the vibration behaviour to contribute to improve the mechanical design and to reduce this undesired effect.

Keywords: Chain Conveyor, Vibration Model, Plastic Chain, Swing Effect, Ergonomics.

1   Introduction

Conveyor Systems based on plastic chain are fairly fresh-baked, being published the first Patent Submission of a POM[1] Conveyor Belt in 1988, in the US [5]. Since its first launch in the market around the end of the last century, the development has been very quick, due to the evident technical advantages of the polymer materials used, like PE, POM, PA, etc. which are for example: Low sliding coefficient, optimal abrasion resistance and a great corrosion tolerance in addition to the product itself: Easy manufacturing, which means a competitive cost, an acceptable mechanical elastic constant in comparison to steel and finally, a density five times less than steel. All these characteristics make possible a lighter, reduced noise, easy and economic mechanic design and also resistant to aggressive and exigent environments.

---

[1] POM. Polyacetal, also known as Polyoxymethylene, a common Engineering Thermoplastic.
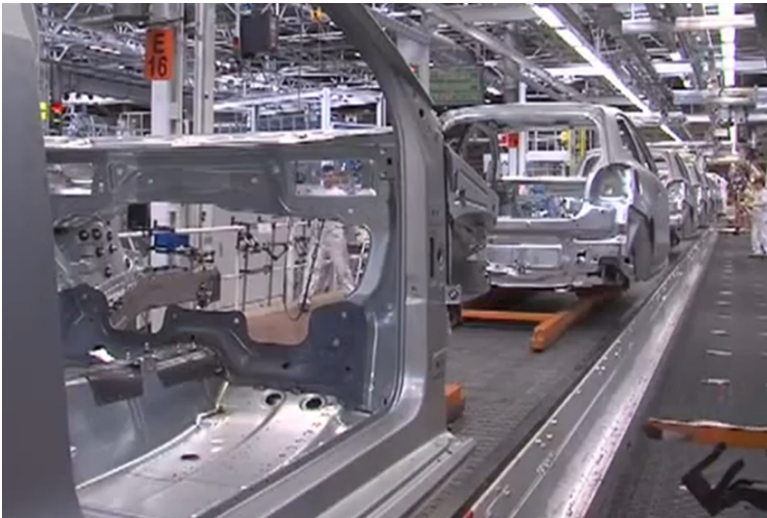
Fig. 1 Overview of a Chain Conveyor

The recent development and market introduction of the POM conveyor systems (Fig. 1) makes difficult to find publications about its dynamic behaviour. Baxter [2] presents an overview of cases describing some vibration problems affecting several types of machinery and Haines [4] describes the design of similar conveyors built with light material but of smaller sizes. However, it is not easy to find vibration models of a POM chain conveyor, which is the subject of our paper. Other authors, as Singhose [7], use a closed-loop regulation in order to reduce the system oscillation.

2   Model Description

The whole system can be described with the mass distribution of the Fig. 2 and represented by the dynamic model of Fig. 3.
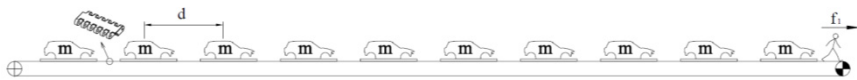
Fig. 2 Overview of a Chain Conveyor
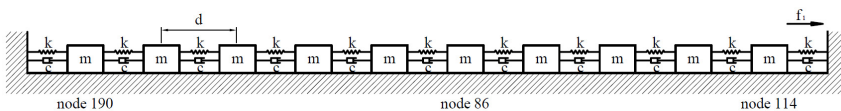
Fig. 3 Dynamic model of the chain conveyor

In order to establish the mathematical model of the dynamical system each node can be represented as shown at Fig. 4:
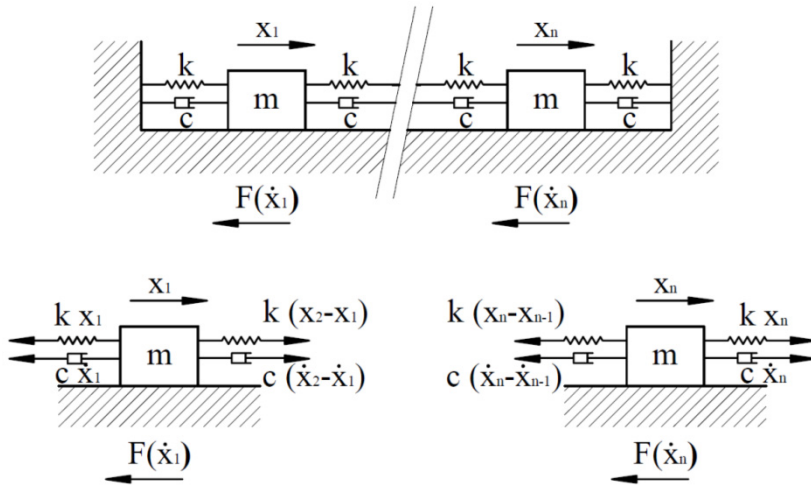
Fig. 4 Dynamic model of a node

For a determined number "n" of bodyworks, the system will be characterized by "n" *DOF's* –Degrees of Freedom-, so its behavior is defined [1] by the following differential equations system Eq. (1):

$$
\begin{pmatrix} m & \cdots & 0 \\ \vdots & \ddots & \vdots \\ 0 & \cdots & m \end{pmatrix} \begin{Bmatrix} \ddot{x}_1 \\ \ddot{x}_2 \\ \vdots \\ \ddot{x}_n \end{Bmatrix} + \begin{pmatrix} 2c & \cdots & -c \\ \vdots & \ddots & \vdots \\ -c & \cdots & 2c \end{pmatrix} \begin{pmatrix} \dot{x}_1 \\ \vdots \\ \dot{x}_n \end{pmatrix} +
$$

$$
+ \begin{pmatrix} \mu mg & \cdots & 0 \\ \vdots & \ddots & \vdots \\ 0 & \cdots & \mu mg \end{pmatrix} \begin{pmatrix} sgn\,(\dot{x}_1) \\ \vdots \\ sgn\,(\dot{x}_n) \end{pmatrix} + \begin{pmatrix} 2k & \cdots & -k \\ \vdots & \ddots & \vdots \\ -k & \cdots & 2k \end{pmatrix} \begin{pmatrix} x_1 \\ \vdots \\ x_n \end{pmatrix} = \begin{pmatrix} f_1 \\ \vdots \\ f_n \end{pmatrix} \tag{1}
$$

Where m is the mass of each vehicle, k is the elasticity constant of a chain track, c is the damping constant and μ is the coefficient of kinetic friction between chain and supporting surface that determinate friction force F at each node. In this case, all the driving forces will be null except from f_1, supposed the only moving worker is located there. The displacement of each mass $x_i(t)$ will be obtained from Eq. (2):

$$
\begin{pmatrix} x_1\,(t) \\ \vdots \\ x_n\,(t) \end{pmatrix} = \begin{pmatrix} X_{11} & \cdots & X_{1n} \\ \vdots & \ddots & \vdots \\ X_{n1} & \cdots & X_{nn} \end{pmatrix} \begin{Bmatrix} \eta_1\,(t) \\ \vdots \\ \eta_n\,(t) \end{Bmatrix} \tag{2}
$$

Where X_{ij} is the modal matrix and $\eta_j\,(t)$ are the modal amplitudes.

3   Simulation

With the help of the mechanical simulation software, *Working Model* [6], a sample chain conveyor model can be defined and tested, with the data of a real conveyor, in order to find their similarities.

The main data of the conveyor and POM chain material are shown at Table 1.

A view of the software interface is presented in Fig. 5:
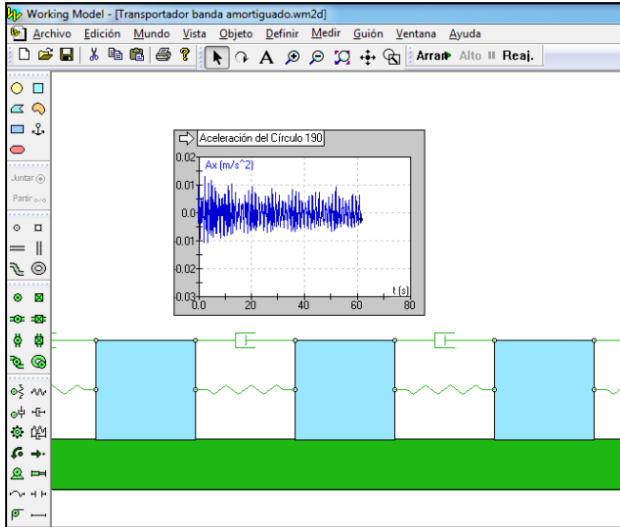
Fig. 5 Software Interface

The f_1 effect is represented as a worker walking strongly over the plastic belt at the front of the conveyor. It is simulated on the software as a 90 kg mass, with a high coefficient of kinetic friction, μ_w= 0.9, attached to a crank-connecting rod system of a diameter of 1m, activated by a simulated engine at 5 rad/s speed.

The worker's movement is transmitted to the base element as a friction force. Each of the cubes reproduces a vehicle with a mass of m = 675 kg over a 5 m chain stretch. The kinetic friction coefficient between the base and the cubes is μ = 0.23, according the manufacturer data sheet, the same value existing in a contact of two POM components.

Each of the springs included has an equivalent elastic constant k of a 5 m chain calculated from a single chain link.

With the help of a FEM program, the elastic constant on a chain link k, can be calculated, taking into account the characteristics of the selected material (see Table 1 and Fig. 6).

Table 1 Main data of the chain conveyor

Load conveyed: 10 vehicles of 650 kg each = 6500 kg
Speed: minimum of $1.6 \, E^{-2} – 0.167$ m/s (minimum and maximum)
Chain dimensions: length of 120 m and width of 1,2 m
Constants of chain material: POM
Density according to DIN 53479: 900 kg/m^3
Coefficient of kinetic friction: 0.23
Elastic modulus: 900 N/mm^2
Yield strength according to DIN 53455: 28 N/mm^2
Chain's width: 1200 mm. Link width: 100mm
Poisson's Ratio: 0.4
Yield Point: 20 N/mm^2
Elastic constant coefficient –calculated- of each POM link: 68455.64 N/mm
Elastic constant coefficient –calculated- of 5 m of POM chain: 20.078N/mm
Damping Coefficient of POM Delrin [3]: 0.0322 Ns/m
Operation Temperature: 5-30°C
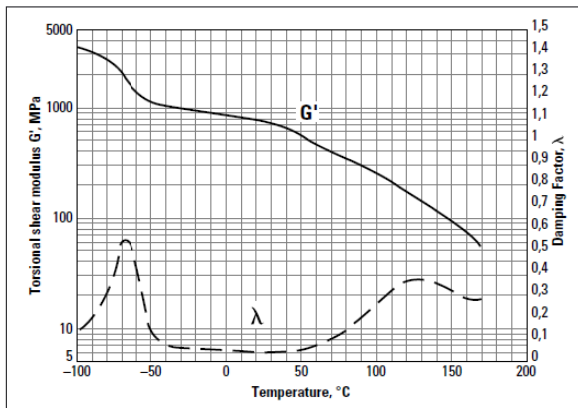
Fig. 6 Damping Factor of POM Delrin with Temperature

The chain link section is as shown at Fig. 7:
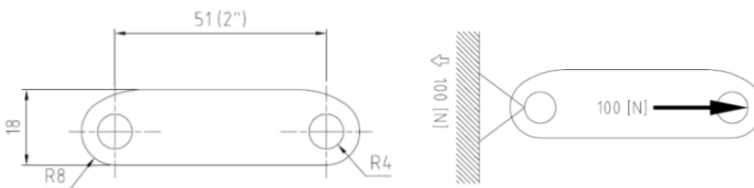
Fig. 7 Link design and forces distribution

By means of a chain link analysis, the linear deformation results are obtained for different values of the applied forces, as it is shown below:
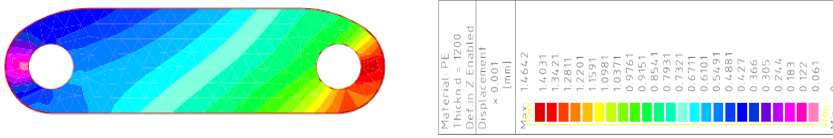
Fig. 8 Deformation of a chain link

For a link of 1200 mm width the elastic constant results to be:

$$k_0 = 68455.64 \text{ N/mm}$$

The joints between links have been simulated as a simple slope beam. The material was stainless steel and its diameter, 8 mm. The distance between both supports is 100 mm, the width of a single link. The elastic constant of the joint results to be:

$$k_e = 2026.75 \text{ N/mm}$$

Links and joints are connected alternately in series. Depending on the number of links "n" connected, the elastic constants "k_0" and "k_e" will perform the equivalent elastic constant "k" as follows:

$$\frac{1}{k} = \sum_1^n \frac{1}{ki} = \frac{n}{ko} + \frac{n}{ke} \tag{3}$$

The final value of the elastic constant in this specific case is:

$$k = \frac{k_0 k_e}{n(ke+k_0)} = 20.078 \text{ N/mm} \tag{4}$$

There is also a damping factor foreseen, took from the manufacturer [3] of the POM material.

There are two determined measuring points: Node 86 in the middle and node 190 at the end, at the center of mass of their respective masses.

The time-simulation is around 60 s, in order to analyze the displacement (in the x-axis) tolerated by the finish line workers.

4   Results

The displacements in x-axis, obtained with the simulation are the following, shown at Fig. 9 and 10.
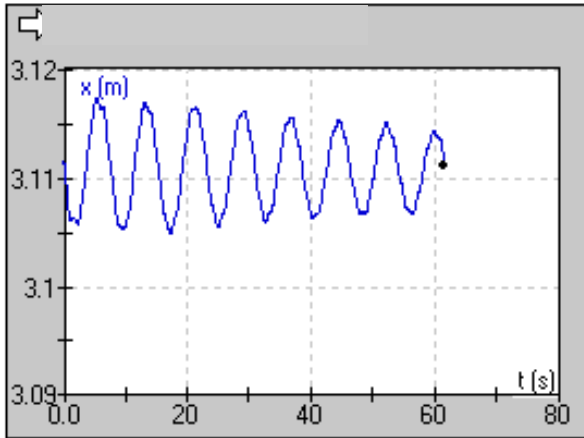
Fig. 9 x-axis displacement of node 86 at the middle of the chain
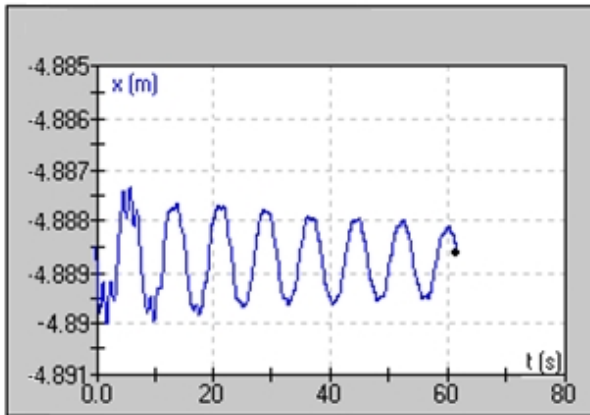
Fig. 10 x-axis displacement of node 114 at the end of the chain

From data obtained is possible to determine the main frequency of the system, as calculated from figure 8 and 9 data. The frequency value obtained in both cases is 0.16 Hz, quite similar to the real values. Furthermore, this value is in the rank of motion sickness ones (kinetosis) and produces important ergonomics effects on workers. On the other hand it provides also interesting data regarding displacement. The displacements are shown in the Table 2, as follows:

Table 2 Maximum x-axis displacements

Displacement Node	X in 190	X in 86	X in 114
Delta (mm)	2.63	12.10	17.51

It can be observed that:

- The displacement is higher in the front of the conveyor than the obtained at the middle and end.
- Due to the damping presence a smooth reduction of the displacement response can be observed.
- The maximum theoretical displacement of the chain is 17.51 mm. This value might also indicate that the conditions for having an ergonomic system are not optimal.

5 Conclusions

The results obtained indicate that proposed model confirms that there is an undesirable movement in the conveyor, which might affect both the ergonomic and comfort conditions of the operators. As the technology involved is very new, there are still not many studies available.

Results obtained from the model permit an improved mechanical design of the conveyor by modifying c and k, i.e. the material and dimensions of the conveyor links, but additional model improvements are needed.

Then, mechanical corrections can be made from the system model in order that the swinging effect can be diminished or even avoided, improving the comfort conditions of the equipment and the quality of the manufactured product.

References

1. Balachandran, B., Magrab, E.B.: Vibrations. Cengage Learning, Toronto (2009)
2. Baxter, N.L.: Troubleshooting Vibration Problems. A Compilation of Case Histories. Defense Technical Information Center, Virginia (2001)
3. Dupont,
   `http://www2.dupont.com/Plastics/en_US/assets/downloads/design/DELDGe.pdf`
4. Haines, M.: Development of a Conveyor Belt Idler Roller for Light Weight and Low Noise. University of New South Wales (2007)
5. Karl, V.P.: Plastic Conveyor Belt. United States Patent Nr. 4,742,907, California (1988)
6. Mitiguy, et al.: Working Model. MSC Software, California (2003)
7. Singhose, W.: Command Generation for Flexible Systems. MIT (2007)

Development of a Trochoidal Gear Reducer with a Slipping Rollers Type Torque Limiter

H. Terada[1], M. Kobayashi[1], and K. Imase[2]

[1] University of Yamanashi, Japan
 {terada,g12mm011}@yamanashi.ac.jp
[2] kamo-Seiko Corporation
 imase@kamo-seiko.co.jp

Abstract. To realize the no-backlash transmission element for wearable human assist robots, a trochoidal gear reducer with a slipping rollers type torque limiter has been developed. This reducer is a kind of a pin gear with planetary motion. That roller-train is fixed only by friction force to slip under an overload. And a preload mechanism has been developed. This mechanism consists of an outer race and a preload generator which have taper contact sections to generate a uniform preload. Also, a calculation method of a trochoidal gear tooth profile by use of polar complex vector geometry is proposed. Then, using the prototype reducer, it is proved that slip occurs in the set torque, and that reducer can rotate without backlash. And it is clear that has the sufficient performances for actuator of wearable human assist robots.

Keywords: reducer, trochoidal, pin gear, torque limiter, slipping roller.

1   Introduction

In Japan, a population of the aging people is increasing abruptly after 1975. So, to support the aging people, a development of a wearable human assist robot is the current trend [5, 10]. These robots assisting human muscles, must deal with various abnormal conditions which are tipping and tripping. In other words, to eliminate danger condition which overloads to a muscle, a torque limiter system is needed. However, conventional mechanical torque limiters are too heavy, so they aren't suitable for assist robots. Therefore, most assist robots use a software torque limiter which excludes some assumptions. And these performances are insufficient. So, the trochoidal gear reducer with a slipping rollers type torque limiter [4] has been developed. This limiter consists of some mechanical structures which doesn't have electric circuit. And that has an adjusting mechanism for the preload. In this report, at first, a calculation method of a trochoidal gear tooth profile is proposed. And the torque limiter mechanism design is proposed. And then, using the prototype reducer, we evaluate the usefulness of the proposed calculation method and the design of a torque limiter.

Output mechanism with eccentricity elimination

Outer race with taper shape

Trochoidal gear

Eccentric input shaft

Bearing support

Roller-train

Housing

Preload generator
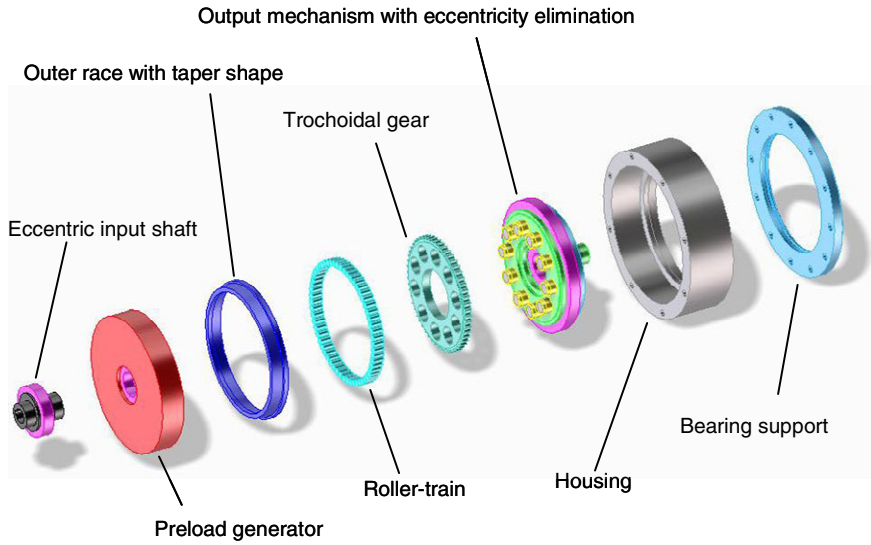
Fig. 1 Structure of the trochoidal gear reducer

2   Structure of a Trochoidal Gear Reducer

A trochoidal gear reducer is a kind of the pin gear with planetary motion. This reducer consists of four sections which are an eccentric motion input section, a reduction section, a motion transmitting section with eccentricity elimination, and a preload generating section, as shown in Fig.1. Especially, many rollers are arranged inside the outer race under the solid-preload. All rollers are pressed each other, and they press the outer race at the uniform force. In other words, the roller-train is fixed only by the friction force. So, when the large force caused by a transmitting torque acts on the roller-train, each roller slips over an outer rotor surface.   And, a preload generator adjusts the slipping torque. Then, considering the no-backlash motion, the constant velocity rotation and the pin gear shape at the reduction section, the trochoidal gear tooth profile is proposed. To generate the high reduction ratio, this reducer rotates with eccentric motion. So, the output mechanism for eccentricity elimination is needed. This structure is similar to the conventional planetary type gearless reducers [7].

   In this report, to calculate a tooth profile, terminologies are defined as Table 1.

Table 1 Terminologies of a trochoidal gear reducer

Symbols	Terminology	Symbols	Terminology
Z_r	Number of rollers	d_r	Roller pitch diameter
Z_c	Number of gear teeth	d_c	Gear pitch diameter
m	Module	y	Offset coefficient

3   Tooth Profiles Calculation Method by Complex Plane Vector Geometry

It is difficult to generate the no-backlash motion and the constant velocity rotation at pin gear using the conventional gear teeth. Because that the interference occurs at the dedendum of a gear tooth. So, we propose the new gear tooth profile calculation method. Using the complex plane vector geometry [6], this gear profile is shown as shown in Fig.2. When the initial center distance a_0 is defined as shown in Eq. (1), the eccentricity a_1 is defined as shown in Eq. (2).

$$a_0 = \frac{(d_r - d_c)}{2} = \frac{(z_r - z_c) \cdot m}{2} \tag{1}$$

$$a_1 = a_0 - y \cdot m \tag{2}$$

And, a relative motion method is used; to generate a tooth profile, at first, we assume that the fixed ring of rollers rotates. So, the $\mathbf{B_2}$ is defined as the rotation vector with relative rotation τ. And the $\mathbf{C_1}$ is defined as a constant vector from the trochoidal gear center to the roller-fixed ring center. The relative rotation $\mathbf{P_3}$ on that gear center is defined as Eq. (3).

$$\mathbf{P_3} = \mathbf{C_1} + \mathbf{B_2} = -a_1 \cdot e^{j\frac{\pi}{2}} + \frac{z_r m}{2} \cdot e^{j\tau} \tag{3}$$

In cases in which the tooth profile is calculated, the coordinate of gear tooth has to be fixed. So, we rotate that gear to the inverse direction as $-\theta$. So, the motion locus of roller meshing with the gear tooth is defined as Eq. (4).

$$\mathbf{P_4} = \mathbf{P_3} \cdot e^{j(-\theta)} \tag{4}$$

In other words, this motion locus conforms to the roller center locus along the tooth profile.

And this tooth profile is the envelope locus of a roller that diameter is defined as d_f, which moves along center locus. The normal direction of that motion locus is needed. So, the tangent vector of motion locus is calculated as Eq. (5).

$$\dot{\mathbf{P}}_4 = s_d \cdot e^{j\phi}$$
$$= j \cdot \dot{\theta} \cdot a_1 \cdot e^{j(\frac{\pi}{2} - \theta)} + j \cdot (\dot{\tau} - \dot{\theta}) \cdot \frac{z_r m}{2} \cdot e^{j(\tau - \theta)} \tag{5}$$

At this equation, a motion speed is defined as s_d, and the tangent direction of locus shows as ϕ. So, the normal vector $\mathbf{B_5}$ from the roller center is shown as Eq. (6). Therefore, the tooth profile is defined as Eq. (7).

$$\mathbf{B_5} = \frac{d_f}{2} \cdot e^{j(\phi - \frac{\pi}{2})} \tag{6}$$

$$\mathbf{P_6} = \mathbf{P_4} + \mathbf{B_5} \tag{7}$$

On the other hand, the output mechanism motion vector geometry is similar to the motion transmitting section of a trochoidal wave ball reducer [9].
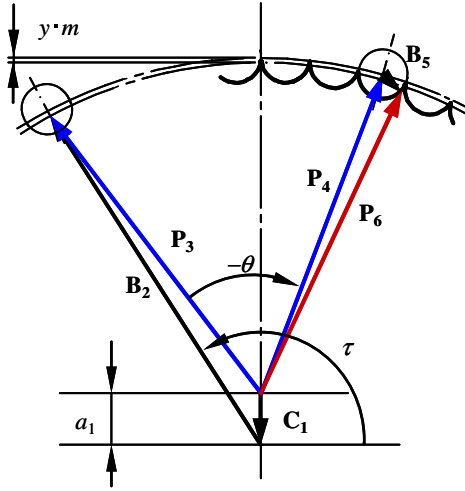
Fig. 2 Vector geometry of a trochoidal gear tooth

4   Preload Generator Designs

At this reducer, many rollers are arranged on the outer race without clearance. Especially, when many rollers are fixed by the elastic deformation and the friction force, the geometrical condition of a roller index angle θ_i has to be satisfied as Eq. (8).

$$\sin \frac{\theta_i}{2} = \sin \left(\frac{\pi}{z_r} \right) < \frac{d_f}{d_r} \tag{8}$$

Then, selections of the roller diameter and the roller pitch diameter are very important to decide the slipping torque. And the radial preload from the outer race generates the similar deformation and the friction force. The deformation and the friction force depend on material hardness and radius of curvature. However, that influence rate cannot separate each other; the friction force cannot set using these conditions directly. Therefore, at first, an elastic deformation has been simulated using the FEM analysis (ANSYS) as shown in Fig.3. At this simulation, the deformation of a center roller which is constrained by both-sides rollers and outer race is simulated. It is assumed that both-sides rollers are fixed, and this assumption is defined as the boundary condition. And that roller is loaded as a radial preload from the outer race. In cases in which the friction coefficient μ is assumed at 0.15, this maximum simulated deformation is 1.91μm under the preload 4818N from the outer race. Also, this simulation data shows that roller deformation isn't uniform, because the outer race and the preload generator have an asymmetry
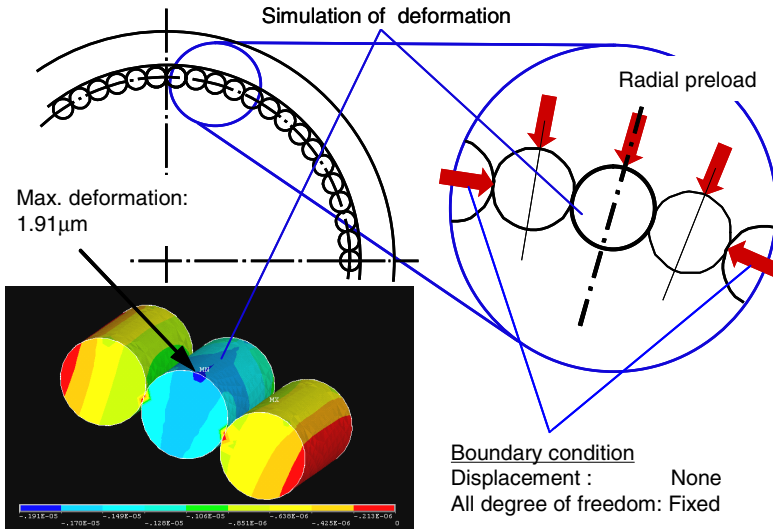
Fig. 3 Simulation of the roller deformation by preload from the outer race
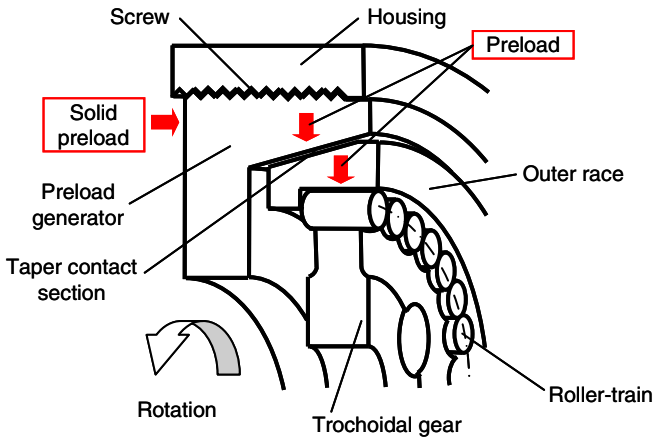
Fig. 4 Preload mechanism with a taper contact section

shape. This non-uniform value is less than 0.4μm; it does not cause the rotating accuracy degradation. And if the high resolution less than $1.75{\times}10^{-3}$ rad is required, we have to investigate the optimized cross section shape of an outer race.

Using this simulation data, we develop the preload mechanism as shown in Fig.4. A thin outer race and a preload generator have taper contacting sections. When that preload generator rotates itself, the taper section of this generator moves linearly. And thin outer race which is located around many rollers is pressed at the taper section from the preload generator, as "wedge effect". Using

this mechanism, the transmission torque can limit at both directions. So, the preload can be set to the arbitrary amount, and the slipping torque can be adjusted as shown in Fig.5. At this case, that preload is controlled by changing the pushing depth from 0μm to 28μm. And the slipping torque depends on a rotation speed.

Especially, the initial slipping torque is about 150% of the rated slipping torque. And at rotation speed over 100rpm, that slipping torque is similar to the rated slipping torque. At the rotation speeds 300rpm, the slipping torque can adjust between 9.5Nm and 10.9Nm. If the higher preload range than the set range is needed, a pitch diameter of an outer race or a roller diameter will be changed.
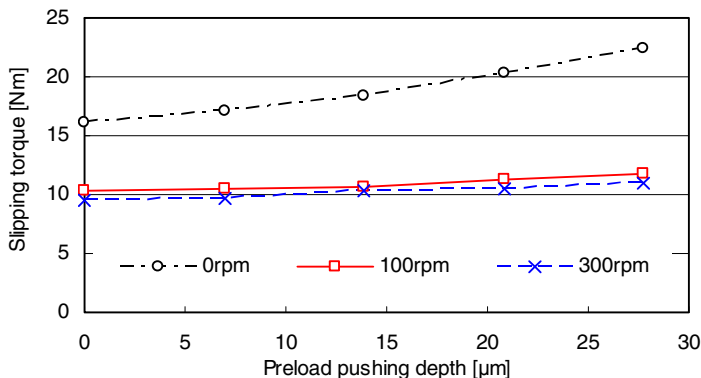
Fig. 5 Relations between the pre-load length and the slipping torque adjustments

5   Verification Test of the Prototype Reducer

Considering the proposed design method, the prototype reducer has been made as shown in Fig.6. That rated torque is 11.0Nm, and the weight is 0.55kgf. A trochoidal gear is made from the temper steel S45C [1]. And the outer race is made from the chromium-molybdenum steel SCM415 [2]. Rollers are made from the bearing steel SUJ2 [3] which have hardness as the Rockwell hardness C58-C60. And then, to confirm the usefulness of a slipping rollers type torque limiter, the transmission efficiency has been tested at 300rpm as shown in Fig.7. At this case, when a slipping torque is set as 8.0Nm, we have confirmed that torque limiter acts certainly. Then, relations between the number of slipping and the slipping torque changes are investigated as shown in Fig.8. At this case we set the initial slipping torque as 11.0Nm. It is clear that slipping torque does not almost change to 200 times. Also, the preload mechanism can adjust the slipping torque in ±0.7Nm; this mechanism can be used during 500 times.

And we evaluate the performances for positioning mechanisms. A hysteresis loss is 3.40×10^{-3} rad, and the spring constant is 1.10×10^{3} Nm/rad. On the other hand, the angle transmission accuracy is 2.52×10^{-3} rad (520.1 arc seconds). They are similar to other type no-backlash reducer [8]. Therefore, it is proved that this type reducer is enough for the actuator of human assist robots.

Reduction ratio	-28
Number of rollers	58
Roller diameter	2.998mm
Roller length	5.0mm
Roller pitch diameter	55.376mm
Number of teeth	56
Teeth width	3.0mm
Eccentric distance	0.764mm
Module	0.955mm
Offset coefficient	0.20

Fig. 6 Prototype reducer
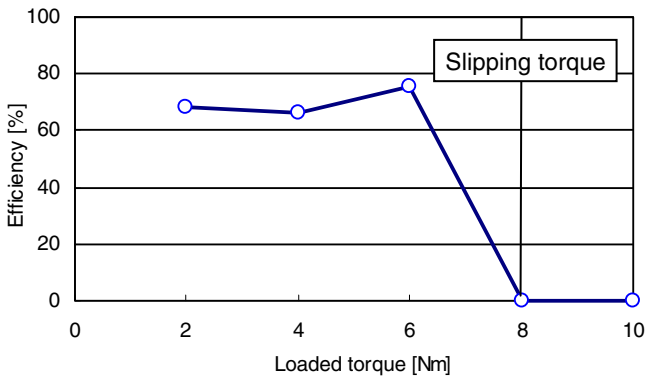
Fig. 7 Efficiency at the slipping torque as 8.0Nm
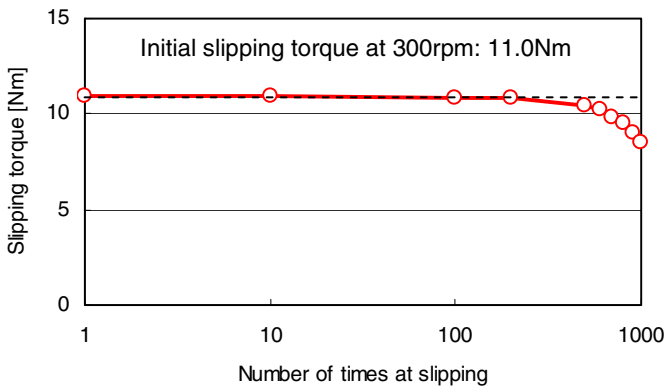
Fig. 8 Relations between the number of times for slipping and the slipping torque changes

6   Conclusions

Trochoidal gear reducer with a slipping rollers type torque limiter has been developed and analyzed geometrically. Especially, the preload mechanism which has a thin outer race and a new preload generator with taper contacting sections has been developed to adjust the slipping torque. Also, using prototype reducer, it is proved that slip occurs in the set torque, and that reducer can rotate without backlash under the set torque. And it is clear that has the sufficient performances for actuator of human assist robots. In future work, to eliminate the non-uniformity of preload, a cross section shape of an outer race will be improved.

References

1. Japanese Industrial Standards: Carbon steels for machine structural use. JIS G 4051 (2009)
2. Japanese Industrial Standards: Low-alloyed steels for machine structural use. JIS G 4053 (2008)
3. Japanese Industrial Standards: High carbon chromium bearing steels. JIS G 4805 (2008)
4. Japanese Unexamined Patent Application Publication: Roller type transmission device. No.2012-26568 (2012)
5. Kawamoto, H., Kanbe, S., Sankai, Y.: Power Assist Method for HAL-3 Estimating Operator's Intension Based on Motion Information. In: Proceedings of the 12th IEEE Workshop on Robot and Human Interactive Communication, 1A1-E04 (2003)
6. Makino, H.: Automatic machine Kinematics, Nikkan kogyo shinbunsha, Japan (1976)
7. Sumitomo Heavy Industry Ltd.: Cyclo Reducer. F0101-2 (1999)
8. Terada, H., et al.: Motion Analysis of a Reciprocating Motion Type Ball Reducer. In: Proceedings of the 12th IFToMM World Congress, Besançon, France, LC-418 (2007)
9. Terada, H., Imase, K.: Motion Analysis of a Multistage Type Trochoidal Wave Ball Reducer. In: Proceedings of X. International Conference on the Theory of Machines and Mechanisms, Liberec Czech Republic, pp. 629–636 (2008)
10. Terada, H., et al.: Development of a Wearable Assist Robot for Walk Rehabilitation after Knee Arthroplasty Surgery. In: Proceedings of International Conference on the Theory of Machines and Mechanisms 2012, Liberec Czech Republic, pp. 65–71 (2012)

Uncertainty Propagation in the Grinding Process of High Contact Ratio Gears for a Planetary Geared Turbofan

A. Martínez-Ciudad, L.N. López de Lacalle, and J. Sánchez

University of the Basque Country, Spain
{alvaro.martinez,norberto.lzlacalle,
joseantonio.sanchez}@ehu.es

Abstract. This article shows the uncertainty propagation in the machining of a planetary speed reducer with HCR (High Contact Ratio) gears for high responsibility applications. It is known that in these applications, failure tolerance of a component is very low, so reliability must be close to 100%. In this way, the tolerances associated to the manufacturing process of the individual parts are typically very narrow in order to find higher function reliability. Therefore, the knowledge of which are the error sources in the manufacturing of the gear it is required, if the maximum repeatability (precision) demanded in those narrow tolerances has to be achieved. Also, tolerances are directly related to the acceptance of several unknown factors on system performance. This work will break down the sources of uncertainty, focusing on the manufacturing process by grinding.

Keywords: Uncertainty, propagation, gear, manufacturing, planetary.

1 Introduction

For airlines companies, the fuel is the highest business cost, and while the price of your car's regular unleaded is skyrocketing, the same applies to jet fuel, and in significant numbers. The New York Times reports that 1 cent increase in the per gallon price of jet fuel translates to an additional cost to the industry of $200 million per year. In this way, it can be seen that one of the key factor to reduce is the fuel consumption.

Nowadays everything that is manufactured must contain an ecological component. The systems must consume less, last more and be tougher. In the aeronautical world it is the same. There are many factors that can reduce the fuel consume of an aircraft: using compound materials in the plane structure, the improvement of the aerodynamics and of course the improvement of the engine efficiency.

2   Choice of the Speed Reductor

Turbofan engines have limits. To increase bypass ratio, the turbine must grow to create more power to drive the larger fan. Fans want to turn at slow speeds, while turbines want to turn at high speed. With the fan and turbine directly connected by the shaft, a compromise must be made to maximize fan diameter (low speed) at the best turbine speed (a slower than optimum speed), as shown in Fig. 1.

A new engine concept introduced is the "geared turbofan" that uses a planetary gear reductor enabling the engine fan to work independently of a low-pressure compressor and turbine. With this change, it results in significant fuel efficiency and reduced fan speed for a quieter ride, and even the emissions are reduced.

When a high speed reduction is needed but there is not enough space, one of the best options that are available is to introduce planetary speed reducer. It has the advantage of being very compact and performing a high efficiency (95-98%).

The components of this speed reductor are considered as high responsibility parts. This means that in case of collapse of one of these parts, the aircraft could not continue flying.
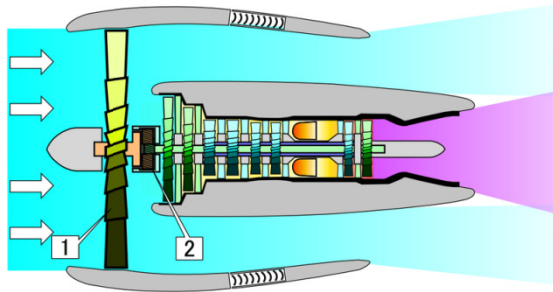
Fig. 1 Geared turbofan. 1- Fan, 2- Planetary gear reducer

3   Study of the Planetary HCR Gear Reducer

This section will show a real problem of a planetary gear reducer used to enable the engine fan to work independently of a low-pressure compressor. It will be analyzed the difference between choosing a tooth like HCR or a standard tooth. This engine is aimed at small motors for business airplanes. Usual features are: thrust force ranging from 1150 N to 3550 N, bypass ratio between 6.5 and 8.2, motor weight near 85kg. Hence, the technical requirements that must be kept for this application are:

- Transmission power: 360 kW
- Input speed: 44750 rpm.
- Output speed: 15680 rpm

With this data it is formulated a planetary gear reducer that is composed of a sun, three planets and a ring. Helical gears were discarded due to low transmission power, being spur gears with high contact ratio (HCR) the most suitable option for this application. Table 1 shows some differences between choosing a HCR gear or a standard gear.

It has no sense showing the differences between the gear quality parameters because independently of whether it is a HCR gear or a standard gear, both must keep the same quality requirements.

Table 1 Differences between a HCR gear and a standard gear

	High Contact Ratio (HCR)			STANDARD GEAR		
	SUN	PLANET	RING	SUN	PLANET	RING
Module (mm)	1.28	1.28	1.28	1.25	1.25	1.25
Number of teeth	31	29	89	31	29	89
Pressure Angle	20°	20°	20°	20°	20°	20°
Addendum	$1.2 \cdot m$	$1.2 \cdot m$	$1.2 \cdot m$	$1 \cdot m$	$1 \cdot m$	$1 \cdot m$
Dedendum	$1.45 \cdot m$	$1.45 \cdot m$	$1.45 \cdot m$	$1.25 \cdot m$	$1.25 \cdot m$	$1.25 \cdot m$
Pitch diameter (mm)	39.68	37.12	113.92	38.75	36.25	111.25
Addendum diameter (mm)	42.752	40.192	110.848	41.25	39.25	108.75
Dedendum diameter (mm)	35.968	33.408	117.632	38.125	36.125	114.375
Ratio of contact	1.934			1.653		
	2.052			1.743		
Manufacturing Cost	HCR > STANDARD GEAR					

In order to make the calculation much faster, only three teeth of each component have to been taken into account in the finite elements model.
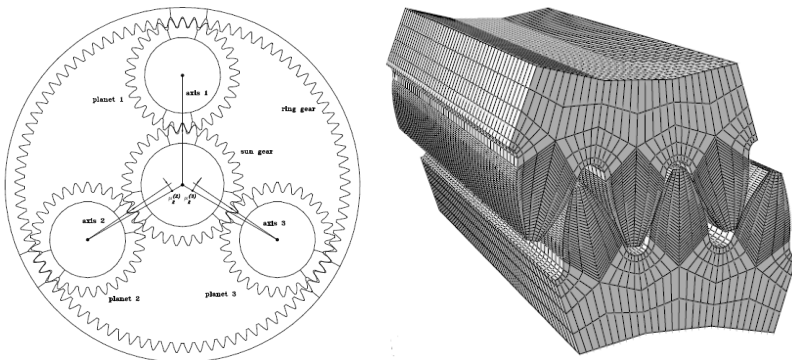
Fig. 2 a) Set up of the planetary gear reducer, b) Meshing of three teeth

4   Manufacturing

4.1   P400G, Gear Grinding Machine

This study is focused on detecting where do the uncertainties sources come from. In this section the machine where the test is going to be made will be presented.

The P400G is a machine developed by the company Gleason®. It is a grinding machine with a profile wheel for grinding gears whose diameters are smaller than 400 mm. The machine is qualified for grinding gears with a quality of DIN 3 according to DIN 3960.

This grinding machine has 10 axis interpolated by CN (*X, Y, Z, Z2, Y3, A, C, S, S2. S3*). *Y3* is the axis of a probe that the machine has included for measuring inside the machine. This case of study is about high precision gears so, this won´t be taken as valid. However, it is an important help for the worker.
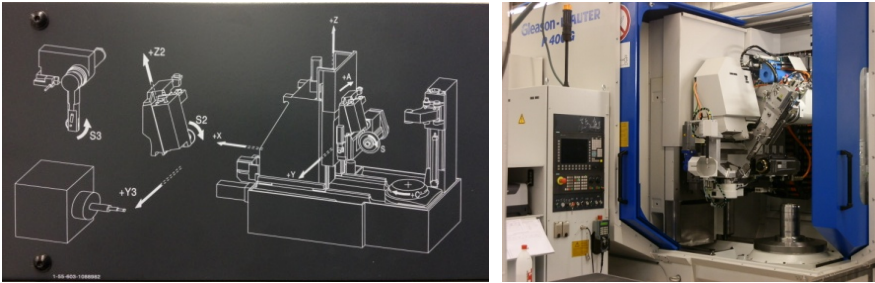
Fig. 3 a) Axis of the machine, b) P400G Gear grinding machine

4.2   Gear Tolerances

There are many tolerances that must be taken into account when a gear is manufactured. Nevertheless, the most difficult ones are the single pitch deviation (f_p), the total cumulative pitch deviation (F_p), the total profile deviation (F_α) and the total helix deviation (F_β) [2].
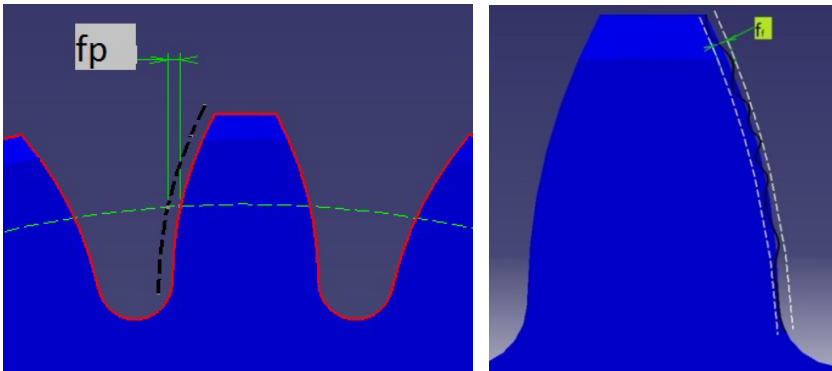
Fig. 4 a) Single pitch deviation (f_p), b) Total profile deviation (f_f)

5   Error Budget

In this study an error budget [4] was made using the method outlined in Slocum [3]. With that procedure it is possible to identify and quantify the sources of errors [5] so that subsequent efforts could be directed at those problems which proved to have most effect on precision and accuracy. The budget includes all the elements that affect the final accuracy of the gear, i.e. the machine, the dresser, the clamping system, the wheel wear and the measurement of the gear. Each error source has been characterized by the following rules [1, 5]:

- An estimate of its effect, an expanded uncertainty U_i, which for a Gaussian distribution may be an expanded uncertainty from a calibration report, a standard deviation, or simply estimated or judged as a 95% estimate.
- A reducing factor k_i to convert U_i, to its equivalent standard uncertainty $u(x_i)$, in this study for simplicity it is assumed as $k=2$

$$u(x_i) = U_i/k \tag{1}$$

The expanded uncertainty (U) and, thus, the combined standard uncertainty (u_c) calculated, respectively, as:

$$U = 2u_c \tag{2}$$

$$u_c^2 = \sum_{i=1}^{N} |c_i u(x_i)|^2 \tag{3}$$

It is necessary to understand that the sum of all the uncertainties must be less than the narrowest tolerance. If the process can assure this fact, all the gears will be made within the quality requirements.

5.1   Uncertainty due to the Axes of the Machine

The machine is fairly new, it has not been possible to run tests in order to quantify the uncertainty that comes from each axis In the next studies all the axis of the machine to know their errors will be analyzed. However, to establish a global uncertainty of the machine, all the quantities on which the result of the measurement depends are varied, its uncertainty can be evaluated by statistical means [1, 5]. Here it is suggested a measurement of a point within the work space from very different positions of the machine. As a result of this, there is an uncertainty of 0.26 µm.

5.2   Uncertainty due to the Thermal Deformation of the Machine

To reduce the uncertainty that comes from the thermal deformation, before starting any job, the machine must be warmed for at least 1 hour. To make this possible, the machine will work (without a part) making the same movements as if it were manufacturing. Making this, the uncertainty that comes from the thermal deformation is supposed nearly zero. Workshop is kept to a run temperature of 20°.

5.3   Uncertainty due to the Dresser

The gear-set is manufactured with a shaped wheel, the space between two teeth will be a copy of the tool. The error in the grinding wheel will come from the error that exists in the dressing process. So before dressing, the dresser must be measured with the highest accuracy in order to write the measured values into the control and ensure the accuracy of the dressing. This dresser's measurement has an uncertainty of 1.23 µm. The uncertainty coming from the dressing will come from the wear of the dresser. Actually this is a study field because it is not easy to understand the wearing process. This work assumes that the dresser is under perfect conditions and there is no wear between one finish dressing and another.

5.4   Uncertainty due to the Clamping System

The uncertainty of the clamping system has been determined by making measurements "insitu", Fig. 5. It must be taken into account that the positioning of the part in the clamping system is made individually trying to leave it in the most optimal way. It is evident that this takes time away from the production but it is necessary when a company searches high quality components. The indicator used in the measurements has an expanded uncertainty of 2 µm. With the entire experimental datum, the uncertainty of the clamping system has been calculated having the value of 3.3 µm. It is true that there are some other clamping systems developed by Hirschmann or Erowa that have less uncertainty. They have a repetitive accuracy (consistency) of < 2 µm. In this study, these kind of systems haven´t been chosen due to the number of parts to manufacture is not high.
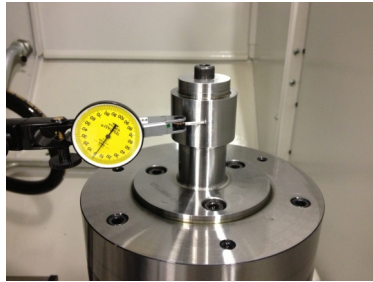
Fig. 5 Clamping system

5.5   Uncertainty due to the Grinding Wheel Wear

The wear of the wheel is corrected with frequently dressings, at least, one before starting the grinding process of the gear. This way, the grinding process has the wheel in the best conditions in order to have the tooth over control. The wear of the wheel leads that the circular thickness of the tooth to become higher.

Furthermore, as the wear is not perfectly symmetric along the wheel it may change the shape of the tooth. Working under these conditions, the wheel has been measured between two dressings in order to know the variability of the wear in the wheel. With this study the uncertainty due to the wheel wear is 2 µm.

5.6   *Uncertainty due to the Measurement of the Gear in the 350 GMS Machine*

This machine has a 0.1 µm high resolution glass scales that allows to keep the expanded uncertainty in 1 µm (in spur gears) as long as the ambient temperature is between 20º C ± 2º C, a thermal fluctuation of =/< 1° C/hour or =/< 1.5° C/day, and a thermal gradient of =/< 1.0° C/meter.

6   **Conclusions**

Searching the continuous improvement and trying to reduce the business cost, this study shows the factors that influence in the final component. Error budget has been used to identify the existing problems in the gear manufacturing.

With this paper it can be probed that the uncertainty of this process comes from:

1- Uncertainty due to the axis of the machine: 0.26 µm
2- Uncertainty due to the dresser: 1.23 µm
3- Uncertainty due to the clamping system: 3.3 µm
4- Uncertainty due to the wheel wear: 2 µm
5- Uncertainty due to the measurement of the gear in 350 GMS machine: 1 µm

The combined standard uncertainty [1, 5] is: 4.2 µm, for each of the datum dimensions, those are single pitch deviation (f_p), the total cumulative pitch deviation (F_p), the total profile deviation (F_α) and the total helix deviation (F_β). The biggest uncertainty comes from the clamping system. Now, it is necessary to see if the uncertainty is inside the tolerances. If it is not, the uncertainty of each component must be reduced. The first one that must be reduced is the easiest one. This is the clamping system. One option to reduce this uncertainty is to make a new design of the clamping system.

References

1. ISO: ISO Guide to the Expression of Uncertainty in Measurement. International Organization for Standarization, Geneva (1993) (corrected & reprinted 1995) ISBN 92-67-10188-9
2. Sato, O., Osawa, S., Kondo, Y., Komori, M., Takatsuji, T.: Calibration and uncertainty evaluation of single pitch deviation by multiple-measurement technique. Precision Engineering 34(1), 156–163 (2010)
3. Slocum, A.: Precision Machine Design. Prentice Hall, New Jersey (1992)
4. Uriarte, L.G., Herrero, A., Zatarain, M., Santiso, G., López de Lacalle, L.N., Lamikiz, A., Albizuri, J.: Error budget and stiffness chain assessment in a micromilling machine equipped with tools less than 0.3mm in diameter. PrecisionEngineering 31(1), 1–12 (2007)
5. Wolfgang, S., Lazos, R.: Guía para estimar la incertidumbre de la medición (2010)

Efficiency Analysis of Shifted Spur Gears

A. Diez-Ibarbia, A. Fernández del Rincón, M. Iglesias, and F. Viadero

University of Cantabria, Structural and Mechanical Department, Spain
`viaderof@unican.es`

Abstract. An efficiency study of spur gears with profile modifications is presented. One of the objectives of this proposal is to make a comparison between efficiency values obtained by an advanced load contact model and reference values obtained from literature. Moreover, two methodologies for calculating the efficiency are presented: a "Numerical method" and an "Analytical method". For the same gear pair, different efficiency values are obtained using each method. The differences among efficiency values are discussed and comparisons between both methodologies are made.

1   Introduction

In the mid-term, an increment in the requirements for gear transmission efficiency is foreseen. This is not only due to the need for higher power density (higher speeds and torques with the same transmission size and therefore higher power losses) but also as a consequence of stricter environmental regulations. In this context, the efficiency study of these systems is a crucial aspect in order to maintain or improve output features.

Furthermore, in multi-stage transmissions (such as in hybrid vehicles and wind turbines), where more than one pair of gears is meshing, improving the efficiency is critical in order to reduce the power losses and lower the operating temperature.

From the literature review [8, 11, 13, 14], it has been concluded that there is not a defined methodology which considers all kinds of power losses in gear transmissions. However, it has been observed that the sources of power losses can typically be classified by their load dependency since only gear elements are taken into account (power losses caused by bearing, seals, shaft, auxiliary elements and other are omitted). The load-dependent losses are caused by friction or rolling forces among gear teeth, while the non load-dependent ones are due to the fluid motion involved (lubricant, refrigerant, air). As in this study high-speed conditions are not used (less than 6.000 rpm speed is used), only load-dependent losses are considered. Besides, as rolling effects contribute less than friction effects in the study conditions to power losses [1, 6], only friction effects are considered for

the efficiency calculation in this work. Thus, this calculation depends mainly on the friction coefficient (FC) and the load sharing (LS) factors.

Considering the importance of these two factors, a review of the FC [13] and the LS [11] formulations is done. From this review, the FC can be approached as (i) variable friction coefficient (VFC) or (ii) constant friction coefficient (CFC) while the LS formulations can be classified as (i) uniform and (ii) non uniform.

Depending on the FC and LS formulations chosen, there are two different ways to calculate the efficiency; analytically and numerically. These approaches are developed in section 2 and are based either on [9, 10] or [11-13] respectively. The numerical approach is implemented in the model developed by the authors [3-5] and assessed taking into account previous results available in the literature [2, 7], which are based on an analytical approach.

The aim of this study is to present the accuracy benefits of using a model based on load effect instead of a model based on kinematic factors. To achieve this goal, the efficiency values obtained from the literature are compared to those obtained using an advanced contact model for shifted gears elaborated by the authors and presented in [3-5]. In this context, profile shifting refers to the manufacturing method for gears that consists in moving the generation tool away or closer in order to make the duration of two different sized meshing gears similar. This modification has an impact on the efficiency of the shifted gear pair. Hence, this aspect is implemented in the load contact model (LCM) developed by authors so that it can be compared with other models. In this work, the shift factors of gears 1 and 2 are constrained to be equal in absolute value with opposite signs ($x_1+x_2=0$ is fulfilled for every case) in order to compare it with those from the literature [2, 7].

2   Efficiency Calculation

Mechanical efficiency is defined as the relationship between energy output and energy input for a given period of time.

$$\eta = \frac{P_{out}}{P_{in}} = \frac{P_{in} - P_{loss}}{P_{in}} \tag{1}$$

The efficiency implemented in the model proposed by the authors has been calculated using a numerical approach, and the results are compared with those using an analytical formulation [2]. Depending on the choice of FC and LS formulations, the implemented approach would be the numerical approach (any FC and LS formulation could be used) or the analytical approach (CFC must be used and LS factor should be predetermined).

Numerical approach

In order to obtain the efficiency, it is necessary to calculate the loading forces, the sliding velocity and the FC for every pair of teeth in contact using a LCM. Once these values are calculated, instantaneous power losses can be obtained by using this equation:

$$P_{loss,inst} = \sum_{z=1}^{N} F_R(\theta) * V_s(\theta) = \sum_{z=1}^{N} \mu(\theta) * F_N(\theta) * V_s(\theta) \qquad (2)$$

Where N is the number of pairs of teeth in contact, μ is the friction coefficient, F_N is the normal load and V_s is the sliding velocity for each contact.

In the proposed model, instantaneous power losses are obtained using:

$$P_{loss,inst} = \sum_{z=1}^{N} (T_{in} * \omega_1 - T_{out} * \omega_2) \qquad (3)$$

Then, average power losses are calculated using the following equation:

$$P_{loss} = \frac{\int_{-\frac{\theta_p}{2}}^{\frac{\theta_p}{2}} P_{loss,inst}\, d\theta}{\theta_p} \qquad (4)$$

Finally, the mechanical efficiency is obtained by means of equation (1).

Analytical approach

This approach is thoroughly explained in [9, 10]. The fundamentals applied in this calculation are the same as in numerical approach, nevertheless some approximations are assumed, as a CFC and uniform LS. Then power losses are obtained using:

$$P_{loss} = F_R(\theta) * V_s(\theta) = \mu(\theta) * F_N(\theta) * V_s(\theta) \qquad (5)$$

The first approximation is to calculate the CFC averaging the FC for the whole mesh (μ_m).

$$P_{loss} = \mu_m * \frac{F_{tmax}}{\cos(\alpha_{wt})} * \frac{V}{p_{et}} * \int_{A}^{E} \frac{F_N(\theta) * V_s(\theta)}{F_{Nmax} * V}\, d\theta \qquad (6)$$

Defining power loss factor (H_v) as:

$$P_{loss} = \mu_m * F_{tmax} * V * H_v = P_{in} * \mu_m * H_v \qquad (7)$$

$$H_v = \frac{1}{\cos(\alpha_{wt})} * \frac{1}{p_{et}} * \int_{A}^{E} \frac{F_N(\theta) * V_s(\theta)}{F_{Nmax} * V}\, d\theta \qquad (8)$$

In order to analytically calculate this factor, another approximation is assumed, that is, LS is uniform and equal for both pairs of teeth (LS=0.5 when N=2 and it is represented in Fig. 2).

Simplifying the power loss factor H_v:

$$H_v = \frac{\pi * (u + 1)}{z_1 * u * \cos(\beta_b)} * (1 - \varepsilon_\alpha + \varepsilon_1^2 + \varepsilon_1^2) \qquad (9)$$

Reordering the mechanical efficiency equation (1):

$$\eta = \frac{P_{out}}{P_{in}} = \frac{P_{in} - P_{loss}}{P_{in}} = \frac{P_{in} - P_{in} * \mu_m * H_v}{P_{in}} = 1 - \mu_m * H_v \qquad (10)$$

Friction coefficient model

As can be seen in both approaches, the FC is an important part of the methodology in order to determine which approach to use. In this study, the FC is obtained using Niemann's formulation because of its widespread use in literature [2, 6, 9, 10]. According to this approach the FC is assumed constant for the whole mesh (CFC) and it is obtained using:

$$\mu_m = 0.048 * \left(\frac{\frac{F_{bt}}{b}}{V_{\Sigma C} * \rho_c}\right)^{0.2} * \eta_{oil}^{-0.05} * R_a^{0.25} * X_L \qquad (11)$$

Where F_{bt} is the normal applied load in the pitch point, $_c$ is the equivalent curvature radius in the pitch point, b is the gear width, η_{oil} is the oil density, R_a is the roughness, and parameters V_c and X_L are defined as:

$$V_{\Sigma C} = 2 * V_t * sen(\alpha_{wt}) \text{ and } X_L = \frac{1}{\left(\frac{F_{bt}(\theta)}{b}\right)^d}; \qquad d = 0.0651 \text{ for mineral oil}$$

In order to get a VFC formulation, some variations in the original equation have been done arriving to equations (12) and (13).

$$\mu(\theta) = 0.048 * \left(\frac{\frac{F_{bt}(\theta)}{b}}{V_{\Sigma C} * \rho_c(\theta)}\right)^{0.2} * \eta_{oil}^{-0.05} * R_a^{0.25} * X_L \qquad (12)$$

$$\mu(\theta) = 0.048 * \left(\frac{\frac{F_{bt}(\theta)}{b}}{V_{\Sigma C} * \rho_c(\theta)}\right)^{0.2} * \eta_{oil}^{-0.05} * R_a^{0.25} * X_L * tgh(\frac{V_s(\theta)}{v_o}) \qquad (13)$$

Then, three different procedures for calculation of FC has been considered in this work designed as (i) CFC (equation (11)), (ii) VFC1 (equation (12)), which considers the variation in the normal applied load and in the equivalent curvature radius and (iii) VFC2 (equation (13)), which includes an additional correction (by the sigmoid function, where v_o is the sliding speed threshold) to avoid the singularity when the contact takes place at the pitch point (the friction force at this instant must be null).

3   Results and Discussion

The geometric parameters of gear and pinion and the operating conditions described by Baglioni et al. [2] are assumed (Table 1) as a reference in order to

compare the proposed model (numerical approach) and the Baglioni et al. model [2] (analytical approach) for shifted gears.

Table 1 Operating conditions and pinion/gear parameters

Operating conditions	Power(kW)	Torque(Nm)	Speed(rpm)
OC1	25	159	1500
OC2	25	40	6000
OC3	50	159	3000
OC4	100	637	1500
OC5	100	159	6000
Main parameters			
Number of the pinion teeth	18	Module	3
Number of the gear teeth	36	Face width	26.7 mm
Pressure angle	20°	Mean Roughness	0.8 μm

The efficiency values calculated with the approach proposed by the authors, considering the three different FC alternatives described in the previous section, are presented in Fig 1. Those values are compared with those obtained from the work of Baglioni et al. [2] in each case.
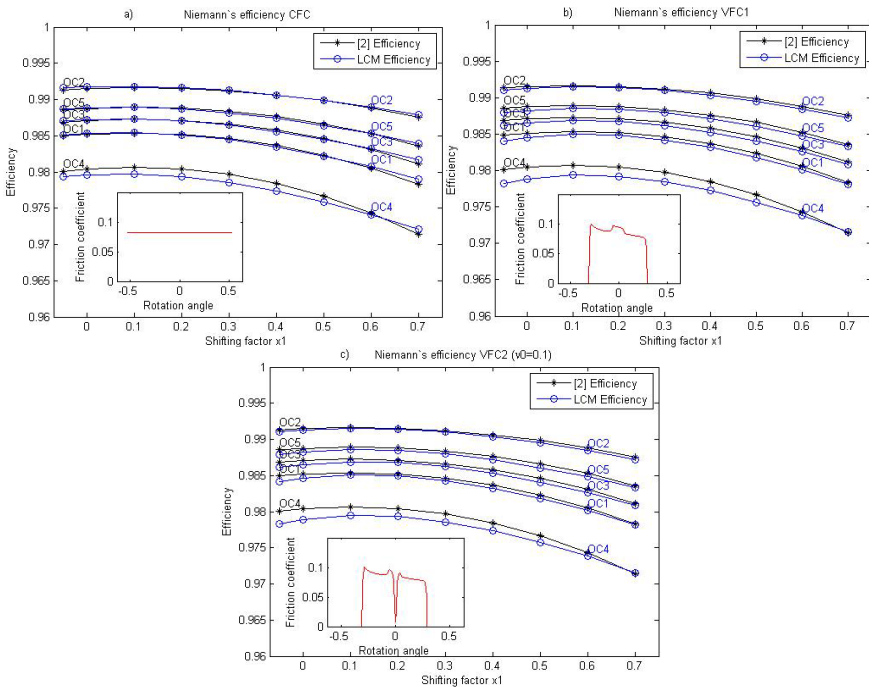
Fig. 1 Comparison between [2] and the LCM efficiency values for a) CFC, b) VFC1 and c) VFC2

As can be seen in Fig. 1, the difference between the efficiency values obtained by both approaches is acceptable. However, it can be seen that when torque is higher (OC4), the difference is bigger. The reason for this behavior is related to the gear body flexibility considered in the proposed model. As a consequence, deflections appear in gear teeth which are not in contact. Then, the starting contact point between pinion and gear occurs earlier than expected for the analytical approach and the ending contact point takes place later than expected, increasing the effective contact ratio. Hence, the analytical contact ratio obtained only taking into account kinematics effects is smaller than the real contact ratio which is considered in the proposed model, explaining why the LCM efficiency values are smaller than those in [2].

This effect is appreciated in Fig. 3, which shows the instantaneous power loss factor (H_{vinst}) for two different levels of applied torque.

$$H_{vinst} = \int_{A}^{E} \frac{\mu(\theta) * F_N(\theta) * V_s(\theta)}{F_{Nmax} * V} d\theta \tag{14}$$

Regarding the efficiency obtained for the three FC alternatives considered, the difference among them is less than 0.1%. That means that the effect of FC formulation has a negligible effect on the calculated efficiency. Otherwise, the torque effect is decisive in the efficiency calculation.
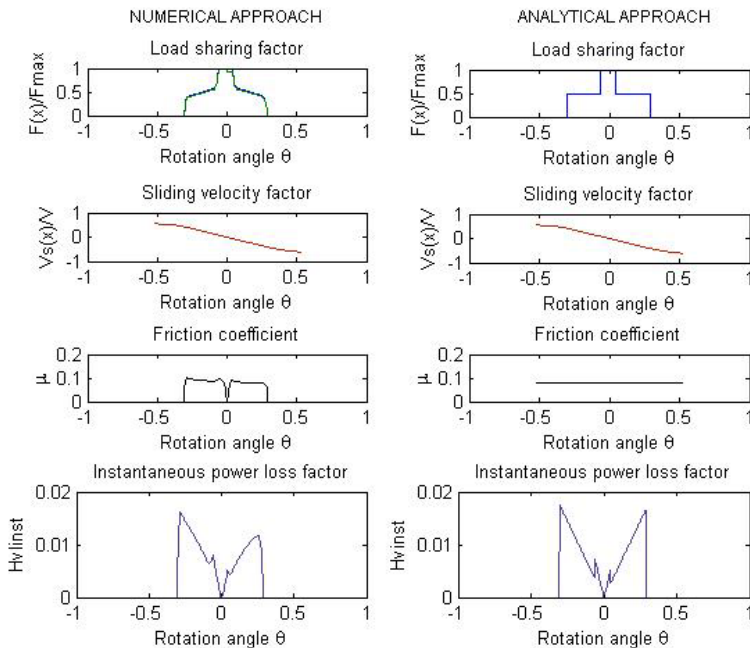
Fig. 2 Comparison between the two approaches. Load sharing, sliding velocity, friction coefficient and instantaneous power loss factor.

In order to explain better the differences between the numerical (with VFC2) and analytical approaches, in Fig. 2, the normalized quantities involved in the calculation of efficiency are presented. As can be seen in Fig. 2, the main difference is related with the FC and LS curves.

The FC is variable in the numerical approach while it is constant when the analytical formulation is considered. On the other hand, regarding LS, the numerical procedure gives a better description of the forces involved along the meshing period while the analytical approach considers a simplified formulation. Recent works [11, 13] considers that the most adequate FC formulation is variable and the LS as non uniform (numerical approach). Thus, it is acceptable to think that the numerical approach values describe better the real efficiency values than the analytical ones.

The difference in FC and LS results in a distinct instantaneous power loss factor as can be seen in Fig. 3. Then, after the integration in a mesh period, the numerical approach provides a greater power loss factor.
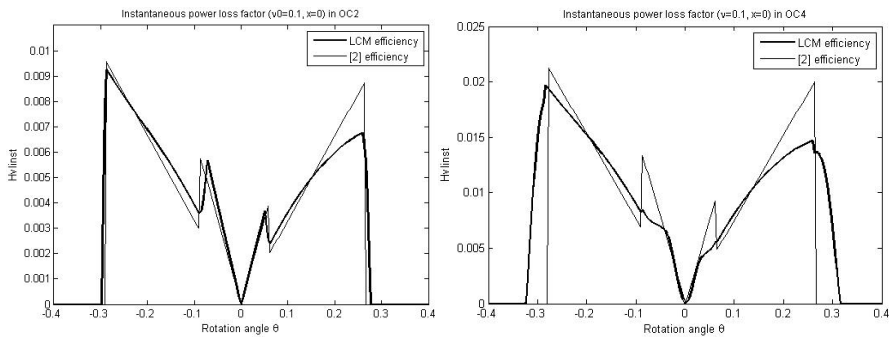
Fig. 3 Comparison between [2] and LCM power loss factor values
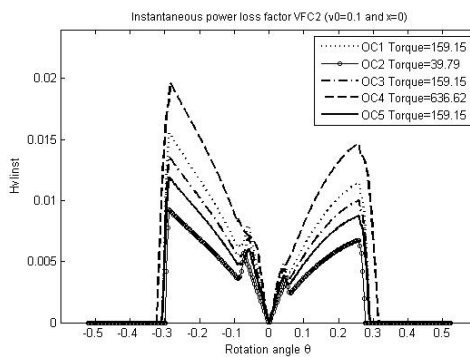
Fig. 4 Power loss factor variation when applied torque values change

In Fig. 4, it can be seen that the power loss factor depends on torque and angular velocity. The power loss factor is greater due to the torque effect rather than due to the angular velocity effect. If only torque is analyzed, the greater it is, the greater the power loss factor is. If the applied torque value is fixed, the power loss factor only depends on the angular velocity. If only angular velocity is analyzed, the lower it is, the greater the power loss factor is.

4   Conclusions

A methodology to calculate efficiency is implemented in the LCM previously developed by the authors [3-5]. Moreover, the model features has been extended in order to include the analysis of shifted gears as they are widely used in real transmissions. Particular attention is given to the formulation used in order to describe the friction coefficient which plays a main role in the power losses.

Several conditions of speed and torque have been analyzed by the proposed methodology and the results in terms of efficiency have been compared with those found in literature (Baglioni et al. [2, 7]) which were derived from an analytical simplified formulation. After comparison it was concluded that the proposed methodology provides similar results when the applied torque is lower than 300 Nm while gives lower efficiency values when the transmitted torque is higher.

This behavior is justified because of the extension of the effective contact ratio considered in the numerical model which takes into account the teeth deflection. Otherwise, the analytical formulation is based only on kinematic assumptions and therefore the contact ratio is not affected by the transmitted torque.

Hence, the choice of approach depends on the accuracy-computational load balance desired. In other words, if a qualitative efficiency calculation is required, the analytical approach is a good approximation of real efficiency values and no computational effort is needed. Nevertheless, if an accurate efficiency calculation is required (i.e in multi-stage transmissions), the analytical approach can overestimate the predicted efficiency and load contact models are needed.

The proposed model has been applied in a reduced number of cases providing valuable results, nevertheless a deeper assessment should be done considering the study of a wider range of transmissions and operation conditions.

References

1. Anderson, N.E., Loewenthal, S.H.: Effect of geometry and operating conditions on spur gear system power loss. J. Mech. Des. Trans. ASME 103(4), 151–159 (1981)
2. Baglioni, S., Cianetti, F., Landi, L.: Influence of the addendum modification on spur gear efficiency. Mechanism and Machine Theory 49, 216–233 (2012)
3. Fernandez Del Rincon, A., Iglesias, M., De Juan, A., Garcia, P., Sancibrian, R., Viadero, F.: Gear transmission dynamic: Effects of tooth profile deviations and support flexibility. Applied Acoustics (in press)

4. Fernandez del Rincon, A., Viadero, F., Iglesias, M., de-Juan, A., García, P., Sancibrian, R.: Effect of cracks and pitting defects on gear meshing. Proc. IMechE Part C: J. Mechanical Engineering Science 226(11), 2805–2815 (2012)
5. Fernandez Del Rincon, A., Viadero, F., Iglesias, M., García, P., De-Juan, A., Sancibrian, R.: A model for the study of meshing stiffness in spur gear transmissions. Mechanism and Machine Theory 61, 30–58 (2013)
6. Höhn, B.: Improvements on noise reduction and efficiency of gears. Meccanica 45(3), 425–437 (2010)
7. Maldotti, S., Botazzi, L., Menegolo, L., Molari, P.G.: L'influenza dello spostamento dei profili sulle perdite di potenza negli ingranaggi. In: Proceedings of 36th National Congress of AIAS, Naples, Italy (2007)
8. Martin, K.F.: A review of friction predictions in gear teeth. Wear 49(2), 201–238 (1978)
9. Michaelis, K., Höhn, B., Hinterstoißer, M.: Influence factors on gearbox power loss. Ind. Lubr. Tribol. 63(1), 46–55 (2011)
10. Ohlendorf, H.: Verlustleistung und erwärmung von stirnrädern (dissertation). TU München (1958)
11. Sánchez, M.B.: Modelo de cálculo resistente de engranajes cilíndricos de alto grado de recubrimiento (dissertation). UNED (2013)
12. Sánchez, M.B., Pleguezuelos, M., Pedrero, J.I.: Enhanced model of load distribution along the line of contact for non-standard involute external gears. Meccanica, 1–17 (2012)
13. Xu, H.: Development of a generalized mechanical efficiency prediction methodology for gear pairs (dissertation). The Ohio State University (2005)
14. Yada, T.: Review of gear efficiency equation and force treatment. JSME Int. J. Ser. C Dyn. Control Rob. Des. Manuf. 40(1), 1–8 (1997)

Interactive Geometric Design of Closed External Single-Range Gearing with Straight Toothing

A.A. Golovin and A.M. Duzhev

Bauman Moscow State Technical University, Russia
`aalgol@mail.ru, alexeyduzhev@ya.ru`

Abstract. Traditional method of geometric design of gearings involves number of simplifications such as taking into consideration only pole-based contact stress instead of using their distribution along line of contact. The purpose of the article is to propose alternative method for interactive geometric design without these disadvantages.

Keywords: Gearing, geometric design, interactive application, contact stress.

1 Introduction

Traditional geometric design of spur gearing is an itrative process [1]:

1. Source data: driven shaft load and rotating velocity; train ratio; train type; operation conditions; gear materials, machining, heat treatment etc.;
2. Preliminary selection of permissible stresses;
3. Preliminary selection of primary train parameters (center distance, number of teeth, module);
4. Selection of load factors and permissible contact stresses in accordance with previously selected parameters;
5. Decision-making of contact stresses value iteration start;
6. Bending check of derived gear;
7. Decision-making of bending stresses value iteration start.

There are two main formulas in the base of geometric design: the Hertz formula for contact between two cylinders with parallel axes and the formula for tooth bending stresses.

There are some doubts about 3, 5 and 7 items laying in:

- taking into consideration only pole-based contact stresses instead of their distribution along line of contact. It makes calculation simply but pole contact stresses are not maximal;
- good preliminary selection of train parameters depends on designer professional skill;

- there are no measures for optimization during stresses value iterations.

Profile correction factors are determined according to State standart for undemanding trains or for another reason [5].

According to this an alternative approach to geometric design of gear train on the basis of dimensionless analysis of train properties is proposed.

2 Dimensionless Properties of Involute Gearing

Parameters that define train properties:

- pressure angle α_w that defines distribution of contact stresses along contact line and minimum velue of contact stresses analogue;
- disposition of contact line depending on outside radiuses $r_{a1,2}$;
- base pitch p_b defining single-paired and double-paired contact lines.
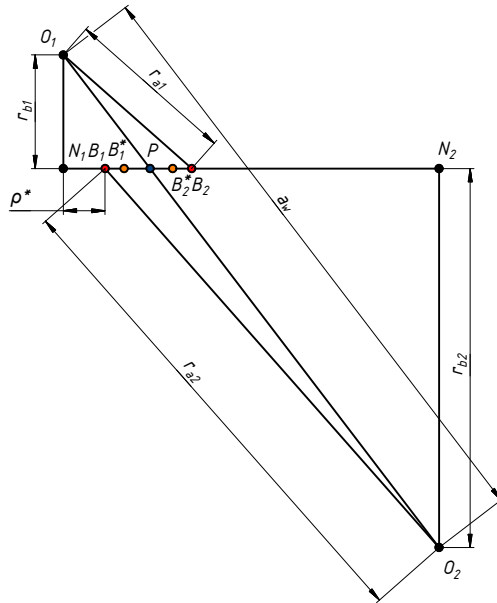
Fig. 1 Gear skeleton

Disposition of contact line and base pitch appoint gear efficiency and power dissipation on verges of single-paired and double-paired contact lines [2].

The notion of gear skeleton introduces to analyze geometry properties. Gear skeleton is a system of O_1, N_1, N_2, O_2 dots on plane (Fig. 1), where:
$O_1N_1 = r_{b1}$, $O_2N_2 = r_{b2}$ — rolling radiuses;

$O_1 = O_2 = a_w$ — center distance;
$\angle N_1 O_1 O_2 = \angle N_2 O_2 O_1 = \alpha_w$ — pressure angle;
P — pole;
$O_1 B_2 = r_{a1}, O_2 B_1 = r_{a2}$ — outside radiuses;
$B_1 B_2^* = B_2 B_1^* = p_b = p \cos \alpha$ — base pitch;
$\rho^* = \frac{N_1 B_1}{N_1 N_2}$.

Line of contact figures on the line of action with B_1, B_1^*, B_2^* and B_2 dots, where segments $B_1 B_1^*$ and $B_2^* B_2$ are double-paired contact lines and segment $B_1^* B_2^*$ is single-paired one.

Minimal number of teeth z_{min}, minimal profile correction factors x_{min}, allowable outside thickness S_{amin} and transverse contact ratio ε_α are constraints of this method while S_{amin} and ε_α constraints are not rigid. Besides, maximal values of contact stress locate on verges of contact line.

As in the traditional method [1], the Hertz formula uses to get value of contact stresses (Poisson's ratio takes equal to 0.3):

$$\sigma_H = 0{,}418 \sqrt{\frac{E Q^n}{b} \left(\frac{1}{\rho_1} + \frac{1}{\rho_2} \right)}. \tag{1}$$

Dimensionless criteria that determine gear properties area 2:

- contact stress analogue (geometric component of Hertz formula) $\sigma = \sigma_Q \sigma_\rho$, where

$$\sigma_Q = \sqrt{\frac{Q^n}{Q_{max}^n}}, \tag{2}$$

$$\sigma_\rho = \sqrt{\frac{1}{\rho_1 / r_{b1}} + \frac{1}{\rho_2 / r_{b1}}}; \tag{3}$$

- power dissipation analogue $f \sigma \frac{v_{s1}}{v^\tau}$, where
  f — constant of kinetic friction;
  v_{s1} — slide velocity;
  v^τ — tangential velocity of point on the one of profiles.

Good lubrication removal is typical for closed gearing we consider. So contact strength is main criterion, bending strength is additional criterion and contact stress analogue is dimensionless one.

Thereafter contact stresses distribution along line of contact is determined by two parametres: pressure angle α_w and location of the point of contact start B_1 (by dimension ρ^*). Fig. 2 shows examples of σ_ρ distribution for different values of α_w (Fig. 2a) and σ distribution for different locations of B_1 dot (dimension ρ^*) (Fig. 2b).
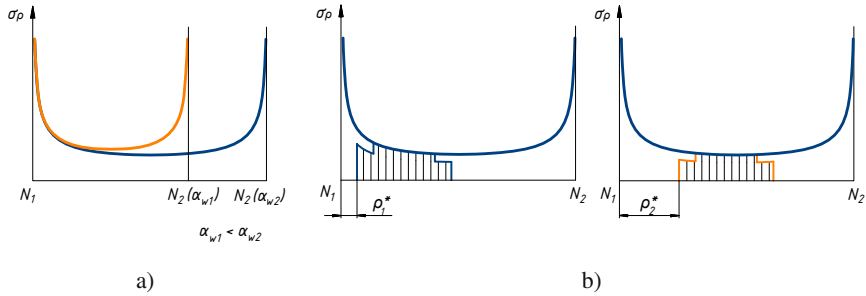
Fig. 2 α_w and ρ^* effect on σ distribution

Therefore, method consists in two-studied iteration:

- dimensionless stresses analogue analysis with fixed α_w and ρ^* variation with subsequent getting of action length $N_1 N_2$, rolling radiuses $r_{b1,2}$ and center distance a_w by using the Hertz formula;
- getting value of Q^n force (from specified torque M_1 or M_2), module m, tooth counts z_1 and z_2 with correction of results.

3   Gearing Geometric Design Application Software

According to these viewpoints, gearing geometric design sequence is offered:

1. Setting the value of pressure angle α_w.
2. Determination of action line relative length:

$$\overline{N_1 N_2} = (u+1)\tan\alpha_w. \tag{4}$$

3. Setting the location of B_1 dot (dimension ρ^*) on the base of σ_ρ distribution along line of action analysis.
4. Determination of $\sigma_{\rho B_1}$:

$$\sigma_{\rho B_1} = \sqrt{\frac{1}{\overline{N_1 N_2}\rho^*(1-\rho^*)}}. \tag{5}$$

5. Determination of constant component of the Hertz formula:

$$A^2 = \frac{[\sigma_H]^2}{\sigma_{\rho B1}^2}. \tag{6}$$

6. Determination of center distance:

$$\alpha_w = \sqrt[3]{0.174\frac{EM_1(u+1)^2}{A^2\psi_{ba}\cos^2\alpha_w}}. \tag{7}$$
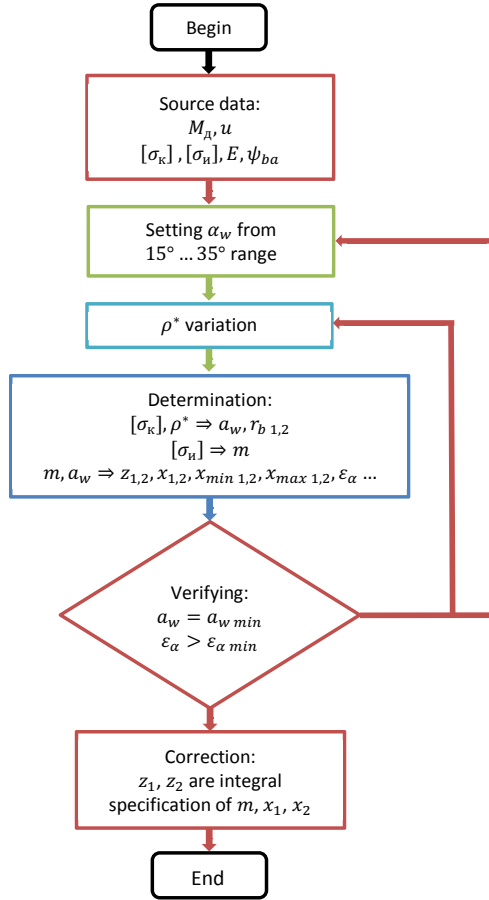
Fig. 3 Block diagram of the offered algorithm

7. Determination of module:

$$m = 5.33 \frac{M_1(u+1)}{a_w^2 \cos \alpha_w \psi_{ba} [\sigma_b]}.$$ (8)

8. Determination of teeth number, profile correction factors etc. Correction of module value with standard series with subsequent recalculation of gear parameters.
9. Leap to item 1 or 3.
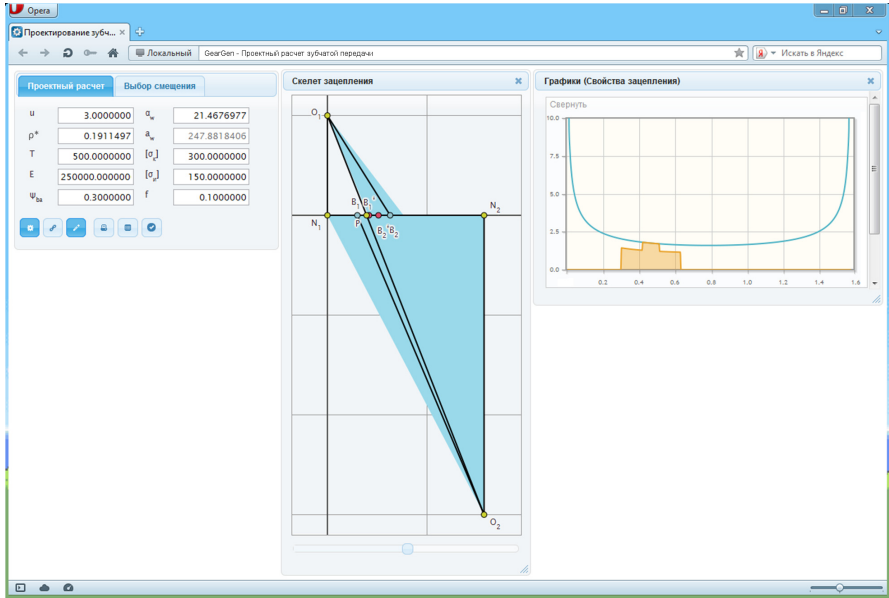
Fig. 4 GearGen graphic interface

4 The GearGen Program

The block diagram of the algorithm executed by the interactive application software
GearGen is presented on Fig.3. The program enables numerical and graphic modes
of gearing geometric design. Graphic interface lets change gear parameters by sight.
This lies in direct dragging of B_1 and N_2 dots along line of action. With N_2 dragging
the pressure angle α_w varies in the range of $15°...35°$. Thus two iteration cycles (ρ^*
and α_w) are realized.

GearGen graphic interface is introduced on Fig.4.

On the left side of the window one can see text fields for numerical data input.
The first tab contains parameters of geometric design: u, M_1, E, ψ_{ba}, $[\sigma_H]$, $[\sigma_b]$, α_w,
ρ^* and read-only parameter a_w. The second tab contains parameters of correction
stage: z_1, z_2, m, α_w, x_1 and read-only parameter x_2.

In the center of window one can see gear skeleton with scale slider under it. Blue
areas show permissible zones for B_1 and B_2 dots.

On the right side of the window there is a graph panel with σ and σ_ρ distributions
diagram shown.

There are six buttons under the data panel. The first three of them control panel's
state (hidden/shown), the second three are to print and show skeleton and additional
parameters (σ_H, σ_b, η etc.) of gear and to start calculation.

5   Examples of the Comparative Gear Analysis

There are two design tasks below that were solved with traditional ([1]) and proposed methods. Allowable contact and bend stresses were used as the basis.

Task 1. Source data: $M_1 = 200\,N \cdot m$, $u = 3$, $\psi_{ba} = 0.15$, $[\sigma_H] = 580\,MPa$, $[\sigma_b] = 210\,MPa$.

Task 2. Source data: $M_1 = 180\,N \cdot m$, $u = 5$, $\psi_{ba} = 0.15$, $[\sigma_H] = 700\,MPa$, $[\sigma_b] = 240\,MPa$.

Results of the calculations carried out in the range of $15°...35°$ are shown in the Fig.5 for Task 1 (grafical interpretation) and the tables 1 (Task 1), 2 (Task 2).
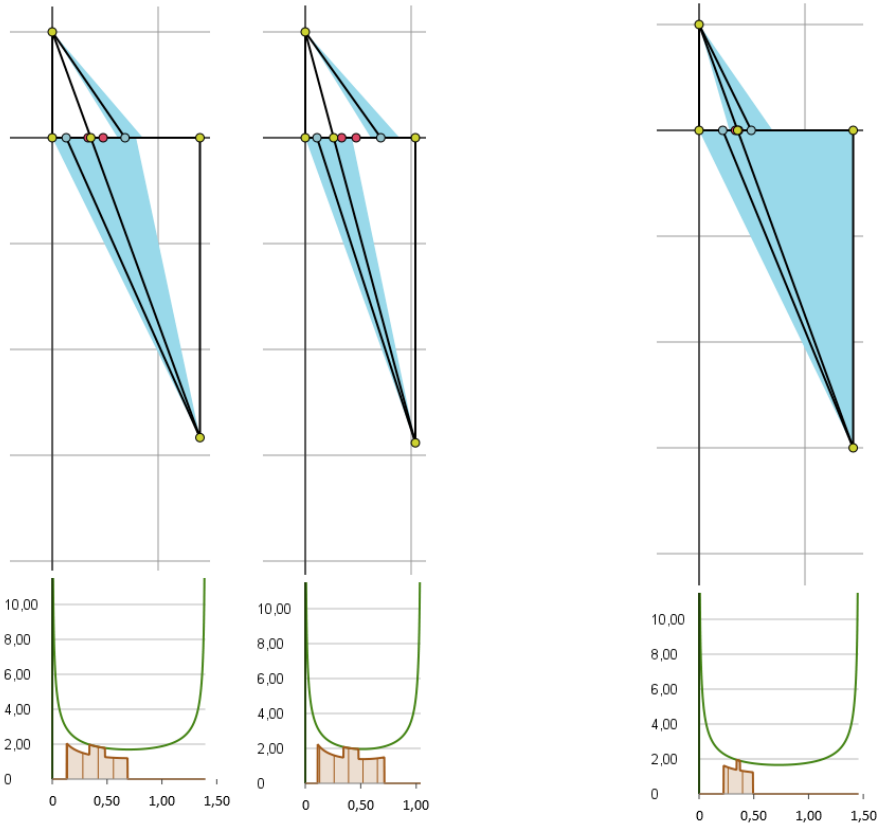
Fig. 5 Graphic results of geometric design (Task 1)

We managed to obtain less center distance a_w and, accordingly, less overall dimensions in comparison with traditional method calculation results in the researched tasks.

Table 1 Results of geometric design (Task 1)

Method	α_w	z_1	z_2	x_1	x_2	$\sigma_{\rho\,min}$	σ_{max}	ε_α	a_w, mm	m, mm
GearGen	20°	18	51	0.263	−0.263	1.693	2.047	1.592	172.5	5.0
GearGen	15°	17	49	0.414	−1.208	1.961	2.247	1.631	160.5	5.0
Traditional method [1]	20°	42	126	0	0	1.693	1.952	1.799	210.0	2.5

Table 2 Results of geometric design (Task 2)

Method	α_w	z_1	z_2	x_1	x_2	$\sigma_{\rho\,min}$	σ_{max}	ε_α	a_w, mm	m, mm
GearGen	20.7°	17	85	0.202	0.038	1.315	2.298	1.596	204.9	4.0
GearGen	15°	17	85	0.422	−1.649	1.577	2.220	1.608	198.5	4.0
Traditional method [1]	20.7°	24	122	0.500	−0.161	1.319	1.747	1.583	220.0	3.0

6 Conclusions

1. Proposed method and software application GearGen let perfomance of multi-version interactive gearing geometric design and are able to become a basis for computer-aided search of the best solution.
2. Comparative analysis of traditional ([1]) and proposed methods (GearGen application) shown advantage of the last one in case of geometric design of closed external single-range gearing with straight toothing performing in accordance with contact stresses minify criteria.

References

1. Reshetov, D.N.: Machinery. Manual for students ofengineering and mechanical specialties. 496 p. (1989) (in Russian)
2. Golovin, A.A.: Higher pair: deterioration geometric analogues, cam machinery and gearings. Electronic Manual (2009) (in Russian)
3. Golovin, A., Borisov, A., Ermakova, A.: Some Examples from History of Machinery in TMM Teaching. In: Proceeding of International Symposium on History of Machines and Mechanisms, pp. 107–118. Kluwer Academic Publishers (2004)
4. Golovin, A., Lafitsky, A., Simushkin, A.: Experimental and Theoretical Research of Cams Wearing of Cams Mechanism. In: Ceccarelli, M. (ed.) Proceeding of EuCoMes 2008, pp. 343–350. Springer (2008)
5. Bolotovskaya, T., Bolotovsky, I., Bocharov, G., et al.: Involute and worm gearings geometric calculation guide (1962) (in Russian)

Adaptive Mechanical Continuously Variable Transmission

K.S. Ivanov[1], A.D. Dinassylov[2], and E.K. Yaroslavceva[3]

[1] Institute of Mechanics and Machine Science after Acad. U.A. Djoldasbekov, Kazakhstan, Almaty University of Power Engineering and Telecommunications, Kazakhstan
ivanovgreek@mail.ru

[2] Almaty University of Power Engineering and Telecommunications, Kazakhstan
adinasylov@yandex.ru

[3] Saint-Petersberg State University of Technology and Design, Russia
yaroslavceva_elena@rambler.ru

Abstract. Adaptive mechanical CVT is executed as differential with the closed contour containing toothed wheels. Kinematic chain of differential with two degree of freedom has an additional geometric constraint, which provides mechanical adaptation to variable technological loading. Work is devoted the kinematic and power analysis and synthesis of adaptive mechanical transmission.

Keywords: adaptive transmission closed contour, synthesis.

1   Introduction

Recently the patents and publications with the description of the self-controlled mechanism in the form of kinematic chain with two degrees of freedom have appeared. Idea of creation the stepless adaptive transmission with constant cogging of toothed wheels in the form of hydrodynamic converter and gear differential with two degree of freedom is presented in patents of S. Croquet [1] and I. Volkov [6]. Mechanism with two degree of freedom and with one entry in the form of gear differential is presented in J. Harries's patent [2]. Various alternatives of designs of gear adaptive transmission in the form of gear differential with two degree of freedom are presented in K. Ivanov's patents [3 and 4]. An additional constraint between links of mechanism with two degree of freedom takes place if the mechanism has a closed contour. It has been theoretically proved in article [5]. The present work is devoted the description of adaptive mechanical continuously variable transmission (CVT) with the additional constraint providing mechanical adaptation to variable load. Work is executed on the basis of regularities of mechanics and mechanisms and machines theory.

2   Research of Motion of Kinematic Chain with Two Degree of Freedom by Means of Picture of Speeds

The investigated adaptive mechanical transmission looks like gear differential with two degree of freedom (Fig. 1). The differential contains rack 0, carrier H_1, satellite 2, block of central wheels 1-4, block of ring wheels 3-6, satellite 5 and carrier H_2. Toothed wheels are forming a closed contour 1-2-3-6-5-4. Sizes of toothed wheels 1, 2, 3, 4, 5, 6 are defined by matching radiuses r_i $i = 1, 2, 3, 4, 5, 6$. Radiuses of carriers are next: $r_{H1} = r_1 + r_2$, $r_{H2} = r_4 + r_5$.
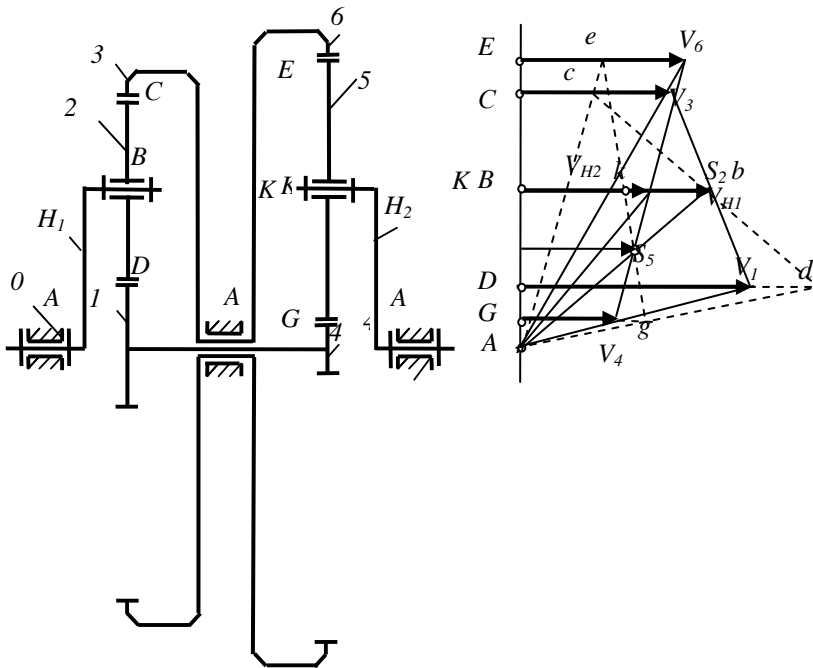
Fig. 1 Gear differential mechanism and a picture of speeds

Picture of links speeds V_i $i = 1, 2, 3, 4, 5, 6$ is presented to the right of mechanism. Linear speeds are next: $V_i = \omega_i r_i$. Linear speeds of carriers are next: $V_{Hi} = \omega_{Hi} r_{Hi}$, $i = 1, 2$.

The initial picture of speeds is shown by full lines. The intermediate picture of speeds is shown by dashed lines. Carrier H_1 angular speed is defined by line Ab. Satellite 2 angular speed is presented by the inclined line, which is passing through point b matching to carrier H_1 point B. Satellite 5 angular speed is presented by the inclined line, which is passing through point k matching to a

carrier H_2 point K. Intermediate picture of speeds is presented by dashed lines. Intersection point S_5 of satellite 5angular speed line eg with carrier H_1 angular speed line Ab is instantaneous centre of turn of satellite 5 concerning carrier H_1. We will prove that satellite 5 instant centre S_5 will have constant position on carrier H_1 angular speed line Ab.

Theorem. In differential wheelwork containing two carriers, two satellites and two blocks of central wheels the satellite has constant instant centre of relative turn on the opposite carrier.

For the demonstration we will consider at first kinematic chain picture of speeds in inverse motion at the motionless carrier H_1 when $V_{H1} = 0$ (Fig. 2). Intersection point S_5 of satellite 5 angular speed line eg with vertical line of zero speeds is the instantaneous centre of turn of satellite 5 concerning motionless carrier H_1. The point S_5 position (size $y = BS_5$) can be univocal determined through mechanism geometric parameters.

Let's define a point S_5 position using similitude of triangles.

The sequence of formulation of the equations matches to sequence of geometrical constructions of picture of speeds on Fig. 2.

1) $\dfrac{Cc}{Ee} = \dfrac{r_3}{r_6}$, $\dfrac{Dd}{Gg} = \dfrac{r_1}{r_4}$. As, $Cc = Dd$

$$\frac{Ee}{Gg} = \frac{r_1 r_6}{r_3 r_4}. \tag{1}$$

2) $\dfrac{Kk}{Ee} = \dfrac{y}{r_5 + y}$, $\dfrac{Kk}{Gg} = \dfrac{y}{r_5 - y}$. From here

$$\frac{Ee}{Gg} = \frac{r_5 + y}{r_5 - y}. \tag{2}$$

From (1) and (2) it is following $\dfrac{r_1 r_6}{r_3 r_4} = \dfrac{r_5 + y}{r_5 - y}$. From here

$$y = r_5 \frac{r_1 r_6 - r_3 r_4}{r_1 r_6 + r_3 r_4}. \tag{3}$$

Eq. (3) is determining the position of instantaneous centre of turn of satellite 5 concerning motionless carrier H_1 univocal. In the valid motion of the mechanism the point S_5 will move together with the carrier H_1 as it is shown in picture of speeds of the moving mechanism (Fig. 1). Hence, satellite has constant instant centre of relative turn on the opposite carrier as was to be shown.
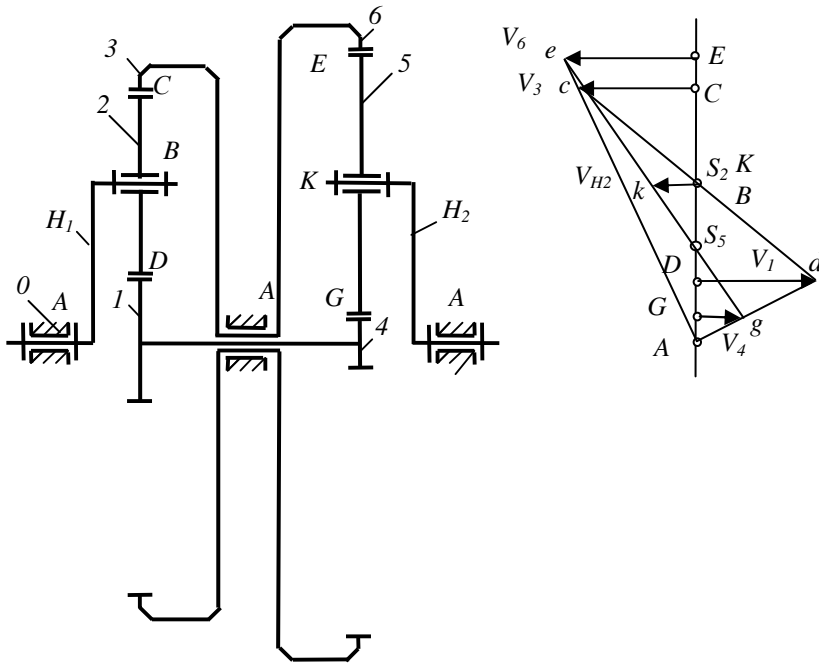
Fig. 2 Gear differential mechanism and picture of speeds of the mechanism in the inverce motion at motionless input carrier

The invariable position of instant centre S_5 on carrier H_1 defines an additional geometric constraint, which takes place in the kinematic chain with two degree of freedom. However, this additional constraint has no constructive performance. The mechanism is remaining the kinematic chain with two degree of freedom mechanically and is keeping the properties of such chain.

Eq. (3) is expressing this additional geometric constraint analytically. As a result, the kinematic chain is becoming definable at presence only one input link. It means that at the given angular speed of the input carrier it is possible to determine speeds of all other mechanism links and points.

The found regularity allows building the conditional replacing mechanism with one degree of freedom (Fig. 3). In the replacing mechanism output satellite is executed in the form of block of wheels 5-7 and affiliated by the higher kinematic pair coinciding with the instant centre to the gear ring 8 on input carrier. The conditional mechanism will move as a single whole without relative mobility of wheels in the closed contour. However, the picture of speeds (Fig. 1) admits relative motion of links for the replacing mechanism. Hence, constructive additional constraint in the form of cogging of toothed wheels 7, 8 of conditional replacing mechanisms is passive.
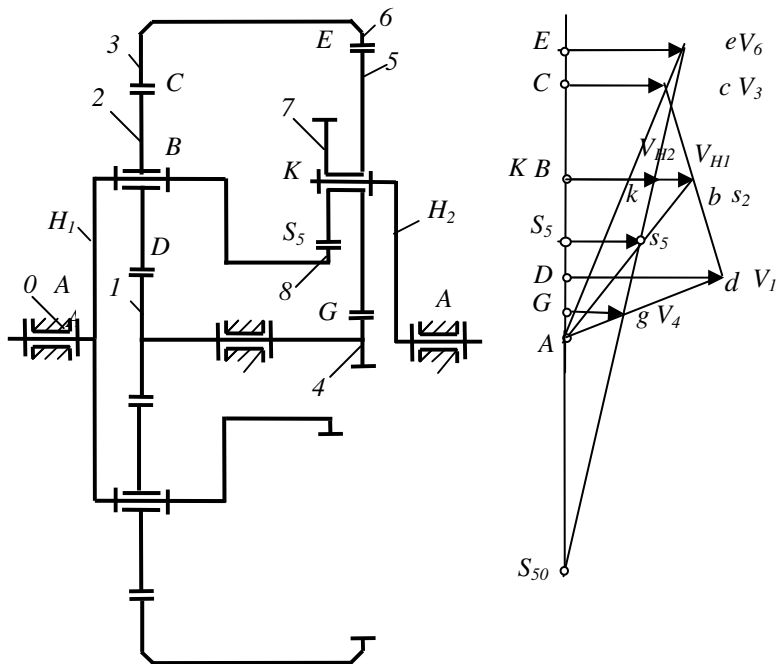
Fig. 3 Conditional replacing mechanism with one degree of freedom and picture of speeds

3 Power Analysis of Adaptive Mechanical Transmission

Considered kinematic chain with two degree of freedom contains two links having generalized co-ordinates (carriers H_1 and H_2) and closed contour affiliated to them containing toothed wheels 1-2-3-6-5-4 having zero mobility.

Statement of problem: two generalized forces (the moments of forces M_{H1}, M_{H2} on carriers H_1 and H_2) are given. It is necessary to determine reactions in kinematic pairs.

Solution

1) Next reactions are transferred from carriers H_1 and H_2 on satellites 2 and 5 of closed contour:

$$R_{H1} = M_{H1} / r_{H1}, \quad R_{H2} = M_{H2} / r_{H2}. \tag{4}$$

2) Reaction R_{H1} in point B and reactions $R_{12} = R_{32} = R_{H1} / 2 = M_{H1} / 2r_{H1}$ in points D and C are acting on satellite 2.

Condition of satellite 2 equilibrium is represented in the form of equality to null of the moments concerning the instant centre of speeds S_{20} (Fig. 3)

$$R_{12} \cdot DS_{20} + R_{32} \cdot CS_{20} = R_{H1} \cdot BS_{20}. \tag{5}$$

3) It is analogous reaction R_{H2} in point K and reactions $R_{45} = R_{65} = R_{H2} / 2 = M_{H2} / 2r_{H2}$ in points G and E are acting on the satellite 5. Condition of equilibrium of satellite 5 presented in the form of equality to null of moments concerning the motionless instant centre of speeds S_{50} (it is not shown at Fig. 3)

$$R_{45} \cdot GS_{50} + R_{65} \cdot ES_{50} = R_{H2} \cdot KS_{50}. \tag{6}$$

4) We will multiplication Eq. (5) on ω_2. With the account $\omega_2 \cdot DS_{20} = V_1$, $\omega_2 \cdot CS_{20} = V_3$, $\omega_2 \cdot BS_{20} = V_{H1}$ we will gain

$$R_{12} \cdot V_1 + R_{32} \cdot V_3 = R_{H1} \cdot V_{H1}. \tag{7}$$

We will multiplication Eq. (6) on ω_5. With the account $\omega_5 \cdot GS_{50} = V_4$, $\omega_5 \cdot ES_{50} = V_6$, $\omega_5 \cdot KS_{50} = V_{H2}$ we will gain

$$R_{45} \cdot V_4 + R_{65} \cdot V_6 = R_{H2} \cdot V_{H2}. \tag{8}$$

Let's add Eq. (7) and Eq. (8)

$$R_{12} \cdot V_1 + R_{32} \cdot V_3 + R_{45} \cdot V_4 + R_{65} \cdot V_6 = R_{H1} \cdot V_{H1} + R_{H2} \cdot V_{H2}. \tag{9}$$

Eq. (9) is containing the forces acting on the closed contour from toothed wheels 1-2-3-6-5-4 affiliated to two carriers (generalized co-ordinates). The left side of Eq. (9) is representing the sum of powers (or works) of internal forces of the closed contour. The right side of Eq. (9) is representing the sum of powers (or works) external forces of the closed contour. We will consider a kinematic pairs of the closed contour as ideal pairs (without friction). Then

$$R_{12} \cdot V_1 + R_{32} \cdot V_3 + R_{45} \cdot V_4 + R_{65} \cdot V_6 = 0. \tag{10}$$

From Eq. (9) is following

$$R_{H1} \cdot V_{H1} + R_{H2} \cdot V_{H2} = 0. \tag{11}$$

Taking into account expressions (4) we will gain

$$M_{H1} \cdot \omega_{H1} + M_{H2} \cdot \omega_{H2} = 0. \tag{12}$$

From Eq. (12) is following: one of the generalized forces should be negative. It is necessary to consider, for example, that M_{H2} is moment of resistance on output carrier H_2 and M_{H1} is driving moment on input carrier H_1. Thus it will appear that in the kinematic chain with two degree of freedom and with the closed contour only one link (input carrier H_1) can have generalized co-ordinate (independent angular speed ω_{H1}). Such kinematic chain will have the kinematic

definability as Eq. (12) allows at the given moments M_{H1} and M_{H2} to determine output angular speed ω_{H2}.

Hence, the kinematic chain with two degree of freedom and with the closed contour at presence only one entry will have static and kinematic definability and will be the mechanism.

From Eq. (12) following

$$\omega_{H2} = \frac{M_{H1} \cdot \omega_{H1}}{M_{H2}} . \qquad (13)$$

Eq. (13) is expressing effect of power adaptation. At the given constant parameters M_{H1} and ω_{H1} of input power the output angular speed ω_{H2} is inversely proportional to given variable output moment of resistance M_{H2}. We will name the mechanism, which is creating the effect of power adaptation as the adaptive mechanism.

4   Synthesis of Gear Adaptive Differential Mechanism

Synthesis of gear adaptive differential mechanism consists in determination of wheels teeth numbers and the carriers sizes for maintenance of a demanded range of transmission ratios

$$u_{12} = \frac{\omega_{H1}}{\omega_{H2}} = \frac{M_{H2}}{M_{H1}} .$$

Range of transmission ratios will change in following limits $1 \le u_{12} \le u_{12\max}$.

From Eq. (6) we have $(M_1 - M_4) \cdot \omega_1 + (M_3 - M_6) \cdot \omega_3 = 0$.

Where M_1, M_4 - the driving moment and the resistance moment on the block of wheels 1-4, M_3, M_6 - the driving moment and the resistance moment on the block of wheels 3-6. The maximum value of output moment of resistance takes place when on one of blocks of wheels there is equilibrium $M_1 = M_4$. Numbers of wheels teeth get out under the formulas resulted in (4).

5   Conclusions

It is proved that kinematic chain with two degree of freedom containing the closed contour has an additional geometric constraint which provides definability of a chain in the presence of one entry. Additional constraint occurs in a picture of speeds of a chain in the form of the instant relative centre of speeds of the satellite and the carrier. This additional constraint can be presented mechanically as passive superfluous constraint. Additional constraint analytically connects force and kinematic parameters of an entry and an exit. This additional analytical constraint

is expressing effect of power adaptation which is providing an overcoming of variable target loading at a constant input power. Mechanical properties of the closed contour are allowing to provide the demanded transfer ratio independently, continuously and automatically without any control.

References

1. Crockett, S.J.: Shiftless, continuously-aligning transmission. Patent of USA 4,932,928, Cl. F16H 47/08, U.S. Cl. 475/51; 475/47, 9 p. (1990)
2. John, H.: Power transmission system comprising two sets of epicyclic gears. Patent of Great Britain GB2238090 (A), 11 p. (1991)
3. Ivanov, K.S., Yaroslavtseva, E.K.: Way of automatic and continuous change of a twisting moment and speed of twirl of the output shaft depending on a tractive resistance and the device for its realization. Patent of Russia RU No. 2398989, 10 p. (September 10, 2010)
4. Ivanov Konstantin, S.: Almaty, KAZ - Owner of the registered sample. The name - Device of automatic and continuous change of a twisting moment – and changes of a corrected speed of output shaft depending on a tractive resistance. The deed on registration of the registered sample No. 20, 101 273.1. Day of Registration 02.05.2012. German patent and firm establishment. Federal Republic Germany, 12 p. (2012)
5. Ivanov, K.S.: Paradox of mechanics – a basis of creation CVT. In: Transactions of 2-d IFToMM Asian Conference on Mechanisms and Machines Science, Tokyo, Japan, November 7-10, pp. 245–264 (2012)
6. Volkov, I.V.: Way of automatic and continuous change of a twisting moment and speed of twirl of the output shaft depending on a tractive resistance and the device for its realization. The invention description to the patent of Russia RU 2 234 626 from 27.03.2004

Design and Characterization of a New Planetary Gear Box

G. Balbayev[1] and Marco Ceccarelli[2]

[1] Almaty University of Power Engineering and Telecommunication, Kazakhstan
  gani_b@mail.ru
[2] University of Cassino and Southern Lazio, Italy
  ceccarelli@unicas.it

Abstract. The aim of the paper is to present a differential planetary gear box. A basic modeling has been formulated to characterize both its design and operation. At constant power input the planetary gear box is able to provide variable speed of the output link. The main purpose of the differential transmission is on the capability to adapt the operation to variable loading. Designed adaptation provides a motion of output link with a speed that is inversely proportional a loading of the link. This enables to use the differential planetary gear box in the transmissions of vehicles, metal cutting tools and in transmissions where it is necessary smooth control of gear ratio.

Keywords: Mechanical Transmission, Gears, Planetary Gears, Design, Analysis.

1   Introduction

In many applications in industry for automobiles, textile, shipping, aerospace, agriculture gear boxes are used extensively. They use different kinds of gear boxes such as automatic gear boxes, manual gear boxes, differential gear boxes, planetary gear boxes. A gear box is a set of gears for transmitting power from one rotating shaft to another. The gears also are used in differential drives of automobiles, final drives of tractors and heavy machineries mainly as reducer. In general planetary gear boxes have lower occupied space and more velocity reduction than other gear boxes, [10].

For example, a gear box with conical gears as a speed reducer consists of 8 conical gears. Two of them are horizontal and 6 pinions are located vertically. Each pairs of pinions are locked together. But in this mechanism design in order to obtain any speed ratios it is necessary to change value of pinion or horizontal gear, [12].

Alternatively cam-based infinitely variable transmission can be used for continuously variable transmission, which can also achieve any transmission ratio. This mechanism consists of two main parts, namely a cam mechanism and a

planetary gear set. Cam-based CVT (continuously variable mechanism) is more complex than others, [2].

Other solutions are magnetic planetary gears, which consist of a sun gear, four planetary gears and a ring gear. Each gear must have an axially magnetized permanent magnet that is sandwiched between two yokes made of electromagnetic soft iron. Magnetic gears have main advantage for a low mechanical loss, but in this mechanism the transmission torque is usually very low, [9].

Planetary gear train with non-circular gears consists of a planet arm, an external gear, intermediate gear and a central gear. This mechanism can be used to generate a variable angular-velocity ratio, [8].

This paper describes a new design of a planetary gear box with two degrees of freedom as differential gear box. It has input and output carriers, two internal gears that are fixed together, two central gears that are fixed together, input and output satellites. This mechanism can be classified as CVT solution since consists only of a planetary gear set. This mechanism is able to adapt its operation to the external applied load, [4, 5, 6]. This paper is aimed to present a new solution for improving efficiency of planetary gear box with two degrees of freedom.

2   Problems for a Gearbox

A mechanism is termed as a planetary mechanism if it contains at least one rigid body which is required to rotate about its own axis and at the same time to revolve about another axis, [7]. Points of this body will generate epicycloids or hypocycloids trajectories. Therefore a planetary mechanism is often called as an epicyclic or cyclic mechanism. A planetary mechanism can be obtained by mounting a rigid body, often referred to as a planet, on a crank pin. The crank is generally called the arm or carrier, [7].

There are several kinds of planetary gear boxes, [7]. Usually planetary gear boxes are composed as shown in the Fig. 1 with a central (sun) gear 1, satellites 4, carrier 3 and epicyclic internal gear 2. Satellites which are hold by carrier, rotate with the carrier around the sun gear. Satellites rotate around their own axes and they rotate around sun gear, but internal gear is fixed. Planetary gears can transmit high torques when compared with other types of transmission. This is because the torque is transmitted by several satellites which can significantly reduce contact pressure on the surfaces of the teeth.

Planetary gears can also be used for stepless transmissions. In this case the mechanism can independently change the gear ratio depending on the load appeared relatively suddenly. This is a mechanism with constant mesh gears as energy transfer device with a continuously variable transmission ratio, [3]. The mechanism is designed as a differential mechanism with two degrees of freedom. It consists of input and output carriers with satellites and the block of the central (sun) gears, the block epicyclic gears, a starting part and a brake. This transmission can independently change the gear ratio depending on the load. In the beginning brake fixes internal gears and transmission will be have one degree of
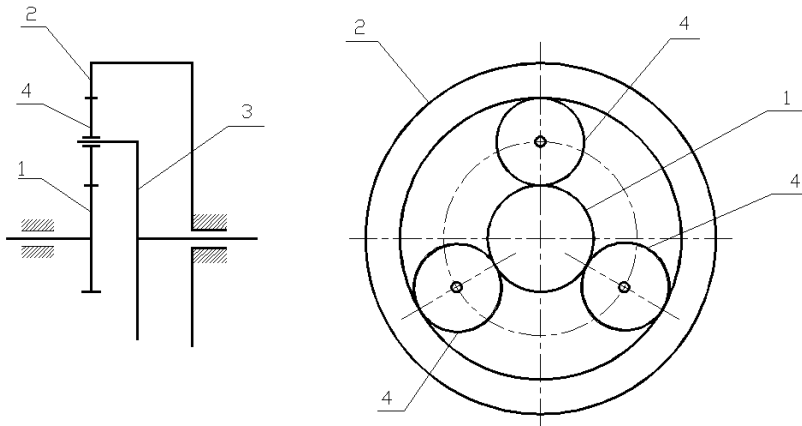
Fig. 1 A general design of planetary gear boxes, [11]

freedom. Transmission can not make force which satellite should to transfer to the output carrier and the output shaft. To start a movement it is necessary to use a brake. A brake stops the block of epicyclic gears and system will be transformed to a system with movable output carrier and fixed ratio. After braking motion begins and the system can work with two degrees of freedom.

In the case continuously transmission, this transmission operates as a hydrodynamic converter and differential mechanism. In this scheme the pump wheel of the hydrotransformer is rigidly connected to the block of the central wheels. The turbine wheel of the hydrotransformer is rigidly connected with input carrier. The torque converter provides an additional differential constraint in the differential gear mechanism with two degrees of freedom, [1]. It provides automatic adaptation of the variable ratio to external loading. Disadvantages of this mechanism are low efficiency due to the use of hydrodynamic converter, low speed range and low reliability at startup.

The above transmissions have main advantage in the possibility to change gear ratio to adapt to a load change. The attached problem can be summarized in a design search for a system with gear box solution with capability of adapting the operation to load change by preserving efficiency and input-output ratio.

3 A Proposal for a New Gear Box

The herein proposed differential planetary gear set is a continuously variable transmission. It consists of a mechanical planetary gear set without additional device such as torque converter or electronic parts. Basic principles of this type of gear box are presented by Ivanov in [4, 5, 6]. In this paper a new solution is considered for improving the efficiency of differential planetary gear box. General design characteristics practical applications for wind turbine installation can be

identified in dimensions with a diameter of 180 mm, a longitudinal size of 95 mm and for a overall weight 3 kg. These parameters have been used for design and simulation of the mechanism.

The new planetary gear box is conceived with two degrees of freedom with a mechanism consisting of an input carrier H_1, an output carrier H_2, central (sun) gears 1 and 4 which are fixed on a shaft, satellites 2 and 5, central internal gears 3 and 6 which are fixed together, Fig. 2.

(a)   (b)
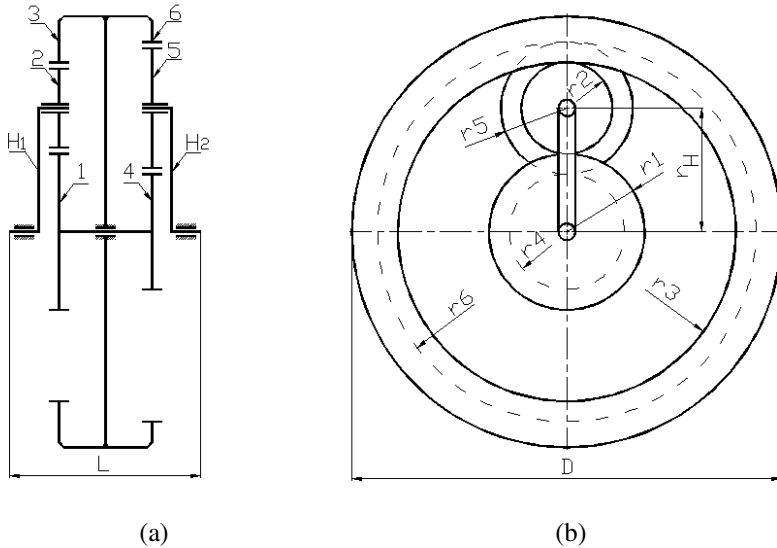
Fig. 2 A kinematic scheme for the new planetary gear box: (a) H_1-input carrier, 1-input sun gear, 2-input satellite, 3-input epicyclic gear, 4-output sun gear, 5-output satellite, 6- output epicyclic gear, H_2-output carrier; (b) r_H-radius of carrier, r_1-radius of sun gear, r_2-radius of input satellite, r_3-radius of input internal gear, r_4-radius of output sun gear, r_5-radius of output satellite, r_6-radius of output internal gear

Gears 2-3-6-5-4-1 form a closed mechanical chain with a differential operation. Carrier H_1 transfers input driving force to the closed mechanical chain and carrier H_2 transfers output resistance force. Motion starts at fixed output carrier with one degree of freedom. At this time satellite 5 is output link. To transmit motion from input carrier H_1 to output carrier H_2 satellite 5 must be locked and this can be obtained thanks to friction at gear contacts. The input carrier H_1 moves gear 2 that pushes both gears 1 and 3 that transmit different forces to gears 6 and 4 correspondingly. Thus, gear 5 moves by different forces coming from its contacts with gears 6 and 4, and therefore carrier H_2 moves. After this the mechanism will be work with two degrees of freedom because the possibility of activating a second degree of freedom. Because of its functioning this mechanism can applied as gearbox of cars, metal cutting machines and where is necessary smoothly to

change reduction ratio of transmissions. This mechanism can start movement without using additional device or controller, when force can overcome friction on the satellites to start movement. This planetary gear box can change reduction ratio as CVT depending on the external load of output carrier.

Main characteristics of the proposed design can be recognized in two input mobile links, two degrees of freedom, stepless operations, smoothly and automatically changing reduction ratio depending on the load of the output link. The operation advantage can be recognized in the possibility of this mechanism to start movement without using any additional device.

4   A Kinematic Characterization

For a kinematic characterization of the proposal gear box the scheme in Fig. 4 is used together with parameters of external torques on the carriers M_{H1}, M_{H2} and the input angular velocity ω_{H1}. From the kinematics the relations among the angular velocities of the gears with z_1, z_2, z_3, z_4, z_5, z_6 teeth can be expressed the form

$$\frac{\omega_1 - \omega_{H1}}{\omega_3 - \omega_{H1}} = u_{13}^{(H1)} \tag{1}$$

$$\frac{\omega_1 - \omega_{H2}}{\omega_3 - \omega_{H2}} = u_{46}^{(H2)} \tag{2}$$

Where

$$u_{13}^{(H1)} = -\frac{z_3}{z_1}$$

$$u_{46}^{(H2)} = -\frac{z_6}{z_4} \tag{3}$$

$$\omega_{H2} = M_{H1}\omega_{H1} / M_{H2} \tag{4}$$

From equation (1) and (2) angular velocities ω_3, ω_1 of gears 3 and 1can be obtained as

$$\omega_3 = \frac{(u_{13}^{(H1)} - 1)\omega_{H1} - (u_{46}^{(H2)} - 1)\omega_{H2}}{u_{13}^{(H1)} - u_{46}^{(H2)}} \tag{5}$$

$$\omega_1 = u_{13}^{(H1)}(\omega_3 - \omega_{H1}) + \omega_{H1} \tag{6}$$

In addition we must take into account the absence of jamming of satellites. Value of driving torque must be more than value of friction torque, in order to get motion. This is

$$M_d > M_f \tag{7}$$

where M_d is the driving torque, M_f the is friction torque. On Fig.3 is shown an example of determining absence of jamming for gear 5, when output carrier is fixed.
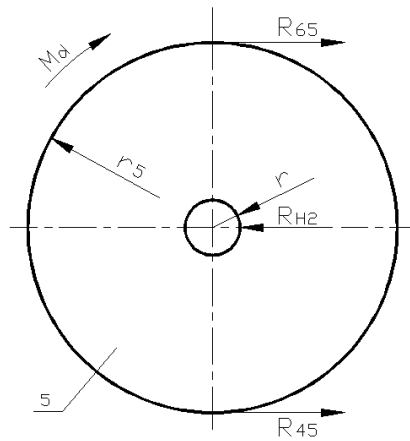
Fig. 3 A free-body diagram for the equilibrium of Gear 5: (R_{65}, R_{45}, R_{H2} - reaction forces; r_5- radius of gear 5; r – radius of axle of gear)

From the scheme in Fig. 3 the equilibrium is expressed by

$$R_{H2} = R_{65} + R_{45} \tag{8}$$

$$M_f = R_{H2}rf \tag{9}$$

where R_{H2} is the force acting on link H_2, R_{65} is the force action from gear 6, R_{45} is the force reaction from gear 4, r is the radius of the axle and f is friction coefficient.

For gear 5 driving torque M_d can be computed as

$$M_d = (R_{65} - R_{45})r_5 \tag{10}$$

where r_5 is the radius of gear 5.

Numerical check is made with an application for a wind turbine as in Fig. 4. Wind turbines are devices that are designed to generate electricity through the natural force of wind. Wind rotates wind turbine that provides rotation to the gear box that transmits rotation to the generator. The generator converts mechanical energy into electricity. For numerical check angular velocity of the input carrier and torques are assumed as ω_{H1}=70 rpm; M_{H1} = 20 Nm; M_{H2} = 15 Nm. The input and the intermediate angular velocities ω_{H2}, ω_1, ω_3 and internal forces can be computed with the proposed model by considering $\omega_4 = \omega_1$, $\omega_6 = \omega_3$. From (4) angular velocity of output carrier is computed as ω_{H2} = 93,3 rpm. From (5) and (6) angular

velocities of gears 1 and 3 are computed as ω_1=15,5 rpm and ω_3=102,6 rpm. The reactions forces in the kinematic pairs are computed using static conditions by the given torques of external forces as R_{12} =0,25 N; R_{23} =0,25 N; R_{45} =0,27 N; R_{56} =0,27 N; R_{H1} =0,71 N; R_{H2} =0,53 N.
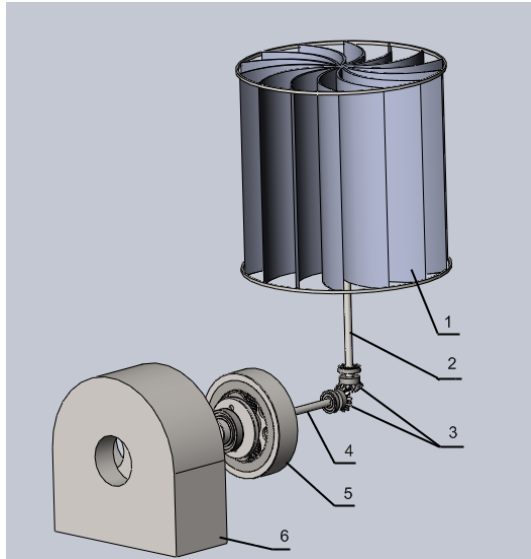
Fig. 4 A wind turbine with a proposed planetary gear box: (1-wind turbine; 2-axis of wind turbine; 3-conical gears; 4-input shaft; 5-gear box; 6-generator)

The operation advantages of this mechanism are in smoothly and automatically changing reduction ratio depending on the load of the output link. This mechanism can be transmission solution for a wind turbine. In this case, gear box is able to adapt its operation to the external applied load of wind.

5   Conclusions

A planetary gear box with two degrees of freedom has been studied from aspects of mechanical design and kinematic modeling. A design of a planetary gear box with two degrees of freedom has been proposed in order to adapt the operation to variable loading. Design of the planetary gearbox is shown in kinematic scheme. A kinematic characterization of a gearbox and equations are worked out taking into account the absence of jamming of satellites. The formulated equations are tested by numerical instances. Numerical check is made with an application for a wind turbine. Results of numerical check show the gars rotate with a proper speed and without jamming.

References

1. Crockett, J.S.: Shiftless, continuously-aligning transmission, Patent of USA 4,932,928, Cl. F16H 47/08, U.S. Cl. 475/51; 475/47 (1990)
2. Derek, F.L., Dennis, W.H.: The Operation and Kinematic Analysis of a Novel Cam-based Infinitely Variable Transmission. In: ASME 2006 International Design Engineering Technical Conferences and Information in Engineering Conference, vol. 3, pp. 1–6 (2006)
3. Harries, J.: Power transmission system comprising two sets of epicyclical gears, Patent of Great Britain GB2238090 (A) (1991)
4. Ivanov, K., Balbayev, G.: Adaptive Drive of Manipulator Module. Applied Mechanics and Materials 186, 266–272 (2012)
5. Ivanov, K.: Design of Toothed Continuously Variable Transmission in the Form of Gear Variator. Balkan Journal of Mechanical Transmissions (BJMT) 2(1), 11–20 (2012)
6. Ivanov, K.: Force Adaptation of Two-Mobile Gear Mechanisms. Textbook. Kazgos INTI Publishing, Almaty (2001)
7. Levai, Z.: Structure and Analysis of Planetary Gear Trains. Journal Mechanisms 3, 131–148 (1968)
8. Mundo, D.: Geometric design of a planetary gear train with non-circular gears. Mechanism and Machine Theory (41), 456–472 (2006)
9. Niguchi, N., Hirata, K.: Transmission Torque Analysis of a Novel Magnetic Planetary Gear Employing 3-D FEM. IEEE Transactions on Magnetics 48(2), 1043–1046 (2012)
10. Patel, P.: Design and Analysis of Differential Gearbox, Report, U.V. Patelcolliege of Engineering, Ganpat University, Kherva (2009)
11. Toyota-club, http://www.toyota-club.net/files/planet/
12. Yaghoubi, M., Mohtasebi, S.: Design and Simulation of a New Bevel Multi-Speed Gear box for Automatic Gearboxes. Science Journal Report and Opinion 2, 1–7 (2010)

The Issues of Spurious Residual Oscillations in the Displacement Laws of Cam Systems

M. Václavík, P. Dostrašil, and P. Jirásko

VÚTS, a.s., Czech Republic
{miroslav.vaclavik,pavel.dostrasil,petr.jirasko}@vuts.cz

Abstract. The paper deals with spurious residual oscillations and compensation methods in the rest areas of the displacements laws of cam system working links. Currently, cam mechanisms are divided into two basic groups, depending on how excitation motion function is implemented. It is then carried out by a conventional cam mechanism, an electronic cam or in a combination of both systems. Between the excitation motion function and the final working link there is usually a function-generating mechanism with constant or non-constant transfer. The structural arrangement is very varied, but typically it is a compliant system which responds to the excitation motion function with undesirable spurious oscillation.

Keywords: Cam, displacement law, residual spectra, indexing drive.

1   The Issues of the Applications of Conventional and Electronic Cams

Both systems have virtually the same, which is the drive of a working link of a processing machine mechanism. As conventional cams we mean compound cam mechanisms with any basic cam mechanisms as described in References [1][4]. Those mechanisms are well known with their pros and cons. Positive properties are for example their high dynamics, relatively low cost and variability of structures; their negatives are their single purpose, the influence of backlashes (clearances), compliances in the input and output kinematic chain, wear (needed as spare parts).

Electronic cams [5] are mechanisms that consist of control (controller) and drive (inverter, servomotor). The positives of electronic cams are their programmability and usability in production systems as elements of flexible automation, low maintenance and reliability. Their negatives are for example: their lower dynamics, higher acquisition costs, high qualification requirements for the preparation and design of an application.

The paper deals with the use of conventional and electronic cams in rigid and flexible automation, which is the implementation of non-periodic (step) movements with structural elements such as are various step mechanisms [3][4] and

turntables in this case. In the one direction, subject of interest is the study of residual oscillation (vibration) in the rest areas of motion functions and finding ways of its minimizing without feedback intervention, i.e., to determine the residual spectra of selected displacement laws and based on them, to set operating speed, angle of displacement or moment of inertia of workload in such a way so that this oscillation is minimal. Then, in the other direction, we study the effect of superposition of the basic displacement law with harmonic compensation (correction) pulse, which minimizes this spurious oscillation [2][5].

2   The Application Research of Conventional and Electronic Cams

For the purposes of experiments, dynamic stands for conventional cam mechanisms and electronic cams were built. In Fig. 1, there is a variant of conventional grooved radial cam with rocker and a pliable driving and driven part with workload. Fig. 2 shows a 3kW system of Yaskawa's electronic cam (controller, inverter, and servomotor) with a pliable driven part with working mass of inertia.

In the following paragraphs, it is then suggested the creation of numerical models of both cam mechanism types. The models were validated by a measurement. The measurement results are not listed due to the limited range of this paper.

Fig. 1 Conventional cam mechanism stand (grooved radial cam with rocker, constant transfer)
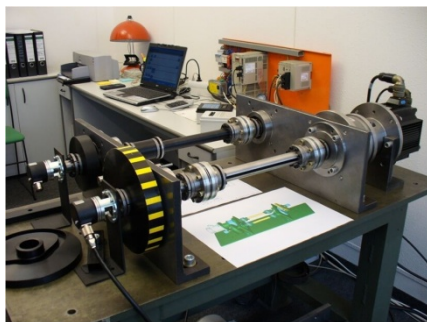
Fig. 2 Electronic cam stand

3   The Discrete Model of Conventional Cam Mechanism with Flexible Constraints

Conventional cam mechanisms with flexible constraints in the driven and driving mechanism parts are characterized by the fact that the combination of two discrete mass system parts with rotational or translational motion, which are part of the

same mechanism link (in terms of kinematic labeling of mechanism links), is implemented by a flexible constraint. The mechanisms of this group have always 1° of degree of freedom at rigid constraints. By introducing flexible constraints, the number of degrees of freedom of the mechanism system that is dependent on the number and arrangements of constraints increases.

Real mechanisms, used for the construction of machines and equipment, are relatively complicated mechanical systems. The starting point for a specific dynamic solution is to determine a suitable computational model. In the class of computational models of mechanisms with flexible constraints, we will include those models of mechanisms by which the appropriate flexible links are considered to be immaterial. The cam mechanism is characterized by a discrete distribution of masses of the individual links of a system that are assumed to be perfectly rigid. The mentioned system has the finite number of degrees of freedom, depending on the number and arrangement of flexible constraints.

For creating the equations of motion for the reference model, there can be used classical Lagrange equations of the 2nd type for independent general coordinates q_i which are the deflections of the links of a cam mechanism due to flexible constraints or also the coordinates of a driving link $q_1(\varphi)$. When deriving the equations of motion, we will use the designation of the positions of the links in absolute coordinates and do not consider the influence of gravity. The discrete model is schematically illustrated in Fig. 3.
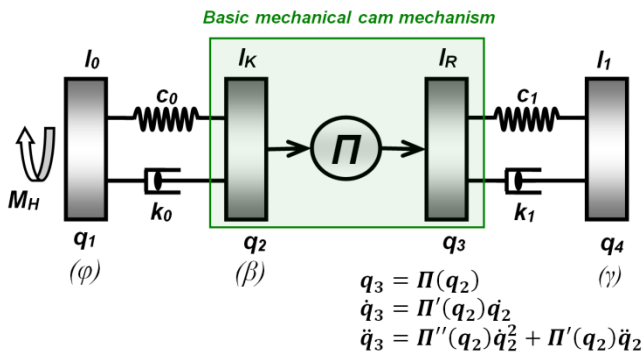
Fig. 3 Discrete model of conventional cam mechanism

By substituting for $q_1 = \varphi \ (= \omega t)$, $\dot{q}_1 = \omega \ (= konst)$, $q_2 = \beta$, $q_4 = \gamma$, we will get the equations of motion in the form of

$$M_H = c_0(\omega t - \beta) + k_0(\omega - \dot{\beta}) \tag{1}$$

$$[I_k + I_R \Pi'^2(\beta)]\ddot{\beta} + I_R \Pi'(\beta)\Pi''(\beta)\dot{\beta}^2 = c_0(\omega t - \beta) - c_1 \Pi'(\beta)[\Pi(\beta) - \gamma] + k_0(\omega - \dot{\beta}) - k_1 \Pi'(\beta)[\Pi'(\beta)\dot{\beta} - \dot{\gamma}] \tag{2}$$

$$I_1 \ddot{\gamma} = c_1[\Pi(\beta) - \gamma] + k_1[\Pi'(\beta)\dot{\beta} - \dot{\gamma}] \tag{3}$$

4   Equations of Motion of the Electronic Cam Discrete Model

We will derive the equations of motion in the same manner as it is in the case of a conventional cam mechanism according to Fig. 3. Due to the analogy with the conventional mechanism, also the links with zero moments of inertia are plotted.
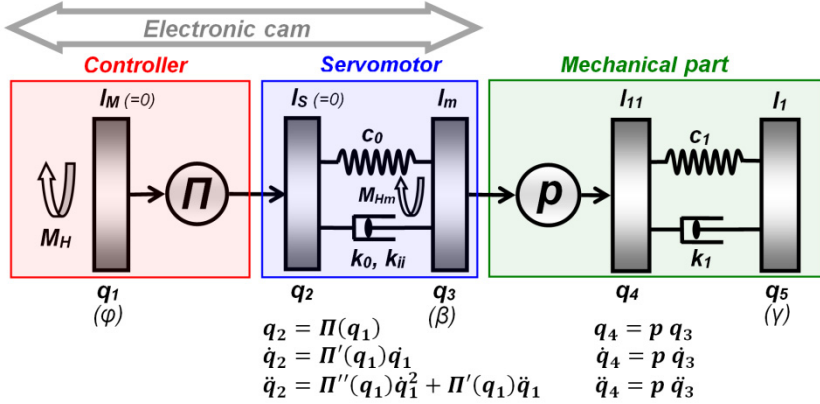
Fig. 4 Discrete model of electronic cam

By substituting for $q_1 = \varphi$, $q_3 = \beta$, $q_5 = \gamma$, we will get the equations of motion of the discrete model of an electronic cam in the form of

$$M_H = \{c_0[\Pi(\varphi) - \beta] + k_0[\Pi'(\varphi)\dot{\varphi} - \dot{\beta}]\}\Pi'(\varphi) \qquad (4)$$

$$(I_m + I_{11}p^2)\ddot{\beta} = c_0[\Pi(\varphi) - \beta] - c_1p(p\beta - \gamma) + k_0[\Pi'(\varphi)\dot{\varphi} - \dot{\beta}] - k_1p(p\dot{\beta} - \dot{\gamma}) \qquad (5)$$

$$I_1\ddot{\gamma} = c_1(p\beta - \gamma) + k_1(p\dot{\beta} - \dot{\gamma}) \qquad (6)$$

where generally $\dot{\varphi} \neq$ konst. Equations (5) and (6) describe the behavior of the electronic cam in the case when coordinate φ is the dependent variable (slave) of the virtual shaft (master). For example, the equations then describe the behavior when starting-up revolutions along a predefined ramp, as it is common with electronic cams. Practically, however, stable operation is solved.

At this point, we will provide a short note to a difference from the numerical solution of a conventional cam mechanism model. Here, we will not describe the principles of controlling servo drives; we will only note that most servo drives have a cascade control structure with torque, speed and position feedback. Controllers are generally proportional (P) and proportionally integral (PI). Thus, we will try to intervene in the numerical solution of equations of motion in such a way so that a characteristic quantity, which is a servo motor positional deviation (PERR: difference of the actual position on the servo shaft from the theoretical one), can correspond to the reality of P/PI modes at most. PERR is a criterion of

the accuracy of the given model and its course was compared with two independent sources. The one is the measurement and the other is the virtual model created in the MSC.ADAMS and MSC.EASY5 program systems [5]. Due to the limited extent of this paper, the results of the comparison are not presented.

5   Residual Spectra of the Displacement Laws

The accuracy of the end position in the rest interval of function of motion is assessed according to the extreme acceleration value of a working link because the links of a cam mechanism are considered as pliable in dynamic models. The criterion of positional accuracy is the residual spectrum of the second derivative (a_R) of the response to the kinematic excitation of a pliable system with a displacement law [1]. The residual spectrum, specific for the given displacement law, will be used for determining the parameters (speed, angle of displacement or moment of inertia) at which the oscillation is minimized. The presented results in the paper are the outcome of a purely numerical solution based on the data file of a displacement law (0th, 1st and 2nd derivative) and the parameters of models with pliable links. In the cycle for/next of relative natural frequency v (in Fig. 5 and 6 as 'ny1'), a numerical solution of equations (1) up to (6) proceeds whose each cycle run is the resulting maximum acceleration in the rest area of the equation of motion. The graphical expression of those values depending on v is the searched residual spectrum. Relative natural frequency v represents the number of oscillations performed in the *time* of one displacement or the implemented angle of displacement (*time period* minus *rest time*). Relationship v[1] with speed n[min^{-1}], angle of displacement ϕ[deg], and moment of inertia of load I_1[kgm^2] is

$$v = \phi f /6n, \quad f = (1/2\pi) \sqrt{c_1/I_1}. \tag{7}$$

With regard to the extent of the paper, there are given only illustrative results for:

- Conventional cam mechanism model (Fig. 5) with a varying input stiffness, output stiffness 1000[Nm/rad], polynomial displacement law of the 5th degree 30[deg] and angle of displacement 90[deg], load 0.1[kgm^2]
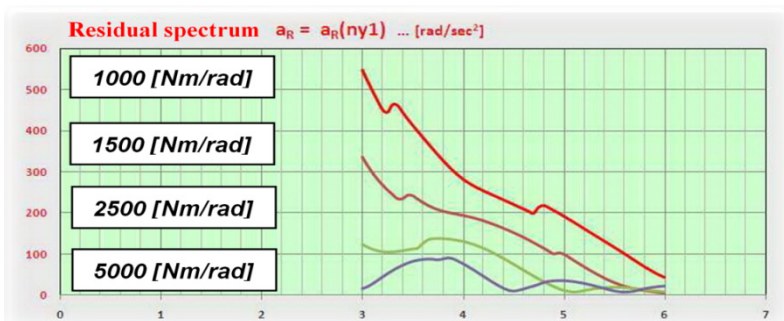
Fig. 5 Residual spectra of a conventional cam mechanism model

- Electronic cam model (Fig. 6) for the polynomial displacement law of 5th degree, harmonic and parabolic with a displacement of 68[deg] and an angle of displacement of 90[deg], load 0.1[kgm^2]
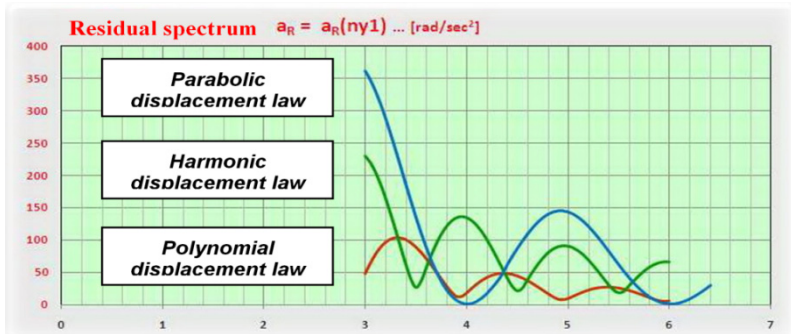
Fig. 6 Residual spectra of an electronic cam model

6   Compensation of Residual Oscillations by Superposition with Harmonic Pulse

The stand model according to Fig. 2 has one natural frequency due to compliance in the driven part of the mechanism. According to [2], there it will come to suppressing the residual oscillations by superposing the basic displacement law with harmonic pulse, which corresponds to the natural frequency of the system with its length (angle of displacement). Intervening manually in the pulse position and compensating (correcting) its amplitude, a desired attenuation will be achieved.

The newly developed system, however, enables us to use the compensation harmonic pulse which may not correspond to the natural frequency of the system, as progressively shown in Figures 7, 8 and 9. Compensation pulse here is 1.3 times the length of the harmonic oscillation with the natural frequency of the system. Furthermore, an algorithm of automatic reach of the position and the amplitude of a 'reasonably general' harmonic compensation pulse was developed. Harmonic oscillations excited by this pulse have the same amplitude as oscillations excited by the initial displacement law, but they act in phase opposition. With a position sensor, we record the position of the oscillating working mass of inertia in the interval of the PLC scan and from it, the sum of the absolute values of the PERR position error is evaluated in the rest part of the motion function in several cycles.

The PC application solves iteratively the new position and amplitude of compensation pulse. The new position of the compensation pulse will be superimposed with a basic displacement law and the new displacement law (superposition)

is transmitted to the controller. The procedure is repeated until the value of the PERR position error achieves an appropriate value. To solve the compensation pulse phase and amplitude, it is not necessary to know the discrete model of the pliable system and its numerical solution according to equations (4) up to (5).

In this phase of the methodology development, the implementation of the iterative task is solved in the external PC. That method can be directly programmed in the PLC electronic cam control system.
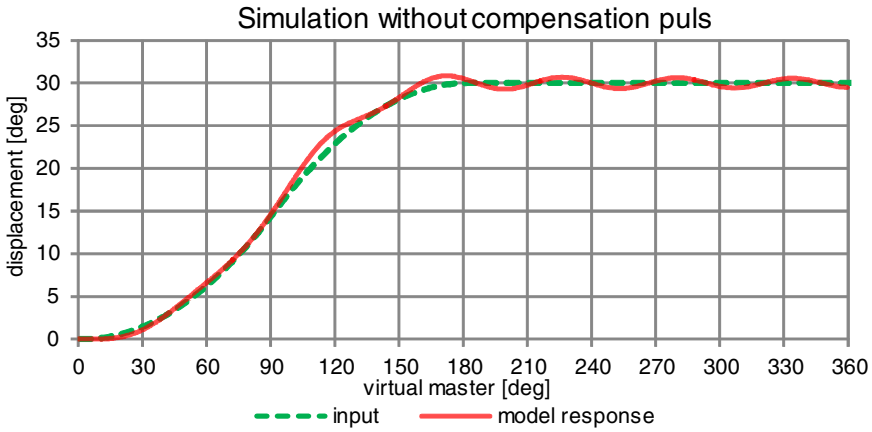
Fig. 7 Basic displacement law
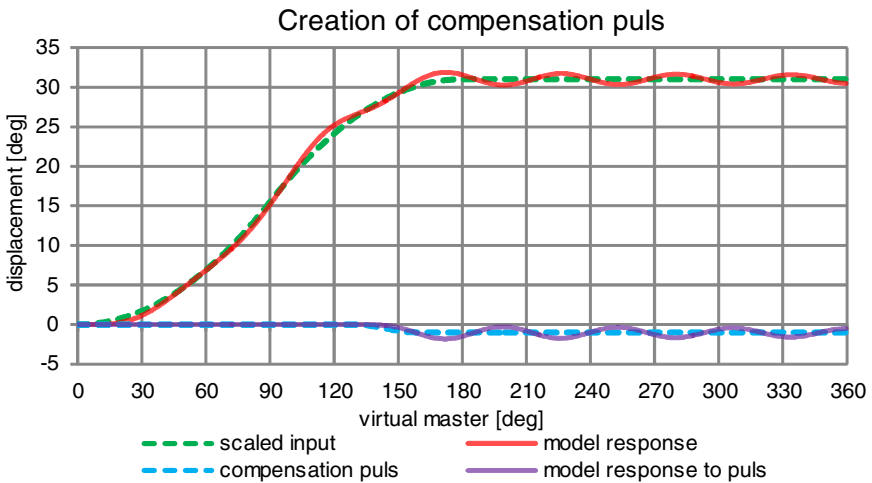
Fig. 8 Creation of compensation pulse
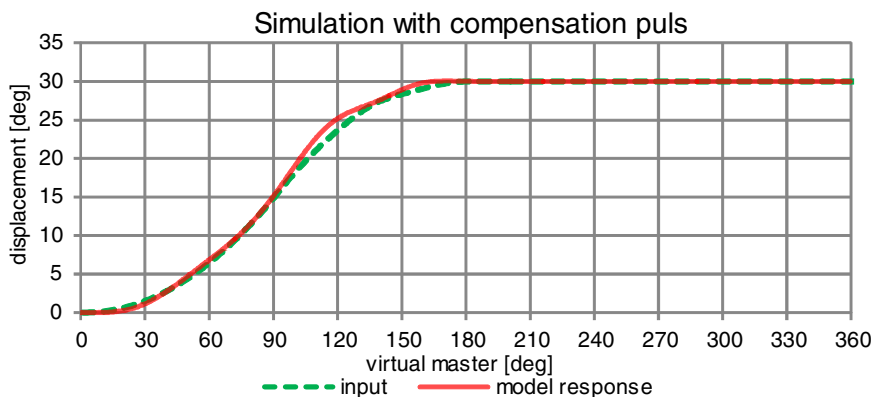
Fig. 9 Superposition of the basic displacement law with compensation pulse

7   Conclusion

Based on the residual spectra of displacement laws, which are the result of a numerical solution of models, it is possible to determine the speed, angle of displacement or moment of inertia in such a way so that residual oscillation (vibration) in the rest area of motion functions is minimal. These conclusions were verified on the dynamic stand according to Fig. 2. One of the interesting results is that the parabolic displacement law preferably compensates residual oscillations, even though the response of the system to this displacement law is the strongest because of its discontinuous course of the 2nd derivative.

The method in accordance with Chapter 6 reliably removes spurious residual oscillations in the rest part of a motion function. We note that we are concerned solely on this rest section because there takes place the specific technological production process. We do not deal with the own positional error in the area of displacement as it is solved by the 'Input Shaping' method.

References

1. Koloc, Z., Václavík, M.: Cam Mechanisms. Elsevier (1993)
2. Václavík, M., Jirásko, P.: Research and Application of Displacement Laws of Electronic Cams. In: 12th IFToMM World Congress, Besançon, France, June18-21 (2007)
3. Václavík, M., Jirásko, P.: Electronic cams in serial and parallel combination with conventional mechanisms in the drive of mechanism working links. In: The First IFToMM Asian Conference on Mechanism and Machine Science, Taipei, Taiwan, October 21-25 (2010)
4. Dostrašil, P., Jirásko, P.: Productive design and calculation of intermittent mechanisms with radial parallel cams. In: WASET (2011)
5. Jirásko, P.: Methodology of electronic cam applications in drives of working links of mechanisms of processing machines. Dissertation TU Liberec CZ (2010)

Mechanism of a Leg Exoskeleton for Walking Rehabilitation Purposes

C. Copilusi[1], Marco Ceccarelli[2], G. Carbone[2], and A. Margine[1]

[1] University of Craiova, Romania
 `cristache03@yahoo.co.uk`
[2] University of Cassino and South Latium , Italy
 `ceccarelli@unicas.it`

Abstract. This paper addresses attention to the conceptual mechanism design of a leg exoskeleton for human rehabilitation purposes. Different mechanism solutions for locomotion rehabilitation are analyzed from a structural and functional viewpoints. By using mobility analysis and considerations on structure design, a new leg exoskeleton is identified with low-cost features and motion ability for rehabilitation purposes.

Keywords: Biped Mechanisms, Human Locomotion, Pantograph-leg Mechanisms, Exoskeleton.

1   Introduction

It is well known that human motions are complex and are extensively studied from experimental viewpoints, theoretical analyses, modelling and simulations, in order to solve different clinical health problems or to apply them to robots.

For many researchers an important point of interest is represented by human walking analysis. This motion was and is applicable to biped robots, walking machines and human locomotion rehabilitation systems or devices.

By studying significant humanoid robot designs as in [2, 5, 6, 7, 9, 13, 15, 16, 17] it can be observed that these are centred on the dynamic control aspects, gait synthesis or interactive studies. Other systems like in [1, 8, 11, 15, 17] use biped walking ability in designs for human walking rehabilitation procedures. In particular leg exoskeletons are used for increasing load capability during human walking. Some of these human walking exoskeletons use a large number of actuators while others have a limited number of actuators like reported in [3, 10, 12, 13]. In this paper the main focus is address to conceive an exoskeleton which can be actuated by few actuators and even by one motor only.

Considering current humanoid robots, walking machines, and rehabilitation exoskeletons, it can be observed that most of them are complex, very expensive or are still at prototype phase.

Other solutions put question marks about mechanism design and leg geometry which can be crucial for human biped stability and motion. Another remark can be outlined as referring to the presence of a large number of actuators which complicate the exoskeleton structure and obviously increases the price of this.

The research aim is represented by finding an optimal solution for an exoskeleton design which can be based on low-cost easy-operation criteria.

This paper is organized as follows. In the first section existing solutions of walking machines are considered as a starting point for a new design. In second section, characteristics of human walking are presented for rehabilitation purposes as obtained on experimental way by using equipment with high-speed recording cameras. Based on analyzed solutions from walking machines, four-bar linkages are analyzed from a structural viewpoint in the third section. These linkages could be used on an exoskeleton structure for main joints such as knee and hip. Other exoskeleton solutions which fulfil also the ankle joint motion during the human gait are analyzed in this section. By combining these structural schemes a low-cost exoskeleton solution with a minimum number of actuators.

2 Human Walking Characteristics for Rehabilitation Purposes

Human walking characteristics can be determined through experimental tests by using special video-analysis equipments. University of Craiova - Faculty of Mechanics owns high-speed video recording equipments called CONTEMPLAS [4]. With this equipment's aid, a database was created, which consists of test results with 10 human subjects. These subjects were half men and half women, with the age between 25-30 years, and the experimental analysis interest was to determine human joints angular variations during a single gait. The analysis procedure consists on monitoring the position of markers that are attached on each joint centre, or on human leg segments. The aim of this analysis was to identify upper and lower limits for hip, knee and ankle joints, in different healthy persons, in order to have experimental reference values. Fig. 1 shows location of markers on human leg during experimental tests for measuring joint ranges during walking by using two cameras. Gait motion was recorded with two high-speed cameras with 350 frames/second. One camera was mounted on lateral side of the analyzed subject, and the other was placed in front. The second camera provides additional data about passive motions of the analyzed joints. Figs. 2 to 4 show measured results for joint angles of hip, knee and ankle, respectively. Those motion ranges have been used to identify motion requirements for exoskeleton design with adaptability to a large variety of human gaits. The difference between this work and earlier work of other researchers [18], consists in a development of a proper database for walking by using experimental determination of human locomotion characteristics from analyzed subjects. Those data can be used as constraints for the design of a parameterized exoskeleton.
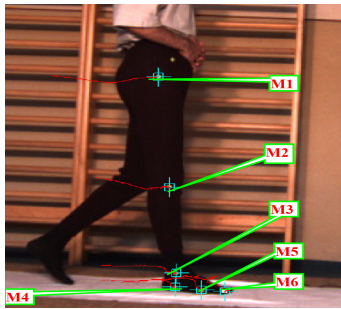
Fig. 1 Location of marker attachment during experimental tests
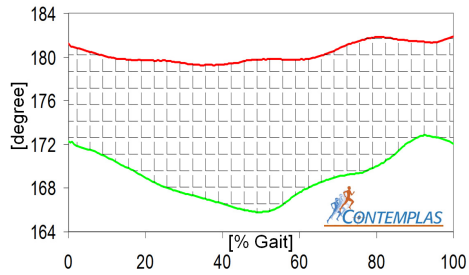
Fig. 2 Measured limits of the hip joint angle as function of % gait phase
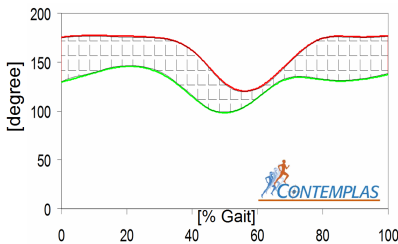
Fig. 3 Measured limits of the knee joint angle as function of % gait phase
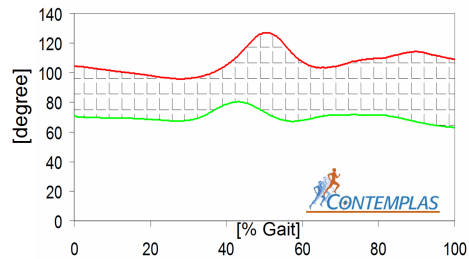
Fig. 4 Measured limits of the ankle joint angle as function of % gait phase

3   Mechanisms for a Leg Exoskeleton

In order to develop a low-cost exoskeleton with a fairly simple mechanism structure it can be convenient to simplify and adapt existing solutions like those in [2, 3, 10]. In Fig. 5 structural solutions are shown as based on a structure with a pantograph and Chebyshev linkage. The mentioned basic structure is considered because of its simplicity and characteristics for efficient reproduction of human walking. A pantograph is useful for human walking reproduction since it can amplify properly an input motion from the body frame to the foot point trajectory. A Chebyshev linkage can be a proper choice for producing an input 'human-like' the path with high mechanical efficiency and fairly simple motion control.

The leg exoskeleton in Fig. 5-a) is a solution proposed in [12]. This solution has a high number of links and joints, and adjustable to the size of the links cannot be different human subjects. In addition, the ankle joint is missing. Nevertheless this exoskeleton mechanism shows a good stability during walking. Thus, considering it, and other ones which uses pantograph or Chebyshev mechanisms as in [3, 10] a new structural scheme was conceived as in Fig. 5 - b). This one has the actuation link - 1, on the front. This solution will cause the impossibility to place a

human subject between exoskeleton legs and the actuator, and the drive link can be placed in the back side. But this solution has no actuation mechanism on ankle joint. A final solution can be identified as in Fig. 5-c), by moving F-joint on C in one joint only.
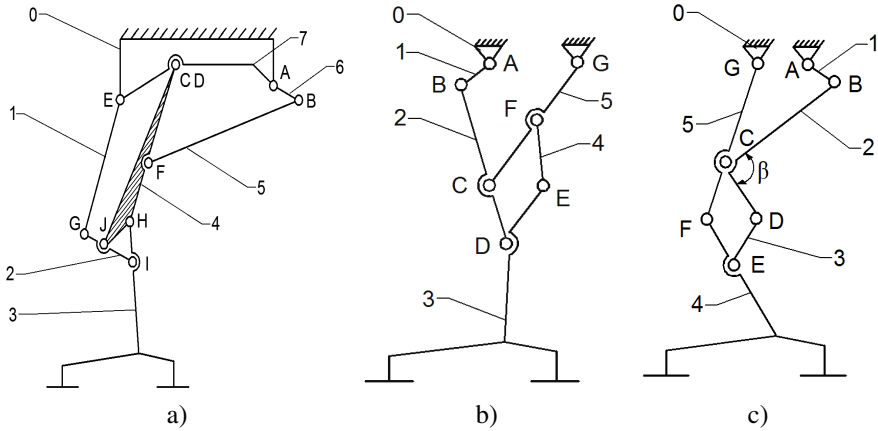
Fig. 5 Structural schemes for leg mechanisms with pantograph: a) design in [12]; b) a new solution; c) the proposed solution

The structural parameters in the solutions in Fig. 5 are listed in Table 1 whose a characterization is given through the range of mobility. The range of mobility M for the structural schemes in Fig. 5 can be computed by:

$$\mathbf{M} = 3\mathbf{e} - \sum_{m=4}^{5} (\mathbf{m} - 3)\mathbf{c}_m \tag{1}$$

where: $\mathbf{e}$ represents the number of elements; $\mathbf{c}_m$ represents kinematic joints of rank $\boldsymbol{m}$.

For the leg exoskeleton solutions in Fig. 5 it is necessary only one actuator that can be placed in joint A on body 0 (the frame). The size of links can be made adjustable only in structural schemes in Fig. 5 - b) and c), in order to adapt a solution to any human body categories. It can be observed that the ankle joint for these solutions is neglected due to the impossibility to place a mechanism near the ankle area. In fact the ankle angular amplitude from Fig. 4 it is between 20-30 degrees and is not small.

The proposed solution in Fig. 5-c) has the joint F from Fig. 5 – b), coupled with joint C and the links 4 and 5 are welded together at a fixed angle β= 90 degrees. For the ankle joint an equivalent mechanism can be proposed as a cam mechanism.

Table 1 A structural comparison of leg mechanism with 1DoF in Fig. 5

Mechanism	Number of links
Fig. 5 a)	7
Fig. 5 b)	5
Fig. 5 c)	5

This represents a novelty principle by implementing cam mechanisms on leg mechanism structure, especially for human final locomotion. But the cam profile needs to develop a human ankle motion law. A structural scheme of an ankle mechanism is presented in Fig. 6 with 4 links, 7 revolute joints, and 1 cam mechanism.
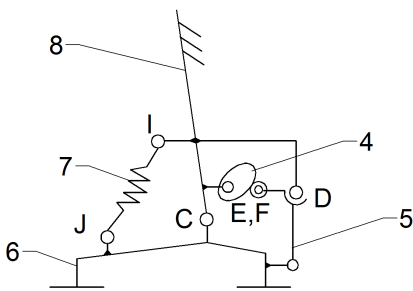
Fig. 6 A structural scheme of the proposed cam mechanism for ankle joint
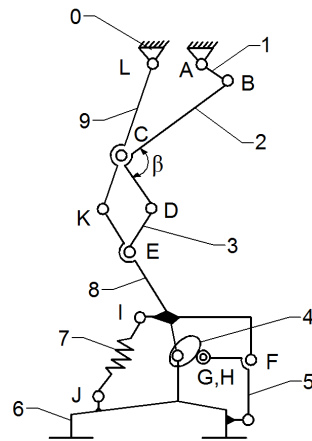
Fig. 7 The proposed leg mechanism with ankle joint actuated through a cam mechanism placed in the ankle joint area

By combining the mechanism in Fig. 5-c) with Fig. 6, the leg mechanism in Fig. 7 can be a final design for a leg mechanism. This leg mechanism cannot be yet proposed for an exoskeleton mechanism solution since the cam mechanism is too large. In fact, a human ankle, including a tibia link, can have an overall size with height of 230 millimetres and width of 180 millimetres. In addition the mobility degree is 2 since one actuator is at joint A, and other at joint G.

In order to reduce the size of the cam ankle mechanism can be installed within a fixed point 1 in the knee area or below at E joint. Thus structural schemes can be modified, as in Fig. 8. A comparison of these solutions is presented in Table 2.

These solutions can fulfil the angular limits that are indicated in the diagrams in Figs. 2 to 4. By decreasing the link 1 length, the hip angular amplitude can be increased (Fig. 2), and also the knee angular amplitude can be with lower limits as in Fig. 3. But the E joint will pass over the upper limit. This can be solved by modifying the links lengths, by adding mechanical devices for adjusting link sizes.
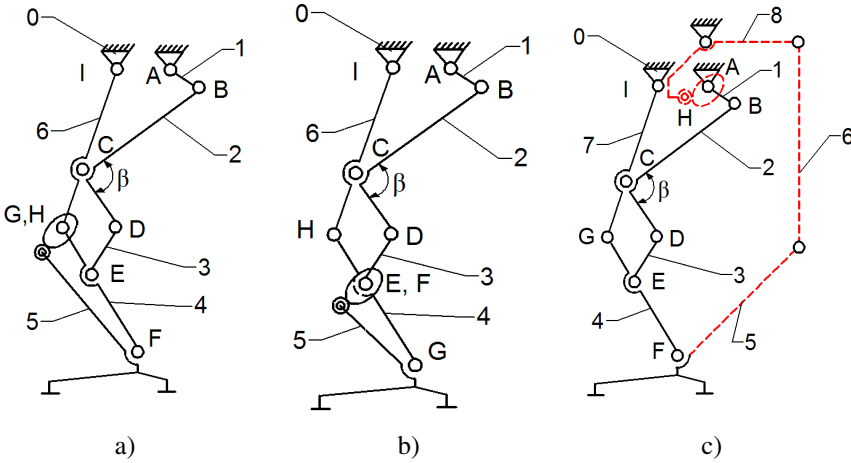
Fig. 8 Low-cost exoskeleton structural schemes with ankle joint mechanism of Fig. 5 connected to different joints: a) at knee joint; b) at a tibia joint; c) at a joint on body frame

Table 2 Leg mechanisms structural comparison (Fig. 8)

Mechanism	Number of links	Number of joints	DoF	Range of mobility
Fig. 8 a)	7	10	1 DoF= 9 joints	2
			2DoF= 1 Cam mechanism	
Fig. 8 b)	7	10	1 DoF= 9 joints	2
			2DoF= 1 Cam mechanism	
Fig. 8 c)	8	12	1 DoF= 11 joints	1
			2DoF= 1 Cam mechanism	

Solutions in Fig. 8 can give leg exoskeletons with large size and weight. Thus, a suitable solution can be identified by installing actuators for the cam mechanisms on a central part of the exoskeleton leg mechanism so that its motion can be transmitted with a link mechanism as in Fig. 8 c). Also this solution has on its base previous works from [2, 3, 10], and it represents a continued work by adding a cam mechanism for ankle joint motion, the drive link is positioned on the mechanism back frame for placing a human subject.

Another alternative solution is to replace the ankle joint actuating mechanism with flexible cables, belts or chain transmissions. In this case from a mechanical viewpoint it is fairly easy to command and control, because it needs only one actuator as it shown in Fig. 9. This solution has 15 links, 17 revolute joints and one cam mechanism with a final conceptual design as in Fig. 9. This solution fulfils complete tasks for each joint for a human like walking, since a proper actuation on all joints for hip, knee and ankle.

The proposed leg mechanism as in Fig. 8 c) or 9 can be used as an exoskeleton in rehabilitation applications since it can be designed with a proper wearable

mechanical design with actuators in the area of hip. In addition the kinematic structure is suitable to have sensors at the joints so that a guided walking can be easily monitored. The ankle joints actuation in the kinematic model case from Fig. 9 will be made through flexible cables and cam mechanisms placed on the drive link no.8. Also the cams must fulfil the ankle joint motion law for walking in case of a parameterized model.
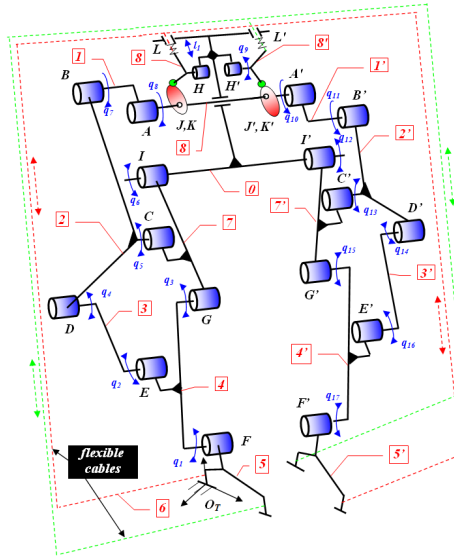
Fig. 9 Kinematic model of the proposed exoskeleton which fulfil the ankle joint motions

4   Conclusions

A conceptual design is presented for a low-cost exoskeleton for human walking rehabilitation. By referring to human walking characteristics a leg mechanism has been conceived with as kinematic structure whose mechanical design can be used for rehabilitation purposes as an exoskeleton wearable by patients. The proposed leg mechanism has been identified with a process of adjusting a linkage based on pantograph. A final solution is proposed with capabilities for motion of hip, knee and ankle. In particular, the ankle motion is obtained by a proper cam mechanism. A database was created in order to identify of human joints upper and lower limit.

References

1. Blaya, J.A., Herr, H.: Control of a variable-impedance ankle-foot orthosis to assist drop-foot gait. IEEE Trans. Neural Syst. Rehabil. Eng. 12(1), 24–31 (2004)
2. Carbone, G., Ceccarelli, M.: Legged Robotic Systems, pp. 553–576. Cutting Edge Robotics ARS Scientific Book, Wien (2005)

3. Liang, C., Ceccarelli, M., Takeda, Y.: Operation Analysis of a One-DOF Pantograph Leg Mechanisms. In: Proceedings of the RAAD 2008. 17th International Workshop on Robotics in Alpe-Adria-Danube Region, September 15-17, pp. 1–10 (2008)
4. CONTEMPLAS Motion Analysis Equipment user manual (2010)
5. Hirai, K., Hirose, M., Haikawa, Y., Takenaka, T.: The development of Honda humanoid robot. In: Proceedings of IEEE International Conference Robotics and Automation, Leuven, Belgium, pp. 1321–1326 (1998)
6. Huang, G.T.: Wearable robots. Technology Review (2004)
7. Kawamoto, H., Sankai, Y.: Power assist system HAL-3 for gait disorder person. In: Miesenberger, K., Klaus, J., Zagler, W.L. (eds.) ICCHP 2002. LNCS, vol. 2398, pp. 96–203. Springer, Heidelberg (2002)
8. Kazerooni, H., Steger, R.: The Berkeley lower extremity exoskeleton. Transactions of the ASME, Journal of Dynamic Systems, Measurements, and Control 128, 14–25 (2006)
9. Liu, J., Tan, M., Zhao, X.G.: Legged robots – an overview. Transactions of the Institute of Measurement and Control 29(2), 185–202 (2007)
10. Li, T., Ceccarelli, M.: An experimental characterization of a rickshaw prototype. Int. Journal of Mechanics and Control 12(2), 29–48 (2012)
11. Pratt, J.E., Krupp, B.T., Morse, C.J., Collins, S.H.: The RoboKnee: an exoskeleton for enhancing strength and endurance during walking. In: Proc. IEEE International Conference on Robotics and Automation, New Orleans, LA, USA, pp. 2430–2435 (2004)
12. Rodriguez, G.A., Rea, P.: A new articulated leg for mobile robots. Industrial Robot: An International Journal 38(5), 521–532 (2011)
13. Shieh, W.B., Tsai, L.W., Azarm, S.: Design and Optimization of a One-Degree-of-Freedom Six-Bar Leg Mechanism for a Walking Machine. Journal of Robotic Systems 14(12), 871–880 (1997)
14. Tavolieri, C., Ottaviano, E., Ceccarelli, M.: Analysis and Design of a 1-DOF Leg for Walking Machines. In: Proceedings of RAAD 2006, 15th International Workshop on Robotics in Alpe-Adria-Danube Region, Balantonfured. CD Proceedings (2006)
15. Walsh, C.J., Pasch, K., Herr, H.: An autonomous, under-actuated exoskeleton for load-carrying augmentation. In: Proc. IEEE/RSJ International Conference on Intelligent Robots and Systems (IROS), Beijing, China, pp. 1410–1415 (2006)
16. Walsh, C.J., Paluska, D., Pasch, K., Grand, W., Valiente, A., Herr, H.: Development of a lightweight, underactuated exoskeleton for load-carrying augmentation. In: Proc. IEEE International Conference on Robotics and Automation, Orlando, FL, USA, pp. 3485–3491 (2006)
17. Walsh, C., Endo, K., Herr, H.: A quasi-passive leg exoskeleton for load-carrying augmentation. Int. Journal H.R. 4(3), 487–506 (2007)
18. Williams, M.: Biomechanics of human motion. Saunders Co., Philadelphia (1996)
19. Zoss, A.B., Kazerooni, H., Chu, A.: Biomechanical design of the Berkeley lower extremity exoskeleton (BLEEX). IEEE ASME Trans. Mechatron. 11(2), 128–138 (2006)

Human Finger Kinematics and Dynamics

Fai Chen Chen, Silvia Appendino, Alessandro Battezzato, Alain Favetto,
Mehdi Mousavi, and Francesco Pescarmona

Center for Space Human Robotics@PoliTo, Istituto Italiano di Tecnologia,
Corso Trento 21, 10129 Torino

Abstract. In the last years, the number of projects studying the human hand from the robotic point of view has increased rapidly, due to the growing interest in academic and industrial applications. Nevertheless, the complexity of the human hand, given its large number of degrees of freedom (DoF) within a significantly reduced space requires an exhaustive analysis, before proposing any applications. The aim of this paper is to provide a complete summary of the kinematic and dynamic characteristics of the human finger as a preliminary step towards the development of hand devices such as prosthetic/robotic hands and exoskeletons imitating the human hand shape and functionality. Kinematics and dynamics are presented for a generic finger; with anthropometric data and the dynamics equations, simulations were performed to understand its behavior.

Keywords: Human finger, Kinematics, Dynamics, Extravehicular Activity.

1   Introduction

The human hand is a complex mechanism; it has a wide range of DoFs, allowing a great variety of movements. In recent years, as robotics has advanced, significant efforts have been devoted to the development of hand-related devices. The two main application fields are prosthetic/robotic hands and exoskeletons. On one side, robotic hands are designed to mimic the human hand characteristics, taking advantage of its variety of movements, thereby avoiding the use of a large number of end-effectors when performing tasks with different objects (e.g. Eurobot [1] and Robonaut [2]). On the other side, exoskeletons are designed to fit onto the human hand, aiming at enhancing performance in the carrying out of daily activities (e.g. improving astronauts' hand performance during Extravehicular Activity [3]) or supporting the rehabilitation stage of hand injury recovery.

There are currently many different projects underway. Schabowsky et al. [4] introduced a newly developed Hand Exoskeleton Rehabilitation Robot (HEXORR); which was designed to provide a full range of motion for all fingers. NASA and General Motors presented a prototype of the Human Grasp Assist device [5]. Worsnopp et al. [6] introduced a finger exoskeleton for hand rehabilitation following stroke, to facilitate movement, especially pinch. Another

project is being developed by Ho et al. [7]: their exoskeleton hand is EMG-driven, again for rehabilitation, but working on all the fingers. All of these projects present a different number of DoFs and different structures, but in general they are developed with the objective of mimicking the main characteristics of the human hand. The current paper provides a general kinematic and dynamic model of a human hand, representing a mathematical tool to conceive and test new robotic hand-related devices.

2   Kinematic Model of the Human Hand

The kinematic model of the human hand here proposed is composed of 19 links corresponding to the bones and 24 DoFs modeled by joints. Two kinematic configurations are considered for the digits: the thumb is modeled as 3 links and 4 joints, while the fingers (index, middle, ring and little) are modeled as 4 links and 5 joints, see Figure 1. In the following, only the four fingers are analyzed, while the thumb is neglected. The direct kinematics, that permits to obtain the fingertip position and orientation according to the joint angles, is here solved. The model equations are calculated by means of Modified Denavit-Hartenberg (MDH) parameters, introduced by J. J. Craig [8].
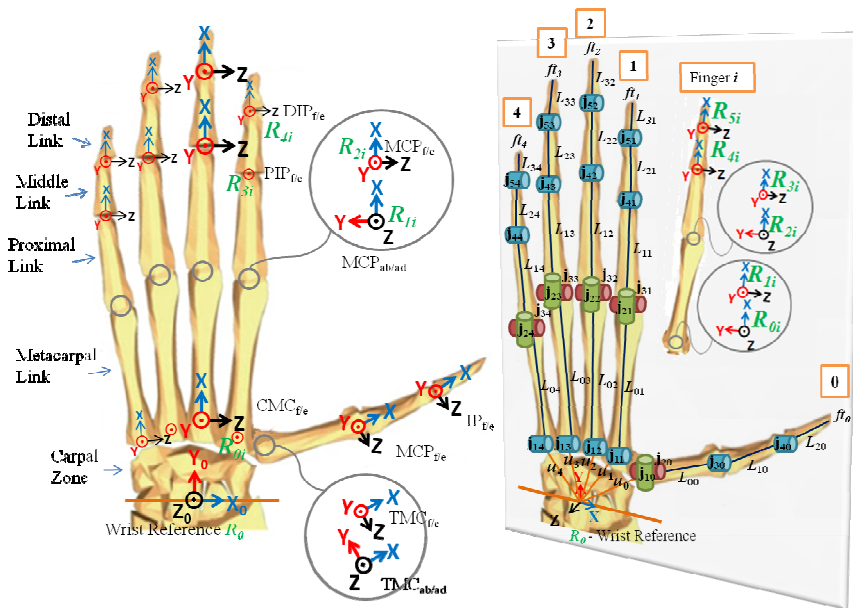
Fig. 1 Kinematic configuration of the human hand

The four bones of each finger correspond to the links of a serial kinematic chain, as represented in Figure 1. Each articulation for these four fingers

corresponds to the joints: CarpoMetaCarpal (CMC), MetaCarpoPhalangeal (MCP), Proximal InterPhalangeal (PIP), and Distal InterPhalangeal (DIP). The CMC joint represents the deformation of the palm, for instance when the hand is grasping a ball, while the MCP joint can be split into 2 DoFs, which carry out the adduction/abduction and flexion/extension movements respectively. All the other joints only allow flexion/extension movements. The digits are numbered from 0 to 4: digit 0 is the thumb and digits 1 to 4 range from the index to the little finger. The following table reports the MDH parameters for all the fingers.

Table 1 MDH parameters of the fingers

Joint	α_{i-1}	a_{i-1}	d_i	θ_i
j_{1i}	$\pi/2$	0	0	$\theta_{CMC_{f/e}}$
j_{2i}	$-\pi/2$	L_{01}	0	$\theta_{MCP_{ab/ad}}$
j_{3i}	$\pi/2$	0	0	$\theta_{MCP_{f/e}}$
j_{4i}	0	L_{11}	0	$\theta_{PIP_{f/e}}$
j_{5i}	0	L_{21}	0	$\theta_{DIP_{f/e}}$

Eq. (1) shows the direct kinematics from index ($i=1$) to the little finger ($i=4$):

$$Q_i = {}^0_0T_i \cdot {}^0_6T_i(\theta_j) = {}^0_0T_i \cdot \prod_{j=1}^{5} {}^{(j-1)}_jT_i(\theta_j) \cdot {}^5_6T_{ft_i} =$$

$$= {}^0_0T_i \cdot {}^0_1T_i(\theta_{CMC_{f/e}}) \cdot {}^1_2T_i(\theta_{MCP_{ab/ad}}) \cdot {}^2_3T_i(\theta_{MCP_{f/e}}) \cdot {}^3_4T_i(\theta_{PIP_{f/e}})$$
$$\cdot {}^4_5T_i(\theta_{DIP_{f/e}}) \cdot {}^5_6T_{ft_i}$$

$$(1)$$

where:

- Q_i is a matrix containing position and orientation of the fingertip of each finger.
- ${}^0_0T_i$ represents a roto-translation matrix taking into account the fact that the fingers are slightly fanned out and allowing to pass from the initial base reference frame (R_o) to the alignment of the i-th finger first reference frame (R_{0i}).
- ${}^0_6T_i(\theta_j)$ is a matrix containing the geometrical transformation between the i-th finger first reference frame and the i-th fingertip (ft_i). The matrix is composed of the concatenation of the transformation matrices of each finger link.
- ${}^{(j-1)}_jT_i(\theta_j)$ is a matrix containing the geometrical transformation between the $(j-1)$-th reference frame and the j-th reference frame of the i-th finger.
- ${}^5_6T_{ft_i}$ represents the position of the fingertip with respect to the distal (5th) reference frame.

j corresponds to each finger's joint $CMC_{f/e}$, $MCP_{ab/ad}$, $MCP_{f/e}$, $PIP_{f/e}$, $DIP_{f/e}$. ft_i stands for the fingertip of i-th finger.

3   Dynamics of a Single Finger

This section provides the dynamics equation system of a generic single finger, represented in Figure 2. The CMC DoF, that deals with the palm, and the MCP abduction/adduction one are neglected, since their range of movement is very low. For sake of brevity, in the following the i index is omitted, and $c\theta_j$ and $s\theta_j$ stand for cosine and sine of θ_j, respectively. The metacarpus is assumed as fixed, while only the finger phalanges are moving parts. Thus, R_2 is the base reference system, and all the equations are written with respect to R_2. The following equations can be recognized as applicable to any 3-R planar serial robot.
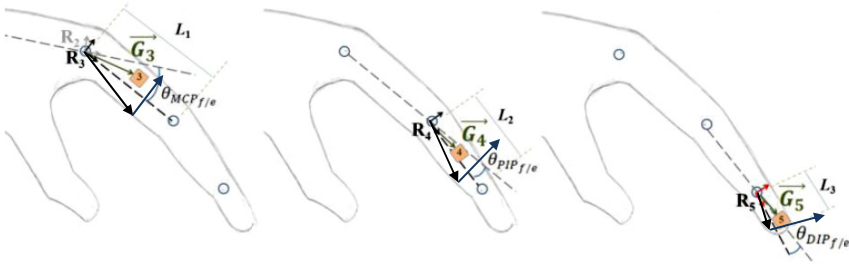
Fig. 2 Dynamic model of a finger

The dynamic model is determined using Euler–Lagrange equations. The kinetic energy is calculated starting from the position vectors of the center of mass of each phalanx with respect to the base reference frame R_2; in general, the position of the center of mass of the j-th phalanx with respect to the j reference frame is $\mathbf{G}_j = [b_{jx} \quad b_{jy} \quad 0]^T$, where j=3,4,5. The mass of the j-th phalanx is m_j and the respective moment of inertia with respect to the axis z is I_j. The following change of coordinates is introduced:

$$\psi_3 = \theta_{MCP_{f/e}} \; ; \quad \psi_4 = \theta_{MCP_{f/e}} + \theta_{PIP_{f/e}} \; ; \quad \psi_5 = \theta_{MCP_{f/e}} + \theta_{PIP_{f/e}} + \theta_{DIP_{f/e}} \quad (2)$$

The generic position vector of the center of mass with respect to the base reference frame R_2 is:

$$\mathbf{G}_j = [G_{jx} \quad G_{jy} \quad G_{jz}]^T = \sum_{q=3}^{j-1} \begin{bmatrix} L_{q-2}c\psi_q \\ L_{q-2}s\psi_q \\ 0 \end{bmatrix} + \begin{bmatrix} b_{jx}c\psi_j - b_{jy}s\psi_j \\ b_{jx}s\psi_j + b_{jy}c\psi_j \\ 0 \end{bmatrix} \quad (3)$$

The velocity of the generic center of mass is obtained:

$$\mathbf{v}_{G_j} = \sum_{q=3}^{j-1} \begin{bmatrix} -L_{q-2}\dot{\psi}_q s\psi_q \\ L_{q-2}\dot{\psi}_q c\psi_q \\ 0 \end{bmatrix} + \begin{bmatrix} -b_{jx}\dot{\psi}_j s\psi_j - b_{jy}\dot{\psi}_j c\psi_j \\ b_{jx}\dot{\psi}_j c\psi_j - b_{jy}\dot{\psi}_j s\psi_j \\ 0 \end{bmatrix} \tag{4}$$

The kinetic energy is thus expressed as:

$$T = \frac{1}{2}\sum_{j=3}^{5}\left(m_j v_{G_j}^2 + I_j \dot{\psi}_j^{\,2}\right) \tag{5}$$

The potential energy includes a gravitational term and an elastic one. Regarding the latter, the stiffness is considered as an average constant value k_j in this study, as a close approximation of the non-linear and anisotropic finger stiffness (i.e. it varies with the direction). k_3, k_4 and k_5 are the stiffness values for the MCP, DIP and PIP joints, respectively [9]. The potential energy is expressed as:

$$U = \sum_{j=3}^{5}\left(m_j g G_{jy} + \frac{1}{2}k_j(\psi_j - \psi_{j-1})^2\right) \tag{6}$$

Moreover, a function of the generalized velocities, usually referred to as the Rayleigh dissipation function F, is introduced for the damping forces; it is expressed as:

$$F = \sum_{j=3}^{5}\left(\frac{1}{2}\beta_j(\dot{\psi}_j - \dot{\psi}_{j-1})^2\right) \tag{7}$$

Where the damping constant β_j stands for the non-conservative contribution, caused by the muscles actuating the finger. Non-conservative forces contributed less than 15% to the total force response to static displacement. Muscle viscosity is dissipative and, hence, non-conservative, resulting in a force field with nonzero curl [9]. To be more precise, values β_3, β_4 and β_5 are the damping values for the MCP, DIP and PIP joints respectively. Considering the generalized coordinates ψ_j the Euler–Lagrange equations become:

$$\frac{d}{dt}\left(\frac{\partial(T-U)}{\partial\dot{\psi}_j}\right) - \frac{\partial(T-U)}{\partial\psi_j} + \frac{\partial F}{\partial\dot{\psi}_j} = \tau_j \tag{8}$$

Where j= 3, 4, 5. The τ_j terms contain the forces applied through the muscles in order to actuate the phalanges and the contact forces. According to the virtual work principle, the generalized force τ_j is:

$$\tau_j = \frac{\sum_{j=3}^{5}\delta W_j}{\delta\psi_j} \tag{9}$$

Where δW_j is the virtual work done by the force applied to the system. Then, it is:

$$\tau_j = (F_{jy}e_{jx} - F_{jx}e_{jy}) + \sum_{q=j+1}^{5} \begin{bmatrix} -L_{(j-2)}s\theta_j \\ L_{(j-2)}c\theta_j \\ 0 \end{bmatrix} \cdot \begin{bmatrix} F_{qx}c\psi_q - F_{qy}s\psi_q \\ F_{qx}s\psi_q + F_{qy}c\psi_q \\ 0 \end{bmatrix} + C_{mj} - C_{m(j+1)}$$

(10)

where the term C_{mj} refers to the torque produced by the muscles on the j-th joint, and $\mathbf{F}_j = [F_{jx} \quad F_{jy} \quad 0]^T$ is the contact force applied to the j-th phalanx at the point defined by the position vector $\mathbf{e}_j = [e_{jx} \quad e_{jy} \quad 0]^T$.

Calculating each element of the Euler–Lagrange equations, the dynamical system in Eq. (8) can be written in matricial form:

$$[A] \cdot [\ddot{\psi}_3 \quad \ddot{\psi}_4 \quad \ddot{\psi}_5]^T = [B]$$

(11)

where the 3x3 matrix [A] contains the coefficients of the accelerations, and the 3x1 vector [B] contains the remaining terms.

Eq. (11) allows the direct dynamics of the finger to be solved, where, given the torques exerted by the muscles on each phalange, the movement of the finger can be calculated. If, on the other side, an inverse dynamics problem is set, it is simple to rearrange Eq. (11) to obtain the trend of the unknown muscle torques from the phalanges motion laws.

4   Simulation

The current section deals with the implementation of the dynamics equations. Anthropometric data [10, 11] and proper numerical constants have been imposed, and a realistic circular grasping movement for a human finger is imposed.

In particular, the simulation shown here deals with an inverse dynamics case study: given the motion law of the system (i.e., the kinematic angles of the phalanges and their time derivatives), the torques exerted by the muscles on each phalanx are calculated. Figure 3 shows the imposed trend of each angle in time, starting from the straight position (angles=0°) and performing a flexion movement, then simulating a circular grasping operation. The angle proportions between the phalanges descend from physiological constraints [12, 13], as well as typical circular grasping proportions. Figure 4 shows the C_{m3}, C_{m4}, and C_{m5} torque values, required to perform this grasping operation. The maximum values of the contact forces used in the simulation were obtained from An et al. [14], which reports the maximum mid-phalangeal joint normal forces exerted by human fingers in a cylindrical power grasp, with values for the index finger of $\mathbf{F}_{max} = [42 \quad 22 \quad 62]^T$N for the proximal, middle and distal phalanx, respectively. Each column in the figure deals with a single simulation: case a) 100% F_{max}; case b) 50% F_{max}; and case c) 25% F_{max}. The a)-column graphs allow a comparison with

the data collected by Hasser [15]: this work states that the maximum torque capabilities of the human hand are $\mathbf{C}_{m\_max} = [4630 \quad 2280 \quad 775]^T$ Nmm for the proximal, middle and distal phalanx, respectively. The maximum torque values of the simulated C_{m4} and C_{m5} are very similar to the literature data, with a difference of 3.2% and 4% respectively. On the other side, the result for C_{m3} is quite different. This may be caused by the fact (not explicitly mentioned) that perhaps not all the three maximum forces can be exerted contemporarily.
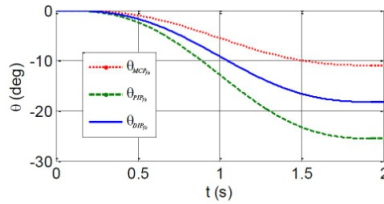
Fig. 3 Behavior of the joint angles in time
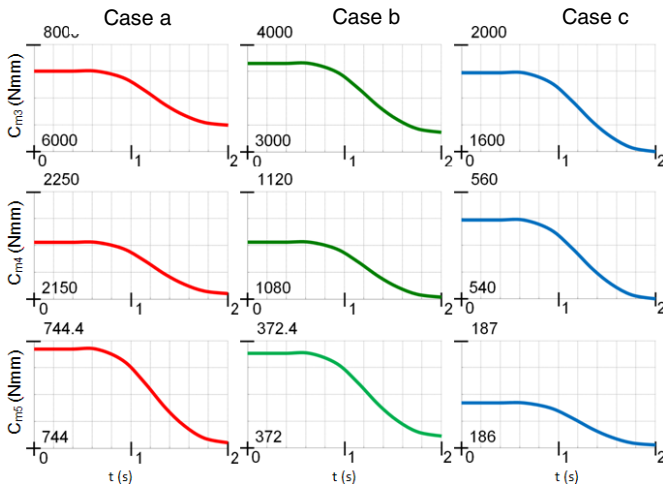
Fig. 4 Inverse dynamics case: behavior of the torques C_{mi} with respect to time

5   Conclusions

An exhaustive study of the human hand was performed, dealing with the kinematics of the human hand and showing the matrices with the MDH parameters and detailed equations to solve the kinematics of the hand. In addition, the dynamics of a single finger was analyzed and solved. A case study was proposed and a simulation was completed using the provided anthropometric data, in order to investigate the capabilities of the proposed analytical system.

The results of the current study can be exploited to conceive future hand devices. In fact, the study of the kinematics and the dynamics constitute a preliminary stage for the development of any structure similar to the human hand, for instance, in robotic or rehabilitation hands projects. Hence, the value of this analytical frame is twofold: to model the finger itself, for example to be used in a control scheme model of a human-machine interface, such as a hand exoskeleton or to model a finger-like architecture, such as a robotic hand.

References

1. Schoonejans, P., Stott, R., Didot, F., Allegra, A., Pensavalle, E., Heemskerk, C.: Eurobot: EVA-assistant robot for ISS, Moon and Mars. In: Proc. 8th ESA Workshop on Advanced Space Technologies for Robotics and Automation, Noordwijk (November 2004)
2. Lovchik, C.S., Diftler, M.A.: The robonaut hand: A dexterous robot hand for space. In: Proc. IEEE Int. Conf. Robotics and Automation (1999)
3. Jordan, N., Saleh, J., Newman, D.: The extravehicular mobility unit: A review of environment, requirements, and design changes in the US spacesuit. Acta Astronautica 59, 1135–1145 (2006)
4. Schabowsky, C.N., Godfrey, S.B., Holley, R.J., Lum, P.S.: Development and pilot testing of HEXORR: Hand EXOskeleton Rehabilitation Robot. Journal of Neuroengineering and Rehabilitation (2010)
5. http://www.nasa.gov/mission_pages/station/main/robo-glove.html
6. Worsnopp, T.T., Peshkin, M.A., Colgate, J.E., Kamper, D.G.: An Actuated Finger Exoskeleton for Hand Rehabilitation Following Stroke. In: Proceedings of the 2007 IEEE 10th International Conference on Rehabilitation Robotics, Noordwijk, The Netherlands, June 12-15 (2007)
7. Ho, N.S.K., Tong, K.Y., Hu, X.L., Fung, K.L., Wei, X.J., Rong, W., Susanto, E.A.: An EMG-driven Exoskeleton Hand Robotic Training Device on Chronic Stroke Subjects. In: 2011 IEEE International Conference on Rehabilitation Robotics Rehab Week Zurich, ETH Zurich Science City, Switzerland, June 29-July 1 (January 2011)
8. Craig, J.J.: Introduction to Robotics, Mechanics and Control, 3rd edn., pp. 67–76. Pearson Education International (1986)
9. Milner, T.E., Franklin, D.W.: Characterization of multijoint finger stiffness: dependence on finger posture and force direction. IEEE Transactions on Biomedical Engineering 45(11), 1363–1375 (1998)
10. Habib, S.R., Kamal, N.N.: Stature estimation from hand and phalanges lengths of Egyptians. Journal of Forensic and Legal Medicine 17(3), 156–160 (2010)
11. Jasuja, O.P., Singh, G.: Estimation of stature from hand and phalange length. Journal of Indian Academy of Forensic Medicine 26(3) (2004)
12. Rijpkema, H., Girard, M.: Computer animation of knowledge-based human grasping. In: Proceedings of Siggraph, pp. 339–348 (1991)
13. Cobos, S., Ferre, M., Sanchez, M., Ortego, J.: Constraints for Realistic Hand Manipulation. In: The 10th Annual International Workshop on Presence, PRESENCE 2007, Barcelona, Spain, October 25-27 (2007)
14. An, K.N., Askew, L., Chao, E.Y.: Biomechanics and Functional Assessment of Upper Extremities. In: Karwowski, W. (ed.) Trends in Ergonomics/Human Factors III, pp. 573–580 (1986)
15. Hasser, C.J.: Force-Reflecting Anthropomorphic Hand Masters. Armstrong Lab Wright-Patterson AFB Oh Crew Systems Directorate, 37 p. (July 1995)

Design and Simulation of a Simplified Mechanism for Sit-to-Stand Assisting Devices

Erika Ottaviano[1], Pierluigi Rea[1], Peru Errea[2], and Charles Pinto[2]

[1] University of Cassino and Southern Lazio, Italy
  `{ottaviano,rea}@unicas.it`
[2] University of the Basque Country, Spain
  `charles.pinto@ehu.es`

Abstract. Standing up deals with the transition from two stable postures, namely the seated and standing ones, with a movement concerning all body segments except the feet. The transfer from sitting to standing and back requires both voluntary movement of different body segments that contribute to the change of posture and equilibrium control during an important displacement of the Centre Of Gravity (COG) of the body. This operation can be considered of great importance for impaired and elderly people to achieve minimal mobility and independence in daily life activities. In this paper we propose the design of a simplified mechanism to be used in assisting device for aiding the sit-to-stand. In particular, experimental tests are carried out to track and record point trajectories and the orientation of the trunk during the sit-to-stand. Twenty healthy adult volunteers were recruited for a trial in order to derive a suitable theoretical trajectory of the point of interest. Finally, according to the experimental results, a proposal and simulation are presented for a novel mechanical system. In particular, in this paper a suitable theoretical trajectory of the point of interest is used to derive a 1-DOF mechanism, which is able to reproduce the requested motion.

Keywords: Sit-to-Stand, Mechanical Design, Assisting Devices, Experimental Evaluation, Simulation.

1   Introduction

Among several daily-life activities, sit-to-stand can be considered one of the most common and it can be defined as a movement in which the base of support is transferred from the seat to the feet. The weight then moves to the front of the feet as the trunk moves forward and the pelvis lifts from the surface [1]. The trajectory of the COG is then characterized by a movement forward and then backward with simultaneous vertical displacement. Consequently, the entire movement requires a strong coordination between posture and movement, but due to several reasons, it may represent a problem for elderly or people with a motion disability.

The analysis of kinematic and kinetic data of the body movement and motion patterns during the sit-to-stand has been subject of several studies, as for example in [1-3], also by considering the contribution of the arms [4]. Most of reported analyses focused on muscle and articulation efforts to determine the correct posture for the task or modification due to ageing or motor impairments.

Several robotic systems have been designed for medical applications [5,6], mechanical devices have been developed to provide support during the walk operation [7] and daily life operations, such as picking objects [8], and aiding during the sit-to-stand [9-11]. An overview on existing assisting devices is reported in [12] focusing the attention on main characteristics but also on limitations. In most of cases robotic devices are bulky and expensive and they are not totally useful for all patients or medical personnel [13]. Among several basic requirements, an assisting device should provide suitable support to the trunk to avoid back pain [14], therefore, experimental data and then numerical simulation can be useful to properly design and then verify the effectiveness of proposed solutions.

In this paper, experimental tests and numerical simulations are developed and reported to design novel assisting devices for the sit-to-stand. In particular, a simplified mechanism having 1-DOF only is proposed and simulated according to the obtained experimental tests.

2   Experimental Evaluation of the Sit-to-Stand

A trial was carried out at the University of Cassino and Southern Lazio by considering 20 healthy and young volunteers (age 20-30). Subjects were asked to be seated on an armless chair set to the 100% of the knee height. The back support of the chair was used to set the trunk in a vertical position. The arms do not participate actively to the movement. The subjects were asked to assume a seated position of readiness and then they were asked to stand up from the chair. During the test the speed of the movement was kept constant, indeed in quasi-static conditions were obtained.

Human detection and tracking is the first step to motion analysis. Recently, due to the high demand there is a fast development of reliable, easy-to-use and economic systems to monitor and determine biomechanical performances, as reported in [15]. One example is the Virtual Sensei Lite, which is a free version of Virtual Sensei software developed and successfully used as a tool for sports club coaches for biomechanical analysis of 3D fast motions [16, 17]. In this context we used the software for the evaluation of the sit-to-stand together with a motion capture system based on cameras. Figure 1 shows the experimental set-up. A study on the sit-to-stand movement pattern reported in [3] demonstrated that the neck, trunk, and pelvis followed similar patterns, moving first into flexion and then into extension as the movement cycle progressed. A similar result was obtained during experimental tests, as it is shown in Figure 2.

a)   b)
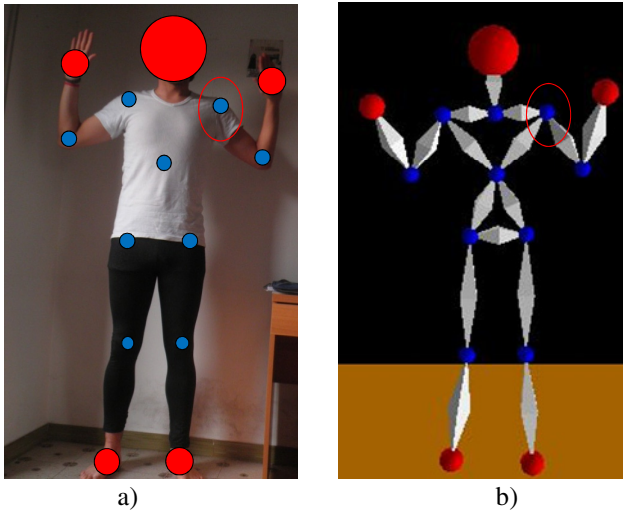
Fig. 1 Experimental set-up: a) subject during the calibration; b) image from Virtual Sensei Lite
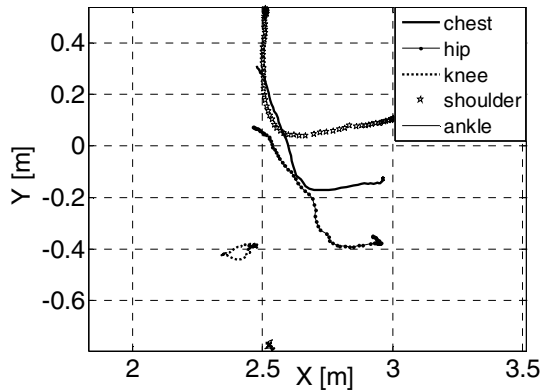
Fig. 2 Trajectories of points for a male subject in Fig.1 obtained during the sit-to-stand

Data in Fig.2 are evaluated in the video capture system reference frame, as the outcome of the Virtual Sensei Lite without any filtering. After a change of reference frame data are expressed in a frame attached to the subject's foot. In the following we focus the attention on the shoulder (as shown in Fig.1) since the device will be developed to lift the person by the armpits. Experimental results obtained during the trial show a large variation in the size its trajectory, but it always possible to recognize a typical shape, which can be referred as trajectory pattern, which can be characterized by four parameters: LF, which is the length of the forward movement, HF, which is the height of forward movement, HL that is the height of the lifting movement, and LL that is the length of the lifting movement. These

parameters have been measured after the experimental tests for all the subjects. Figure 3 shows trajectory patterns for male and female subjects, and a referred trajectory pattern, which is an average of the reported trajectories. The derivation of a referred trajectory pattern can be used for the design of a mechanism that is able to reproduce the requested movement during the Sit-To-Stand. Figure 4 shows a comparison of such trajectory pattern and an interpolating polynomial, which can be used to design a mechanism as path generator by referring to a coupler point curve. It is worth noting that according to the experimental results, the orientation of the trunk can be also derived, therefore, it is possible to implement a study on the design of a mechanism that reproduces a rigid body motion.
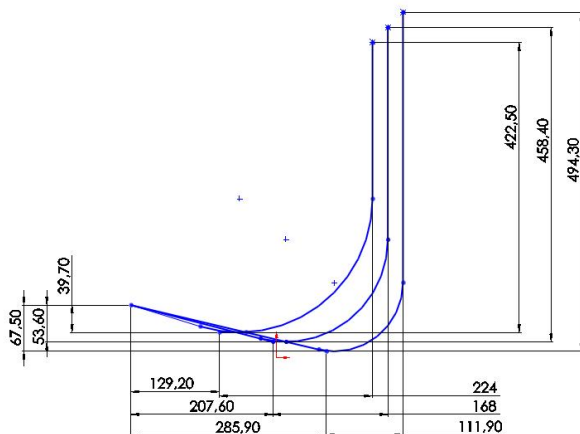
Fig. 3 Trajectories patterns of the point of interest typical for male and female subjects, and the referred trajectory pattern (average) for the trial
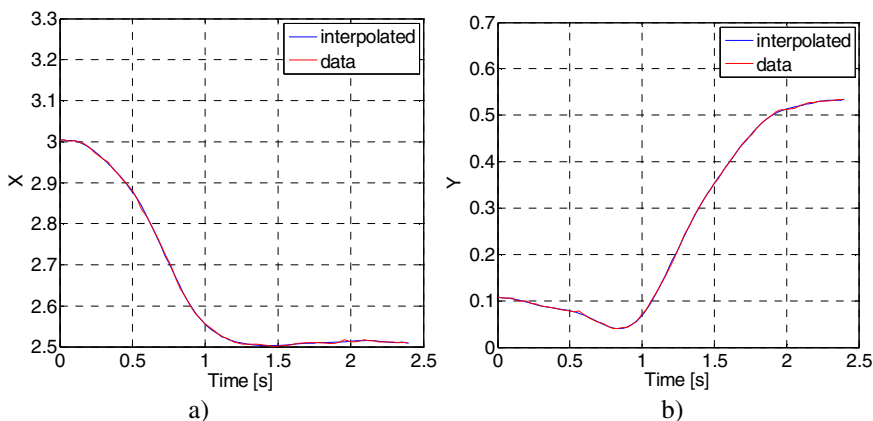
Fig. 4 Comparison between polynomial expression interpolating: a) x displacement; b) y displacement, as function of time

3   Design Considerations

The central premise of the study of the Sit-To-Stand is that there is enormous variation of motion patters, in fact, not only are there obvious differences in the anthropometric data of individuals, but everybody has their own unique style of movement as distinctive as their personality, but also according to the age, weight strength in muscles. Furthermore, each individual will never repeat exactly the same movement from trial to trial. The myriad of factors that influence these variations are too numerous to control, so we have chosen in our study of the human movement and in developed procedures, to consider these variations by using four parameters only, as shown in the trajectory patterns in Figs. 3 and 5.

Referring to the design of the assisting device, it will composed by a mechanical part that will be responsible of the requested movement, an actuation system to give suitable power to lift and sustain the person, and interfaces to sustain the person at the armpits. In addition, any security system to prevent accidental falls and brake system should be included in the overall design.

Focusing the attention on the mechanism devoted to reproduce a desired movement, the designer should find a linkage that will meet the requirements: the device should posses 2-DOFS in saggittal plane to accomplish the requested trajectories, which vary according to anthropometric data of the subject, and his/her physical conditions. Then, an additional DOF can be included to provide a suitable orientation for the trunk support. According to these initial specifications, the designer should determine the topology of the kinematic chain underlying the mechanical structure, indeed choosing among serial, parallel or hybrid structures. Since the requested motion is obtained in the saggital plane, a planar mechanism instead of spatial one can be considered. Among many solutions, we have chosen to simplify the design problem reducing the number of DOFS, mainly because 1) the system should be easy-in-use for non-expert generic users; 2) it leads to simpler control units and less expensive system related to the actuation system than a 3-DOFS system. Furthermore, a large number of commercialized systems are lifters with just 1-DOF that lifts the person without giving any particular trajectory to the trunk. In the following we propose a 4-bar linkage obtained starting from an initial guess solution and performing a parametric iterative study focusing the attention on the referred trajectory pattern in Fig. 5 and related values of the movement parameters given in Table 1. The obtained mechanism gives the required trajectory with good efficiency in reproduction of the trajectory pattern and force transmission. It is worth noting that a type of slider-cranks described in [18] can be also used for obtaining the requested trajectory.

Table 1 Values for the movement parameters of the trajectory pattern

HF: height of forward movement	LF: length of the forward movement	LL: length of the lifting movement	HL: height of the lifting movement
0.053 m	0.207 m	0.168 m	0.458 m
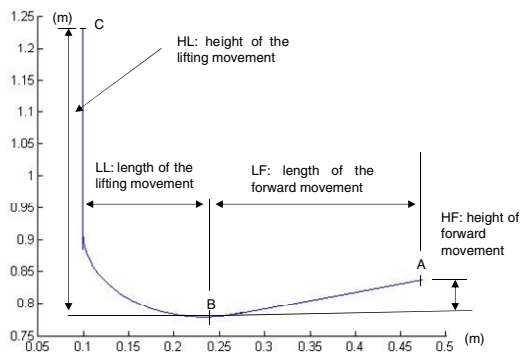
Fig. 5 A sketch and main parameters for the required trajectory pattern

4   A Proposal for a Device for the Sit-to-Stand

According to the requirements obtained by experimental tests and considerations reported in previous Section, we have designed a mechanical system for the sit-to-stand as shown in Fig. 6. The device can be either positioned frontally or posteriorly having 1-DOF in order to reproduce the trajectory given in Fig. 5. Due to lack of space more details of the design are not reported in this paper. At this first stage we have not considered a support for the trunk. In the future, this aspect and other special features as a sling system will be also taken into account.
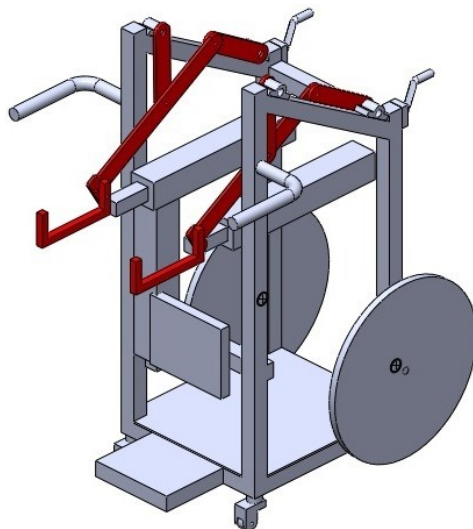
Fig. 6 A sketch for the mechanical design of the device for the sit-to-stand

5 Numerical Results

Simulations were carried out in Solidworks environment. Figure 7 shows a sequence for a simulation with the proposed design solution. It is worth noting that that the body mass has been simulated by including forces on the armpits supports.
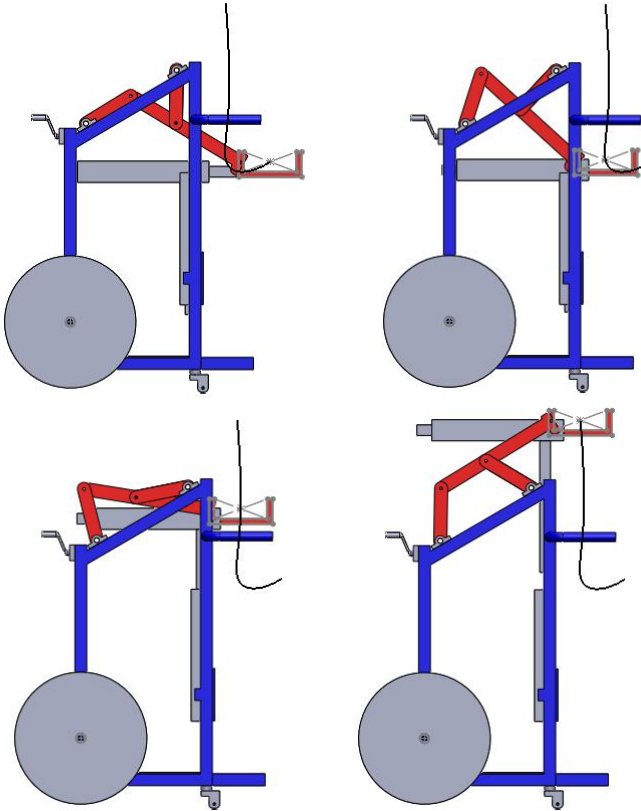
Fig. 7 A motion sequence for the proposed device for the sit-to-stand

6 Conclusions

In this paper the sit-to-stand has been analyzed to identify requirements for design purposes. Results of a trial were used for the design and simulation of a novel device for the sit-to-stand, which has been based on a four-bar linkage. A simulation of the operation of the system was presented. Future development of the work is the simulation including a human body model and construction of a prototype.

References

1. Schenkman, M., Berger, R.A., Riley, P.O., Mann, R.W., Hodge, W.A.: Whole-body movements during rising to standing from sitting. J. Physical Therapy 70, 638–651 (1990)
2. Mourex, F., Pozzo, T., Rouhier-Marcer, I., Didier, J.-P.: A kinematic comparison between elderly and young subjects standing up from and sitting down in a chair. J. Age and Ageing 27, 137–146 (1998)
3. Nuzik, S., Lamb, R., Vansant, A., Hirt, S.: Sit-to-Stand Movement Pattern A Kinematic Study. J. Physical Therapy 66(11), 1708–1713 (1986)
4. Seedholm, B.B., Terayama, K.: Knee forces during the activity of getting out of a chair with and without the aid of the arms. J. Biomed. Eng. 11, 278–282 (1976)
5. Pisla, D., Gherman, B., Vaida, C., Suciu, M., Plitea, N.: An active hybrid parallel robot for minimally invasive surgery. Robotics and Computer-Integrated Manufacturing 29(4), 203–221 (2013),
   http://dx.doi.org/10.1016/j.rcim.2012.12.004
6. Pisla, D., Szilaghyi, A., Vaida, C., Plitea, N.: Kinematics and workspace modeling of a new hybrid robot used in minimally invasive surgery. J. Robotics and Computer-Integrated Manufacturing 29(2), 463–474 (2013),
   http://dx.doi.org/10.1016/j.rcim.2012.09.016
7. Yu, H., Spenko, M., Dubowsky, S.: An adaptive shared control system for an intelligent mobility aid for the elderly. J. Autonomous Robots 15, 53–66 (2003)
8. Graf, B., Hans, M., Rolf, D.S.: Care-O-bot II - development of a next generation robotic home assistant. J. Autonomous Robots 16, 193–205 (2004)
9. Nagai, K., Nakanishi, I., Hanafusa, H.: Assistance of self-transfer of patients using a power-assisting device. In: IEEE Int. Conf. on Rob. and Automation, Taipei, pp. 4008–4015 (2003)
10. Mederic, P., Pasqui, V., Plumet, F., Bidaud, P., Guinot, J.C.: Design of a walking-aid and sit-to-stand transfer assisting device for elderly people. In: 7th Int. Conf. on Climbing on Walking Robots (CLAWAR 2004), Madrid (2004)
11. Castelli, G., Ottaviano, E.: Modelling, Simulation and Testing of a Reconfigurable Cable-Based Parallel Manipulator as Motion Aiding System. J. Applied Bionics and Biomechanics 7(4), 253–268 (2010)
12. Martins, M.M., Santos, C.P., Frizera-Neto, A., Ceres, R.: Assistive mobility devices focusing on Smart Walkers: Classification and review. J. Robotics and Autonomous Systems 60(4), 548–562 (2012)
13. Ottaviano, E.: Design issues and application of cable-based parallel manipulators for rehabilitation therapy. J. Applied Bionics and Biomechanics 5(2), 65–75 (2008)
14. Rea, P., Ottaviano, E., Conte, M., D'Aguanno, A., De Carolis, D.: The design of a novel tilt seat for inversion therapy. J. of Imaging and Robotics (IJIR) 11(3) (2013) ISSN 2231-525X
15. Ottaviano, E., Castelli, G.: A Procedure for Experimental Evaluation of the Sit-to-Stand for the Design of Assisting Devices. In: New Trends in Mechanism and Machine Science, Proc. of the EUCOMES 2012, pp. 487–495. Springer (2012) ISBN 978-94-007-4902-3
16. Timmi, A., Pennestrì, E., Valentini, P.P., Aschieri, P.: Biomechanical Analysis of Two Variants of the Karate Reverse Punch (Gyaku Tsuki) Based on the Evaluation of the Body Kinetic Energy from 3D Mocap Data. In: Proc. of the Multibody Dynamics ECCOMAS, Brussels (2011)
17. Virtual Sensei website (2013), http://www.virtualsensei.it/
18. Figliolini, G., Rea, P.: Effects of the design parameters on the synthesis of Geneva mechanisms. In: Proc. of the Institution of Mechanical Engineers. PART C, J. of Mechanical Engineering Science, pp. 1–10 (2012) ISSN: 0954-4062, doi:10.1177/0954406212466194

Collision Free Design of Dental Prosthesis

E. Solaberrieta, L. Barrenetxea, E. Bilbao, O. Etxaniz, N. Goikoetxea,
R. Minguez, E. Sierra, and A. Uribarri

University of the Basque Country, Spain
eneko.solaberrieta@ehu.es

Abstract. This research project presents the construction of a Dental Virtual Articulator that permits the design of collision-free geometry on dental prostheses. Thanks to this articulator kinematic analysis can be taken into account in the design of dental prostheses. This is an improvement of the utmost importance in this field. Several steps have been followed in the development of this virtual articulator. First, in order to obtain a digitalized data of each individual patient, plaster models of his/her upper and lower parts of the jaw were scanned. Afterwards, depending on the required accuracy or on the patient's setting data available in each case, the type of articulator was selected. Then, using a CAD system, the missing teeth were statically modelled. Also, the opening/closing movements and the lateral occlusion were simulated with the CAD system in order to analyze possible occlusal collisions and modify the design accordingly. Finally, this paper discusses the still existing shortcomings of virtual articulator simulation and provides a detailed research prospect as well. The main practical implications of this paper are, on the one hand, the improvement in dental CAD/CAM systems by adding the kinematic analysis, and on the other, since each of them has an individual pattern of movement, the analysis of the simulations of different articulators.

Keywords: collision free design, dental CAD/CAM, virtual articulator, prosthesis design.

1   Introduction

This project arises out of the need to design a Dental Virtual Articulator in order to design dental prostheses with a collision-free geometry. This can be achieved by means of CAD systems and Reverse Engineering tools, simulating and analyzing mandibular movements.

This development has been made at the Product Design Laboratory (PDL, www.ehu.es/PDL), in the Faculty of Engineering of Bilbao, University of the Basque Country. This Laboratory has focused its investigation on Reverse Engineering and Rapid Prototyping knowledge areas and is currently looking for new fields of application for these new design methods in an effort to promote technological transference with neighboring companies.

The PDL is developing the design of this virtual articulator in collaboration with the Department of Prosthetic of the Martin-Luther University of Halle (Germany). In addition, the Dentistry Department at our university - University of the Basque Country- has supported this project with some useful advice and technical support.

To begin with, different articulators were selected to be modelled through different CAD systems (SolidEdge and CATIA). The design process was carried out using the measuring tools and Reverse Engineering tools available at the PDL. These tools are: the Handyscan EXAscan 3D scanner and its software (VXscan), the Reverse Engineering and Computer-Aided Inspection Software (Geomagic Studio and Qualify), the Rapidform XOR, as well as the ATOS I rev.2 GOM 3D scanner.

After a thorough analysis of the results obtained with different articulators in different systems, the Panadent PSH articulator and the ATOS I scanner were selected, together with the Rapidform and Solidedge software.

In this process, the articulator is first digitized. Then, the next stage consists in obtaining the upper and lower dentures digitally. Apart from this, it is necessary to register the relative location of the occlusal surface referred to the intercondilar axis. This is achieved by means of the face bow. Afterwards, the design of the dental prosthesis is carried out using the CAD system and finally, mandibular movements are simulated. The ultimate aim of this process is to optimize the design of the dental prosthesis whilst avoiding collisions during the excursive movements.

The main tool used in this project is the dental articulator presented in this chapter, together with the complementary registration systems.

1.1 Dental Mechanic Articulators
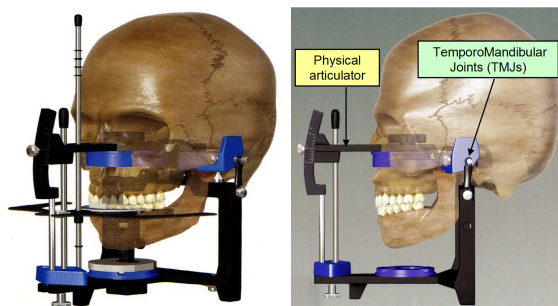
Fig. 1 Dental physical articulator with skull

Physical dental articulators (Fig. 1) are tools that simulate the movements of the human lower jaw and the TemporoMandibular Joints (TMJ-s). They have been used for more than 100 years for different purposes in dentistry [1] (Fig. 2). Since

they simulate specific patients for dental technicians in their laboratory work, they have become indispensable instruments for dentists in their diagnostic activity. Physical dental articulators enable technicians to carry out a study of the occlusal relations between dental arches and to detect harmful occlusal interferences on models before more sophisticated occlusal equilibration procedures are performed on the patient. This equilibration of partial and full dentures is also carried out in dental articulators. Together with the wax-up technique, articulators enable technicians to construct fixed or removable prostheses in the dental laboratory according to the particularities of the different movements of each patient. Nowadays, this procedure is considered standard, so current efficient dentistry necessarily involves the use of physical dental articulators.
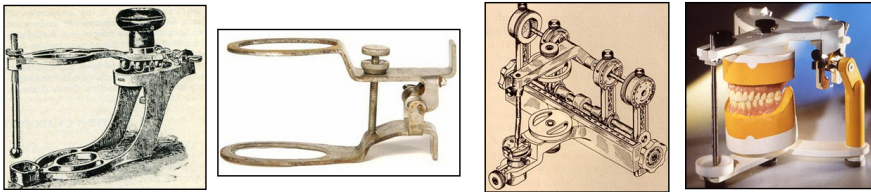
Fig. 2 Articulators of Luce, Kerr, Hanau-Kineskope and Stratos-200

Over the last 120 years, hundreds of different articulators have been developed [2] [3]. Nevertheless, there has been no remarkable conceptual development in articulators. Today's articulators are handy, functional and more precise in both construction and operation. Many differences can be pointed out among them: adjustment, cost, Arcon and Non-Arcon, versatility, etc.

In order to reproduce the individual parameters of each patient, the articulator must be adjustable. First, the setting data are measured on the patient and, using the face bow, the relative location of the occlusal plane is transferred from the patient onto the physical dental articulator.

Due to its three-dimension condilar trajectory, the Panadent PSH semiadjustable articulator was chosen for this project [4] [5].

1.2 Registering Systems

To simulate the specific movements of each patient, the articulator must be adjusted with the specific setting obtained from each patient. Different registration systems are used for this purpose: face-bow, interocclusal registrations and electronic registering systems.

1.3 Design Processes

Over the last few years, the design process of dental prostheses has changed and technicians can now design a complex prosthesis virtually.
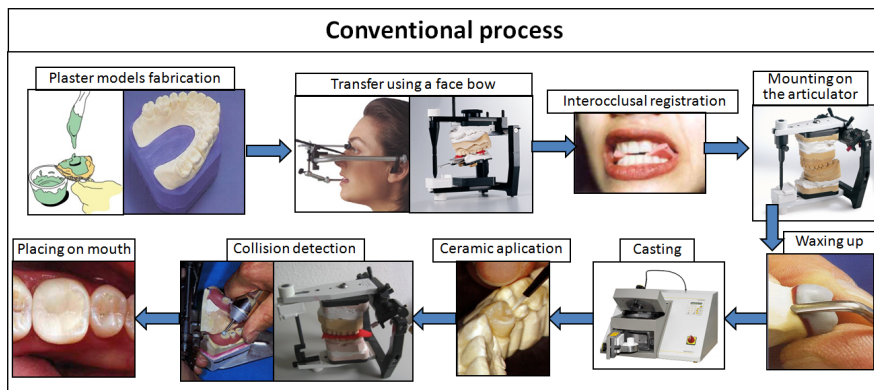
Fig. 3 Conventional design process

In order to have an overall view of the current situation in this field, the coexisting design processes will be briefly presented. The first one (Fig. 3) is the most widely used design process and is still in use in the majority of dental laboratories. The structure of the prosthesis is generated using the wax-up technique (drop by drop) [6]. Then, the ceramic is added, generating the occlusal surface, which should fit with the antagonist. Apart from this, the excursive movements (lateral and protrusive) are applied to check out for possible interferences. If found, they are removed. Once the final design is generated, a thermal treatment is carried out on the ceramic part, which is finally located in the mouth.

Nowadays, the most advanced dental laboratories work with CAD/CAM systems and follow the process described in Fig. 4. This change has involved some significant improvements in terms of time, data registration, material resistance, parameters control, etc. Besides this, CAD/CAM systems are using new materials such as zirconium oxide, calcinable polymers, feldespathic ceramics, etc., being this aspect one of the differential factors among CAD/CAM systems. The future of prostheses design will undoubtedly be based on these systems.

On the other hand, these systems present some deficiencies. The most remarkable one is that they do not take into account the kinematics of the mandible. In other words, the prostheses designed using these systems could generate pathology due to the existence of occlusal interferences during the movements.
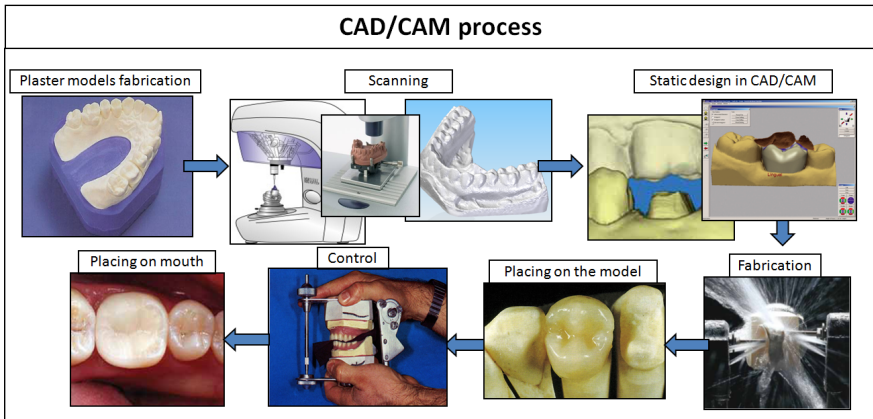
Fig. 4 CAD/CAM design process

Therefore, this paper presents a novel methodology to design collision-free dental prostheses. These virtual design processes [7] (Fig. 5) do not require a physical articulator. All the steps are computer-aided till the prosthesis is located in the mouth.
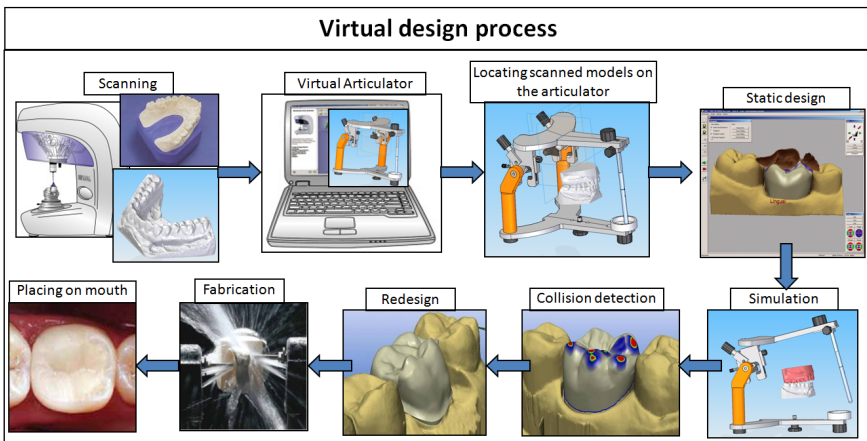
Fig. 5 Virtual design process

1.4 Virtual Articulator

Over the recent years, two virtual articulators have been developed by Kordass and Szentpétery, who were the first developers of such software. By using these articulators it is possible to:

- simulate human mandibular movements
- move digitized occlusal surfaces against each other according to these movements
- correct digitized occlusal surfaces to enable smooth and collision-free movements

The virtual articulator developed by Kordass and Gaertner [8] [9] from the Greifswald University in Germany was designed to record the exact movement paths of the mandible with an electronic jaw movement registration system called Jaw Motion Analyser (Zebris Medizintechnik GmbH, Tübingen/Germany) and move digitized dental arches along these movement paths on the computer. This software is able to calculate and visualize static and kinematic occlusal collisions. However, it must be pointed out that the electronic jaw recording system required by this virtual articulator is very sophisticated and expensive.

The virtual articulator developed by Szentpétery, from the Martin-Luther University of Halle [10] [11] [12] is based on a mathematical simulation of the movements that take place in an articulator. It is a fully adjustable three-dimensional virtual dental articulator, capable of reproducing the movements of an articulator. In addition, mathematical simulation contributes to offer some possibilities not offered by some physical dental articulators, such as the curved Bennet movement or different movements in identical settings. This makes it more versatile than a physical dental articulator. The graphic interface is currently being improved.

Besides, different firms presented their virtual articulators integrated in the CAD/CAM systems at the IDS´13 (International Dental Show 2013, Cologne, Germany). These virtual articulators permit the simulation of protrusive and lateral movements, whilst collisions are visualized in real time. The main disadvantage of this articulator is that the models have to be mounted with gypsum onto the mechanical articulator to scan them in this position, and this step requires time.

2 Results

As it has been explained, the first purpose is to build up a virtual articulator. Firstly, different types of articulators were selected (Fig. 6). Second, several tests were carried out using different scanning systems, Reverse Engineering software and different CAD systems. After a thorough analysis of the results and the difficulties involved in each case, the Panadent PSH and the ATOS I scanner were selected, together with Reverse Engineering software Rapidform and Solidedge as CAD systems.
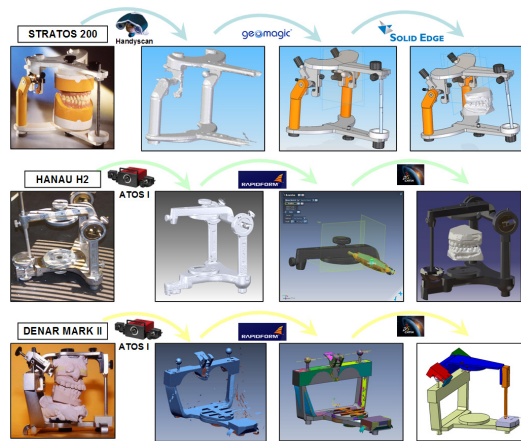
Fig. 6 Modelling processes of different articulators

The following Fig. 7 presents in detail the modelling of the Panadent PSH:
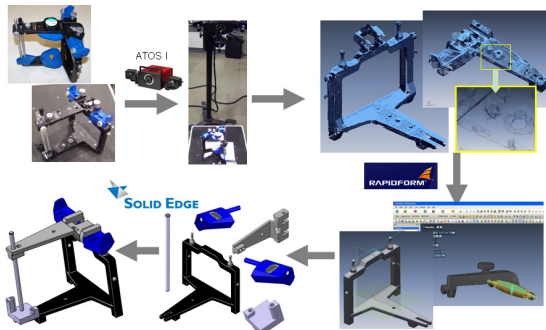
Fig. 7 Modelling process of Panadent

The main result of this project is the construction of the virtual articulator and its validation. Whilst for the other existing virtual articulators, unless a complex registration system is used, physical articulators are still necessary, for this design process, physical articulators are not necessary. This fact reduces the required time and increases the automation of the process.

Another result is the parametrization of the condilar fossa. This involves a greater control of the condilar trajectory. Using the parametrization, it is possible to introduce new parameters. When working with physical articulators, this is certainly impossible.

3   Conclusions

In summary, this project arises from the implementation of CAD systems and Reverse Engineering systems in the construction of a dental virtual articulator. Following the proposed system, producing a dental prosthesis digitally has proven to be possible. The currently commercialized CAD/CAM system does not take into account the kinematics and the existing virtual articulators require a complex registering system or several manual steps to mount models on the physical articulator. The proposed system reduces the amount of manual steps and at the same time, computer aided design becomes more important.

Another certainly important conclusion is that when the collided part is removed, the result is still valid. However, these interferences should be integrated on the re-design process while improving the geometry. This accounts for the importance of visualizing collisions so that, according to them, an optimum geometry can be generated in real time.

References

1. Hoffmann-Axthelm, W.: History of Dentistry. Quintessence Publishing Co. (1976)
2. Mitchell, D.L., Wilkie, N.D.: Articulators through the years. Part I. Up to 1940. J. Prosthet. Dent. 39, 330–338 (1978)
3. Mitchell, D.L., Wilkie, N.D.: Articulators through the years. Part II. From 1940. J. Prosthet. Dent. 39, 330–338 (1978)
4. Hobo, S., Herbert, T., Whitsett, D.: Articulator Selection for Restorative Dentistry. Journal of Prosthetics Dentistry 36, 35–43 (1976)
5. Lee, R.: Jaw movements engraved in solid plastic for articulator controls. Part I. Recording apparatus. Journal of Prosthetic Dentistry 22, 513–527 (1969)
6. Sharry, J.J.: Prostodoncia dental completa. Toray, ed. (1977)
7. Colombo, G., Filippi, S., Rizzi, C., Rotini, F.: A Computer Assisted Methodology to Improve Prosthesis Development Process. In: Proceedings of CIRP Design Conference, Design Synthesis, Twente, Netherlands (2008)
8. Kordass, B.: The virtual articulator-concept and development. Dent. Clin. N. Am., 493–506 (2002)
9. Gaertner, C., Kordass, B.: The Virtual Articulator: Development and Evaluation. Int. Jour. Computerized Dent. 6, 11–23 (2003)
10. Padrós, E.: Bases diagnósticas, terapéuticas y posturales del funcionalismo craneofacial. Tomo II. Ed.Ripano, 894–901 (2006)
11. Szentpétery, A.: Computer Aided Dynamic Correction of Digitized Occlusal Surfaces. J. Gnatho. 16, 53–60 (1997)
12. Szentpétery, A.: 3D Mathematic movement simulation of articulators and its application by the development of a software articulator. Martin-Luther University of Halle. Thesis (1999)

Kinematics Simulation and Validation of a Medical Robot

A. Szilaghyi, D. Pisla*, C. Vaida, B. Gyurka, and N. Plitea

Technical University of Cluj Napoca, Research Center for Industrial Robots Simulation and Testing, Memorandumului 28, RO-400114 Cluj-Napoca, Romania
{Andras.Szilaghyi,Doina.Pisla,Calin.Vaida,Bela.Gyurka,
Nicolae.Plitea}@mep.utcluj.ro

Abstract. A simulation model of a parallel medical robot is presented in this paper. The robot consists of two modules: the PARAMIS robot and an additional parallel module. The parallel module is used to obtain a mechanically fixed remote center of motion (RCM), enabling the structure to manipulate active instruments. The new structure provides the necessary motion control with respect to the particularities and restrictions of minimally invasive applications. A simulation based on the developed kinematic models is performed using the Simulink software from MATLAB. Another simulation of the imposed motion is performed using the CAD model of the structure. The numerical results obtained during the simulations are compared and show that the robotic structure is correctly modelled and reliable.

Keywords: Parallel robot, Simulation, Kinematics, Matlab, Simulink, Control.

1 Introduction

Medicine has known a continuous evolution animated by the ultimate goal of improving the life time and quality of humankind. In surgery, the latest revolution began 25 years ago, when appeared for the first time the concept of minimally invasive surgery (MIS). As a result of the latest developments in this field, robots have been introduced as advanced tools for surgeons in complex medical procedures. An important particularity shared by any robotic device for minimally invasive procedures refers to the special motion of the manipulated tool which passes through a fixed point in space. This point represents the entry port inside the patient body and for the manipulating devices it is often called remote center of motion (RCM) [14]. The mechanisms for MIS can be divided into two groups based on their handling of the entry port. The first group uses it as a passive (virtual) RCM which means that the manipulated device will use the entry port as guidance for its orientation. These structures, which use the "natural" 4 DOF joint, are easy to be controlled and have relatively low occupied space in OR but their precision is low and they cannot be

---

* Corresponding author.

used for the handling of active instruments which enter in direct contact with tissues. The second group imposes mechanically the RCM as a fixed point and the relative position between the robot and the patient superposed it over the entry port in the body. These solutions have complex kinematic chains, have large occupied space in OR, use a "virtual" 4 DOF joint but are capable of manipulating active instruments. Referring to their range of applications in the operating room, the robotic structures can be divided into 2 major groups: the first group integrates the laparoscope holders, the second one integrates complex surgical systems. Several laparoscope holders were developed, the most important being: AESOP [5], FreeHand [3], ViKY [17] and LAPMAN [9]. In the second group several solutions were achieved: The platform of AESOP was later used to create a multi-arm robotic system, named Zeus, able to manipulate different instruments [1], the da Vinci system, which reached a worldwide spread, providing real benefits in numerous surgical procedures. Other complex systems are Amadeus [15] and DLR MiroSurge [4].

The author's first achievement in this field is the 3-DOF laparoscope holder PARAMIS, [8], [16], which uses the entry port in the patient, as a virtual RCM, to guide the endoscope. Following the idea of modularity and the positive feedback from the surgeons, the development of a supplementary module for PARAMIS was chosen, in order to replace the virtual RCM with the mechanically imposed one. The robots with mechanically constraint RCM can be used for the manipulation of the active instruments in MIS and also for needle placement therapies. Needle placement therapies, covers applications like biopsies, fluid extraction from internal organs (heart, lungs) or placement of radioactive seeds in different body organs in minimally invasive cancer therapy, brachytherapy [12].

The paper presents some kinematic simulations of a medical parallel robot with five motors, performed by using the digital control model. Section 2 presents the kinematic scheme and a short description of the studied parallel robot. Sections 3 and 4 deals with the kinematic simulations and illustrates the numerical results of them, followed by the conclusions and references.

2   The Kinematic Scheme of the Parallel Robot

The analyzed parallel robot with five motors is based on an already existing robot and an attachable parallel orientation module, assuring high rigidity due to its closed chains. The robotic arm consists of a positioning parallel module PARAMIS with 3 motors and an orientation parallel module with 2 motors, presented in figure 1. This figure presents also a detail of the parallel module. From the first three active joints, actuated from the robot basis, two of them are prismatic and one is rotational. Two additional active joints are used in the module positioned on the tip of the arm with the length r_A, one of them is rotational and the other one is a prismatic joint [13].

To solve the geometric model, a mobile frame AX'Y'Z', attached to the end-effector in point A is used. The active coordinates of the robot are denoted by q_1, q_2, q_3, q_4 and q_5 and the notations b, h, e_2, d, r_1, r_2, e_3 and β were used for the geometrical parameters (Figure 1). Concerning the solving of the direct geometric
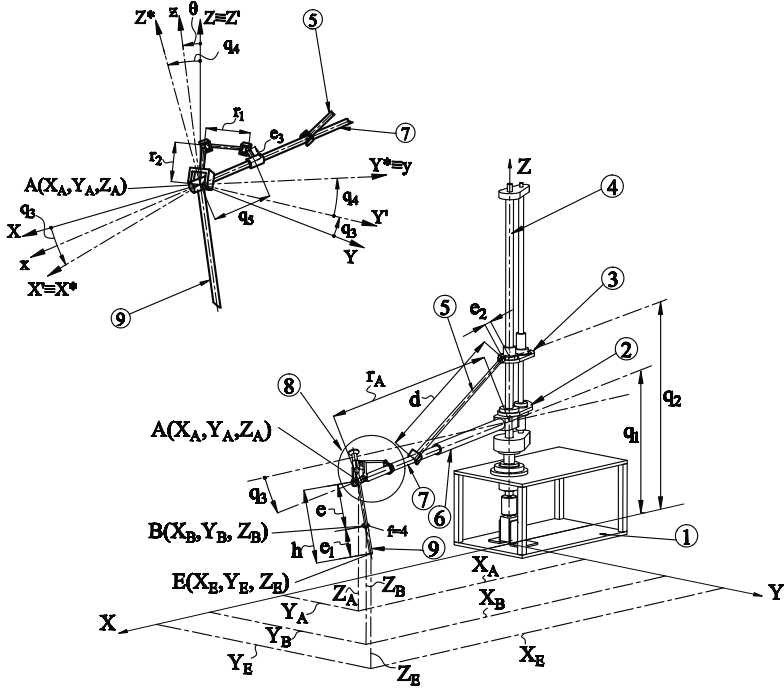
Fig. 1 The kinematic scheme of the robot: The structure and a detail of the parallel module

model, the displacements in motor coordinates q_1, q_2 and q_3 are given along with the coordinates of the insertion point B. The end-effector coordinates are to be determined, namely the point $E(X_E, Y_E, Z_E)$ - the tip of the end-effector, and the two rotation angles ψ and θ, which represents the Euler angles. The instrument must pass through the fixed point B, which means that the coordinates q_4 and q_5 have to be imposed , based on the coordinates of point B. For the inverse geometric model, the generalized coordinates of the active joints along with the rotational angles ψ and θ, have to be determined using the generalized coordinates of the end effector X_E, Y_E, Z_E.

3 Simulink Modeling

Considering the advances of the control theory and computer techniques, the computer aided control system design (CACSD) has been developed. Different tools are used for the analysis of kinematics and dynamics of robotic manipulators [10], for off-line programming, for testing different control algorithms, optimization of the mechanical structures [2] and setup of the robotic cells and production lines. A simulation is useful in order to create an embedded application for a specific robot without being dependent on the "real" structure.

Matlab [6] has become the most widely used software package for modeling and simulating mechanical systems and with its Simulink package is one of the representatives of the high-performance languages for the CACSD. Simulink provides a graphical user interface (GUI) for building models as block diagrams, using click-and-drag mouse operations. Simulink is widely used in control theory and digital signal processing for multi-domain simulation and Model-Based Design [11].

For control studies of the robot, based on the kinematics a Simulink model is built, without frictions in joints, but respecting the constructive dimensions and their geometrical parameters of the mechanical structure. The Simulink model of the robot is made up of the controlled object (the mechanical structure) and the controllers (the five actuators). Figure 2 shows the robot mechanical structure layout, assembled using the Simulink block diagrams. As input data for simulation, the analytically calculated displacements, velocities and accelerations of the actuators were used.
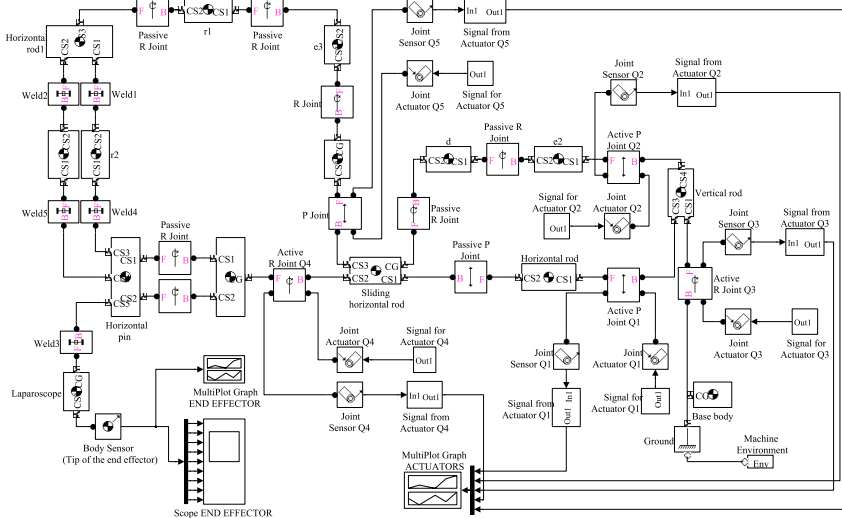
Fig. 2 Simulation: The robot layout based on Simulink block diagram

Using a subsystem for each actuator, the numerical values of the linear/angular position, velocity, and acceleration, are imported in Simulink and bundled into one motion signal. Using a sensor block attached to the tip of the end-effector, the displacements, velocities and accelerations can be measured in that point. The sensor block is a dedicated tool used to determine the geometric parameters of a body, relative to the local or the global coordinate system. With the "Multi Plot" or the "Scope" block diagram (Figure 2), the variations of the measured time dependent parameters of the moving components can be represented in graphical form.

4 Simulation and Validation of the Kinematics

4.1 Simulation with Simulink

For the simulation experiment it was chosen the command MOVE IN, which means a motion of the end-effector with 10 mm into the patient body. In kinematics terms, the command represents a translational motion, along the longitudinal axis of the end-effector, starting from the initial pose.

Using a set of initial coordinates ($X_{Ei} = 990[mm]$, $Y_{Ei} = 255[mm]$, $Z_{Ei} = 420[mm]$) for the tip of the end-effector and following the MOVE IN command, the coordinates of the final position were determined ($X_{Ef} = 991.22[mm]$, $Y_{Ef} = 263.13[mm]$, $Z_{Ef} = 414.31[mm]$), respecting the imposed geometrical restriction represented by the fixed point B with coordinates ($X_B = 975[mm]$, $Y_B = 155[mm]$, $Z_B = 490[mm]$). Regarding the motion parameters, were used the following values for the actuators:
- the maximum speed of the active joints:
$V_{q1} = 22.44[\frac{mm}{s}]$, $V_{q2} = 22.44[\frac{mm}{s}]$, $V_{q3} = 3.20[\frac{deg}{s}]$, $V_{q4} = 6.48[\frac{deg}{s}]$, $V_{q5} = 3.95[\frac{mm}{s}]$
- the maximum acceleration of the active joints:
$A_{q1} = 64.1[\frac{mm}{s^2}]$, $A_{q2} = 64.1[\frac{mm}{s^2}]$, $A_{q3} = 0.75[\frac{deg}{s^2}]$, $A_{q4} = 0.15[\frac{deg}{s^2}]$, $A_{q5} = 8.2[\frac{mm}{s^2}]$
Knowing the initial and final pose of the end-effector, using the inverse geometric model, the initial and final positions of the actuators were determined. Calculating the displacement for each active joint and respecting the imposed geometrical restriction imposed by the fixed point B, the necessary velocity and acceleration of each actuator were determined for the imposed movement. Regarding the motion generation profiles, were taken into consideration two cases, the triangular profile for velocities, when the actuators do not achieve the maximum speed and the trapezoidal profile, when the actuators achieve its maximum speed. In function of the initial and final positions of the actuators, one of the above mentioned cases is used, in order to determine the switching times for the velocities and accelerations (equations (1) and (2)) [7], finally the variations in time of the positions, velocities and accelerations of the active joints are obtained, which represents the inputs of the simulation.

The relations for the switching times, if the maximum velocity is reached

$$t_1 = \frac{v_{max}}{a_{max}}, t_2 = \frac{|p_f - p_i|}{v_{max}}, t_3 = \frac{|p_f - p_i|}{v_{max}} + \frac{v_{max}}{a_{max}} \tag{1}$$

and in case of the maximum velocity is not reached the equations become:

$$t_{12} = \sqrt{\frac{p_f - p_i}{a_{max}}}, t_3 = 2 \cdot t_{12} \tag{2}$$

These numerical values (Figure 3) were imported in the Simulink block diagram as inputs for the joint actuators. Simulating the imposed motion in Simulink were obtained the variations of the time dependent parameters of the end-effector.
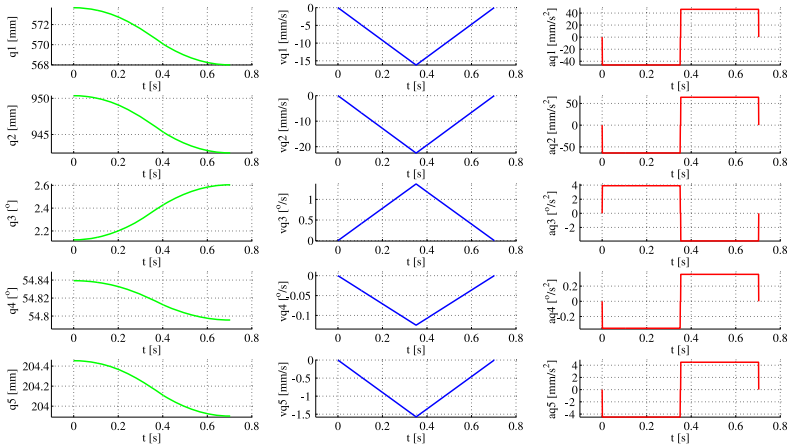
Fig. 3 Time history diagrams - positions, velocities and accelerations of the actuators

4.2   Simulation with SolidWorks

A CAD model of the 5 DOF hybrid robot was developed in SolidWorks (Figure 4) in order to realize some tests with a virtual model of the structure before the construction of the experimental model. In this case for the simulation experiment it was chosen the same command (MOVE IN), presented above in order to compare the SolidWorks simulation with the Simulink results.

As inputs a set of data was used for each actuator, representing the switching times determined above and the velocities at that times, and based on the linear interpolation implemented in the SolidWorks Motion module, were automatically
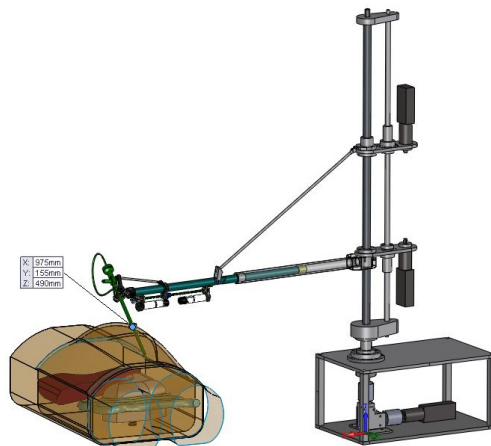
Fig. 4 CAD model of the PARAMIS 5M-P

calculated the time variation of the positions, velocities and accelerations for the actuators. Using the available sensor types in SolidWorks Motion the variation of the time dependent end-effector parameters were measured.

4.3 Comparison of the Numerical Results

Comparing the time history diagrams (Figure 5), obtained by following the numerical simulation of the direct kinematics in Simulink and from the simulation made on the CAD model of the studied structure, the results prove to be identical.
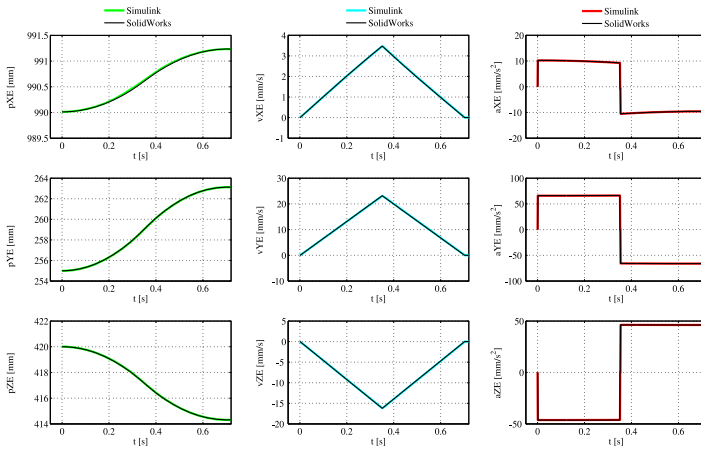
Fig. 5 Time history diagrams - positions, velocities and accelerations of the end-effector

Analyzing the plots in figure 5, the trajectories of the end-effector obtained analytically in Simulink correspond with the behavior of the mechanical structure in SolidWorks, validating the designed parallel robot. Considering the medical restrictions and requirements imposed for a robot applied in MIS procedures, where the imposed precision for the positioning of the end-effector is 1 millimeter, this structure is viable for such applications. The obtained results are compared and thus the accuracy of the developed kinematic models is confirmed.

5 Conclusions

A Simulink and a CAD model of the PARAMIS 5-MP parallel robot and its motion simulation, based on the direct kinematics, are presented. The simulation experiments were performed using as inputs digital motion signals for the actuators. The comparison of the presented simulations shows that the developed kinematics models for the robotic structure are reliable and can be used in the control system of the

experimental model of the PARAMIS 5-MP robot. The motion accuracy and the use of a mechanically constraint RCM allow the structure to be used for the handling of active instruments which enter in direct contact with tissues and also the PARAMIS 5-MP structure is a viable candidate for brachytherapy, where the motion is identical to the MOVE IN function in MIS.

References

1. Brown University, Division of Biology and Medicine (2012),
   `http://biomed.brown.edu`
2. Figliolini, G., et al.: Effects of the design parameters on the synthesis of Geneva mechanisms. J. of Mechanical Engineering Science (November 9, 2012), doi:10.1177/0954406212466194
3. Finlay, P.A.: A New Miniature Manipulator for Laparoscopic Camera Control. In: WC on Medical Physics and Biomedical Eng., Germany (2009), doi:10.1007/978-3-642-03906-5-34
4. Hagn, U., et al.: DLR MiroSurge: a versatile system for research in endoscopic telesurgery. IJCARS 5(2), 183–193 (2009)
5. Kraft, B.M., et al.: The AESOP robot system in laparoscopic surgery: Increased risk or advantage for surgeon and patient? Surgical Endoscopy 18(8), 1216–1223 (2004)
6. Matlab - the language of technical computing, 6th edn. The Mathworks Inc., Natick (2001)
7. Pisla, D.: Kinematic and dynamic modeling of parallel robots. In: DACIA (2005) ISBN 973-35-1941-3 (published in romanian)
8. Plitea, N., et al.: Innovative development of Parallel Robots. In: Meditech 2007, Cluj-Napoca, Romania, pp. 201–206. Published in Acta Electrotehnica (2007) ISSN 1841-3323
9. Polet, R., Donnez, J.: Using a Laparoscope Manipulator (LapMan) in Laparoscopic Gynecological Surgery. Surg. Tech. Int. XVII 17, 187–191 (2008)
10. Rea, P., et al.: The Design of a Novel Tilt Seat for Inversion Therapy. Int. J. of Imaging and Robotics 11(3) (2013) ISSN 2231-525X
11. Reedy, J., Lunzman, S.: Model Based Design Accelerates the Development of Mechanical Locomotive Controls, SAE Technical Paper 2010-01-1999 (2010)
12. Strassman, G., et al.: Advantage of robotic needle placement on a prostate model in HDR brachytherapy. Strahlenther. Onkol. 187(6), 367–372 (2011)
13. Szilaghyi, A., Stoica, A., Pisla, D., Vaida, C., Plitea, N.: Kinematics Analysis of a Parallel Surgical Robot. In: Latest Advances in Robot Kinematics, pp. 333–340 (2012)
14. Taylor, R.H., et al.: Remote center-of-motion robot for surgery. Robotics and Computer-Integrated Manufacturing 11(4), II (1994)

15. Titan Medical Homepage, `http://www.titanmedicalinc.com`
16. Vaida, C., et al.: Development of a Control System for a Parallel Robot used in Minimally Invasive Surgery. In: Meditech 2009. IFMBE Proceedings Series (2009) ISSN 1680-0737
17. Voros, S., et al.: ViKY Robotic Scope Holder: Initial Clinical Experience and Preliminary Results Using Instrument Tracking. IEEE/ASME Trans. on Mech. 15(6), 879–886 (2010)

Experimental Design and Control Approach of an Active Knee Prosthesis with Geared Linkage

E.-C. Lovasz[1], V. Ciupe[1], K.-H. Modler[2], C.M. Gruescu[1],
U. Hanke[2], I. Maniu[1], and D. Mărgineanu[1]

[1] Politehnica University of Timişoara, Romania
  `erwin.lovasz@mec.upt.ro`
[2] Technische Universität Dresden, Germany
  `karl-heinz.modler@tu-dresden.de`

Abstract. The main purpose of this paper is to develop a novel experimental design of knee prosthesis for trans-femoral amputees, which uses a geared linkage in order to generate a rotational movement of the knee joint. The geared linkage with linear actuator can reproduce an approximately linear transmission function for a very large rotation angle. This property of the geared linkage allows an easier control of the walking gait. Such prosthesis becomes active by empowering it with an electro-pneumatic circuit and an electro-pneumatic control unit, which allows the control of the swing phase.

Keywords: knee prosthesis, geared linkage, prosthesis design, control approach.

1   Introduction

The development in the field of knee prostheses pursues a biological static and dynamic behaviour of the lower human limb, an uniform distribution of the body weight both on the prosthetic limb and the healthy limb, ensuring the walking stability and identical movement for both limbs. All these requirements improve the life quality and the work capacity of the amputees.

In order to insure the walking stability, usually a large series of mechanical, pneumatic and hydraulic solutions is used for the knee prosthesis. These prostheses are designed either as passive or active systems. The mechanical solutions can use a simple and least expensive cinematic joint with dampening system or polycentric (physiological) hinge [1].

In [2] the purposed design of the active prosthetic knee (APK) is an inverted slider crank, using a screwball system accompanied by a high-speed brushed servomotor to provide one degree of freedom and the full necessary torque at the knee joint. In [3] a prosthetic system for trans-femoral amputees C-Leg is described. It is based on a hydraulic knee joint with electronic control of both swing and stance phase. The required resistance for flexion or extension of the knee is calculated and then provided by a hydraulic unit equipped with electronic servo

valves. The design and evaluation of knee joint controllers, used for controlled driving of the knee actuator is presented in [4]. The paper work [5] develops a knee-ankle-foot orthesis with a joint unit that controls knee movements using a microcomputer. By means of using sensors the gait phase is optimized [6]. A new technique for dynamic damping control is presented in [7] based on natural humanoid walk for above knee prosthesis which exploits biologically inspired central pattern generator (CPG).

Authors of [8] propose a design of active and passive knee prosthesis system, using a slider crank mechanism with its own hydraulic acting system. This prosthesis allows the blocking of the knee joint in the extended limb position through the geometry of the piston and crank. A solution for the knee prosthesis with geared linkages and linear displacement actuator is presented in [9], [10] and [11].

The geared linkages with linear displacement actuator have the property to allow the movement for a very large rotation angle. In the presented prosthesis, the knee is substituted with a simple joint. The electro-pneumatic control unit helps to control the swing phase. The pneumatic controlled knee prosthesis contains pistons that adjust the swing phase resistance as gait changes.

The aim of the paper refers to a new design and a control approach of an active knee prosthesis that uses a geared linkage and a linear displacement actuator.

2   Synthesis of the Geared Linkage as Knee Prosthesis

The solution of knee joint allows a rotation movement with an angle of 130°. As presented above, the active prostheses with 1 DOF uses an inverted slider-crank (Fig.1 a,b) or a slider crank. These mechanisms are actuated by a double acting hydraulic cylinder (Fig.1c) assembled in parallel with a throttle [1]. Such mechanism structures provide a non-linear transmission function and allow a limited rotation angle between the thigh and the leg.
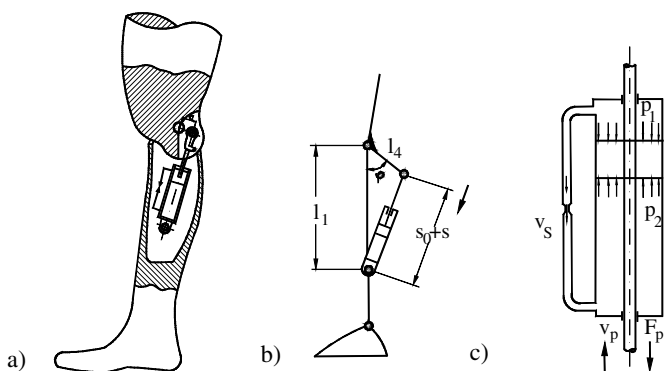
Fig. 1 Knee joint (a). Kinematic schema of the inverted slider-crank (b). Hydraulic or pneumatic double acting cylinder (c)

In order to avoid the disadvantages of the inverted slider-crank it is recommended to use a geared linkage and a linear displacement actuator. Therefore, the synthesis of the geared linkage with linear actuator, used as driving mechanism of the knee prosthesis joint is further developed. The geared linkage contains an inverted slider-crank as basic structure connected in parallel with a gear train. One of the gears is connected with the slider of the basic structure and performs a planetary motion (Fig. 2). The input parameter is the stroke s of the slider and the output parameter is the rotation angle of the output gear χ. In order to obtain an approximately constant transmission ratio for a large rotation angle, an optimization synthesis is recommended.
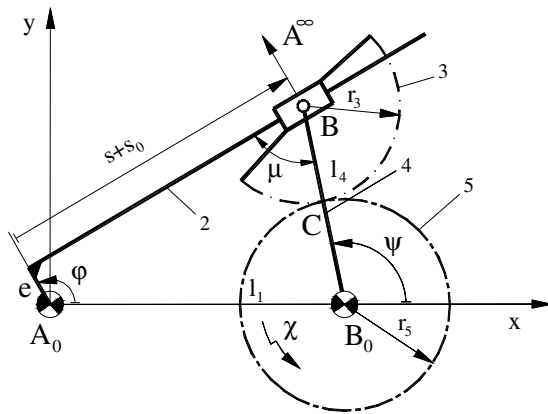
Fig. 2 Geared linkage with inverted slider-crank

The target function is defined as difference between the instantaneous transmission ratio and the desired constant transmission ratio. The target function is:

$$F(\mathbf{x}) = \int_{0}^{s_H/l_1} |\chi'(s, \lambda_2, \lambda_4) - \chi'_{desired}| \, ds := \text{Min!} \tag{1}$$

where s_H - the imposed stroke, $\chi'(s, \lambda_2, \lambda_4)$ - instantaneous transmission ratio (first order transmission function) and $\chi'_{desired}$ - desired transmission ratio, defined as:

$$\chi'_{desired}(s) = \frac{\chi_{max}}{s_{max}} = ct. \tag{2}$$

with χ_{max} - the maximum rotation angle of the output gear, s_{max} - maximum stroke of the input element.

The transmission function $\chi(s)$ of the geared linkage results in the form of:

$$\chi(s) = (1 - \rho) \cdot \psi(s) + \rho \cdot \varphi(s), \tag{3}$$

where

$$\rho = \pm r_3/r_5 , \tag{4}$$

$$\varphi(s) = 2\arctan((B \pm \sqrt{A^2 + B^2 - C^2})/(A - C)), \tag{5}$$

with

$$A = 2 \cdot l_1 \cdot e , \quad B = 2 \cdot l_1 \cdot (s_0 + s) , \quad C = -l_1^2 - e^2 - (s_0 + s)^2 + l_4^2 \tag{6}$$

and

$$\psi(s) = \arccos((e^2 + (s_0 + s)^2 - l_1^2 - l_4^2)/2 l_1 l_4) . \tag{7}$$

The instantaneous transmission ratio correlated with (4) to (7) gives:

$$\chi'(s) = (-(s_0 + s) + \rho \cdot l_1 \sin\varphi)/(l_1 l_4 \sin\psi) . \tag{8}$$

For the optimization problem, the expression $\mathbf{x} = (\lambda_2, \lambda_4)^T$ is considered as variable vector, with the non-dimensional variables:

$$\lambda_2 = e/l_1 , \quad \lambda_4 = l_4/l_1 . \tag{9}$$

The restrictions are given as inequations, which describe the start and end from geometrical conditions:

$$(\lambda_4 - 1)^2 - \lambda_2^2 - (s_0/l_1)^2 < 0 , \tag{10}$$

$$-(\lambda_4 + 1)^2 + \lambda_2^2 + ((s_0 + s_H)/l_1)^2 < 0 . \tag{11}$$

The condition for a convenient transmission angle $\mu > \mu_{min}$ at the start position is further used to determine the start unitary displacement s_0/l_1:

$$\left(\frac{s_0}{l_1}\right) = -\lambda_4 \cdot \cos\mu_{min} + \sqrt{1 - [(\lambda_2 - \lambda_4) \cdot \sin\mu_{min}]^2} . \tag{12}$$
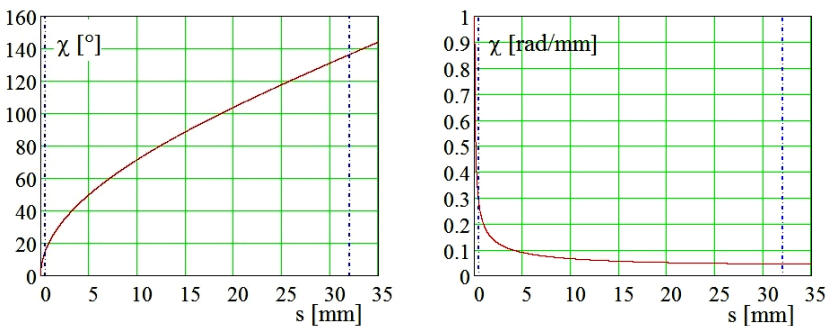
Fig. 3 Transmission function and instantaneous transmission ratio of the geared linkage with inverted slider-crank used for the knee joint

The imposed parameters for the optimization problem are the gear ratio, $\rho = 0.62$, the minimal transmission angle $\mu_{min}° = 10°$, needed to limit the rotation angle, and the maximum unitary stroke $s_H / l_1 = 0.08$. One local minimum value for the non-dimensional links lengths results from the contour line diagram for $\lambda_2 = 0$ and $\lambda_4 = 0.9$. The links lengths are $l_2 = 0$ mm and $l_4 = 36$ mm for the frame length of $l_1 = 400$ mm. This mechanism allows a maximum rotation angle of $\chi_{max}° \cong 144°$ for a start position $s_0 = 364$ mm and a stroke $s_H = 36$ mm. The rotation angle is limited to $120°$ (Fig. 3) with the displacements $s_1 = 0.5$ mm and $s_2 = 32$ mm, which means that for the knee-joint, the start position and the stroke are $s_0 = 364.5$ mm and $s_H = 396$ mm, respectively.

a)   b)
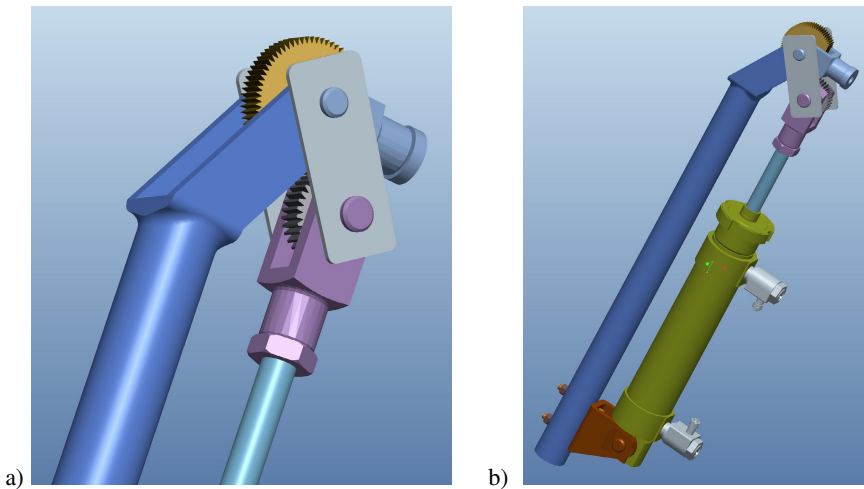
Fig. 4 CAD model of the knee joint prosthesis

A double acting cylinder drives the prosthesis. Because the requirement of stability while stepping, the double acting cylinder is more suitable in use with this prosthesis. The CAD model of the actual prosthesis (Fig. 4 a,b) illustrates the construction of the geared linkage and assembly of the actuator [12].

The actual active prosthesis was manufactured as a demonstrative model (Fig. 5) developed with sensorics for controlling the valves (myoelectric sensors) and monitoring the velocity of the components on different loads.

The control of the braking action is based on adjustment of throttles. Different levels of screwing the throttles on both ends of the cylinder lead to different braking actions on each end of the cylinder. This action is necessary in order to mimic the human gait in the best way.
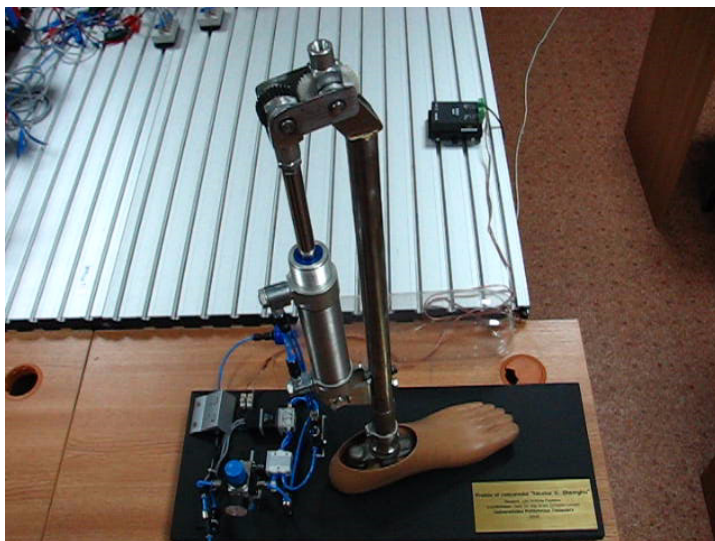
Fig. 5 Active knee prosthesis demonstrator

3   The Electro-pneumatic Control Circuit

The prosthesis uses an electro-pneumatic assembly and an electronic assembly for its control functions. It also needs two different power sources, compressed air (reservoir) and electricity (battery).

In order to control the prosthesis (Fig. 6), a set of 2x3 myoelectric sensors are attached to two of the wearer's muscles, one set (3 sensors) for extension and one set (the other 3 sensors) for flexion. The very weak electrical signal collected by the sensors is then amplified by two amplifier stages and then fed as a higher voltage analog signal to the ADC of the electronic control unit. In turn, this unit monitors the converted values for the two signal channels and decides whether the prosthesis is required to extend or to flex. Also based on the values from the sensors, 3 discrete speed values of the prosthesis can be selected.

The interface between the low power ECU and the high power electro-valves is achieved with a relay board. This board contains 4 relays: 2 of them feed power to the appropriate valves for extending the pneumatic cylinder or retracting it and the other two provide the power to the throttled valves that control the air flow in the cylinder and thus the velocity of the prosthesis.

The pneumatics consists of the cylinder, the electro-valves group, the compressed air conditioning group (filtering, pressure limiting, 3-way valve for refill) and the air reservoir. Pressure inside each chamber of the cylinder is controlled individually so that the force exerted by the prosthesis can be tuned according to the application. The pneumatic circuit also involves two electrically piloted check valves that restrict the air evacuation form the cylinder when there is no command to move it. In this state, the prosthesis behaves like having a slightly damped elastic element that provides the wearer with a level of compliance.
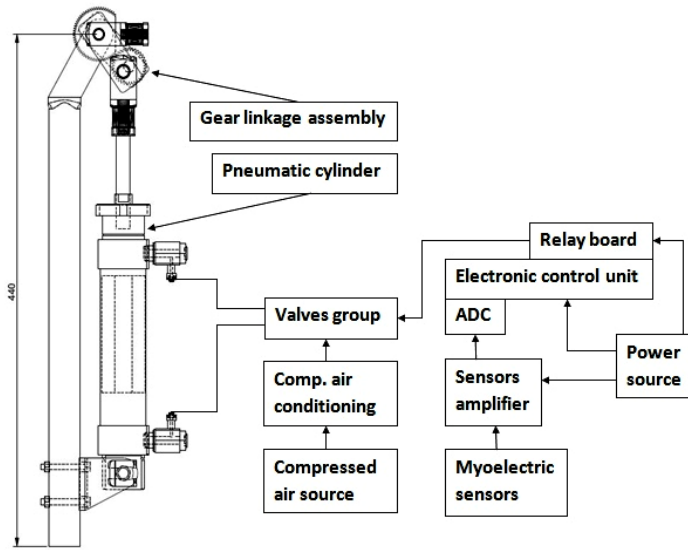
Fig. 6 Active knee prosthesis demonstrator

The working pressure of the system is 0.4 MPa and the pressure limit inside the pneumatic circuit is 1.0 MPa so if a high pressure air reservoir (~2.0 MPa) is to be used (which can increase autonomy), another intermediate pressure regulator must be used. Since the air consumption of the current demonstrator is ~1.10 nl/min, another possibility for providing extended autonomy for a functional prosthesis is to wear a small and silent compressor, but at the expense of increased total weight (from the compressor and additional batteries).

4   Conclusions

The paper proposes an original solution of knee prosthesis, designed and manufactured in the laboratories of the Politehnica University of Timisoara.

The prosthesis implements a geared linkage in order to mimic the movement of the human knee during the flexure/extension. The extension of the rotation and its forward/backward sense is controlled by means of a geared linkage with inverted slider crank basic structure. The optimal dimensioning of the links was performed on the criterion of getting natural values of movement extension. A pneumatic system actuates and controls the mechanical parts' movement.

The prosthesis is original in regard of the used mechanism which allows a large rotation angle, small weight at simple and sturdy construction. The linear transmission function was achieved by means of a fairly simple and reliable system.

Manufacturing and assembling of the prosthesis allows future laboratory testing in order to validate the theoretical optimization approach.

References

1. Hutten, H.: Biomedizinische Technik. Springer, Graz (1991)
2. Borjian, R.: Design, Modeling, and Control of an Active Prosthetic Knee. PhD Thesis, Waterloo, Ontario, Canada (2008)
3. Dietl, H., Kaitan, R., Pawlik, R., Ferrara, P.: C-Leg – Ein neues System zur Versorgung von Oberschenkelamputationen. Orthopädie-Technik 3, 197–221 (1998)
4. Scandaroli, G.G., Araújo Borges, G., Ferreira da Rocha, A., Assis de Oliveira Nascimento, F.: Adaptive Knee Joint Control for an Active Amputee Prosthesis. In: IEEE Latin American Robotic Symposium, pp. 164–169 (2008)
5. Suga, T., Kameyama, O., Ogawa, R., Matsuura, M., Oka, H.: Newly designed computer controlled knee-ankle-foot orthosis (Intelligent Orthosis). Prosthetics and Orthotics International 22, 230–239 (1998)
6. von Wilmsdorff, H., Stinus, H.: Biomechanik und Beurteilung des mikroprozessorgesteuerten Exoprothesenkniegelenkes C-Leg. Zeitschrift für Orthopädie und ihre Grenzgebiete 138, 278–282 (2000)
7. Anand, H.K., Rastogi, R., Nandi, G.C.: Techniques for Dynamic Damping Control in Above Knee Prosthesis. In: Proc. of the 13th National Conference on Mechanisms and Machines (NaCoMM 2007), IISc, Bangalore, December 12-13, pp. 289–295 (2007)
8. Gramnaes, L.: Combined active and passive leg prosthesis, Patent WO 2006112774, Göteborg, Swiss (October 26, 2006)
9. Lovasz, E.-C., Modler, K.-H., Hollman, C.: Auslegung der Räderkoppelgetriebe mit linearem Antrieb. In: Internationales Kolloquium, TU Ilmenau, September 23-26, vol. 47, pp. 316–317 (2002)
10. Modler, K.-H., Hollmann, C., Lovasz, E.-C., Perju, D.: Geared Linkages with Linear Displacement Actuator Used as Function Generating Mechanisms. In: Proc. of the 11th World Congress on TMM, Tian Jin, April 01-05, pp. 1254–1259 (2005)
11. Lovasz, E.-C., Modler, K.-H., Drăghici, A., Văcărescu, V.: Studies for a new prosthesis design for the work capacity rehabilitation. In: The 20th International DAAAM Symposium Intelligent Manufacturing & Automation: Theory, Practice & Education, Vienna, Austria, November 25-28, pp. 1381–1382 (2009)
12. Popescu, I.A., Lovasz, E.-C., Ciupe, V.: Active Prosthesis for Lower Limb Amputated Above Knee. Robotica & Management International Journal 15(1), 59–60 (2010)

Motion Control and Fall Prevention for an Active Walker Mobility Aid

S. Irgenfried and H. Wörn

Karlsruhe Institute of Technology KIT
Institute of Process Control, Automation and Robotics IPR
{stephan.irgenfried,woern}@kit.edu

Abstract. In this paper we present concept, prototype and first experimental results of a force/ torque-sensor based motion control and fall prevention system for an active walker mobility aid to support walking and the sit to stand transfer. For detection of the user intention and for characterization of possible fall situations a 6D-force/torque sensor is used in combination together with a real-time SIMULINK® signal pre- and postprocessing. To improve situation awareness of the signal processing, a mathematical model of the human body is used in the background. Finally we present first experimental results acquired with a passive type rollator using our lab test course.

Keywords: Mobility Aid, Force-Torque-Sensor, Human Body Modeling, Intention Detection, Fall Prevention.

1 Introduction

With the increasing expectation of life in most countries in the world, the number of people attaining a great age raises year by year. One of the key expectations of this group of people is to live as self-determined as they were used to in the first decades of their life. For them it is important to be able to fulfil the activities of daily life without being dependent on the help through caregivers [1]. A key factor for this is mobility. Suffering from restricted mobility has negative effects on the physiological as well as on the psychological well-being and can start a vicious circle of physical and mental degradation. The source of restricted mobility could either be temporal, e.g. a surgery or accident, or permanent, e.g arthrosis or muscle weakness. The range of limitations starts with a limited sphere of action around the home and can range to total dependence on caregivers due to impossibility to perfom a sit to stand transfer without external help. For those situations, different aids are already available or under current reseach. While passive tools like canes, crutches or passive walkers or rollators can be bough in many variations, the area of active aids is still under research of geriatric as well as robotic scientific community. With this work we present the design and implementation for a control system of a

motorized mobility aid to support users walk, support the sit to stand transfer process and act as fall prevention tool. The main aim of the system is to allow people with restricted mobility to live a self-determined life at home and to prevent or prolong the need for caregivers or to move to a nursed home. With a small footprint the system is designed to be used in accessible environments.

The rest of the paper is organzied as follows: section 2 gives an overview on the work of others in the field of walking aids, especially active ones. Following this chapter, in section 3 we present our work. In section 4 we present experimental results before concluding in chapter 5. Since this is work published during the project is in progress, we give an outlook on ongoing and future work in section 6.

2   Related Work

A very good survery paper on the current state of research on mobility aids was recently published by Dune and Gorce [4]. Our work was inspired by the previous works of Mederic et al. [8] and Merlet [9]. The work of Alwan [1], Frizera Neto [6, 5] and Wasson [10] is focused on deriving gait characteristics from a FTS-signal using passive type walking aids.

3   Our Work

In the following we describe our approach for design and implementation of a control system for an active mobility aid for handicapped persons designed to support the user walk (including an active fall prevention), stand up and sit down. For our research work, we decided for a two step approach: In the beginning, we modified an existing rollator system to make its mechanical and sensor layout match the final system configuration. Based on the results, a motorized version of the final system is designed and built.

3.1   Mechanical and Electrical Setup

Since the final system will have a height adjustable horizontal bar that the user grasps to hold and control the mobility aid, we replaced the handles of a standard rollator by the construction shown in figure 2. The induction point of forces and torques is centered in the middle of the virtual axis connecting the two rear wheels of the rollator. The height of the handle bar is fixed to match an average person's hands position if holding them loosely bent in front of the body. The mechnical connection between the handle bar and the rollator is performed using a 6D-force/torque sensor (FTS) as shown in figure 2. The sensor is an ATI Mini45 force/torque sensor with the technical specifications listed in table 1.This passive system was used to gather information on the expected way how users will interact with the mobility aid and about the necessary dimensioning of sensors and actors in the final system by identifying the forces and torques required to be measured to detect user

intention. Depending on the desired use of the final system, the 6D-FTS could be replaced by a simpler (and also cheaper) sensor principle like 1D-force sensing for particular axis only or by mechanically damping the connection between handle and system body and measuring the user commands using e.g. a mini-joystick. For in-deep monitoring of the user's gait characteristics, we still suggest using an 6D-FTS sensor because it delivers the biggest amount of direction-dependent motion information. Also the software framework for detecting the user navigation commands in the sensor data was implemented using this device. The user command detection can work in two operating modes: Use forces and torques directly as input data for position control or analyze a sequence of data samples using a lookup table or neural network and output pre-defined control patterns to the motors. For both operating modes the torque applied to the Z-Axis is converted into a desired turning rate of the system and then added to the forward motion signal. Figure 1 gives an overwiew on the system.
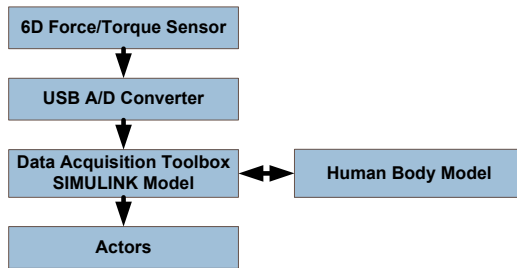
Fig. 1 System overview of the mobility aid control system

An electromechanical prototype of the final system is currently under construction. The planned way of using the final device is shown in figure 5(b). Two major parts of the system will be motor-driven: Based on the idea of a standard rollator, our final device will have 2 motor driven rear wheels and 2 free turning caster wheels at the front. The second motor driven part will be the height-adjustable top table with the handle bar attached.

Table 1 Rated (Full-Scale) Loads and measurement uncertainty (95% confidence level, percent of full-scale load) of our ATI Mini45 Force/Torque Sensor

F_x	F_y	F_z	T_x	T_y	T_z
290 N	290 N	580 N	10 Nm	10 Nm	10 Nm
1.00%	0.75%	0.75%	1.25%	1.50%	1.00%
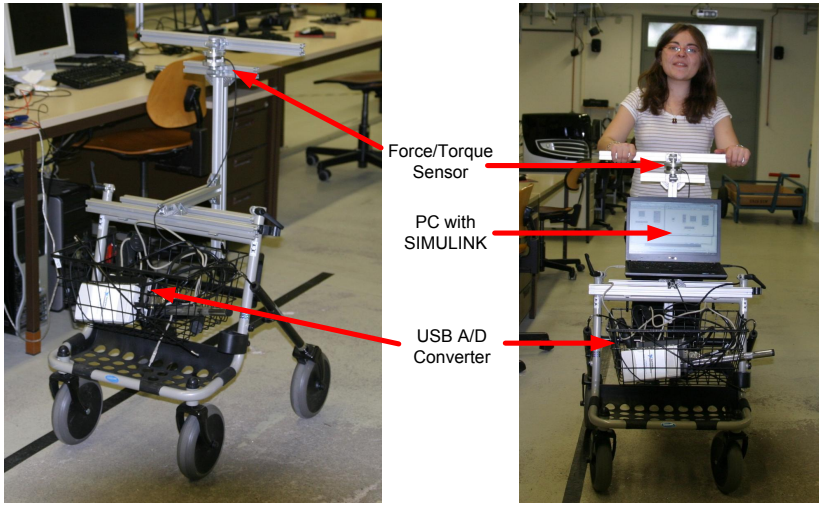
Fig. 2 Rollator equipped mith Force/Torque-Sensor, PC and USB powered A/D converter

3.2 Mathematical Model of the Human Body

Based on the work of Hanavan [7], a mathematical model of the human body was used in the control software. As shown in figure 3, in this model, human body is split into 15 geometric solids. The work describes the dimensions of the body parts as well as their weights and moments. Finally the work provides measurements for 5 subjects and 31 different poses. To adapt the model to the desired user group we used the information provided in the german standards DIN 33402-1 and DIN 33402-2 which provide the average size of body parts and the average weight by gender and age groups for german people [3, 2]. Figure 4 shows a drawing from the standards document. We implemented the model using standard geometries and joints in SimMechanics to be able to animate it and use it as basis for the extraction
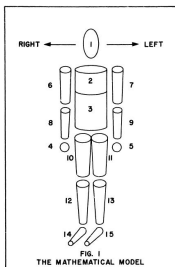
Fig. 3 Model of the human body [7]
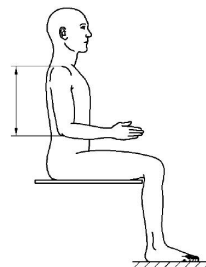
Fig. 4 Upper arm length [2]

of the user navigation commands from the FTS signals. Figure 5(a) shows the model of a human arm using the parts described in the mathematical model. One of the key motivations behind using the mathematical model is the ability to pre-configure the device for a particular user weight and proportions and adjust the motor control profile to adapt to user requirements or preferences.The model also helps to detect possible fall situations in the FTS signals by helping to seperate gait induced variations from the ones creating by the user stumbling.

(a)   SimMechanics model of the arm

(b) Model of mobility aid with user
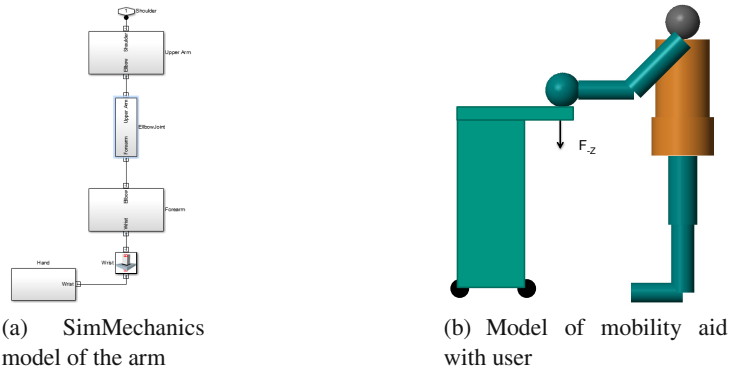
Fig. 5 System model created with Matlab SimMechanics Toolbox

4   Experiments

In this section we describe the experiments we did with young and healthy subjects in the lab at the IPR. With these experiments we wanted to check the correctness of using the mathematical model of the human body described in section 3.2 together with the mechanical design and the sensor concept. After verifying the basic functionality of this system components, dynamic tests using a test track in our lab were performed.

4.1   Static Experiments

The first experiment was carried out by the test person encompassing the handle with both hands without moving the system. The person mass was entered into the mathematical model. The calculated values for the relevant body parts are:

Table 2 Mass of body parts of test persons. Calculated using [7]

Person	Mass	Head-Neck-Torso	Upper arm (L+R)	Lower arm (L+R)	Hand (L+R)
1	58 kg	33.79 kg	3.32 kg	2.09 kg	0.89 kg
2	75 kg	43.31 kg	4.68 kg	2.77 kg	1.06 kg

For the static experiments, the user was standing upright. Person 1 was holding the upper arms in parallel to the torso, the upper arm of person 2 was forming an angle of 45 degrees with the upper body like shown in figure 5(b). The values expected to be measured for $-F_Z$ for person 1 was 14.7 N, for person 2 35.1 N. Results are shown in figure 6. The error for this experiment was 0.3 N (2%).
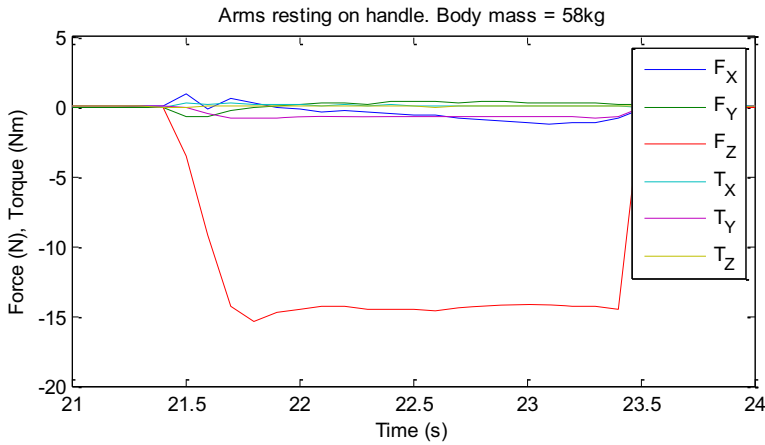
Fig. 6 Sensor values for static test with person 1. Average value for $-F_Z$ = 14.4 N.

4.2 Dynamic Experiments

2 experiments were carried out with test person 2 (75 kg). The first was a test course with 2m of straight walk, then stop, turn left by 90 degrees, then walk straight again and stop. The results are shown in figure 7.
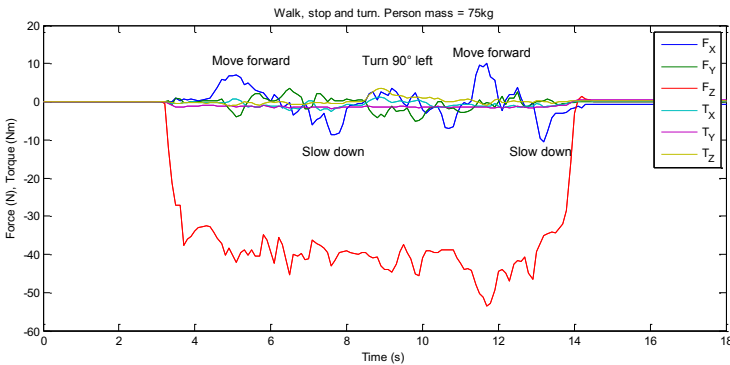
Fig. 7 Sensor values for dynamic test with person 1

The second experiment started with a straight walk continued with an insinuated stumbling by tripping over a carpet-style barrier fixed to the lab floor. The results of this experiment are shown in figure 8. The diagram shows a cleary visible and detectable peak in the sensor values, which can be used for detection of an arising fall situation and to slow down or stop the system to give the user a safe stand. The amplitude of the peak is about 3 times higher (-150N) compared to average normal walking condition.
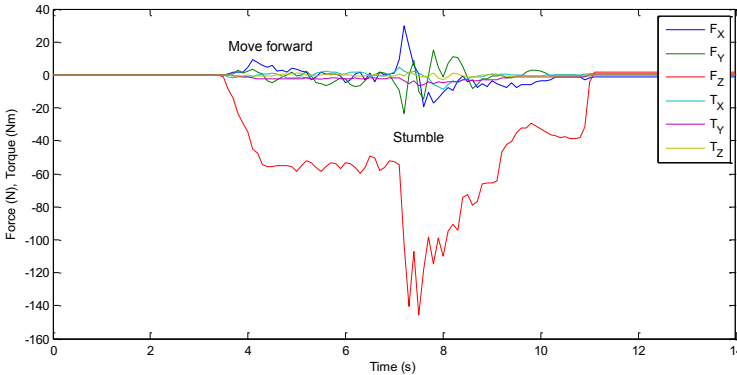
Fig. 8 Sensor values for person 1 stumbling in sagittal plane

Together with the mathematical model of the human body this experimental information is used for dimensioning a stable final system and choose robust mechanical components.

5   Conclusions

We presented our work of a system design for motor control and fall prevention for a motor-driven mobility aid. A mathematical model of the human body is used to adapt the system to the user preferences and to improve the situation awareness for detection of possible fall situations. The electro-mechanical concept was described and first experiments were carried out.

6   Future Work

Currently the protoype system is under construction. The suggested control concept and the mathematical human body model will be implemented as part of the control system.

References

1. Alwan, M., Ledoux, A., Wasson, G., Sheth, P., Huang, C.: Basic walker-assisted gait characteristics derived from forces and moments exerted on the walker's handles: Results on normal subjects. Medical Engineering & Physics 29(3), 380–389 (2007)
2. DIN Deutsches Institut für Normung e.V.: Din 33402-2: Ergonomie – körpermaße des menschen – teil 2: Werte (December 1, 2005)
3. DIN Deutsches Institut für Normung e.V.: Din 33402-1:ergonomie – körpermaße des menschen – teil 1: Begriffe, messverfahren (January 15, 2008)
4. Dune, C., Gorce, P., Merlet, J.P.: Can smart rollators be used for gait monitoring and fall prevention? In: Spalazani, A., Daney, D., Simonin, O., Merlet, J.P. (eds.) IROS 2012 International Workshop on Assistance and Service Robotics in a Human Environment, pp. 59–65 (2012)
5. Frizera Neto, A., Gallego, J.A., Rocon, E., Abellanas, A., Pons, J.L., Ceres, R.: Online cadence estimation through force interaction in walker assisted gait. In: ISSNIP (ed.) ISSNIP Biosignals and Biorobotics Conference 2010, pp. 1–5 (2010)
6. Frizera Neto, A., Gallego, J.A., Rocon, E., Pons, J.L., Ceres, R.: Extraction of user's navigation commands from upper body force interaction in walker assisted gait. BioMedical Engineering OnLine 9(1), 37 (2010)
7. Hanavan, E.P.J.: A mathematical model of the human body. amrl-tr-64-102. Wright-Patterson Air Force Base and Ohio (1964)
8. Médéric, P., Pasqui, V., Plumet, F., Bidaud, P.: Sit to stand transfer assisting by an intelligent walking-aid, Paris (2004)
9. Merlet, J.P.: Ang, a family of multi-mode, low-cost walking aid. In: Spalazani, A., Daney, D., Simonin, O., Merlet, J.P. (eds.) IROS 2012 International Workshop on Assistance and Service Robotics in a Human Environment, pp. 77–82 (2012)
10. Wasson, G., Sheth, P., Alwan, M., Granata, K., Ledoux, A., Cunjun, H.: User intent in a shared control framework for pedestrian mobility aids. In: Proceedings. 2003 IEEE/RSJ International Conference on Intelligent Robots and Systems, IROS 2003, vol. 3, pp. 2962–2967 (2003)

Workspace and Tension Analysis of a Cable-Based Parallel Manipulator for Lower Limb Rehabilitation

J.C.M. Carvalho, A.M. Barbosa, and R.S. Gonçalves

Federal University of Uberlândia, Brazil
`{jcmendes,rsgoncalves}@mecanica.ufu.br,`
`andremarkez@yahoo.com.br`

Abstract. The development of robotic devices to apply in rehabilitation process of human lower limbs is justified by the large number of people with lower limb problems due to stroke and/or accidents. In this paper is presented a cable-based parallel manipulator for lower limb rehabilitation which is composed by a fixed base and a moving platform that can be connected from two to six cables performing the movement of human gait and the individual movements of hip, knee and ankle. In this paper an optimization analysis of the motors position is made using Genetic Algorithms, considering its workspace, in such way that the cables have a minimum tension on it. For this, the static force analysis is made using the Jacobian matrix.

Keywords: Cable-based parallel manipulator, rehabilitation, lower limb, workspace, optimization.

1   Introduction

The science of rehabilitation shows that repeated movements of human limbs can to help the patient regain the function of the injured limb. Mechanical systems under automatic control can be more efficient in performing these exercises than humans because they can perform the necessary rehabilitation movement as well as record information like position, trajectory, force and velocity, maximizing motor performance during active movements, and guiding the movement of a patient's limb attached to it. All trajectory data can be archived and then compared to check the progress of patients in therapy.

Different mechanical systems have been developed and applied for rehabilitation. These mechanical systems can be divided in: robots, exoskeletons, and cable-based manipulators [4].

The cable-based parallel manipulator (or cable-driven parallel manipulator) consists of a fixed base and a moving platform which are connected by multiple cables that can extend or retract. Then, a cable-based parallel manipulator can

move the end-effector by changing the cables lengths while preventing any cables becoming slack. Therefore, feasible tasks are limited due to main static, or dynamic, characteristics of the cables because they can only pull the end-effector but do not push it [1, 7].

These structures have characteristics that make them suitable for rehabilitation purposes. They have large workspace which may be adapted to different patient and different training. The mechanical structure is easy to assembly and disassembly which makes it easier to transport, and can be reconfigured in order to perform different therapies. In the clinical point of view the use of cables instead to rigid links makes the patient fell less constrained which is important to help it to accept the technology. These characteristics make the cable-based parallel manipulators an excellent alternative for rehabilitation. The drawbacks related to the use of cable-based parallel manipulators are the physical nature of cables that can only pull and not push and the workspace evaluation becomes forces dependent and can have a complex and irregular shape [7, 11].

This paper presents a new cable-based parallel manipulator for rehabilitation of the lower limb human movements and its workspace analysis. The structure can be assembled from two to six cables that allow the individual movements of hip, knee, ankle and the human gait simulation with different limits and speed. The development of this robotic device is justified by the large number of people with lower limb problems. The paper is organized as: first the kinematics model of the cable-base parallel manipulator is obtained. Secondly the static force analysis is made by using the Jacobian matrix and, finally, it was carried out the optimization process for the actuators location applied to the human gait. One note that the aim of the propose structure is to assist health professionals and not to replace them.

2   Kinetostatic Modeling

The cable-based parallel manipulator, proposed in this paper, can be assembled from two to six cables arranged in a rigid structure (fixed platform) having a splint as moving platform, Fig. 1(a). Figure 1(b) shows the prototype built at the Laboratory of Robotics and Automation at Federal University of Uberlândia, assembled with four cables, which they are driven by a 24 VDC motor, 45 Nm, an encoder with 500 pulses per revolution and pulley. For initial studies, for graphic simulations and experimental tests, was used a wooden puppet with anthropometric characteristics and 1.80 m tall to simulate the human body, Fig. 1(b).

To obtain the kinematic model of a cable-based parallel manipulator one can do in the same way that those used for the traditional parallel structures [3]. The inverse kinematic model consists in finding the cables lengths, ρ_i, as function of the end-effector pose and the forward kinematic problem consists of finding the end-effector poses for a given set of cables lengths, ρ_i. For the kinematic model, the used parameters are shown in Fig. 1(c).
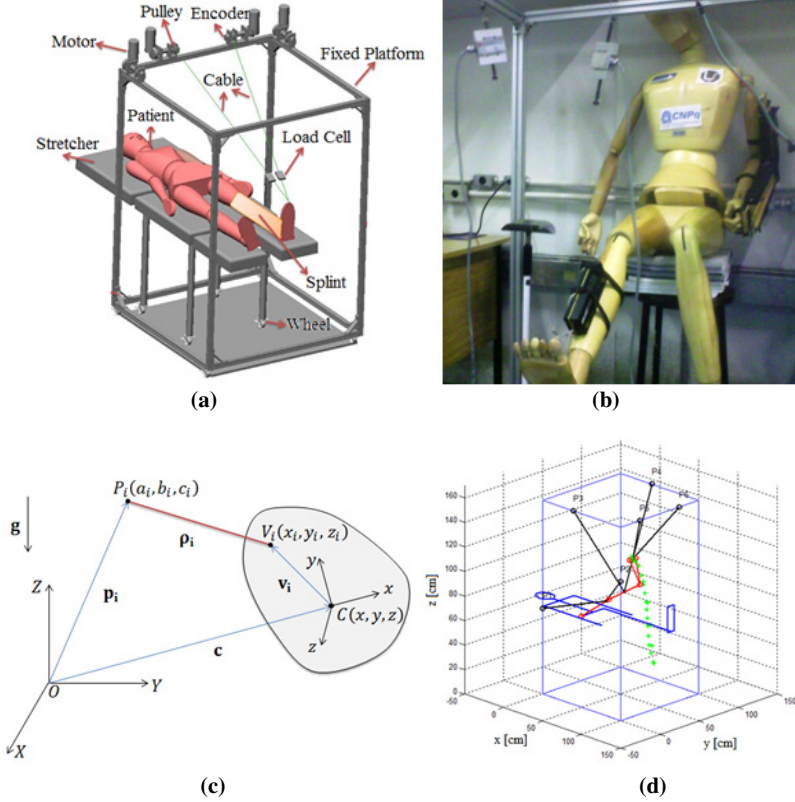
Fig. 1 (a) Scheme of the proposed parallel structure; (b) Prototype; (c) Kinematic parameters; (d) gait simulation with the proposed structure

From Figure 1(c) the inverse kinematic model of the proposed parallel structure can be found by

$$\rho_i = \left\| c + Q\, v_i - p_i \right\| \tag{1}$$

$$Q = \begin{bmatrix} \cos\beta\,\cos\gamma & -\cos\beta\,\sin\gamma & \sin\beta \\ \sin\theta\,\sin\beta\,\cos\gamma + \cos\theta\,\sin\gamma & -\sin\theta\,\sin\beta\,\sin\gamma + \cos\theta\,\cos\gamma & -\sin\theta\,\cos\beta \\ -\cos\theta\,\sin\beta\,\cos\gamma + \sin\theta\,\sin\gamma & \cos\theta\,\sin\beta\,\sin\gamma + \sin\theta\,\cos\gamma & \cos\theta\,\cos\beta \end{bmatrix} \tag{2}$$

Where the subscript i represents the number of cables; $p_i\,(a_i, b_i, c_i)$ is the position vector of point P_i , defining the motor/cable position at the fixed structure, related to the fixed reference frame; $v_i\,(x_i, y_i, z_i)$ is the position vector of point V_i , defining the position where the cable is attached at the moving platform (splint), related to the moving frame; $C\,(c_x, c_y, c_z)$ is the position vector of the center of gravity of the moving platform; Q is the rotation matrix between the fixed and moving frames obtained by means of three successive rotations θ , β and γ about axes X, Y_1 and Z_2 and, ρ_i is the distance between points P_i and V_i (length of cable i).

2.1   Static Force Analysis

When the cable-based manipulator performs a given task, the end effector exerts force and moment on the external environment, and the forces are transmitted by extending and retracting cables, ensuring the condition of pulling cables. The static force analysis is important to determine the quality of force transmission, which is a fundamental aspect of the energetic efficiency of the manipulator and it is necessary in order to obtain a feasible workspace. Therefore, the static analysis is done taking into account that all cables must remain in tension under any load.

The equilibrium equations for forces and moments acting on each cable can be given by

$$\sum_{i=1}^{n} F_i = \sum_{i=1}^{n} F_i\, \hat{\rho}_i = P \quad \text{and} \quad \sum_{i=1}^{n} t_i = \sum_{i=1}^{n} \hat{\rho}_i \times Q v_i = M \tag{3}$$

Written in matrix form:

$$[J]^T [F] = [W] \tag{4}$$

Where vector $[F]$ represents the cable tension, which are forces that must be done by actuators, $[W]$ is the vector of external forces and moments applied to the system, which are the limb and the splint weights, $[J]$ is the Jacobian matrix of the structure and, $\hat{\rho}$ is the unitary vector defining the cable direction from the mobile platform to the actuator. For the structure with i cables, the Jacobian can be written as Eq. (5).

Then, Equations (3) and (5) are used to evaluate the cable tension for a known trajectory for a cable-based parallel manipulator.

$$J = \begin{bmatrix} \hat{\rho}_1 & \hat{\rho}_2 & \dots & \hat{\rho}_i \\ \hat{\rho}_1 \times Q v_1 & \hat{\rho}_2 \times Q v_2 & \dots & \hat{\rho}_i \times Q v_i \end{bmatrix} \tag{5}$$

3   Workspace Analysis

One of the most important characteristics of manipulators is its workspace. In the present case, the workspace is the set of position and orientation configurations in which the end effector is controllable; tensions in cables are positive; forces on cables are between a minimum, F_{min}, and a maximum, F_{max}, in order to maintain cables in tension and to avoid breaking of cables; the end effector is far from singularities, and the wrapping of cables is avoided [6, 9]. As the workspace depends on the existing forces, the static analysis was presented before. Therefore, a computer program can be written to search the statically reachable combined workspace, starting from an initial workspace, under the following conditions [5].

$$[F] = [J]^{-T} [W]$$

$$under \begin{cases} F_i \in [F_{\min}, F_{\max}] \\ F_i > 0 \rightarrow i = 1,2,...,m \\ \rho_i \leq \rho_{\max} \end{cases} \tag{6}$$

To simulate the sequence of movement of the human step were used the angles of the hip, knee and ankle as shown in Fig. 2, obtained from [10]. Details about human lower limb movements and joints limits can be found in [8]. The rehabilitation of the human foot is not purpose of this work.
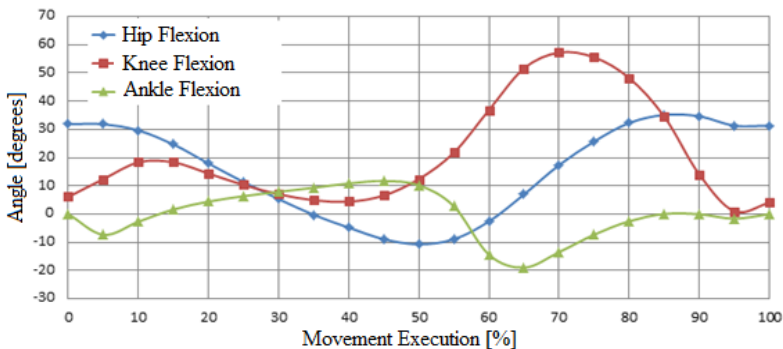
Fig. 2 Values of the hip, knee and ankle angles for a human gait

During the rehabilitation movements it is possible that at least one cable has no traction, leading to a region of non-movement control in the structure, since cables cannot push the lower limb but only pull it. To avoid this, it is necessary that forces on cables are positive during the movement otherwise, it is not possible to move the limb in all required positions for the rehabilitation process.

Thus, in this paper was used Genetic Algorithms optimization (GAO) method [2, 6] to determine the best position of motors in the fixed platform according to the required movement. It was used the toolbox "gatool" of MatLab® software which is necessary input the objective function as well as the lateral limits of the problem.

For simulating the human gait it was used six cables, where the variables are the positions of the six motors in the structure and the objective function to be minimized is the number of negative or very low force on cables throughout the movement. The lower and upper limits are the coordinates that the motor can be attached on each axis. For the GAO algorithm was used a population of 100 subjects and 100 generations. In this case the program gives real-time solution of the objective function.

A gait motion simulation is shown in Fig. 1(d) using the prototype dimensions, emphasizing the points achieved by the tip of the foot during the movement. In the

left side of Figure 3 are shown the cable tension and its length without optimization process, where one can note an overlapping of cables due to the symmetry of the positioning of the motors and due to the puppet being situated in the middle of the structure, so the cable length 1 is equal to cable 2, cable length 3 = 4, cable length 5 = 6. The coordinates of attachment of motors are presented in Table 1.

Table 1 Motor Coordinates before and after optimization

Coordinates [cm]	Axis X before	Axis X after	Axis Y before	Axis Y after	Axis Z before	Axis Z after
Motor 1	0	0	0	0	70	79.9
Motor 2	0	0	100	100	70	81.8
Motor 3	40	10.3	0	0	158	158
Motor 4	40	13.8	100	100	158	158
Motor 5	100	100	25	10.8	158	158
Motor 6	100	100	75	87.6	158	158
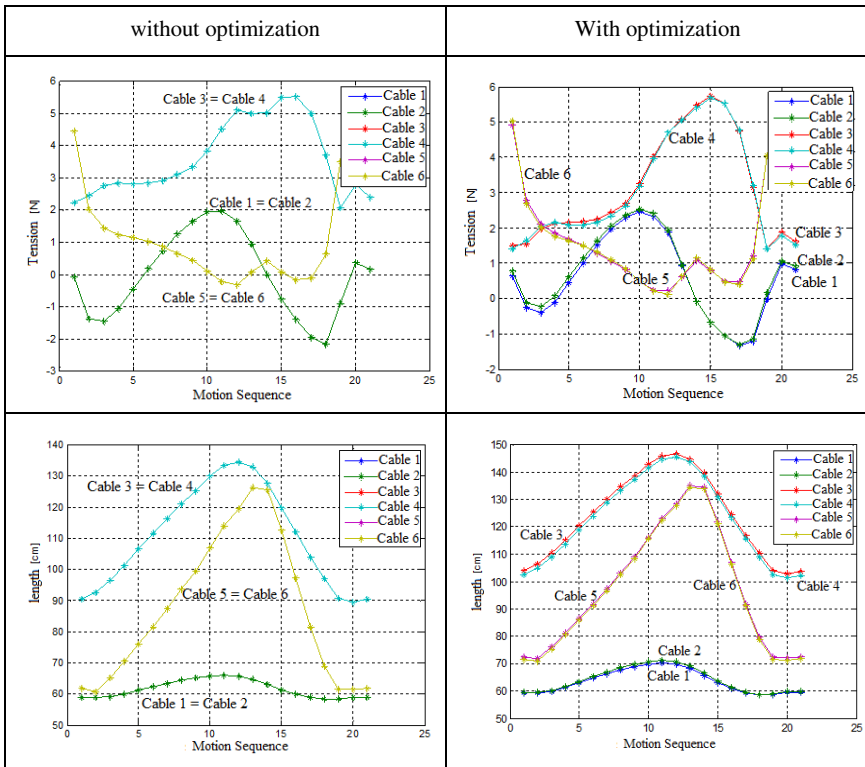
Fig. 3 Simulations of the human gait before and after optimization

For simulations one considered that the minimum traction force on cables is 0.5 N. For the example, without optimization, the analysis had shown that in 126 analyzed poses, at 46 poses there was no sufficient cable traction force.

To apply the optimization method were considered the motors P1 and P2 in the Z-axis, the motors P3 and P4 in the X-axis, and the motors P5 and P6 in the Y-axis (coordinate values are shown in bold in Table 1).

For motors P1 and P2, the lateral limits are between 50 cm and 150 cm. For motors P3, P4, P5, and P6, the allowable range is between 10 cm and 90 cm. It was given a limit of 10 cm after the beginning and before the end of the bar to ensure the assembling of the motor, Fig. 1.

Thus, the optimization program provided the optimal positions of the motors in order to reduce the regions in which the forces on the cables were insufficient to perform the movement. Results for the motor position obtained by the optimization algorithm are shown in Table 1 and noted as "after" optimization.

Using the GAO program, for the same analyzed 126 poses one obtained 28 poses where the tensile strength of at least one cable was less than the minimum then, a reduction of 18 poses.

Results of cable forces and length in both cases are shown in Fig. 3 where one can see the behavior of cables before and after the optimization process.

4 Conclusions

The number of people with lower limb problems grows at each day due to car accidents, stroke and others, which justify studies for developing new structures for rehabilitation process. In this paper a cable-based parallel manipulator for rehabilitation of the lower limb movements has been presented. The application of this structure is illustrated for gait human movement.

The developed cable-based parallel manipulator structure can be assembled from two to six cables that connect the fixed platform and the mobile platform (splint), allowing the realization of the major movements of the lower limb. The kinetostatic model was obtained for the proposed structure.

The analysis of the workspace of the proposed structure is performed considering the necessity of all cables stay tensioned during the rehabilitation process.

The optimization analysis of the motors position was made using Genetic Algorithms, considering its workspace, in such way that the cables must maintain a minimum tension on it.

Experimental tests using an anthropometric puppet to simulate human body are still undergoing to validate the proposed structure for several lower limb movements.

References

1. Cannella, G., Ottaviano, E., Castelli, G.: A cable-based system for aiding elderly people in sit to stand transfer. In: The Int. Symp. on Multibody Systems and Mechatronics, MUSME 2008, San Juan, pp. 8–12 (2008)
2. Chong, E.K.P., Żak, S.H.: An Introduction to Optimization, 2nd edn. John Wiley & Sons, Inc. (2001)
3. Côté, G.: Analyse et conception de mécanismes parallèles actionnés par cables. M.Sc. dissertation, Université Laval, Quebec (2003) (in French)
4. Gonçalves, R.S., Carvalho, J.C.M.: Robot Modeling for Physical Rehabilitation. In: Service Robots and Robotics Design and Application, pp. 154–175. An imprint of IGI Global (2012)
5. Hamedi, J., Zohoor, H.: Kinematic modeling and workspace analysis of a spatial cable suspended robots as incompletely restrained positioning mechanism. World Academy of Science, Engineering and Technology: Mechanical and Aerospace Engineering 2(2) (2008)
6. Haupt, R.L., Haupt, S.E.: Practical Genetic Algorithm, pp. 25–48. John Wiley G. Sons Inc., New York (1998)
7. Hiller, M., Hirsch, K., Bruckmann, T., Brandt, T., Schramm, D.: Common Aspects in Methods for the Design of Mechatronic Systems - Applications in Automotive and Robotic Systems U. of Duisburg-Essen, Germany. In: XII International Symposium on Dynamic Problems of Mechanics, Angra dos Reis, RJ (2009)
8. Kapandji, A.I.: The Physiology of the Joints, 6th edn., Churchill Livingstone. Lower Limb, vol. 2 (2010)
9. Merlet, J.-P.: Analysis of the influence of wires interference on the workspace of wire robots. In: On Advances in Robot Kinematics, pp. 211–218. Kluwer Academic Publishers (2004)
10. Perry, J., Burnfield, J.: Gait Analysis: Normal and Pathological Function, 2nd edn. Slack Incorporated (2010)
11. Surdilovic, D., Bernhardt, R.: String-man: A New Wire Robot for Gait Rehabilitation. In: Proceedings of the 2004 IEEE International Conference on Robotics & Automation, New Orleans (2004)

Tool for the Analysis of New Skills Biped Pasibot

H. Rubio, A. Bustos, C. Castejón, J. Meneses, and J.C. García Prada

University Carlos III de Madrid, Spain
`hrubio@ing.uc3m.es`

Abstract. The aim of this work is to explain the advances made in the development of biped robot PASIBOT. The wish of add mimetic skills to the basic robot lead us include a pair of linear actuators in the hip of the robot. In order to determine the best trajectories that will define these mimetic skills, a mathematical model is developed and implemented in Matlab, creating a user interface with the aim of facilitate the researcher's work. This software not only solves the equations, but also offers several options to visualize the results obtained. The correct definition of these trajectories will be the input data for further analysis, including dynamics in Msc.Adams and on the physical prototype. Unfortunately, the lack of space for this paper prevent us from developing the control strategies in a suitable way.

Keywords: biped, walking robot, leg mechanism, simulation, gait.

1   Introduction

Despite of the great advances performed until now in the field of the biped robots, there is still a lot to do. The major disadvantages walking robots present are related to the weight and the power consumption, as they reproduce the human leg with all its joints (hip, knee and ankle) and actuators.

However, several researchers prefer to emulate the human gait movement using classical mechanisms [5, 11]. By this way, robots can walk in a similar way as humans do, but they minimize the energy required to make this action. Walking chairs developed in the last years are a perfect example of this philosophy, but only Ceccarelli et al. (Laboratory of Robotics and Mechatronic, LARM) have been working in a continued way in this line, firstly with the biped robot EP-War II [3] and lately with the designs of the legs of the low-cost humanoid CALUMA [9] and others [4, 6, 12].

Having in mind this philosophy, MAQLAB group of University Carlos III of Madrid have been designing and manufacturing the biped PASIBOT, Fig. 1, about which several mechanical studies have been presented [1, 2, 7, 8, 10]. This biped is a 1 DOF mechanical system based on the combination of classical mechanism

that widely reproduces the human walking. In order to improve the robot and get a higher maneuverability, some mimetic skills will given to the biped by means of two small linear actuators, one horizontal and other vertical.

This work will focus on developing an application on Matlab that solves the kinematic equations that define the movement of the biped. By this way, it will be able to study several trajectories of the biped's foot, some of which will make the mimetic skills up. Once the possible trajectories are defined, the model will be implemented in Msc.Adams in order to check if the dynamic behavior is as expected, and then, add all these new skills to the physical prototype.
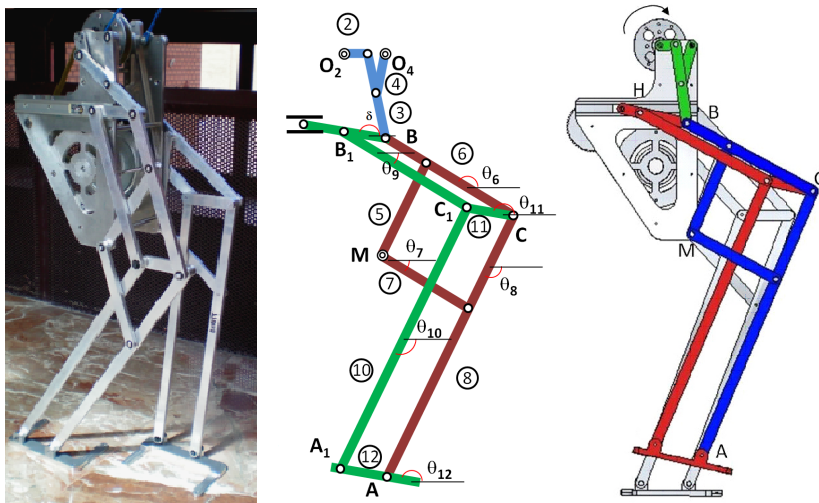
Fig. 1 PASIBOT robot and its main kinematic chains

2   The Biped PASIBOT

The biped robot PASIBOT (Fig. 1) is a 1 DOF (Degree Of Freedom) mechanical system based on the smart combination of classical mechanism to widely reproduce the human walking. In fact, the design characteristics PASIBOT must achieve are: Passive mechanical walking must be performed by the walking robot, the number of actuators must be lower than the number of joints and it must use articulated mechanism as links for the leg design in sagittal plane.

Two basic mechanisms make the robot up: a Tchebychev mechanism gives the robot the basic trajectory of the gait (as it generates an almost straight line trajectory) and a pantograph mechanism reverses and amplifies this movement. The pantograph's central point (point M) is fixed to the hip, being driving by the

short side (point B) and obtaining the final foot trajectory on the long side (point A). A stabilization system must be added to ensure that the foot will be parallel to the ground without additional actuation, which will get the correct walking of the robot.

The improvement of the robot with the addition of the mimetic skills motivates the change of name: PASIBOT will be called MIMBOT from now. MIMBOT must be able to develop some skills humans do -as lengthening or shortening the gait, or up/down one step – in a simple and effective way. The main difference between PASIBOT and MIMBOT is the addition of two small linear actuators on each side of the robot's hip. This will give the robot a total of 5 DOF. Two actuators (one on each side) will work horizontally, whereas the others will work vertically. The rod of both actuators must be attached to the fixed point of pantograph mechanism (point M) because in this way the geometry of the mechanism is modified, and consequently, the gait (trajectory of point A) will change to get the desired mimetic skill.

3   MIMBOT Software

The parametric mathematical model defining the robot's kinematics is implemented in Matlab and, in order to get an easy way to solve and modify the robot characteristics, a user interface is developed using the tool GUIDE, embedded in Matlab. As it will be seen later, the developed software is very useful to check the suitability of modifications executed.

As this model has been widely explained in other works [7, 8], here we will refer only to relevant equations for the mimetic skills. Once the Tchebychev's mechanism is solved, next step is solving the kinematic chain belonging to the pantograph mechanism (the darkest highlight in Fig. 1). Its closure relation is showed in Eq. (1). After this, just two loops remain to be solved, those related to the stabilization system (the two darkest highlights in Fig. 1) whose closure relations are showed in Eq. (2) and Eq. (3)-.

$$\overrightarrow{MB} + r_6 e^{j\theta6} + r_8 e^{j\theta8} = 0 \tag{1}$$

$$r_C e^{j\theta7} + r_{11} e^{j\theta11} = r_f e^{j\delta} + r_9 e^{j\theta9} \tag{2}$$

$$r_A e^{j\theta8} + r_{12} e^{j\theta12} = r_{11} e^{j\theta11} + r_{10} e^{j\theta10} \tag{3}$$

Developing the equations, it is able to obtain every interesting angle as, for example, the angles between the horizontal and the femur (θ_6) and the tibia (θ_8) or the inclination angle of foot respect to the horizontal, Eqs (4-7).

$$F = MB_Y^2 + MB_X^2 + r_8^2 - r_6^2 \tag{4}$$

$$\theta_8 = -\cos^{-1}\left(\frac{-F \cdot MB_X - MB_Y\sqrt{4r_8^2\left(MB_X^2 + MB_Y^2\right) - F^2}}{2r_8\left(MB_X^2 + MB_Y^2\right)}\right) \tag{5}$$

$$\theta_6 = \arccos\frac{MB_X + r_8\cos\theta_8}{r_6} \tag{6}$$

$$\theta_{12} = \cos^{-1}\left(\frac{r_{11}\cos\theta_{11} - r_A\cos\theta_8 + r_{10}\cos\theta_{10}}{r_{12}}\right) \tag{7}$$
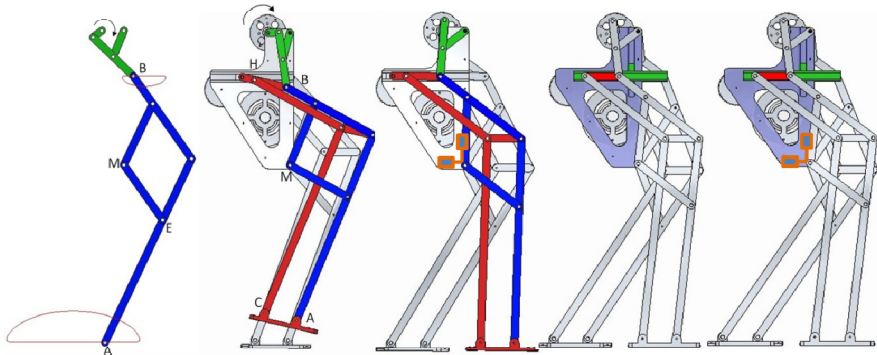
Fig. 2 Five steps in evolution of PASIBOT

The software is divided in five modules, each of them corresponding to a different level of evolution of the robot, see Fig. 2. The first one is a simple scheme of the two main mechanisms, the second one adds the stabilization system and the third adds also two linear actuators to give some mimetic capabilities. Fourth and fifth modules are similar, respectively, to the second and third ones, but they replace the original stabilization system with a new design. The MIMBOT software flow chart is showed in Fig. 3.

In all cases, a window in which writing the initial conditions of simulation will appear; Fig. 4 shows the window for the third module. After inputting the necessary data, "Calculate" and "Next" buttons must be pressed; the program will solve the equations and open a new window to see the results, as showed in Fig. 5. These results can be analyzed by means of graphs (up to 174) or exported to a plain text file for further analysis. Finally, pressing the "Animation" button, the software will show a schematic representation of the robot movement with some controls to manage the animation showed in Fig. 5.

Going back to the input data window, in modules 3 and 5 there is an extra panel in the right side of window, see Fig. 4. This panel defines 6 predefined movements of linear actuators:
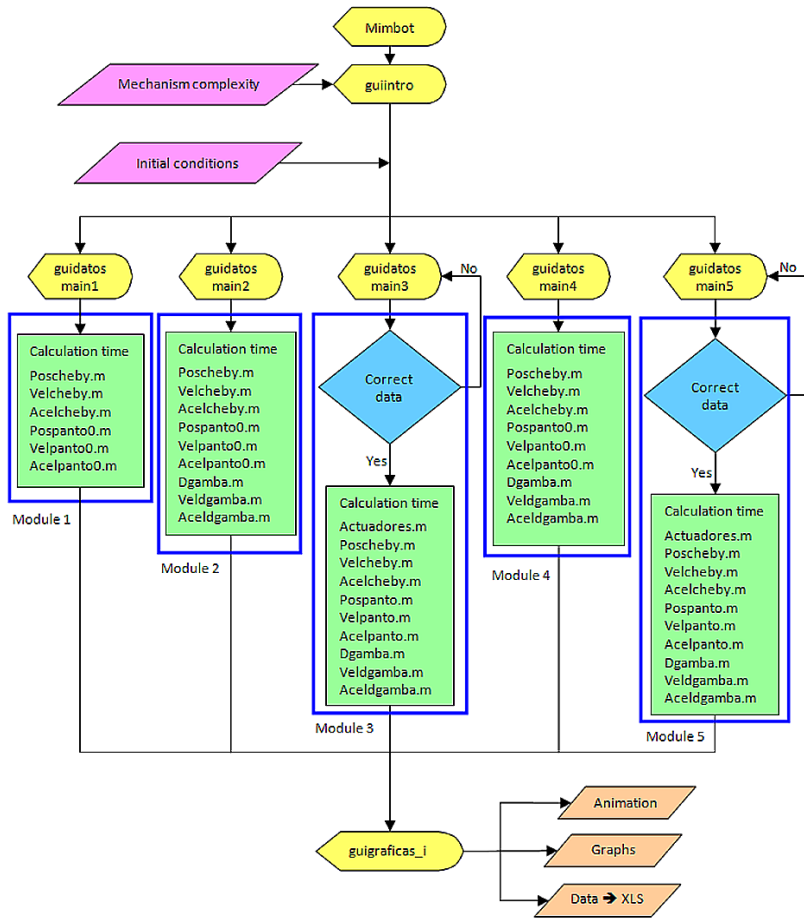
Fig. 3 Flow chart of MIMBOT software

Fig. 6 shows the consequences that some of these movements generate in point A of robot. The first graph – Fig. 6-a - shows the influence of front modification of gait applied by the actuator in point M, lengthening the gait. The same effect is professed if the rear modification is performed –Fig. 6-b-, but obviously, it occurs at the rear part of the gait. Fig. 6-c shows the effect of inclination of foot. As it can be observed, this option elevates the foot not only in the flight phase, but also in the support phase. In the other hand, Fig. 6-d illustrates the elevation of foot, which indeed moves upwards the foot in the flight phase. An example of the effect of trapezoidal movement is presented in Fig. 6-e. As this is an open option, it may generate undesired effects. The last image, Fig. 6-f, shows the combination of the front modification of gait and inclination of foot, in a clear example of how to climb a step.

Fig. 7 shows a detailed analysis of the four joints that make the ankle (A and A_1) and the knee (C and C_1) for the gait drawn in Fig. 6-f. It is clearly visible the greater path (in both axes, horizontal and vertical) performed by the ankle and the knee, as well as the variation of its respective angles, when the actuators modify the regular robot's gait.
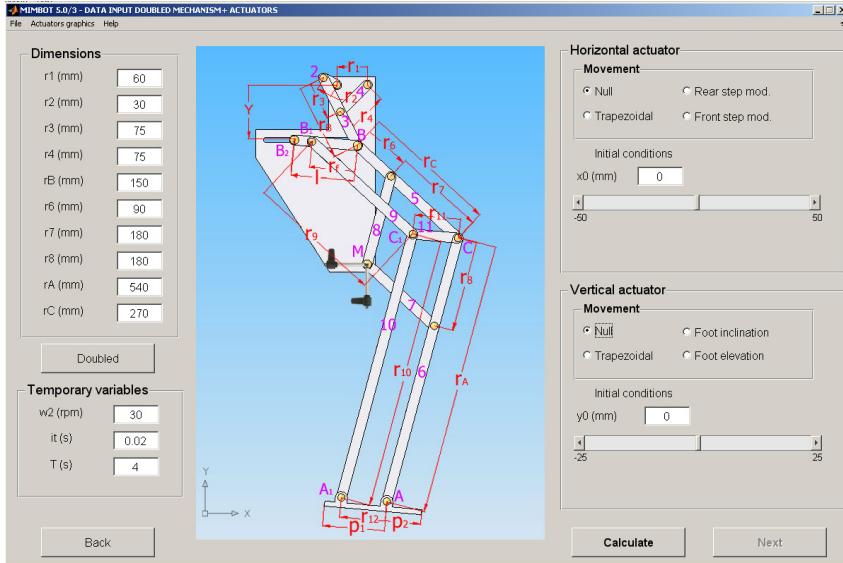
Fig. 4 Input data window
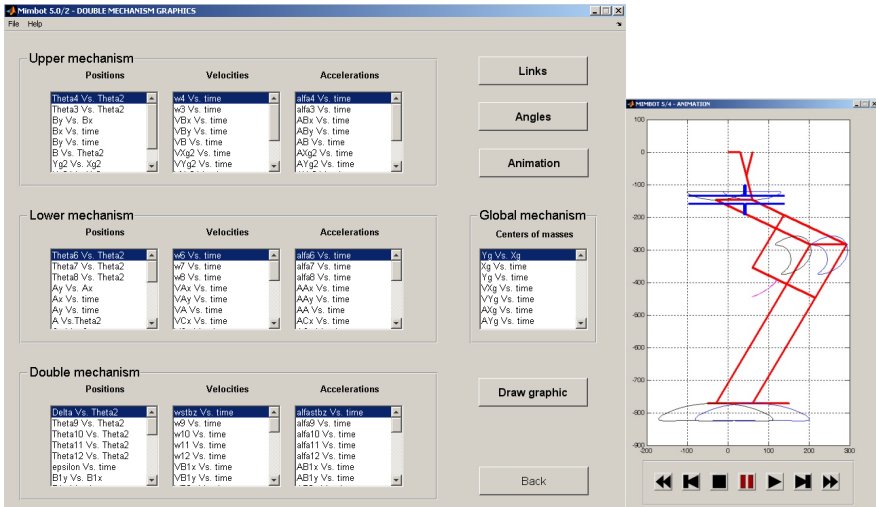
Fig. 5 Results and graphs window (left) and animation window (right)
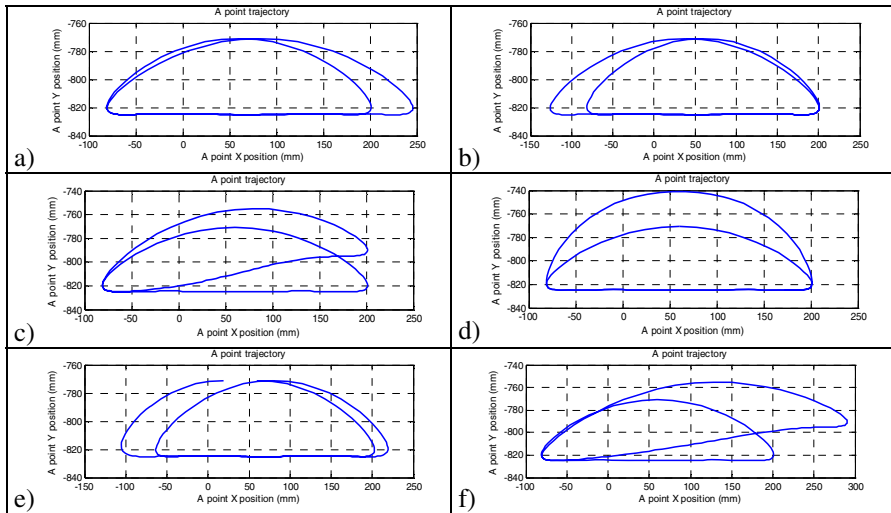
Fig. 6 Possible trajectories of the point A, using the options offered by MIMBOT software
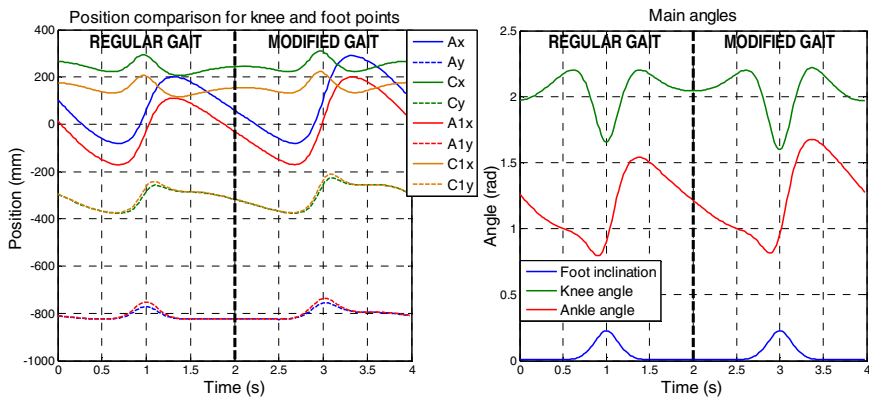
Fig. 7 Position comparison for main joints and angles of regular and modified gait

All these examples have been made with positive value for the options, a negative value will shorten or lower the gait. Combining the different options with different values for each one will provide a lot of possible trajectories to study.

Once the trajectories of interest have been determined, the robot is implemented in Msc.Adams with the aim of verifying the results obtained in the developed software. Also, it will give the possibility of analyzing the robot dynamics, checking the ZMP (Zero Moment Point) is within the support area, although it isn't the objective of this work. Finally, the implementation in Msc.Adams let us decide if the solution adopted is good enough to be added to the physical prototype of MIMBOT.

4 Conclusions

This work presents the PASIBOT biped robot, which is based on the articulated mechanism and with only one actuator. It has also been developed a parametric mathematical model that describes in detail the kinematics of MIMBOT biped robot based on low cost technology, whose basic mechanical system consists of two legs resulting from the combination of classical mechanics (Tchebychev, pantograph and a stabilization system).

The parametric mathematical model has been developed having in mind to include a pair of linear actuators located at the biped's hip, with the future intention of developing some mimetic skills. Besides, a graphic interface was built in order to enable easy and fast design variations, which facilitates the research and optimization of trajectories that will give the robot its new mimetic skills.

The usefulness of this new software has been proved with the illustration of results obtained from different simulation varying the actuation parameters of both linear actuators. These results are the inputs for detailed dynamic analysis, including the verification of ZMP, made in Msc.Adams.

References

1. Alba, D.M., Garcia-Prada, J.C., Meneses, J., Rubio, H.: Center of Percussion and Gait Design of Biped Robots. Mechanism and Machine Theory 45(11), 1681–1693 (2010)
2. Escobar, M.E., Rubio, H., García-Prada, J.C.: Analysis of the Stabilization System of Mimbot Biped. Journal Applied Research and Technology 10(2), 206–214 (2012)
3. Figliolini, G., Ceccarelli, M.: Walking programming for an electropneumatic biped robot. Mechatronics 9, 941–964 (1999)
4. Gu, H., Ceccarelli, M., Carbone, G.: Design and Operation of 1-DOF Anthropomorphic Arm for Humanoid Robots. In: Proceedings of the 17th Int. Workshop on Robotics in Alpe-Adria-Danube Region RAAD 2008, Ancona. CD Proceedings (2008)
5. Hu, Y., Nakamura, H., Takeda, Y., et al.: Development of a Power Assist System of a Walking Chair Based on Human Arm Characteristics. Journal of Advanced Mechanical Design, Systems and Manufacturing 1(1), 141–154 (2007)
6. Liang, C., Ceccarelli, M., Takeda, Y.: Operation analysis of a Chebyshev-Pantograph leg mechanism for a single DOF biped robot. Frontiers of Mechanical Engineering 7(4), 357–370 (2012)
7. Meneses, J., Rubio, H., Castejón, C., Ottaviano, E., Ceccarelli, M.: Modelo cinemático del robot bípedo Pasibot. In: IX CIBIM, Las Palmas de Gran Canaria, Spain (2009)
8. Meneses, J., Castejón, C., Rubio, H., García, J.C.: Kinematics and dynamics of the quasi-passive biped PASIBOT. Journal of Mechanical Engineering 57(12), 879–887 (2011)

9. Nava, N.E., Carbone, G., Ceccarelli, M.: Design Evolution of Low-Cost Humanoid Robot CALUMA. In: Proceedings 12th IFToMM World Congress, Besançon, France (2007)
10. Rubio, H., Meneses, J., Castejon, C., et al.: Mechanical design of walking robot Pasibot. In: Parametric Model and Gait Analysis. In: 12th International Conference on Climbing and Walking Robots, CLAWAR 2009, Istambul, Turkey (2009) ISBN 13-978-981-4291-26-2
11. Sugahara, Y., et al.: Walking up and down stairs carrying a human by a biped locomotor with parallel mechanism. In: IROS 2005, vol. 2(6), pp. 1489–1494 (2005)
12. Tavolieri, C., Ottaviano, E., Ceccarelli, M., Di Rienzo, A.: Analysis and Design of a 1-DOF Leg for Walking Machines. In: Proceedings of RAAD 2006, 15th International Workshop on Robotics in Alpe-Adria-Danube Region, Balantonfured. CD Proceedings (2006)

Hybrid Quadruped Robot – Mechanical Design and Gait Modelling

M. Olinski and J. Ziemba

Wroclaw University of Technology, Poland
{michal.olinski,jacek.ziemba}@pwr.wroc.pl

Abstract. The study aimed to develop a walking mobile robot and model its four-legged gait. At first, a review of existing structures was conducted and then the robot's purpose and design parameters were specified. On this basis, the kinematic structure and the geometry of the robot's legs were determined. After that, a numerical model of the quadruped robot was built in MD Adams. Mechanical structure of construction was designed and relevant drawings of individual parts were made using Inventor. General algorithm of four-legged gait used for this robot was specified. Simulations of the model's actions in MD Adams were performed to determine the kinematic and dynamic properties of the movement. Among others, walking on wheels and on feet, using the lateral surfaces of wheels, were examined and results have been presented.

Keywords: wheel-legged robot, hybrid robot, simulations.

1   Introduction

The issue of four-legged gait had been addressed by many researchers. One of them was Hildebrand [2], who analyzed different ways of horse's motion. Quadruped robot's gait has been widely studied [9, 10]. The popularity of this topic results from a fairly obvious advantage possessed by the walking machines over the more popular and simpler in construction wheeled and tracked machines. Their superiority lies in the process of moving. Robots with legs can move in much more difficult terrain and get where the wheeled and tracked robots cannot, for which only half of the earth's surface is available.

In recent years, walking robots have been becoming more widely applied in various fields. It is worth to mention, the Boston Dynamics constructions, BigDog and its bigger brother AlphaDog (LS3) [7]. Their amazing movement abilities and usage in military cargoes transport incline thinking, that in the near future walking robots will find wider and more practical applications than before. However, it cannot be forgotten, that wheeled robots are superior to walking ones as far as movement speed on flat and even surface is concerned. Because of this, appropriate is combining features of these two classes of robots and creating a hybrid robot equipped with both wheels and legs. Also this topic has already been exploited by

many researchers, which resulted in construction of a wide range of wheeled robots with high mobility [8]. Within this group, the robot Roller-Walker is worth attention [1]. It has the ability to rotate wheels to the side and to walk on theirs lateral surfaces, using wheels as feet.

2   Wheel-legged Robot "Wonderworker"

This paper discusses the problem of modelling the gait of a mobile quadruped robot. In order to determine the algorithm and conduct tests a wheel-legged robot named **W**onde**rw**orke**r** (**W**heels **R**otating **W**alking **R**obot) has been designed. The robot can perform a variety of tasks such as transport, surroundings examination, field measurements, inspection and diagnostics. An important area of this robot's application can be military tasks such as: seeking, inspecting and neutralizing mines and improvised explosives, reconnaissance, area observation and active support of combat operations. In regard to the applications that have been intended for the robot, several requirements were identified: the ability to move in various terrains and to generate different types of gaits, as well as the adaptability to changing terrain and overcoming obstacles [4]. Based on these assumptions, the kinematic diagram and geometry of the machine have been determined [5]. The design of the robot was patterned on other constructions including the Roller-Walker. However one of Wonderworker's advantages over Roller-Walker are driven wheels which allow it to move more efficiently up the slope. Moreover, far larger wheels have been applied, which turned to the function of feet will prevent problems with movement on muddy or loose surfaces.
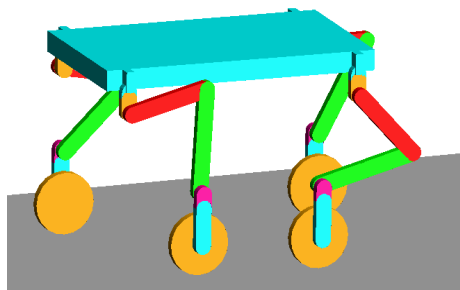
Fig. 1 Robot's model built in MD Adams [3]

Determining the robot's kinematics and geometry allowed building dynamic model in MD Adams (Fig. 1). Individual components were created and had relevant material and mass properties assigned. Then, components were connected using kinematic pairs. It was also necessary to model contact type kinematic pairs between wheels and ground [3].
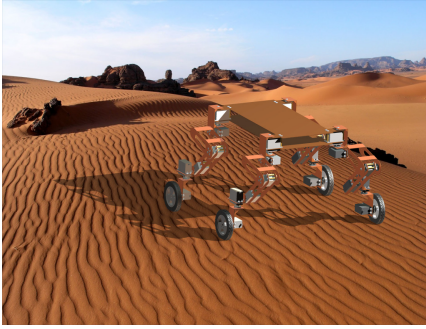
Fig. 2 Robot's view in 3D - driving position with widely placed wheels [4]
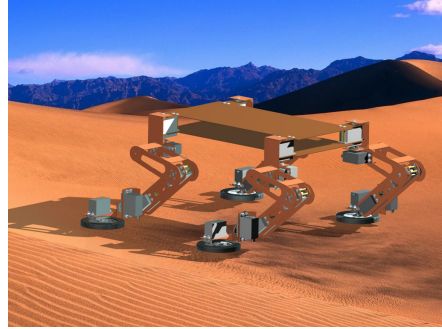
Fig. 3 Robot's view in 3D while walking on feet (typical for mammals position of legs) [4]

Individual components were designed in 3D using Inventor. Figures 2 and 3 show 3D views of the whole Wonderworker robot with four designed legs attached, in two positions [4].

3   The Control Algorithm – Model of Four-Legged Gait

Walking is a very common way of moving on land. It is achieved by limbs conversion sequence, repeated from time to time, called the period of gait. This is a complex way of moving and its implementation in robots requires an accurate control algorithm. Walking is characterized by many parameters and exists in many variations. In addition to the different postures, walking can be divided according to the length of stance phase for individual legs. For quadrupeds, symmetrical gaits among others can be distinguished (Fig. 4). They are characterized by an identical time of stance phase for each leg, while asymmetric gaits do not meet this condition [11]. Another feature of the gait is the order of limbs conversion. For four-legged gaits six sequences can be distinguished. When it comes to walking robot's control, one should pay attention to the possible shapes of the trajectory of feet relative to the body. The most commonly used are triangular (Fig. 5), trapezoidal and rectangular trajectories [11].

To realize walking of Wonderworker, posture typical for mammals, quadruped crawl with a triangular trajectory of step and the sequence of legs conversion: left front, right rear, right front, left rear, were selected. It was also assumes, that the period of gait consists of 12 equal parts and the swing phase for each leg takes 2/12 of the period. As a result, the length of step was divided into 10 parts [11].
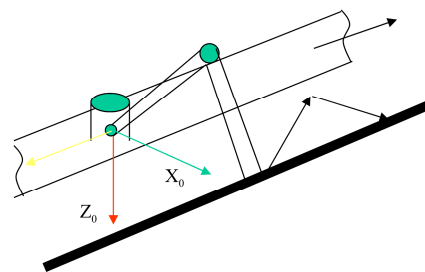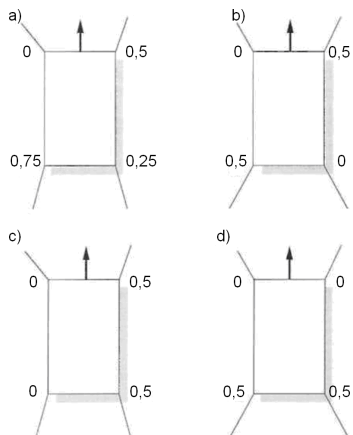
Fig. 4 Symmetrical gaits: a) quadruped crawl, b) trot, c) pace, d) bound [11]

Fig. 5 The triangular motion trajectory of leg's end [3]
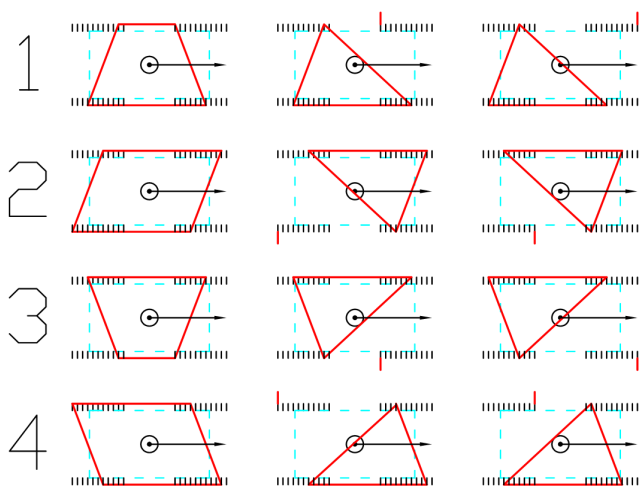
Fig. 6 Successive support polygons analyzed for robot's gait [3]

For the selected type of gait with predetermined motion parameters, analysis of the body's centre of gravity movement relative to the ends of the limbs while walking was performed to determine the stability. The result was obtaining a sequence of support polygons and positions of the centre of gravity (Fig. 6) [11]. The diagram should be analyzed from left to right, row by row. The dashed line outlines the body, while the point in the middle stands for the centre of gravity. Thick lines indicate support polygons. Short segments of thick vertical lines show locations where leg has just left the ground or where in a second it is going to

make contact with the ground. Successive views of support polygons indicate that the robot should maintain static stability at every moment of walk. The reason is the fact that, the body's centre of gravity stays always within the current support polygon. This is true for considerations without taking into account the dynamic relations and influence of legs' masses on position of the robot's centre of gravity. Furthermore, at some points the centre of gravity is dangerously close to the boundary of the polygon, which may lead to a loss of balance [3].

A good solution to the mentioned problem is monitoring the state of the robot, in order to enable the control system to react properly and avoid an overturn. Placing pressure sensors in the wheels (feet) of the robot would also be very helpful. They would allow keeping proper load on each leg, thus helping to maintain the balance [3].

4   Simulations of Robot's Walk

Using the presented earlier dynamic model in the MD Adams, a number of simulations were carried out. Among others, walking on wheels was modeled (Fig. 7). Leg's trajectory of motion relative to the body achieved through inverse kinematics is shown in Fig. 8.
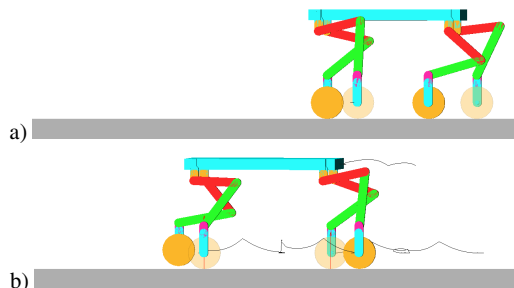
Fig. 7 View of walking on wheels – with a marked motion tracks of the body and wheels of front left and rear right legs [6]

The horizontal line at the height y = 75 mm (Fig. 9), indicates the expected positions of wheels during the stance phase. For each leg in this phase, the wheel is lower than it should. This means that while walking, the body and legs' attachment points to the body are too high. Thus there are moments when one of legs at the end of the swing phase does not reach the ground. The reason is the fact that, trajectories between the predefined points are circles' arcs (Fig. 8). As an example of the error, in Fig. 9 the arrow marks the point of maximum deviation for the left front leg [6].
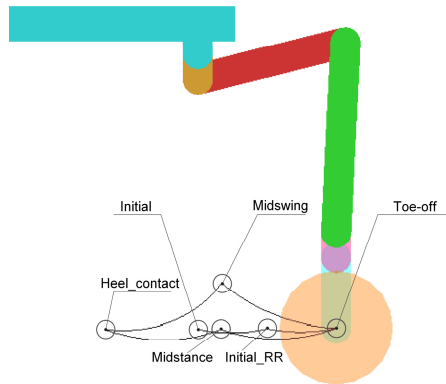
Fig. 8 Motion trajectory of the leg relative to the body, while walking on wheels [6]
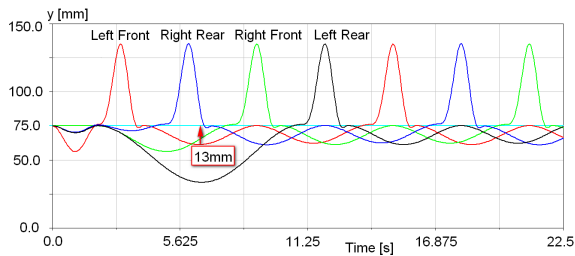
Fig. 9 Graph of positions, along y-axis, of centres of wheels for particular legs while walking, according to fixed body [6]

Moreover, gait with the use of wheels in function of feet was developed (Fig. 10). The reconfiguration of the robot from its initial position, where it stands on wheels, to the position where all wheels are rotated to the position of feet takes 14 s. Sequentially for successive legs, wheels change to positions of feet during the first second of swing phase, while moving from point toe-off to point midswing (Fig. 8) [3].
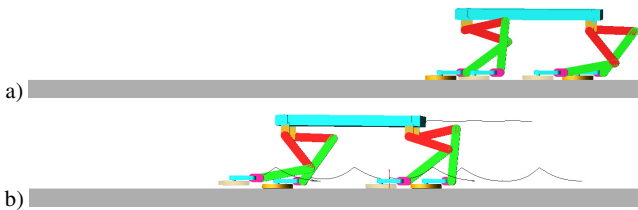
Fig. 10 View of walking on feet – with a marked motion tracks of the body and wheels of front left and rear right legs [3]

The graphs (Fig. 11, 12) show the results starting from 12 s, and they are completely correct only after 14 s, because it is as long as it takes the robot to change to the initial position. Each leg is set in appropriate phase of movement and wheels are rotated to positions of feet [3].
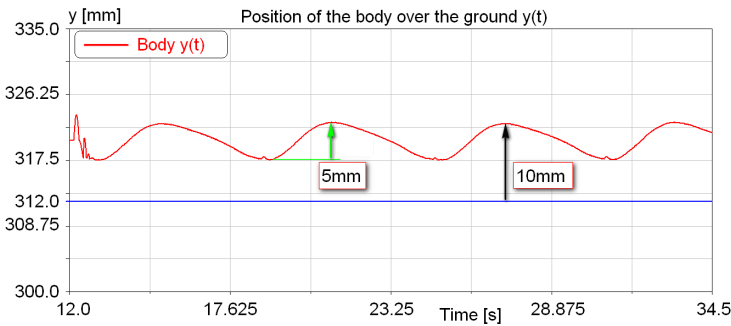
Fig. 11 The graph of the height of the body above the ground y(t), while walking on feet [3]

The problem mentioned at the simulations of walking on wheels occurs also in this case and causes the distance of the robot's body from the ground to increase by approximately 10 mm, in regard to the expected position (horizontal line in Fig. 11). However, fluctuations of the height of body's position are rare and their amplitude is not greater than 5 mm (Fig. 11) [3].
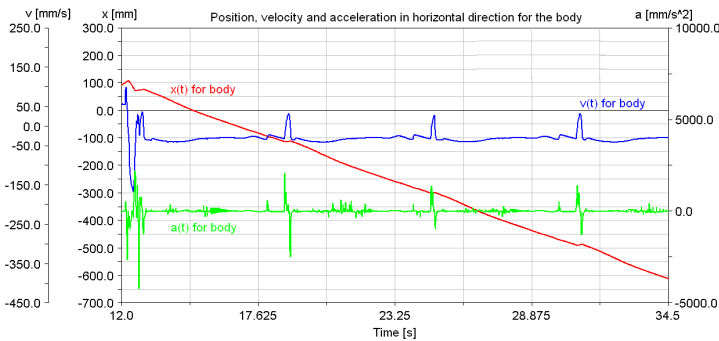
Fig. 12 Graph of position (x), velocity (v) and acceleration (a), along x-axis against time [3]

Based on the characteristics of the body's movement (Fig. 12) it is concluded that the robot traveled 700 mm in 22 s. Therefore, the absolute value of average speed is equal to 32 mm/s. It is also confirmed by average value obtained from the speed curve v(t). The body's movement speed is quite constant, there are no large fluctuations and its value never changes the sign. However, there are sudden changes in the values of velocity and acceleration [1]. The timing of these abnormalities is consistent for both. They appear about every 6 s. Thanks to that and observations of motion it have been concluded that they correspond to the phases

of movement when one of the front legs is in a heel contact phase. Due to the mentioned problem of incorrect vertical positions of feet, the front leg is not touching the ground. There is a slight forward tilt and the leg gently hits the ground. In addition, there are little slips of wheels in the first moments of stance phases [3].

5   Conclusions

The type of gait shown in the simulations of walking is the best obtained during various tests of robot's motion on flat surface. Further improvements of the gait would be possible by adding more trajectory points. This would lead to small differences between the expected and achieved trajectory. As a result, smaller errors of body and legs' positions would be achieved. This would improve the stability of gait and decrease the fluctuations in speed and acceleration of body movements. In addition, the errors that occur during the initial phase should be eliminated by improving the gait's control algorithm. It would result in achieving movements, leading to the initial position of walking and rotating wheels to position of feet, being as smooth as in the repeated gait cycle.

References

1. Endo, G., Hirose, S.: Study on Roller-Walker. Energy efficiency of Roller-Walk. In: International Conference on Intelligent Robots and Systems, pp. 5050–5055 (2011)
2. Hildebrand, M.: Symmetrical Gaits of Horses. Science 150, 701–708 (1965)
3. Olinski, M.: Preliminary design and simulation of mobile robot with many degrees of freedom. Master thesis Wroclaw UT (2011) (in Polish)
4. Olinski, M.: Preliminary design of leg walking robot. Bachelor thesis Wroclaw UT (2013) (in Polish)
5. Olinski, M.: Preliminary design of mechanics and control of a mobile robot's limb. Collective work edited by Szrek, J.: Interdisciplinarity of Scientific Research. Oficyna Wydawnicza Politechniki Wrocławskiej, Wrocław (2013) (in Polish)
6. Olinski, M.: Simulation of mobile robot with many degrees of freedom. Collective work edited by Zarzycki J.: The Computer-Aided Scientific Research XVIII. Wrocławskie Towarzystwo Naukowe, Wrocław, Poland (2011) (in Polish)
7. Raibert, M., Blankespoor, K., Nelson, G., Playter, R.: The BigDog Team: BigDog, the Rough-Terrain Quadruped Robot. Boston Dynamics Corp. (2008), http://www.bostondynamics.com/img/BigDog_IFAC_Apr-8-2008.pdf
8. Shah, R., Ozcelik, S., Challoo, R.: Design of a Highly Maneuverable Mobile Robot. Procedia CS 12, 170–175 (2012)
9. Wang, B., Hu, R., Zhang, X., Huai, C.: Gait planning and intelligent control for a quadruped robot. Journal of Control Theory and Applications 7(2), 207–211 (2009)
10. Yi, S.: Reliable gait planning and control for miniaturized quadruped robot pet. Mechatronics 20, 485–495 (2010)
11. Zielińska, T.: Walking Machines Basics, design, control and biological patterns. Wydawnictwo Naukowe PWN, Warszawa, Poland (2003) (in Polish)

Wheel-Legged Robot – Construction and Obstacle Detection Sensors

A. Gronowicz[1], P. Sperzyński[1], J. Szrek[1], and J. Jakubiak[2]

[1] Wrocław University of Technology, Division of Machine Theory
and Mechatronic Systems, Poland
`jaroslaw.szrek@pwr.wroc.pl`
[2] Wrocław University of Technology, Institute of Computer Engineering,
Control and Robotics, Poland
`janusz.jakubiak@pwr.wroc.pl`

Abstract. This paper presents the general structure of wheel-legged robot module and sensory systems. The scheme, interfaces and system components will be presented. Basing on initial experiments the sensor properties and suitability for a particular task – detection, identification and overcoming encountered obstacles on the robot's path were assessed.

Keywords: Wheel-legged, control system, levelling, obstacle detection, overcoming.

1   Introduction

The possibility of an autonomous mobile robot moving in the presence of obstacles has been the subject of research of the scientific and industrial centers for many years. Such systems are used, among others in the inspection, transport and operation in difficult to reach areas. One of the topics of publications is navigation and the planned path of the robot in the presence of obstacles. Usually, it is assumed that autonomous vehicle, usually wheeled, encounters an obstacle on its path, which it will be able to evade. This type of task is now successfully resolved - an example can be competition organized by DARPA - Grand Challenge and Urban Challenge [13].

Another problem of operating in the presence of obstacles is when a robot can not avoid obstacles and must overcome them by treading. First, the robot must be equipped with a suspension that will have the required mobility and range of movement to perform this operation. This is achieved by using special suspension systems: wheeled, tracked, legged or - based on their combinations – hybrid systems. Hybrid systems make it possible to move on wheels when ground is flat, providing the required speed of movement. In the more challenging terrain - uneven surfaces or obstacles presence - robot can overcome it by treading.

Wheel-legged suspension systems have a special kinematic structure and thus may be more versatile, particularly when performing more complex tasks, such as moving up the stairs [4]. Examples of wheeled robots with the ability to walk are: Sojourner rover, four-limb robot WorkPartner [9] and Shrimp, which has additional support wheels for obstacle overcoming. Other examples of similar solutions have been presented in [5, 6, 8]. Another example of wheel-legged robot is LegVan [7, 8] and LegVan II - robot built in the Division of Machine Theory and Mechatronic Systems at Wroclaw University of Technology (Poland).

The robot has four limbs with a wheel attached to each. All the wheels are driven wheels, two of them being also turning wheels [7, 11]. The robot has a special suspension system designed to best perform the levelling and walking functions by means of a minimum number of drives [1, 2, 12]. In order to determine the actual mechanical properties of the robot's leg and to test the control system it was decided to build a rig for testing a single robot leg (Fig. 1)
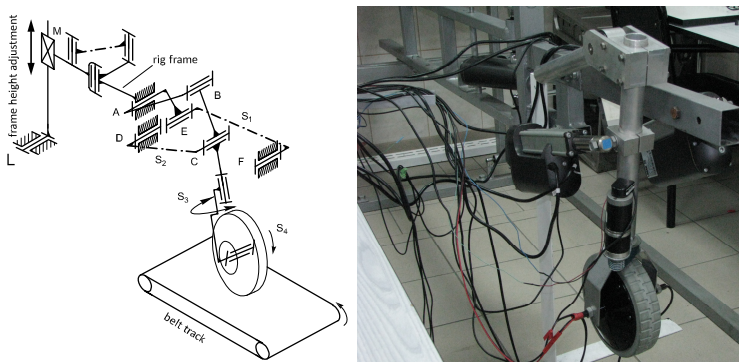
Fig. 1 View of the robot's limb rig and its kinematic structure
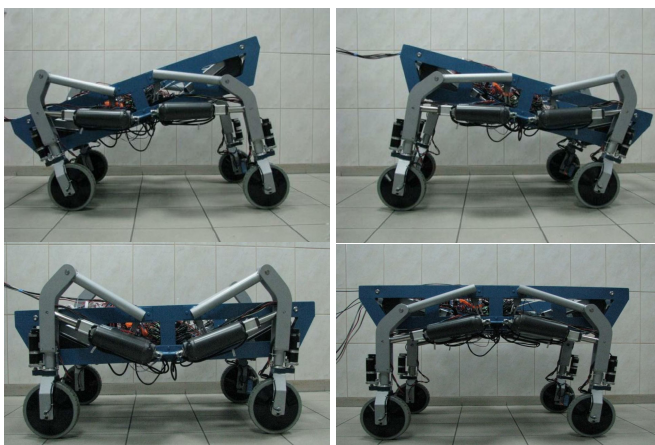
Fig. 2 Robot's motion capabilities

Displacement abilities of the robot are shown in Fig. 2. A characteristic feature of the robot limb is specially designed kinematic structure - where without compromising traction, the number of controlled drives has been reduced to four [8, 12].

Important elements of the robot are integrated sensors and control algorithms, that in addition to the process of overcoming obstacles must be used to ensure the stability of the robot. Detection of obstacles and their proper classification, as well as obtaining information about how to overcome the encountered obstacles is still a challenge [3, 4, 10].

This paper presents preliminary results of a research on the development of sensory systems of a wheel-legged robot allowing obstacles autonomous detection and overcoming by treading.

Chapter 2 presents the assumptions on robot motion and obstacle type that should be recognized. Chapter 3 presents the design of the sensory and the analysis of its components. The summary is contained in Chapter 4.

2 Assumptions

In principle, the robot has to operate in urban areas mainly moving on wheels. On their way they may face obstacles such as slopes, steps, thresholds and curbs, whose defeat requires a walking motion.

The sensory system of the wheel-legged robot should provide both the internal state of the robot measurements and the information about the environment, in particular – detection and approaching to obstacles.

Unequivocal interpretation of space, especially fast-changing is a very difficult task, due to the fact that the initial type of obstacle is restricted. It is assumed that the robot will have to face an obstacle located in front of one wheel, two wheels (type barrier curb or wall) and a multi-level obstacle - stairs.

3 The Sensory System

The control system, whose function is to control the object should have the suitable structure and the computing power required to process all the data, particularly from the robot's environment.

3.1 Structure of the Sensory System

The third figure shows a diagram of the robot's control system. As a part of the measuring system the internal state of the robot included in the proposed system is to handle data of wheels pressure on the ground, obtained by strain gauges (POZ) which constitute a crank in the structure of all four limbs of the robot.
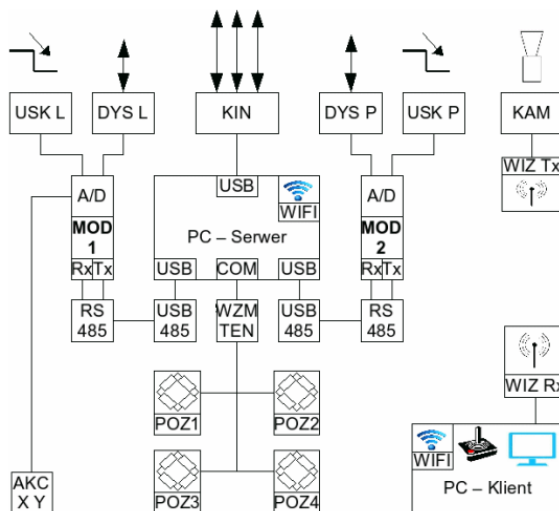
Fig. 3 Structure of the environment's sensory system of the wheel –legged robot LegVan II

To obtain information about the environment of the robot the central group of sensors, which are responsible for the measurement of environment and two further groups of sensors associated with front legs to ensure the detection of obstacles in front of the robot are used. Groups of sensors associated with the limbs contain short-range distance sensors (DYS) and step detectors (USK).

The sensors are located in the front legs at the height of the left and right wheels' axis. The signal from the sensor is processed via analog-to-digital local microcontroller module (MOD), and then goes to the robot's main computer (PC-Server).

The main part of the central group of sensors is a sensor (KIN) providing an array of depth of the robot's front area. Measurement data is complemented by an additional image from the camera (CAM) located on the robot.

An image of the robot's environment goes by independent wireless connection to the remote computer (PC Client), where the current parameters of the robot are visualized.

3.2 Measurement of Force Reaction and Deviation from the Horizontal Position

In order to measure the wheel load (reaction of ground) a tensometric beam was applied. The beam also serves as a crank (Fig. 4) transforming servomotor elongation into the rotational motion of the leg for the lifting function.

Owing to the fact that the sensor is part of the leg and is located on the crank it is possible to read the force directly connected with the pressure exerted by the leg on the ground. The force is not disturbed by any other components.

The tensometric beam supplies information about wheel/ground contact loss instants, which is useful for negotiating obstacles by walking.

Fig. 4 Lifting drive with measuring beam

Last sensor provides information about the deviation of the platform from the horizontal position. It is delivered by 2D digital accelerometer located in the geometric center of the robot.

3.3   The Distance Measuring

The location of the obstacles encountered in front of the robot's wheels is carried out by two laser distance sensors SICK DT 10.

The sensors, mounted on the robot limbs provide distance information in the range of 50-500mm. Figure 5 shows a view of the detection of a obstacle. The analog signal from range 4-20 mA is fed to the analog-to-digital converters inputs.
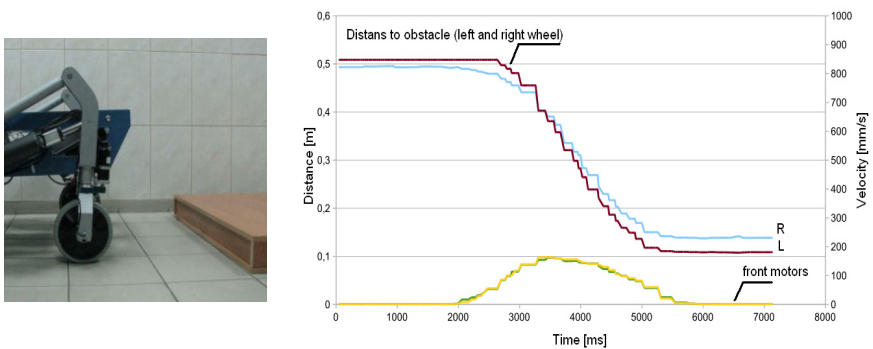
Fig. 5 Contactless distance sensor SICK DT10 – detection and stop in front of the obsctacle

Another distance sensor is responsible for detecting the encountered step. For this purpose the Sharp GP2D120 infrared sensor has been used with a measuring range 40-300mm. The advantage of the sensor is a relatively low price in comparison to the sensor SICK DT 2, with a similar range.

3.4   The Robot's Environment Analysis

For the analysis of the area in front of the robot a Kinect from Microsoft has been used. Kinect is a device for extending the interaction capabilities of XBOX360 console. The device generates an RGB image with dimensions of 640x480 pixels, and depth map of the same size with resolution of 10 or 11 bits.

In particular, the sensor is used to track the figures of two (and also theoretically more) people situated in front of the sensor. Its capabilities and a relatively low price caused that it was used in robotic applications [14].
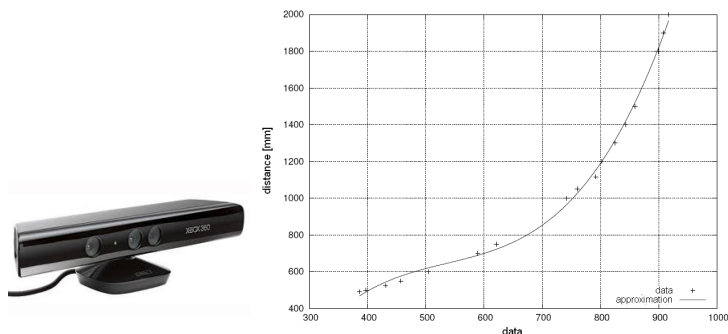
Fig. 6 Kinect Sensor with characteristics

In the case of wheel-legged robot the depth map returned by the Kinect has been used. Measurement of depth is in the range of 57 degrees horizontal and 43 degrees vertical. The sensor detects objects at the distance of slightly less than 0.5 to 4 m. The dependence of the actual distance d from the sensor readings r is non-linear. For the purposes of the application, the measured characteristic is approximated by a polynomial (1) (Fig. 6).

$$d = 1.86134e - 05r3 - 0.0299318r2 + 16.8096r - 2630.95 \qquad (1)$$

The characteristics also show that the distance measurement resolution decreases from 10 readings per cm for a distance of 50cm to about 1 reading per cm at a distance of 2m. Therefore, in the obstacle detection application of wheel-legged robot the range was established from 50 to 200cm, as more useful.

For detection of obstacles, 3 zones of interest are dealt: the center, left and right. Zones: left and right are tracks where the wheels will move the robot in the case of linear motion. The width of these zones is 300 mm, which corresponds to the width of the limbs and drive motors. The central zone has a width equal to the distance between the wheels of the robot – about 355mm.

Measuring zones extend in the whole range of the analyzed distance - from 50 to 200cm.

Step: Right	d=677, h=247
Step Left	d=1488, h=268
Step: Right	d=677, h=250
Step Left	d=1488, h=268
Step: Right	d=677, h=250
Step Left	d=1488, h=262
Step: Right	d=677, h=247
Step Left	d=1488, h=268
Step: Right	d=677, h=247
Step Left	d=1488, h=268
Step: Right	d=677, h=247
Step Left	d=1488, h=268
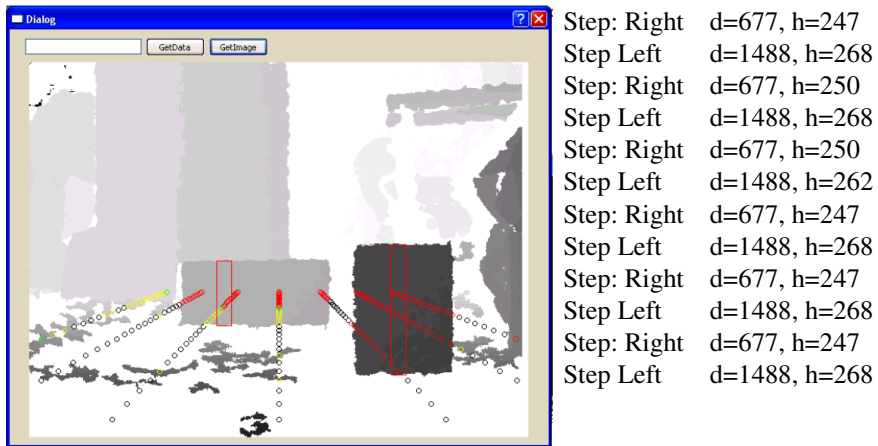
Fig. 7 The information sent by the server sckinect, on the left: image with marked detected obstacles, on the right: the text messages about detected obstacles

Analysis of the distance is performed independently in each of the three zones. In the area of limbs' measurement, module provides information about obstacle of any type (curb, threshold, wall). In the central zone of the analysis is stopped only when it detects an obstacle with a height greater than the clearance under the housing of the robot, which is between 250-550mm, depending on the current configuration. The results (view of scene and data) sent by the obstacle detection module (server sckinect) are shown in Fig. 7.

4   Conclusions

The aim of the wheel-legged robot's sensors system is to enable the implementation of a robot moving in an unknown, but a structured field. The sensors included in the system have been tested for their suitability to carry out an assumed task. Proposed sensor system is sufficient to achieve the task of obstacle localization when a class of encountered obstacles is limited (to several groups).

A further step will be integration of the data obtained from each sensor to ensure a reliable and autonomous movement of the robot in an unknown space.

Experiments show that the measurement error of the distance to an obstacle and height of rectangular obstacles is less than 30mm. This is a sufficient value to decide how to overcome the obstacles, or if necessary to change the direction of motion.

Preliminary experiments indicate that the Kinect sensor is useful for the preliminary robot's path planning and the navigation of mobile robots, providing information about obstacles detected at a distance up to 2-3m. Due to several centimeters accuracy and dead zone at a distance of less than 50cm, the sensor can not be used alone. Only a fusion with other sensors provide adequate precision of measurement and robot motion.

References

1. Bałchanowski, J.: Mobile wheel-legged robot: researching of suspension leveling system. In: Beran, J. (ed.) Advances in Mechanisms Design: Proceedings of TMM 2012, pp. 3–12. Springer, Dordrecht (2012)
2. Bałchanowski, J., Gronowicz, A.: Design and simulations of wheel-legged mobile robot. Acta Mechanica et Automatica 6(2), 11–16 (2012)
3. Cunha, J., et al.: Using a depth camera for indoor robot localization and navigation. In: Proceedings of the Robotics Science and Systems 2011 Workshop on Advanced Reasoning with Depth Cameras, Los Angeles, California, USA (July 2011)
4. Gonzalez, A., Ottaviano, E., Ceccarelli, M.: On the kinematic functionality of a four-bar based mechanism for guiding wheels in climbing steps and obstacles. Mechanism and Machine Theory 44(8), 1507–1523 (2009)
5. Grand, C., et al.: Stability control of a wheel-legged mini-rover. In: Proc. of CLAWAR 2002: Proceedings of the 5th Int. Conf. on Climbing and Walking Robots, Paris, France, pp. 323–330 (2002)
6. Grand, C., et al.: Stability and traction optimization of a wheel-legged robot. International Journal of Robotics Research 23(10-1), 1041–1058 (2004)
7. Gronowicz, A., Szrek, J.: Design of LegVan wheel-legged robot's mechanical and control system. In: SYROM 2009 Red. Ion Visa, pp. 145–158. Springer, Netherlands (2009)
8. Gronowicz, A., Szrek, J.: Idea of a quadruped wheel-legged robot. Archive of Mechanical Engineering 56(3), 263–278 (2009)
9. Halme, A., et al.: Hybrid locomotion of a wheel-legged machine. In: Proceedings CLAWAR 2000 (2000)
10. Henry, P., et al.: RGB-D mapping: Using depth cameras for dense 3D modeling of indoor environments. In: Proceedings RGB-D: Advanced Reasoning with Depth Cameras Workshop, vol. 1 (2010)
11. Sperzynski, P., Szrek, J., Gronowicz, A.: Synteza geometryczna mechanizmu realizującego trajektorieprostoliniowa ocechowana. Acta Mechanica et Automatica 4(2), 124–129 (2010)
12. Szrek, J.: Metoda syntezy układu zawieszenia kołowo – krocz˛acego robota mobilnego. In: Proceedings XX Konferencja Naukowo – Dydaktyczna Teorii Maszyn i Mechanizmów, Zielona Góra, Wrzesień (2006)
13. Buehler, M., Iagnemma, K., Singh, S. (eds.): The DARPA Urban Challenge. Autonomous Vehicles in City Traffic. STAR, vol. 56. Springer, Heidelberg (2009)
14. Open Kinect Project, http://openkinect.org/wiki/Main_Page

Control of Constrained Dynamic System of Leg of Wheel-Legged Mobile Robot

P. Sperzyński and J. Szrek

Wroclaw University of Technology,
Division of Machine Theory and Mechatronic
{przemyslaw.sperzynski,jaroslaw.szrek}@pwr.wroc.pl

Abstract. This paper proposes a general formulation of the dynamic model of constrained, articulated limb of wheel-legged mobile robot. Dynamic model of the system has been formulated in terms of actuated joints using Euler-Lagrange formulation. Implicit kinematic model is used to provide dependences between articulated and unarticulated joint rates, velocities and accelerations used in the model. Based on dynamic model of the system a nonlinear controller has been proposed. Numerical model of the limb has been built in order to verify the validity of the control laws. Exemplary simulations have been presented to show asymptotic stability of control system.

Keywords: dynamics, nonlinear control, constrained multibody system, mobile robot.

1   Introduction

A wheel-legged mobile robot is formed from connection of two categories of robots – Wheeled and legged [1, 3]. The considered robot (Fig. 1) has a suspension system that allows for execution of significant displacement of the wheels. This characteristic (walking function) is useful particularly in the situation of overcoming obstacles like: curb, step, these which robot with passive suspension system based on driven wheels. Another advantage of this hybrid type of suspension system is the possibility of fast navigation on wheels on the even surface. Structure of the limb has a special well-matched geometry, where lifting function is executed only by one from two actuators placed in the limb [2]. In the meantime, second actuator is formed on a particular length, which is being changed only during the process of walking. Control system of the limb has been considered in [4, 5]. This paper presents nonlinear control system of the robot's limb, based on the dynamic model of the leg. In order to derive the dynamic model a kinematic analysis of the limb has been presented, together with singularity analysis of the system.
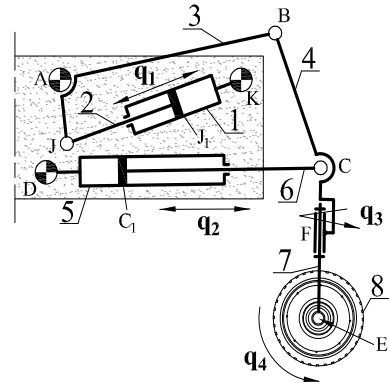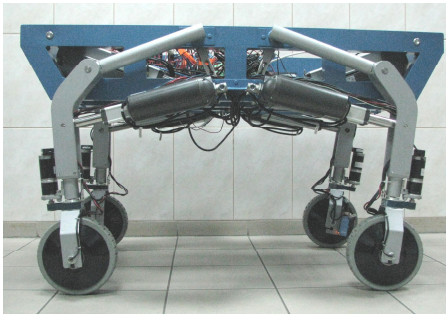
a)   b)

Fig. 1 a) view of constructed wheel-legged mobile robot, b) kinematic scheme with denoted elements and q drives

2   Kinematic Formulation of the Leg of Mobile Robot

The limb scheme is presented in the Fig. 2. In order to describe the dynamics of the system, kinematic dependences of the mechanism have been derived. The configuration of the limb's system has been described through vector equations with closed-loop kinematic chain. The joint variables have been divided for independent – controlled $\mathbf{q} = [q_1, ..., q_n]^T$, and dependent variables – uncontrolled $\mathbf{p}(\mathbf{q}) = [p_1, ..., p_m]^T$. The dimensions of the structure have been described through constants $\mathbf{a} = [a_1, ..., a_k]^T$ and $\boldsymbol{\alpha} = [\alpha_1, ..., \alpha_l]^T$.
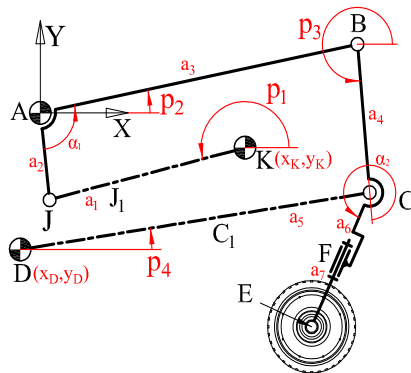
Fig. 2 Assumed limb's parameters

With such parameters local coordinate systems $\mathfrak{F}_i$ of all elements of the mechanism have been assumed. Below, transformations between base reference frame and local frames have been presented:

$$\begin{aligned}
&\mathfrak{F}_1 = T_x(x_K)T_y(y_K)R_z(p_1) && \mathfrak{F}_5 = T_x(x_D)T_y(y_D)R_z(p_4) \\
&\mathfrak{F}_2 = \mathfrak{F}_1 T_x(q_1 - a_1) && \mathfrak{F}_6 = \mathfrak{F}_5 T_x(q_2 - a_5) \\
&\mathfrak{F}_3 = R_z(p_2) && \mathfrak{F}_7 = \mathfrak{F}_4 T_x(a_4)R_z(\alpha_2)T_x(a_6) \\
&\mathfrak{F}_4 = \mathfrak{F}_3 T_x(a_3)R_z(p_3) && \mathfrak{F}_8 = \mathfrak{F}_7 R_x(q_3)T_x(a_7)
\end{aligned}$$

where $T_{x,y}$ – translation matrix along X, Y axes, $R_{x,z}$ – rotation matrix along X or Z axis (global reference frame is placed in point A, as showed in Fig. 2) in form of Euclidean group SE(3).

Kinematics of the system is described in implicit form of active variables $\mathbf{q}$ and passive $\mathbf{p}$. Equations can be rewritten as:

$$\varphi_i\big(\mathbf{q}, \mathbf{p}(\mathbf{q}), \mathbf{a}, \boldsymbol{\alpha}\big) = 0, \, i = 1 \ldots m. \tag{1}$$

Next assuming $\mathbf{q} = \mathbf{q}(t)$, $\mathbf{p} = \mathbf{p}(t)$, position equations have been differentiated with respect to time, to obtain velocities terms:

$$\boldsymbol{\Phi}_p \dot{\mathbf{p}} + \boldsymbol{\Phi}_q \dot{\mathbf{q}} = 0 \qquad \Rightarrow \qquad \dot{\mathbf{p}} = -\boldsymbol{\Phi}_p^{-1} \boldsymbol{\Phi}_q \dot{\mathbf{q}}, \tag{2}$$

where $\boldsymbol{\Phi}_p$ and $\boldsymbol{\Phi}_q$:

$$\boldsymbol{\Phi}_p = \frac{\partial \boldsymbol{\varphi}}{\partial \mathbf{p}}, \qquad \boldsymbol{\Phi}_q = \frac{\partial \boldsymbol{\varphi}}{\partial \mathbf{q}}, \tag{3}$$

are Jacobian matrices of constrained kinematic system due to active and passive variables.

Following, accelerations analysis leads to equations:

$$\begin{aligned}
&\dot{\boldsymbol{\Phi}}_p \dot{\mathbf{p}} + \boldsymbol{\Phi}_p \ddot{\mathbf{p}} + \dot{\boldsymbol{\Phi}}_q \dot{\mathbf{q}} + \boldsymbol{\Phi}_q \ddot{\mathbf{q}} = 0 \Rightarrow \\
&\ddot{\mathbf{p}} = -\boldsymbol{\Phi}_p^{-1}\Big(\boldsymbol{\Phi}_q \ddot{\mathbf{q}} + \big(\dot{\boldsymbol{\Phi}}_q - \dot{\boldsymbol{\Phi}}_p \boldsymbol{\Phi}_p^{-1} \boldsymbol{\Phi}_q\big)\dot{\mathbf{q}}\Big)^{.}
\end{aligned} \tag{4}$$

Eq. φ (1) as closed-loop equations are obtained by means of closed vectors loops:

$$\boldsymbol{\varphi} = \begin{cases} \overrightarrow{AK} + \overrightarrow{KJ} - \overrightarrow{AJ} \\ \overrightarrow{AB} + \overrightarrow{BC} - \overrightarrow{AD} - \overrightarrow{DC} \end{cases} = 0. \tag{5}$$

Further, extending (4) into scalar coordinates, equations take the form of:

$$\boldsymbol{\varphi} = \begin{cases} x_K + q_1\cos(p_1) - a_2\cos(p_2 - \alpha_1) \\ y_K + q_1\sin(p_1) - a_2\sin(p_2 - \alpha_1) \\ a_4\cos(p_3) + a_3\cos(p_2) - x_D - q_2\cos(p_4) \\ a_4\sin(p_3) + a_3\sin(p_2) - y_D - q_2\sin(p_4) \end{cases} = 0. \qquad (6)$$

Upon above Eq. (6), first two have to be solved to provide solution of the $p_2(q_1)$ joint rate, which respectively need to be used to solve next two of $p_3(p_2, q_2)$ and $p_4(p_2, q_2)$.

2.1 Solution of Kinematic Constraints

Dividing the Eq. (6) into two pairs as has been described above that can be transformed into the form of:

$$\varphi_i = C_{Si}\sin(p_i) + C_{Ci}\cos(p_i) + C_{Oi}, \qquad (7)$$

which only depends on one of passive variable p_i.

Eq. (7), can be solved with respect to $\sin(p_i)$ and $\cos(p_i)$ term, as:

$$\sin(p_i) = \frac{-C_{Oi}C_{Si} \pm \sqrt{C_{Ci}^4 - C_{Ci}^2 C_{Oi}^2 + C_{Ci}^2 C_{Si}^2}}{C_{Ci}^2 + C_{Si}^2}$$

$$\cos(p_i) = \frac{-C_{Oi}C_{Ci} \pm \sqrt{C_{Si}^4 - C_{Si}^2 C_{Oi}^2 + C_{Ci}^2 C_{Si}^2}}{C_{Ci}^2 + C_{Si}^2}. \qquad (8)$$

Therefore analytic solution of the p_i takes form:

$$p_i = \arctan\left(\frac{\sin(p_i)}{\cos(p_i)}\right) \qquad (9)$$

2.2 Singularities of the System

Singularity analysis of the system with respect to passive joint rates $\dot{\mathbf{p}}$ gives following expression of the determinant of the Jacobian matrix $\boldsymbol{\Phi}_p$:

$$\det(\boldsymbol{\Phi}_p) = q_1 q_2 a_3 a_4 \sin(p_3 + p_4)\sin(p_1 + p_2 - \alpha_1) \qquad (10)$$

The determinant of the Jacobian matrix will be equal to zero, if the lengths of the actuators q_1 or q_2 are 0 or the sum of the angles p_3+p_4 and $p_1+p_2-\alpha$ equals 0 or π. That means singular positions (where assuming q_1 and q_2, passive joint rates cannot be solved) can be reached when AJ, JK links are collinear, similarly as BC, CD links. The parameters of the limb have been chosen to avoid such singular position for the assumed q_1 and q_2 actuators stroke lengths.

3   Dynamic Model Formulation of the System

Dynamic model of the system has been established using Euler-Lagrange formulation [6], assuming actuated variables vector $\mathbf{q}$, as independent variable vector. Equations take form:

$$\mathbf{M}(\mathbf{q},\mathbf{p})\ddot{\mathbf{q}} + \mathbf{C}(\mathbf{q},\dot{\mathbf{q}},\mathbf{p},\dot{\mathbf{p}})\dot{\mathbf{q}} + \mathbf{G}(\mathbf{q},\mathbf{p}) = \mathbf{Q}, \tag{11}$$

where $\mathbf{M}$ – mass forces matrix, $\mathbf{C}$ – centrifugal and Coriolis forces matrix, $\mathbf{G}$ - potential (gravity) forces vector, $\mathbf{Q}$ – vector of generalized forces and torques.

Equations of motion (11) are obtained from Lagrange function L as follows:

$$\frac{d}{dt}\frac{\partial L(\mathbf{q},\dot{\mathbf{q}},\mathbf{p}(\mathbf{q}),\dot{\mathbf{p}}(\mathbf{q},\dot{\mathbf{q}},\mathbf{p}))}{\partial \dot{\mathbf{q}}} - \frac{\partial L(\mathbf{q},\dot{\mathbf{q}},\mathbf{p}(\mathbf{q}),\dot{\mathbf{p}}(\mathbf{q},\dot{\mathbf{q}},\mathbf{p}))}{\partial \mathbf{q}} = \mathbf{Q}. \tag{12}$$

Lagrange function L is given as:

$$L = K - V, \tag{13}$$

where K – kinetic energy of the multibody system, V – potential energy.

$$K = \frac{1}{2}\sum_i \left(m_i \dot{\mathbf{c}}_i^T \dot{\mathbf{c}}_i + \boldsymbol{\omega}_i^T \mathbf{I}_i \boldsymbol{\omega}_i\right), \quad V = -\sum_i m_i \mathbf{g}^T \mathbf{c}_i, \tag{14}$$

where m_i – element mass, $\mathbf{c}_i$ –centres of mass position, $\boldsymbol{\omega}_i$ – angular velocity, $\mathbf{I}_i$ – inertia tensor with respect to base reference frame, $\mathbf{g}$ – gravity vector. The centre of mass reference frame $\mathfrak{F}_{ci}$ is described in assumed local reference frames $\mathfrak{F}_i$ of the mechanism elements as : $\mathfrak{F}_{ci}=\mathfrak{F}_i T_x(x_{Ci})T_y(y_{Ci})R_z(\alpha_{Ci})$.

In a first step, $\partial K/\partial \dot{\mathbf{q}}$ term has to be computed in order to calculate M mass forces matrix. As follows, $\partial K/\partial \dot{\mathbf{q}}$ takes form of:

$$\frac{\partial K}{\partial \dot{q}_i} = f_i(\mathbf{q},\dot{\mathbf{q}},\mathbf{p},\dot{\mathbf{p}},\frac{\partial \dot{\mathbf{p}}}{\partial \dot{\mathbf{q}}}) \Rightarrow \frac{d}{dt}\frac{\partial K}{\partial \dot{q}_i} = f_i(\mathbf{q},\dot{\mathbf{q}},\ddot{\mathbf{q}},\mathbf{p},\dot{\mathbf{p}},\ddot{\mathbf{p}},\frac{\partial \dot{\mathbf{p}}}{\partial \dot{\mathbf{q}}},\frac{d}{dt}\frac{\partial \dot{\mathbf{p}}}{\partial \dot{\mathbf{q}}}), \tag{15}$$

It can be demonstrated, that $\partial\dot{\mathbf{p}}/\partial\dot{\mathbf{q}}$ depends only on configuration of the mechanism $\mathbf{p}$ and $\mathbf{p}(\mathbf{q})$ joint positions. From Eq. (2) can be obtained:

$$\frac{\partial\dot{\mathbf{p}}}{\partial\dot{\mathbf{q}}} = -\boldsymbol{\Phi}_p^{-1}\boldsymbol{\Phi}_q, \ \frac{d}{dt}\frac{\partial\dot{\mathbf{p}}}{\partial\dot{\mathbf{q}}} = -\frac{d\boldsymbol{\Phi}_p^{-1}}{dt}\boldsymbol{\Phi}_q - \boldsymbol{\Phi}_p^{-1}\frac{d\boldsymbol{\Phi}_q}{dt}, \tag{16}$$

which depends only on p and q, therefore mass forces matrix M can be computed collecting $\ddot{\mathbf{q}}$ and $\ddot{\mathbf{p}}$ coefficients from Eq. (15):

$$\mathbf{M} = \left[m_{ij}\right]_{n\times n} = \mathbf{M}_q\ddot{\mathbf{q}} + \mathbf{M}_p\ddot{\mathbf{p}} = \left(\mathbf{M}_q - \mathbf{M}_p\boldsymbol{\Phi}_p^{-1}\boldsymbol{\Phi}_q\right)\ddot{\mathbf{q}}, \tag{17}$$

where $\mathbf{M}_q$ – matrix of $\ddot{\mathbf{q}}$ coefficients, $\mathbf{M}_p$ – matrix of $\ddot{\mathbf{p}}$ coefficients

Centrifugal forces matrix $\mathbf{C}$ can be obtained using property of the E-L dynamic model, which brings $\mathbf{C}$ matrix definition as terms of Christoffel symbols of first kind:

$$\mathbf{C} = \left[c_{kj}\right]_{n\times n}, c_{kj} = \sum_i\left(\frac{\partial m_{kj}}{\partial q_i} + \frac{\partial m_{ki}}{\partial q_j} - \frac{\partial m_{ij}}{\partial q_k}\right)\dot{q}_i, \tag{18}$$

In order to compute c_{kj}, the partial derivatives $\partial\mathbf{p}/\partial\mathbf{q}$ have to be established, that can be obtained using (9).

Further, dynamic model formulation is ended by description of vector of potential forces $\mathbf{G}$, as:

$$G_i = \frac{\partial V}{\partial q_i}, \tag{19}$$

which needs partial derivatives $\partial\mathbf{p}/\partial\mathbf{q}$, as c_{jk} symbols.

4   Nonlinear Controller of the System

Upon dynamic model (11) the control system has been proposed based on [2]. The control law is defined by expression:

$$\mathbf{Q} = \mathbf{M}(\mathbf{q},\mathbf{p})\ddot{\mathbf{q}}_{ref} + C(\mathbf{q},\dot{\mathbf{q}},\mathbf{p},\dot{\mathbf{p}})\dot{\mathbf{q}}_{ref} + \mathbf{G}(\mathbf{q},\mathbf{p}) + \mathbf{K}\mathbf{s}, \tag{20}$$

where $\mathbf{q}_d$, $\dot{\mathbf{q}}_d$, $\ddot{\mathbf{q}}_d$, – desired positions, velocities, and accelerations, $\mathbf{M}$, $\mathbf{C}$, $\mathbf{G}$ – matrices given by dynamic model of the system (11), $\mathbf{K}$ – gain matrix (diagonal matrix), $\dot{\mathbf{q}}_{ref}$, $\ddot{\mathbf{q}}_{ref}$ – reference positions and velocities, $\mathbf{s}$ – slide, defined as:

$$\ddot{\mathbf{q}}_{ref} = \ddot{\mathbf{q}}_d - \Lambda\left(\dot{\mathbf{q}} - \dot{\mathbf{q}}_d\right), \dot{\mathbf{q}}_{ref} = \dot{\mathbf{q}}_d - \Lambda\left(\mathbf{q} - \mathbf{q}_d\right), s = \dot{\mathbf{q}}_d - \dot{\mathbf{q}} + \Lambda\left(\mathbf{q} - \mathbf{q}_d\right), \tag{21}$$

Gains of the controller **K**, are adapted based on slide variable as follows:

$$\mathbf{K} = diag\{K_i\}, K_i = K_p \int s_i^2(t)dt + K_0 .$$

(22)

Stability of the algorithm has been proven in [7].

4.1   Simulation Example

The parameters of the limb (Fig. 2) have been assumed as: $x_K = 0.42$m, $y_K = 0$m, $x_D = -0.07$m, $y_D = -0.15$m, $a_1 = 0.3$m, $a_2 = 0.16$m, $a_3 = 0.303$m, $a_4 = 0.162$m, $a_5 = 0.3$m, $a_6 = 0.2$m, $a_7 = 0.1507$m, $\alpha_1 = 90°$, $\alpha_2 = 332.5°$. The centres of masses, masses and inertia tensors have been assumed according to real limb parameters.

a)   b)
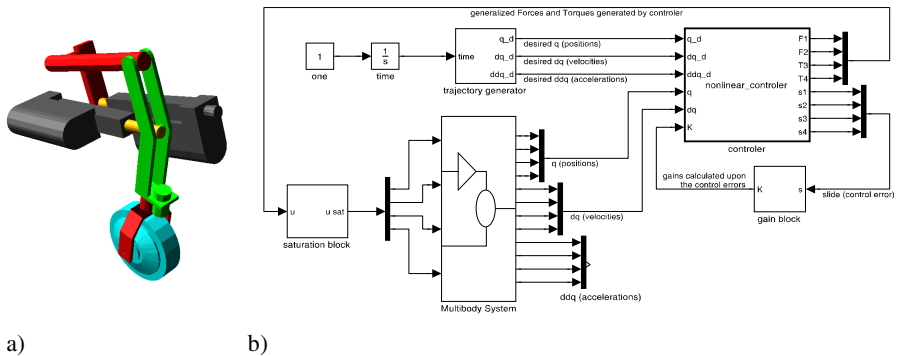
Fig. 3 a) Numerical model of the mechanism MSC/ADAMS, b) control system in MATLAB/SIMULINK

Based on the obtained dynamic system equations, controller system in MATLAB/SIMULINK environment and numerical multibody model of the limb mechanism (MSC/ADAMS) have been created. (Fig. 3). Below exemplary simulation's results have been presented (Fig. 4).

Two different sine desired trajectory for q_{1d} and q_{2d} actuators were assumed:

$$q_{id}(t) = A_i \sin\left(\frac{2\pi}{T_i}t + \theta_i\right) + q_{i0} ,$$

(23)

The parameters have been chosen as follows: $A_1=A_2=0.05$m, $T_1=7$, $T_2=5$, $\theta_1=\pi/2$, $\theta_2=-\pi/2$, $q_{10}=q_{20}=0.425$m, desired trajectory for the other two actuators q_3 and q_4 were set to constant point 0. The derivatives with respect to time were computed in order to provide $\dot{\mathbf{q}}_d$ and $\ddot{\mathbf{q}}_d$. Results of the simulations as controls tracking errors (difference between obtained and desired configuration $\mathbf{e}=\mathbf{q}-\mathbf{q}_d$) have been presented in Fig. 4.

a)   b)
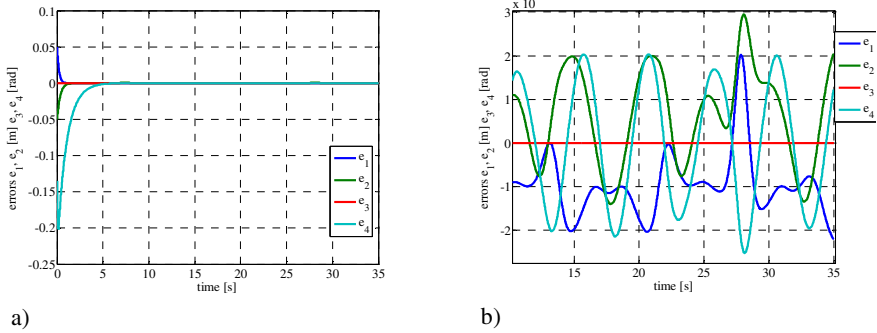
Fig. 4 a) tracking error obtained during the simulation, b) closer look into the tracking errors after 10s of the simulation

5   Conclusions

In the paper, nonlinear controller of the constrained mechanical system has been introduced. The case of reaching time independent set point and time dependent trajectory has been studied.

Fig. 4a) presents asymptotic stability of the algorithm (tracking errors, leads to 0), however after closer look into the simulation errors (Fig. 4b), they cannot go below $2 \cdot 10^{-4}$[m, rad] level. In the paper q_1 and q_2 actuators as transitional joints have been assumed, but in the future screw joint has to be considered.

References

1. Bałchanowski, J., Gronowicz, A.: Design and simulations of wheel-legged mobile robot. Acta Mechanica et Automatica 6(2), 11–16 (2012)
2. Gronowicz, A., Sperzyński, P.: Dimensional Synthesis of Suspension System of Wheel-Legged Mobile Robot. In: SYROM 2009 Red. Ion Visa, pp. 633–644. Springer, Netherlands (2009)
3. Gronowicz, A., Szrek, J.: Design of LegVan wheel-legged robot's mechanical and control system. In: SYROM 2009 Red. Ion Visa, pp. 145–158. Springer, Netherlands (2009)
4. Gronowicz, A., Szrek, J., Wudarczyk, S.: The force reaction control of the wheel-legged robot's limb prototype. In: Beran, J. (ed.) Advances in Mechanisms Design: Proceedings of TMM 2012, pp. 303–308. Springer, Dordrecht (2012)
5. Gronowicz, A., Szrek, J., Wudarczyk, S.: A rig for testing the leg of a wheel-legged robot. Acta Mechanica et Automatica 6(2), 48–52 (2012)
6. Shabana, A.: Dynamics of multibody systems. Cambridge University Press (2005) ISBN 0-13-9780511115837
7. Slotine, E., Li, W.: Applied nonlinear control. Prentice Hall, Englewood Cliffs, ISBN 0-13-040890-5

Planning an Optimal Step Motion
for a Hybrid Wheeled-Legged Hexapod

F. Gómez-Bravo[1], M. J. Aznar[1], and G. Carbone[2]

[1] University of Huelva, Spain
 fernando.gomez@diesia.uhu.es
[2] University of Cassino and South Latium, Italy
 carbone@unicas.it

Abstract. This paper addresses the path planning problem for an hybrid wheeled–legged hexapod. In particular, the proposed procedure is aiming to identify optimal trajectories for a leg when it has to step over an obstacle. The proposed procedure is a combination of a quick random search algorithm together with an optimisation method. This combination is used to achieve a good compromise between computational costs and path planning performance. The optimization method is efficiently solved by using a genetic algorithm to achieve properly smooth leg movements. A case of study is numerically solved by referring to a built prototype of Cassino Hexapod at LARM in Cassino.

Keywords: Hybrid wheel-legged vehicles, Collision free trajectories, Motion Planning.

1   Introduction

Autonomous navigation of wheeled robot has been widely addressed in literature. The ability of these vehicles to move and maneuver justifies the interest of the scientific community on them. However, the main drawback of these robots is their limited capability of motion on uneven terrains. These situations use to happen, for instance, on exploration missions of unknown outdoor scenarios, where unexpected obstacles, that cannot be overcome using wheels, can appear [5]. Thus, navigation of mobile robot in irregular terrains represents a new challenge in the field of robotics research [5]. In this context, hybrid wheel-legged vehicles are a possible way to enhance the locomotion performance of an autonomous mobile platform [6]. This type of mobile robot combines the efficiency of the wheels and the walking machines. The robot will move on wheels and when it faces an obstacle which cannot be avoided, it will overcome it by passing over it. For this purpose, an efficient strategy for stepping over the obstacle is needed.

This paper, presents a new methodology for planning leg motions of a hexapod hybrid walking machine designed and built at the Laboratory of Robotics and Mechatronic (LARM) of the Cassino University [2]. This hexapod walking

machine is composed of six legs having a modular anthropomorphic architecture with a wheel as foot at its extremity. The proposed approach provides optimum trajectories that allow a leg of the hexapod to step over an obstacle. The method generates leg motions that present a trade off between the length of the path and the distance to the obstacle. The planning technique is based on combining a random search algorithm with an optimization procedure, namely a Genetics Algorithm (A.G.) [3, 9].

2   The Cassino Hexapod

The Cassino Hexapod [2] is a hybrid wheeled-legged robot that can be used for rolling locomotion on a flat ground and at the same time, can walk on irregular terrains (see Fig. 1a). On the one hand, the robot can move fast using its wheels, without consuming a lot of energy. On the other hand, it can use the legs in order to overcome situations in which wheeled motions are not possible. The proposed design has been conceived for developing a wheeled-walking system by using mainly low-cost industrial components into a suitable design for the whole system. Expected field of application for this prototype can be the inspection and operation in non-accessible sites as outlined in [5]. As a hexapod the robot consists of six legs and proper walking motion is possible by synchronizing the motion of all those [2]. In particular, each leg has on board three DC motors. Thus, a total of 18 DC motors are controlled for the operation of this walking machine. These six legs have been connected to a suitable body in order to build the prototype that is shown in Fig. 1b. This walking machine can fit into a cube of 0.6m x 0.6m x 0.5m and it has an overall weight of 180N. It can carry on-board its own control board. The weight of a leg is about 25 N. As an articulated body, each leg presents two revolute joint.

a)   b)

Fig. 1 Cassino Hexapod prototype: a) the whole robot; b) a single leg with main components

A leg includes a drive wheel as traction system. Each joint is driven by a commercial DC motor. Fig. 1b shows a built prototype of the proposed leg. It has a total height of 0.5 m and a weight of about 25 N and its maximum step size is 155mm. Kinematics and dynamic models have been previously reported in [5].

Programming the movement of one leg is very important for the successful movement of the robot. Various operation strategies have been analyzed and implemented on the built prototype [2]. In particular, if an obstacle is detected the neighborhood legs can be lifted up. Then, the hexapod robot can move forward by means of the wheels. The leg can go back to the straight configuration and afterwards other legs can be lifted up. This procedure can continue until the robot overcomes the obstacle(s). A commercial PLC Siemens S7-200 series has been chosen as main control unit together with additional I/O boards. A commercial DC power source provides the power supply for both the PLC and DC motors [2].

3   A Case of Study: Step over an Obstacle

The aim of this work is the study of the hexapod capability of stepping over obstacles. Instead of applying a traditional obstacle avoidance strategy for wheeled mobile robot, the robot has to move the legs in order to pass over the obstacle. Obviously this strategy can only be applied if the size of the obstacle allows the leg to move over it without colliding. For this purpose, this article focuses attention on the motion of a leg of the hexapod to overcome the obstacle.

The leg will evolve in a planar motion even though the study is accomplished with a 3D model. It is assumed that the control of the leg has three Degrees Of Freedom (DOF); two due to the revolute joints motion (that represents the first and second articular variables q1 and q2) and the third is the forward or backward motion of the robot (that represents the third articular variable q3). Fig. 2a illustrates the 3D representation model, presenting the articular variables, and the parameters that define the scenario. Fig. 2b shows the limit of the articular motion. Is important to note that during motion, the weight of the robot will be supported on the other legs, therefore it is also assumed that the height of the body robot will remain constant during the leg motion.

Thus the basic idea is to study different situations in which a leg can face an obstacle. These situations will consider different sizes of the obstacle, and different initial and final configuration of the leg. On the one hand, a rectangular prism has been considered in order to model the obstacles, and then the height (H) and width (W) are two fundamental values for determining the collision situation (see Fig. 2a). On the other hand, the initial and final configuration is defined by the distance of the leg to the obstacle (D) and also the leg joint angles (q1, q2). In future works, the existence of more than one obstacle will be considered.

From this point of view, the strategy consists on applying a motion planning algorithm that provides solutions to different situations. Thus, a procedure for planning optimal joint trajectories and avoid obstacle collision in articulated robots has been applied [3]. The idea is to solve the planning problem off-line so

that the motion of the leg can be learned from previous calculated solutions. Then, the learned trajectories can be applied in real time applications. Thus, the time consumed by the planning algorithm is not a critical parameter at this stage.

a)   b)
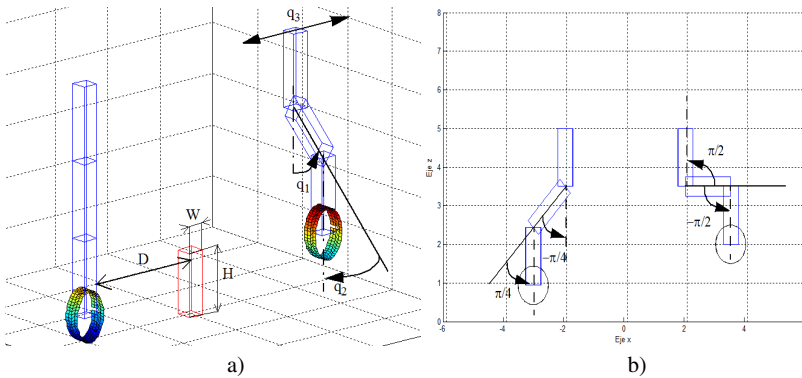
Fig. 2 Schemes of leg a) a 3D model; b) Leg motion limits

4   Optimal Leg Motion Planning

The method applied for building the leg trajectory has been previously developed for motion planning purposes in hybrid and parallel manipulators [3, 4]. The technique is based on searching collision free trajectories in the leg Joint Space Ω. For this purpose, the collision free sub-space ($\Omega_f \in \langle \Omega$), i.e. the set of configurations in which no collision exist, has to be determined. Thus, the planning method has to provide a sequence of joint configurations (a joint path) $^j\Xi = \{\ ^jq_1, ..., ^jq_n\ \}$, accomplishing $^jq_i \in \Omega_f$. Then, the first step of the method consist on generating a solutions set $\Lambda = \{\ ^j\Xi\}$, j=1..m, i.e, a collection of collision free paths $^j\Xi$ that connect the initial and the final configurations. In the second step, a Genetics Algorithm is applied to Λ so that the optimum solution is provided according to a trade off considering safety, reliability and length of the obtained trajectory. Then, the optimization method tries to obtain the shorter path which, at the same time, is far enough from collision, both in the joint space. A path far from obstacles decreases the possibility of collision if the path is not exactly followed (safety and reliability). Moreover, shorter path in the configuration space implies decreasing the length of motor's motion.

The solution set is obtained by means of a random generation's algorithm, represented by the "Rapidly Exploring Random Trees" (RRT) [1]. The RRT Algorithm is based on the construction of a tree of configurations that grows, seeking the final configuration position from a starting point. The objective of the RRT methods consists of constructing an exploration tree which covers randomly the

whole collision-free space. RRT is a planning method that can be used in any dimensional space where there are occupied zones, i.e. configurations where collision with obstacles exits, among collision-free configuration areas. The inconvenience of this method rests on the complexity of the obtained solution and the tendency of the path to lay very close to the obstacles. There are in the bibliography several procedures to improve the obtained solutions [1, 8]. In this work the use of Genetics Algorithms (G.A.) has been proposed [7].

The G. A. applied in this article is based on the typical procedures of this technique [7]. It accomplishes a set of operations (cross, mutation, evaluation and selection) over a population of possible solutions using an opportune encoding of the problem. The objective is to generate a solution that optimizes a fitness function. In this approach, each phenotype is a path $^j\Xi$, i.e. a sequence of adjacent joint configurations that enable to connect the initial with the final configuration without collision. The number of genes is not bounded so that trajectories of different length can be obtained. Thus, from an initial population Λ of non optimal free collision trajectories provided by RRT, the algorithm is capable of providing a solution that improves the fitness function. Finally during the selection procedure, the population members are evaluated against the fitness function in order to establish the members that will compose the next generation. An elitist technique that selects the best individuals (those with minor value for fitness function) has been chosen in order to implement the aforementioned selection. Thus, according to the evaluation, the worse phenotypes are discarded, maintaining constant the size of the population.

The fitness function that has been proposed for evaluating a joint path $^j\Xi$ is:

$$J(^j\Xi) = \Gamma + \sum_{i=1}^{m} d\left(^j q_i, {}^j q_{i+1}\right) + k_i \cdot \beta \tag{1}$$

The first component Γ has the mission of penalizing the existence of collision in accordance with:

$$\Gamma = \begin{cases} \infty & if \;\; {}^j q_i \notin \Omega_f \\ 0 & otherwise \end{cases} \tag{2}$$

The second component of the fitness function is the summation of two terms for the m configurations that composes the evaluated trajectory. The term $d(^j q_i, {}^j q_{i+1})$ represents the Euclidean distances between each two consecutive configurations. The term k_i weights the proximity to the obstacles using the following expression:

$$k_i = \begin{cases} 1 & if \;\; \rho_i < \delta \\ 0 & otherwise \end{cases} \tag{3}$$

where ρ_i is the distance from the configuration ${}^j q_i$ to the nearest collision configuration. According to this fitness function, the algorithm will supply the shorter trajectory that is far enough to the obstacles both in the joint space. It is worth highlighting that, shorter path in the joint space represent less effort and energy consumption as the motion of the actuator are shorter. Likewise, being far of the obstacles in Ω means that not only one element of the leg but the whole leg is taken into account for avoiding collision.

5   Simulation Results

Regarding the configuration of the Genetic Algorithm, after performing many numerical experiments, the maximum number of generation has been fixed to 100 and the population size to 50, in order to achieve a trade of between time consuming and the quality of the solutions. The crossover probability is equal to 1, i.e. all the phenotypes of the population are paired off randomly at this operation, providing new phenotypes composed by different parts of the progenitors: two phenotypes are generated from each couple. With this high crossover factor, although the algorithm works slower, the crossover operation positively influences in the quality of the solutions. The mutation probability is equal to 0.05.
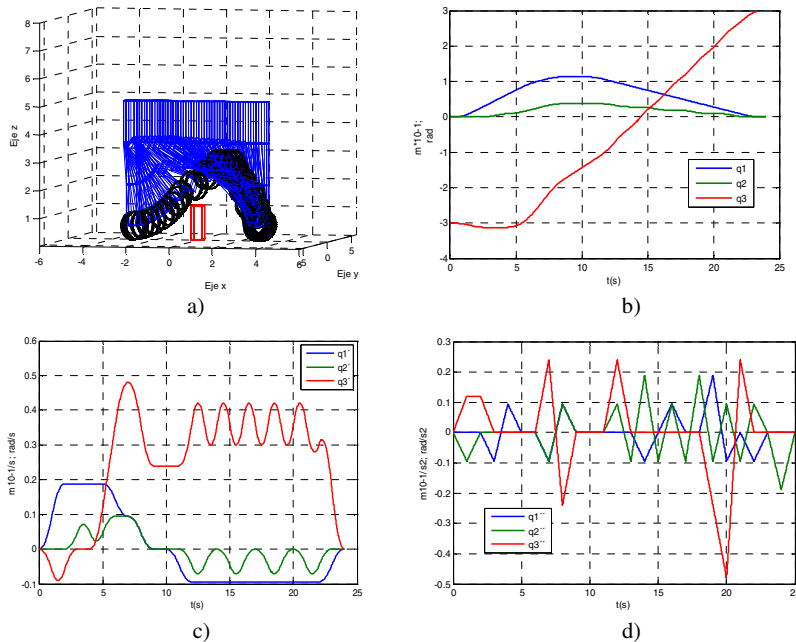
Fig. 3 Simulation results: a) bird-like step; b) joints evolution; c) joint velocities; d) joint accelerations

Table 1 Fitness Function Values

H=0.125 m ;W=0.1 m	D=0.1 m	D=0.2 m	D=0.4 m
Bird-like step	2.601457e+005	2.0018726e+005	3.2021623e+005
Human-like step	4.2010618e+005	3.2011990e+005	4.2019020e+005
Best Initial Phenotipe	1.120167e+006	1.0801824e+006	1.2003406e+006
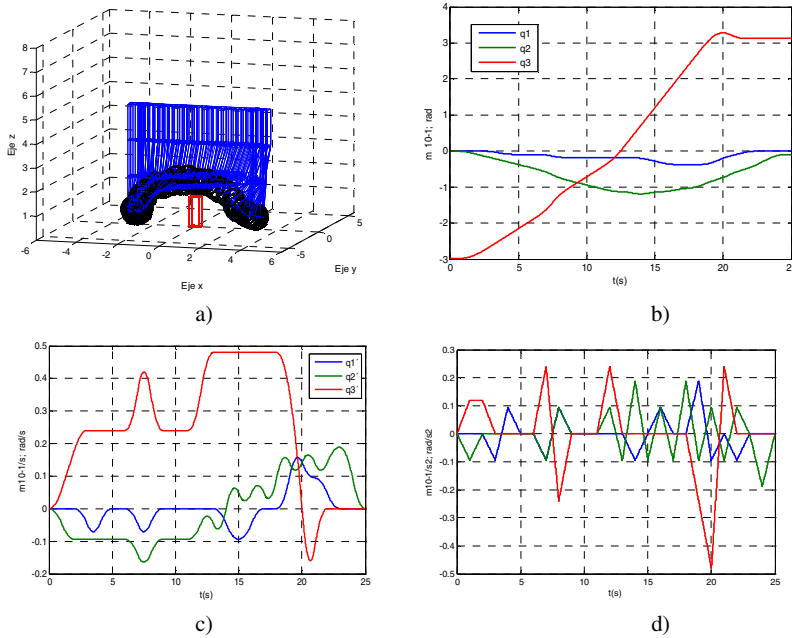
Fig. 4. a) human-like step; b) joints evolution; c) joint velocities; d) joint accelerations

Many experiments have been performed, considering the angular constraint of the leg, different initial conditions and obstacles size. In general the optimum solution is highly dependent on the value of these parameters. However, for medium size obstacles, and the constraints $q1 \in [-\pi/4\ \pi/2]$ and $q2 \in [-\pi/2\ \pi/4]$ (the constraint of the real robot) one type of optimal solution has been found: the bird-like step. This paper presents this solution, and compares it with a typical human-like step by taking into account the value of the fitness function of both trajectories in the same scenarios. Note that both solutions have been obtained automatically by the algorithm, just specifying the initial conditions and the joint constraint. In the experiment presented in this paper, the distance to the obstacle is 0.3m., and the size of the obstacle is given by H = 0.125m., and W = 0.1m. On the one hand, the bird-like step is shown in Fig. 3a. Fig. 3b, Fig. 3c and Fig. 3d illustrate the evolution of the joint variables their velocities and accelerations respectively. On the other hand, Fig. 4a represents the human-like step. This solution is similar to

the human way of walking; in this case, q1 and q2 evolve following a backward motion. The evolution of the joint variables, their velocities and accelerations are represented in Fig. 4b, Fig. 4c and Fig. 4d. This solution has been provided by the algorithm by constraining the joint variables according to q1 ∈ [-π/4 0] and q2 ∈ [-π/2 0], so that forward motions are not allowed. Table 1 shows the value of the fitness function considering, in the same scenario, different initial conditions, for the bird-like solution, the human-like solutions and the best initial phenotype. This table demonstrates that the algorithm minimizes the value of the fitness function and that the bird-like solutions represent the best option.

6   Conclusions

This paper, presents a new methodology for planning leg motions for a wheel–legged hexapod in order to step over obstacles. The technique is based on applying a random generation method RRT and an optimization procedure G.A. so that optimum solutions are obtained. Several simulations have been carried out also to identify the most convenient trajectories. The obtained results show that bird-like leg motion solutions are the most convenient path solutions for overcoming obstacles as based on the constraints of the Cassino Hexapod. Further works will consider the study of more general obstacles sizes and complex obstacle avoidance strategies, involving the motion of several legs.

References

1. Lavalle, S.M.: From dynamic programming to RRTs: Algorithmic design of feasible trajectories. In: Bicchi, A., Prattichizzo, D., Christensen, H.I. (eds.) Control Problems. STAR, vol. 4, pp. 19–37. Springer, Heidelberg (2002)
2. Carbone, G., Ceccarelli, M.: A Low-Cost Easy-Operation Hexapod Walking Machine. International Journal of Advanced Robotic Systems 5(2) (2008)
3. Gómez-Bravo, F., Carbone, G., Fortes, J.: Collision free trajectory planning for hybrid manipulators. Mechatronics 22(6), 836–851 (2012)
4. Carbone, G., Gómez-Bravo, F., Selvi, O.: An Experimental validation of collision free trajectories for parallel manipulators. Mechanics Based Design of Structures and Machines: An International Journal 40(4), 414–433 (2012)
5. Cigola, M., Pelliccio, A., Salotto, O., Carbone, G., Ottaviano, E., Ceccarelli, M.: Application of robots for inspection and restoration of historical sites. In: Proceeedings of 22nd International Symposium on Automation and Robotics in Construction ISARC 2005, Ferrara, paper 37 (2005)
6. Carbone, G., Ceccarelli, M.: A mechanical design of a low-cost easy-operation anthropomorphic wheeled leg for walking machines. The International Journal Robotica & Management 9(2), 3–8 (2004)
7. Houck, C.R., Joinez, J.A., Kay, M.G.: A Genetic Algorithms for Function Optimization: a Matlab Implementation, NCSU-IE Technical Reported (1995)
8. Lin, C.S., Chang, P.R., Luh, J.Y.S.: Formulation and Optimization of Cubic Polynomial Joint Trajectories for Industrial Robots. IEEE Trans. Automt. Contr. 28, 1066–1073 (1983)

Geometrical Synthesis Approach for Compliant Mechanisms – Design of Applications Exploiting Fibre Reinforced Material Characteristics

J. Ehlig[1], U. Hanke[1], E.-C. Lovasz[2], M. Zichner[1], and K.-H. Modler[1]

[1] TU Dresden, Germany
   `Jana.Ehlig@tu-dresden.de`
[2] Politechnica University of Timişoara, Romania
   `erwin.lovasz@mec.upt.ro`

Abstract. Compliant mechanisms have several advantages, especially smaller number of elements and therefore less movable joints. The flexural members furthermore allow an integration of special functions like balancing or locking. To take advantage of compliant elements in applications a robust synthesis tool is needed. Most of the common synthesis methods focus on energy storage or shape optimization. The purely geometrical approach presented in this paper concentrates on solving guidance tasks with maximum design freedom within the installation space. An easy to use step-by-step synthesis procedure is provided through which the user is able to design mechanisms with a compliant beam element. The necessary analysis of the compliant beam element can be done by numerical analysis as well as through experiments. The synthesis method is presented using an application for a cup holder mechanism made of fibre reinforced material.

Keywords: Compliant mechanisms, large deflections, synthesis.

1 Introduction

Typical applications of classical four or six bar linkages are hinges as shown in Fig. 1a. Most of these applications need additional elements (i.e. springs: C_0C) for balancing or locking, which gives rise to the structure complexity (Fig. 1b).

Comparing such a classical structure with a compliant mechanism structure (Fig. 1c) the benefit of using compliant elements is evident. In this special case the linkage can be reduced to a two part assembly, which also fulfills the motion task. The integrated compliant section allows the implementation of locking, so that additional springs are not required.

There are different practical ways to integrate a cantilevered compliant beam in a mechanism. Besides non-linear finite element analysis [1] or optimization methods [2] it is common to create a pseudo-rigid-body model [3, 4, 5] that unifies the compliant and rigid-body mechanism theories. These methods often concentrate on kinematic and stress constraints or energy storage to aim for optimal solutions. In
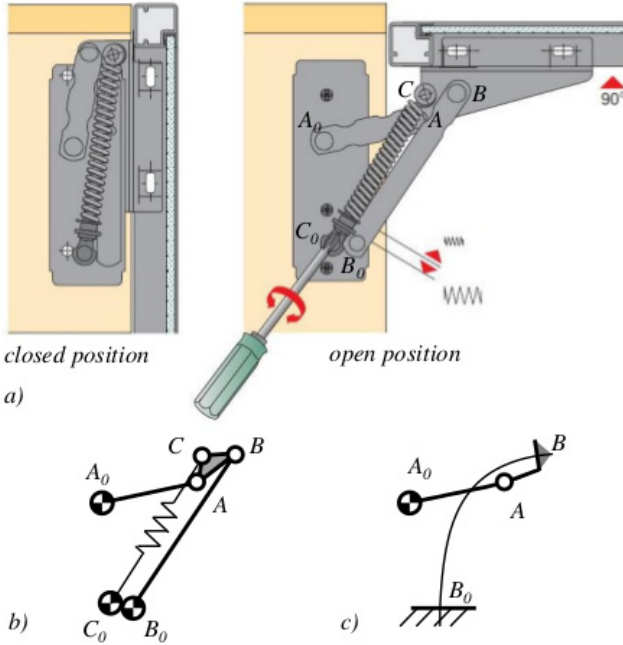
Fig. 1 Hinge mechanisms: a) Hinge mechanism b) classical four bar mechanism c) compliant mechanism

contrast to that, the scope of this paper is the development of a geometric based synthesis method, which allows a direct use in the design process providing maximum design freedom with regard to position and size of the mechanism.

2   Geometrical Synthesis of Compliant Mechanism Structures

2.1   Theoretical Background

The general structure consists of a RR-joint pair A_0A, which is directly coupled to the guidance link AB (s. Fig. 1c). The compliant beam section B_0B is integrated in the guidance link and acts like a spring element. For the synthesis model the large deflections of this beam section are only introduced by a force/moment load, defined through the RR-joint pair. Its implementation is problematic, due to the fact that the kinematic behavior of the beam is directly coupled to the force/moment action. The problem can be solved by coupling the force/moment action to the pole. After this, it is possible to implement the results through the analysis of a normalized beam into the given synthesis task. The pole is now the center for the classical synthesis of the RR-joint pair as well as for the compliant beam section.

2.2 Analysis of Compliant Beam Element

Before starting with the synthesis it is essential to describe the bending behavior of a cantilevered compliant beam under different load conditions as shown in Fig. 2. An initially undeflected beam loaded with a moment M_0 and a force F at the beam end is shown. The force F is acting at an angle φ. The deflection of the compliant beam depends on its material parameters (Young's modulus E, cross section and resulting moment of inertia I), its length L and the load conditions.
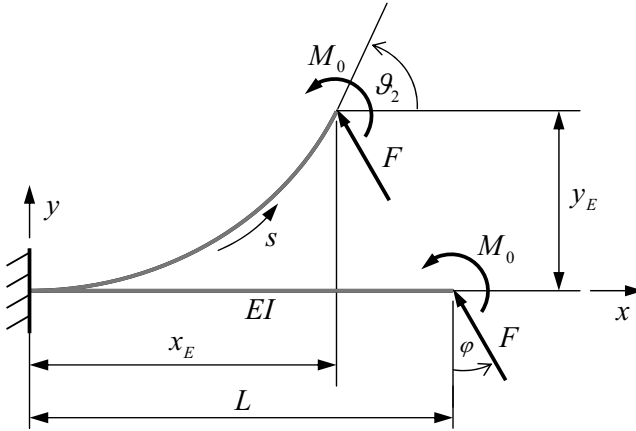
Fig. 2 Deflection of a cantilevered compliant beam under external load

The mathematical description of large-deflection behavior of cantilevered beams is subject to several scientific publications. The following statements and equations are based upon the considerations of HOWELL [5].

The Bernoulli-Euler equation is the vital element when dealing with large-deflection analysis. It says that the curvature κ can be written as

$$\kappa = \frac{d\vartheta}{ds} = \frac{d^2y/dx^2}{[1 + (dy/dx)^2]^{3/2}} = \frac{M}{EI}. \tag{1}$$

For a single moment end load ($F = 0$) the moment along the beam is constant and so is the curvature. For a single force end load ($M_0 = 0$) the internal moment can be written as $M = F \cos \varphi (x_E - x) + F \sin \varphi (y_E - y)$ and has to be substituted into Eq.(1). After performing a number of mathematical transformations and with $\kappa(s = L) = 0$ as well as $\vartheta(s = L) = \vartheta_2$ the equation results in

$$L = \sqrt{\frac{EI}{2F}} \int_{\vartheta_1=0}^{\vartheta_2} \frac{d\vartheta}{\sqrt{\cos \varphi (\sin \vartheta_2 - \sin \vartheta) - \sin \varphi (\cos \vartheta_2 - \cos \vartheta)}}. \tag{2}$$

A mixture of both moment and force load is equivalent to a single force load acting at a distance m (s. Fig. 4) to the beam end. In this case the boundary condition for the curvature at the beam end is $\kappa(s = L) = mF/(EI)$. The solution of the differential equation (2) can be found in different ways [5, 8] and leads to the location B_2 for the angle ϑ_2 of the beam end for the compliant beam element. So we have two positions $B_1(\vartheta_1)$ (undeflected beam) and $B_2(\vartheta_2)$ (deflected beam) which define the pole:

$$P_{12} = B_1 + \frac{B_2 - B_1}{2\sin(\vartheta_{12}/2)} i e^{-i\vartheta_{12}/2} \text{ with } \vartheta_{12} = \vartheta_2 - \vartheta_1. \tag{3}$$

For a pure moment load it can be shown that all poles P_{12} lie on a straight line through $(L/2, 0)$ perpendicular to the undeformed beam [6]. The starting point of all centrodes is the instantaneous center of rotation IC. The complexity of the centrodes depends on the beam load. For small deflections equation (3) can be used to describe IC. With $B_1 = L$, $B_2 = L + iFL^3/(3EI)$ and $\vartheta_{12} = FL^2/(2EI)$ [7] for $\vartheta_{12} \approx 0$ equation (3) can be simplified to

$$IC = L - \frac{FL^3}{3EI \cdot 2\vartheta_{12}/2}(1 - i\vartheta_{12}/2) = L/3 + i\frac{FL^3}{6EI}. \tag{4}$$

Therefore the instantaneous center of rotation for a beam with pure force load starts at $(L/3, 0)$. Fig. 3 shows exemplarily two centrodes $p_{F,\varphi}$ for different force angles φ. All poles as a consequence of mixtures of force and moment end load for $m \geq 0$ lie in between p_M and the corresponding $p_{F,\varphi}$.
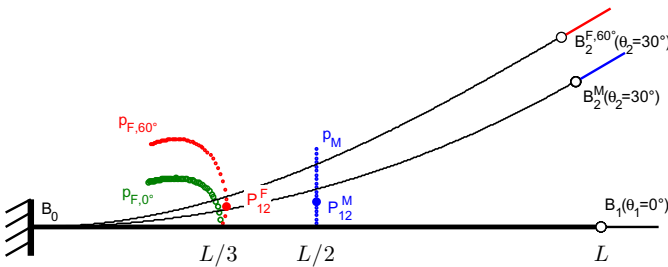
Fig. 3 Centrodes $p_{F,0°}, p_{F,60°}, p_M$ for different end load conditions

The beam element used in a mechanism structure like the one in Fig. 1c gets its moment load troughout a force pair. The direction and the point of acting of this pair results from the shortest distance m (s. Fig. 4) of the beam end and the force axis f. Therefore the moment can be expressed by $M_0 = mF$. This helps to find a generalized expression of (4) for the instantaneous center of rotation when $F \approx 0$

$$IC = \frac{1}{3}\frac{3m + L}{2m + L}L + i\,g(F) \text{ with } g(F) \approx 0. \tag{5}$$
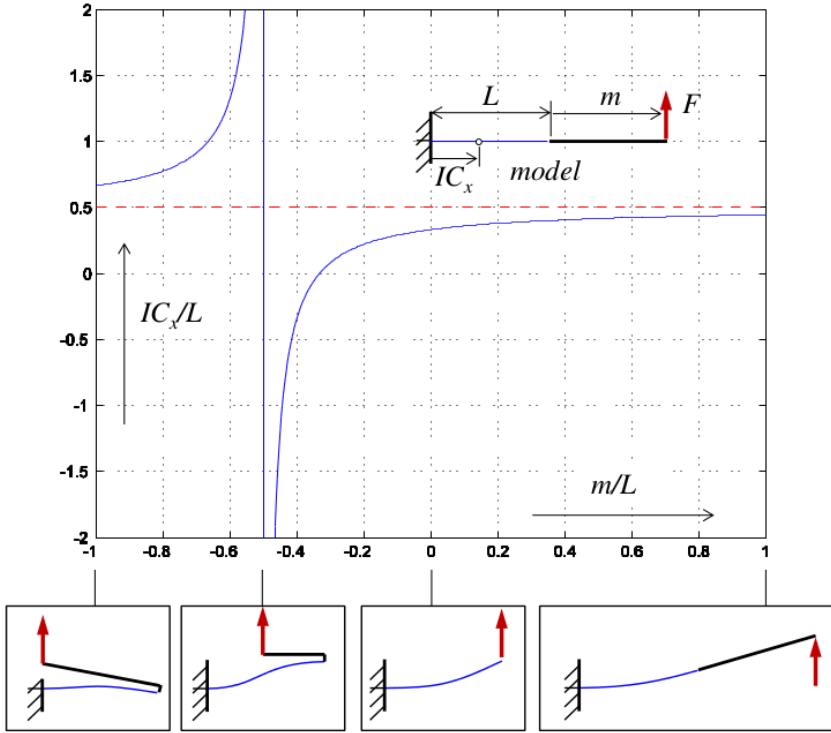
Fig. 4 Force pair distance m with respect to the horizontal pole location IC_x

A pure force load at the beam end is equal to $m = 0$, and a pure moment load introduced by a force pair is at $m = \infty$. The horizontal pole location IC_x normalized to the beam length L with respect to the normalized distance m leads to the diagram shown in Fig. 4. A technically interesting case occurs when $m = -0.5$. Here the motion of the beam end is equal to a pure translation. With $m < -0.5$ the direction of rotation is opposite to the case $m > 0.5$.

2.3 Synthesis

The synthesis belonging to the structure shown in Fig. 1c is based on a two pose task: Position 1 with an undeflected beam ($\vartheta_1 = 0$) and position 2 with a deflected beam as the compliant element. For a normalized beam with given deflection end angle ϑ_2 different possible end load sets can be found (Fig. 3). This set of moment and force load can be distinguished by its ratio $m = M_0/F$ and the force direction angle φ (s. Fig. 2). The following synthesis is based on these two important parameters.

The basic idea of the synthesis is to start with the classical RR-joint pair for the two pose task. With the location of $A_0 A_2$ for the deflected beam element, the force axis f is defined (Fig 5a). Usually there is an idea of the general orientation γ of the undeformed beam element. With γ and the axis f the force direction angle φ can be found. With the help of φ, the deflection of a normalized beam element (E, I, L) as shown in Fig. 5b can be calculated. Starting with a pure force load $(m' = 0)$ the deformation from B_1' to B_2' for $\vartheta_{12} = \vartheta_2 - \vartheta_1$ defines the pole P_{12}'. With P_{12}' the model beam can be used to find the dimensions of the compliant element of the mechanism. The whole procedure is based on the similarity between the model beam $B_0' B'$ and the beam element in the mechanism solution $B_0 B$. Therefore the dimensions are defined by scaling and rotating (similarity transformation) the model beam in reference to the pole:

$$B_k = P_{12} + (B_k' - P_{12}') \cdot \lambda \, i e^{i(\gamma - \varphi)}, \text{ with } k = 0, 1, 2. \tag{6}$$

The scaling factor λ in equation (6) can be obtained by the distance ratio $\lambda = a/a'$ (s. Fig. 5c). Introducing an additional moment at the beam end only affects the scaling of the compliant beam element. With the previously defined moment-force ratio m it is possible to apply the previously explained method. The ratio m is equal to the distance of the force pair, which defines the moment $M_0 = mF$. The scaling factor λ therefore changes to $a/(a' + m')$. It follows that $m \neq 0$ (Fig. 5d) leads to a scaling of the beam, whereby the beam length for $m \neq 0$ is always smaller than the beam length for $m = 0$ (pure force load at beam end).

The described method simplifies the implementation of compliant beam elements in a geometrical synthesis to the use of two parameters: force direction angle φ and moment-force ratio m. While the force direction angle φ defines the general beam location, changes in the moment-force ratio m lead to an altered beam dimension.

Besides the theoretical way of finding the pole it is also possible to do the synthesis with a real model beam. The pole can be found by measuring the model beam or a compliant element tool kit [9]. The result will be less exact, but will still give good preconditions for the design process.

With this background the synthesis of a RR-joint pair coupled to a compliant beam element leads to the general scheme with the following steps (Fig. 5):

1. Pose a_1 and a_2 define the pole P_{12}.
2. Placing the ground joint A_0 with respect to the boundary conditions.
3. The pole P_{12} and joint A_0 define the moving joint A in position A_2.
4. With A_0, A_2 the force axis f is defined and therefore distance a.
5. Defining the general beam position by angle γ.
6. The solution of the real beam position for a beam with pure force load at the beam end can be find by equation (6) with the scaling factor $\lambda = a/a'$ and the angles γ, φ.
7. The final beam position with force and moment load at beam end can be found iteratively by varying the moment-force ratio m. The usage of the diagram in Fig. 4 helps to reduce the iteration steps.
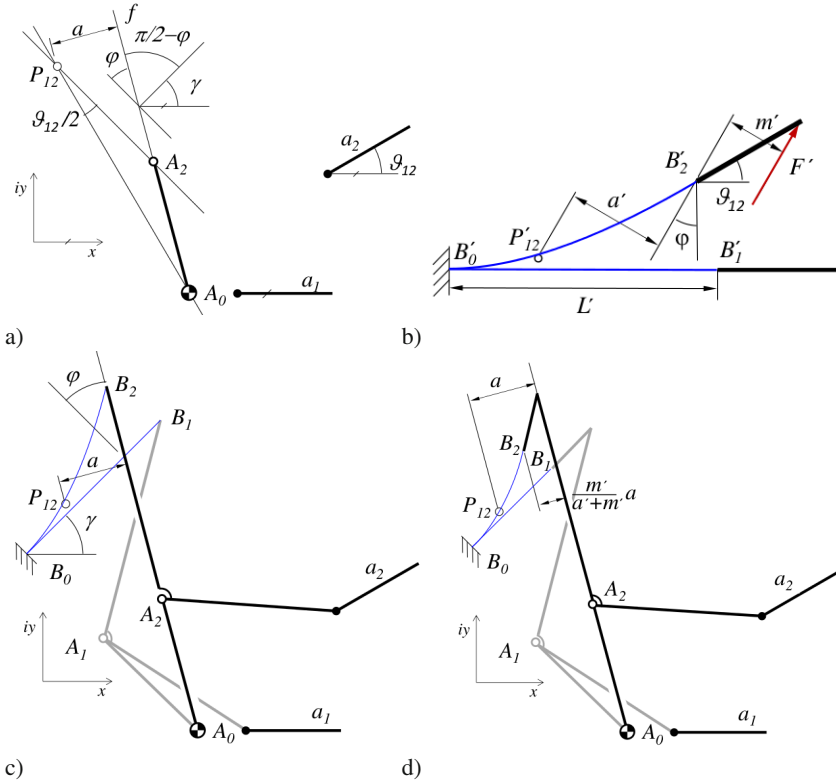
Fig. 5 Synthesis: a) task with RR-chain A_0A_2 b) normalized beam modell c) solution for pure force load at the beam end d) solution for mixed force and moment load at the beam end

3 Application

The described synthesis will be used to derive a cup holder mechanism as we can find in mobile vehicles [10]. The aim is the reduction of parts via integration of all locking functions within the compliance of the mechanism structure.

Table 1 Task and solution parameters

i	$a_i(x, y, \vartheta)$	$A_i(x, y)$	$B_i(x, y)$
0	-	100, 80	$-23.561,\ 0.000$
1	10, 0, 0°	10, -80	49.432, 0.000
2	20,10,90°	100, 10	20.000,49.432
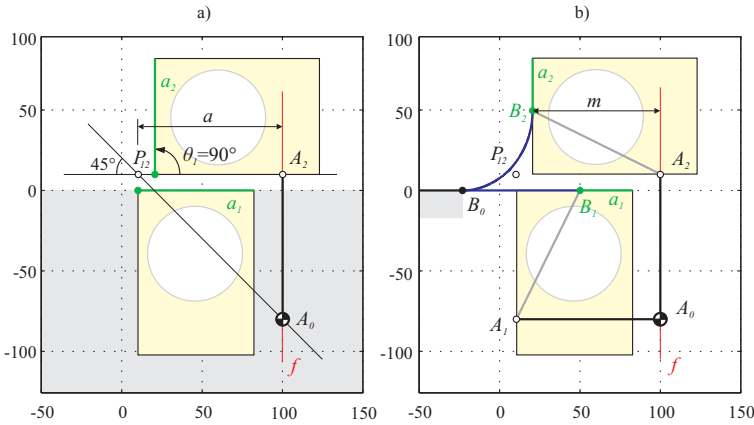
Fig. 6 Compliant cup holder mechanism: a) task b) solution

The synthesis task is a two pose task (s. Table 1 and Fig. 6a). In the initial position a_1 the cupholder should be hiding behind the front board. The second position a_2 offers a panel with a circular hole to place the cup. The two required positions define the beam position for the undeflected beam. When the holder is not in use the frontend should flush with the surface of the board. The ground joint A_0 position should be behind this board in the grey marked area and the moving joint A may be best placed on the cup holder. By applying the synthesis plan presented in the previous chapter on this particular problem we can find a solution as shown in Fig. 6b and Table 1. If the cup holder is closed the system is force free. The load introduced by the beam element in the open position is carried by link A_0A_2 in a stable position. The design of the cup holder mechanism by using fibre reinforced material is shown in Fig. 7.
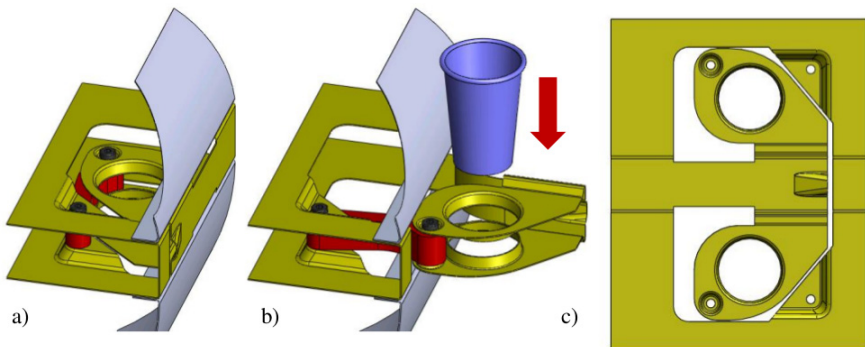
Fig. 7 CAD model of the compliant cup holder mechanism: a) closed postion b) open position c) unfolded textile preform of fibre reinforced material

4 Conclusions

Within the frame of research the deflection of a cantilevered model beam has been described theoretically to find the pole and instantaneous center of rotation subject to altering load conditions. Through these investigations it was possible to identify two parameters that allow the geometrical synthesis for mechanisms with a compliant beam element. Finally, it has been shown that with the help of a subsequently developed synthesis scheme the mechanism designer has a great influence on size and position of the compliant structure.

References

1. Albanesi, A.E., Pucheta, M.A., Fachinotti, V.D.: A new method to design compliant mechanisms based on the inverse beam finite element model. Mechanism and Machine Theory 65, 14–28 (2013)
2. Otomori, M., Yamada, T., Izui, K., Nishiwaki, S.: Level set-based topology optimisation of a compliant mechanism design using mathematical programming. Mechanism Science 2, 91–98 (2011)
3. Su, H.-J.: A Pseudo Rigid Body 3R Model for Determining Large Deflection of Cantilever Beams Subject to Tip Loads. ASME Journal of Mechanism and Robotics 1(2), 021008-1–021008-9 (2009)
4. Dado, M.H.: Variable parametric pseudo-rigid-body model for large deflection beams with end loads. International Journal of Non-Linear Mechanics 36(7), 1123–1133 (2001)
5. Howell, L.: Compliant Mechanisms. Wiley-Interscience (2001)
6. Modler, N., et al.: Optimization of a Test Bench for Testing Compliant Elements Under Shear-Force-Free Bending Load. Procedia Materials Science 2, 130–136 (2013)
7. Beitz, W., Küttner, K.-H.: Dubbel - Taschenbuch für den Maschinenbau, vol. 18. Springer, Heidelberg (1995)
8. Venanzi, S., Giesen, P., Parenti-Castelli, V.: A novel technique for position analysis of planar compliant mechanisms. Mechanism and Machine Theory 40, 1224–1239 (2005)
9. Limaey, P., Ramu, G., Pamulapati, S., Ananthasuresh, G.K.: A compliant mechanism kit with flexible beamsand connectors along with analysis and optimal synthesis procedures. Mechanism and Machine Theory 49, 21–39 (2012)
10. Barej, M., Hüsing, M., Corves, B.: Teaching Mecanism Theory - From Hands-on Analysis to Virtual Modeling. Mechanism and Machine Science 7, 703–710 (2001)

Derivation of Input/Output Relationships for the Bennett 6R Linkages Based on the Method of Decomposition

R.I. Alizade, G. Kiper, M.İ.C. Dede, and E. Uzunoğlu

İzmir Institute of Technology, Turkey
`alizada_rasim@hotmail.com,`
`{gokhankiper,candede}@iyte.edu.tr,`
`elmoremre@gmail.com`

Abstract. The Bennett overconstrained 6R linkages are the double-planar, the double-spherical and the plano-spherical 6R linkages. These mechanisms are obtained by combining simple planar and/or spherical mechanisms and then removing one of the common links. This paper presents the derivation of the input/output relationships for these mechanisms using the decomposition method. This method is based on writing the input/output equations for the two imaginary loops comprising the 6R mechanism and then eliminating the imaginary joint variable. It is found that the resulting input/output equations contain up to 4th power of trigonometric terms, such as $\cos^4\theta$.

Keywords: Bennett 6R linkages, passive joints, input/output relationship, method of decomposition.

1   Introduction

The first reported overconstrained mechanism is due to Sarrus in 1853 [1]. The Sarrus linkage is a spatial 6R linkage obtained by assembling two planar dyads in perpendicular planes and it can be interpreted as two slider crank mechanisms with a common slider, axis of which is along the intersection of the perpendicular planes. The angle between the intersecting planes is arbitrary and the two triplets of parallel joint axes may be positioned arbitrarily and the linkage will be still mobile. We will call such a generalized Sarrus linkage as the double-planar 6R linkage (Fig. 1a). As far as the authors know, such a form of the general Sarrus linkage as shown in Fig. 1a is presented nowhere else. The relative motion between the links with nonparallel joint axes is linear translation and hence a prismatic joint can be inserted between the two. Such a joint is called a passive joint [2].

In 1905 Bennett worked on the Sarrus linkage and proposed two new families of overconstrained linkages known as the double-spherical and the plano-spherical 6R linkages [3]. The double-spherical linkage is obtained by merging two
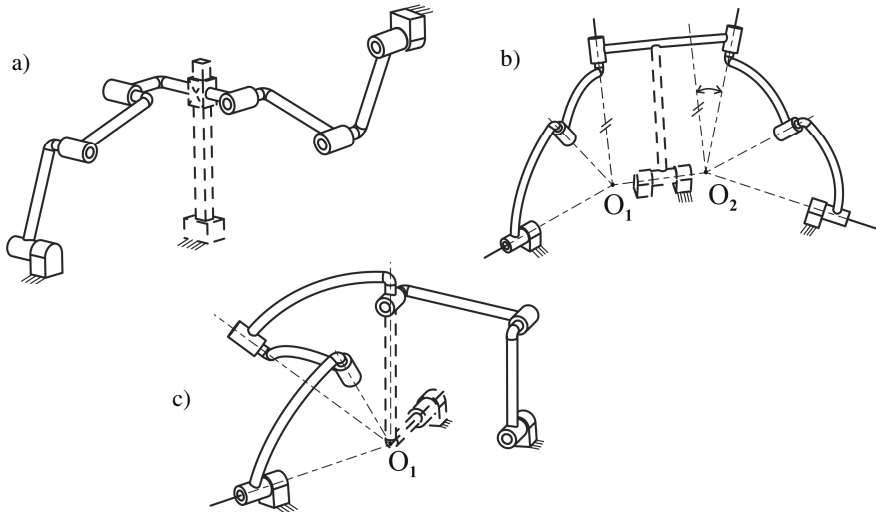
Fig. 1 a) Double-planar (generalized Sarrus) linkage, (b) double-spherical linkage, and (c) plano-spherical linkage together with their passive joints (adapted from [4])

spherical four-bar mechanisms with two common links (Fig. 1b) and the plano-spherical linkage is obtained by merging a planar four-bar mechanism and a spherical four-bar mechanism with two common links (Fig. 1c). Both of these linkages have a passive revolute joint. For the double-spherical linkage, the passive joint axis is through the line connecting the sphere centers O_1 and O_2. For the plano-spherical linkage the passive joint axis is normal to the plane and passes through the sphere intersecting the plane. The plano-spherical linkage and the double-planar linkage can be obtained from the double-spherical linkage by sending one or both of the sphere centers to infinity [4]. The Bennett 6R linkages are examples of linkages obtained from intersections of Euclidean subspaces [2].

A special case of the double-spherical 6R linkage is the well known double-Hooke's-joint linkage for which the twist angles are 90°, 90°, 0°, 90°, 90° and arbitrary angle between the fixed joints. Baker [5] derived the input/output (I/O) relationship for the double-spherical 6R linkage starting from the double-Hooke's-joint linkage. In this paper we present an alternative formulation based on the method of decomposition [6].

The method of decomposition originates from a simple idea: since the above-mentioned mechanisms are obtained as merging two simple loop mechanisms and then removing the passive joint, the original single loop may be decomposed into two imaginary loops. By taking the input and output joints as the fixed joints, the I/O equations for each imaginary loop are obtained. The passive joint is output for the first loop and input for the second loop. Eliminating the passive joint variable from the two I/O equations, the I/O equation for the 6R mechanism is obtained. Also, these linkages prove useful in function synthesis when the method of decomposition is applied. The synthesis methods are left for future studies.

2   The Double-Planar 6R Linkage

Together with the passive prismatic joint, the double-planar 6R linkage may be considered to be composed of a pair of slider-crank mechanisms. The sliding direction in both slider-cranks is common and intuitively it can be verified that the angle between the planes of motion of the two planar mechanisms does not affect the I/O relationship. The planes of motion have to be nonparallel, but, there is no harm in considering the two slider-crank mechanisms in the same plane as long as the prismatic joint is included. Let ϕ be the input ange, θ be the output angle and s be the passive joint variable of the double-planar 6R mechanism shown in Fig. 2.
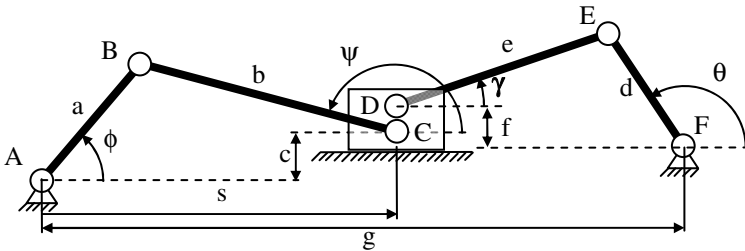
Fig. 2 Double-planar 6R linkage

Loop closure equation for loop ABC:

$$\overrightarrow{AB}=\overrightarrow{AC}+\overrightarrow{CB} \quad \Rightarrow \quad \begin{array}{l} a\cos\phi=s+b\cos\psi \\ a\sin\phi=c+b\sin\psi \end{array} \tag{1}$$

Eliminating ψ from Eq. (1):

$$b^2=\left(a\cos\phi-s\right)^2+\left(a\sin\phi-c\right)^2 \Rightarrow s^2=2a\cos\phi s-a^2+b^2-c^2+2ac\sin\phi \tag{2}$$

Loop closure equation for loop DEF:

$$\overrightarrow{DE}=\overrightarrow{DF}+\overrightarrow{FE} \quad \Rightarrow \quad \begin{array}{l} e\cos\gamma=g-s+d\cos\theta \\ e\sin\gamma=-f+d\sin\theta \end{array} \tag{3}$$

Eliminating γ from Eq. (3):

$$e^2=\left(g-s+d\cos\theta\right)^2+\left(-f+d\sin\theta\right)^2$$
$$\Rightarrow s^2=2\left(g+d\cos\theta\right)s-d^2+e^2-f^2-g^2-2dg\cos\theta+2df\sin\theta \tag{4}$$

Equating the right hand sides of Eqs. (2, 4):

$$s=\frac{a^2-b^2+c^2-d^2+e^2-f^2-g^2-2ac\sin\phi-2dg\cos\theta+2df\sin\theta}{2\left(a\cos\phi-d\cos\theta-g\right)} \tag{5}$$

Substituting s from Eq. (5) into Eq. (2):

$$
(A-2ac\sin\phi-2dg\cos\theta+2df\sin\theta)^2+4(B-2ac\sin\phi)(a\cos\phi-d\cos\theta-g)^2
$$
$$
-4a\cos\phi(A-2ac\sin\phi-2dg\cos\theta+2df\sin\theta)(a\cos\phi-d\cos\theta-g)=0 \tag{6}
$$

where $A=a^2-b^2+c^2-d^2+e^2-f^2-g^2$ and $B=a^2-b^2+c^2$. Eq. (6) is the implicit I/O relation of the double-planar 6R linkage, which contains up to 3rd power of trigonometric terms, such as $\cos^3\theta$.

3 The Double-Spherical 6R Linkage

Let ϕ, ψ and θ be the respective input, passive joint and output angle of the double-spherical 6R mechanism shown in Fig. 3. O_1D and O_2E are skew with a twist angle of γ. The radii of the spheres do not affect the I/O relationship, so without loss of generality assume both radii as 1. Also notice that the distance $|O_1O_2|$ has no effect on the I/O relationships.
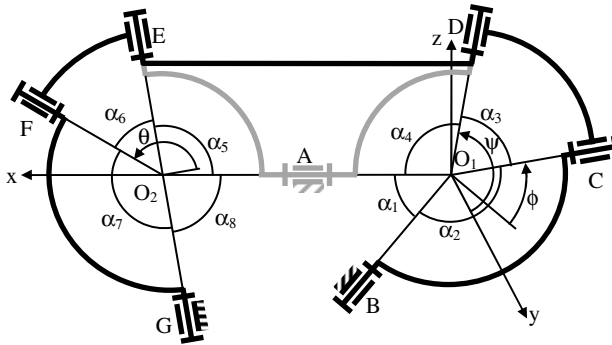
Fig. 3 Double-spherical 6R linkage

Coordinates of B, C, D can be found as follows:

$$
\begin{bmatrix} B_x \\ B_y \\ B_z \end{bmatrix} = Z[\alpha_1]\begin{bmatrix} 1 \\ 0 \\ 0 \end{bmatrix} = \begin{bmatrix} c_1 \\ s_1 \\ 0 \end{bmatrix} \quad , \quad \begin{bmatrix} D_x \\ D_y \\ D_z \end{bmatrix} = X[\psi]Z[\alpha_4]\begin{bmatrix} 1 \\ 0 \\ 0 \end{bmatrix} = \begin{bmatrix} c_4 \\ s_4\,c\psi \\ s_4\,s\psi \end{bmatrix} \quad ,
$$
$$
\begin{bmatrix} C_x \\ C_y \\ C_z \end{bmatrix} = Z[\alpha_1]X[\phi]Z[\alpha_2]\begin{bmatrix} 1 \\ 0 \\ 0 \end{bmatrix} = \begin{bmatrix} c_1\,c_2-s_1\,s_2\,c\phi \\ s_1\,c_2+c_1\,s_2\,c\phi \\ s_2\,s\phi \end{bmatrix} \tag{7}
$$

where X[.] and Z[.] represent rotation matrices about x and z axes, respectively and $c_i = \cos\alpha_i$, $s_i = \sin\alpha_i$ for i = 1, 2, 3, 4 and other c and s are short for cosine and sine, respectively. The angle between O_1C and O_1D is α_3, so

$$\overrightarrow{O_1C}\cdot\overrightarrow{O_1D}=c_3 \Rightarrow c_1 c_2 c_4 -c_3 -s_1 s_2 c_4 c\phi+s_1 c_2 s_4 c\psi+c_1 s_2 s_4 c\phi c\psi+s_2 s_4 s\phi s\psi=0 \quad (8)$$

Eq. (8) gives the I/O equation for the first loop. For the second loop the coordinates of E, F and G with respect to O_2 can be calculated as follows:

$$\begin{bmatrix} E_x \\ E_y \\ E_z \end{bmatrix}=X[\psi+\gamma]Z[\pi-\alpha_5]\begin{bmatrix} 1 \\ 0 \\ 0 \end{bmatrix}=\begin{bmatrix} -c_5 \\ s_5 c\gamma c\psi-s_5 s\gamma s\psi \\ s_5 c\gamma s\psi+s_5 s\gamma c\psi \end{bmatrix} \quad ,$$

$$\begin{bmatrix} F_x \\ F_y \\ F_z \end{bmatrix}=Z[\pi-\alpha_8]X[\theta]Z[\alpha_7]\begin{bmatrix} 1 \\ 0 \\ 0 \end{bmatrix}=\begin{bmatrix} -c_7 c_8 -s_7 s_8 c\theta \\ c_7 s_8 -s_7 c_8 c\theta \\ s_7 s\theta \end{bmatrix} \quad , \quad \begin{bmatrix} G_x \\ G_y \\ G_z \end{bmatrix}=Z[\pi-\alpha_8]\begin{bmatrix} 1 \\ 0 \\ 0 \end{bmatrix}=\begin{bmatrix} -c_8 \\ s_8 \\ 0 \end{bmatrix} \quad (9)$$

The angle between O_2E and O_2F is α_6, so

$$\overrightarrow{O_2E}\cdot\overrightarrow{O_2F}=c_6 \Rightarrow c_5 c_7 c_8 -c_6 +c_5 s_7 s_8 c\theta+s_5 c_7 s_8 c\gamma c\psi-s_5 c_7 s_8 s\gamma s\psi$$
$$-s_5 s_7 c_8 c\gamma c\theta c\psi+s_5 s_7 c_8 s\gamma c\theta s\psi+s_5 s_7 c\gamma s\theta s\psi+s_5 s_7 s\gamma s\theta c\psi=0 \quad (10)$$

ψ is to be eliminated from Eq. (8) and Eq. (10). Notice that Eq. (8) and Eq. (10) are linear in terms of $c\psi$ and $s\psi$. Writing these equations in matrix form:

$$\begin{bmatrix} P_1 & Q_1 \\ P_2 & Q_2 \end{bmatrix}\begin{bmatrix} c\psi \\ s\psi \end{bmatrix}=\begin{bmatrix} R_1 \\ R_2 \end{bmatrix} \quad (11)$$

where the coefficients are functions of link parameters α_i, γ, input angle ϕ and output angle θ only: $P_1=s_1 c_2+c_1 s_2 c\phi$, $Q_1=s_2 s\phi$, $R_1=(-c_1 c_2 c_4+c_3+s_1 s_2 c_4 c\phi)/s_4$, $P_2=c_7 s_8 c\gamma-s_7 c_8 c\gamma c\theta+s_7 s\gamma s\theta$, $Q_1=-c_7 s_8 s\gamma+s_7 c_8 s\gamma c\theta+s_7 c\gamma s\theta$ and $R_2=(-c_5 c_7 c_8+c_6-c_5 s_7 s_8 c\theta)/s_5$. The linear set Eq. (11) can be solved using Cramer's rule and put into $s^2\psi + c^2\psi = 1$ to get

$$c\psi=\frac{\begin{vmatrix} R_1 & Q_1 \\ R_2 & Q_2 \end{vmatrix}}{\begin{vmatrix} P_1 & Q_1 \\ P_2 & Q_2 \end{vmatrix}}, \quad s\psi=\frac{\begin{vmatrix} P_1 & R_1 \\ P_2 & R_2 \end{vmatrix}}{\begin{vmatrix} P_1 & Q_1 \\ P_2 & Q_2 \end{vmatrix}} \Rightarrow (R_1Q_2-R_2Q_1)^2+(P_1R_2-P_2R_1)^2=(P_1Q_2-P_2Q_1)^2 \quad (12)$$

Eq. (12) is the implicit I/O relation of the double-spherical 6R linkage and it contains up to 4th power of trigonometric terms, such as $\cos^4\theta$.

4   The Plano-spherical 6R Linkage

Fig. 4 illustrates a plano-spherical 6R linkage. ϕ is the input and ψ is the output, or vice versa. The I/O relationship for the spherical loop is the same as for the double-spherical 6R linkage and is given by Eq. (8). The planar loop moves parallel to the yz-plane, so the x coordinates are irrelevant. The y, z coordinates for the joints E and F of the planar four-bar loop are found as

$$\begin{bmatrix} E_y \\ E_z \end{bmatrix} = X[\psi+\gamma]\begin{bmatrix} a_5 \\ 0 \end{bmatrix} = \begin{bmatrix} a_5 c(\psi+\gamma) \\ a_5 s(\psi+\gamma) \end{bmatrix} \quad , \quad \begin{bmatrix} F_y \\ F_z \end{bmatrix} = \begin{bmatrix} 0 \\ a_8 \end{bmatrix} + X[\theta]\begin{bmatrix} a_7 \\ 0 \end{bmatrix} = \begin{bmatrix} a_7 c\theta \\ a_8 + a_7 s\theta \end{bmatrix} \quad (13)$$

The distance between E and F is a_6, so

$$\left(E_y - F_y\right)^2 + \left(E_z - F_z\right)^2 = \left[a_5 c(\psi+\gamma) - a_7 c\theta\right]^2 + \left[a_5 s(\psi+\gamma) - a_8 - a_7 s\theta\right]^2 = a_6^2$$

$$\Rightarrow a_5^2 - a_6^2 + a_7^2 + a_8^2 - 2a_7 a_8 s\theta - 2a_5 a_7 c(\psi+\gamma-\theta) - 2a_5 a_8 s(\psi+\gamma) = 0 \quad (14)$$

$$\Rightarrow 2a_5\left[a_7 c(\theta-\gamma) + a_8 s\gamma\right]c\psi + 2a_5\left[a_7 s(\theta-\gamma) + a_8 c\gamma\right]s\psi = a_5^2 - a_6^2 + a_7^2 + a_8^2 - 2a_7 a_8 s\theta$$

Eqs. (8) and (14) constitute a linear set of equations in terms of $c\psi$ and $s\psi$ as in Eq. (11), but this time $P_2 = 2a_5\left[a_7 c(\theta-\gamma) + a_8 s\gamma\right]$, $Q_2 = 2a_5\left[a_7 s(\theta-\gamma) + a_8 c\gamma\right]$, and $R_2 = a_5^2 - a_6^2 + a_7^2 + a_8^2 - 2a_7 a_8 s\theta$. $c\psi$ and $s\psi$ are linearly solved and ψ is eliminated as in Section 3 to obtain the I/O relation of the plano-spherical 6R linkage and once again it contains up to 4th power of trigonometric terms in terms of θ and ψ, such as $\cos^4\theta$.
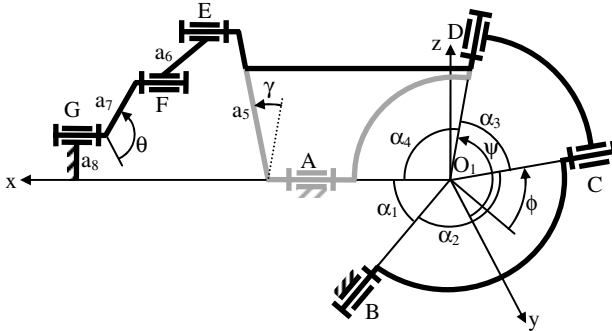
Fig. 4 Plano-spherical 6R linkage

5   Conclusions and Discussions

The Bennett 6R mechanisms are special overconstrained 6R mechanisms in that they can be dissected into planar slider crank or planar four bar or spherical four bar loops once the imaginary joint is inserted in between the loops. This allows us

to formulate the I/O equations for the loops separately and then eliminate the passive joint variable to obtain the I/O relation for the 6R mechanism without conducting spatial kinematics calculations. The method of decomposition is applied to Bennett 6R mechanisms for the first time. This method is not only useful in analysis, but also it has numerous advantages in synthesis. Synthesis methods based on the formulations in this paper will be the scope of further studies.

References

1. Sarrus, P.T.: Note sur la transformation des mouvements rectilignes alternatifs, en mouvements circulaires, et reciproquement. Academie des Sciences 36, 1036–1038 (1853)
2. Selvi, Ö.: Structural and kinematic synthesis of overconstrained mechanisms. PhD Thesis in Mechanical Engineering, İzmir Institute of Technology (2012)
3. Bennett, G.T.: The parallel motion of Sarrus and some allied mechanisms. Philosophy Magazine, 6th Series 9, 803–810 (1905)
4. Chen, Y., You, Z.: Spatial overconstrained linkages—the lost jade. In: Koetsier, T., Ceccarelli, M. (eds.) Explorations in the History of Machines and Mechanisms. HMMS, vol. 15, pp. 535–550. Springer, Heidelberg (2012)
5. Baker, J.E.: Displacement-closure equations of the unspecialized double Hooke's-joint linkage. Mech. Mach. Theory 37, 1127–1144 (2002)
6. Alizade, R.I., Aydazade, K.P., Novruzbekov, I.G.: Analysis and synthesis of planar mechanisms by using decomposition method. J. Mechanics of Machines, The Academy of Sciences of the USSR 57, 26–32 (1980)

Non-smooth Behaviour of a Linkage Mechanism with Revolute Clearance Joints

A. Krinner and T. Thümmel

Institute of Applied Mechanics, Chair: Prof. Daniel J. Rixen,
Technische Universität München, Germany
{andreas.krinner,thuemmel}@tum.de

Abstract. Mechanisms including friction and multiple clearance contacts usually could be modelled by continuous or discontinuous force laws. In this contribution the non-smooth behaviour of a planar 6-bar linkage mechanism with revolute clearance joints is simulated by the methods of unilateral contacts. Within a non-commercial simulation framework flow separation as well as high frequency tangential pendulum motion in the clearance joints can be detected and a spring as a device of reaction force balancing is analysed.

Keywords: multibody dynamics, unilateral contacts, clearance joints, linkages.

1   Introduction

High-speed mechanisms have a broad spectrum of application in processing machinery like textile, packing, forging, pressing, cutting or printing. The dynamic response and quality characteristic of high- or slow-speed mechanisms could be limited by nonlinear, so-called secondary mechanical problems. Especially, unilateral contact mechanics within revolute joints involves additional physical phenomena, like e.g. clearance-impact-noise phenomenon, stick-slip vibrations, multiple impact interaction in different contacts, dissipation or wear. Here, HAINES [2] gives an overview, while DRESIG/ HOLZWEISSIG [1] summarize the primare and global dynamics of rigid body mechanisms.

Early experimental and numerical investigation of a planar four-bar mechanism with multiple clearance joints was done by HORIE et al. [3]. In a more recent work FLORES [4] gives a parametric study of a planar slider crank mechanism with multiple clearance joints. SCHWAB et al. [7] compare different revolute clearance joints models for a planar rigid as well as elastic slider-crank mechanism.

At our institute an experimental setup of a crank-and-rocker mechanism has been used to investigate various phenomena of high-speed mechanism dynamics including friction-clearance contacts amongst others, see THÜMMEL [8] − [11]. In [10] motion trajectories of the bolt in a clearance revolute joint have been measured and

simulated, based on friction and impact modelling by corner laws and LCP's according to PFEIFFER and GLOCKER [6]. With the same approach, a planar slider-crank mechanism with five unilateral contacts was simulated [9].

By the present paper the authors apply the method of non-smooth mechanics including unilateral contacts to a planar six-bar mechanism with multiple friction clearance joints. Thus, secondary oscillation phenomena can be detected at an early stage of development of the kinematic and kinetic synthesis of the mechanism, which shall be used as a driving unit in a cutting press. Hence, theoretical preliminary studies for the development of the driving unit are presented, without having an experimental set-up of the mechanism yet. In section 2 an overview of joint modelling and the applied numerical framework is given. Section 3 delivers the model description of the investigated mechanism and the simulation results in section 4 show the good practicability of the method in analysing the secondary oscillating problems flow separation and pendulum motion.

2   Joint Model and Simulation Environment

2.1   Modelling of Revolute Clearance Joints with Dry Contact

In a broad sense, clearance joints with dry contact can be modelled by a continous or a discontinous approach, see [5].

Within the continous approach a regularized formulation of the force law, comparable to a spring-damper element, is applied to the equation of motion, when a contact occures, see Fig. 1(a). The continous force law can therefore be linear, such as the KELVIN-VOIGT model, or nonlinear, such as the HERTZ law, and captures elasticity effects as it allows small penetrations of the colliding bodies.

The second approach solves the discontinouity in the velocities of the mechanical elements caused by an impact. The time of an impact is assumed to be instantaneous and the momentum equations are solved for each closing contact. The method uses an unilateral formulation of the force law, which prevents penetration of the colliding bodies, see [6]. Within this paper, the 2-dimensional unilateral contact within the revolute joint is parameterized in normal direction by the gap g_N and the contact force value λ. The different normal vectors at the bolt and at the hole generate the pair of reaction forces in the revolute joint, see Fig. 1(b).
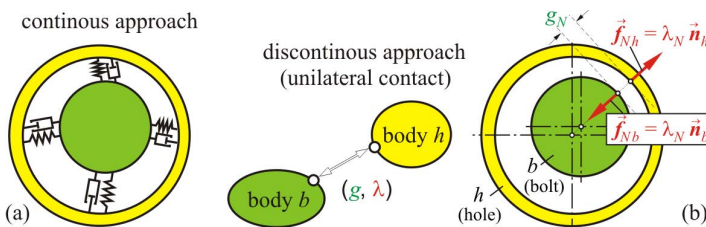
Fig. 1 Continous and discontinous approach for planar revolute joints modelling

2.2   Simulation Environment

In this paper the clearance is modelled by the discontinous approach with unilateral constraints. The simulation environment MBSIM (freely available at http://code.goo gle.com/p/mbsim-env/), which was developed at the Institute of Applied Mechanics, is used. It is based on a framework for the efficent simulation of multibody systems with unilateral contacts. The framework comprises the description of the system dynamics as well as numerical methods as provided in [13]. A brief overview follows.

Equation of motion and impact equation: The non-smooth dynamics of a system with bi- and unilateral contacts is described by the measure differential equation

$$\mathbf{M}d\mathbf{u} = \mathbf{h}dt + \mathbf{W}d\Lambda \tag{1}$$

$\mathbf{M} = \mathbf{M}(\mathbf{q})$ denotes the symmetric mass matrix, which depends on the vector of generalized coordinates $\mathbf{q}$, $d\mathbf{u}$ denotes the acceleration measure and the vector $\mathbf{h} = \mathbf{h}(\mathbf{u},\mathbf{q},t)$ contains all smooth external, internal and gyroscopic forces. The reaction measure in the contacts $\mathbf{W}d\Lambda$ is the product of the generalized force directions $\mathbf{W} = \mathbf{W}(\mathbf{q})$ and the magnitudes $d\Lambda$.

Assuming that impacts occure at times $t_i \in M_S$ integration of Eq. (1) yields the classical equations of motion at times $t \notin M_S$

$$\dot{\mathbf{q}} = \mathbf{u}, \quad \mathbf{M}\dot{\mathbf{u}} = \mathbf{h} + \mathbf{W}\lambda \qquad \forall\, t \notin M_S \tag{2}$$

as well as the impact equations at the discontinuities t_i

$$\mathbf{q}_i^+ = \mathbf{q}_i^-, \quad \mathbf{M}_i(\mathbf{u}_i^+ - \mathbf{u}_i^-) = \mathbf{W}_i\Lambda_i \qquad \forall\, t_i \in M_S \tag{3}$$

both with so far unknown contact reactions λ and Λ_i, respectively. Thus, additional contact laws have to be constituted. Contacts between bodies in the system are modelled as discrete point contacts with totally rigid contact zone. Hence, a contact corresponds to a constraint. Two types of contacts with different contact laws are considered: persisting contacts which are always closed; and contacts that may be open or closed.

The contact reactions

$$\mathbf{W}d\Lambda = \begin{pmatrix} \mathbf{W}_N\ \mathbf{W}_T \end{pmatrix} \begin{pmatrix} d\Lambda_N \\ d\Lambda_T \end{pmatrix} = \begin{pmatrix} \mathbf{W}_B\ \mathbf{W}_U\ \mathbf{W}_T \end{pmatrix} \begin{pmatrix} d\Lambda_B \\ d\Lambda_U \\ d\Lambda_T \end{pmatrix} \tag{4}$$

are decomposed into components normal (index N) – split up in bilateral (B) and unilateral (U) – and tangential (T) to the contact plane.

Force laws for smooth transitions: For the smooth transition between impacts ($t \notin M_S$) a bilateral contact on position level can be expressed in the form

$$g_B = 0, \qquad \lambda_B \in \mathbb{R} \tag{5}$$

where g_B is the normal distance of the interacting bodies in the contact point. A unilateral contact also allows detachment leading to in-activity of kinematic restriction

$$g_U \geq 0, \qquad \lambda_U \geq 0, \qquad g_U \lambda_U = 0 \tag{6}$$

The respective force laws are shown in Figs. 2(a) and 2(b).

For both bi- and unilateral constraints, dry friction is considered. Using the force component $\lambda_N \in \{\lambda_B, \lambda_U\}$ normal to the contact plane and the relative tangential velocity $\dot{g}_T$, COULOMB's friction law is given by

$$\text{if} \quad \dot{g}_T = 0 \quad \Rightarrow \quad |\lambda_T| \leq \mu_0 |\lambda_N| \tag{7}$$

$$\text{if} \quad \dot{g}_T \neq 0 \quad \Rightarrow \quad |\lambda_T| = -\frac{\dot{g}_T}{|\dot{g}_T|} \mu |\lambda_N| \tag{8}$$

Fig. 2(c) shows the force law of a tangential frictional contact for the planar case.

(a) Bilateral constraint   (b) Unilateral constraint   (c) COULOMB friction
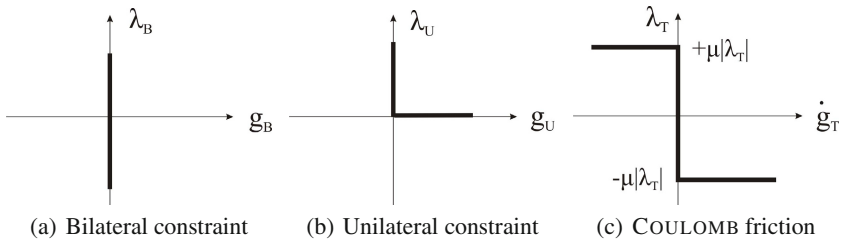
Fig. 2 Force laws for bi- and unilateral contacts and friction

Impact laws: In contrast to persisting and detaching contacts, a closing contact leads to a discontinuity in the vector **u** of generalized velocities. Hereby, the exchange of discrete impacts Λ_i affects all closed bilateral and unilateral contacts.

The impact law for a bilateral contact is given by

$$\dot{g}_B^+ = 0, \qquad \Lambda_B \in \mathbb{R} \tag{9}$$

and ensures that relation of Eq. (5) is not violated after collisions. For the post-impact velocity for a unilateral contact the NEWTON's impact law holds

$$\dot{\bar{g}}_U \geq 0, \qquad \Lambda_U \geq 0, \qquad \dot{\bar{g}}_U^+ \Lambda_U = 0 \tag{10}$$

which allows to choose between elastic ($\varepsilon = 1$) and plastic ($\varepsilon = 0$) impact behaviour by defining the kinematic coefficient of restitution ε in $\dot{\bar{g}}_U = \varepsilon \dot{g}_U^- + \dot{g}_U^+$.

In tangential direction, COULOMB friction law is formulated on impulse level:

$$\text{if} \quad \dot{g}_T = 0 \quad \Rightarrow \quad |\Lambda_T| \leq \mu_0 |\Lambda_N| \tag{11}$$

$$\text{if} \quad \dot{g}_T \neq 0 \quad \Rightarrow \quad |\Lambda_T| = -\frac{\dot{g}_T}{|\dot{g}_T|} \mu |\Lambda_N| \tag{12}$$

3   Model of the Application Object with Imperfect Joints

Fig. 3 shows the model of the planar linkage mechanism with the crank (2), the coupler (3), the rocker (4), the piston rod (5) and the ram (6). Besides, the stroke and the velocity of the ram are plotted. The joints C and E are modelled as imperfect joints with dry contact in the discontinuous manner as described in subsections 2.1 and 2.2. These two joints are analysed because they pass through more complex trajectories than the other joints during one rotation.

The integration is performed using a half-explicit time-stepping integrator with constant step size, which is adapted individually to every simulation. In Table 1 the parameters for the dynamic simulations are listed.
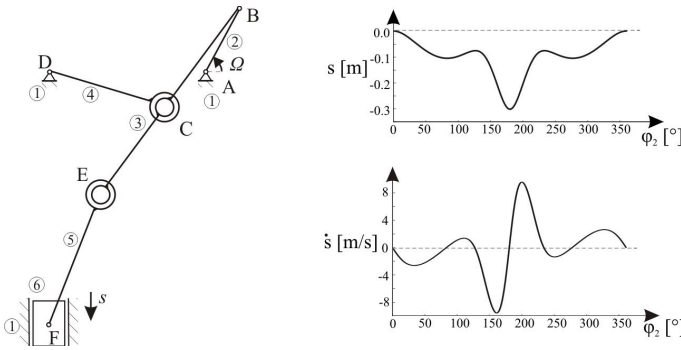
Fig. 3 Planar model and kinematics of application object

Table 1 Parameters used in the dynamic simulations

	flow sep.	pend. motion
nominal bearing diameter [mm]	11	10.05
nominal journal diameter [mm]	10	10
diametric clearance [mm]	1	0.05
coefficient of restitution ε	1	1
coefficient of friction μ	0.1	0.04
rotation speed [rpm]	220	220

4   Simulation Results

4.1   Analysis of Flow Separation

In a first step the flow separation in joint C and E is examined. Therefore the numerical parameters with the unrealistic high clearance in Table 1 are used. This high value for the joint clearance serves for detecting critical positions very rapidly.

(a) g_N in joints C and E

(b) trajectory of joint E
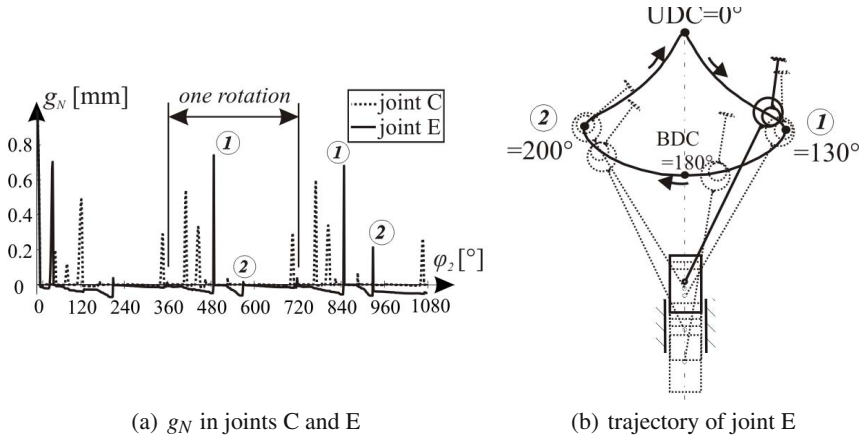
Fig. 4 Flow separation in joints C and E of the linkage mechanism

Fig. 4(a) shows the minimal gap between journal and bearing in the two joints. The first rotation is always neglected in order to prevent errors due to initial conditions. The small penetrations result from the used time-stepping scheme. Compared to the trajectory of joint E in Fig. 4(b) the two states of separation in joint E can be assigned to the two peripher points 1 and 2 with a high curvature. This agrees with guideline [12], which states out that a very low value of the reaction force F_i and a rapidly changing force direction δ are significant for a loss of contact, meaning a high coefficient

$$\kappa = \left| \frac{\dot{\delta}}{F_i} \right|_{max} \tag{13}$$

For the contact loss in joint C the nearly vanishing reaction force is responsible.

In press machines a frequently used measure for joint force balancing is a hydraulic spring to prestress the whole mechanism. The effect of such a device is tested for the analysed linkage mechanism, which can be seen in Fig. 5(a). For this simulation all five joints are modelled as imperfect joints. Fig. 6 shows how the spring changes the reaction forces in joint C and E.

In the diagram of Fig. 5(b) the gaps between the journals and the bearings of the joints C, D and E under the preload of the spring are plotted. It can be seen that contact loss can not completly be avoided, as flow separation in joint C still occurs at a crank position of 80°. The reason can be found again in the polar diagram in Fig. 6(a): Despite the spring, the reaction force still vanishes at this very position, what means an undetermined load situation, compared to Eq. (13). In contrast, no contact loss occurs in joint E, as there is no zero crossing of the reaction force in the prestressed mechanism any more, see Fig. 6(b). As also can be seen in Fig. 5(b), the contact loss in C leads to an impact, which initiates contact loss in joint D.

(a) effect in E   (b) g_N in joints C, E and D with undetermined load situation at 80°
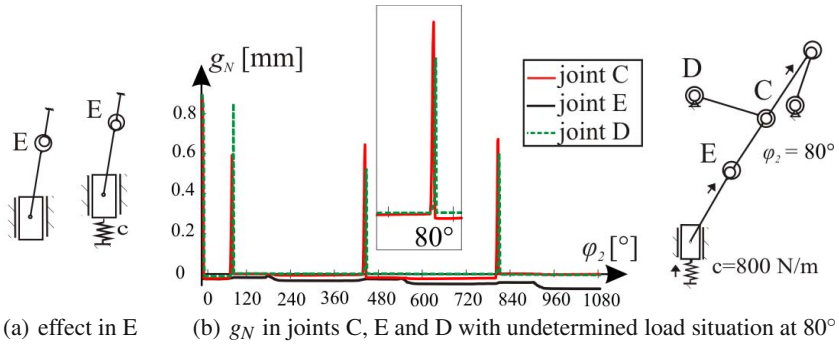
Fig. 5 Joint balancing of the linkage mechanism with a spring
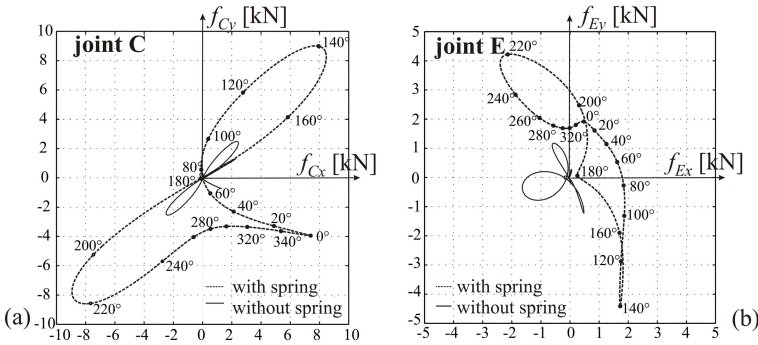
Fig. 6 Polar diagram of reaction forces with and without spring

4.2 Analysis of Oscillation Phenomena (Pendulum Motion)

Due to [12] high-frequency oscillations of the journal in the bearing shell can arise in a mechanism, even if no contact loss occurs. GINZINGER and THÜMMEL analysed this effect experimentally and numerically for a crank and rocker mechanism [10].

(a) journal positions   (b) contact angle
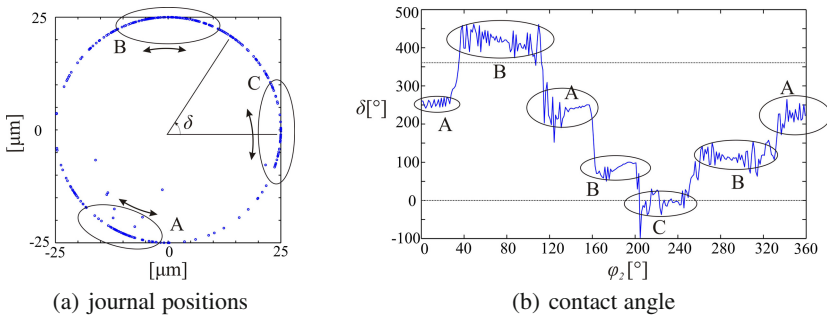
Fig. 7 Tangential pendulum motion in joint E

Here, the appearance of such oscillations is investigated in joint E of the linkage mechanism. Therefore, only joint E is modelled as imperfect and the numerical setup in Table 1 with the small clearance is applied. Fig. 7(a) shows the position of the journal in the bearing during one rotation of the crank. Around angles $\delta = 0°, 90°$ and $240°$ more often contacts are detected. Compared to the diagram of the angle δ in Fig. 7(b), it can be seen that high-frequency oscillations arise at these positions.

5   Conclusions

Within this contribution the non-smooth behaviour of a 6-bar linkage mechanism with clearance joints was analysed by a discontinous method within the simulation environment. This method is useful for efficently detecting and analysing secondary effects in a mechanism, since only three parameters - the clearance size, the restitution and the friction coefficient – are necessary. In detail, it was shown that the arising contact losses in the joints can be avoided by a spring device except at one position, where an undetermined load situation still remains. Furthermore, the existence of pendulum motion in one joint of the 6-bar mechanism was shown. Since secondary effects highly depend on the parameter set as well as the operation condition, further investigation have to follow and an experimental matching has to be done in a next step.

References

1. Dresig, H., Holzweißig, F.: Dynamics of Machinery. Theory and Applications. Springer (2010)
2. Haines, R.S.: Survey: 2-dimensional motion and impact at revolute joints. Mechanism and Machine Theory 15(5), 361–370 (1980)
3. Horie, M., Funabashi, H., Ogawa, K., Abe, H.: Dynamic Characteristics of Planar Link Mechanisms with Clearances. Bulletin of the JSME 29(252), 1888–1899 (1986)
4. Flores, P.: A parametric study on the dynamic response of planar multibody systems with multiple clearance joints. Nonlinear Dynamics 61, 633–653 (2010)
5. Flores, P., Ambrósio, J., Pimenta Claro, J.C., Lankarani, H.M.: Kinematics and Dynamics of Multibody Systems with Imperfect Joint. LNACM, vol. 34. Springer, Heidelberg (2008)
6. Pfeiffer, F., Glocker, C.: Multibody Dynamics with Unilateral Contacts. John Wiley Inc. (1996)
7. Schwab, A.L., Meijaard, J.P., Meijers, P.: A comparison of revolute joint clearance models in the dynamic analysis of rigid and elastic mechanical systems. Mechanism and Machine Theory 37, 895–913 (2002)
8. Thümmel, T., Brandl, M.: Active Balancing of Joint Forces in High-speed Linkages by Redundant Drives and Learning Control. In: Proceedings of ASME DETC Conference, Irvine, California (1996)
9. Thümmel, T., Funk, K.: Multibody Modelling of Linkage Mechanisms including Friction, Clearance and Impact. In: Proceedings of 10th World Congress on TMM, Oulu, Finland (1999)

10. Thümmel, T., Ginzinger, L.: Measurements and Simulations of a Crank and Rocker Mechanism including Friction, Clearance and Impacts. In: Proceedings of the IX. International Conference on the Theory of Machines and Mechanisms, Liberec, Czech Republic (2004)
11. Thümmel, T., Roßner, M.: Introduction to Modelling and Parameter Identification Methodology of Linkages by Measurements and Simulation. In: Proceedings of the 13th World Congress in Mechanism and Machine Science, Guanajuato, Mexico (2011)
12. VDI Guideline 2149 Part 1: Dynamics of mechanisms – Rigid body mechanisms. Issue German/English. Beuth Verlag GmbH (2008)
13. Zander, R., Schindler, T., Friedrich, M., Huber, R., Förg, M., Ulbrich, H.: Non-smooth dynamics in academia and industriy: recent work at TU München. Acta Mechanica (2008)

Design of a Dynamometric Wheel Rim

Jesús Blasco, Francisco Valero, Antonio Besa, and Francisco Rubio

CITV Universitat Politècnica de València, Spain
fvalero@mcm.upv.es, jeblallo@upv.es

Abstract. Dynamic simulation and advanced control are two areas that are becoming important in the field of design and industrial production. Dynamic simulation is a design tool now consolidated and commonly used in industries such as automobile and the related ones because it replaces the expensive tests with prototypes. Well, the results can provide simulation tools such as advanced control techniques critically depend on the quality of the data from which the mechanical model systems are generated. Direct measurement of these data or physical parameters (mass, location of centers of gravity, inertia tensors, friction parameters, etc) is problematic in systems that are being designed. We also have to consider that these parameters may change significantly over the life of the mechanical system. The alternative measurement is the identification of these parameters from experimental data acquired during the operation of mechanical systems. The actual proposal of this work is to design a wheel rim for light vehicle able to determinate the forces and moments that are transmitted to the axis of the vehicle wheel during use. The necessary instrumentation is designed using extensometry techniques, and the design process focuses on the study of the wheel rim deformations associated with the different forces acting on it. The study of strain performed on models analyzed by finite element techniques considering the different types of forces acting on the rim. Modeling the deformations behavior of the wheel rim, and doing a proper instrumentation based on the FEM analysis the results will be develop the procedure for the instrumentation of the rim to obtain the desired measurements.

Keywords: extensometry, tire, parameters identification, forces measurement, strain gauges.

1 Introduction

The authors of this paper are developing a project that has the identification of physical parameters in vehicles among its objectives. That is, known applied forces and the dynamic response of a vehicle to follow a path, it is expected to obtain an estimation of the dynamic parameters of the system, thus, mass, position of the center of mass, inertial matrix for each of the components of the system, and the friction parameters of the defined links, as well as the damping and stiffness in these components.

For measuring the loads transmitted from the ground there is already specific instrumentation. Companies such as Kistler or RS Technologies offer it at high cost. These wheels work by a triaxial load cells implementation mounted on a special rim so that it enables to measure the three forces and three moments acting in the vehicle wheel. Dynamometric wheels have been used, for example, in [5] and [3] to obtain the forces transmitted by the ground and to apply them in solving problems of identification of physical parameters in vehicles, in combination with other instrumentation that allows obtaining paths and the determination of pitch and roll angles among others. They have also been used those sensors to verify models of tire lateral load behavior [4].

Specific sensors for specific applications are sometimes developed, such as fatigue life studies based on road data acquired using road load data acquisition and strain gauges strategically positioned at critical stress locations to directly reflect the input loads experienced by the components [1]. Also, special instrumented wheel bearings, which can act as load cells, have been used to measure the strains caused by the elastic deformation of the bearings [2].

The design process of a dynamometric wheel rim subject to a number of constraints given by the need to use existing equipment to achieve lower costs is presented. So measurements are made in each tire using four strain gauge channels. Since the conventional wheel having a high rigidity, it was decided to modify the junction between the hub and the rim to improve sensitivity. This alternative allows to work with existing instrumentation and to make designs and modifications on the wheel rim in the facilities of CITV at a lower cost.

In the second part of this article the technique of measurement which will be use is described. In the third one the process of design of a wheel rim is explained. The fourth part explains the calibration process. And in the last part results of the designed rim are presented.

2   Measurement Techniques

The design is conditioned by the telemetry equipment available, this equipment has four measurements channels for wheel.

The work is developed with a Cartesian reference system where Y axis is coincident with the axis of rotation of the wheel and the axes X and Z in the midplane thereof, as shown in Figure 1. The loads measured on the wheel rim are due to the load transmission between the tire contact patch with the ground and the hub that supports the wheel are three forces F_x, F_y, F_z, and one moment M_z. If it is supposed that the contact point between the tire and the ground it is satisfied the following equation:

$$M_y = -R_e \cdot F_x \text{ and } M_x = R_e \cdot F_y, \tag{1}$$
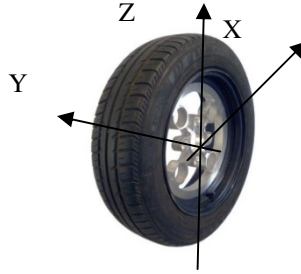
being R_e the tire radius.

Fig. 1 Coordinate system

Assuming the possible error associated with asymmetries of load on the contact patch and the rolling resistance. So to minimize these effects will be set a pressure of 400 kPa (4 bar) in the tires.

Direct measurements are obtained from four strain gauge channels, each of these channels will be sensitive to the six basic solicitations (three forces F_1, F_2, F_3 and three moments F_4, F_5, F_6). All these measurements are function of the position of the wheel rim relative to the contact point with the ground α, so the output of the measurement channel i is in volts,

$$\Delta V_i = \sum_{j=1}^{6} F_j \cdot SF_{ij}(\propto), \tag{2}$$

being $SF_{ij}(\propto)$ function of the position $\propto$ in V/N for j=1, 3 and V/Nm for j=4, 6. Replacing (1) in (2) and reordering it results as;

$$\Delta V_i = F_1 \cdot \left(SF_{i1}(\propto) - R_e \cdot SF_{i5}(\propto)\right) + F_2 \cdot \left(SF_{i2}(\propto) + R_e \cdot SF_{i4}(\propto)\right) + F_3 \cdot SF_{i3}(\propto) + F_6 \cdot SF_{i6}(\propto). \tag{3}$$

Setting the equation (3) in matrix form:

$$\{\Delta V\} = [SF]_\alpha \{F\} \tag{4}$$

$[SF]_\alpha$ is the sensitivity matrix of dimension 4x4, $\{\Delta V\}$ is the measurements vector and $\{F\}$ is the load vector that contains a F_x, F_y, F_z, M_z, that can be calculated as:

$$[SF]_\propto^{-1}\{\Delta V\} = \{F\} \tag{5}$$

The expression (5) will allow, for a position, to get the vector of loads, known the measurements vector and the sensitivity matrix.

For accurate results a sensitivity matrix without numerical problems to perform operations and whose terms do not contain significant errors is required. This requires good core design of the rim, so that it is sensitive to a similar magnitude in the measurements, and conducting proper calibration, both issues are discussed in the following sections.

3   Design

A pre-design stage was to analyze the behavior of existing commercial rims, checking that their high rigidity prevents from taking direct measurement. So the design of a customized rim with lower rigidity at a lower cost is proposed, so that in designing a specific geometry for the central area of the rim corresponding to the junction between the outer ring that supports the tire and the hub will be worked (see Fig. 1).

The objective of the design process is to determine a geometry that allows precise measurements and therefore, this geometry will be conditioned by the instrumentation used. Thus, high deformation zones are obtained to achieve good sensitivity to the strain gauge measuring techniques. (See figure 2).

The design process is iterative and is developed according to the sequence detailed below.

1. Establishment of geometry. It details the geometry accurately.
2. FEM analysis respect to one of the load cases of interest. Considering the wheel rotation analysis is performed by rotating the load at intervals of 10°. Figure 2 shows the strain when the position of the radial load, F_z, is aligned with a radius.
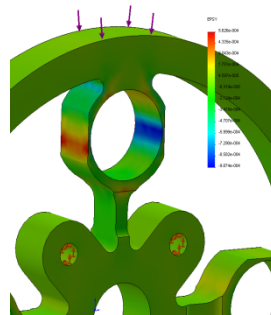
Fig. 2 Plot of calculated strain by FEM

3. Determination of the measurement points. The results of analysis in step 2 determine the most suitable areas to apply strain gauges so that they can compose full Wheatstone bridges. The procedure is iterative, going back to step 1 to achieve enough sensitivity.
4. Study of sensitivity to other load cases. Analysis is performed by a FEM analysis of strain corresponding to the loads that weren't applied in step 2.
5. Change of the load case. The process for all load cases is repeated, being established the geometry when for all types of load the step 4 is exceeded.

The bridge 1, composed of strain gauges 1, 2, 3 and 4 (figure 4a), has been discussed above.

The bridge 2, composed of strain gauges 5, 6, 7 and 8, is similar to bridge 1 with the difference of being rotated 90°. Both bridges are noticeably sensitive to the loads F_z and F_x and torque M_y. But the influence of the lateral force F_y and moments M_x and M_z is really small.

The bridge 3, composed of strain gauges 9, 10, 11 and 12 (See Figure 4c), is much more sensitive to the torque M_y than to the rest of the loads, and the result obtained along the spin remains stable as it is shown in the figure 3.
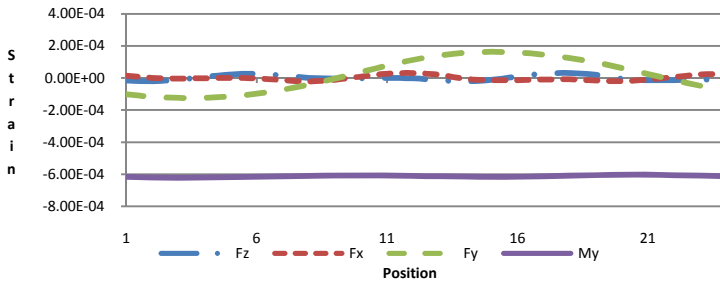
Fig. 3 Representation of strain associated with different load cases in the bridge 3

And the bridge 4 is composed of strain gauges 13, 14, 15 and 16. Its behavior is similar to the bridge 3. It is much more sensitive to the force F_y than to the rest loads. The result obtained also remains stable along the wheel spin.

a)   b)
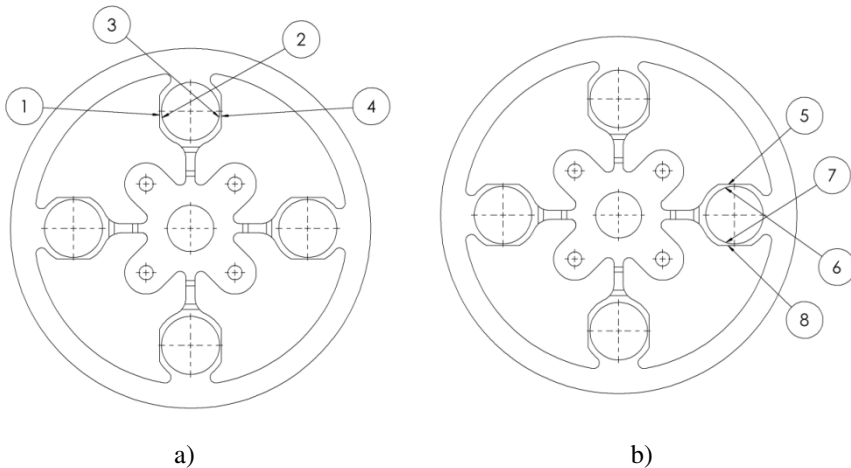
Fig. 4 Position of the strain gauges of the bridge1 (a), bridge2 (b), bridge3 (c) and bridge4 (d)

c)   d)
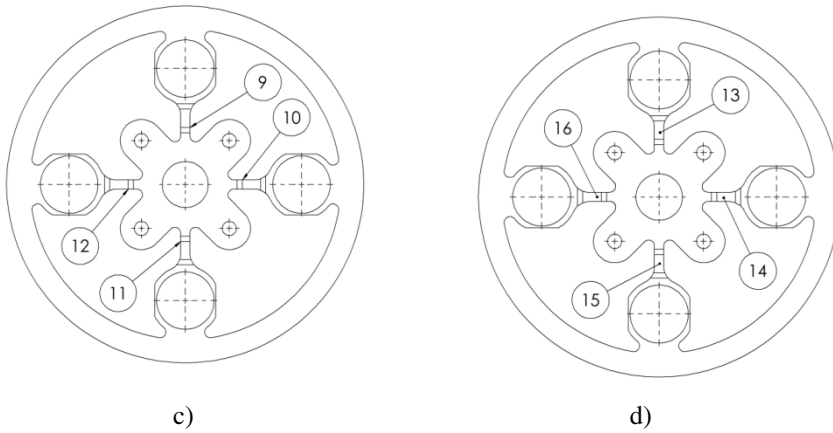
Fig. 4 (*continued*)

4 Calibration

The calibration aims to obtain the 24 values of $SF_{ij}(\propto)$ for each position α that appears in expression (2), that are required to obtain the sensitivity matrix $[\mathbf{SF}]_\alpha$ that allows, applying the expression (5), the calculation of the load as a function of the instrumentation inputs.

The process is performed for each wheel individually. This is repeated for each load to a set of discrete positions. The following summarizes the calibration sequence:

1. Firstly the wheel rim is fixed on the frame in a given position α, and a low magnitude load is applied, coming from the vector of six components $\{F_\propto\}_l$, obtaining the reading of the four components of $\{V_\propto\}_l$.
2. Load is increased to a significant known value and within the measuring range $\{F_\propto\}_h$, taking the pertinent input $\{V_\propto\}_h$, and the increment is calculated. $\{\Delta V_\propto\} = \{V_\propto\}_l - \{V_\propto\}_h$ and $\{\Delta F_\propto\} = \{F_\propto\}_l - \{F_\propto\}_h$.
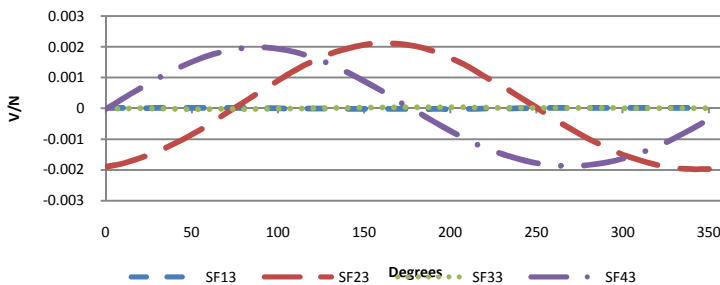
Fig. 5 Coefficients SF_{i3}

3. The process exposed above in steps 1 and 2 is repeated for six independent load cases, and since eq. (2) gives 4 equations for each load case, it yields a system of 24 independent linear equations, that allows to calculate $SF_{ij}(\propto)$ for the α position, and known R_e the matrix $[SF]_\alpha$

4. Repetition of the steps 1 to 3 for all the desired positions, in this case every 10°, therefore there are 36 angular positions.

5. 10 repetitions were performed from step 1 to 4, getting the bounded averaging of each term of the sensitivity matrix for each of the 36 desired positions.

Through these data, the calibrated matrix of the wheel $[SF]_\alpha$ is obtained.

5   Conclusions

To check the calibration output, combined loads have been applied in different angular positions, representing both the calculated values and those used in Fig. 6. The average relative error obtained for these test loads was 3.49%.
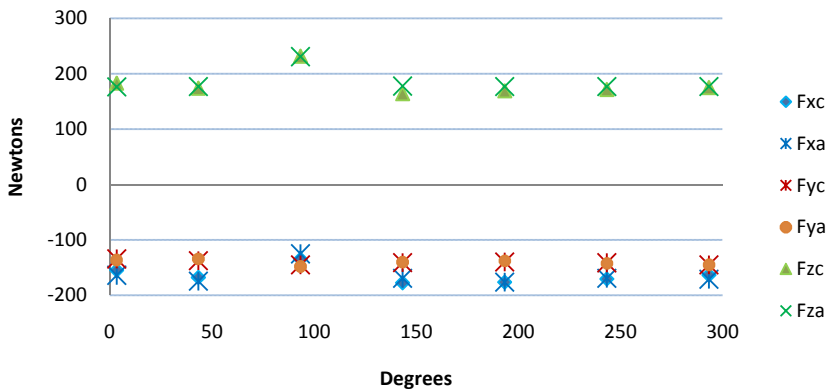
Fig. 6 Representation of applied loads on calculated loads by the calibrated wheel

A low cost dynamometric wheel rim has been designed and built. This rim is able to meet the needs of the dynamic test of the IDEMOV project, since the errors obtained are compatible with the parameter identification procedures.

References

1. Azrulhisham, E., Asri, Y.M., Dzuraidah, A.W., Nik Abdullah, N.M., Che Hassan, C.H., Shahrom, A.: Application of road simulator service loads in automotive component durability assessment. The Open Industrial & Manufacturing Engineering Journal 4, 1–7 (2011)
2. Jayashankar, A.: Experimental & modeling study of the influence of support stiffness on load sensing bearings. Department of Precision and Microsystems Engineering. T.U. Delft
3. Doumiati, Victorino, A., Charara, A., Lechner, D.: A method to estimate the lateral tire force and the sideslip angle of a vehicle: Experimental. In: 2010 American Control Conference, June 30-July 02. Marriott Waterfront, Baltimore (2010)
4. Venture, G., Ripert, P.-J.: Modeling and identification of passenger car dynamics using robotics formalism. Department of Precision and Microsystems Engineering. IEEE Transactions on Intelligent Transportation Systems 7(3) (september 2006)
5. Venture, G., Khalil, W., Gautier, M., Bodson, P.: Dynamicmodelling and identification of a car P.S.A. Peugeot Citroën/ Institut de recherche en Communications et Cybernétique de Nantes (IRCCyN)
6. Martín i Batlle, M.: Galgues extensomètriques. Universitat Politècnica deCatalunya (1992)

Design of a Feeder with the Use of the Path Synthesis Method

J. Buśkiewicz

Poznan University of Technology, Poland
`jacek.buskiewicz@put.poznan.pl`

Abstract. The paper presents the adaptation of the technique for motion and path synthesis to the problem in which the motion equations of two links are coupled. The method is employed to design a feeder for carrying products between two points. The feeder is assumed to be an one degree of freedom system of six links connected by means of revolute joints. The jaws of the gripper catch the product and transports to other work stand where the gripper releases the product and moves back to its initial position. No extra drive of the gripper is needed as the movement of the jaws is driven by the active link of the feeder. The mathematical basis of the method is presented. The problem is formulated as an optimization task. An exemplary solution is presented and discussed.

Keywords: mechanism synthesis, motion synthesis, path synthesis, four-bar linkage, feeder.

1   Introduction

Typical problems of dimensional mechanism synthesis involve the determination of the dimensions the mechanism to realize required performance. In the basic approach the requirements specify the motion of the working link, which is to perform technical functions with a prescribed accuracy. Nonetheless, in many design problems a mechanism satisfies its functions when the motions of a few links are coupled. The mechanism synthesis is a problem of great mathematical complexity [4, 5], therefore at present mainly computer methods are developed. The optimization problem is defined by design parameters, an objective function, an optimization algorithm and constraints. The evolutionary algorithms and neural networks are employed to synthesis purposes since they search for the optimal solution in the whole defined space, whereas the deterministic methods, as is the case with gradient methods, converge to the local minimum in the proximity of the initial parameters. The effectiveness of the method depends essentially on the number of design parameters and, as a consequence, on the structure of the objective function. Therefore, mechanism synthesis addresses also the techniques minimizing the number of design parameters [2, 3, 6, 7, 10]. Every additional parameter increases the computational cost and affects the quality of the solution

obtained. In most techniques presented in the literature the point is rather to develop and enhance algorithms minimizing an objective function and construct new error functions [8, 9, 11-18]. Some papers present methods for synthesis of multilink mechanisms realizing special motions [19, 20], the others deal with the linkages generating the coupler curve a part of which is an approximate straight line [21].

The paper presents the adaptation of the technique for optimal path/motion synthesis without time prescription of four link planar mechanisms [1, 2] to the synthesis problem in which the motion of two links has to be coupled in the working phase of the motion. The method is employed to design a feeder for carrying a product between two points. The feeder is assumed to be an one degree of freedom system of six links connected by means of revolute joints. In the utilized method the angular position of the coupler is approximated by means of periodical function *sine*. Such an approach enables decreasing the number of design parameters describing dimensions, orientation and position of a path/motion generator. Non-optimized geometric parameters are determined when the optimization process is accomplished.

2   Formulation of the Problem

Fig. 1 presents the mechanism of the third class, applied in industry to transport products between two work-stands. The feeder is designed so that the moveable jaw of the gripper should not rotate when moving to the left. This is the working stage of the motion in which a product is shifted. The gripper is open when sliding back to the very right position to catch the next product. This device has some disadvantages which can be divided into two groups. The first group refers to mathematical complexity of the synthesis problem - relatively large number of links separating input and output links, kinematic analysis of the third class mechanisms is a complex problem, and the synthesis of such mechanisms is much more complex task. The second group addresses some technical problems which prevent the device from wide industrial applications. The guiding link that guides the gripper has to be mounted between the points where the product is caught and released. This is sometimes disadvantageous because of the fact that the elements of the feeder have to be built in the existing system of work stands. Moreover, slight relative rotational motion between jaws of the gripper exists when the product is transported. A six-link kinematic system is proposed as an alternative solution. The system is Stephenson mechanism based on four-bar linkage. There are no guiding links, the jaws of the gripper can work far away from the remaining links, which gives bigger possibilities for embodying the feeder into housing. The concept of the method and application of its own were described in [1, 2]. Compared to these works the method was modified in order to widen the number of geometric input data, i.e. by prescribing the positions of ground pivots.
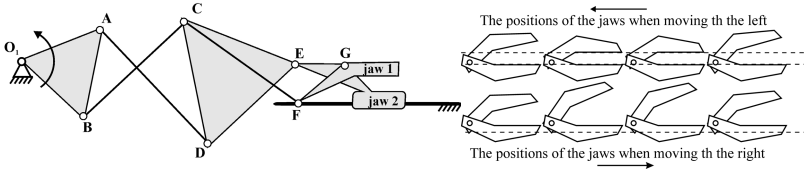
Fig. 1 The geometric scheme of an exemplary feeder (a), the positions of the jaws when transporting the product to the left and returning to the right (b)

3   Description of the Synthesis Method

We consider a four-bar linkage shown in Fig. 3. Let us disconnect the coupler from the four-bar linkage. We assume that point D of the coupler traces a required open path, given parametrically:

$$x = x(s), \quad y = y(s), \tag{1}$$

where $0 \le s < 1$. Simultaneously the coupler rotates according to the function:

$$\theta_{2L} = v_1 \sin(v_2 s + v_3) + v_4. \tag{2}$$

The parameters of function (2) either can be prescribed when motion synthesis problem is considered or are design parameters in path synthesis problem. One has to specify the locations of joints A and B with respect to the point D to connect the coupler with rotating input and output links. In the ideal case these joints move on arcs of circles. Let us denote: $|AD| = l_5$, $|BD| = l_6$, β is an angle between segments DA and DB. Hence, to solve the synthesis problem for the four bar linkage as a path generator one has to determine: the lengths of the coupler l_5, l_6, angle β and the coefficients of function (2): v_1, v_2, v_3, v_4, so that the revolute joints A and B of the coupler would trace as close as possible the trajectories which they trace in the assembled mechanism when point D traces required trajectory (1).

   Seven parameters have to be determined. In motion synthesis parameters v_1, v_2, v_3 and v_4 are given. Then, three parameters are optimized. In the papers [1, 2] the author proved that the angular motion of the coupler can be expressed by means of sine function (2). The method belongs to the group of methods aimed at decreasing the number of optimized design parameters. The geometry of the four bar linkage as an open path generator is defined by 11 parameters (Fig. 2): coordinates of the fixed ground pins: x_{O1}, y_{O1}, x_{O2}, y_{O2}, links lengths: l_1, l_2, l_3, l_5, the angle between arms AD and AB of the coupler θ_4, and the boundaries of the angle through which the active link rotates when a path is traced θ_{1s}, θ_{1e}.
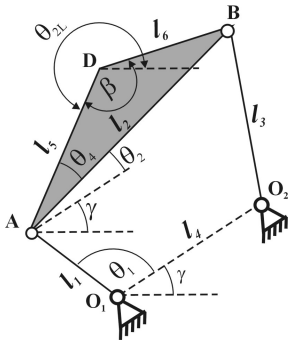
Fig. 2 The geometric scheme of
the four bar linkage
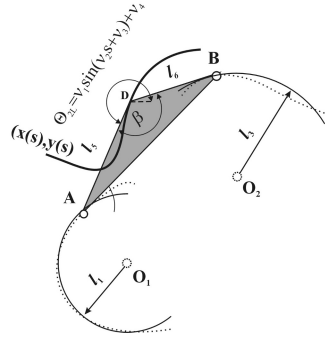
Fig. 3 Computed paths of joints A and B
and circular arcs approximating these paths

The design parameters are optimized by means of evolutionary algorithm. The algorithm itself involves no special improvements. The objective function measures the deviation of joints A and B from ideal circles, which was presented in [1, 2]. To put it short, let us assume that the path of joint A is discretized by 20 points. We determine the circles passing through three points A_i, A_{5+i} and A_{10+i}, $i = 1..10$. Then, we obtain 10 circles. We compute the centroid of their centers and the average value of their radiuses. In this manner we obtain the position of joint O_1 and the length of the active link l_1. The same procedure enables the coordinates of the output link ground pin O_2 and the output link length $l_3 = |O_2B|$ to be determined. The objective function has the form:

$$E_1 = \frac{\max|O_1A_i| - \min|O_1A_i|}{l_1} + \frac{\max|O_2B_i| - \min|O_2B_i|}{l_3}. \tag{3}$$

An engineer frequently cannot arbitrarily locate the ground pins when machine designing. Then, the objective function is a measure of deviation of joints A and B trajectories from the circles with centers at prescribed points O_1 and O_2.

4 Adaptation of the Method to the Mechanism Synthesis with Coupled Motion Conditions of Two Links

On the basis of the proposed method we can propose the following concept to design the feeder. This approach does not require the modification of the presented method. We synthesize the four-bar linkage O_1ABO_2, which draws the trajectory a part of which is the circle of radius R and with center at point O_3. In other words, point D of the coupler traces the circular arc of radius $R = |O_3D|$, centered at O_3 and spanned by a given angle (Fig. 4). Let the mechanism be in the

initial position, in which point D is located at the beginning point of the arc. We fix additional link O_3N to the ground at the pivot O_3. The length of the link $l_7 = R$. We choose an arbitrary point M on the coupler and we connect the coupler to link MN by means of the revolute joint at this point. The links MN and NO_3 are connected by revolute joint N. In the initial position the coordinates of points N and D are equal to each other (Fig. 5a). The location of point M is arbitrary and may be changed, e.g. when dead position occurs. The proper choice of point M allows for optimizing the kinematic and dynamic properties of the mechanism. Joint N moves along the arc of the circle with center at point O_3 and in the ideal case its position is coincident with the position of point D, the point which approximates this arc.
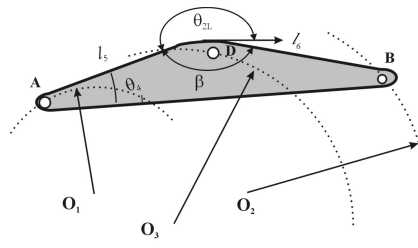
Fig. 4 The motion of the coupler joints and the path of point D

In this phase of motion link MN and the coupler rotate with the same angular velocity. The relative angular motion is a result of slight deviation of the trajectory of point D from the required trajectory. One jaw of the gripper is attached to the coupler, the other one is attached to link MN (Fig. 5b).
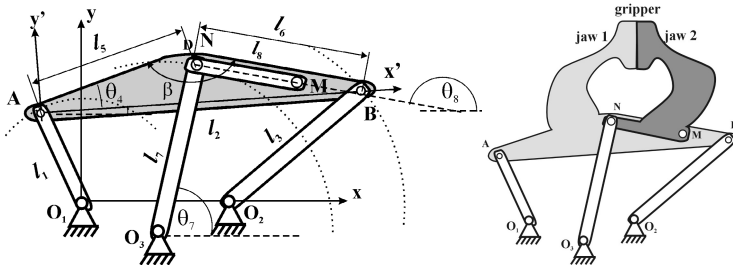
Fig. 5 The geometric scheme of the feeder (a), the feeder with the gripper (b)

When point D is in its initial position, i.e. it starts drawing the arc, the jaws of the gripper catch the product, shut and keep closed as long as point D moves along the arc. Subsequently, the gripper opens, the product is taken away and point D moves back to its initial position along the remaining part of the coupler curve. The locations of the jaws of the gripper on the coupler and on link MN determine the trajectory of the product and they can be prescribed in this stage of designing.

The global coordinate system O_1xy originated at joint O_1 constitutes a fixed reference system. The local system $Ax'y'$ moves with the coupler. The coordinates of point M(x'_M, y'_M) in the global system are as follows:

$$r_M = (x'_M + iy'_M)e^{i\theta_2} + (x_A + iy_A), \quad x_M = \mathrm{Re}(r_M), \quad y_M = \mathrm{Im}(r_M), \quad i = \sqrt{-1}. \tag{5}$$

The coordinates of joint N in the local system are $x'_N = l_5 \cos\theta_4$, $y'_N = l_5 \sin\theta_4$. We have to determine the angular positions of links NM and O_3N. Lets us denote: $\Delta x = x_M - x_{O3}$, $\Delta y = y_M - y_{O3}$. From the equations $l_7 \cos\theta_7 + l_8 \cos\theta_8 = \Delta x$ and $l_7 \sin\theta_7 + l_8 \sin\theta_8 = \Delta y$ one can compute the angular positions of link 8 and 7:

$$\theta_{81,2} = 2\arctan \frac{\Delta y \pm \sqrt{\Delta x^2 + \Delta y^2 - H^2}}{H + \Delta x}, \quad \text{where } H = (\Delta x^2 + \Delta y^2 + l_8^2 - l_7^2)/(2l_8),$$

$$\cos\theta_7 = \frac{\Delta x - l_8 \cos\theta_8}{l_7}, \quad \sin\theta_7 = \frac{\Delta y - l_8 \sin\theta_8}{l_7}.$$

5   Numerical Solutions and Conclusions

The nondimensional input data are as follows: coordinates of joint O_1(-5,0), coordinates of joint $O_2(x,0)$, where $0 < x < 10$, the lengths of links have to be less than 10, coordinates of joint $O_3(0,0)$. The evolutionary algorithm is employed to synthesize the four-bar linkage which traces the arc of the circle with center at (0,0), of radius $R = 5$ and spanned by the angle $2 \cdot 0.524$ rad. The parametric equations of this path are as follows:

x = 5cos((π-2·0,524)s+0,524), y = 5sin((π-2·0,524)s+0,524), 0 ≤ s < 1.

We get the following outcome: l_5=5.00, l_6=5.036, β=3.149 rad, and the parameters of the angular position of the coupler:

$$\theta_{2L} = 0.206\sin(-0.846s - 1.166) - 2.924 \text{ rad}.$$

Further on the basis of these outputs we compute: the lengths of rotating active and passive links: l_1=4.93, l_3=5.101, the horizontal coordinate of point O_2 fixation x_{O2}=5.029, the angle $\theta_4 = 0.004$ rad, the angle through which the active link rotates when the arc is traced: θ_{1s}=0.4992 rad, θ_{1e}=2.646 rad.

Joint N has the coordinates $(l_5 \cos\theta_4, l_5 \sin\theta_4)$ in the local coordinate system. The following coordinates of joint M in the local coordinate system are taken: $(1.2l_2,2)$. The motion of the feeder, the positions of the gripper and the trajectories of the jaws are shown in Figs 6a-f. The difference between the angular positions of the both links supporting the jaws is very small, as shown in Fig. 7, so one can assume that this concept is a good starting point for further dynamic analysis.
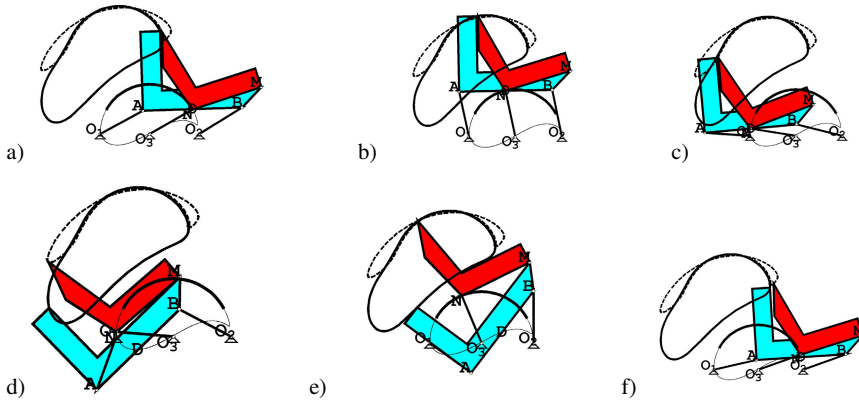
Fig. 6 The positions of mechanisms when the product is transported (a-c). The return motion of the feeder (d-f). The trajectories of the jaws (when the trajectories overlaps, the jaws are closed)
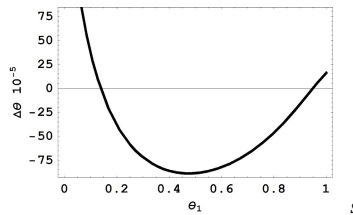
Fig. 7 The relative angular motion of jaws in the phase of the product transportation

By changing the position of jaws one can change the trajectory of the product. This trajectory has not to be given in the stage of the problem formulation. The position of point M can be also changed. These choices are conditioned by concrete design requirements and are not considered in this paper.

The results prove that the utilized method can be effectively applied to many types of synthesis problems. The proposed feeder is simple, six-link system driven by one rotor. It requires no extra hydraulic, pneumatic or electric drive to control the position of griper's jaws. In the phase of the product transportation the relative rotation of the jaws is less than 0.0015 radian. The position of the system shown in Fig. 1 is determined by the position of the work-stands, at which the product is caught and released, whereas the proposed system can be fit into existing housing condition by changing positions of fixations of jaws. In terms of these features it compares favourably with the system presented in Fig. 1. It should be noted that the paper deals only with geometric synthesis. The further studies is the optimization of kinematic and dynamic features of the feeder.

References

1. Buśkiewicz, J.: Synthesis Method of Planar Mechanisms Approximating Open Paths. In: Proceedings of the 10th IFToMM International Symposium on Science of Mechanisms and Machines, SYROM 2009, vol. XXII, pp. 597–609. Springer Science+Business Media B.V. (2009) ISBN: 978-90-481-3521-9
2. Buśkiewicz, J.: Minimization of the dimension of the solution space in optimal mechanism synthesis. Dissertations no. 442. Publishing house of Poznan University of Technology (2009)
3. Buśkiewicz, J.: Use of shape invariants in optimal synthesis of geared five-bar linkage. Mechanism and Machine Theory 45, 273–290 (2010)
4. Suh, C.H., Radcliffe, C.W.: Kinematics and mechanism Design. Wiley, New York (1978)
5. Erdman, A.G., Sandor, G.N., Kota, S.S.: Mechanism Design: Analysis & Synthesis, 4th edn. Web Enhanced, vol. I. Prentice-Hall (2001)
6. McGarva, J., Mullineux, G.: Harmonic representation of closed curves. Appl. Math. Model. 17(4), 213–218 (1994)
7. Ullah, I., Kota, S.: Optimal synthesis of mechanisms for path generation using fourier descriptors and global search methods. Journal of Mechanical Design 119, 504–510 (1997)
8. Wen-Yi, L.: A GA–DE hybrid evolutionary algorithm for path synthesis of four-bar linkage. Mechanism and Machine Theory 45(8), 1096–1107 (2010)
9. Penunuri, F., Peón-Escalante, R., Villanueva, C., Pech-Oy, D.: Synthesis of mechanisms for single and hybrid tasks using differential evolution. Mechanism and Machine Theory 46(10), 1335 (2011)
10. Sanchez Marin, F.T., Gonzalez, A.P.: Open-path synthesis of linkages through geometrical adaptation. Mechanism and Machine Theory 39, 943–955 (2004)
11. Lio, M.D., Cossalter, V., Lot, R.: On the use of natural coordinates in optimal synthesis of mechanisms. Mechanism and Machine Theory 35(10), 1367–1389 (2000)
12. Akcali, I.D., Dittrich, G.: Path generation by subdomain method. Mechanism and Machine Theory 24(1), 45–52 (1989)
13. Lio, M.D.: Robust synthesis of linkages–synthesis by solving non-linear optimization problem. Mechanism and Machine Theory 32(8), 921–932 (1997)
14. Matekar, S.B., Gogate, G.R.: Optimum synthesis of path generating four-bar mechanisms using differential evolution and a modified error function. Mechanism and Machine Theory 52, 158–179 (2012)
15. Gogate, G.R., Matekar, S.B.: Optimum synthesis of motion generating four-bar mechanisms using alternate error functions. Mechanism and Machine Theory 54, 41–61 (2012)
16. Avilés, R., Vallejo, J., Fernández de Bustos, I., Aguirrebeitia, J., Ajuria, G.: Optimum synthesis of planar linkages using a strain–energy error function under geometric constraints. Mechanism and Machine Theory 45, 65–79 (2010)
17. Sancibrian, R., Viadero, F., García, P., Fernández, A.: Gradient-based optimization of path synthesis problems in planar mechanisms. Mechanism and Machine Theory 39(8), 839–856 (2004)

18. Bulatovic, R.R., Dordevic, S.R.: On the optimum synthesis of a four-bar linkage using differential evolution and method of variable controlled deviations. Mechanism and Machine Theory 44, 235–246 (2009)
19. Chao, C., Jorge, A.: A novel family of linkages for advanced motion synthesis. Mechanism and Machine Theory 43, 882–890 (2008)
20. Radovan, R., Bulatović, R.R., Dordević, S.R., Dordević, V.S.: Search algorithm: A metaheuristic approach to solving the problem of optimum synthesis of a six-bar double dwell linkage. Mechanism and Machine Theory 61, 1–13 (2013)
21. Vidosic, J.P., Tesar, D.: Selections of four-bar mechanisms having required approximate straight-line outputs, Part I, II, III. Journal of Mechanisms 2, 23–44, 45–59, 61–76 (1967)

A Fairly Simple Mechanism Design
for a Rural Water Pump

Marco Ceccarelli[1] and Jorge Alencastre Miranda[2]

[1] University of Cassino and South Latium, Italy
 `ceccarelli@unicas.it`
[2] Pontifical Catholic University of Perù, Perù
 `jalenca@pucp.edu.pe`

Abstract. In this paper a driving linkage is designed with a fairly simple procedure for a fairly simple structure for implementation in a rural water pump in Andes regions. The aim is to provide a mechanism solution that can be easily implemented for comfort and efficiency issues with proper adjustments and available materials in rural environments with very limited resources.

Keywords: Rural Machines, Design, Linkages.

1 Introduction

Rural machines are needed in places where people can have difficulties not only to buy machines but mainly to operate them with industrial-like facilities, [4]. Thus, in general rural machines are constrained in design, material, operation features to be systems that can be handled in rural fields with reduced power without any supporting environment. The design and operation of rural machines must be possible so that the machine can be manufactured and assembled in rural places where they will be operated, without any technical support, [1, 3]. Consequently, main characteristics of a rural machine can be considered in a fairly simple structure and human-sized operation with locally available materials. In addition, it is to note that the acceptance and use of rural machines strongly depends on how they are introduced within the social and anthropological frames of a specific rural community in order to respect and indeed integrate the cultural identity and life environment of the rural community, as stressed in the ITACAB report, [3].

In this paper a design procedure is outlined to conceive and size mechanisms for rural machines but to propose their improvements for better efficiency and ergonomics that can facilitate the acceptance and indeed the use in rural fields by operators without any technical background. Thus, a design procedure and performance characterization are proposed with handsome calculations as based on geometrical models and formulation.

2   A Water Rural Pump

This specific case of study refers to a water pumping systems for small sized-water spring hole in its form that has been originally developed for application in rural areas in Andes region in Perù, Fig1. The pump is composed of a rope, piston heads, an upper wheel with crank, a bottom underwater small wheel with weight, and a pipeline. All components can be made with natural materials, like wood from local trees and other common available materials. The piston heads are attached along the rope at an interval of 1 m or less, so that they can push the water ahead to the top when the rope is run inside the pipeline with suitable diameter with respect to the size of the piston heads. With such a design a prototype, Fig.1, was tested to prove a water flow of about 1.5 litre per revolution with a manpower of 5 W.

a)   b)
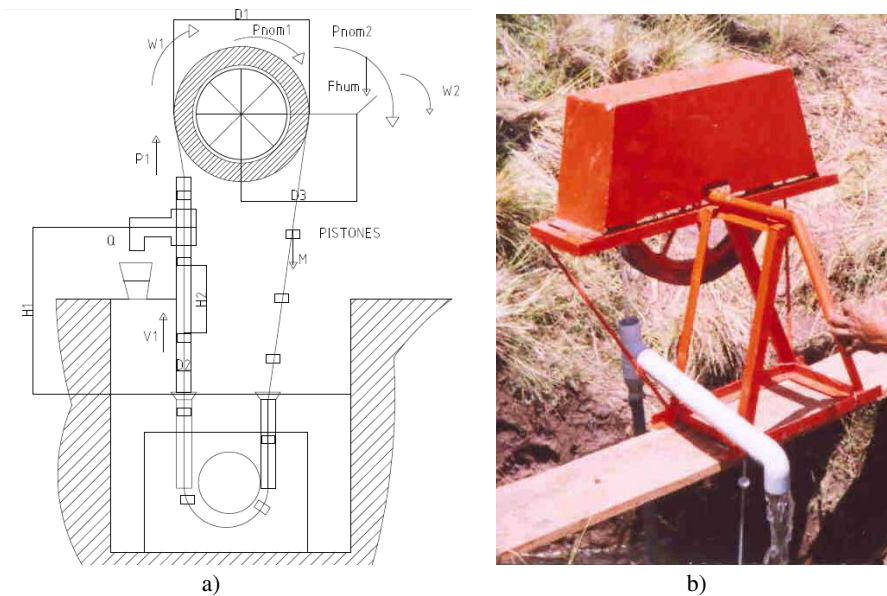
Fig. 1 A design of a rural water pump as applied in Andes areas of Perù: a) diagram and parameters of a current solution; b) a prototype of a current solution at the Pontifical Catholic University of Perù

In Fig. 2 experimental results are reported to show the action force of a human operator in driving the water pump through the crank rotation. Results are illustrated as function of number of turns by an operator as measured at given crank angles during each rotation. A peak force value is experienced as 19.80N where as the average maximum force during the operation can be considered with about 11N near the upward position of the crank.

A design procedure for the system development in Fig.1 was based preliminarily on the rules in the German standard VDI 2222-1, as outlined in [1], and

consists on evaluation criteria for considering both local and technical require-
ments, computation efforts for identification of morphological matrix and func-
tions structures for the specific machine, and finally calculations for an optimal
design. In this case of rural machines for Andes areas main attention has been
addressed to local requirements for identification not only technical constraints
for design issues but mainly for feasible expectations for a proper use and
understanding from potential users.
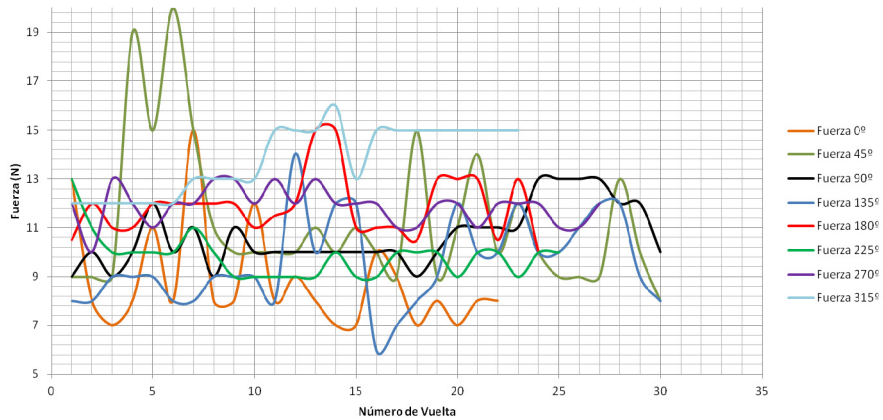
Fig. 2 Measured operator action during crank revolution of the upper wheel for rural pump
in Fig.1

Direct experiences on site have shown that main problems are related to the ac-
ceptance of the water pump machine with proper functioning. Reluctance has been
experience as due to understanding the technical system by potential users both for
their limited education (not only in technical matters) and capability of operating
the system at high altitude with proper action in not even long operation. By let-
ting potential users contribute in the development but assembling and installation
of a rural water pump will obtain both acceptance and understanding for a proper
use of the system, as successfully experienced in a similar case with another rural
machine, [1]. This requires to conceive the system fairly simple with components
that can be easily adjusted both in materials and manufacturing with range of tol-
erance for the final result.

The latter aspect, e. g. proper action and comfort in operating the water pump
by manual operation, is the problem that is addressed with the solution proposed
in this paper. The current solution in Fig. 1 is operated through a crank that is
attached directly to the upper wheel. The upper wheel has been designed with a
proper small size whose diameter that can range from 40 cm to 60 cm and it can
be installed with the center at a height of 40 cm to 70 cm from the ground, as at-
tempted in the prototype of Fig. 1. This design solution, although amenable for
components in manufacturing and assembling in rural sites, can give problems for

a human operator in rotating the crank with proper force in a long operation. Comfort issues will require the crank at a height that does not need too many other motion of the human body of an operator and the driving force can be transmitted to the upper wheel at a proper ratio from human action.

Comfort and proper human action have motivated a conception of a new fairly simple solution by using the mechanism in Fig. 3.

3   A Design Solution with a Driving Linkage

Design problem for enhancing the rural water pump in Fig.1 has been focused for a better efficiency with comfort solution for an operator working the pump in standing up position with a limited man power. In addition, constraints were considered in planning not to modify the original structure of the rural system and its sizes and materials as in Fig. b). Thus a solution has been conceived by proposing to add a mechanism to the axle of the upper wheel with the aim to achieve a proper functioning with suitable comfort of an operator. Thu, the scheme of Fig.3 has been considered as based on a 4-bar linkage whose crank is connected to the upper wheel and the input link can be powered through an handle by a human operator in a standing up position to alternate the input motion though the designed follower behavior. Ergonomic features are represented by the length h for the handle link and the swinging angle $\Delta\theta$ as function of the motion capability of human operators. Efficiency is considered by sizing the 4-bar linkage so that the required torque M_w for the upper wheel is obtained with a force F_h at the handle with values that can be feasible for human operators in rural places.
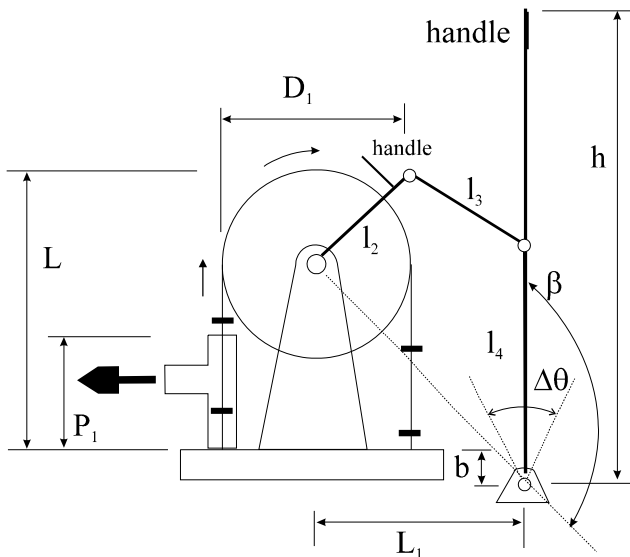
Fig. 3 An improved design of the rural water pump in Fig.1 with a driving linkage mechanism and its parameters

Beside the sizes of links as l_1, l_2, l_3, l_4, the linkage is characterized the by handle link with length H and a frame whose position can be adjusted with respect to the upper wheel frame through distances L_1, D_1, and b. the frame link has a size l1 given by

$$l_1^2 = L_1^2 + (b + L - D_1/2)^2 \tag{1}$$

A suitable comfort operation is related to a suitable approximate straight path of handle corresponding to a proper value of $\Delta\theta_4$ for l_4. In order to achieve a design solution with a computation procedure that can be easily understood and even updates on site, the scheme of Fig.4 has been used for the dead centre configurations of a 4-bar linkage as in [3]

$$l_1^2 + l_4^2 - 2\,l_1 l_4 \cos\psi_1 = (l_2 + l_3)^2$$

$$l_1^2 + l_4^2 - 2\,l_1 l_4 \cos\psi_2 = (l_3 - l_2)^2 \tag{2}$$

with

$$\psi_1 = \pi - \beta + \theta\,; \quad \psi_2 = \pi - \beta - \theta\,; \quad \beta = \frac{\pi}{2} + \tan^{-1}\left(\frac{b + L - D_1/2}{L_1}\right)$$

By using Eqs. (1) -(2) and Fig.4 data are obtained for design solution for different cases as reported in Table 1.
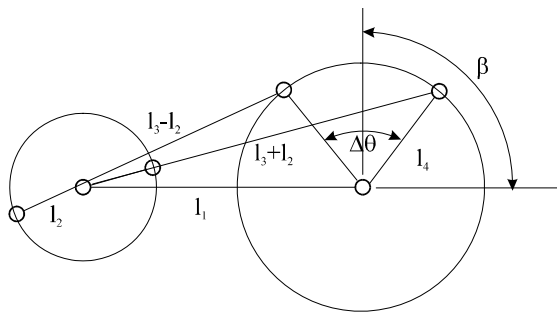
Fig. 4 A design scheme for a fairly easy calculation of dimensional synthesis of the linkage in Fig.3

Table 1 Design data for a driving linkage mechanism in Fig.3 with $\Delta\theta$ = 30 deg for the prototype in Fig.1b) with D_1= 40 cm and L = 50 cm.(lengths in cm)

Design case	L_1	b	l_1	l_2	l_3	l_4
I	50	10	60.3	20.0	64.7	22.1
II	50	0	58.3	20.0	58.6	20.9
II	80	10	89.4	20.0	89.5	20.4

As regarding force transmission for operation efficiency, a 4-bar linkage offers the possibility of a fairly simple computation of the relationship between a required driving torque M_w for the upper wheel and human action Fh_1 at the input link handle in the form

$$F_h = \frac{M_w \ \omega_2}{V_h \ \cos \varphi} \tag{3}$$

with $M_w = F_w \ r_w$ where F_w is the weight and force due to the lifting rope with water acting at the radius r_w of the upper wheel. An analysis has been carried out to derive computation expressions also for the force transmission as based on geometrical schemes that both help for intuitive understanding and allow handsome computations. Referring to the scheme in Fig.5, by using expressions for lines IA and IB with I as instantaneous center of rotation for link l_3, [3], the velocity V_h of the handle point and its orientation angle φ with respect to the horizontal human driving force F_h can be computed after some algebraic manipulations as

$$V_h = \omega_2 \frac{l_2 \ IB}{l_4 \ IA} \quad \text{and} \quad \cos \varphi = \frac{y_B}{l_1 - x_B} \tag{4}$$

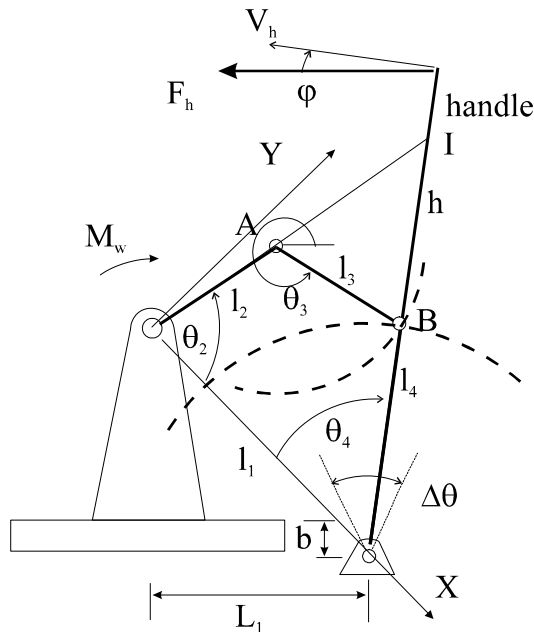with IB as distance of I from B and IA as distance of I from A.

Fig. 5 A design scheme for a calculation of driving human action of the linkage in Fig.3

The coordinates of I can be computed as intersection of lines IA and IB as

$$x_I = \frac{-l_1 \, t_B}{t_A - t_B} \quad \text{and} \quad y_I = t_A \, x_I \tag{5}$$

where $t_A = y_A / x_A$ and $t_B = y_B / (x_B - l_1)$, when $x_A = l_2 \sin(\theta_2)$ and $y_A = l2_2 \cos(\theta_2)$.

The coordinates of B are obtained by intersecting the mobility circles that are centered in A with radius l_2 and centered at frame joint of follower with radius l_4 as

$$x_B = \frac{-b + \sqrt{b^2 - 4a\,c}}{2a} \quad \text{and} \quad y_B = \sqrt{l_4^2 - l_1^2 - x_B^2 + 2 l_1 \, x_B} \tag{6}$$

with

$$a = 4(l_1 - x_A)^2 - 4 \, y_A^2 \,,$$

$$b = -8 \, l_1 \, y_A^2 + 4(l_1 - x_A)\left(x_A^2 + y_A^2 + l_4^2 - l_1^2 - l_3^2\right)$$

$$c = -4 \, y_A^2 \left(l_4^2 - l_1^2\right) + \left(x_A^2 + y_A^2 + l_4^2 - l_1^2 - l_3^2\right)^2$$

Design results from Eqs. (3) to (6) as related to the design solutions in Table 1 give suitable values of human action force with maximum values below 100 N when the speed of the driving upper wheel is moved for a speed of 360 deg /sec.

In particular, the above expressions Eqs. (3) to (6) can be computed through a drawing scheme like in Fig.5 from which parameters can be easily obtained for a handsome calculations with only geometrical data to obtain the required force F_h to operate the water pump as

$$Fh = \frac{F_w \, r_w}{\omega_2 \, h} \frac{l_4}{l_2} \frac{IA}{IB} \frac{l_1 - x_B}{y_B} \tag{7}$$

The design procedure has been formulated as based on the schemes of Figs. 3 and 5 with a geometrical approach that can be used to explain the linkage solution with its parameters but even to perform computations for necessary adjustments on field, even by the operators in rural frames.

In Fig. 6 a CAD output is shown as a proposal to potential users in rural frames to help to understand the design and its operation feasibility within their rural frames as well as the manufacturing and assembling of the components with fairly simple geometry. An additional flywheel is also added in the opposite side of the upper wheel both for balancing purposes and energy storage to help human operating power. The simple geometry of components is overstressed to facilitate fairly simple solutions of implementation both in materials and manufacturing. The CAD fairly simple representation with essential geometry and construction details is also aimed to show the fairly simple design and its assembling as well as operation features of the system.
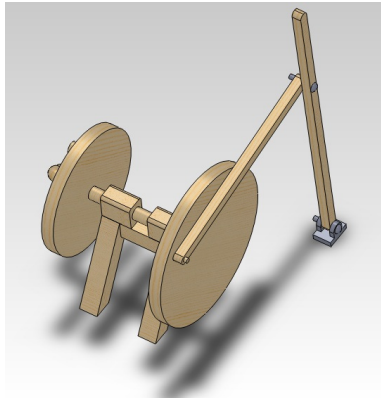
Fig. 6 A CAD mechanical design of the solution I in Table 1 that has been computed with the scheme in Fig.3

4 Conclusions

The results of this paper are focused in using a 4-bar linkage as driving mechanism for a rural water pump with the possibility to enhance its use both in mechanical efficiency and operator comfort. Adaptations will be surely needed on site and a design solution has been elaborated with fairly simple calculations that can be also handsome and able to ensure suitable operation adaptation of the man-powered system as based on fairly simple geometrical schemes.

References

1. Alencastre Miranda, J., Malpartida de la Cruz, I.: Metodologia de Diseno aplicada a la obtenciòn de una venteadora de granos. In: CD Proceedings of 7th Bolivarian Conference of Mechanical Engineering, Cusco (2012)
2. ITACAB (Institute for Technological Transfer to Marginal Sectors), Report Andrès Bello, Lima (2005)
3. Lopez-Cajùn, C.S., Ceccarelli, M.: Mecanisms: Kinematic Fundamentals for design and optimization of machinery, Trillas, Ciudad de Mexico (2008) (in Spanish)
4. Zakiuddin, K.S., Sondawale, H.V., Modak, J.P., Ceccarelli, M.: History of Human Powered Threshing Machines: a Literature Review. In: Koetsier, T., Ceccarelli, M. (eds.) Explorations in the History of Machines and Mechanisms. HMMS, vol. 15, pp. 431–446. Springer, Heidelberg (2012)

Adjustable Low-Cost Robot Link

C. Teichgräber[1], M. Berger[1] and J. Müglitz[2]

[1] Chemnitz University of Technology, Germany
 {carsten.teichgraeber,maik.berger}@mb.tu-chemnitz.de
[2] ZIS Industrietechnik GmbH, Meerane
 joerg.mueglitz@zis-meerane.de

Abstract. The paper deals with a low-cost robot link concept. By simplifying common means for the development of parallel kinematic machines, a means to optimize the dimensioning, regarding link stiffness, is found. To underline the utility of the design concept, called rigid hexapod, a way for geometric adjustment of the lightweight structure is presented.

Keywords: robot link design, TCP-fixed wrist, stiffness optimization, adjustment, rigid hexapod.

1   Introduction

The design of robotic devices often demands expensive manufacturing techniques in order to assure high precision requirements. Essentially the resulting costs are dominated by two main influences. Namely there are shape and position tolerances defined within the dimensioning process and the usage of fixtures to assist the assembly process. Positioning and repeat accuracy of the working robotic manipulator depend directly on its deformation when exposed to forces, i. e. its stiffness.

Especially serial robots suffer from these circumstances. However the widespread universal-task-robots can be offered at relatively low prices due to an effective mass production. The disadvantages increase for special machinery, designed for own usage. In this case creative engineering and a thoughtful relaxation of the requirements may lead to a low-cost solution of acceptable performance.

The problem under observation in this paper will be the adjustment of two rotary axes, which are part of a robot's wrist mechanism. The mechanisms task is the orientation of an oxyfuel torch.

The wrist has a spherical design. Its redundant kinematic structure is somewhat unconventional [2]. Fig. 1a shows the wrist in its stretched pose with torch on the edge of the reachable workspace. The rotary axes of each separate link include the angle γ_k ($k = 1, .., 4$; Fig. 1b) and intersect at a common point, which coincides with the wrist's tool-center-point (TCP). The TCP also lies on the beam direction

of the cutting tool, that is rigidly fixed on the distal link. This configuration allows torch rotation about the TCP within $\varphi \in [\,0°, 360°]$, $\psi \in [\,0°, 45°]$ without encountering a singular pose.
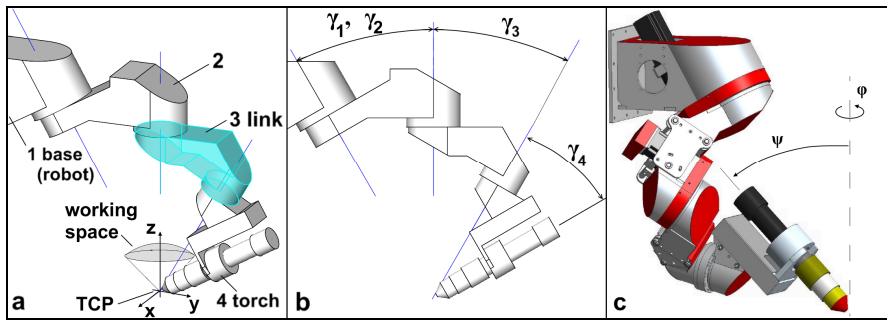
Fig. 1 a) Redundant serial wrist b) link scheme c) prototype design (©ZIS Industrietechnik)

2   Design Issues

The purpose of each link with two revolute joints is to keep the angle γ_k (between the rotary axes) within minimal deviation. Furthermore the two axes have to lie in the same plane, thus they have to intersect. These two geometric constraints are given by the spherical structure. The first prototype of the wrist was realized as a welded sheet metal construction (Fig. 1c). Significant precision deficits were observed due to

  (i)   thermal deformation after the joining operation as well as
  (ii)   the static weight loads on the one hand and
  (iii)   dynamic inertia and damping forces of the torch pipe on the
          other hand.

Obviously the influence of (i) may be reduced by a proper adjustment mechanism, while the effects of (ii, iii) require selective stiffness modifications. This analysis led to a design review, aiming to combine both of these demands without additional costs, but by reducing mass and clearance and increasing stiffness.

3   Rigid Hexapod Concept

To solve the problems mentioned above the idea of a hexapod structure with rigid legs (Fig. 2a) came up. The term 'hexapod' is sometimes imprecisely used for parallel kinematic machines in general. In this paper any structure consisting of two rigid bodies, connected to each other via six linkages, is called a hexapod. One of the two bodies is defined as base while the other one is called platform.

For this application it has proofed advantageously to make sure, that there are no redundant joint bindings within the mechanism, whose degree of freedom equals zero. There are six legs, each with two spherical joints. A verification with Grübler's formula reveals, that the platform is statically determinate, whereas the six legs' ability to rotate has no noteworthy effect (Fig. 2a).
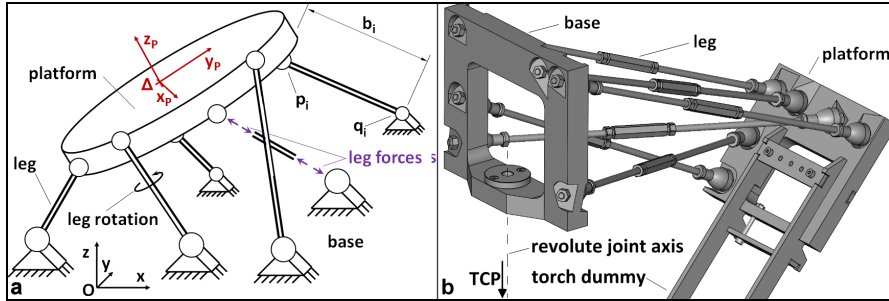

Fig. 2 a) Rigid hexapod concept b) test link with revolute joint (to robot) and torch dummy

A well designed hexapod possesses truss-like properties due to its kinematical structure. This application tries to benefit from the high load capacity to weight ratio. The dimensioning below will be done geometrically and statically, based on roughly estimated mass and process force, as well as an appropriately chosen typical movement. The geometric parameters are the center point coordinates of the six ball joints on the base and the platform respectively. The diameter of the legs and the spherical joints' size depend primarily on the load.

4   Geometric Dimensioning

The question of interest, when choosing the ball joint positions on both the base and the platform, leads to a problem of some kinematic complexity. Provided that the six linkages are designed with two spherical joints, the analysis described in the next sections is valid. More complex kinematic chains, with more links between base and platform, result in even more involved mechanical models. These models then have some similarity to robotic multi-fingered grasps (for a thorough discussion see e. g. [3]).

Solving the geometric dimensioning problem means finding the positions of the fixed joints $\mathbf{q}_i$ on the base and the platform joints $\mathbf{p}_i$ (with $i = 1, ..., 6$ see Fig. 2a). $\mathbf{p}_i^{\,0}$ are the ball joint centers with respect to the platform fixed frame $\{x_P, y_P, z_P\}$. In this paper names of variables will be bold for vectors/points, while capital bold letters are used for two-dimensional matrices.

To minimize displacements under load the force/translation or torque/rotation ratio for each spatial direction need to be maximized. The simplified model assumes both the base and the platform as rigid bodies connected by the legs and spherical joints being compliant. Therefore forces applied to the platform will only

cause (longitudinal) leg forces (Fig. 2a). Modeling the linkages between base and platform as linear springs promises to be a simple means for displacement calculation. Only the relation between the forces/torques applied to the platform and the leg forces will be needed.

The mapping of the platform forces/torques to the longitudinal leg forces is the inverse Jacobian. To take this matrix into account is a usual way to evaluate the stiffness of a hexapod robot with six driven telescopic legs. An adequate method to judge the stiffness of a hexapod robot is presented in [1] (p. 259-268). The author provides a suggestion for the stiffness matrix of linear elastic legs as

$$\mathbf{K} = \mathbf{J}^{-T} \cdot diag(k_i) \cdot \mathbf{J}^{-1}, \tag{1}$$

with the legs' and joints' stiffness k_i determined from

$$\frac{1}{k_i} = \frac{b_i}{ES_i} + \frac{2}{k_{BJ}} . \tag{2}$$

where E is Young's modulus, S_i is the area of one leg's cross-section and b_i is the link length. The strut and joints are considered as serial connected strings. By using the unit $[\,k_i\,] = 1\ N/\mu m$ the figures should remain at a manageable scale.

The influence of the spherical joint stiffness k_{BJ} also has to be looked at. A curve with the relation between displacement and force is gained from a physical test. Typically this non-linear curve can be approximated by a linear function whose slope depends on the tilting angle of the leg. However in the case of a rigid hexapod k_{BJ} is constant for all of the twelve identical spherical joints.

The inverse Jacobian $\mathbf{J}^{-1}$ in Eq. (1) can be deduced from considerations regarding the force equilibrium of the mechanism or the velocity transmission [1]. In this paper the latter way was taken using a common geometric approach from [4].

For the six points $\mathbf{p}_i$ are fixed to the rigid platform and are also guided by the leg vectors of length b_i the following constraint holds

$$f_i = b_i^2 - (\mathbf{p}_i - \mathbf{q}_i)^2 = 0 . \tag{3}$$

The platform position and orientation coordinates $\mathbf{x} = (\Delta x\ \Delta y\ \Delta z\ \alpha\ \beta\ \varphi)^T$ locate the frame $\{x_P, y_P, z_P\}$ with respect to the base frame $\{x, y, z\}$ in Fig. 2a. $\mathbf{x}$ may occur in a parameterized representation of the points $\mathbf{p}_i = \mathbf{p}_i(\mathbf{x}, \mathbf{p}_i^0)$. High index '0' indicate the local point coordinates with respect to the platform frame.

The leg length b_i then equals

$$b_i = \sqrt{(\mathbf{p}_i(\mathbf{x}) - \mathbf{q}_i)^2} . \tag{4}$$

The derivation of Eq. (3) with respect to the platform coordinates $\mathbf{x}$ leads to

$$b'_i = \tfrac{1}{b_i}(\mathbf{p}_i(\mathbf{x}) - \mathbf{q}_i)^T \mathbf{P}'_i(\mathbf{x}) \cdot \mathbf{x}' . \tag{5}$$

Eq. (5) describes the relation between the variations in leg deformation **b** and the platform displacement **x**. Thus the vector of coefficients in Eq. (5) equals the i-th row of the inverse Jacobian $\mathbf{J}^{-1}$. The 3x6-matrix $\mathbf{P}'(\mathbf{x})$ contains the partial derivatives of $\mathbf{p}_i(\mathbf{x})$ with respect to the coordinates of **x**. It depends directly on the parameters, that were chosen to express the platform position and orientation.

As mentioned before, this calculation is done to find the maximum hexapod stiffness by varying the local coordinates of the points $\mathbf{p}_i^0$ on the platform. Therefore the scalar objective function Z may be used for a numerical optimization

$$Z(\mathbf{p}_i^0) = \left\| \mathbf{K}(\mathbf{p}_i^0) \right\| \tag{6}$$

using the stiffness matrix **K** from Eq. (1). There is some literature to be found on norm criteria, e. g. [4]. The spectral norm was used for this 6x6-matrix in Eq. (6). Special attention also needs to be paid to the different units of translation and rotation within **K**. The translation/rotation scaling should be chosen in such a manner, that the elements of the upper rows ($i = 1, 2, 3$) of **J** have similar values to those of the lower ones ($i = 4, 5, 6$). Thus the usage of screw coordinates can be spared.

For a successful optimization an appropriate set of constraints is essential. In this case the available space in the link design has to be considered. In a prior estimation the possible ranges of the Cartesian coordinates of $\mathbf{p}_i^0$ were set as

$$\begin{pmatrix} x_i^{min} & y_i^{min} & z_i^{min} \end{pmatrix}^T \leq \mathbf{p}_i^0 \leq \begin{pmatrix} x_i^{max} & y_i^{max} & z_i^{max} \end{pmatrix}^T \quad \text{(see Fig. 3a).} \tag{7}$$

Additionally a leg crossover must not occur. To achieve that, the legs' minimal distance to each other e must be greater than their diameter d:

$$e_{i,j} = \left| \mathbf{u}_{i,j}^T \mathbf{v}_{i,j} \right| > \tfrac{1}{2}(d_i + d_j) \quad i,j = 0, ..., 5; \quad i < j ; \tag{8}$$

$$\text{with} \quad \mathbf{v}_{i,j} = \mathbf{p}_j - \mathbf{p}_i \quad \text{and} \quad \mathbf{v}_{i,j} = \tfrac{1}{b_i b_j}(\mathbf{p}_i - \mathbf{q}_i) \times (\mathbf{p}_j - \mathbf{q}_j).$$

Eq. (8) checks the distance of the lines between the points $\mathbf{p}_{i/j}$ and $\mathbf{q}_{i/j}$ while for our case only the line segments between them is of interest. The formulation lacks the ability to detect whether $e_{i,j}$ is found between these points or not. In this case

$$g_{i,j} = [(\mathbf{p}_j - \mathbf{q}_i) \times (\mathbf{p}_j - \mathbf{q}_j)]^T \mathbf{v} . \tag{9}$$

and

$$h_{i,j} = [\mathbf{u} \times (\mathbf{q}_j - \mathbf{p}_i)]^T \mathbf{v} . \tag{10}$$

have different signs. If not ($g_{i,j}$ and $h_{i,j}$ have the same sign) then the minimal crossing distance of the examined line segments according to Fig. 3b is

$$\tilde{e}_{i,j} = \min\left(\left| \mathbf{p}_i - \mathbf{p}_j \right|, \left| \mathbf{p}_i - \mathbf{q}_j \right|, \left| \mathbf{q}_i - \mathbf{p}_j \right|, \left| \mathbf{q}_i - \mathbf{q}_j \right| \right). \tag{11}$$

It may be advantageous to repeat the optimization process for the base joints holding the platform points $\mathbf{p}_i$ fixed thus converting Eq. (6) into $Z(\mathbf{q}_i^0) = \|\mathbf{K}(\mathbf{q}_i^0)\|$.
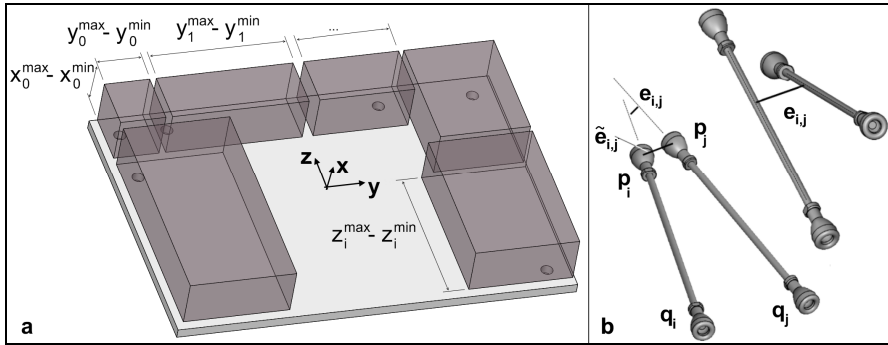

Fig. 3 a) Design space for each of the platform joints' coordinates b) leg distances

5   Link and Joint Dimensions

The loads being applied on the wrist during normal operation are known and can be described as a collection of several load cases $\mathbf{f}_m$, expressed in the fixed frame $\{\mathbf{x}, \mathbf{y}, \mathbf{z}\}$. The normal forces $\boldsymbol{\tau}_m$ along the struts can easily be calculated [1] (p. 259) for each load case by

$$\boldsymbol{\tau}_m = \mathbf{J}^T \mathbf{f}_m \tag{12}$$

when inverting $\mathbf{J}^{-T}$ found in Eq. (5). Based on the maximum forces a start value for S_i in Eq. (2), regarding the above optimization problem, is generated. It seems reasonable to perform a buckling analysis with the largest value of b_i to gain the legs' diameter d. In accordance with the linear stiffness of the most compliant leg (see first term in Eq. (2)) now an appropriate joint size has to be chosen.
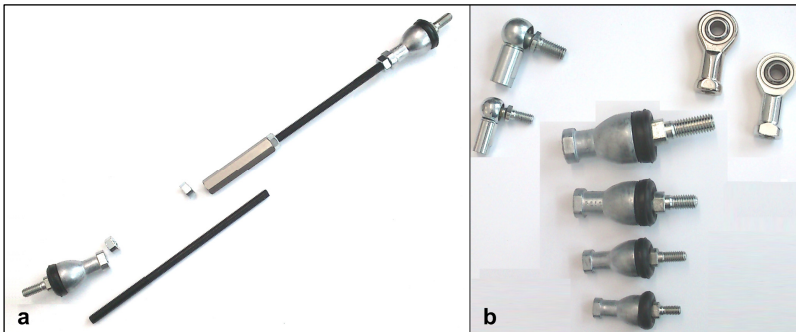

Fig. 4 a) Leg assembled from left-hand and right-hand threaded bars and a coupling b) ball joints

A brief study on joint characteristics, using a tension testing machine, led to several preliminary assumptions, that should be verified in future work:

(i)   Even joints with literally no backlash seem to have a settling behavior when first being put under compression (stiffening effect after load relieve).

(ii) The load-displacement graph for compression has an almost linear section above ≈15% of the joint's static load capacity.

(iii) If the joint's nominal size equals a leg's diameter d the joint stiffness k_{BJ} (Eq. 2) can be neglected when increasing b_i by one joint length (half the length on both sides, see Fig. 4a).

As a conclusion either the use of tight-fitted ball joints is recommended (Fig. 4b upper right) or a pre-load of them, using springs between the base and the platform. As a consequence the joint stiffness remains nearly constant during operation and there is no backlash. Further tests will be conducted, as there were only few test objects (Fig. 4b) and the investigations concerned only static rigidity.

6   Geometric Adjustment

After the assembly of the wrist, which is done without special fixtures, there will be deviations from the desired mechanism geometry. This results in positioning errors measured at the TCP when orientating the end-effector. For this measurement a dummy torch with a ball at the TCP is used. The resulting TCP-curve can be decomposed in a radial ε_r and an axial ε_a error (see Fig. 5), as well as a tilting angle ε_γ. An ideally assembled link would mean no TCP-movement at all.
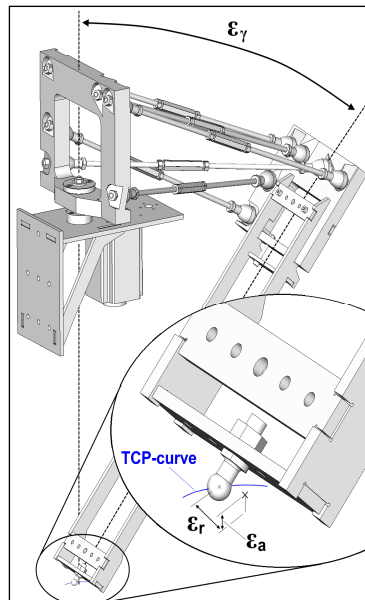
Fig. 5 Error measures for calculation the adjustment

With the error information a change of the leg lengths can be calculated in order to have the errors vanish or at least decrease beneath $\delta = 0.1$mm. The actual adjustment is done by defined turns of the fine threaded nuts. Several measurement series may be conducted to achieve satisfying results.

Computing the real leg lengths is a problem similar to the inverse kinematics of parallel kinematic machines. It is the authors' proposal to include the errors $\boldsymbol{\varepsilon}_{1,...,n} = (\varepsilon_{rx}\,\varepsilon_{ry}\,\varepsilon_a)^T$ into Eq. (3). Then f_i is minimized by varying b_i, considering all n measured points of the curve. Newton's method is an effective means, as there are very good starting values. Furthermore it allows the inclusion of other adjustment parameters, if wanted.

7   Conclusion and Prospect

This paper deals with an adjustable robot link design concept using a rigid hexapod, which is a hexapod inspired truss with rigid legs. The central part of the paper is a formulation of a method to find the optimal leg position regarding the link stiffness. Therefore an objective function is defined, using the hexapods Jacobian and the leg's dimensions as well as material properties.

The structure possesses the ability of leg length adjustment, which makes it similar to a parallel kinematic machine. With an appropriate measurement the influence of assembly- and manufacturing tolerances can be determined and compensated.

In future research the investigation of more and different spherical joint designs including is planned. Interesting possibilities offer flexural pivots and "monolithic" legs, that can be adjustable more accurate by elastic deformable regions. The final target is a hexapod, that is made by one solid body with joints, designed by local stiffness reduction and with no clearance, high stiffness and low manufacturing and assembling costs.

References

[1] Merlet, J.-P.: Parallel Robots. Solid Mechanics and Its Applications. Springer (2006)
[2] Müglitz, J., Berger, M., Wegert, E.: Roboterhandgelenke zum thermischen Schneiden. In: Berger, M. (ed.) Kolloquium Getriebetechnik. vol. 9, Technische Universität Chemnitz (2011)
[3] Murray, R.M., Li, Z., Sastry, S.S.: A Mathematical Introduction to Robotic Manipulation. CRC Press (1994)
[4] Schönherr, J.: Evaluation and optimum design of parallel manipulators having defined workspace. In: ASME Design Engineering Technical Conferences and Computers and Information in Engineering Conference Baltimore, Maryland (2000)

2D Scan-Head Motion Characterization and Machine-Tool Integration

E. Ukar, S. Martínez, A. Lamikiz, and I. Tabernero

Dept. of Mechanical Engineering of UPV/EHU, Spain
eneko.ukar@ehu.es

Abstract. This work is focused in the integration of a scan-head in a machine tool for laser processing of large areas. The scan-head is a device typically used for marking operations and provides very high linear speeds. Despite scanners present high accuracy for marking speeds below 5,000 mm/s, over this limit, accuracy problems were found. In this kind of device the motion is controlled using high precision actuators but there is no positioning closed-loop and workspace area is typically limited to small working areas. On the other hand, the positioning error varies also with working area plane positioning. This becomes a problem for processing complex shape surfaces. The work presented deals with characterization of the scan head, to identify the parameters affecting the error, the influence of the error with working plane positioning and with the integration of fast rotary axes of the scan head with conventional linear axes of a machine-tool. The proposed solution is based on a NC parent program controlling the linear axis of the machine-tool with integrated subprograms that control rotary axes of the scan-head.

Keywords: laser, scan-head, machine-tool, motion, integration.

1   Introduction

Scan-heads are devices mainly used for laser marking operations. The beam positioning is controlled with two mirrors. These mirrors are moved with high precision rotary actuators [1]. The lightness of the mirrors enables fast rotation and linear motion of the beam on the surface. This device uses an F-Theta lens to keep the laser beam focused in a flat plane while scanning the entire scan field. 3D scan-heads have another linear mirror to control the focal distance in order to keep the beam focused on complex surfaces. The main application of this equipment is for industrial laser marking, although its use is spreading to other processes that need very fast movements of laser beam like, surface texturing, remote laser processes or laser hardening operations, where fast beam movement enables customizing energy density on the hardening area. An advantage provided by this system is the high speed and motion agility that can be achieved, since the motion of the mirrors is performed directly with a small digital drive and present virtually

no inertia. However, like any mechanical system, scanners presents a series of positioning errors due to response delays, assembly errors, etc. Currently, manufacturers use a number of standardized tests intended for calibrating scanners, however, do not provide information about the accuracy of positioning the scanner to different velocities and trajectories. In high precision applications, such as the glass marking [2], the polymer micro-processing [3], or when it is important to know the actual speed of the beam, the information provided by the manufacturer is insufficient. One of the main characteristics of the use of a scanner is the need to correct the workspace because of optical distortions due to the use of optical lenses. These distortions also include effects due to lack of alignment, assembly and thermal expansion [4]. During the installation, some correction parameters are introduced, but these parameters remain constant independently of the application or the scanning parameters used. Some authors proposed systems for the correction of the distortion of the field of work within the workspace [5-6].

However, there is an additional source of error associated with the delay and advance times introduced to ensure no sudden changes in accelerations and corner interpolations. Such forward and delay times result in rounding errors edges and contours closures, depending on the feed rate. This means that the error depends on the feed rate. Although time can be adjusted, in a device such as a scanner, these parameters cannot be changed during the process. For this reason it is interesting characterize different process parameters and evaluating the error function of the feed rate used in each case for certain parameters. Thus, one of the aims of the work presented here is the identification of the main parameters of the scanner and quantification of the errors depending on the process parameters to define a process window with maximum feed rates depending on the expected accuracy.

On the other hand, some applications need larger workspace and accurate control of beam positioning. Commercial solutions are focused on marking operations and the programs used to control beam paths enable few control on beam positioning. To reach larger working areas, such us for remote welding or cutting operations, there is a necessity of the integration of the scan-head axes with the machine-tool axes. Thus, in this work a solution based on independent but synchronized programs is proposed to move both kinematics at the same time.

2   Scan-Head Error Parameter Definition

From literature and previous tests, a number of errors that directly affect the quality of the result were identified. The errors can be resumed in three different effects:

- Distortion of the processed area geometry.
- Overexposed areas in corners at high speeds.
- Delays in the laser on and off.

The motion is controlled using different commands. The errors take place between two successive operating commands execution, so previously it is important

to identify the motion commands correctly. The commands used are classified in jump, marking and polygon commands. The jump commands are used to make a displacement along a vector with the laser turned off. The marking command allows performing a movement along a vector with the laser switched on. Switching on the laser at the beginning and switching it off at the end. Finally, polygon command allows marking a polygon at programmed feed rate. Once the first vector of the polygon is marked, the laser remains on and executes the following vector of the polygon until the last vector of the polygon is marked.

3 Experimental Characterization of Workspace

Experiments were carried out in an adapted and retrofitted conventional milling machine KONDIA B500. In this machine the spindle was replaced by own developed laser processing multi-purpose head and all actuators and control unit were replaced (Fig. 1). The multi-purpose head includes two optical fibers coming from ROFIN FL010 1 kW fiber laser. A 600 microns fiber attached to a laser cladding nozzle and 100 microns fiber attached to 2D Hurry Scan 25 scan-head from SCANLAB. This scanner provides a work area of 120 x 120 mm and a maximum scanning speed of 7,000 mm/s and it is controlled by Visual Laser Marker (VLM) commercial software. VLM software is oriented to marking operations and includes correction parameters adjusted by the manufacturer.
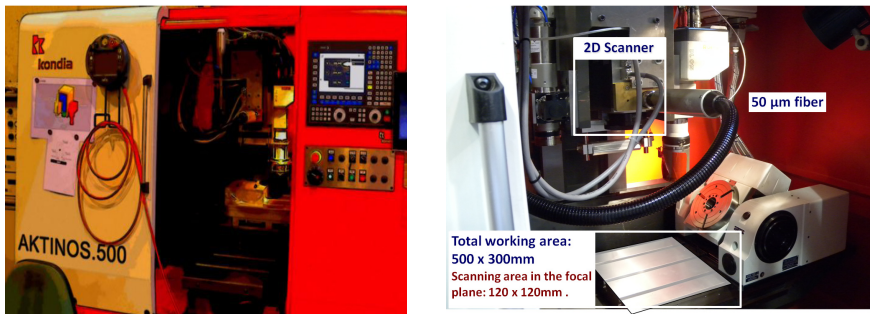

Fig. 1 Laser center with attached scan-head

The characterization was performed at two levels. In the first one it was necessary to study the influence of the errors in the focused marking area with the scanning speed. At the second level, the error at different points of the workspace was studied. So, in the first level two test were performed, first one to check the influence of the feed rate in the error, and the second one, to check if there is a variation in the feed rate when scanning direction is changed. The test consisted on rectangles of 11x11 mm and 8x8 mm marked at 7,000 mm/s and 500 mm/s respectively. The laser power was set constant at 50W.

In laser marking there are three main parameters that control path accuracy. These parameters are laser on, laser off and polygon delay, which represents the time taken by to switch on laser once the motion is started, the time to switch off before finishing the path and the time to start the motion of an axis when reaching a corner. These delays control over exposures on the part and the smooth motion, avoiding maximum acceleration and deceleration.

The delays were measured experimentally by marking an open rectangle at constant feed rate, as shown in Fig. 2 left and measuring the difference between theoretical path and the marked trajectory. Measured laser on delay was of 0.041 ms, the laser off delay was 0.141 ms and the polygon delay was of 0.186 ms.

To confirm that feed rate remains constant, various marking angles were performed at constant speed in pulsed mode as it is shown in Fig. 2 right. The distance between marked spots was constant, so feed rate remains constant independently of the marked angle.
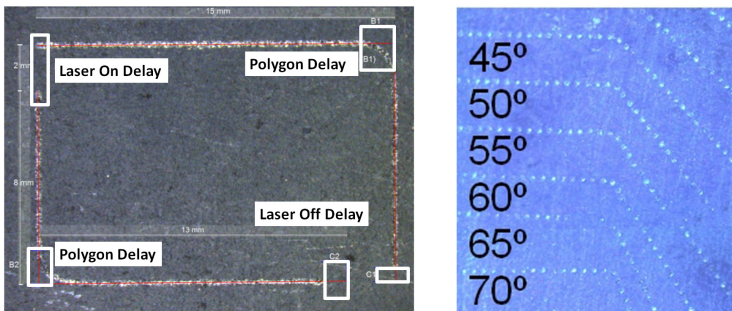
Fig. 2 Left) Laser on, laser off and polygon delay characterization test and right) feed rate test

With factory settings at speeds above 4,000 mm/s, the trajectory described by the scanner clearly deviates from the theoretical path in corners, being more noticeable the effect of the delay at higher feed rates.

At feed rates above 5,000 mm/s, the effect is also significant in the laser off and laser on delays, with unmarked segments within the target path. However, for feed rates below 1,500 mm/s it is given the opposite effect, where appear overexposed areas. In the same way it was observed that polygon delay has no relevant effect at feed rates between 1,000 mm/s and 2,000 mm/s because the delay time is high enough and there is no deviation from theoretical path.

Considering the results two different working configurations can be identified. With the manufacturing settings the scan-head was found to be adapted to scan speeds between 1,000 mm/s and 5,000 mm/s, whereas the maximum feed rate without inertia problems recommended by the manufacturer is 7,000 mm/s. Both, feed rates below 1,000 mm/s and feed rates above 5,000 mm/s have shown significant marking errors and need a laser on, laser off and polygon delay modification. With the solution provided by the manufactures with VLM control software these

parameters must be adapted to each working conditions and is not possible to work using whole range of feed rates.

Another point to consider is the accuracy at different points of the workspace. To find out this point another experimental test was carried out. The aim is to quantify the distortion in all the work area at different heights from the focal plane. A regular grid with maximum dimensions of 120 x120 mm was marked using a photo-sensible paper as it is shown in Fig. 3. Each rectangle of the grid presents a theoretical square shape of 2.5 x 2.5 mm and enables measuring the error at different points. The test were carried out at focal distance and defocusing the beam up to 50 mm. The results were measured using a profile projector MITUTOYO PJ - H3000 F.
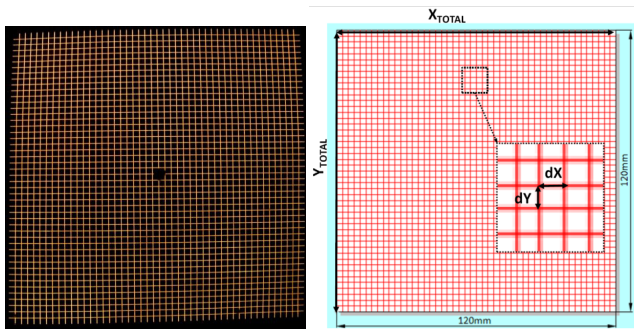
Fig. 3 left) resulting grid after marking photo-sensible paper and right) theoretical grid shape

To evaluate the result, first Y Total and X Total distances were measured with the results shown in Table 1.

Table 1 Work plane maximum dimensions for different offsets

ΔZ from focal plane [mm]	Duty Cycle [%]	Power [W]	X Total [mm]	Y Total [mm]	Feed [mm/s]
-20	100	1	112,005	115,555	200
-10	100	1	115,664	117,661	200
0	100	2	118,659	119,749	1000
10	100	1	122,429	121,412	200
20	100	1	125,836	123,218	200
30	100	1	129,229	125,447	200
40	20	50	132,104	126,859	200
50	30	50	134,706	129,022	200

Considering the shape distortion of the small squares (dX, dY), the deformation depends both, on the work plane position and defocusing distance. In order to study the maximum error rates, the measurement was carried out at the maximum defocusing distance ΔZ= +50 mm. This defocusing also corresponds with the working conditions in laser hardening process with scan-head, so it is of special interest to study the positioning errors within the working area in this situation. The results are shown in Fig. 4. The error is different in each axis due to the compensation parameters of F-Theta lens used to keep laser focused in a plane and with normal incidence angle to surface. To consider effects in both axes the error in the grid was calculated following mean square error formula Eq. (2).

$$E_m = \sqrt{E_{dX}^2 + E_{dY}^2} \, [\%] \tag{2}$$

Through these measures in defocusing conditions, which is a working situation in processes like laser hardening with scan-head, the central area of the work plane presents the highest error in absolute value (with distortion reaching 15 %), but it is the most stable area since no significant variation is appreciated within this area. In the border area the error is less significant, with minimum value of 7 %. However, in this area more variations can be appreciated between different working points. Thus, when defocusing the laser beam, the central workspace has to be considered the optimum area with reduced dimensions of 60 x 80mm.
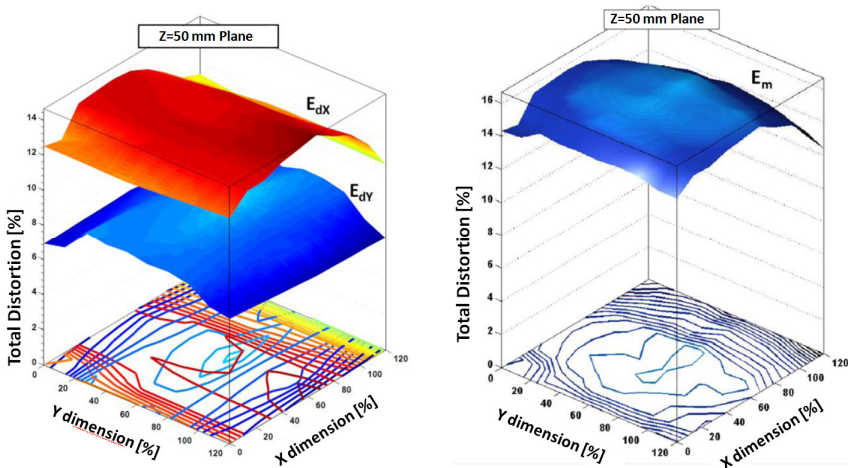

Fig. 4 Local distortion along the workspace in the plane Z = +50 mm

4   Machine Tool and Scan-Head Integration

Once characterized the scan-head motion is possible to develop an integration system for synchronized movement of both machine tool and scan-head. The proposed solution integrates both control programs in just one parent program.

However this control cannot be performed using marking software like VLM. The marking software is prepared to work with contours but gives no option to control the laser position. So, this software decides laser position using its own built-in algorithms and these cannot be manipulated externally.
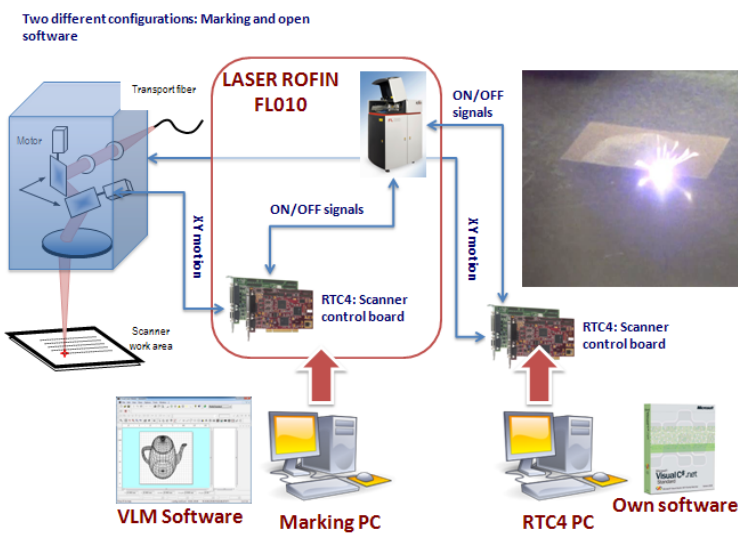

Fig. 4 Motion integration scheme

One option is to control laser movement independently using external programming executed towards the control card of the scan head. In this case programming based on vector movement sentences was carried out on external RTC4 SCANLAB control card. Following this configuration, the program runs directly using scan-head control code instead of using marking software as interface to generate the code.

Once direct programming of the scan-head is solved, it is necessary to integrate both motions: machine-tool and scan-head motion. This was solved starting from the CAD geometry of the target marking area and its division in two independent movements, machine-tool and scan-head motion. Thus, the machine performs long linear and slow motions while the scanner gives transverse motion at high feed rates. Characterization tests carried out previously showed that scanning speed remains almost constant even with direction changes. So, considering the scanning path and the programmed feed rate is possible to control the total time that takes executing the scanner program. In order to get optimal results it is possible to split the scanner motion in short programs to make synchronization easier. On the other hand, the machine-tool motion can be almost considered at constant feed rate since the trajectory is composed by long linear movements at slow feed rates. Once motions are decoupled the NC program controlling machine-tool actuates like a *parent program*. This program includes call sentences to scan-head to

execute the second level program. Fig. 5 shows schematically the proposed solution. Thus, following this scheme is possible to process large areas becoming an optimal solution for several processes like remote welding, remote cutting, laser polishing or texturing and laser scan-head hardening.

5   Conclusions

- The scan-head motion presents three ranges of accuracy considering feed rate: Below 1,000 mm/s, between 1,000 and 5,000 mm/s and over 5,000 mm/s.
- Each range needs different delay parameters values.
- The error of the scan-head in Y direction is significantly lower when compared with X direction.
- The most stable working area is in the center of the workspace. This is more noticeable for highly defocused working planes.
- The proposed solution enables synchronized motion of machine-tool and scan-head axes with external control of the scanner. This solution becomes very interesting for applications that need enlargement of the workspace.

References

1. Chen, M.F., et al.: A scribing laser marking system using DSP controller. Optics and Lasers in Engineering 46, 410–418 (2008)
2. Dumont, T., Lippert, T., Wokaun, A., Leyvraz, P.: Laser writing of 2D data matrices in glass. Thin Solid Films 453-454, 42–45 (2004)
3. Delmdahl, R., Tapie, J.L.: Excimer lasers drive large area microprocessing. Applied Surface Science 258, 9123–9127 (2012)
4. Chen, M.F., Chen, Y.P., Hsiao, W.T.: Correction of field distortion of laser marking systems using surface compensation function. Optics and Lasers in Engineering 47, 84–89 (2009)
5. Xie, J., Huang, S., Duan, Z., Shi, Y., Wen, S.: Correction of the image distortion for laser galvanometric scanning system. Opt. Laser Technology 37, 305–311 (2005)
6. Chen, M.F., Chen, Y.P.: Compensating technique of field-distorting error for the CO_2 laser galvanometric scanning drilling machines. Int. J. Machine Tools & Manufacture 47, 1114–1124 (2007)

Development of a Pneumatic End-Effector for a 3-DOF Robotic Local Structure

S. Kurtenbach, M. Kochniss, A. Cousin, and B. Corves

Department of Mechanism Theory and Dynamics of Machines (IGM),
RWTH Aachen University, Germany
{Kurtenbach,Kochniss,Cousin,Corves}@igm.rwth-aachen.de

Abstract. The handling system developed at the IGM enables a quick adaption of the kinematic structure to a new motion task through a modular and versatile concept. Several parallel kinematic robotic arms integrate an object in the kinematic structure by adapting to the object with the end-effectors. Current developments provide the manipulation only of ferromagnetic objects. This paper introduces the development process of an end-effector for a 3-DOF robotic structure using a design methodology increasing the range of objects to be manipulated. Through definition of a solution set with subsequent systematic analysis different concepts for a vacuum gripper are developed. Compressed-air is used as power supply. The robotic local structure is a spherical linkage where the pneumatic hose must be integrated.

Keywords: wrist joint, vacuum gripper, reconfigurable handling system, spherical linkage.

1   Introduction

Now-a-days parallel handing devices are used in various application areas. The Department of Mechanisms Theory and Dynamics of Machines (IGM) at RWTH Aachen University developed a new and innovative handling system basing on a reconfigurable structure with modular layout [1, 2, 3, 4]. The handling system moves the object with six degrees of freedom in space, using a parallel kinematic structure. This results only through the integration of the object using several robotic arms. This makes it a part of the parallel kinematic structure. Figure 1 shows the entire handling system with all three robotic arms adapted to the object. A single robotic arm has six degrees of freedom; three rotational degrees of freedom in the robotic regional structure and further three in the robotic local structure. The regional structure represents a hybrid structure. A planar five-bar linkage can be rotated around a previously located main axis of rotation. Drives (servo motors) are provided solely for the three degrees of freedom of the regional structure. The end-effector is operated in a purely passive form. This is to reduce the number of drives for the entire handling system to nine servo motors to move an object with three translational and three rotational degrees of freedom. Similar applications, in comparison, for three serial industrial robots require 18 drives.
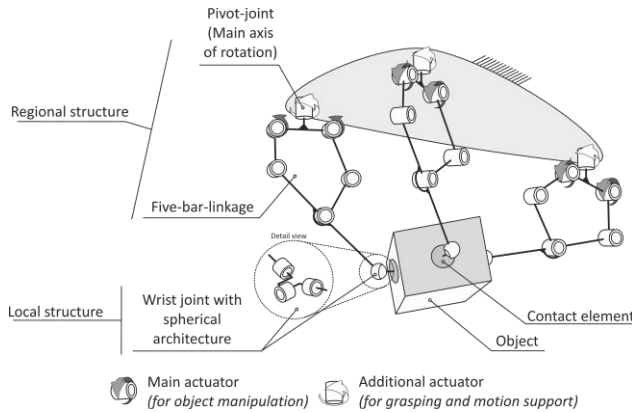
Fig. 1 PARAGRIP

The current local structure of the robotic arms comprises a spherical arrangement of the wrist. Figure 2a schematically shows the spherical structure with the notation of various axes. The integration of the object in the kinematic structure has been achieved in previous developments by using an electromagnet. This magnet represents the end-effector (Figure 2b). The electrical energy is passed through the entire spherical structure by collector ring contacts, which are provided on the corresponding axes of rotation. In order to avoid a collision between the wrist joint and the object during docking, the R-axis is equipped and actuated by a stepping motor, which serves merely to pre-position the wrist joint. It is switched passive immediately after the object has been gripped.
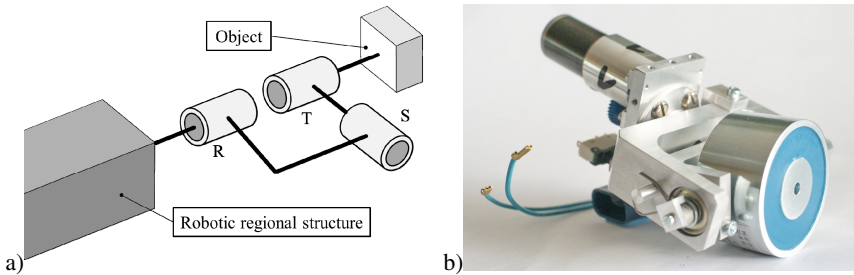
Fig. 2 Schematic representation (a) and image (b) of the current wrist joint

The S-axis has a balancing and restoring spring element that holds the solenoid in the center position while not in contact with the object. To meet the requirements in terms of low spring forces, the focus of design and construction of the end-effector must be on the S-axis. A disadvantage of the current contact principle is the required ferromagnetism of the objects. In this paper, the systematic development of two different end-effectors is presented. These wrist joints must have restrictive contact principles enabling the manipulation of any object independent of the material. Therefore, a vacuum gripper is developed.
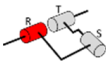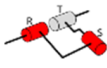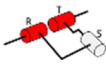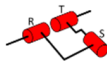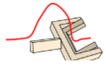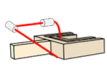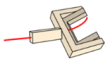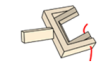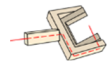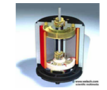
2   Requirements, Systematic and Solution Set

The development of the solution set of a pneumatic-end-effector for a 3-axis robotic local structure was been on the concept of design methodology according to Pahl/Beitz [5]. In a requirements list, all requirements for the local structure are documented. Based on the main feature list of Pahl/Beitz and the scenario technique, the most important requirements are determined.

Connecting and integrating the new developed end-effector to the existing structure of the manipulator is one of the main requirements. This puts additional restrictions on the geometry, the type of energy for actuation and the connectivity. To ensure a light and compact design of the end-effector; the main focus on the individual components and sub-assemblies is to have them as close to the respective axes of rotation as possible, in order to have low moment of inertia. The pneumatic hose for vacuum and the internal forces should not influence the movement and should not cause a collision of the assembly. To ensure a successful integration of the new designs in the overall handling system, the weight and size of these concepts should be comparable to that of an electromagnetic end-effector. From the kinematic point of view, it is required to have minimized moments of inertia about the three axes of rotation for the end-effector.

The following text presents the solution set of the concepts. Along with the various end-effector designs, various actuation principles and actuation concepts have also been introduced in Table 1.

Table 1 Solution set

Functions	1	2	3	4	5
Drive of the local structure	Driven R-Axis	Driven R- und S-Axis	Driven R- and T- Axis	Driven R-, S- and T- Axis	-
Hose pipe system	Outside, not mounted	Guided outside and mounted	Mount integrated in R- and T-Axis	Mount integrated in S- and T-Axis	Mount completely integrated
Rotational drives (Gripper orientation)	Electric servo drive with gearbox	Electric servo drive	Electric stepping motor	Pneumatic (Gear driven piston)	X No drive
Type of gripper	Flat suction pads (round or oval)	Bellows suction pads (round or oval)	-	-	-

Apart from the constraint that the S-axis is balanced and restored by a spring the S-axis and T-axis are free to rotate. This leads to a passive motion of the end-effector, as soon as the object is integrated in the multi arm structure. The adaptation of the wrist for different end-effectors may require additional drive axes. The drive of the R-axis for the pre-positioning of the end-effector can be combined with the drive of the S-axis or the T-axis for the entire coupling process. Regarding the hose pipe of the system, five sensible options can be considered. Similar to the drive of the end-effector, again, all possibilities are considered here generally and then only the most meaningful are selected for further analysis.

In the case of pneumatic components, there are many technological options to realize the hose pipe in the system. For example, pneumatic rotary joints could be used. For the synthesis of the new concept vacuum grippers are considered as end-effectors. Flat-suction pads or bellows-suction pads can be used, either with a round or an oval design. The gripper is dimensioned that the maximum load of the object (5 kg) can be held by just one wrist joint so that the object won't crash uncontrolled.
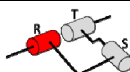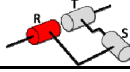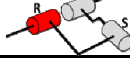
By sensible combination of established principles, various concepts are generated basing on the morphological constraints. At the end, the found principle combinations will be listed and evaluated with the following qualitative criteria (Table 2) and pre-selected with regard to the quality of the performance function.

The three principle combinations (PC) are illustrated in Table 3. They differ only by the type of hose pipe system. On base of the pre-selection the other functions turn out to be worse than the chosen ones. These may be integrated only in the R-and T-axes (PC 1); in the S-and T-axes (PC 2) or completely in all three axes (PC 3). This has the advantage that the pipe cannot collide or be wound up as it can be done in PC 1 and PC 2. The problem of integrating the end-effector into the local structure is solvable. The path of the hose pipe system through the local structure thus represents the crucial distinguishing feature amongst the three combinations and the much bigger problem to be solved.

Table 2 Qualitative evaluation criteria

Criterion
• Mass of the wrist joint
• Stiffness of the wrist joint
• Design space of the wrist joint
• Technical feasibility
• Mobility of the wrist joint (cable)
• Level of functional performance

Table 3 Principle combinations

	Drive of the end-effector	Hose pipe system	Gripper type
PC 1			
PC 2			
PC 3			

3 Concepts

The synthesis and the qualitative evaluation of the concepts is followed by a rough design of the combinations (Table 4). In order to ensure comparability with respect to objective and quantitative evaluation criteria, all concepts are designed towards a comparable detailing. Thus the general functionality of all the concepts is ensured by considering all the requirements. The main task is to reduce the installation space of the bearings and rotational joints on the axes of rotation. For a force-free hose pipe system, the rotary distributors are arranged coaxially to the roller bearings. Concept 1 shows the spherical wrist joint with the hose pipe fed through the R- and T-axes. The rotary distributor is used so that the axis of rotation lies on the S-axis itself. The focus of the assembly is that it restores itself on the S-axis, and also on the rotation axis. This requires the use of stronger return springs. In comparison, concept 2 shows the hose pipe through the stock of S-axis using a straight rotary distributor. Thus the return springs can be dimensioned smaller. The design and manufacturing of the most expensive solution is the concept 3, where the complete hose pipe system is integrated in the structure through a system of holes and piped connections. Rotation-symmetric flat-suction pads do not require to be adjusted before the coupling process in contrast to bellows-suction-pads. It is sufficient to maintain the drive of the R-axis and design the remaining axes passively. Particularly challenging is the integration of the rotary distributors. They are not designed to transmit forces, and therefore provide only a support so that the hose pipe is not damaged by internal twisting. In all three concepts, the rotary distributors are combined with mechanical bearings. The bearing on the T-axis is made up of a radially double-split body, through which its assembly and mounting ability are ensured.

Table 4 Concepts for the vacuum gripper

| Concept 1 | Concept 2 | Concept 3 |
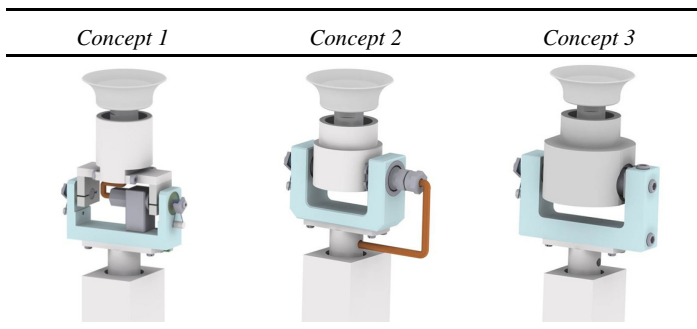
4 Evaluation

For the final selection based on the rough concepts described above, they are subject to the following evaluation [6]. The distinguishing features within the

concepts are compiled in the form of evaluation criteria. Subsequently they are weighted against each other in a preference matrix using a pair wise comparison. In the next step, all the concept-specific data are related and charged as per evaluation criteria. All the collected data are put into an evaluation scheme and a solution concept is determined. The evaluation criteria are determined using the previously created list of requirements and are shown in Table 5.

Table 5 Evaluation Criteria

Number	Criterion
1	Low Mass
2	Ease of design / manufacturing
3	Less construction space
4	Low restoring torque
5	Low mass moment of inertia
6	High postional accuracy
7	Low Cost

The total mass relates to the inertial forces which occur during the movement, as well as the static gravitational behavior of the robots local structure. The individual masses of the components can be determined using the CAD-System.

In order to facilitate the maintenance and easy replacement of components, attention is paid to ensure a simple design and easy manufacturing. Under simple design and low production cost all those criteria are summarized, that affect the number of components, assembly facilities and the level of complexity of individual modules and components. The evaluation can be done by direct comparison with each other. The design space is a direct measure of the compactness of the local structure and is important for a fast start-up movement for coupling to the object. These dimensions can also be found in the CAD-system.

In order to decouple the object, the restoring moment has to be overcome and the wrist joint must be brought back to a predefined position of the S-axis. Thus, in order to have a minimum restoring torque, the torsion springs must have the least possible stiffness.

To determine the restoring moments on the respective assemblies, the distance of their centre of gravity is measured from the axis of rotation and analyzed. The maximum restoring torque is obtained by multiplying the weight of the assembly with its distance to the rotation axis considering the worst case.

The mass moments of inertia can be used as a criterion for evaluating the dynamic behavior of the redesigned robot local structure. The mass moment of inertia has to be considered for all the three axes of rotation of the local structure.

For high positioning accuracy a high stiffness of the assembly and low backlash is required. The moving components must not influence the positioning accuracy of the system. Therefore, the internal reactions must be minimized.

The costs of the wrists are secondary, since it is a prototype. The main costs consist of the pneumatic rotary distributors and the bearings, which differ in number and type depending on the different concepts developed. For all concepts the production costs are nearly the same.

The summarized results of the evaluation are presented in Table 6. Concept 2 (hose pipe integrated into S- and T-axis) emerges as the winning concept from the evaluation. Concept 1 is only slightly worse. An exhaustively conducted vulnerability analysis shows the disadvantages of some concepts, those that could not be directly compared.

Table 6 Evaluation

Evaluation criterion	Weighting	Concept 1	Concept 2	Concept 3
Low mass	0,2	2	1	0
Ease of design	0,04	3	2	1
Low design space	0,22	2	1	1
Low restoring moment	0,2	0	2	1
Low moment of inertia	0,1	2	2	1
High accuracy	0,2	2	3	3
Low costs	0,04	3	2	2
Total	1	1,68	1,78	1,24

5   Further Design

Figure 3 shows the final version of the vacuum gripper basing on concept 2. The rotary distributors provided by manufacturers are comparably huge. They were exchanged by smaller ones, which are a proprietary development, so that the design space is reduced further. This reasons the complete integration of the hose pipe into the structure. Furthermore, the restoring spring-system was improved. The both torsion springs were replaced through compression springs, where an adjustment enables to define the necessary restoring force.
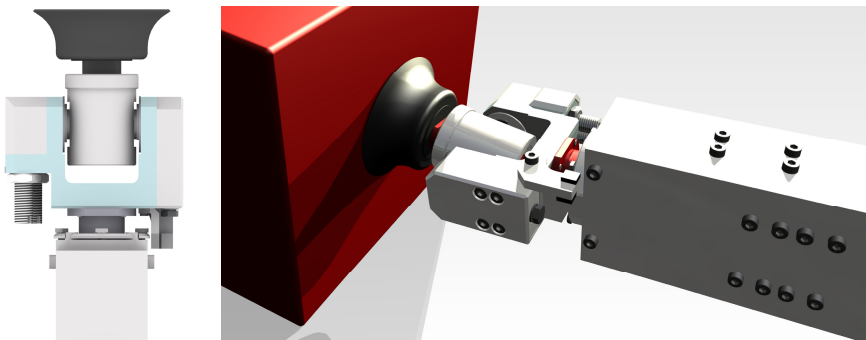
Fig. 3 Image of the developed vacuum gripper

6   Summary

This paper presents a conceptual approach to the development of a new wrist joint as end-effector for a parallel-handling device. With this end-effector – a vacuum gripper – objects can be moved in space with six degrees of freedom, regardless of their material properties. The local structure has three revolute joints and integrates the object into the kinematic structure.

Taking into account the requirements, a solution set is determined, which allows different concepts to be identified. These concepts are further designed in following steps. This allows a quantitative evaluation based on the extractable data from the CAD-system.

Finally the designed wrist joint is presented. The whole power supply for the end-effector – the pneumatic hose system – is completely integrated into the kinematic structure.

References

1. Müller, R., Riedel, M., Vette, M., Corves, B., Esser, M., Hüsing, M.: Reconfigurable Self-Optimising Handling System. In: Ratchev, S. (ed.) IPAS 2010. IFIP AICT, vol. 315, pp. 255–262. Springer, Heidelberg (2010)
2. Riedel, M., Nefzi, M., Huesing, M., Corves, B.: An adjustable gripper as a reconfigurable robot with a parallel structure. In: Proceedings of the Second International Workshop on Fundamental Issues and Future Research Directions for Parallel Mechanisms and Manipulators, pp. 253–260 (2008)
3. Müller, R., Corves, B., Hüsing, M., Esser, M., Riedel, M., Vette, M.: Rekonfigurierbares selbstoptimierendes Bauteilhandling. In: 8. Kolloquium Getriebe-technik Aachen 2009, pp. S.297–S.311. Verlagshaus Mainz, Aachen (2009) ISBN: 3-86130-984-X
4. Riedel, M., Nefzi, M., Corves, B.: Performance analysis and dimensional synthesis of a six DOF reconfigurable parallel manipulator. In: IFToMM Symposium on Mechanism Design for Robotics 2012, Mexico City, Mexico, September 28-30 (2010)
5. Pahl, G., Beitz, W., Feldhusen, J., Grote, K.-H.: Engineering Design - A Systematic Approach. Springer, London (2007) ISBN: 978-1-84628-318-5
6. VDI-Fachbereich Produktentwicklung und Mechatronik, Design engineering methodics - Engineering design at optimum cost - Valuation of costs. In: VDI 2225 Blatt 3. Beuth Verlags GmbH, Berlin (1998)

Enhancement of Mechanism Design Process by Interaction with Haptic Feedback-Systems

T. Kölling, M Hüsing, and B. Corves

Department of Mechanism Theory and Dynamics of Machines
at RWTH Aachen University, Germany
`{koelling,huesing,corves}@igm.rwth-aachen.de`

Abstract. The category of Haptic Feedback-Systems (HFS) is presented. These systems allow the operator to interact intuitively with a chosen simulation scenario. The systems reaction is unlike usual output tactile and kinaesthetic perceptible. The fundamentals of haptic will be illustrated as well as the basic structure of HFS. Subsequently a general survey of the state of the scientific and technical knowledge is given and fields of application are discussed. The process of mechanism design and development is emphasized. HFS are practically not used in this process up to now. The conventional procedures for dimensioning technical devices do not permit statements according ergonomic questions or perception of actuating forces. To allow proper evaluation usually a time-consuming and cost intensive prototype has to be built. The application of a universal HFS to interactively support certain phases of the mechanism design process is envisioned.

Keywords: mechanism design, design theory, haptic feedback, digital prototype, human engineering.

1 Introduction to Haptics

Haptic perception can be considered along with sight, hearing, smell and taste as one of the five human senses. It allows objects, their properties and external influences to be felt. In addition to pain and thermal stimuli, the different receptors of the human skin also register touch, pressure and vibration. According to [7, 8], the latter are received in particular by the Pacinian corpuscles, which have the fastest transmission properties, as they deal with changes in pressure speed and thus acceleration. Thus vibration frequencies of 100-400 Hz can be resolved. In addition, the distinction is made between superficial sensibility and proprioception. Superficial sensibility allows tactile perception, i.e. touch, by means of skin receptors. Proprioception, on the other hand, refers among other things to kinaesthetic perception, i.e. a sense of bodily movement as well as relative position and orientation in space afforded by different receptors in the muscles and joints. The main interest of this study is kinaesthetic perception alone or in combination with tactile perception.

2 Haptic Feedback-Systems

A Haptic Feedback-System (abbreviated below as HFS) is responsible for generating a perceptible haptic reaction on the basis of a selected virtual scenario and the effects on these scenarios.

2.1 Setup of an HFS

An HFS is composed of multiple components. The supposedly primary device is the input/output device. This is able both to import information about position (as a mouse does for a PC) or load and to create haptically perceptible feedback to the user. As the determining factor is the force, this is also referred to as "force feedback". However, cases of a qualitative, imprecise feedback are frequently included in this conception. But the overall system also comprises the connections, the data processing, the simulation model of the observed scenario and, in a certain sense, the user him/herself. A more accurate illustration of the individual mechatronic components of a general HFS provides Fig. 1.
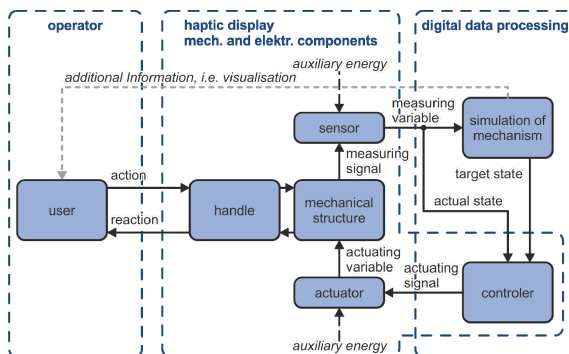
Fig. 1 Mechatronic structure of a generalised HFS

The user generally grips a handle. This handle may be specially designed for the particular application, but usually has a universal shape, such as a ball- or sylus-shaped handpiece. The user acts on the device by activating the handle, whereupon he experiences a reaction based on the simulated model. The handle therefore represents the immediate interface to the user and can be referred to accordingly as the "user interface" (UI). The handle is in turn connected firmly with the mechanical hardware. The concrete structure used for this mechanism is subject to variation. Typical structures are those with serial kinematics, i.e. the individual elements are always only connected with the next element via driven joints. Not quite as common are parallel kinematic structures, i.e. structures which the working platform connects with the frame via multiple branches. This induces both passive joints and the possibility of mounting the drives in the frame and of

thereby reducing the mass being moved, as shown in Fig. 2. Another viable option is a hybrid solution combining both of the above. Depending on the implementation, the mechanism used offers a varying range of movement.
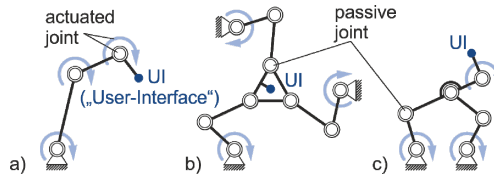
Fig. 2 Structures of movement units (here: 3 DOF)

According to the implemented control approach sensors are used to measure kinetic and/or load values on the mechanism. These measurements are sent to the simulation and the controller for data processing. In the simulation, a setpoint is calculated on the basis of this input quantity and the other parameters usually predefined prior to beginning the simulation and provided to the controller. Via electromechanical actuators, the controller induces a transfer of the mechanism and thus a perceptible feedback to the user. As these components would leave the user in the dark, an additional visual feedback (e.g. a monitor or a HMD/HUD for higher VR-immersion) of information is almost imperative. The control and output unit in this regard is what is referred to as the "haptic display". An HFS also includes the computer hardware required for simulation and control and the required software. If the simulation routines are not implemented on the host computer, the system may also include executing target computers. Because an immediate interaction takes place with the user, the data has to be processed in real-time. Due to the responsiveness of human sensory organs as described in the first section, in haptics typical clock rates are 1 kHz or higher for individual systems.

2.2 Control Concepts

According to [2], three basic control concepts for kinaesthetic feedback systems must be distinguished which have varying requirements with respect to hardware and in particular the sensor system used. The most widespread concept applied in HFS is that of "open loop impedance controlled systems", as it has the lowest technological requirements. The only measured quantity is the position (or sometimes the orientation) of the user interface (UI). This value enters into the simulation and is compared by the controller with the setpoint value in order to induce a force or torque as feedback. Another concept is that of "closed loop impedance controlled systems". In this case, the sensors also provide the force/torque as a control variable. The position is only required for the simulation. Finally, "closed loop admittance controlled systems" are also imaginable. Unlike the other concepts, here the position and orientation represent the retroactive variable controlled via the force and torque deviation.

2.3   Common Applications of Feedback-Devices

Haptic feedback systems are typically implemented when additional force feedback represents a possible further use or a condition for use at all. An overview of different applications provides Fig. 3.
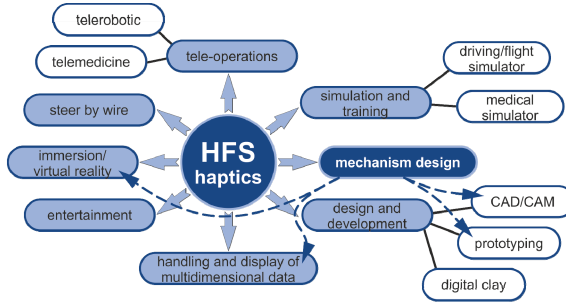
Fig. 3 Conventional and new areas of HFS-applications

HFS clearly enjoys the broadest use in the entertainment and handheld industries. However, it is only used here to produce technically rather imprecise vibrations as tactile feedback, e.g. as alarm signal for calls or when activating virtual buttons of a touch screen. A large area of application and research is that of tele-operations. Through HFS, the user receives information about which strains are being placed on the executing unit. Only this makes it possible, for example, to conduct medical operations from a remote location or to handle hazardous goods. Haptic feedback makes acting within a virtual world all the more realistic. Training simulations of medical interventions, such as injections or laparoscopic operations, as well as of road vehicle or aircraft applications can only reasonably approach the goal of the greatest possible realism by using a haptic feedback system. Other applications include handling complex data volumes, designing and drafting, e.g. when modelling freeform surfaces or collusion monitoring.

3   State of the Scientific and Technical Knowledge of HFS

In addition to the international commercial providers, there are a large number of users, some of which make modifications, and research groups who develop entirely new devices. The application conditions imply a broad spectrum of device requirements. In addition to device specifications like the number of degrees of freedom, resolution and repeat accuracy, as well as the achievable rigidity, the size of the workspace and the feedback force are important for selecting a device. Typically, a force feedback is constantly provided according to the position or vice versa. For this reason, the market overview provided in Fig. 4 maps the workspace over the maximum achievable force. The dimension used for the workspace is, on the one hand, the length along the main axis of the specified effectively

usable workspace and, on the other, the largest length that can be registered. As there are many non-commercially developed devices for which the specifications are not always available, the overview represents selected prominent devices and e.g. most telesurgery systems (compare Fig. 3) are excluded.
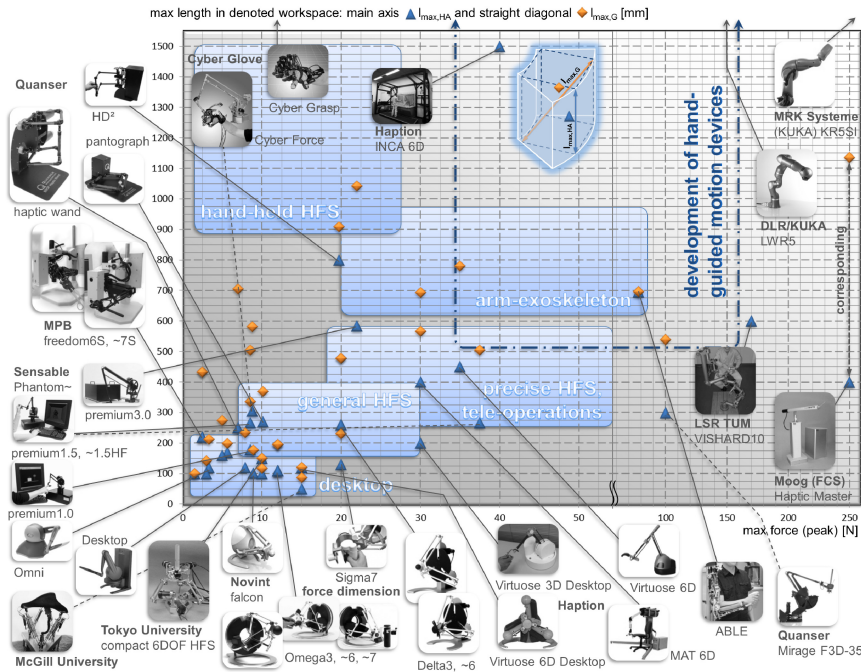
Fig. 4 Overview of current HFS (sources: see manufacturers' data in figure)

The represented range of haptic feedback devices can be subdivided into individual sections as in the figure for the sake of simplicity. The largest range of products is that of desktop devices with a correspondingly small workspace and force potential. This transitions to the area of general devices with enhanced properties. Some applications, for instance teleoperations, require a certain magnitude, while some designs, such as exoskeletons for fastening on the arm or portable devices, e.g. which individually act on the fingers of one hand, already possess this. The structure variations described in Section 2.1 can all be found here.

4 Usage of HFS in the Designing Process

As shown in [4], the use of an HFS in the mechanism designing process is very promising. The following will first discuss the generalised process and then the application advantages of an HFS before finally depict some implementations.

4.1 Designing Process for Hand-Guided Motion Devices

When considering the general designing process it is apparent that almost any description contains analytic processes. The entire design process can be subdivided into subordinate phases. They range from gathering the requirements to the finished product. An outline based on [3] shows Fig. 5. If the objective of the process is to develop a mechanism as a motion device, then according to [5] the sequence of synthetic activities is accompanied by analytic processes in which it is decided whether the results of the preceding phase are suitable for the further designing phases. The next phase can only be entered after a positive conclusion. Otherwise, a return to the preceding phase for improvement is required. The process is therefore strongly recursive in character and is only executed linearly in exceptional cases. After the conclusion of the final examination, an evaluation of the design solution is made which ensures that all requirements have been fulfilled.
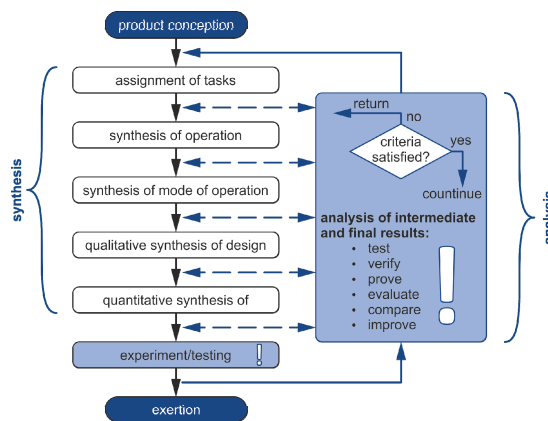
Fig. 5 Structure of the mechanism design process according to [3, 5]

When designing motion devices, [1] cites the structural synthesis, i.e. determination of the optimal kinematic structure, as well as the dimensional synthesis, i.e. the determination of the optimal kinematic dimensions, as being particularly important. Synthesis is intimately connected with analysis, as the kinematic and dynamic properties must be determined and checked.

4.2 Assistive Use of HFS during Mechanism Design

It is evident that the evaluation and assessment at the end of each design phase represents a central, recurring and essential part. Conventional analytic tools offer, for example, a calculation of maximum forces or a path of movement, possible also a force developing superimposed over this in the form of a hodograph. However, an assessment with respect to ergonomic questions or those of human

capability can be difficult in certain situations. Anthropometric standards also fail to offer a basis for decision in this case, as there are generally no specifications of distribution of capable forces in the workspace. This makes it necessary either to make do with an estimation or to produce a prototype as a physical test setup. According to [6], models and prototypes are often already appropriate in the early concept phase but unusual.

When using a suitable HFS, however, it is possible to develop this prototype digitally and to apply it as an enhancement of the conventional digital mock-up.

For this purpose, the previous results are used at the end of the development phase to construct and parameterise a simulation model. This can then be used to create haptic signals via the HFS. The use of a digital virtual prototype together with the output possibility of a universal HFS thereby provides the use in early phases of development, simplifies direct comparisons of multiple variants, as only parameters have to be altered digitally, and dispenses with the time- and cost-intensive usage of physical prototypes. In addition, the lower amount of effort required for an existing HFS allows an earlier and more frequent use of a proto-type. According to [4], statements can also be made with respect to handling, con-venience and ergonomics. The statements gained are occasionally subjective and can be used in point scales, as for example with the common method of cost-utility analysis. This way, the entire process can be improved and even acceler-ated, which in turn corresponds to the Rapid Product Development (RPD) approach.

When limiting the scope to the designing process of hand-guided mechanisms, it is striking that these usually represent planar guidance mechanisms. A work-space of al least 0.5 m in one axial direction with a force feedback of approx. 35-150 N seems plausible. The resultant area is also indicated in Fig. 4. An ac-cordingly adequate device for this application would therefore have to be derived from this area or meet even higher specifications as well as cover the remaining requirements. In contrast to most teleoperations a reality like, quantitative exact behaviour is seeked. As the motion devices which come into question for simula-tions often only use part of the path, stops must most probably be provided at the end positions. According to [2], closed loop admittance control is therefore the best choice, as it affords quick reaction behaviour and, at the same time, high ri-gidity. - The described area of application and the interfaces to the preceding areas are added in Fig. 3.

4.3   Scenarios of Implementation

A large number of applications are imaginable for the strategy described above. Fig. 6 shows a tailgate mechanism, a window system and a kitchen wall unit, all of which require an initiating hand-activated motion. The mechanical structures are straightforward and have a staggered arrangement symmetrical to the handle. However, unsymmetrical cases, such as kitchen corner units, are also conceivable.
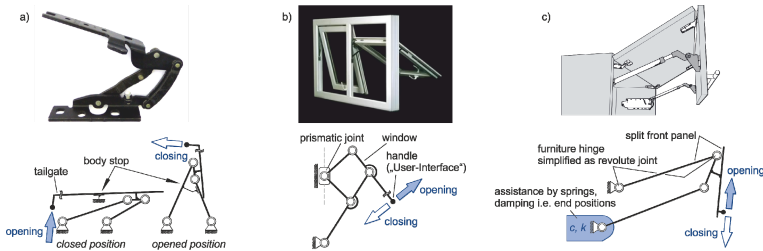
Fig. 6 Selection of hand-guided mechanisms: a) car tailgate, b) window opening to the outside - Neptun Outside from Alpina Hochwasserschutzfenster GmbH (source: www.lantenhammer.net), c) kitchen wall unit - Aventos HF from Julius Blum GmbH (source: www.blum.com)

5   Conclusions

This study gives an introduction to haptics and the principles of haptic feedback systems. It explains the structure of such systems and the most important system properties. In addition, the study shows which areas already make use of haptic devices and provides an extensive overview of commercially available devices and research work. Finally, the conventional designing process for hand-guided mechanisms is introduced, on the basis of which the idea is developed of how the interactive use of universal HFS can improve this process by increasing effectivity and lowering costs already in early developmental phases. The use of HFS can lower prototype costs and enhance the digital prototyping. Requirements are defined in reference to the market overview and the illustrated application scenarios.

References

1. Kerle, M., Pittschellis, R., Corves, B.: Einführung in die Getriebelehre – Analyse und Syntheseungleichmäßig übersetzender Getriebe. Teubner, Wiesbaden (2007)
2. Kern, T.A. (Hrsg.): Entwicklung haptischer Geräte, pp. 97–104. Springer, Heidelberg (2009)
3. Koller, R.: Konstruktionslehre für den Maschinenbau – Grundlagen zur Neu- und Weiterentwicklung technischer Produkte, pp. 74–83. Springer, Heidelberg (1994)
4. Kölling, T., Hüsing, M., Corves, B.: Möglichkeiten der Einbindung eines haptischen Feedback-Systems in den Entwicklungsprozess von Mechanismen. In: Beiträge der Ergonomie zur Mensch-System-Integration, Manching. DGLR-Bericht Bonn (2008)
5. Niemeyer, J.: Methodische Entwicklung von Prinziplösungen bei der Auslegung ungleichmäßig übersetzender Getriebe unter Verwendung eines praxisorientierten interaktiven Wissens-speichers. Dissertation, IGM RWTH Aachen (2002)
6. Pahl, G., Beitz, W., Feldhusen, J., Grote, K.-H.: Konstruktionslehre – Grundlagen, p. 199, 566–567. Springer, Heidelberg (2007)
7. Schmidt, R.F., Thews, G. (Hrsg.): Physiologie des Menschen, pp. 216–221. Springer, Heidelberg (1997)
8. Silbernagel, S., Despopoulos, A.: Taschenatlas Physiologie, pp. 316–319. Georg Thieme, Stuttgart (2007)

Giuseppe Antonio Borgnis and Significance of His Handbooks on Representation and Terminology of Machines

Michela Cigola and Marco Ceccarelli

University of Cassino and South Latium, Italy
{cigola,ceccarelli}@unicas.it

Abstract. This paper presents considerations on the valuable contributions of Giuseppe Antonio Borgnis in the 19-th century developments on Mechanism Design in terms of representation of machine mechanical designs and terminology for the rising discipline on Theory of mechanisms.

1 Introduction

A need to survey available variety of machines arose since Renaissance both to show designers' expertise and to attempt classification of mechanisms and machines, [3]. A tradition was established with the Theatrum Machinarum treatises that evolved into technical handbooks in 19th century during Industrial Revolution. The book collection by Borgnis is one of the first of those technical handbooks of machinery in which a historical background is still present but it also contains novel characters in terms of contents as well as approaches of presentation of machines. The Borgnis handbook collections started a modern discussion and elaboration of machine classification that was initiated by Monge's concepts in the milestone work by Lanz and Betancourt in 1808, [5]. Even the presentation of machine designs is attached with modern perspectives of technical views with the aim to direct a machine survey specifically to professionals of a technical community growing rapidly.

This paper is an attempt to identify those characters of novelty in Borgnis handbook collection mainly as related to graphical aspects of drawing representation as results of such a technical approach for a technical community. In this study examples of machine representations are reported to show an evolution of graphical representation operated by Borgnis as linked both to a modernization of that time for traditional machines and enhancement of machine performance in old and new solutions.

2 Biographical Notes on Giuseppe Antonio Borgnis

Giuseppe Antonio Borgnis, Fig. 1, was born on April 15, 1781 in Craveggia, Italy, from a well established family since the father Giovanni was a banker in Paris. He was well educated with special interest on mathematical disciplines and although the revolution time affected the family he was able to graduate as engineer. He got a position as naval engineer in Venice where he gained so valuable expertise to write a book on machines on 1809. This gave him a good reputation and got the possibility to attend the Ecole Polytechnique in Paris. During this period he deepened his expertise on machine design both on theoretical studies and practical applications. He evolved views from the Monge's approach as to propose his own classification on mechanism variety for machine applications, [5]. Developing in more details his views he published ten books from 1818 up to 1823 [1-2], as a handbook on machine designs and applications, as a practical implementation of his new classification for an overall view, Fig. 2 b), [1]. Once returned in Italy he got the position of professor at the University of Pavia where because of his repute and further activities he became also rector in 1848.

He was well reputed professor of applied mathematics and civil transportation architecture, as combining his interests and activities in theory and engineering designs, during the first period of industrial revolution all around Italy, although he was in the north east state within in the Austrian-Hungarian Empire.

Fig. 1 A portrait of Giuseppe Antonio Borgnis (1781-1863)

(The grand-grand child Massimo Borgnis is thankfully acknowledged for the portrait and additional biographical notes)

3   Handbooks by Borgnis

The encyclopedic handbook is organized by Borgnis from a classification over-view up to specific studies of category of machines, by discussing design and operation characteristics, [1]. A last book is on terminology with synthesis of concepts and understanding of terms that are related to design, operation, and manufacturing of machines. In particular, the content of those volumes [1] is summarized in the following:

1 – **"De la composition des machines"** (450 pages, published in 1818), Fig.2, which contains classification and description of mechanical devices in agree-ment with the approach proposed by Gaspard Monge. The treatise is com-pleted with drawing of 1,200 mechanical devices, which are also compared in term of figure and operation characteristics. The classification is summarized in Tables, which give a synopsis of available mechanisms at that time.

2 – **"Du mouvement des fardeaux"** (334 pages, published in 1818), which con-tains a description of mechanical design and operation characteristics of the machines that can be used for transportation and lifting all kind of weights.

3 – **"Des machines employées dans les constructions diverses"** (336 pages, published in 1818), which describes the design and operation of machines that are used for construction in the field of civil engineering, hydraulic engineer-ing, naval engineering and military applications.

4 – **"Des machines hydrauliques"** (295 pages, published in 1819), which con-tains an overview of machines that can be used in hydraulic systems. An in-depth study is reported for machines applied in agriculture and mining.

5 – **"Des machines d'agriculture"** (295 pages, published in 1819), which con-tains description of equipment and machines used in agriculture. Detailed stu-dies are reported on mechanisms that are used for harvesting machines, winding and drilling machines, and devices for production of oil and wine.

6 – **"Des machines employèes dans diverses fabrications"** (285 pages, pub-lished in 1819), which contains the description of machines used in industrial plants for production of metal components, paper products, textile manufac-tures, and tannery products.

7 – **"Des machines qui servent à confectioner les ètoffes"** (335 pages, published in 1820), which contains description of procedures for spinning of vegetal or animal material, comparative analyses of mechanical means for industrial spinning and equipment of different kind of machines for different kind of products in textile manufacturing.

8 – **"Des machines imitatives et des Machines théatrales"** (285 pages, pub-lished in 1820), which contains a description of mechanical device that are used for any kind of transportation and movement, including devices mimick-ing animal motions. The text includes an Appendix with interesting descrip-tion of old machines for theatres and how to adapt their use to current needs and other aims.

9 – **"Thèorie de la Mecanique usuelle"** (published in 1821), which contains an
   introduction to the mechanics applied to practical industrial applications and
   refers to principles of Statics, Dynamics, and Hydraulics. Detailed descrip-
   tions and formulation are presented on main mechanical transmissions.

Borgnis completed the encyclopedic work with publication of the **"Diction-
naire de Mecanique appliquèe aux arts"** in 1823, [2]. This is a brilliant synthet-
ic dictionary with technical terminology for Mechanical Science, with a vision
anticipating the modern time that lead only in 2003 to IFToMM terminology, [4].

The encyclopedic work by Borgnis on mechanisms and machines in 9 volumes
was used as reference handbook by practicing engineers along the whole XIX
century, as a first modern technical handbook, in Italy and in whole Europe. It was
also considered as reference for further studies on classification and evolution of
mechanical engineering handbooks.

Borgnis attached the variety of machines by looking at practical aspects from
successful operations. Thus, his classification is an amplification of the theoretical
approach of Monge in indicating operation characteristics as related to the action
of motor components and output purposes of machines. The background of me-
chanism analysis is till persistent as shown in table 2 b) from the first volume, but
the structures are more near to full machines than basic mechanisms. In fact, as
indicated also of the organization of machines in the above-mentioned volumes,
Borgnis focused the attention on full machines and important has considered the
mechanical and operation performance of functioning in quite long descriptions
and discussions.

a)   b)
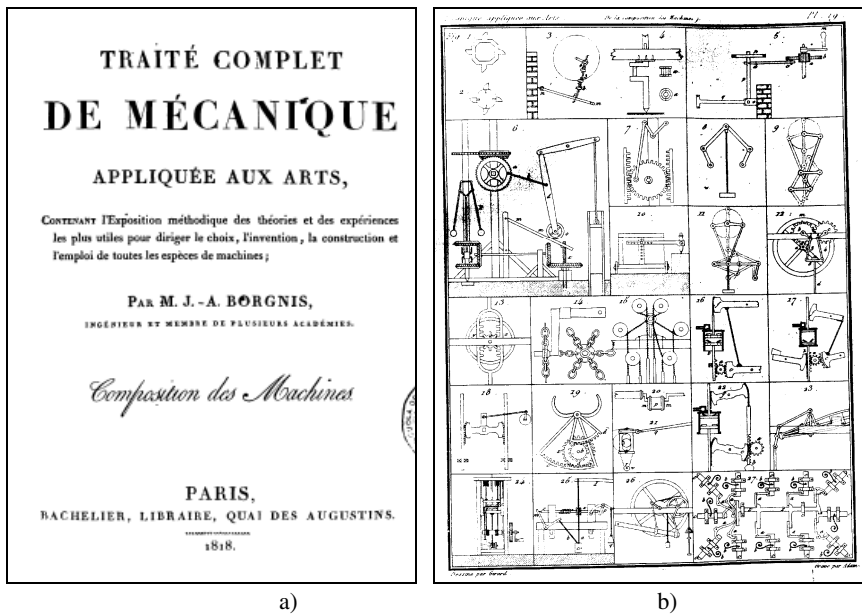
Fig. 2 Mechanism classification by Borgnis: a) book title page; b) part of a summary table

4 Machine Representation

The machine representation by Borgnis with clear drawings is considered part of the presentation and discussion of machine properties even for further developments. Although he represented machines with drawings of mechanical design along the well established tradition, nevertheless he attempted to advance technical representation of machines in approaching descriptions with essential characters for a full understanding by professionals (not really a large public) whose community was growing rapidly within the merging Industrial Revolution. Few examples of those aspects are commented in the following

Figure 3 a) shows a water pump system whose drawing is within a tradition of the representation of hydraulic machines that appear frequently in the manuals and texts since the oldest times. Everything is drawn with strong definition and precision. The drawing of mechanical parts is synthetic and essential, while the drawing of the building in which the machines are located, is expressed with more naturalistic representation, such as a pictorial figure of stone pieces in the walls.

Figure 3 b) demonstrates clearly the French formation of Borgnis as focused on Encyclopèdie by Diderot and D'Alembert. In fact, the clock assembling recalls very closely a table of Encyclopèdie, but nevertheless the representation is much more concise with less characteristics towards chiaroscuro and decorations. This is a sign that Borgnis well understood coming trends towards abstraction and synthesis that characterizes the modern technical drawing as directed to professionals.

a) b)

Fig. 3 Machine designs by Borgnis: a) a water pump system; b) clock assembling

a) b)

Fig. 4 Mechanism designs by Borgnis: a) a on-field crane; b) mechanical system for gun production

Fig. 5 Machine design by Borgnis for a textile manufacturing system

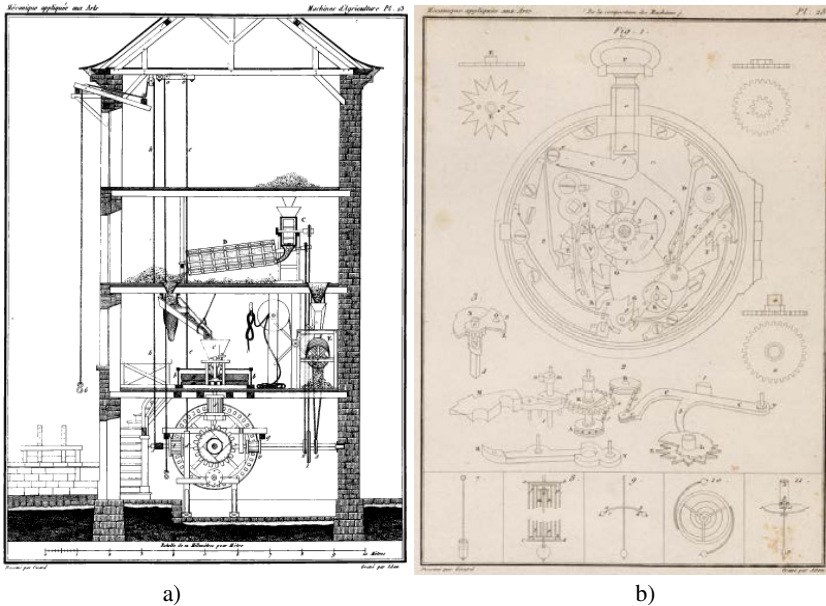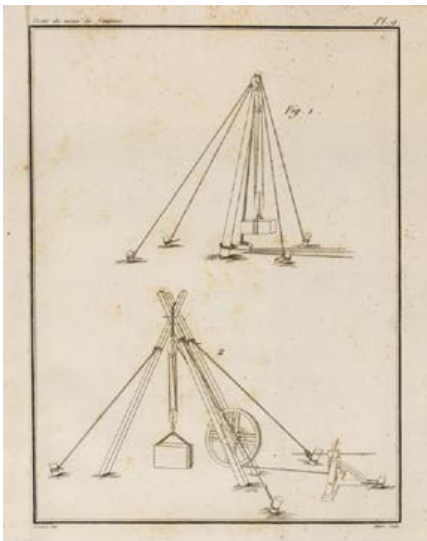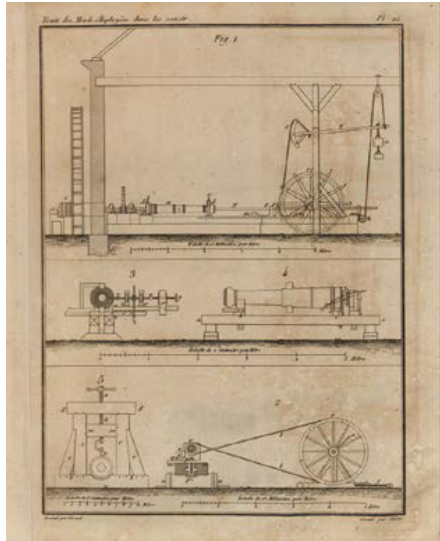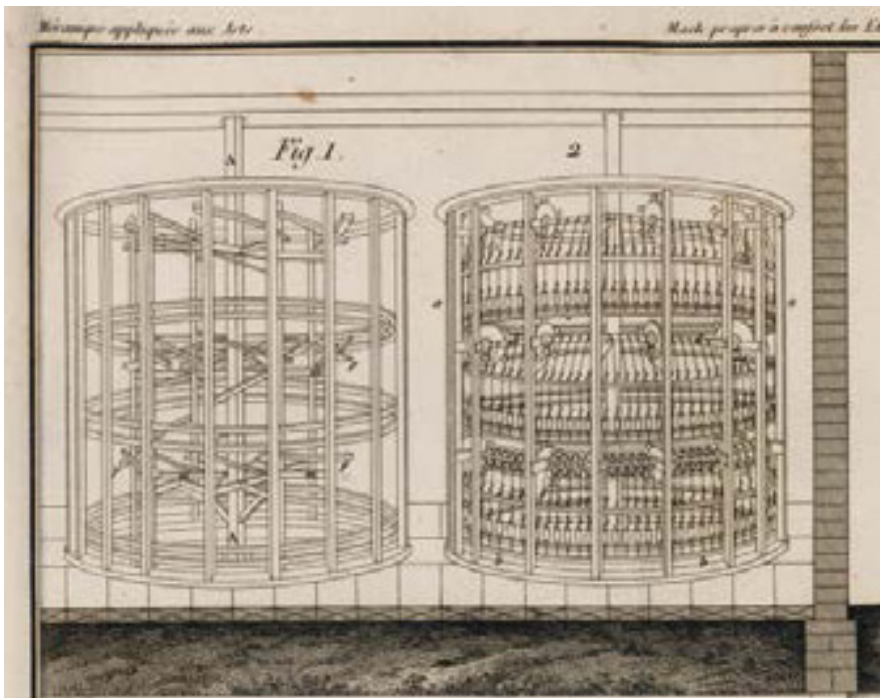Figure 4 a) shows one of the machines that are part of patrimony of ancient technological heritage. The same machine are presented by Vitruvius in De Architectura book X. We can find this type of machine for lifting weights (on-field crane) in all editions of Vitruvius, since Frà Giocondo edition in 1511 to Perrault's French edition of 1673. In this drawing Borgnis seems to be inspired by Perrault edition, [7], but even in this case he deleted graphic complacency and landscape details as to focus on the device and its functioning only.

Figure 4 b) is another proof of the importance of French period in Borgnis' formation and later professional experience. He studied at the École Polytechnique, where he certainly came into contact with Gaspard Monge. In this figure he recall almost exactly Monge text on guns [6], bringing nearly identical portions of the plates of Monge. Even in this case, the drawing is more concise without shadows that enriched the volume of objects as represented by Monge.

Figure 5 presents a textile manufacturing system which you can find in many of the treatises of Theatrum Machinarum from the 16th and 17th century. Also in this case the Borgnis' representation gives the object without decoration that can confuse the attention of a professional reader. Even machine location is indicated with synthetic and concise frames as focused on the functioning of the machine, although the representation of the cylindrical complex is not without a certain graphic virtuosity.

5   Machine Terminology

The technical presentation of machines led Borgnis to the need to identify and to collect a commonly accepted terminology for machinery as a natural complement of the language of a graphical representation. The 10th volume of the handbook is on terminology as a milestone work attempting a technical dictionary that today is well recognized necessary in all scientific areas, as stated in the several standards of ISO. In the specific area of machine design Borgnis started a need that was solved only in 1990_s within IFToMM activity leading to the last IFToMM collection of standardization and terminology in 2003, [4].

As Borgnis stated in the book preface, the terminology collection is aimed to summarize the most used terms on machinery with a well defined and accepted understanding. Examples are reported in this paper to show the synthetic characters but technical clarity of Borgnis description of the terms. A comparison is proposed with the corresponding IFToMM terminology. Machine is described by Borgnis as "general name that is used for several combinations of mechanical devices which are used frequently in Industry. Within the Statics treatment, it is possible to distinguish the names of elementary machines of lever, pulley, inclined plan, screw, wedge and belt machine". In IFToMM machine is defined as "Mechanical system that performs a specific task, such as the forming of material, and the transference and transformation of motion and force".

While in IFToMM even the term of mechanism is specifically described, in Borgnis terminology it is not defined. But specific components are properly indicated, like for example a crank is described as 'a link that rotates about an axis and at whose extremity is applied a force. There are cranks with simple, double, triple structure". In IFToMM a crank is "a link able to rotate completely about a fixed axis".

Borgnis specified terminology also for machine operation within the definition of a term. Thus, for example he defined as lifter a combination of gears with a worm and a crank whose aim is to produce a large force through a small sized device. Within brackets he indicated to refer to the motion of weights as additional characterization of the device. In general, definitions of terms by Borgnis are synthetic but additional indications are suggested to a reader as to refer to other terms. In addition specific hints are given to mention literature on arguments of a wide topic. For example in specifying the term steam, as also referring to steam machines, Borgnis added a quite long list of references on the topics, even by mentioning past designers like Watt, Wolf, and Evans.

Thus, the terminology by Borgnis contains technical definitions and operation descriptions with theoretical background including historical notes and indications of common applications.

6   Conclusions

Giuseppe Antonio Borgnis was a personality in TMM developments in the first half of 19-th century both for his life activity and his works. In this paper we have stressed his contributions mainly in term of machine design as graphical representation combining with the novel need of a terminology for a common understanding both by professionals and users.

References

1. Borgnis, G.A.: Traitè complet de mecanique appliquée aux arts, Bachelier, Paris, 9 vols., pp. 1818–1821
2. Borgnis, G.A.: Dictionnaire de mecanique appliquèe aux arts, Bachelier, Paris (1823)
3. Ceccarelli, M.: Classifications of mechanisms over time. In: Proc. of International Symposium on History of Machines and Mechanisms, HMM 2004, pp. 285–302. Kluwer, Dordrecht (2004)
4. Ionescu, T. (ed.): Special issue: Standardization and terminology, Mechanism and Machine Theory, vol. 38 (2003)
5. Lanz, J.M., Betancourt, A.: Essai sur la composition des machines, Paris (1808)
6. Monge, G.: Description de l'art de fabriquer les canons, Paris (1794)
7. Perrault, C.: Les dix livres d'architecture de Vitruve, Paris (1675)

A Comparative Study on Application of Decomposition Method in Function Generation Synthesis of Over-Constrained Mechanisms

O.W.N. Maaroof[1] and M.İ.C. Dede[2]

[1] Mosul University, Mosul, Iraq
 `omarmaaroof@uomosul.com`
[2] İzmir Institute of Technology, İzmir, Turkey
 `candede@iyte.edu.tr`

Abstract. Double-spherical six-bar linkage is one of the Bennett over-constrained 6R linkages. Kinematic synthesis of such linkages can be tedious and impossible to solve for analytically. In order to cope with higher number of unknowns in these types of linkages, decomposition method is a valuable tool. This paper focuses on the function generation synthesis of double-spherical six-bar linkage. Two procedures for applying decomposition method are explained. Two numerical studies are conducted for both procedures to evaluate the performance of each procedure.

Keywords: Kinematic Synthesis, over-constrained Mechanism, double-spherical six-bar mechanism, interpolation approximation, equal spacing, decomposition method.

1   Introduction

There have been numerous studies on kinematic synthesis procedures for spherical four-bar linkages to solve for path generation [1], function generation [2, 3, 4, 5]. Also, there have been recent studies on function generation synthesis with increased number of independent parameters [6].

   The nonlinearity in analytical equations increases as number of independent parameters increases. Hence, function generation of linkages with higher number of independent parameters can become very tedious if not impossible to solve for analytically. This study focuses on the decomposition method, which is presented in [7], to decompose the double-spherical six-bar linkage into two serially connected spherical four-bar mechanisms with a passive revolute joint in between. Validity of such a method and the explanation of the synthesis procedure was given in [8] and also briefly discussed in Section 2 and 3 respectively.

   Aim of this paper is to investigate and evaluate two possible procedures in using interpolation approximation method for function generation of double-spherical six-bar mechanism. Through this investigation, findings can be extrapolated for remaining Bennett over-constrained 6R linkages.

2   Description of the Double-Spherical Six-Bar Linkage

A mechanism with a single general constraint, such as double-spherical six-bar linkage, has motion in subspace $\lambda=5$. Six revolute joints are arranged in such a way that while joint axes of first three are intersecting at one center, joint axes of remaining three intersect at a different center. In Fig. 1, joint axes that denote these two groups of three revolute joints are S_{14}-S_{12}-S_{10} and S_6-S_4-S_2. It must be noted for readers that vectors are denoted with bold fonts throughout this paper.

   Decomposition method enables to decompose this linkage into two spherical four-bar mechanisms by adding a passive revolute joint whose rotation axis is aligned with virtual line that connects two centers that was described in the previous paragraph. Rotation axis of passive joint is denoted with S_8 in Fig. 1. Therefore, passive joint is included in both spherical four-bar mechanisms that can be separately indicated as S_{14}-S_{12}-S_{10}-S_8 and S_8-S_6-S_4-S_2 spherical four-bar linkages. Overall, for input-output function synthesis of the double spherical linkage, mechanism is described as two spherical four-bar linkages as shown in Fig. 1. It can be observed from Fig. 1 that as passive joint, $\widetilde{\psi}$, is output for the first spherical mechanism with input ϕ, it is also the input of second spherical four-bar mechanism that has output denoted as ψ. In order to relate unit vectors assigned in Fig. 1, transformation unit vector equation described in [9] is used. With respect to formulation given in [9], for each S_i (l_i, m_i, n_i) that rotates around $S_j(l_j, m_j, n_j)$ by angle α_{ik}, $S_k(l_k, m_k, n_k)$ can be calculated as shown in Eq. (1).

$$S_k = S_i \cos \alpha_{ik} + S_{ji} \sin \alpha_{ik} \qquad\qquad (1)$$

where, $S_{ji} = S_j \times S_i$. Screws defined for revolute pairs of double-spherical six-bar mechanism are shown as joint unit vectors, where $S_1 = (1,0,0)$ and $S_2 = (0,0,1)$. Other screws are found as indicated in Table 1.

3   Objective Functions for the Spherical Linkages

There will be a single objective function for the whole mechanism. However, since decomposition method is used, objective functions for both decomposed spherical four-bar mechanisms have to be formulated independently. Input-output relation/equation, which is commonly called as objective function in function generation synthesis, of first four-bar is calculated presented in Eq. (2), and (3). In equations, cosine and sine functions are abbreviated as $C\alpha = \cos\alpha$ and $S\alpha = \sin\alpha$.
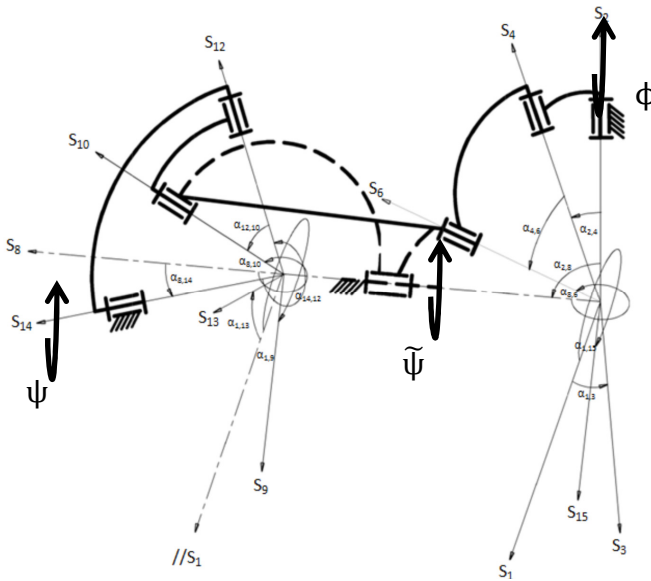
Fig. 1 Double-spherical six-bar linkage mechanism with joint axes [8]

Table 1 Calculation of the screws of the double-spherical six-bar linkage

First four-bar of the mechanism	Second four-bar of the mechanism
S_1 , S_2 and $\alpha_{1,3} \rightarrow S_3$; S_2 , S_3 and $\alpha_{2,4} \rightarrow S_4$	S_8 , S_1 and $\alpha_{8,14} \rightarrow S_{14}$; S_1 , S_{14} and $\alpha_{1,13} \rightarrow S_{13}$
S_2 , S_1 and $\alpha_{2,8} \rightarrow S_8$; S_1 , S_8 and $\alpha_{1,15} \rightarrow S_{15}$	S_{14} , S_{13} and $\alpha_{14,12} \rightarrow S_{12}$; S_1 , S_8 and $\alpha_{1,9} \rightarrow S_9$
S_8 , S_{15} and $\alpha_{8,6} \rightarrow S_6$	S_8 , S_9 and $\alpha_{8,10} \rightarrow S_{10}$

$$S_6 . S_4 = C\alpha_{4,6} \tag{2}$$

When the values of S_4 and S_6 are substituted and Eq. (2) is re-arranged and the function is re-written in polynomial form, Eq. (3) can be formulated. Necessary manipulations to formulate Eq. (3) are explained in [8].

$$P_0 f_0(\phi) + P_1 f_1(\phi) + P_2 f_2(\phi) + P_3 f_3(\phi) - F(\phi) = 0 \tag{3}$$

where $P_0 = \left(C\alpha_{4,6} - C\alpha_{2,4} C\alpha_{2,8} C\alpha_{8,6}\right)/\left(S\alpha_{2,4} S\alpha_{8,6}\right)$, $P_1 = -C\alpha_{8,6} S\alpha_{2,8}/S\alpha_{8,6}$, $P_2 = -C\alpha_{2,8}$, $P_3 = C\alpha_{2,4} S\alpha_{2,8}/S\alpha_{2,4}$, $f_0(\phi) = 1$, $f_1(\phi) = C\phi$, $f_2(\phi) = C\phi C\widetilde{\psi}$, $f_3(\phi) = C\widetilde{\psi}$, $F(\phi) = S\phi S\widetilde{\psi}$.

Objective function for the second four-bar is calculated similarly by using Eq. (4).

$$S_{12} . S_{10} = C\alpha_{10,12} \tag{4}$$

The function for the second spherical four-bar that is written in the polynomial form using similar manipulations is detailed in [8].

4   Equal Spacing and Precision Points

In decomposition method, a given function can be decomposed into a function of function and therefore, the overall function can be shared between two spherical four-bar linkages. Procedure for function generation synthesis by decomposition method starts with selecting an overall double-spherical six-bar linkage function, function, $y = f(x)$. Following this, an arbitrary function $\acute{y} = h(x)$ can be selected as first function. Range of x is given as $x_0 \leq x \leq x_m$ and respectively $\acute{y}_0 \leq \acute{y} \leq \acute{y}_m$ where $\acute{y}_0 = h(x_0)$ and $\acute{y}_m = h(x_m)$.

First, the arbitrary function $\acute{y} = h(x)$ is scaled for input (ϕ) and output $(\widetilde{\psi})$ of first mechanism. When range of input is $\phi_0 \leq \phi \leq \phi_m$ and a range of output is selected as $\widetilde{\psi}_0 \leq \widetilde{\psi} \leq \widetilde{\psi}_m$, and scaling equations are calculated as $\phi = \acute{a}_1 x + \acute{a}_2$, $\widetilde{\psi} = \acute{b}_1 \acute{y} + \acute{b}_2$.

Selected function for output angle for first mechanism becomes by $\widetilde{\psi} = \acute{b}_1 h\left(\frac{\phi - \acute{a}_2}{\acute{a}_1}\right) + \acute{b}_2$. A function is found by making synthesis of first four-bar linkage after defining input-output relations as indicated in Eq. (5).

$$\widetilde{\psi} = h(\phi, \bar{c}) \tag{5}$$

where $\bar{c}$ is the vector containing the designed construction parameters of first four-bar linkage. Following the design of construction parameters for first four-bar linkage, function for second spherical four-bar linkage is calculated. The calculation is conducted to find a function $y = g(\acute{y})$, where $y = g(h(x)) = f(x)$. It should be noted that range of input for second spherical linkage is selected to be the same as the range of output of first spherical linkage. In addition, range of output should be selected as the range of output for whole mechanism, $\psi_0 \leq \psi \leq \psi_m$. Scaling equations are with respect to these criteria are $\widetilde{\psi} = \acute{b}_1 \acute{y} + \acute{b}_2$, $\psi = b_1 y + b_2$.

Desired function for output angle of whole mechanism is calculated as $\psi = b_1 g\left(\frac{\widetilde{\psi} - \acute{b}_2}{\acute{b}_1}\right) + b_2$. After defining the input output relations, a function is found by making synthesis of the second four bar linkages as;

$$\psi = g(\widetilde{\psi}, \bar{d}) \; . \tag{6}$$

Substituting Eq. (5) in Eq. (6), objective function for double-spherical six-bar mechanism can be calculated as $\psi = g(h(\phi, \bar{c}), \bar{d})$, where $\bar{c}$ and $\bar{d}$ are designed construction parameters of first and second four-bar linkages respectively.

Interpolation approximation is used for finding the construction parameters of the mechanism. For exact solution, 4 positions of the mechanism are required four unknown parameters for each spherical linkage must be determined. Thus, $n = 4$ (n is number of equations or precision points) and as an example, precision points are distributed for exact synthesis equally in range of x from $x_0 = 1$ to $x_m = 2$ as $x_n = x_{n-1} + \delta \; ; n = 1,2,3,4$, where $\delta = (x_m - x_0)/(n + 1)$ for $n = 4$. y values of given and selected functions can be calculated by $y_i = f(x_i)$, $i = 0, n + 1$.

Constant parameters are calculated using Eq.(7) for first and second linkage. Using equal spacing for the second mechanism is not the only option towards a solution. Another option is using outputs of first spherical four-bar mechanism's precision points as precision points for second spherical four-bar mechanism. In this way, it is foreseen that in total error calculation of whole mechanism, there will be exactly four locations where error will be zero and these will be for precision points set for input of mechanism while solving for first spherical four-bar.

$$\acute{a}_1 = (\phi_0 - \phi_m)/(x_0 - x_m), \qquad \acute{a}_2 = (x_m\phi_0 - x_0\phi_m)/(x_m - x_0)$$
$$\acute{b}_1 = (\widetilde{\psi}_0 - \widetilde{\psi}_m)/(\acute{y}_0 - \acute{y}_m), \qquad \acute{b}_2 = (\acute{y}_m\widetilde{\psi}_0 - \acute{y}_0\widetilde{\psi}_m)/(\acute{y}_m - \acute{y}_0) \tag{7}$$

5 Derivation of Design Equations of Spherical Four-Bar

Generalized equations for objective function of both spherical four-bar mechanisms are shown in Eq. (8). Number of precision points is four, thus, four linear equations with four unknowns are required for each objective function. After arranging equations as matrices, values of P_i and R_i are found by using Cramer's rule, and unknown construction parameters of first spherical four-bar linkage are determined as shown in [8]. Thus, construction parameters for both mechanisms are calculated as; $\bar{c} = \{\alpha_{2,8}, \alpha_{2,4}, \alpha_{8,6}, \alpha_{4,6}\}$, and $\bar{d} = \{\alpha_{8,14}, \alpha_{14,12}, \alpha_{8,10}, \alpha_{12,10}\}$.

$$\sum_{k=0}^{n-1} P_k f_k(\phi_i) - F(\phi_i) = 0, \quad i = 1, n$$
$$\sum_{k=0}^{n-1} R_k g_k(\widetilde{\psi}_i) - G(\widetilde{\psi}_i) = 0, \quad i = 1, n \tag{8}$$

6 Numerical Examples

Two sets of numerical example studies are conducted. Equal spacing is used for both spherical four-bar designs in first set of numerical examples. In second set, equal spacing is used only for first spherical four-bar mechanism and output of the precision points set for first bar are used as precision points for second mechanism. Procedure for equal spacing and calculation method of errors are explained in [8]. First function to be generated by double-spherical six-bar is $y = x^{1.3}$. This function is shared between two mechanisms as $\acute{y} = x^{0.8}$ and $y = \acute{y}^{1.625}$. Second function is $y = e^{2x}$. This function is divided into two as $\acute{y} = e^{1.2x}$ and $y = \acute{y}^{(2/1.2)}$.

Since the method of choosing the precision points for second spherical four-bar and its effect on the whole mechanism's design precision is in question, only construction parameters of second spherical four-bar mechanisms and error graphs of second four-bar mechanisms double-spherical six-bar linkage are presented. Errors are calculated for second four-bar by $e_2 = \left| \left(b_1 g \left(\frac{\widetilde{\psi} - \acute{b}_2}{\acute{b}_1} \right) + b_2 \right) - g(\widetilde{\psi}, \bar{d}) \right|$ and similarly for the whole mechanism.

6.1   Results by Using Equal Spacing

Precision points and designed construction parameters of the second spherical four-bar mechanisms for both functions are presented in Table 2 and 3 with respect to the appearance of the function in Section 6.

Error for first function is calculated to be e_2= 0.0993 for a step size of $\Delta\widetilde{\psi} =$ 0.0314. Error calculated for second function is e_2= 0.2342 for a step size of $\Delta\widetilde{\psi} = 0.0314$. Total error of double-spherical six-bar linkage is calculated as e_{total}= 0.0738 for a step size of $\Delta\phi = 0.0377$ and e_{total}= 0.0744 for a step size of $\Delta\phi = 0.0377$ respectively for both functions. Total error graph for both functions are presented in Fig. 2 (a) and (b). It is clearly observed that errors do not go to zero at four points for whole mechanism.

Table 2 Precision points & construction parameters for 2nd spherical four-bar with $y = \acute{y}^{1.625}$

i	$\acute{y}_i$	y_i	$\widetilde{\psi}_i$(rad)	ψ_i (rad)	R_i	Second four-bar parameters (rad)
1	1.1186	1.1998	0.5655	1.7377	-0.4954	$\alpha_{8,14} = 0.8245$
2	1.2668	1.4686	0.8797	1.9623	0.8375	$\alpha_{14,12} = -0.7198$
3	1.4150	1.7578	1.1938	2.2040	-0.6789	$\alpha_{8,10} = 0.5035$
4	1.5632	2.0667	1.5079	2.4620	-1.3329	$\alpha_{12,10} = 0.9214$

Table 3 Precision points & construction parameters for 2nd spherical four-bar with $y = \acute{y}^{(2/1.2)}$

i	$\acute{y}_i$	y_i	$\widetilde{\psi}_i$(rad)	ψ_i (rad)	R_i	Second four-bar parameters (rad)
1	4.5526	12.5054	0.5655	1.7032	-3.3772	$\alpha_{8,14} = 1.5969$
2	6.0932	20.3271	0.8796	1.9056	3.8417	$\alpha_{14,12} = -0.2546$
3	7.6338	29.5961	1.1938	2.1455	0.0261	$\alpha_{8,10} = 0.1952$
4	9.1744	40.2065	1.5080	2.4201	-5.0564	$\alpha_{12,10} = 1.4302$

(a)   (b)

Fig. 2 Total error graph using equal spacing for function (a) $y = x^{1.3}$ (b) $y = e^{2x}$

6.2 Results by Using the Outputs of First Four-Bar

In this case, outputs of first spherical four-bar mechanisms for its four precision points are taken as the precision points for seond spherical four-bar mechanism. Precision points and designed construction parameters of the second spherical four-bar mechanisms for both functions are presented in Table 4 and 5 with respect to the appearance of functions in Section 6.
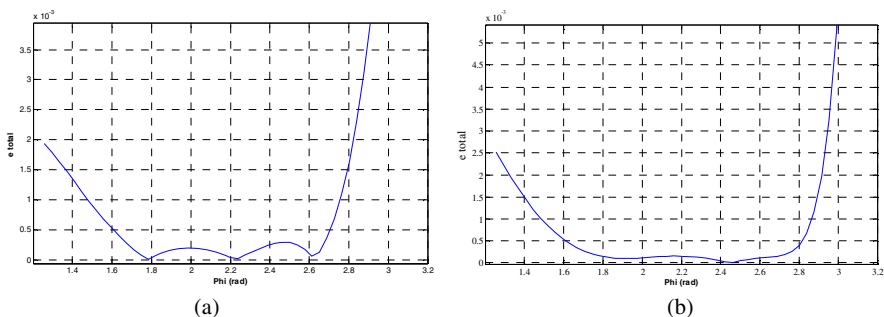
Table 4 Precision points & construction parameters for 2nd spherical four-bar with $y = \acute{y}^{1.625}$

i	x_i	$\acute{y}_i$	y_i	$\widetilde{\psi}_i(rad)$	$\psi_i\ (rad)$	R_i	Second four-bar parameters (*rad*)
1	1.2200	1.1724	1.2950	0.6796	1.8173	-2.6165	$\alpha_{8,14} = 1.9330$
2	1.4200	1.3238	1.5775	1.0005	2.0533	2.9938	$\alpha_{14,12} = -0.3027$
3	1.6200	1.4710	1.8723	1.3125	2.2996	0.3544	$\alpha_{8,10} = 0.2322$
4	1.8200	1.6146	2.1782	1.6168	2.5552	-3.9540	$\alpha_{12,10} = 1.7210$

Table 5 Precision points & construction parameters for 2nd spherical four-bar with $y = \acute{y}^{(2/1.2)}$

i	x_i	$\acute{y}_i$	y_i	$\widetilde{\psi}_i(rad)$	$\psi_i\ (rad)$	R_i	Second four-bar parameters (*rad*)
1	1.2800	4.6460	12.9358	0.5845	1.7143	-3.6848	$\alpha_{8,14} = 1.7265$
2	1.4800	5.9062	19.2980	0.8415	1.8790	4.1595	$\alpha_{14,12} = -0.2332$
3	1.6800	7.5082	28.7892	1.1682	2.1246	0.1551	$\alpha_{8,10} = 0.1791$
4	1.8800	9.5448	42.9484	1.5835	2.4910	-5.4560	$\alpha_{12,10} = 1.5676$

Error for the first function is calculated to be $e_2 = 0.1751$ for a step size of $\Delta\widetilde{\psi} = 0.0312$. The error calculated for the second function is $e_2 = 0.1891$ for a step size of $\Delta\widetilde{\psi} = 0.0333$. Total error of the double-spherical six-bar linkage is calculated as $e_{total} = 0.1233$ for a step size of $\Delta\phi = 0.0377$ and $e_{total} = 0.0486$ for a step size of $\Delta\phi = 0.0377$ respectively for both functions. Total error graph for both functions are presented in Fig. 3 (a) and (b). It is clearly observed that the errors go to zero at four points for the whole mechanism.

(a)   (b)
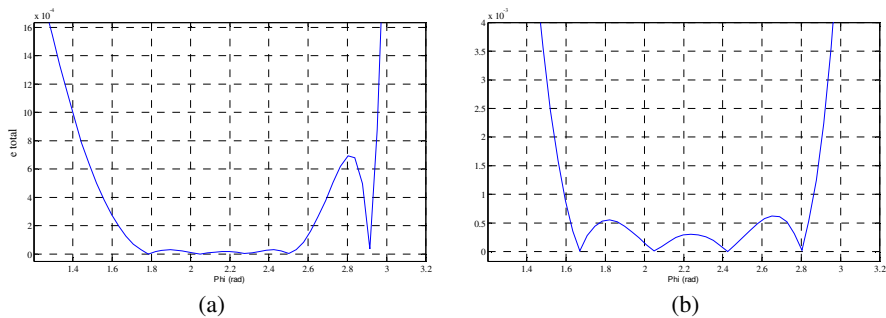
Fig. 3 Total error graph using the outputs of first four-bar for function (a) $y = x^{1.3}$ (b) $y = e^{2x}$

7   Conclusions and Discussions

Decomposition method with interpolation approximation is used for function generation synthesis of procedure of double-spherical six-bar linkage by using four precision points. While synthesis procedures of both four-bars are similar, selection of precision points for second spherical four-bar can be a different procedure. One of the options is to use equal spacing in between set limits as it is the case for first spherical four-bar and the other option is to use outputs of precision points at passive joint as precision points for the second spherical four-bar synthesis. Second option guarantees that total error for double-spherical six-bar mechanism is zero at exactly four points. This is clearly observed in the error plots presented in Fig. 3. On the contrary, in error graphs drawn for first option, in one of the function generations there are three locations that total error goes to zero while in the other function generation total error does not approach to zero at any point.

Total error using second option is increased with respect to the result obtained for first option when first selected function is generated. However, when second function is generated, second option produced decreased total error with respect to the first option. Therefore, although second option for selecting precision points for synthesis of second spherical four-bar is shown to guarantee that total error goes to zero at exactly four points for four precision point synthesis, it does not guarantee that total errors decrease with respect to the first option.

References

1. Tong, S.H., Chiang, C.H.: Syntheses of planar and spherical four-bar path generators by the pole method. Mech. Mach. Theory 27(2), 143–155 (1992)
2. Denavit, J., Hartenberg, R.S.: Kinematic synthesis of linkages. McGraw-Hill, New York (1964)
3. McCarthy, J.M.: Geometric Design of Linkages, 1st edn. Springer, New York (2000)
4. Alizade, R.I.: Synthesis of four-bar spherical mechanism on five parameters. J. Mech. Eng., Russian Academy of Science (ANR) 6 (1994) (in Russian)
5. Alizade, R.I., Kilit, O.: Analytic synthesis of function generating spherical four-bar mechanism for five precision points. Mech. Mach. Theory 40(7), 863–878 (2005)
6. Alizade, R.I., Gezgin, E.: Synthesis of function generating spherical four bar mechanism for the six independent parameters. Mech. Mach. Theory 46(9), 1316–1326 (2011)
7. Alizade, R.I., Aydazade, K.P., Novruzbekov, I.G.: Analysis and synthesis of planar mechanisms by using decomposition method. J. Mechanics of Machines, The Academy of Sciences of the USSR 57, 26–32 (1980)
8. Maaroof, O.W.N., Dede, M.İ.C.: Kinematic synthesis of over-constrained double-Spherical six-bar mechanism. Under Review in Mech. Mach. Theory
9. Alizade, R.I.: Structural synthesis of robot manipulators. In: Proc. Int. Symp. Mech. Mach. Sci., Izmir, Turkey, pp. 11–32 (2010)

A Novel 4 DoFs (3T-1R) Parallel Manipulator with Actuation Redundancy – Workspace Analysis

Samah Shayya[1], Sébastien Krut[2], Olivier Company[2],
Cédric Baradat[1], and François Pierrot[2]

[1] TECNALIA FRANCE– MIBI Building,
 672 Rue du Mas de Verchant, 34000 Montpellier, France
 `www.tecnalia.com`
[2] LIRMM –Université Montpellier 2 - 161 rue Ada, 34095 Montpellier, France
 `{samah.shayya,cedric.baradat}@tecnalia.com`
 `{krut,company,francois.pierrot}@lirmm.fr`

Abstract. This paper presents a novel 4 dofs (3T-1R[1]) parallel actuatedly redundant mechanism and its workspace analysis, based on a performance index involving velocity and force capabilities. The robot is capable of performing a half-turn[2] about the z axis. Moreover, having all of its prismatic actuators along one direction; the x motion is independent- only limited by the stroke of the prismatic actuators. The mechanism is characterized by elevated dynamical capabilities having its actuators at base.

Keywords: Parallel mechanism, actuation redundancy, 4 dofs mechanism, large rotational capacity, velocity and force performance index.

1   Introduction

For most industrial applications (such as machining) 6 dofs are too much. Thus studies have been conducted regarding the synthesis of 3 dofs (3T), 4 dofs (3T-1R) and 5 dofs (3T-2R) parallel manipulators. In fact, regarding some tasks, 4 dofs (3T-1R) parallel manipulators are sufficient. In others, where another rotation is required it can be provided either by the table or by an additional actuator in series with the parallel mechanism. Many 3T-1R parallel manipulators exist in literature such as the famous Delta robot [2] (with the **R**-U-P-U[3] chain), the Kanuk [10], the SMG in [1], the H4 in [8], the I4 in [6], the Par4 in [7] with its industrialized version Adept Quattro [9] (fastest industrial pick-and-place robot).

---

[1] 3T-1R: Three-translational degrees of freedom (dofs) and one rotational degree of freedom.
[2] Complete rotation is constrained by unavoidable collisions.
[3] R, U, and P: correspond to rotational, universal, and prismatic joints. Bold faced letter means actuated, and underlined letter means the joint position is measured.

Also, an interesting family of fully-isotropic parallel 4 dofs (3T-1R) manipulators, in addition to decoupled manipulators, has been synthesized in [4]. In [4], there is an elaborated referencing to other 4 dofs manipulators.

However, these and other existing manipulators have some drawbacks. For example, in the case of Delta with a huge workspace (even much larger with linear Delta), the presence of the RUPU chain connecting the base to the platform to supply the rotational dof is a weak element reducing the workspace. Others present problems of singularities, limitation of workspace (and particularly) in rotational capability, complexity of obtaining analytical expressions for the direct geometric model, and /or the use of transmission systems with the articulated platform as in the case [6-9] which impacts the accuracy of the robot. The manipulators in [4], despite their interesting isotropic property, have a limited workspace, are complex from manufacturability point of view, and have poor rigidity.

In this paper we present, a 4 dofs (3T-1R) parallel mechanism with two degrees of actuation redundancy that responds to the major requirements: large operational workspace, high rotational capability, absence of singularities, design simplicity, high rigidity, and high dynamical capabilities with analytical expressions for the inverse and direct geometric models. The paper introduces the mechanism in section 2, its geometrical elements, its inverse geometric model and the inverse jacobian matrix. Then section 3 describes the new performance index and workspace analysis of this mechanism. The paper ends with section 4 giving the conclusions.
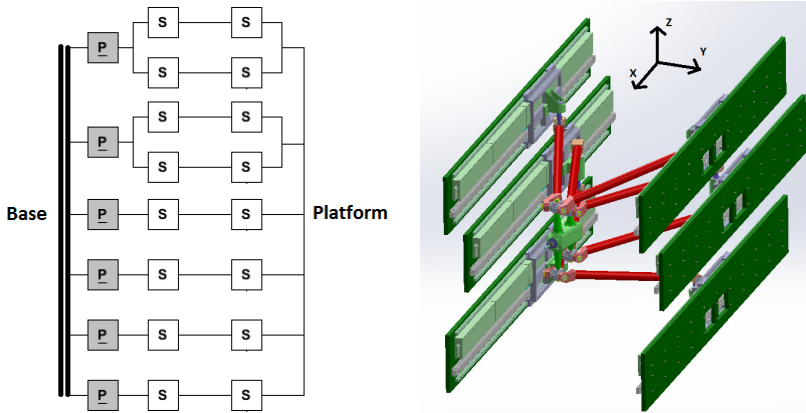
2   The New 4 DoFs (3T-1R) Manipulator (ARROW)

The graph diagram of the four dofs (3T-1R) parallel mechanism, called **ARROW** (**A**ccurate **R**apid **R**obot with Large **O**perational **W**orkspace), is shown with its CAD drawing in Fig. 1. In Fig.2 we show the frontal view of the robot and platform details.

The robot consists of six actuators along the same direction (x-axis) and can perform four motions x, y, z and Θ (rotation about z-axis). The robot is redundant (having two extra actuators). It is quite clear that this robot can move along x independently of the other motions y, z and Θ. This motion along x is only limited by the available stroke for the prismatic actuators. The role of parallelograms in chains (III) and (IV) (see Fig. 2) is to constraint the platform rotation about any axis that is perpendicular to the z axis of the base frame.

These two parallelogram arms cooperate with the other four simple arms to position the TCP and control the platform orientation about the z axis.

Let L_i be the length of ith arm $A_i B_i$ (all simple arms are of equal length L_s and parallelogram arms of equal length L_p) with $A_i = \begin{pmatrix} q_i & y_i & z_i \end{pmatrix}^{\text{T}}$ and $B_i = \begin{pmatrix} x_{b_i} & y_{b_i} & z_{b_i} \end{pmatrix}^{\text{T}}$ in the base frame. Note that $B_i^{\, m} = \begin{pmatrix} x_{b_i}^{\, m} & 0 & z_{b_i}^{\, m} \end{pmatrix}^{\text{T}}$ in

Fig. 1 Graph diagram of the mechanism on the left and CAD drawing of the robot with its base frame on the right. P: prismatic joint, S: spherical joint[4]. Gray box means actuated, while white box means passive. The underlining signifies that the joint position is being measured.

platform frame and the terms y_i and z_i can be determined from Fig. 2. Denote $P = \begin{pmatrix} x & y & z \end{pmatrix}^T$ (TCP coordinates) and the pose $x = \begin{pmatrix} x & y & z & \theta \end{pmatrix}^T$ (θ : rotation about z-axis). Then the inverse geometric model (IGM) is given by:

$$q_i = x_{b_i} - \sqrt{L_i^2 - (y_{b_i} - y_i)^2 - (z_{b_i} - z_i)^2}, \ \forall i = 1...6 \tag{1}$$

$$\boldsymbol{B}_i = \boldsymbol{P} + \boldsymbol{R}\, \boldsymbol{B}_i^m, \text{ with } \boldsymbol{R} = \begin{bmatrix} \cos(\theta) & -\sin(\theta) & 0 \\ \sin(\theta) & \cos(\theta) & 0 \\ 0 & 0 & 1 \end{bmatrix} \tag{2}$$

The inverse jacobian $\boldsymbol{J}_m$ is determined by equiprojectivity of velocities, giving ($\dot{\boldsymbol{q}} = \boldsymbol{J}_m \boldsymbol{v}$, $\boldsymbol{v} = \begin{pmatrix} \dot{x} & \dot{y} & \dot{z} & \dot{\theta} \end{pmatrix}^T$, $\dot{\boldsymbol{q}} = \begin{pmatrix} \dot{q}_1 & \cdots & \dot{q}_6 \end{pmatrix}^T$)[5]:

$$\boldsymbol{J}_m = \boldsymbol{J}_q^{-1} \boldsymbol{J}_x;\ \boldsymbol{J}_q = \mathrm{diag}\left(\boldsymbol{A}_1 \boldsymbol{B}_1^T \boldsymbol{e}_x, ..., \boldsymbol{A}_6 \boldsymbol{B}_6^T \boldsymbol{e}_x\right),\ \boldsymbol{J}_x = \begin{bmatrix} \boldsymbol{A}_1 \boldsymbol{B}_1^T & -\boldsymbol{A}_1 \boldsymbol{B}_1^T \left(\boldsymbol{PB}_1 \times \boldsymbol{e}_z\right) \\ \vdots & \vdots \\ \boldsymbol{A}_6 \boldsymbol{B}_6^T & -\boldsymbol{A}_6 \boldsymbol{B}_6^T \left(\boldsymbol{PB}_6 \times \boldsymbol{e}_z\right) \end{bmatrix} \tag{3}$$

---

[4] Note that spherical joints practically can be replaced by three revolute joints as to overcome the problem of limited angular deviations in commercial spherical joints.

[5] Note that $\dot{f} = \dfrac{df}{dt}$ is the time derivative of a function $f(t)$. Note also that $\boldsymbol{e}_x$, $\boldsymbol{e}_y$ and $\boldsymbol{e}_z$ are the unit vectors along x, y, and z axes of the base frame.
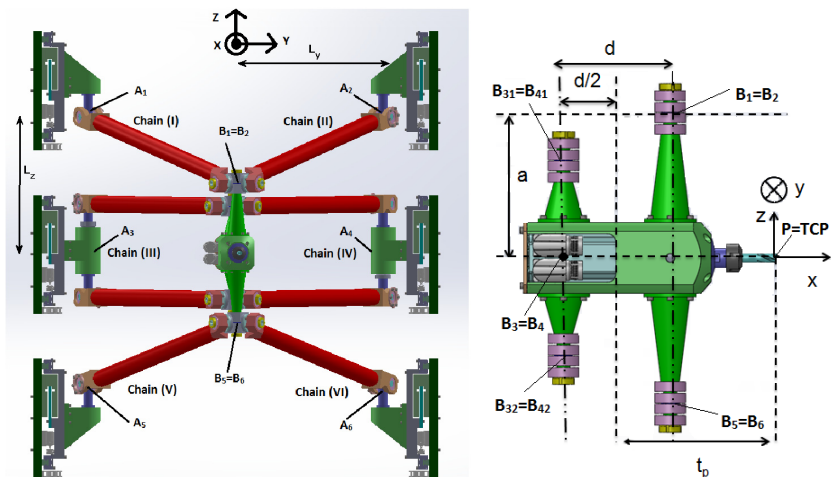
Fig. 2 Frontal view of the robot on the left and platform details on the right (TCP at origin of base frame with zero rotation). The L_y and L_z are related to y_i and z_i coordinates of point A_i. Note that chains (III) and (IV) are parallelograms. The points A_3 and B_3 are along the virtual axis of parallelogram (III) (mid-line). The same applies for chain (IV). The TCP (tool center point) is shown also and is denoted by P and it is the origin of the platform moving frame.

The singularity analysis (although is not discussed here in details due to space limitation) shows that if the mechanism is to have parallel type singularities they are necessary coincident with serial type singularities which cannot take place except at the boundary of the geometrically accessible workspace (when one of the arms happens to be in the yz plane provided that the corresponding pose is geometrically accessible). Hence, we can assure that there are no singularities of any type (serial or parallel) within the geometrically accessible workspace excluding its boundary.

3   Workspace Analysis

The workspace analysis can be limited to investigating the yz region that allows a half-turn (or a certain range of rotation) and where the value of the chosen performance index is within the acceptable range. There are several indices in literature that might be used to evaluate the robot's performance [5, 11, 12] and each has its own limitations. However, in our case, we are interested in assuring a certain minimal kinetostatic performance in all directions; more precisely assuring a minimal speed capability while being capable at the same time of supporting a minimal external force, regardless of the velocity or force direction. The robot under study being redundant, the singular values of the jacobian matrix are no longer

significant regarding this aspect and so is the condition number based on the ratio of largest singular value to the minimal one. So, in our study and evaluation of the workspace, we have defined the following index:

$$FVI = \min\left(\frac{v_w}{v_{wl}}, \frac{f_w}{f_{wl}}\right) \tag{4}$$

The terms v_w and f_w are the worst speed and the worst force respectively, whereas v_{wl} and f_{wl} are the desired lower bounds for the worst speed and worst force (not inducing internal stresses), respectively. Actually, v_w is nothing except the largest isotropic speed (radius of the largest sphere included in the zonotope of the operational velocities), and f_w is similarly the largest isotropic force (radius of largest sphere included in the operational force zonotope not inducing internal stresses). In our case, we have chosen $v_{wl} = 0.25\dot{q}_{\max}$ and $f_{wl} = 0.25\tau_{\max}$. The terms $\dot{q}_{\max}$ and $\tau_{\max}$ are respectively the maximum speed and maximum force of the linear actuator (all actuators are considered identical).

Since we have mixed dofs (translation and rotation), it is mandatory to homogenize J_m before evaluating the index at each pose if we are interested in all dofs (as to detect singularity while evaluating kinetostatic analysis)[6]. For this purpose, we may use a suitable characteristic length... However, in our case, we are only interested in the translational dofs (x, y and z motions), so we will consider only the translational part of J_m, call it J_{mp} composed of the first three columns of J_m. Note that this would not be sufficient unless a separate singularity analysis prior to this has been made and it is our case here (the study is not included here due to space limitation, but it is done). The terms v_w and f_w are given by:

$$v_w = \min_{i=1...6}\left(\frac{1}{\| j_{mpr_i} \|}\right)\dot{q}_{\max} \;,\; f_w = \min_{i=1...6}\left(\frac{1}{\| j_{pc_i} \|}\right)\tau_{\max} \tag{5}$$

The terms j_{mpr_i} and j_{pc_i} mean the ith row vector of matrix J_{mp} and i[th] column vector of the matrix J_p, the pseudo-inverse of J_{mp}. The proof of Eq. (5) is similar to the proof of the dynamic index introduced in [3].

In what follows we have established the yz region with zero orientation ($\theta = 0°$) and the yz region with rotation $\theta \in [-45° \quad 45°]$ despite the fact that the robot can produce half-turn (±45° being sufficient for our application) (see Fig. 3).

---

[6] Note that we can show that when $v_w = 0$, we have serial-type singularity and when $f_w = 0$ we have parallel-type singularity. So the closeness of FVI to zero can serve as a singularity measure as well.

Regarding the case of yz region with rotation, we have evaluated *FVI* for a set of different rotational angles particularly ±45°,±30° and 0° for the purpose of reducing computation time and we assumed the worst value of this index for the corresponding (y, z) position (in this case the minimal value of *FVI*). For this study, we used the following optimized parameters: $L_s = 0.72m$, $L_p = 0.86m$, $L_y = 0.35m$, $L_z = 0.314m$, $d = 0.12m$, $a = 0.164m$, and $t_p = 0.18m$.

Notice that the robot has its workspace symmetric with respect to xz and yz planes, and convex. The latter property, namely convexity, is very advantageous regarding trajectory planning; any two points in the workspace can be connected by a straight line trajectory.

To avoid collision with slider guides, the TCP should be at least at a distance $t_l = 0.2m$ in case of rotation ±45° and at a distance $t_w = 0.073m$ in case of zero rotation. Note that t_w and t_l are generally imposed by the platform dimensions, spindle motor and tool size. These plots show that the yz region with and without orientation is large, especially when we consider the available space between its slider guides and collision limits with the sliders, which is quite interesting.

For better insight on the results regarding the workspace areas and variations of the index, we have tabulated them (see Table 1).
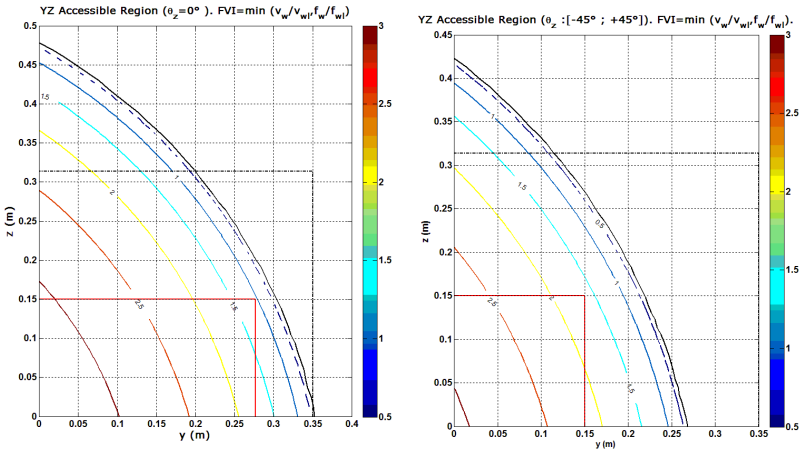
Fig. 3 Accessible yz regions for θ=0° (left) and for θ between -45° and +45° (right): quarter of the region is shown since it is symmetric with respect to y-axis and z-axis. The red solid lines show the boundaries that should not be exceeded by the TCP to avoid collisions with the sliders (vertical red line) and inter-arm collisions (horizontal red lines).. Dotted black line shows the available space within the linear sliders.

Table 1 Workspace analysis and FVI index variations over the workspace

		Area (m^2)	Area/$(4*L_y*L_z)$	Mean Value	Standard Deviation
Collisions not considered	Workspace $\theta=0°$ (no limits)	0.441	1.00	2.01	0.76
	Workspace $\theta=0°$ (FVI≥1)	0.387	0.88	2.19	0.62
	Workspace $\theta:\pm45°$ (no limits)	0.288	0.65	1.79	0.70
	Workspace $\theta:\pm45°$ (FVI≥1)	0.243	0.55	2.00	0.53
Collisions considered	Workspace $\theta=0°$ (no limits)	0.165	0.38	2.55	0.52
	Workspace $\theta=0°$ (FVI≥1)	0.165	0.38	2.55	0.52
	Workspace $\theta:\pm45°$ (no limits)	0.089	0.20	2.48	0.31
	Workspace $\theta:\pm45°$ (FVI≥1)	0.089	0.20	2.48	0.31

4   Conclusions and Future Work

In this paper, we have presented a new 4 dofs (3T-1R) parallel redundant mechanism (**ARROW**). It has 6 actuators for 4 dofs; the interest in this actuation redundancy is eliminating singularities and improving performance. The geometric models and inverse jacobian were derived. Singularity analysis results were briefed due to space limitation. We have then calculated the different workspaces and presented a new kinetostatic performance index " *FVI* " which is suitable for redundant and non-redundant robots equally well.

The workspace of this mechanism along x direction is independent of the other motions and only limited by the available stroke of the linear actuators, which is one of its major advantages. The yz accessible regions are large in both cases with and without orientation, especially when compared to the space between its slider guides. The mechanism is particularly interesting having the capability to perform a half-turn (complete rotation is not possible due to unavoidable collisions).

Besides, having the arms connected to the platform and actuators via spherical joints, puts these arms under tension/compression forces making it easier to model deformation and compensate for it. In brief the simplicity of the design, the actuation redundancy, the actuation at base, and the high stiffness of the mechanism contribute to the high dynamical capabilities (regarding pay-load, acceleration and velocity) as well as to its enhanced performance regarding accuracy. Regarding the future work, the introduced robot is currently being under further study (regarding dynamics) and under optimization in the sense of implementing it and producing a prototype on which real performance can be evaluated.

References

1. Angeles, J., Caro, S., Khan, W., Morozov, A.: The kinetostatic design of an innovative Schonflies-motion generator. Proceedings of the Institution of Mechanical Engineers, Part C: Journal of Mechanical Engineering Science 220(7), 935–943 (2006)
2. Clavel, R.: Une nouvelle structure de manipulateur parallèle pour la robotique légère. In: APII, vol. 23(6), pp. 371–386 (1985)
3. Corbel, D., Gouttefarde, M., Company, O., Pierrot, F.: Towards 100G with PKM. Is actuation redundancy a good solution for pick-and-place? In: 2010 IEEE International Conference on Robotics and Automation, Anchorage, Alaska, USA, May 3-8 (2010)
4. Gogu, G.: Structural synthesis of fully-isotropic parallel robots with Schonflies motions via theory of linear transformations and evolutionary morphology. European Journal of Mechanics A/Solids 26, 242–269 (2007)
5. Gosselin, C., Angeles, J.: Global performance index for the kinematic optimization of robotic manipulators. Transaction of the ASME, Journal of Mechanical Design 113(3), 220–226 (1991)
6. Krut, S., Company, O., Benoit, M., Ota, H., Pierrot, F.: I4: A new parallel mechanism for Scara motions. In: Proc. of the 2003 Int. Conf. on Robotics and Automation, Taipei, Taiwan, pp. 1875–1880 (September 1880)
7. Nabat, V., Company, O., Krut, S., Rodriguez, M., Pierrot, F.: Par4: very high speed parallel robot for pick-and-place. In: Proc. IEEE International Conference on Intelligent Robots and Systems (IROS 2005), Edmonton, Alberta, Canada (August 2005)
8. Pierrot, F., Company, O.: H4: a new family of 4-dof parallel robots. In: Proc. of the IEEE/ASME Int. Conf. on Advanced Intelligent Mechatronics, Atlanta, USA, pp. 508–513 (1999)
9. Pierrot, F., Nabat, V., Company, O., Krut, S.: From Par4 to Adept Quattro. In: Proc. Robotic Systems for Handling and Assembly - 3rd International Colloquium of the Collaborative Research Center SFB, Braunschweig, Germany, vol. 562 (2008)
10. Rolland, L.: The Manta and the Kanuk: Novel 4 dof parallel mechanism for industrial handling. In: Proc. of ASME Dynamic Systems and Control Division IMECE 1999 Conference, Nashville, USA, November 14-19, vol. 67, pp. 831–844 (1999)
11. Salisbury, J.K., Craig, J.J.: Articulated hands: force control and kinematic issues. International Journal of Robotics Research 1(1), 4–17 (1982)
12. Yoshikawa, T.: Manipulability of robotic manipulators. International Journal of Robotics Research 4(2), 3–9 (1985)

Two Parallel Robots with Actuators Situated on the Base

A.V. Kozyrev and V.A. Glazunov

Institute of Machines Science named after A.A. Blagonravov
of the Russian Academy of Sciences, Russia
lexxko@yandex.ru,
vaglznv@mail.ru

Abstract. Mechanisms and manipulators having parallel structure are rapidly spreading. Designs of mechanisms are constantly evolving, new ones appearing. According to that, the study of designs with some special features is rather relevant. In this paper, the parallel translational mechanism, in which all linear actuators located on the base, was considered. The Plucker coordinates matrix and the solution of the inverse kinematics problem were obtained. Also an improvement of the manipulator was proposed, and the Plucker coordinates matrix and the solution of the inverse kinematics problem were obtained for this advanced mechanism.
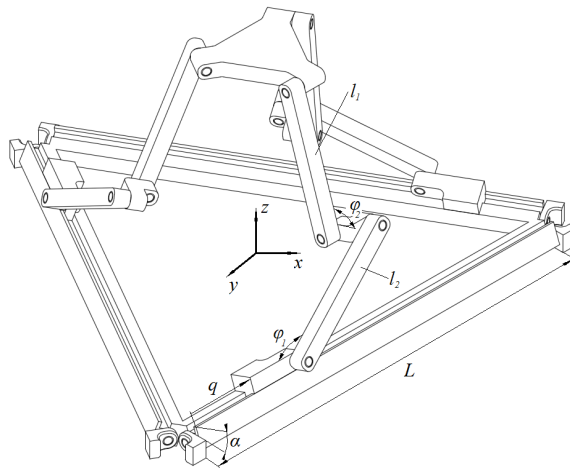
Keywords: parallel manipulators, Plucker coordinates, inverse kinematics problem.

1   Introduction

Among parallel mechanisms comprising several kinematic chains connecting the base with the end-effector, translational mechanisms are of the particular interest. There are different ways to design limbs providing such translational motion [3-6].

One of the possible mechanism configurations (Fig. 1) was proposed in [1]. The mechanism includes the base connected with the end-effector (moving platform) via three identical limbs, comprising the horizontally disposed linear actuator each. It is important to note that, firstly, all the drives are arranged in a horizontal plane, simplifying design of the base and, secondly, there are only rotational joints what increase the manufacturability of the mechanism.

In this paper, the advanced version of mechanism was proposed (Fig. 2). In this manipulator all actuators are set at an angle β relative to the base. It can improve some characteristics such as the pressure angles. The Plucker coordinates matrix was calculated for the both versions of the manipulator. Analysis of this matrix is a basic tool for studying the parallel mechanisms, and allows us to solve the following problems: the problem of singularities, the problem of speed and the power analysis. Also the paper presents the solution of the inverse kinematics problem.

Fig. 1 The general version of the manipulator
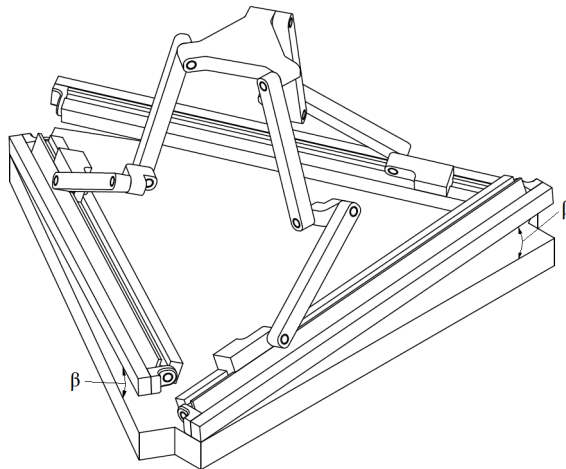
Fig. 2 The improved version of the manipulator

2   Plucker Coordinates Matrices

The most comprehensive and versatile tool for the exploration of the structure of parallel manipulators is studying of the kinematic and power screws vectors characterizing the geometry of the mechanism obtained by the methods of the screw calculus and the Plucker coordinates matrix composed of these screws [2,3].

The unit screw is a vector comprising six parameters: the coordinates of the unit vectors located in each of the kinematic pair, and the momentum of each unit vector relative to the origin. Knowing the single screws, the equivalent power screws which are used in the analysis of the manipulator can be found.

The mechanism comprises three kinematic chains, each of which has one translational pair (linear actuator) and four passive rotational joints. Each unit vector is oriented along the axis of the corresponding kinematic pair. The momentum of the unit vector relative to the origin is the vector product of the vector and the radius vector pointing from the origin to the center of the kinematic pair. The single screws are formed from the collected data, and using the linear transformations reciprocal power screws can be obtained.

Adding the rotation angles α_1, α_2, α_3 is due to avoid singularities of the mechanism throughout workspace [1]: each limb constrains the rotational movement of the end-effector about the z-axis only, and uncontrolled rotations about the x-axis and the y-axis are possible. Using these angles prevents uncontrolled motion. These angles are set once and aren't changing during the mechanism operation.

The computation of the power screw of the one limb is shown below. Since all limbs in the mechanism are identical, the calculations for the remaining power screws are made similarly.

The unit vector in the translational kinematic pair has coordinates:

$$\mathbf{e}_{10} = \begin{pmatrix} 1 \\ 0 \\ 0 \end{pmatrix} \tag{1}$$

The radius vector from the origin to the translational kinematic pair:

$$\mathbf{\rho}_{10} = \begin{pmatrix} \cos\left(\pi+\dfrac{\pi}{6}\right) & -\sin\left(\pi+\dfrac{\pi}{6}\right) & 0 & q_1 \\ \sin\left(\pi+\dfrac{\pi}{6}\right) & \cos\left(\pi+\dfrac{\pi}{6}\right) & 0 & 0 \\ 0 & 0 & 1 & 0 \\ 0 & 0 & 0 & 1 \end{pmatrix} \begin{pmatrix} R \\ 0 \\ 0 \\ 1 \end{pmatrix} = \begin{pmatrix} q_1 - \dfrac{L}{2} \\ -\dfrac{\sqrt{3}\cdot L}{6} \\ 0 \\ 1 \end{pmatrix} \tag{2}$$

Moving on to the standard form:

$$\mathbf{\rho}_{10} = \begin{pmatrix} q_1 - \dfrac{L}{2} \\ -\dfrac{\sqrt{3}L}{6} \\ 0 \end{pmatrix} \tag{3}$$

The momentum of the unit vector of the translational kinematic pair relative to the origin:

$$\mathbf{e}_{o10} = \mathbf{\rho}_{10} \times \mathbf{e}_{10} = \begin{pmatrix} 0 \\ 0 \\ 0 \end{pmatrix} \tag{4}$$

Performing the same calculations for the remaining kinematic pairs, the unit screw Plucker coordinates was obtained:

$$\mathbf{e}^1_0 = (\mathbf{e}_{10_0} \quad \mathbf{e}_{10_1} \quad \mathbf{e}_{10_2} \quad \mathbf{e}_{o10_0} \quad \mathbf{e}_{o10_1} \quad \mathbf{e}_{o10_2})$$
$$\vdots$$
$$\mathbf{e}^1_4 = (\mathbf{e}_{14_0} \quad \mathbf{e}_{14_1} \quad \mathbf{e}_{14_2} \quad \mathbf{e}_{o14_0} \quad \mathbf{e}_{o14_1} \quad \mathbf{e}_{o14_2})$$

(5)

where:

$$\mathbf{e}^1_0 = (1 \quad 0 \quad 0 \quad 0 \quad 0 \quad 0)$$

(6)

$$\mathbf{e}^1_1 = \left(0 \quad -\sin(\alpha_1) \quad \cos(\alpha_1) \quad -\frac{\sqrt{3} \cdot L\cos(\alpha_1)}{6} \quad -\cos(\alpha_1)\left(q_1 - \frac{L}{2}\right) \quad -\sin(\alpha_1)\left(q_1 - \frac{L}{2}\right)\right)$$

(7)

The other expressions are not given, as more complex.

Further it is necessary to find the power screw. To do so the set of five equations should be solved. Each equation means the momentum of the power screw relative to the momentum of the kinematic screw. These equations should be zero because the power screws are reciprocal to the unit ones. The power screw has six components, and there are only five equations, so one of the coordinates is set arbitrarily, but in such a way that the set of the equations has a nonzero solution.

The set of the equations is as follows:

$$\mathbf{r}_{o1x}\mathbf{e}_{10_0} + \mathbf{r}_{o1y}\mathbf{e}_{10_1} + \mathbf{r}_{o1z}\mathbf{e}_{10_2} + \mathbf{r}_{1x}\mathbf{e}_{o10_0} + \mathbf{r}_{1y}\mathbf{e}_{o10_1} + \mathbf{r}_{1z}\mathbf{e}_{o10_2} = 0$$
$$\vdots$$
$$\mathbf{r}_{o1x}\mathbf{e}_{14_0} + \mathbf{r}_{o1y}\mathbf{e}_{14_1} + \mathbf{r}_{o1z}\mathbf{e}_{14_2} + \mathbf{r}_{1x}\mathbf{e}_{o14_0} + \mathbf{r}_{1y}\mathbf{e}_{o14_1} + \mathbf{r}_{1z}\mathbf{e}_{o14_2} = 0$$

(8)

The arbitrary coordinate of the power screw:

$$\mathbf{r}_{o1z} = 0$$

(9)

By solving the set of the equations the following result was obtained:

$$\mathbf{r}^1_1 = \begin{pmatrix} 0 \\ 0 \\ 0 \\ 0 \\ 0 \\ \cot(\alpha_1) \end{pmatrix}$$

(10)

As a result, the power screw reciprocal to the five unit screws has been found for the first kinematic chain. Performing the same computations for the remaining

two kinematic chains the matrix of the Plucker coordinates whose rows contain the power screws coordinates was obtained. It has the following form:

$$
\mathbf{R} = \begin{pmatrix} 0 & 0 & 0 & 0 & \cot(\alpha_1) & 1 \\ 0 & 0 & 0 & \dfrac{\sqrt{3}\cot(\alpha_2)}{2} & -\dfrac{\cot(\alpha_2)}{2} & 1 \\ 0 & 0 & 0 & \dfrac{-\sqrt{3}\cot(\alpha_3)}{2} & -\dfrac{\cot(\alpha_3)}{2} & 1 \end{pmatrix} \tag{11}
$$

Since the matrix obtained has only the moment part, the limbs restrict only rotation of the platform about the three axes. This implies that the mechanism has three translational degrees of freedom.

Plucker coordinates matrix for the improved version of the manipulator has been computed the same way. It has the following form:

$$
\mathbf{R} = \begin{pmatrix} \mathbf{r}_{1x} & \mathbf{r}_{1y} & \mathbf{r}_{1z} & \mathbf{r}_{o1x} & \mathbf{r}_{o1y} & \mathbf{r}_{o1z} \\ \mathbf{r}_{2x} & \mathbf{r}_{2y} & \mathbf{r}_{2z} & \mathbf{r}_{o2x} & \mathbf{r}_{o2y} & \mathbf{r}_{o2z} \\ \mathbf{r}_{3x} & \mathbf{r}_{3y} & \mathbf{r}_{3z} & \mathbf{r}_{o3x} & \mathbf{r}_{o3y} & \mathbf{r}_{o3z} \end{pmatrix} \tag{12}
$$

Where

$$
\mathbf{r}_{1y} = (\sin(\varphi_{12}) - \cos(2\beta)\sin(\varphi_{12}))\,/
$$
$$
/(2q_1\sin(\beta)\sin(\varphi_{12}) - L\sin(\beta)\sin(\varphi_{12}) + 2l_1\cos(\alpha_1)\cos(\varphi_{11})\cos(\varphi_{12}) + \tag{13}
$$
$$
+2l_1\cos(\varphi_{11})\sin(\alpha_1)\sin(\varphi_{12}))
$$

$$
\mathbf{r}_{o1x} = -\sin(\beta)^2 \tag{14}
$$

The other expressions can't be shown as much more complicated.

3   Inverse Kinematics Problem

The aim of solving the inverse kinematics problem is to find the positions of the all drives for the given position of the end-effector. For the each limb the calculation is made separately. The solution reduces to searching of the conditions in which the coordinates at the junction point of the two links of the kinematic chain obtained geometrically from the origin center of the platform would be equal to the coordinates of this point obtained by moving from the actuator. The solutions are similar for the all kinematic chains. Below is the solution for one of the three kinematic chains.

Moving from the first point of the platform to the point where the two links are connected is carried out by the rotation at the angle φ_2 around the x-axis and by the negative displacement along the z-axis at the distance l_2:

$$
\mathbf{a}^1 = \begin{pmatrix} 1 & 0 & 0 & x \\ 0 & \cos(\varphi_{12}) & -\sin(\varphi_{12}) & y-r \\ 0 & \sin(\varphi_{12}) & \cos(\varphi_{12}) & z \\ 0 & 0 & 0 & 1 \end{pmatrix} \begin{pmatrix} 0 \\ 0 \\ -l_2 \\ 1 \end{pmatrix} = \begin{pmatrix} x \\ y-r+l_2\sin(\varphi_{12}) \\ z-l_2\cos(\varphi_{12}) \\ 1 \end{pmatrix}
\tag{15}
$$

Further it is necessary to get the coordinates of the same point, relatively to the origin. The computation of the actuator position in relation to the origin is performed by the rotation at the angle $\dfrac{7\pi}{6}$ around the z-axis and by the positive displacement along the x-axis at the distance R (the radius of the circle triangular base):

$$
\mathbf{q}^1 = \begin{pmatrix} \cos(\pi+\frac{\pi}{6}) & -\sin(\pi+\frac{\pi}{6}) & 0 & x \\ \sin(\pi+\frac{\pi}{6}) & \cos(\pi+\frac{\pi}{6}) & 0 & 0 \\ 0 & 0 & 1 & 0 \\ 0 & 0 & 0 & 1 \end{pmatrix} \begin{pmatrix} q_1 \\ 0 \\ -l_2 \\ 1 \end{pmatrix} = \begin{pmatrix} q_1 - \dfrac{L}{2} \\ -\dfrac{\sqrt{3}L}{6} \\ 0 \\ 1 \end{pmatrix}
\tag{16}
$$

Moving from the actuator to the point where the two links are connected performed by the rotation at the angle α around the x-axis, by the rotation at the angle φ_1 around the z-axis and by the negative displacement along the y-axis at the distance l_1:

$$
\mathbf{b}^1 = \begin{pmatrix} 1 & 0 & 0 & q_0^1 \\ 0 & \cos(\alpha_1) & -\sin(\alpha_1) & q_1^1 \\ 0 & \sin(\alpha_1) & \cos(\alpha_1) & q_2^1 \\ 0 & 0 & 0 & 1 \end{pmatrix} \begin{pmatrix} \cos(\varphi_{11}) & -\sin(\varphi_{11}) & 0 & x \\ \sin(\varphi_{11}) & \cos(\varphi_{11}) & 0 & 0 \\ 0 & 0 & 1 & 0 \\ 0 & 0 & 0 & 1 \end{pmatrix} \begin{pmatrix} 0 \\ l_1 \\ 0 \\ 1 \end{pmatrix} = \begin{pmatrix} q_1 - \dfrac{L}{2} - l_1\sin(\varphi_{11}) \\ l_1\cos(\alpha_1)\cos(\varphi_{11}) - \dfrac{\sqrt{3}L}{6} \\ l_1\cos(\varphi_{11})\sin(\alpha_1) \\ 1 \end{pmatrix}
\tag{17}
$$

Next, it necessary to equate the coordinates of the point of connection of the two links obtained by the two methods ($\mathbf{a}^1 = \mathbf{b}^1$) and to solve the resulting set of the equations. Solving these equations, following result was obtained:

$$q_1 = \frac{L}{2} + x - l_1 \cdot \sqrt{1 - \frac{\left(z + l_2 \cdot \cos\left(\alpha_1 \pm \arccos\left(\frac{\sin(\alpha_1) \cdot \left(y - r + \frac{\sqrt{3} \cdot L}{6} \right) - z \cdot \cos(\alpha_1)}{l_2} \right) \right) \right)^2}{l_1^2 \cdot \sin(\alpha_1)^2}} \tag{18}$$

The expression showing the relationship between the coordinates of the mobile platform and the position of the actuator of the first kinematic chain was found. Performing the similar calculations for the other two limbs, the remaining expressions were found. They have a similar form and weren't given in this paper.

The solution of the inverse kinematic problem for the advanced version of the manipulator was made the same way. It has the following form for the first kinematic chain:

$$q_1 = \frac{x + z - l_2 \cos(\varphi_{12}) + \frac{1}{2} L \cos(\beta) + l_1 \cos(\beta) \sin(\varphi_{11}) - \frac{1}{2} L \sin(\beta)}{\cos(\beta) - \sin(\beta)} -$$
$$- \frac{l_1 \sin(\beta) \cos(\varphi_{11}) \sin(\alpha_1) + l_1 \sin(\beta) \sin(\varphi_{11}) + l_1 \cos(\beta) \cos(\varphi_{11}) \sin(\alpha_1)}{\cos(\beta) - \sin(\beta)} \tag{19}$$

Where

$$\varphi_{11} = \pm \arccos\left(\frac{y - r + l_2 \sin(\varphi_{12}) + \frac{\sqrt{3} \cdot L}{6}}{l_1 \cos(\alpha_1)} \right) \tag{20}$$

and φ_{12} is highly complicated and it is difficult to give it here.

4   Conclusions

Two translational parallel robots were observed in this paper. The Plucker coordinates matrix was made and the inverse kinematics problem was solved for the each mechanism.

References

1. Bamberger, H., Wolf, A., Shoham, M.: Architectures of Translational Parallel Mechanism for MEMS Fabrication. In: The 12th World Congress IFToMM, Besançon, France, June 18-21, 6 p. (2007)

2. Glazunov, V.: Design of decoupled parallel manipulators by means of the theory of screws. Mechanism and Machine Theory (45), 239–250 (2010) (in Russian)
3. Glazunov, V.A., Koliskor, A.S., Krainev, A.F.: Spacial parallel mechanisms, 95 p. Nauka, Moscow (1991) (in Russian)
4. Kong, X., Gosselin, C.: Type Synthesis of Parallel Mechanisms, 275 p. Springer (2007)
5. Merlet, J.P.: Parallel robots, 372 p. Kluwer Academic Publishers (2000)
6. Tsai, L.-W.: Robot analysis: the mechanics of serial and parallel manipulators, 505 p. John Wiley & Sons (1999)

Geometric, Kinematic and Dynamic Analysis of Four Degrees of Freedom Manipulating Robot, Using Methods of Nonlinear Programming

A. Evgrafov and A. Kornishov

St. Petersburg State Polytechnical University, Russia
`a.evgrafov@spbstu.ru,`
`akornishov@gmail.com`

Abstract. This article considers the five-link spatial mechanism of manipulating robot with revolute and prismatic kinematic pairs. It is shown that making geometric analysis using classical methods is not rational. This article presents a numerical method of geometric analysis, kinematic and dynamic calculations of a mechanism.

Keywords: spatial manipulating robot, numerical method, geometric, dynamic and kinematic analysis.

1   Introduction

Geometric, kinematic and dynamic analysis methods for manipulating robots with degrees of mobility $n \leq 3$ are well studied and described in many sources (for example [3, 8]). However, using a more complex design of mechanisms with $n \geq 4$ sometimes may be considered as a more reasonable decision. Multidirectional robots have considerable diversity of designs and a wide range of applications [1, 9]. Geometric analysis of these mechanisms can be produced using various methods, the applicability of which depends on the specific problem and required accuracy of output link movements. The numerical method for solving the inverse problem of geometric analysis, the following kinematic and dynamic calculations of the mechanism are proposed in this paper. Dynamic analysis is made in two different ways: using the equations of kinetostatics and Lagrange equation of the second kind.

   Figure 1 shows the appearance of the experimental robot, built in the program «Solid Works». Linear dimensions of the links have been chosen in such a way as to exclude the appearance of geometrically indeterminate points in the operating zone of the robot. Guiding ways 1 are linked to slider 2 allowing him to move linearly, L-shaped rod 3 is mounted on the top of the slider and revolves on its axis. A small slider 4 moves linearly along the facet of the rod forming a revolute pair with the grabber 5.
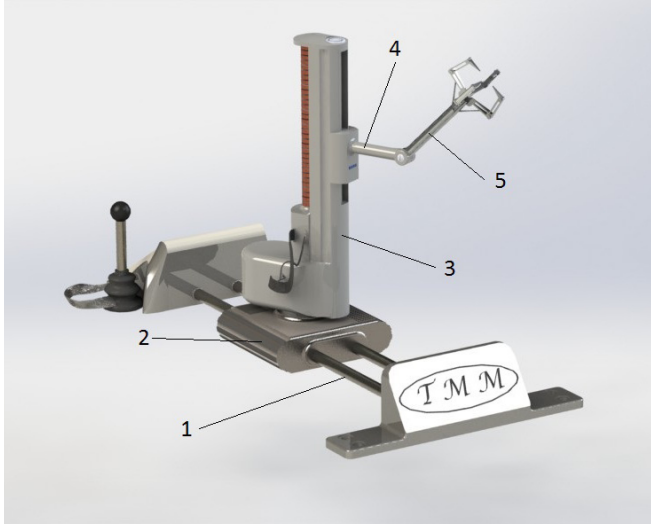
Fig. 1 Appearance of the experimental robot

2   Direct Problem of Geometric Analysis

Geometric analysis, the basic steps of which are described in work [6], should be started with finding a solution for the direct problem of geometric analysis. The problem is solved by using Denavit-Hartenberg parameters [4]. Figure 2 shows the kinematic diagram of the robot with local coordinate systems (LCS) $x_i y_i z_i$ (where i=1..4) rigidly connected to links 2-5 respectively.

Absolute coordinate system (ACS) $X_0 Y_0 Z_0$ is connected to link 1 (guiding ways of the mechanism), the pole of ACS is marked as 0. All generalized coordinates define positions of each subsequent LCS relative to the previous, and marked as q_i. For example, q_1 describes the translational motion of slider 2 and LCS, connected to it, along the guiding ways 1 (Fig.1); q_3 describes the same between links 3 and 4; q_2 reflects the rotational motion of link 3 relative to the axis y_1 of the link 2 and q_4 reflects the same between links 4 and 5. If the angle of rotation follows the arrow sign, it should be considered as positive angle, otherwise negative. All linear dimensions of the links are labeled in Latin letters for convenience.

Let us require the validity of the following equation:

$$H_{01}^{P}(q_1) \cdot H_{12}^{R}(q_2) \cdot H_{23}^{P}(q_3) \cdot H_{34}^{R}(q_4) \cdot \mathbf{R}_m^{(4)} = \mathbf{R}_\mathbf{m}^{(0)}, \tag{1}$$

where $\mathbf{R}_\mathbf{m}^{(4)}$ — coordinates of the point M in the fourth LCS, $\mathbf{R}_\mathbf{m}^{(0)}$ — coordinates of the point M in the ACS, $H_{i,i+1}^{P}$ and $H_{i,i+1}^{R}$ — transformation matrixes for the $(i+1)$-th and i-th LCS of prismatic and revolute kinematic pairs respectively.
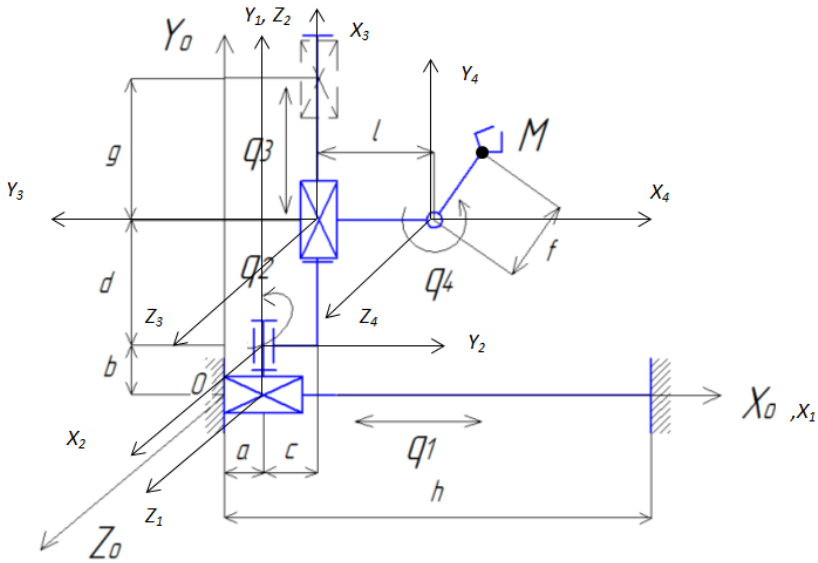
Fig. 2 Kinematic diagram of the robot

Equation (1) gives us the following:

$$\mathbf{R}_m^{(0)} = \begin{pmatrix} \cos q_2 (\cos q_4 \cdot f + l + c) + a + q_1 \\ \sin q_4 \cdot f + d + q_3 + b \\ -\sin q_2 (\cos q_4 \cdot f + l + c) \\ 1 \end{pmatrix}. \tag{2}$$

System of equations, consisting of three equations and four variables (q_1, q_2, q_3, q_4), may be retrieved from (2).

3   The Inverse Problem of Geometric Analysis

Obviously, system of equations, retrieved from (2) does not have a unique solution, since the number of independent variables exceeds the number of equations. The solution for this problem is selection of numerical values of q_i, followed by interpolation in the selected area, carried out in following sequence:

1. The coordinates of two points: A (x_A^0, y_A^0, z_A^0) and B (x_B^0, y_B^0, z_B^0) are given in the operating zone of the robot. Spatial curve drawn through the points A and B is the motion path of the point M of grabber 5.

2. Coordinates of the points, which belong to the curve *AB*, are defined by parametric equations (3) (parameter - time *t*) in the ACS.
3. Equations (2) and (3) are used for numerical selection of q_i values in the program «*Matlab*».
4. Continuous series of q_1 values must be interpolated in order to obtain the general law $q_1(t)$.
5. With the help of equations (2) and the resulting law $q_1(t)$ unique solutions for functions $q_{2,3,4}(x_m^0, y_m^0, z_m^0, t)$ may be finally found.

Let us form equations (3) as follows:

$$\begin{cases} x_{AB}^0(t) = -\dfrac{0,35}{\pi} \cdot \sin\left(\dfrac{\pi}{5} \cdot t\right) + 0,07 \cdot t, \\[2mm] y_{AB}^0(t) = 0,43 \cdot x_{AB}^0(t) + 0,5, \\[2mm] z_{AB}^0(t) = 0,14 \cdot x_{AB}^0(t) + 0,2, \end{cases} \tag{3}$$

where $t \in [0;10]$, coordinates of the boundary points of segment *AB*: $A(0; 0,5; 0,2)$, $B(0,7; 0,8; 0,3)$.

Numerical selection of q_i values is done by using «*fmincon*» [5, 7] function, which uses an interior point method [2] in order to find the solution for system of equations with *n* independent variables and a minimum of arbitrarily given function. We require that the selection of values must be carried out with the minimum of function $F=1$.

In conditions when there is a necessity to minimize one of the q_i values, function *F* can take this value.

Figure 3 shows a graph made of fitted q_1 values. Interpolation is made by using «*Microsoft Excel*» resources.
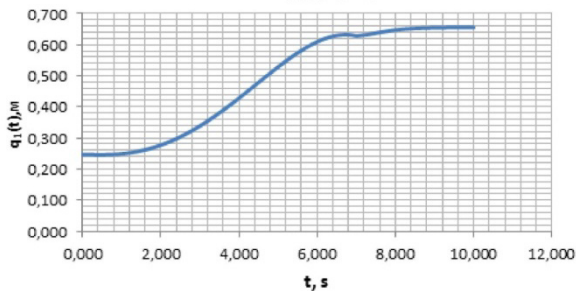
Fig. 3 Graph of function $q_1(t)$

Whole graph is divided into two areas:

$$t \in [0;7], \; q_1(t) = -5{,}1466878 \cdot 10^{-4} t^4 + 4{,}2754936 \cdot 10^{-3} t^3 + 3{,}9178021 \cdot 10^{-3} t^2$$
$$-5{,}9658774 \cdot 10^{-3} t + 2{,}4734661 \cdot 10^{-1}, \tag{4}$$

$$t \in [7;10], \; q_1(t) = 6{,}7019965 \cdot 10^{-4} t^6 - 3{,}5456170 \cdot 10^{-2} t^5 + 7{,}7957242 \cdot 10^{-1} t^4$$
$$-9{,}1161840 t^3 + 59{,}780243 t^2 - 208{,}35002 t + 302{,}00832. \tag{5}$$

As seen from equations (4) and (5), four and six degree polynomial interpolation has been performed. With this arrangement of polynomial coefficients variation from the originally specified trajectory of the gripper is less than a thousandth part of a millimeter.

Functions $q_{2,3,4}(x_m^0, y_m^0, z_m^0, t)$ are determined from the equations (2), (4), (5) and can be brought to the following form:

$$\begin{cases} q_2(x_m^0, y_m^0, z_m^0, t) = K \cdot \arccos\left(\dfrac{x_{AB}^0(t) - a - q_1(t)}{\cos q_4(x_m^0, y_m^0, z_m^0, t) \cdot f + l + c} \right), \\[2mm] q_3(x_m^0, y_m^0, z_m^0, t) = y_{AB}^0(t) - \sin q_4(x_m^0, y_m^0, z_m^0, t) \cdot f - d - b \\[2mm] q_4(x_m^0, y_m^0, z_m^0, t) = K \cdot \arccos\left(\dfrac{\sqrt{(x_{AB}^0(t) - a - q_1(t))^2 + z_{AB}^0(t)^2} - l - c}{f} \right), \end{cases} \tag{6}$$

where $K = \pm 1$ – determines the configuration of links of the robot in general case. For given trajectory of the gripper $K = -1$ and $K = +1$ for q_2 and q_4 respectively.

Generalized velocity and acceleration $\dot{q}_i(t), \ddot{q}_i(t)$ can be found using equations (4), (5), (6).

4   Kinematic Analysis

Kinematic analysis of the mechanism should be started with a determination of angular velocities of the links. In general case absolute angular velocity of i-th link in LCS connected to this link, may be found using formula (7):

$$\boldsymbol{\Omega}_i^{(i)} = A_{i-1,i}^T \cdot \boldsymbol{\Omega}_{i-1}^{(i-1)} + \boldsymbol{\omega}_i^{(i)}, \tag{7}$$

where $\boldsymbol{\Omega}_{i-1}^{(i-1)}$ – absolute angular velocity of i-th link in LCS, $\boldsymbol{\omega}_i^{(i)}$ – relative angular velocity of i-th link, and $A_{i-1,i}^T$ – transposed direction cosine matrix.

Angular accelerations may be determined from the equation (8):

$$\mathbf{E}_i^{(i)} = A_{i-1,i}^T \mathbf{E}_{i-1}^{(i-1)} + \boldsymbol{\varepsilon}_i^{(i)} + \boldsymbol{\Omega}_i^{(i)} \times \boldsymbol{\omega}_i^{(i)}, \tag{8}$$

where $\mathbf{E_i^{(i)}}$- absolute angular acceleration of i-th link in LCS, $\mathbf{\epsilon_i^{(i)}}$ - relative angular acceleration of i-th link.

Velocities of LCS poles, rigidly connected to each link, can be found using formula (9):

$$\mathbf{v_{0i}^{(i)}} = A_{i-1,i}^{T}\,(\mathbf{v_{0i-1}^{(i-1)}} + \mathbf{v_{r0i}^{(i-1)}} + \mathbf{\Omega_{i-1}^{(i-1)}} \times \mathbf{r_{0i}^{(i-1)}})\,, \tag{9}$$

where $\mathbf{v_{r0i}^{(i-1)}}$ – relative velocity of i-th LCS pole in $(i$-1$)$-th LCS, $\mathbf{r_{0i}^{(i-1)}}$ – column of i-th LCS pole coordinates in $(i$-1$)$-th LCS. Velocities of mass centers of the links are defined by formula:

$$\mathbf{v_{si}^{(i)}} = \mathbf{v_{oi}^{(i)}} + \mathbf{\Omega_i^{(i)}} \times \mathbf{r_{si}^{(i)}}\,, \tag{10}$$

where $\mathbf{v_{si}^{(i)}}$ – velocity of mass center of i-th link in LCS, connected to this link, $\mathbf{r_{si}^{(i)}}$ – column of mass center's coordinates of i-th link in LCS, connected to this link.

Accelerations of LCS poles can be determined using formula (11):

$$\mathbf{w_{0i}^{(i)}} = A_{i-1,i}^{T}(\mathbf{w_{0i-1}^{(i-1)}} + \mathbf{E_{i-1}^{(i-1)}} \times \mathbf{r_{0i}^{(i-1)}} + \mathbf{\Omega_{i-1}^{(i-1)}} \times (\mathbf{\Omega_{i-1}^{(i-1)}} \times \mathbf{r_{0i}^{(i-1)}}) + \mathbf{w_{r0i}^{(i-1)}} + 2\mathbf{\Omega_{i-1}^{(i-1)}} \times \mathbf{v_{r0i}^{(i-1)}})\,, \tag{11}$$

where $\mathbf{w_{r0i}^{(i-1)}}$ – relative acceleration of i-th LCS pole in $(i$-1$)$-th LCS. Accelerations of mass centers of the links are defined by formula:

$$\mathbf{w_{si}^{(i)}} = \mathbf{w_{0i}^{(i)}} + \mathbf{E_i^{(i)}} \times \mathbf{r_{si}^{(i)}} + \mathbf{\Omega_i^{(i)}} \times (\mathbf{\Omega_i^{(i)}} \times \mathbf{r_{si}^{(i)}})\,. \tag{12}$$

5   Dynamic Analysis

The resulting expressions are used in dynamic analysis of the mechanism in order to find all inertial forces and their moments.

Inertial forces and their moments in relation to the centers of mass of the links can be determined by the following equations:

$$\mathbf{\Phi_i(t)} = -m_i \cdot \mathbf{w_{si}^{(i)}(t)}\,; \qquad \mathbf{M_s(\Phi_i)} = -I_{si} \cdot \mathbf{E_i^{(i)}} - \mathbf{\Omega_i^{(i)}} \times (I_{si} \cdot \mathbf{\Omega_i^{(i)}})\,, \tag{13}$$

where I_{si} – inertia tensor of i-th link in relation to the mass center of this link and $\mathbf{\Phi_i}$ -inertial force of i-th link. Moments of inertial forces in relation to the LCS can be determined using formula (14):

$$\mathbf{M_0(\Phi_i)} = \mathbf{r_{si}} \times \mathbf{\Phi_i(t)} + \mathbf{M_s(\Phi_i)}\,. \tag{14}$$

Moments of gravity forces in relation to the LCS are defined by formula (15):

$$\mathbf{M_{0i}(G_i)} = \mathbf{r_{si}} \times \mathbf{G_i(t)}\,, \tag{15}$$

Where $\mathbf{G_i}$ -gravity force of i-th link. Resultant vectors of forces and their moments are determined by the equations of kinetostatics (16) and (17) respectively:

$$\mathbf{V_{i-1,i}} - \mathbf{V_{i,i+1}} + \mathbf{G_i} + \mathbf{\Phi_i} = 0, \tag{16}$$

where $\mathbf{V_{i-1,i}}$ – resulting force vector which acts on the $(i-1)$-th link from the position of i-th link, and $\mathbf{V_{i,i+1}}$ – resulting force vector which acts on the i-th link from the position of $(i+1)$-th link.

$$\mathbf{M_{0i}}(\mathbf{V_{i-1,i}}) - \mathbf{M_{0i+i}}(\mathbf{V_{i,i+1}}) - \mathbf{r_{0i+1}} \times \mathbf{V_{i,i+1}} + \mathbf{M_{0i}}(\mathbf{G_i}) + \mathbf{M_{0i}}(\mathbf{\Phi_i}) = 0, \tag{17}$$

where $\mathbf{r_{0i+1}}$ – column of $(i+1)$-th LCS pole coordinates in i-th LCS.

Projecting the expressions (16) and (17) on the axis of i-th coordinate system, we obtain the following expressions:

$$\mathbf{V}_{i-1,i}^{(i)} = A_{i,i+1} \mathbf{V}_{i,i+1}^{(i)} - (\mathbf{G}_i^{(i)} + \mathbf{\Phi}_i^{(i)}), \tag{18}$$

$$\mathbf{M}_{0i}^{(i)}(\mathbf{V_{i-1,i}}) = A_{i,i+1}\mathbf{M}_{0i+1}^{(i+1)}(\mathbf{V_{i,i+1}}) + \mathbf{r}_{0i+1}^{(i)} \times A_{i,i+1}\mathbf{V}_{i,i+1}^{(i)} - (\mathbf{M}_{0i}^{(i)}(\mathbf{G_i}) + \mathbf{M}_{0i}^{(i)}(\mathbf{\Phi_i})) = 0. \tag{19}$$

Expressions (18) and (19) allow us to find the interaction forces between the links and generalized driving forces ($R_{i-1,i}$ and Q_i respectively):

$$\mathbf{V}_{i-1,i}^{(i)} = \begin{pmatrix} Q_i \\ R_{i-1,iy} \\ R_{i-1,iz} \end{pmatrix}; \quad \mathbf{M_{0i}}(\mathbf{V_{i-1,i}}) = \begin{pmatrix} M_{0ix}(R_{i-1,i}) \\ M_{0iy}(R_{i-1,i}) \\ Q_i \end{pmatrix}. \tag{20}$$

Generalized driving forces can be also found using the Lagrange equation of the second kind:

$$\frac{d}{dt}\frac{\partial T}{\partial \dot{q}_i} - \frac{\partial T}{\partial q_i} = Q + Q_R, \tag{21}$$

where Q – required generalized driving force, Q_R – generalized resistance force, T – kinetic energy of the mechanism, defined as follows:

$$\begin{aligned} T &= \frac{1}{2}(m_1 \mathbf{v_{s1}^T} \cdot \mathbf{v_{s1}} + m_2 \mathbf{v_{s2}^T} \cdot \mathbf{v_{s2}} + m_3 \mathbf{v_{s3}^T} \cdot \mathbf{v_{s3}} + m_4 \mathbf{v_{s4}^T} \cdot \mathbf{v_{s4}}) + \\ &\frac{1}{2}(\mathbf{\Omega_1^T} \cdot \mathbf{I_{s1}}\mathbf{\Omega_1} + \mathbf{\Omega_2^T} \cdot \mathbf{I_{s2}}\mathbf{\Omega_2} + \mathbf{\Omega_3^T} \cdot \mathbf{I_{s3}}\mathbf{\Omega_3} + \mathbf{\Omega_4^T} \cdot \mathbf{I_{s4}}\mathbf{\Omega_4}) \end{aligned} \tag{22}$$

6   Conclusion

In conclusion, the proposed method of numerical selection of q_i values can be used even in case of calculating the $n > 4$ degree of freedom robot, since the program does not constrain the limit of independent variables in the system of equations (4).

References

1. Ceccarelli, M.: The Challenges for Machine and Mechanism Design at the Beginning of the Third Millennium as Viewed from the Past. In: Proceedings of Brazilian Congress on Mechanical Engineering COBEM 2001, Uberlandia, Invited Lecture, pp. 132–151 (2001)
2. Deakin, I.: The method of interior points in the linear and nonlinear programming, 120 p. KRASAND, Moscow (2010) (in Russian)
3. Evgrafov, A., Kolovsky, M., Petrov, G.: Theory of Mechanisms and Machines, 248 p. Publishing House of SPbSPU, St. Petersburg (2009) (in Russian)
4. Hartenberg, R.S., Denavit, J.: Kinematic synthesis of linkages. McGraw-Hill series in mechanical engineering, 435 p. McGraw-Hill, New York (1965)
5. Recktenwald, G.W.: Introduction to Numerical Methods and MATLAB: Implementations and Applications. Prentice Hall (2001) ISBN: 0201308606
6. Kolovsky, M.Z., Evgrafov, A.N., Semenov, Y.A., Slousch, A.V.: Advanced Theory of Mechanisms and Machines, 396 p. Springer (2000)
7. Chapman, S.J.: MATLAB (r) Programming for Engineers. Brooks / Cole Pub. Co. (1999) ISBN: 0534951511
8. Petuya, V., Alonso, A., Pinto, C., Altuzarra, O., Hernandez, A.: A new general-purpose method to solve the forward position problem in parallel manipulators. Advances Robotics 22, 395–409 (2008)
9. Solomentsev, Y., Zhukov, K., Pavlov, Y., et al.: Industrial robots in machine engineering: Album of plans and designs, Moscow, 140 p. (1986) (in Russian), Edited by Solomentsev, Y.

Robust Model Based Predictive Control for Trajectory Tracking of Parallel Robots

A. Zubizarreta[1], I. Cabanes[1], M. Marcos[1], Charles Pinto[2], and J. Corral[2]

[1] Automatics and System Engineering Dpt., University of the Basque Country, Spain
`asier.zubizarreta@ehu.es`
[2] Dpt. of Mechanical Engineering, University of the Basque Country, Spain

Abstract. Model Based Predictive Control (MPC) is an interesting approach due to its ability to consider the constraints of the controlled system and easily adapt to the future reference changes. In this paper, a novel robust MPC controller is presented, which considers the effect of the Tool Center Point (TCP) estimation errors and the model uncertainties of the mechanical structure. In order to show its effectiveness, its application to the 5R parallel manipulator is detailed. Simulation validation is provided to demonstrate that the proposed approach can exploit all the theoretical capabilities of the mechatronic system.

Keywords: Parallel Robots, Model Based Predictive Control, Robust Control, Five Bar Mechanism.

1 Introduction

Parallel robots [8], have recently drawn attention from both academy and industry due to their performance when handling high-speed, high-precision or heavy load handling tasks. This performance is derived from their parallel structure, composed by multiple kinematic chains, or "limbs". However, its complexity presents some drawbacks, such as a reduced workspace, presence of singularities or highly coupled kinematics and dynamics.

In order to reduce the effect of these disadvantages, an optimized mechanical design, adequate actuator selection and proper control law that allows to exploit all the capabilities of the mechatronic system is required. In the literature, many different control approaches have been proposed, such as simple independent joint control approaches based on PID [3, 9] , or more advanced, model based control laws such as the Computed Torque Control (CTC) [11], adaptive control [5] or robust control [7]. However, none of the aforementioned approaches considers the physical limitations of the parallel robot (torques, workspace, speed) in the control law or adapts in a predictive way to the programmed reference trajectory.

Model Based Predictive Control (MPC) [4] groups a set of control strategies that use the dynamic model of a process to predict its behaviour in a finite future time window (the horizon). This way, its future error can be minimized by calculating a proper control action. Moreover, this control action can be calculated considering the physical constraints, which guarantees near optimal performance of the process and its actuators. These features are very interesting in robot control, as the potential of the mechatronic system can be maximized, actuator limits considered and workspace singularities avoided.

However, MPC controllers are usually complex and computationally intensive, and most approaches are based on constant references in the prediction horizon [10, 2]. In this paper, a novel, robust MPC for trajectory tracking (RMPC-T) is presented, based on the one developed in [1]. This approach presents three main features over the ones previously proposed: 1) it considers the physical constraints of the parallel robot, 2) it is robust against model uncertainties, and 3) it allows tracking of changing references, which enhances significatively the tracking capabilities of parallel robots. In order to detail this approach, the rest of the paper is structured in three sections. First, the robust MPC approach for tracking control law formulation is detailed for a generic system. Then, the application to the 5R parallel robot is detailed. Third, the effectiveness of the approach is demonstrated by simulation. Finally, the most important ideas are summarized.

2 Robust MPC for Trajectory Tracking

The novel robust MPC for trajectory tracking (RMPC-T) presented in this section is based on the one developed by Alvarado *et al* in [1]. However, while in the mentioned work constant trajectories are considered in the prediction horizon, in the formulation presented in this paper, changing trajectories are considered, which are more appropriate for parallel robots.

Next, the formulation of the MPC for a generic system is presented. For the sake of simplicity, some definitions are not fully detailed in this section. The reader is referred to [12] for more detail in the formulation and the concepts involved.

Consider the following uncertain system, defined in discrete time using state-space formulation,

$$
\begin{aligned}
\mathbf{x}(k+1) &= \mathbf{A}\mathbf{x}(k) + \mathbf{B}\mathbf{u}(k) + \mathbf{w}(k) \\
\mathbf{y}(k+1) &= \mathbf{C}\mathbf{x}(k) + \mathbf{D}\mathbf{u}(k)
\end{aligned}
\tag{1}
$$

where $\mathbf{x} \in \mathbb{R}^n$ represents the state, $\mathbf{u} \in \mathbf{R}^m$ the control input and $\mathbf{y} \in \mathbf{R}^p$ the system output. $\mathbf{w} \in \mathcal{W}$ are the external additive disturbances that model parameter uncertainties and measurement errors. The system of Eq. (1) is considered to be time-invariant and controllable.

All sets are considered bounded, so that a convex polytope can be defined for each set to represent all points included within the bounds,

$$
\mathscr{Z} = \left\{ \mathbf{z} = \left[\mathbf{x}^T \; \mathbf{u}^T \right]^T \in \mathbb{R}^{n+m} : \mathbf{A_z}\mathbf{z} \leq \mathbf{b_z} \right\}
$$

where $\mathbf{A_z}$ and $\mathbf{b_z}$ are used to define the bounds of the set in the *h-representation* of a convex polytope.

The objective of the RMPC-T controller is, for each time step k, to stabilize the system and steer the state $\mathbf{x}$ to a neighbourhood of a steady state $\mathbf{x_s}$ associated to a setpoint $\mathbf{r}$, guaranteeing all the constraints even in presence of disturbances. For that purpose, a three level control approach is defined: a local robust control to reduce the effect of disturbances, a MPC controller which ensures feasibility with the system constraints and a local tracking controller to ensure convergence to the desired state.

The **local robust controller** is designed to avoid the exponential growth of the prediction error due to unknown $\mathbf{w}$ disturbances. Its goal is to ensure that the *real* state $\mathbf{x}$ lies within a bounded hipertube arround the trajectory of the nominal state $\overline{\mathbf{x}}$ (without disturbances), which is characterized by a *Robust Positively Invariant* (RPI) set [6] Φ_K. Hence, the local control law

$$\mathbf{u}(k+j) = \overline{\mathbf{u}}(k+j) + \mathbf{K}\left(\mathbf{x}(k+j) - \overline{\mathbf{x}}(k+j)\right) \tag{2}$$

where the nominal system $\overline{\mathbf{x}}, \overline{\mathbf{u}}, \overline{\mathbf{y}}$ is the *ideal* one and presents no disturbances. The gain matrix $\mathbf{K}$ is defined so that the error caused by the disturbances $\mathbf{w} = \mathbf{x} - \overline{\mathbf{x}} \in \Phi_K$ lies always in a bounded and fixed RPI set Φ_K. So, a bounded trajectory tube is generated for $\mathbf{z}$ that considers all possible uncertainties,

$$\overline{\mathscr{X}} = \mathscr{X} \ominus \Phi_K \ , \ \overline{\mathscr{U}} = \mathscr{U} \ominus \mathbf{K}\,\Phi_K \ , \ \overline{\mathscr{Z}} = \mathscr{Z} \ominus (\Phi_K \times \mathbf{K}\,\Phi_K) \, , \ \overline{\mathbf{z}} = \left[\overline{\mathbf{x}}^T \ \overline{\mathbf{u}}^T\right]^T \in \overline{\mathscr{Z}}$$

where $\ominus$ is the Pontryagin difference.

Using the local robust control law defined in Eq. (2), it is ensured that the trajectory of the real state $\mathbf{x}$ lies within a bounded tube. This allows to consider the nominal trajectory of the state $\overline{\mathbf{x}}$ in the predictions of the MPC and the calculation of a feasible nominal control action $\overline{\mathbf{u}}^*$ that satisfies the contraints. However, in order to ensure convergence to the desired reference, the final predicted state of the MPC must lie within a neighbourhood of the desired steady state. This neighbourhood is defined as an *Invariant Set for Tracking* $\Omega^a_{t,\overline{\mathbf{K}}}$ and ensures that once reached this set both the state and internal reference $\boldsymbol{\theta}$ associated to the changing trajectory setpoint $\mathbf{r}$, evolve within the bounds of this set[1].

Based on the aforementioned sets and local controllers, the **MPC control law** is calculated by solving the minimization problem V_t^*,

$$V_t^* = \min_{\overline{\mathbf{u}}, \overline{\mathbf{x}}, \overline{\theta}} \mathbf{V}_t\left(\mathbf{x}(k), \boldsymbol{\theta}; \overline{\mathbf{u}}, \overline{\mathbf{x}}, \overline{\theta}\right) \ \text{s.t.} \ \begin{cases} \overline{\mathbf{x}}(k) \in \mathbf{x}(k) \oplus (-\Phi_K) \\ \left[\overline{\mathbf{x}}(k+j)^T \ \overline{\mathbf{u}}(k+j)^T\right]^T \in \overline{\mathscr{Z}} \\ \left[\overline{\mathbf{x}}_s(k+j)^T \ \overline{\mathbf{u}}_s(k+j)^T\right]^T = \mathbf{M}_{\boldsymbol{\theta}}\,\overline{\boldsymbol{\theta}} \\ \left[\overline{\mathbf{x}}(k+h)^T \ \overline{\theta}(k+h)^T\right]^T \in \Omega^a_{t,\overline{\mathbf{K}}} \end{cases} \tag{3}$$

where h is the prediction horizon, i.e, the number of time steps into the future that the controller uses to calculate the optimal control action sequence $\overline{\mathbf{u}}^*(k)$, $\boldsymbol{\theta}$ is the

sequence associated to the changing trajectory setpoint $\mathbf{r}$, $\Omega_{t,\overline{\mathbf{K}}}^{a}$ is the Invariant Set for Tracking, Φ_K is the robust positively invariant set and the cost function,

$$
\begin{aligned}
\mathbf{V}_t\left(\mathbf{x}(k), \boldsymbol{\theta}; \overline{\mathbf{u}}, \overline{\mathbf{x}}, \overline{\theta}\right) =& \sum_{j=0}^{h-1} \left(\overline{\mathbf{x}}(k+j) - \overline{\mathbf{x}}_s(k+j)\right)^T \mathbf{Q}\left(\overline{\mathbf{x}}(k+j) - \overline{\mathbf{x}}_s(k+j)\right) \\
&+ \sum_{j=0}^{h-1} \left(\overline{\mathbf{u}}(k+j) - \overline{\mathbf{u}_s}(\mathbf{k+j})\right)^T \mathbf{R}\left(\overline{\mathbf{u}}(k+j) - \overline{\mathbf{u}}_s(k+j)\right) \\
&+ \left(\overline{\mathbf{x}}(k+h) - \overline{\mathbf{x}_s}\right)^T \mathbf{P}\left(\overline{\mathbf{x}}(k+h) - \overline{\mathbf{x}_s}\right) \\
&+ \sum_{j=0}^{h} \left(\overline{\theta}(k+j) - \boldsymbol{\theta}(k+j)\right)^T \mathbf{T}\left(\overline{\theta}(k+j) - \boldsymbol{\theta}(k+j)\right)
\end{aligned}
$$

where $\mathbf{Q}$, $\mathbf{R}$, $\mathbf{T}$ and $\mathbf{P}$ are ponderation matrices, whose tuning is discussed in [12].

Finally, the real one control action by means of the **local tracking controller**, which considers the error generated by disturbances,

$$
\mathbf{u}^*(k) = \overline{\mathbf{u}}^*(k) + \mathbf{K}\left(\mathbf{x}(k) - \overline{\mathbf{x}}^*(k)\right) \tag{4}
$$

3 Application to the 5R Parallel Robot

The control law detailed in the previous section is defined for discrete, space state time invariant systems, and requires the definition of bounds in order to be implemented. In this section the procedure to implement the RMPC-T to parallel robots is detailed by analyzing a study case based on the 5R parallel robot. However, it should be noted that this procedure can be applied to any parallel robot.

The first requirement to be fulfilled is to linealize the dynamics of the 5R parallel robot (Fig. 1), which can be calculated using the traditional formulation in the *task space* $\boldsymbol{\tau} = \mathbf{D}\ddot{\mathbf{q}} + \mathbf{H}(\mathbf{q}, \dot{\mathbf{q}})$, where $\mathbf{q} = \begin{bmatrix} x \, y \end{bmatrix}^T$ are the Tool Center Point (TCP) cartesian coordinates[13]. Table 1 summarizes the parameters selected for this study case.
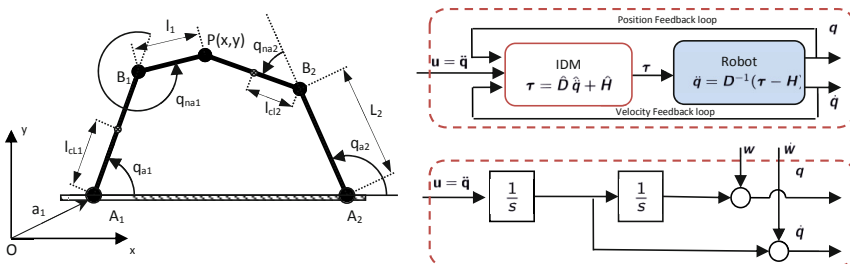
Fig. 1 5R Parallel Robot and nonlinear feedback linearization approach

Table 1 5R parallel robot model parameters (IS units)

Parameter	Real Value	Identified Value (MPC Model)
$\mathbf{a_1}$	$\begin{bmatrix} -0.5 & 0 \end{bmatrix}^T$ (m)	$\begin{bmatrix} -0.4950 & -0.005 \end{bmatrix}^T$ (m)
$\mathbf{a_2}$	$\begin{bmatrix} 0.5 & 0 \end{bmatrix}^T$ (m)	$\begin{bmatrix} 0.4950 & -0.005 \end{bmatrix}^T$ (m)
$L_1 = L_2$	0.5 (m)	0.495 (m)
$l_1 = l_2$	1 (m)	0.995 (m)
m_c	0.5 (kg)	0.6 (kg)
m_{L_1}	0.4239 (kg)	0.3239 (kg)
m_{L_2}	0.4239 (kg)	0.4239 (kg)
$m_{l_1} = m_{l_2}$	0.8477 (kg)	0.7477 (kg)
$I_{L_1} = I_{L_2}$	$8.800 \cdot 10^{-3}$ (kg m^2)	$8.800 \cdot 10^{-3}$ (kg m^2)
$I_{l_1} = I_{l_2}$	$7.070 \cdot 10^{-2}$ (kg m^2)	$7.770 \cdot 10^{-2}$ (kg m^2)
I_c	$8.3333 \cdot 10^{-4}$ (kg m^2)	$8.3333 \cdot 10^{-4}$ (kg m^2)

For that purpose, the linearization by nonlinear feedback technique is used, so that in the ideal case, if no model errors arise, the linearized system can be reduced to a set of two decoupled double integrator systems (Fig. 1) $\mathbf{u} = \ddot{\mathbf{q}}$. Hence, the state vector of the linealized system can be defined as $\mathbf{x} = \begin{bmatrix} \mathbf{q}^T & \dot{\mathbf{q}}^T \end{bmatrix}^T$.

One of the main issues in parallel robotics is the difficulty measuring the real TCP position and speed, which is usually estimated using the actuated joint data and the use of the kinematic relations. In presence of uncertainties, this estimation can present errors, so that the real state $\mathbf{x}$ and the estimated one $\hat{\mathbf{x}}$ diverge. In general, it is possible to bound this error within the operational workspace of the robot, so that the linearized dynamic model can be approximated to,

$$\begin{aligned} \hat{\mathbf{x}}(k+1) &= \mathbf{A}\hat{\mathbf{x}}(k) + \mathbf{B}\mathbf{u}(k) + \mathbf{w}'(k) \\ \mathbf{x} &= \hat{\mathbf{x}} + \mathbf{v} \end{aligned} \rightarrow \begin{aligned} \mathbf{x}(k+1) &= \mathbf{A}\mathbf{x}(k) + \mathbf{B}\mathbf{u}(k) + \mathbf{w}(k) \\ \mathbf{w}(k) &= \mathbf{w}'(k) + (\mathbf{I} - \mathbf{A})\mathbf{v}(k) \end{aligned} \quad (5)$$

where $\mathbf{v}(k) = \mathbf{x} - \hat{\mathbf{x}}$ models estimation errors and $\mathbf{w}'(k)$ models errors due to the uncertainties of the dynamic model and uncompensated dynamics of the robot. Hence, if the real state $\mathbf{x}$ is considered for application of the MPC control law, $\mathbf{w}(k)$ group the disturbances of both types.

If a sample time of $T_s = 10ms$ is selected, the discretized dynamics of the set of double integrator systems in the 5R parallel manipulator is,

$$\mathbf{A} = \begin{bmatrix} 1 & 0 & 0.01 & 0 \\ 0 & 1 & 0 & 0.01 \\ 0 & 0 & 1 & 0 \\ 0 & 0 & 0 & 1 \end{bmatrix} \quad \mathbf{B} = \begin{bmatrix} 5 \cdot 10^{-5} & 0 \\ 0 & 5 \cdot 10^{-5} \\ 0.01 & 0 \\ 0 & 0.01 \end{bmatrix}$$

In order to implement the proposed MPC, all variables have to be bounded, and the disturbances maximum and minimum values defined. For that purpose, first the operational workspace of the 5R parallel robot will be defined arbitrarily in a

(a) Operational Worskpace   (b) Invariant sets
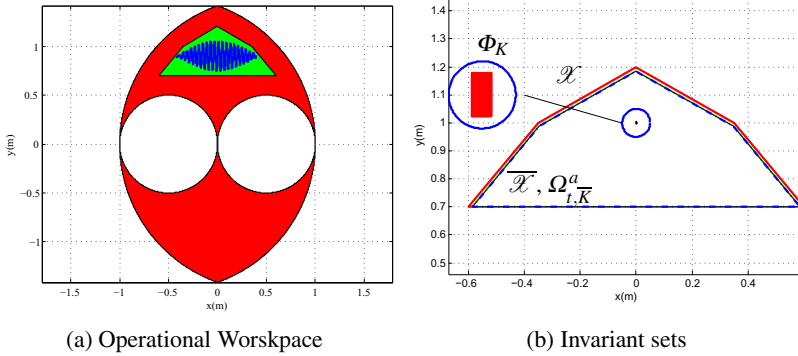
Fig. 2 Validation trajectories, operational workspace and invariant sets

nonsingular region of its workspace associated to a fixed working and assembly mode. This region will be defined by a set $\mathscr{X}$. However, as the real state $\mathbf{x}$ cannot be measured directly, the MPC will be implemented using the estimated one $\hat{\mathbf{x}}$. The RMPC-T controller will ensure that the real state $\mathbf{x}$ will be always within the tube of trajectories defined by the estimated one $\hat{\mathbf{x}}$ and the RPI Φ_K,

$$\hat{\mathbf{x}} \in \hat{\mathscr{X}} = \mathscr{X} \ominus \Phi_K \Rightarrow \hat{\mathbf{x}}' \in \hat{\mathscr{X}} \tag{6}$$

where $\mathscr{X}$ is defined by a polytope defined in *XY* plane, Fig. 2a, and the maximum linear speed of the TCP, which has been limited to $\pm 3 m/s$.

The bounds of the estimation error $\mathbf{v}$ are calculated by discretizing the operational workspace defined for $\mathscr{X}$ and measuring the speed and positioning errors for each set. In order to bound the state disturbance $\mathbf{w}'$, the performance of the ideal double integrator system and the linearized dynamics of the 5R parallel robot considering the parameters of Table 1 are considered. The resulting bounds are,

$$
\begin{aligned}
v_x &\in [-0.0014, 0.0016] \text{ (m)} & w_x &\in \left[-5.4131 \cdot 10^{-5}, 2.6455\,10^{-5}\right] \text{ (m)} \\
v_y &\in [0.0025, 0.0091] \text{ (m)} & w_y &\in \left[-6.1584 \cdot 10^{-5}, 1.1981\,10^{-4}\right] \text{ (m)} \\
v_{\dot{x}} &\in [-0.0324, 0.0324] \text{ (m/s)} & w_{\dot{x}} &\in [-0.01131, 0.0039132] \text{ (m/s)} \\
v_{\dot{y}} &\in [-0.0425, 0.0425] \text{ (m/s)} & w_{\dot{y}} &\in [-0.0093394, 0.022516] \text{ (m/s)}
\end{aligned}
\tag{7}
$$

Finally, the system input is bounded. For that purpose, the inverse dynamic model is required $\mathbf{u} = \hat{\mathbf{D}}^{-1} \left(\boldsymbol{\tau} - \hat{\mathbf{H}} \right)$, which relates the input of the linearized robot, $\mathbf{u}$ and the torque exerted by the motors $\boldsymbol{\tau}$. Being nonlinear and dependent on the state $\mathbf{x}$, a conservative approach is considered, in which the set of all possible admissible sets for $\mathbf{u}$ are calculated considering all admissible states $\mathbf{x} \in \mathscr{X}$. Then, the intersection of all sets is considered as the admissible set $\mathscr{U}$.

4 Simulation Results

The linealized dynamic model and the bounded sets defined previously have been used to implement the RMPC-T. The prediction horizon has been set in $h = 3$ steps and the ponderation gains and local robust controller gains have been tuned following the procedure detailed in [12]. The resulting invariant sets are defined in Fig. 2b.

In order to demonstrate the effectiveness of the robust MPC for tracking approach, it has been compared with the robust MPC for tracking proposed in [1] (RMPC) and the classical Computed Torque Control (CTC) approach. Both controllers have been tuned to achieve maximum performance within the defined physical constraints. A senoidal trajectory in the *XY* plane and within the operational workspace has been selected as reference (Fig. 2a).

TCP positioning errors and mean of the squared error (mse) performance indexes are shown in Fig. 3. As it can be seen, the best performance is achieved by the RMPC-T, reducing the tracking error in 47% in comparison with the RMPC and 30% with respect to the CTC. Hence, the proposed RMPC-T is able to adapt to the future changing trajectory before changes actually occur, resulting in very low tracking error. The RMPC [1], however, considers a constant reference in its prediction horizon, which penalizes its performance. Finally, the classical CTC is not able to anticipate to future reference changes, and focuses in compensating the actual error, which leads to larger trajectory tracking errors. Hence, the main advantage of the proposed RMPC-T controller is demonstrated, which can be implemented to reduce significantly the tracking error of parallel robots.
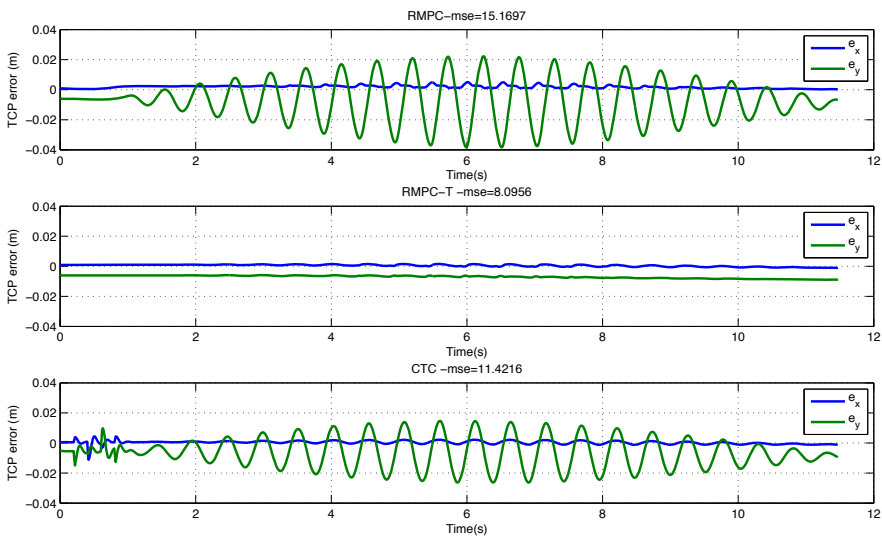
Fig. 3 Performance of Robust MPC, Robust MPC for traj. tracking and Computed Torque Control approaches

5 Conclusions

Control is a key issue in parallel robotics, as proper control approaches are required in order to exploit the theoretical capabilities. In this work a novel Robust Model Predictive Control approach for trajectory tracking (RMPC-T) has been presented, and its application to a 5R parallel robot prototype detailed. Simulation results show that this approach can provide enhanced tracking capabilities to parallel robots in comparison with classical CTC or MPC approaches.

References

1. Alvarado, I.: Model predictive control for tracking constrained linear systems. Ph.D. thesis, Escuela Técnica Superior de Ingenieros Universidad de Sevilla (2007)
2. Belda, K., Böhm, J., Valášek, M.: State-Space Generalized Predictive Control for Redundant Parallel Robots. Mechanics Based Design of Structures and Machines 31(3), 413–432 (2003)
3. Brecher, C., Ostermann, T., Friedrich, D.: Control concept for pkm considering the mechanical coupling between actuator. In: Proceedings of the 5th Chemnitz Parallel Kinematics Seminar, pp. 413–427 (2006)
4. Camacho, E., Bordons, C.: Control predictivo: Pasado, presente y futuro. Revista Iberoamericana de Automtica e Informtica Industrial (RIAI) 1(3) (2004) (in Spanish)
5. Honegger, M., Codourey, A., Burdet, E.: Adaptive control of the hexaglide, a 6 dof parallel manipulator. In: IEEE International Conference in Robotics and Automation (1997)
6. Kolmanovsky, I., Gilbert, E.G.: Theory and conmputation of disturbance invariant sets for discrete-time linear systems. Mathematical Problems in Engineering: Theory, Methods and Applications 4, 317–367 (1998)
7. Lee, S.H., Song, J.B., Choi, W.C., Hong, D.: Position control of a stewart platform using inverse dynamics control with approximate dynamics. Mechatronics 13, 605–619 (2003)
8. Merlet, J.-P.: Parallel Robots, 2nd edn. Kluwer (2006)
9. Stan, S., Manic, M., Maties, M., Balan, R.: Kinematics analysis, design, and control of an isoglide3 parallel robot (ig3pr). In: Proc. 34th Annual Conference of the IEEE Industrial Electronics Society, pp. 1265–1275 (2008)
10. Vivas, A., Poignet, P.: Model based predcitive control of a fully parallel robot. In: Proceedings of the 7th IFAC Symposium on Robot Control (SYROCO 2003), pp. 253–258 (2003)
11. Yen, P., Lai, C.: Dynamic modeling and control of a 3-dof cartesian parallel manipulator. Mechatronics 19(3), 390–398 (2009)
12. Zubizarreta, A.: Estrategias de control avanzado para robots paralelos. Ph.D. thesis, University of the Basque Country, UPV/EHU (2010) (in spanish)
13. Zubizarreta, A., Cabanes, I., Marcos-Muñoz, M., Pinto, C.: Experimental validation of the extended computed torque control approach in the 5r parallel robot prototype. In: Su, C.-Y., Rakheja, S., Liu, H. (eds.) ICIRA 2012, Part II. LNCS (LNAI), vol. 7507, pp. 509–518. Springer, Heidelberg (2012)

A Calibration Method for a Six-Degree-of-Freedom Parallel Manipulator with a Redundant Passive Chain

T. Oiwa[1] and H. Ikuma[2]

[1] Shizuoka University, Japan
   `tmtooiw@ipc.shizuoka.ac.jp`
[2] Graduate school, Shizuoka University, Japan

Abstract. This paper examines parameter identification for six-degree-of-freedom (6-DOF) parallel manipulators, from the point of view of measurement redundancy. A redundant passive chain with a displacement sensor is installed between the moving stage and the machine frame, and is passively expanded and contracted by actuation of the 6-DOF manipulator. Linear encoders built in seven prismatic joints in the passive chain and six actuated chains measure change in length of the chains during traveling of the end-effector. Moreover, length error in one of the seven chains can be calculated from the forward kinematics of a 6-DOF parallel manipulator consisting of the remaining 6 chains. Consequently, comparison between the measured seven lengths and calculated seven lengths reveals seven length errors at each pose of the end-effector because seven combinations are possible. The least-squares method using a Jacobian matrix corrects 37 kinematic parameters so that the length errors of the seven chains are minimized. The above calculations were repeated until convergence in both numerical simulations and experiments employing a coordinate measuring machine based on the parallel manipulator. Moreover, coordinate measurement using a 3-D ball plate was performed to verify the identified parameters. The measurement result demonstrated that the average coordinate error of 0.161 mm was reduced to 0.066 mm.

Keywords: parallel manipulator, hexapod manipulator, kinematic calibration, redundant passive chain.

1   Introduction

For the last half-century, many types of parallel kinematic manipulators have been applied to various industry fields, such as flight simulators, high-speed robots, and machine tools, because these manipulators allow for and provide dexterity, stiffness and high-speed capability. Parallel manipulators have great promise for application in precision machines such as coordinate measuring machines (CMMs) and precision positioning stages, because the parallel mechanism has

many advantages for improving the motion accuracy, such as higher stiffness, non-cumulative motion errors, smaller inertial mass of moving parts and Abbe-error free due to observable angular motions[1].

These advantages allow the parallel manipulator to have great repetitive motion accuracy. However, it is difficult to improve absolute motion accuracy, namely volumetric accuracy, which is usually a systematic error caused by kinematic parameter errors of the manipulator. Various methods have been proposed to solve this problem via the kinematic calibration of such parameters [2], including 1) directly measuring the kinematic parameters, such as the position of a joint or the size of a link with other measurement devices, 2) changing the position and orientation of an end-effector and modifying the parameters until there is no difference from the target value, and 3) increasing the DOF of the measuring system in the manipulator, that is, adding more sensors so that there are more sensors than there are DOF of the manipulator's motion. In other words, these methods use redundancy of the measuring system to identify the kinematic parameters [3–7]. Moreover, the third method includes mounting a sensor on a passive joint for redundancy or constraining one or more DOF of the manipulator's motion for redundancy.

Here we discuss parameter identification based on measurement redundancy employing an additional sensor. A redundant passive chain equipped with a linear encoder to measure change in the length of the chain was installed between the moving stage and the machine frame of a Gough platform manipulator. The results of numerical simulations and experiments are reported.

2   Calibration Method with One Redundant Chain

Figure 1 illustrates a hexapod-type 6-DOF parallel manipulator, the so-called Gough platform, consisting of 6-SPS or 6-SPU chains. When each prismatic joint is actively moved by an actuator, the change in length of the chain can be measured by a displacement sensor installed in the prismatic joint. In addition, a redundant passive chain consisting of two spherical joints and a prismatic joint is installed between the moving stage and the machine frame. When the passive chain is expanded and contracted by actuation of the manipulator during traveling of the moving stage in its working space, a length sensor installed in the prismatic joint measures the change in length of the passive chain. Meanwhile, because six prismatic joints of the manipulator's chains also have length sensors, the pose of the moving stage can be calculated by using the forward kinematics of the hexapod manipulator. Thus, change in length of the passive chain can also be calculated by using the pose of the moving stage. However, there is a difference between measured length and calculated length, because the kinematic parameters of the forward kinematics contain geometrical errors before calibration. The least-squares method using a Jacobian matrix corrects the kinematic parameters so that the length errors of this passive chain are usually minimized. However, the change in length of the passive chain becomes extremely small when the stage moves

perpendicular to the passive chain axis, and in such a case, kinematic parameters cannot be accurately identified. Employing a double-ball-bar system to measure the change in distance between the end-effector and a ball fixed on the surface plate eliminates this problem [6, 8], because the bar axis varies in direction during operation.
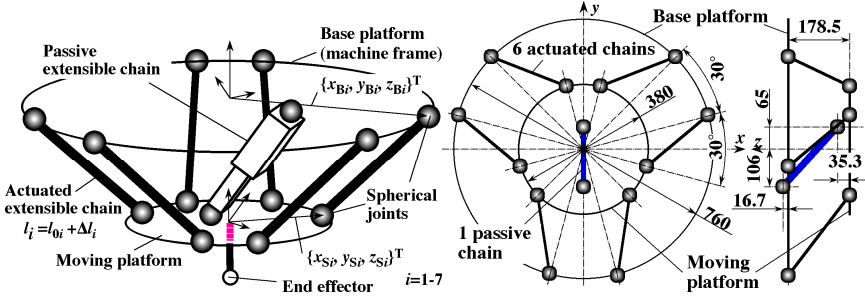
Fig. 1 Kinematic parameters of 6-DOF parallel manipulator with one passive redundant chain

In our previous study for calibrating a 3-DOF parallel manipulator[9], one passive chain was sequentially placed in three configurations with approximately right angles to each other for ensuring reliable expansion and contraction during traveling of the moving stage in its working space. In the present study, not only one passive chain but also six active chains are used for calculating the length error to minimize. In other words, length error in one of the seven chains can be calculated from forward kinematics of a 6-DOF manipulator consisting of the remaining six chains. Therefore, comparison between the measured seven lengths and calculated seven lengths reveals seven length errors at each pose of the end-effector, because seven combinations are possible. The least-squares method using a Jacobian matrix corrects 37 kinematic parameters so that the length errors of the seven chains are minimized. Consequently, we believe this method avoids the insensible problem in measured length of the passive chains, because seven chains are configured in different directions.

Figure 1 also depicts 37 kinematic parameters to be identified in this report, consisting of 30 parameters of 14-joint positions at the ends of chains, and seven parameters of the initial lengths of the seven chains, l_{0i}. The i is the chain number ($i=1,...,7$). Note that 12 coordinates of these 14 joints' positions are fixed to two coordinate systems on the base platform and the moving stage, and are exempted from parameter identification. The length errors of seven chains at one pose of the end-effector, Δl_i, can be expressed by

$$\Delta l_i = J\Delta\phi \ , \tag{1}$$

where J is a Jacobian matrix, $\Delta\phi$ is the error of the kinematic parameters. The length errors at n poses of the end-effector are

$$\Delta l_{in} = \left[\Delta l_{i1}, \Delta l_{i2}, \cdots, \Delta l_{in}\right]^T \ . \tag{2}$$

The Jacobian matrixes at n poses are

$$A = \left[J_1, J_2, \cdots, J_n\right]^T \ . \tag{3}$$

Therefore, by using ordinary least-squares, we have

$$\Delta\phi = \left(A^T A\right)^{-1} A^T \Delta l_{in} \ . \tag{4}$$

During each iteration, the nominal parameter values are updated by above $\Delta\phi$. This procedure is iterated 30 times in this paper. After that, the $\Delta\phi$ were less than 1 µm in calibration simulation.

3   Calibration Simulation

Before calibrating for an actual parallel manipulator, we performed a computer simulation to verify the calibration method based on one passive chain. First, assuming geometrical errors of the manipulator's mechanical elements, we introduced random errors within ±1 mm into 37 kinematic parameters. Figure 1 also indicates the link configuration of the manipulator used in both the simulation and the experiment. In addition, considering measurement errors of the displacement sensors including spherical joints' runouts in six chains, we added random errors with ±1-µm amplitude to calculated lengths of the seven chains, because pose errors were successfully diminished to approximately zero after calibration without the measurement errors. Positions of the end-effector were located as equally as possible on the 7 planes shown in Figure 2, and the orientations of the end-effector were randomly configured within ±0.2 rad around x, y and z axes. The number of calibration   poses increased from 50 to 300.
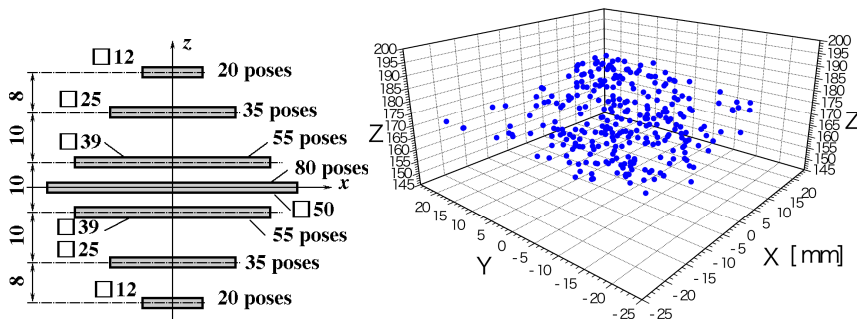
Fig. 2 300-pose distribution in working space for calibration simulation and experiment
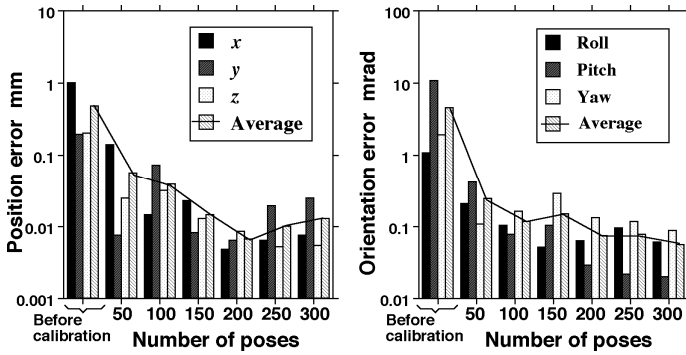
Fig. 3 Mean deviation of pose errors before and after calibration simulation

As a result of the identification, the average length error of seven chains decreased from 1.77 mm to 0.11 µm (less than 10^{-4}), even when 100 calibration poses were used. Figure 3 depicts the mean deviation of position errors and orientation errors of the end-effector before and after calibration. Although the pose error was mm-order and 10-mrad-order before calibration, the errors decreased to approximately 0.01 mm and 0.1 mrad when using more than 200 poses. These bar charts also indicate that the pose error decreased in inverse proportion to the number of calibration poses. Moreover, introduced measurement errors of the seven chains ie. ±1 µm strongly affected on the calibration results. For instance, tenfold errors produce single-digit increase of the pose errors. In addition, parameter identification based on length errors measured by only one passive chain diverged the calculation, and not converged even when the measurement errors were introduced into only passive chain.

4   Calibration Experiment

The calibration method based on one redundant passive chain was demonstrated in an experimental manipulator shown in Fig. 4. The manipulator consisted of six active chains with two spherical joints (Hephaist seiko Co., Ltd., SRJ016C) and a prismatic joint. Each prismatic joint is expanded and contracted by an AC servomotor and a ball screw. Six linear scale units (Sony Laser Scale BS77+ BD11, measuring range: 70 mm, system accuracy: ±0.08 µm, measuring resolution: 0.01 µm) measured the change in length of six active chains when the end-effector moved to as many as 300 target poses, as in the calibration simulation. A plunger-type linear encoder (Heidenhain length gauge, MT60K, measuring range: 60 mm, system accuracy: ±0.5 µm, measuring resolution: 2 nm) equipped with two spherical couplings (Heidenhain, ID206310-01) at both ends was used as the passive chain. The length error of the seven chains was calculated by comparing the measured length with the length calculated from the forward kinematics. Identification of the kinematic parameters was performed by the least-squares method in the same manner as in the simulation. After 100 iterations, the kinematic parameters were identified, because the correcting value of all parameters completely converged to less than one micrometer.
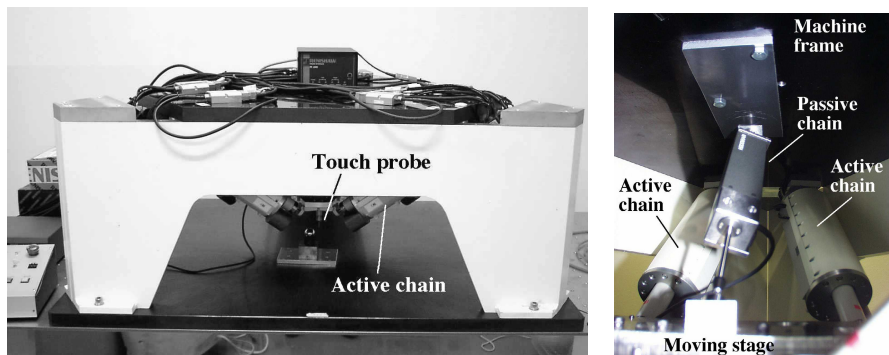
Fig. 4 Experimental manipulator and passive chain installed between frame and moving stage
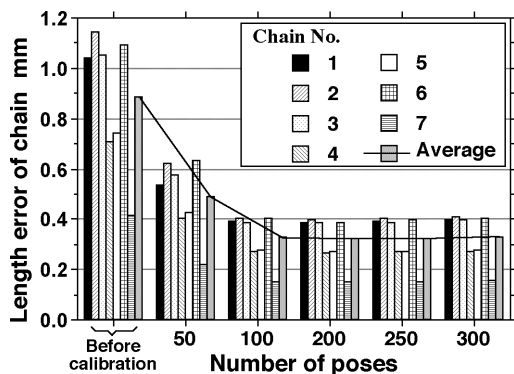
Fig. 5 Averaged length error of seven chains before and after calibration

Figure 5 depicts the mean deviation of chains' length errors before and after calibration. This means that parameter identification reduced the average length error of seven chains from more than 1.1 mm to less than 0.4 mm. The reduction ratio was approximately one third in the experiment although it was one ten-thousandth in the simulation described in chapter 3. It is expected that actual measurement error of the passive chain including runouts of the spherical joints were significantly worse than ±1µm assumed in the simulation. In addition, thermal deformation of the machine structure certainly spoiled the measurement accuracy because the measuring or 300-pose data acquisition lasted several hours in ordinary temperature environment.

To verify the identified parameters after the calibration, we had the manipulator shown in Fig. 3 measure the balls' respective coordinates on the three-dimensional ball plate shown in Fig. 6, because this manipulator has a touch trigger probe system (Renishaw TP200) as an end-effector, and has a function of CMM. The ball plate measures 20x20x7 mm^3 and consists of five 3/8"-diameter balls having a

sphericity error less than 0.13 µm. A commercial conventional CMM (Brown & Sharpe, Chameleon 765) calibrated the ball plate before the verification.

The bar chart on the left side of Fig. 6 indicates the result of the ball plate measurement. Although mean deviation of measured coordinate errors of five balls were 0.161 mm_{MD} (peak-to-peak value: 0.448 mm_{p-p}) before calibration, the parameter identification decreased these errors to 0.066 mm_{MD} (41%) and 0.258 mm_{p-p} (58%), respectively.
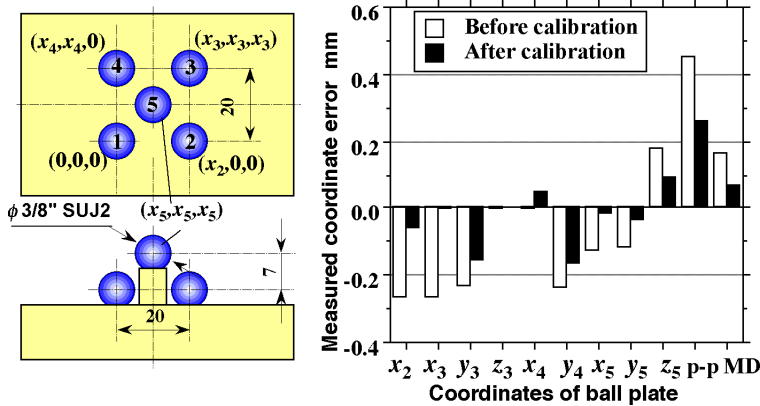
Fig. 6 Configuration of 3-D ball plate and verification result for identified parameters

5   Discussion

In the verification experiment, the balls' coordinates were calculated by the forward kinematics with not only the identified parameters but also unidentified parameters related to the end-effector or the touch trigger probe. Using the method described in this paper, we were not able to identify these probe parameters in principle, because these parameters' errors have no effect on the length error of the passive chain. In other words, this method requires another identification only for probe parameters. The authors are considering identifying the probe parameters by using the coordinate errors of the 3-D ball plate.

6   Conclusions

A calibration method based on measurement redundancy has been described for identifying 37 kinematic parameters of a 6-DOF parallel manipulator. One passive chain was installed in the manipulator. Change in lengths of seven chains were calculated when the moving stage moves in the working space. During identification iterations, length errors of seven chains were reduced to approximately one 10-thousandth in numerical simulation and one third in the

experiment. Verifications for the identified parameters were performed in experimental measurement with a 3-D ball plate. The experiment showed that the identification reduced the measured deflections to approximately half of that before calibration.

References

1. Oiwa, T.: Precision Mechanisms Based on Parallel Kinematics. International Journal of Automation Technology 4(4), 326–337 (2010)
2. Merlet, J.-P.: Parallel Robots, p. 289. Springer (2006)
3. Nahvi, A., Hollerbach, M.J.: Calibration of a Parallel Robot Using Multiple Kinematic Closed Loops. In: Proc. IEEE Int. Conference on Robotics and Automation, pp. 407–412 (1994)
4. Zhuang, H.: Self-Calibration of Parallel Mechanisms with a Case Study on Stewart Platforms. IEEE Transactions on Robotics and Automation 13(3), 387–397 (1997)
5. Wampler, W.C., Hollerback, M.J., Arai, T.: An Implicit Loop Method for Kinematic Calibration and Its Application to Closed-Chain Mechanisms. IEEE Trans. Robotics and Automation 11(5), 710–714 (1995)
6. Patel, J.A., Ehmann, F.K.: Calibration of a hexapod machine tool using a redundant leg. International Journal of Machine Tools and Manufacture 40(4), 489–512 (2000)
7. Chiu, Y.-J., Perng, M.-H.: Self-calibration of a general hexapod manipulator with enhanced precision in 5-DOF motions. Mechanism and Machine Theory 39(1), 1–23 (2004)
8. Takeda, Y., Shen, G., Funabashi, H.: A DBB-Based Kinematic Calibration Method for in-Parallel Actuated Mechanisms Using a Fourier Series. Journal of Mechanical Design 126, 856–865 (2004)
9. Oiwa, T., Daido, H., Asama, J.: A calibration method for a three-degree-of-freedom parallel manipulator with a redundant passive chain. Applied Mechanics and Materials 162, 171–178 (2012)

Non-singular Transitions Based Optimal Design Methodology for Parallel Manipulators

M. Urízar, V. Petuya, M. Diez, E. Macho, and A. Hernández

University of the Basque Country, Faculty of Engineering in Bilbao
Mechanical Engineering Dept., Bilbao, Spain
monica.urizar@ehu.es

Abstract. In this paper, an optimal design methodology for three-degree-of-freedom planar or spatial parallel manipulators is presented. In particular, cuspidal manipulators, which own the ability of performing non-singular transitions, are addressed. The design procedure incorporates the transitioning ability into the design criteria. An initial stage of the procedure comprises the analysis of different designs by means of characterizing configuration space entities. This gives an overall insight into the capacities of the robot. Then, the dimensional synthesis focuses on cuspidal designs in order to find the set of optimum design parameters such that the operational workspace is as larger as possible having also a regular shape. So as to illustrate the methodology, the 3-S$\underline{P}$S-S spatial orientation manipulator is used.

Keywords: parallel manipulator, non-singular transition, configuration space, dimensional synthesis.

1   Introduction

The design of parallel manipulators is usually approached by searching for the design parameters such that certain important requirements are achieved. From the kinematic point of view, dimensional optimization processes are mainly focused on: workspace [4, 5], kinematic performance indices [1], task development [6], accuracy [2], etc.

In this paper, a design methodology basing on the ability of some parallel manipulators to perform non-singular transitions is presented [9, 3, 8]. In general, this ability enables extending the range of motion of the manipulator, as the robot can move between different regions of the workspace in a safety and controlled way. Therefore, it is desirable to consider this property at the design stage.

Through this paper the guidelines of the proposed design methodology, valid for planar or spatial three-degree-of-freedom parallel manipulators, will be explained making use of the 3-S$\underline{P}$S-S spatial orientation manipulator. Spatial orientation manipulators have a broad range of applications, such as: orienting a tool or a workpiece,

camera devices, solar panels and space antennas, haptic devices, robotic wrists, etc. It will be shown that some designs of the manipulator under study present the *cuspidality property*, and this influences significantly on the resultant operational workspace. The dimensional synthesis will be approached using the design parameter space, in which the set of possible designs are evaluated according to different indicators. The workspace evaluation is considered in the optimization process, searching for optimum designs that have a wider and regular workspace.

2   Guidelines of the Design Methodology

The design procedure aims at the optimization of the workspace exploiting the transitioning ability. The latter refers to the capacity of some parallel manipulators to move among different solutions of the Direct Kinematic Problem (DKP) without crossing any singularity. The main steps of the methodology are (highlighted in the flow chart of Fig. 1):

- **Kinematic problems:** This includes solving the position and velocity problem, and obtaining the characteristic polynomial (assess the number of DKP solutions) and singularity loci.
- **Configuration space:** Analyze the entities of the configuration space, such as the joint space, workspace and reduced configuration space. The visualization of these entities for different designs gives an overall insight into the transitioning ability.
- **Locus of cusp points:** Verify the existence of cusp points in singularity curves inside joint space sections. For a manipulator under study, some particular designs can have or not the *cuspidality* property.
- **Dimensional synthesis:** An optimization process based on the *design parameter space* is proposed. The set of geometric parameters establishes three-dimensional graphs, each point of the graph corresponding to a specific design. Each design is characterized according to different features, two main design goals being the existence of cusps in the joint space and the workspace evaluation, regarding its size and shape.

3   Case Study: 3-S$\underline{P}$S-S Parallel Manipulator

3.1   *Kinematics*

The spatial orientation 3-S$\underline{P}$S-S parallel manipulator shown in Fig. 2a will be studied. It is made up of a moving platform $OB_1B_2B_3$, a base platform $OA_1A_2A_3$, and three extensible limbs denoted by l_i. Both platforms take the form of a tetrahedron, connected one to each other by a fixed spherical joint at point O. The robot has 3-DoF, the Euler angles (ϕ, θ, ψ), defining the orientation of the moving platform.

The fixed spherical joints A_i are located on the principal axes of the fixed frame $\mathscr{F}\{\mathbf{x}, \mathbf{y}, \mathbf{z}\}$ fulfilling $|\overrightarrow{OA_i}| = R$, for $i = 1, 2, 3$. Besides, joints B_i are located with respect to the moving frame $\mathscr{M}\{\mathbf{u}, \mathbf{v}, \mathbf{w}\}$ (see Fig. 2b) as follows:
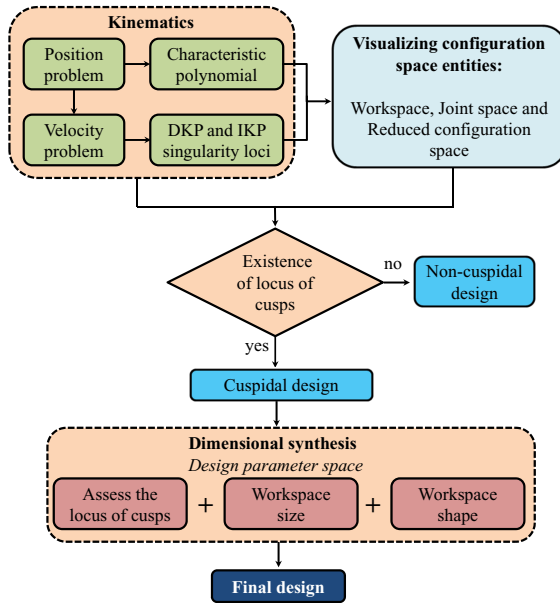
Fig. 1 Flow chart of the proposed design methodology

$$^{\mathcal{M}}\mathbf{b}_1 = L\,[0,0,1]^T \tag{1}$$

$$^{\mathcal{M}}\mathbf{b}_2 = L\,[b_{2u},0,b_{2w}]^T = L\,[c\beta_2,0,s\beta_2]^T$$

$$^{\mathcal{M}}\mathbf{b}_3 = L\,[b_{3u},b_{3v},b_{3w}]^T = L\,[c\beta_3c\gamma_3,c\beta_3s\gamma_3,s\beta_3]^T$$

The vector $^{\mathcal{F}}\mathbf{b}_i$, or simply $\mathbf{b}_i$, expressed with respect to the fixed frame $\mathcal{F}$ is:

$$\mathbf{b}_i = [b_{ix},b_{iy},b_{iz}]^T = {}_{\mathcal{M}}^{\mathcal{F}}\mathbf{R}\,{}^{\mathcal{M}}\mathbf{b}_i \tag{2}$$

The loop-closure equation for each limb is $\mathbf{l}_i = \mathbf{b}_i - \mathbf{a}_i$, which results in the following system for $i = 1,2,3$:

$$l_i^2 = \mathbf{a}_i^2 + \mathbf{b}_i^2 - 2\mathbf{a}_i^T\mathbf{b}_i \tag{3}$$

From Eq. 3, the inverse kinematics yields one possible solution for l_i. The direct kinematics, solved in Tsai [7], presents a maximum of eight DKP solutions.

So as to solve the velocity problem the loop-closure equations are differentiated with respect to time, obtaining the Jacobian matrices:

$$\mathbf{J}_{DKP} = \begin{bmatrix} (\mathbf{b}_1 \times \mathbf{l}_1)^T \\ (\mathbf{b}_2 \times \mathbf{l}_2)^T \\ (\mathbf{b}_3 \times \mathbf{l}_3)^T \end{bmatrix} ; \quad \mathbf{J}_{IKP} = \begin{bmatrix} l_1 & 0 & 0 \\ 0 & l_2 & 0 \\ 0 & 0 & l_3 \end{bmatrix} \tag{4}$$
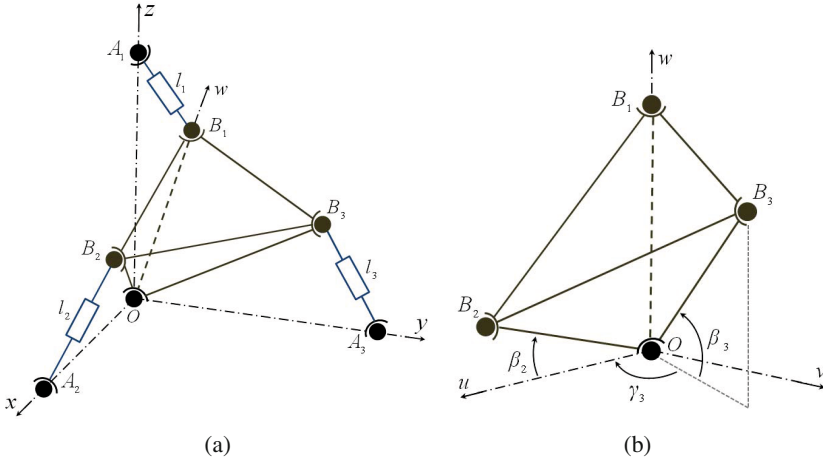
Fig. 2 (a) Spatial orientation 3-SPS-S parallel manipulator; (b) Design parameters of the moving platform

The inverse Jacobian matrix, $\mathbf{J}_{IKP}$, is singular only whenever any of the prismatic limbs has zero length, which cannot be achieved in practice. Hence, we focus on the analysis of the DKP singularity locus, given by the nullity of the determinant:

$$|\mathbf{J}_{DKP}| = -R^3 L^3 \cdot s\theta \cdot \xi \tag{5}$$

where

$$
\begin{aligned}
\xi = {} & c^2\phi c\theta (b_{2w}(b_{3u}s\psi + b_{3v}c\psi) - b_{3w}(b_{2u}s\psi)) - c^2\phi s\theta (b_{3v}b_{2u}) \\
& + c^2\psi s\theta (b_{2u}b_{3v}) + s\theta c\psi s\psi (b_{2u}b_{3u}) - c\theta (b_{2w}(b_{3u}s\psi + b_{3v}c\psi)) \\
& + s\phi c\phi (b_{2w}(b_{3u}c\psi - b_{3v}s\psi) - b_{3w}b_{2u}c\psi)
\end{aligned}
\tag{6}
$$

Equation 5 shows that the determinant of $\mathbf{J}_{DKP}$ factorizes into three terms:

- The constant $R^3 L^3$ does not affect the shape of the DKP singularity locus. Without loss of generality, the values $R = 1$ and $L = 0.5$ will be assigned.
- The second term corresponds to the function: $s\theta$. So as to avoid the singularity planes $\theta = 0$ and $\theta = \pm\pi$, the interval $\theta \in (0, \pi)$ will be considered.
- The expression ξ depends on the output variables (ϕ, θ, ψ), and on parameters $(\beta_2, \gamma_3, \beta_3)$. Thus, $(\beta_2, \gamma_3, \beta_3)$ comprise the set of design parameters.

3.2 Configuration Space Entities

The entities belonging to the configuration space such as workspace, joint space and reduced configuration space are characterized for different designs, analyzing the influence of the non-singular transitioning ability.

- **Case 1:** Similar Platforms

The first case under study establishes a design of the moving platform such that it is similar to the fixed base. For that, the geometric parameters are: $\beta_2 = \beta_3 = 0$ and $\gamma_3 = 90°$. The expression of the DKP singularity locus, given by Eq. 6, yields:

$$\xi = s\theta(c\psi - c\phi)(c\psi + c\phi) \tag{7}$$

It is factorized into the function $s\theta$, and the product of two planes. These planes divide the workspace (ϕ, θ, ψ) into eight aspects, so $V_{case1} = V_T/8$ being $V_T = 4\pi^3 rad^3$ the total volume. Each DKP solution lies inside each aspect, non-singular transitions being not possible. This is corroborated with the non-existence of cusp points inside any section of the joint space.

- **Case 2:** Joints (B_2, B_3) on a plane

The second case under study locates joints (B_2, B_3) on the **uv**-plane, such that $\beta_2 = \beta_3 = 0$ and $\gamma_3 \in (0, 90°)$. The singularity locus yields:

$$\xi = s\theta[c\gamma_3 s\psi c\psi + s\gamma_3(c^2\psi - c^2\phi)] \tag{8}$$

Yet again, expression ξ factorizes into the function $s\theta$, and a trigonometric expression depending on outputs (ϕ, ψ) and geometric parameter γ_3. Let us analyze a design of Case 2 having $\gamma_3 = 30°$. The workspace for θ *const* is shown in Fig. 3a. Contrary to Case 1, only four aspects exist, so that the operational workspace is duplicated $V_{case2} = 2V_{case1} = V_T/4$, because the robot can move between solutions located inside the same aspect. This is in accordance with the existence of cusp points in joint space sections (see Fig. 3b). Non-singular transitions can be performed between regions where different solutions lie, as for example regions 1 and 2 in Fig. 3a. It is interesting to search for designs that yield a regular workspace, such that the range of motion of the output variables is as much invariant as possible. The ratio $H = h/r$ serves as an indicator of regularity. Its evolution depending on γ_3 is represented in Fig. 3c. Small values of γ_3 yield a more regular workspace ($H \approx 1$). One of the extreme values, $\gamma_3 = 90°$, coincides with Case 1, and verifies $H = 0$, no connection between different regions is possible. The other extreme, $\gamma_3 = 0$, is a very special case, in which the moving platform is planar and the singularity curves evolved into planes.

- **Case 3:** General design

The last case corresponds to a general design of the moving platform. The three dimensional parameters $(\beta_2, \gamma_3, \beta_3)$ can be assigned any value in the range $(0, 90°)$. Let us analyze one arbitrary design: $\beta_2 = \beta_3 = 45°$ and $\gamma_3 = 70°$. The workspace presents two aspects, as shown in Figs. 4a and 4b. Consequently, designs of Case 3 exhibit the maximum operational workspace: $V_{case3} = V_T/2$. Nevertheless, the shape that the singularity surface acquires in the workspace, and in the joint space (Fig. 4c), is much more complex. Cusp points exist in the joint space, and visualizing the reduced configuration space for $l_1 = 1.2$ (Fig. 4d) the possibility of transitioning among solutions S_1 and S_2 is easily observed.
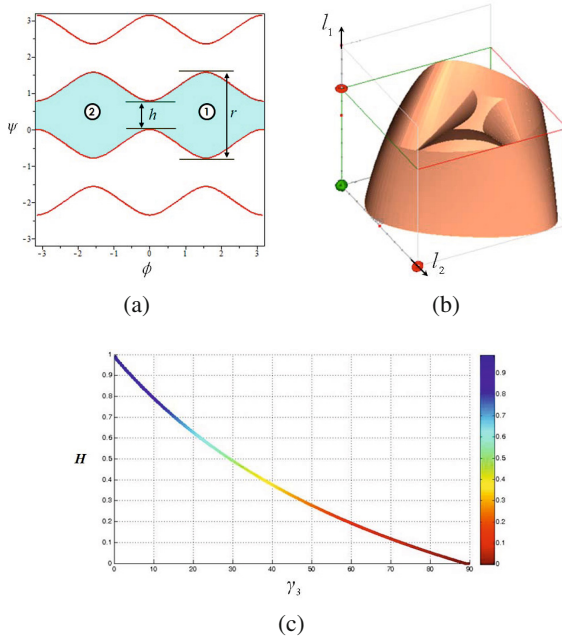
Fig. 3 Case 2: (a) Workspace section; (b) Joint space; (c) Ratio $H = h/r$

3.3 Dimensional Synthesis

The design optimization process is based on the *design parameter space* proposed in [4]. It is a 3D graph formed by a set of points (that constitute all possible designs), each point being assigned a numeric value regarding the feature under evaluation. The process does not strictly achieve an optimum design, but that a set of most favorable designs that comply with the established requirements is obtained.

The designs of Case 3 have the maximum workspace, but the drawback of these designs lies in the complexity of the singularity locus. Hence, following the idea proposed in Case 2, two indicators to evaluate the workspace are implemented. The first one, R_1, evaluates the regularity of the singularity curves among different sections of $\theta_i \in (0, \pi)$. The second indicator, R_2, assesses the quality of the curves in each θ_i section, penalizing the designs for which the curves cover a larger region. The design parameter space, formed by parameters $(\beta_2, \gamma_3, \beta_3)$, is shown according to R_1 and R_2 in Figs. 5a and 5b respectively. The blue colored points indicate the geometric parameters corresponding to optimum designs, and the red ones the worst. The optimum design parameter space can be computed by intersecting the best values of both graphs. Any point belonging to the resultant optimum space constitutes a valid design complying with the established requirements. For example, the following design: $\beta_2 = 15°$, $\gamma_3 = 10°$ and $\beta_3 = 20°$ is an optimum design with regular workspace, maintaining a similar pattern of the singularity curves in different sections of the workspace.
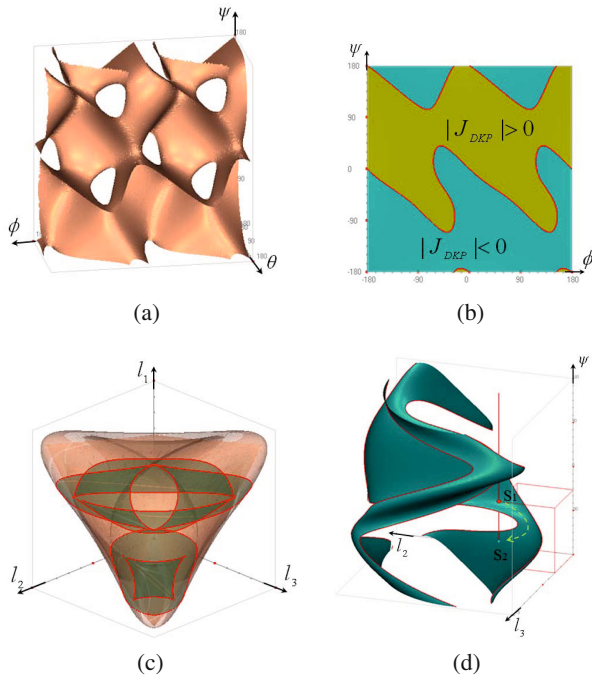
Fig. 4 (a) Workspace, (b) section; (c) Joint space; (d) Reduced configuration space
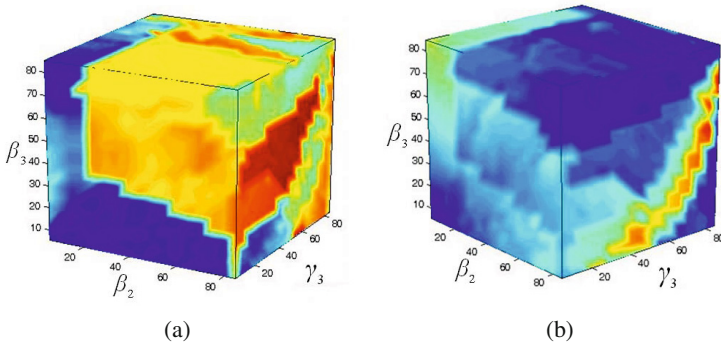
Fig. 5 Design parameter space according to indicators (a) R_1 and (b) R_2

4 Conclusions

In this paper, a design methodology for planar or spatial 3-DoF parallel manipulators, that exploits the transitioning ability of cuspidal manipulators has been presented. In order to show the potential of the methodology, it has been applied to the 3-SPS-S manipulator. The procedure bases on the characterization of configuration space entities so as to analyze the influence of the transitioning capacity on

the resultant workspace. Then, making use of the design parameter space approach, indicators that assess the operational workspace are proposed. Future work could enlarge the methodology by incorporating additional indicators as for example dexterity evaluation or other significant features.

References

1. Gosselin, C., Angeles, J.: A global performance index for the kinematic optimization of robotic manipulators. Journal of Mechanical Design 113(3), 220–226 (1991)
2. Hao, F., Merlet, J.P.: Multi-criteria optimal design of parallel manipulators based on interval analysis. Mechanism and Machine Theory 40, 157–171 (2005)
3. Husty, M.: Non-singular assembly mode change in 3-RPR-parallel manipulators. In: Kecskeméthy, A., Müller, A. (eds.) Computational Kinematics. Springer (2009)
4. Merlet, J.: Parallel Robots. Kluwer Academic Publishers (2000)
5. Ottaviano, E., Ceccarelli, M.: An Analytical Design for CaPaMan with Prescribed Position and Orientation. In: Proc. of the ASME Design Engineering Technical Conference and Computers and Information in Engineering Conference, Baltimore (2000)
6. Riedel, M., Nefzi, M., Huesing, M., Corves, B.: An Adjustable Gripper as a Reconfigurable Robot with a Parallel Structure. In: 2nd Int.Workshop on Fundamental Issues and Future Research Directions for Parallel Mechanisms and Manipulators, Montpellier, France (2008)
7. Tsai, L.-W.: Robot Analysis: The Mechanics of Serial and Parallel Manipulators. John Wiley and Sons (1999)
8. Urízar, M., Petuya, V., Altuzarra, O., Hernández, A.: Assembly Mode Changing in the Cuspidal Analytic 3-RPR. IEEE Transactions on Robotics 28(2), 506–513 (2012)
9. Zein, M., Wenger, P., Chablat, D.: Non-singular assembly mode changing motions for 3-RPR parallel manipulators. Mechanism and Machine Theory 43(4), 480–490 (2008)

On the Fatigue Strength of Ball Burnished Mechanical Elements

R. Avilés, J. Albizuri, A. Rodríguez, and L.N. López de Lacalle

University of the Basque Country, Spain
{rafael.aviles,joseba.albizuri,
adrian.rodriguez,norberto.lzlacalle}@ehu.es

Abstract. This work presents the quantification of the improvement in the high-cycle fatigue strength of machine parts manufactured with medium-carbon steels by means of low-plasticity burnishing. A complete experimental study has been performed on specimens: surface integrity, in-depth residual stresses, residual stresses relaxation, alternating bending fatigue tests and fractographic analysis. The tests show that the fatigue strength of ball-burnished components is significantly improved in the range 10^4 to 10^6 cycles, and the fatigue limit is increased by 20%. The residual stresses in the surface layer are non-isotropic biaxial compressive stresses varying in time because of stress relaxation. The quantitative data here provided are the modifying coefficient for the Marin equation and a uniaxial effective mean stress for each stress level. For fatigue calculations, this effective constant mean stress is equivalent to the effects produced by ball burnishing, and is an alternative to the calculations based on modifying coefficients.

Keywords: Machine design, Fatigue analysis, Ball burnishing, Medium carbon steels, Life prediction.

1   Introduction

Surface treatments are an effective way to improve the fatigue behaviour of mechanical elements. Ball burnishing, or low-plasticity burnishing (LPB), is a relatively new finishing process based on pressing and rolling a hydraulically floated ball along the surface of the component being treated [4], in such a way that the surface asperities are plastically deformed (see Fig. 1). As a result, the surface roughness is improved and a field of compressive residual stresses is generated in the outer layers of the burnished component; both effects help to the improvement of the fatigue strength.

Fatigue calculations of machine parts are usually based in the Basquin curve, obtained from the strength-lifetime curve of the material by means of the Marin equation using the modifying coefficients of the fatigue limit. The literature on machine design gives recommended values of these coefficients [1], which are meant to quantify the differences between the specimens used in the fatigue tests
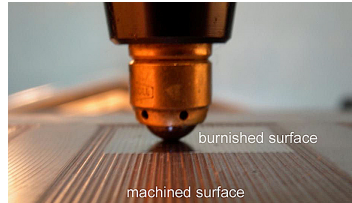
Fig. 1 Ball burnishing of a machined surface

and the actual components being designed. However, few values of the modifying coefficients can be found for modern manufacturing processes, as LPB, being the motivation of the research presented here.

LPB can be included in the same group as other surface treatments such as shot-peening (SP), laser shock-peening (LSP), cavitation shotless peening and surface rolling. These techniques cause compressive residual stresses in the surface of the treated component, improving the material's fatigue behaviour. Additionally, some of these processes produce a mirror-finished surface, which also contributes to enhanced high-cycle fatigue strength. Most of these processes generate isotropic residual stresses, which differs from the orthotropic residual stresses generated by LPB. Also, the surface finish in ball-burnished specimens has a quasi-mirror quality instead of the dimpled surface produced by shot-peening and other techniques. In summary LPB is a surface mechanical treatment generating high compressive residual stresses in the surface layers and producing a high quality surface finish.

2 Experimental Set-Up

The material chosen for this research was AISI 1045 steel. Ball burnishing of the fatigue specimens was carried out in a turning centre (see Fig. 2). The burnishing system consisted of a high-pressure hydraulic pump and a 6 *mm* diameter burnishing tool connected via high-pressure hoses. The process was performed using an emulsion-type coolant (92% water, 8% coolant). The pressure was supplied by a hydraulic pump capable of pumping at a maximum of 40 *MPa*. A ceramic ball was pressed against the surface of the work-piece, to make the material flows from the peaks to the valleys of the surface micro-irregularities. In this hydrostatic technology, the normal force depends only on the pump pressure. The choices of the burnishing parameters is based in previous works from the authors [5] and are listed here: fluid burnishing pressure 10 *MPa*, burnishing feed per revolution 0.05 *mm/rev* and burnishing speed 75 *m/min*. A total of 120 DIN 50113 (150 *mm* length, 8 *mm* diameter) fatigue specimens were manufactured; 60 of them were then ball-burnished in the zone shown in Fig. 2.
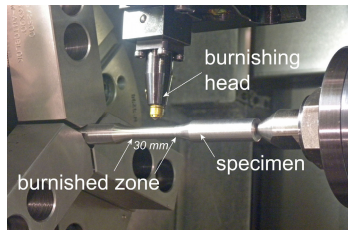
Fig. 2 Ball burnishing set-up and DIN 50113 fatigue specimen

The tensile properties of the material were obtained by means of four specimens; the average value of the tensile strength σ_{ut} is 869 *MPa* and the yield strength σ_{yp} is 727 *MPa*. The surface roughness was measured with an optical profilometer using a Gaussian filter with a 0.8 *mm* cut-off. The average roughness R_a is 0.68 *μm* for the original specimens and 0.12 *μm* for the ball-burnished ones. Fig. 3 shows the 2D profiles of the surface roughness of the untreated and ball-burnished specimens.
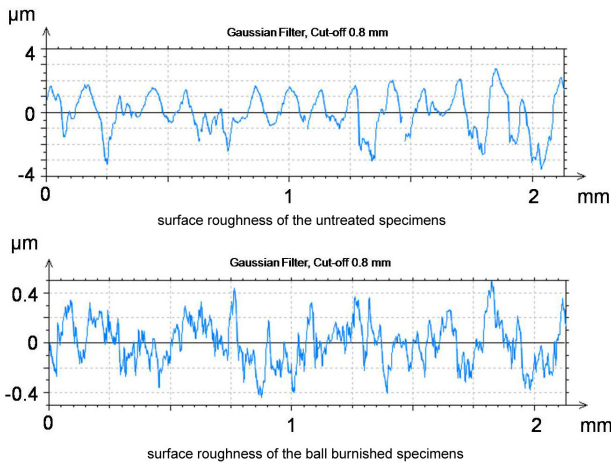
Fig. 3 Surface roughness of the fatigue specimens

The thickness of the layer of material deformed during LPB is 10 to 20 *μm*. The hardness of the ball burnished specimens is increased up to 20%, to a depth of about 0.3 *mm* with a maximum of 360 *HBN*, the hardness in the centre zone of the ball-burnished specimens, about 275 *HBN*. The grain size in the affected zone is reduced to a 50%. The in-depth residual stresses were measured in the axial direction in the surface zone (to 0.45 *mm* depth) in the middle section of one untreated and one ball-burnished specimen; the results are presented in Fig. 4. The untreated specimens have a compressive surface residual stress of 60 *MPa* (up to -140 *MPa* under the surface). LPB produces a 0.4 *mm* thick compressive layer where the outer surface residual stress is about -600 *MPa*.
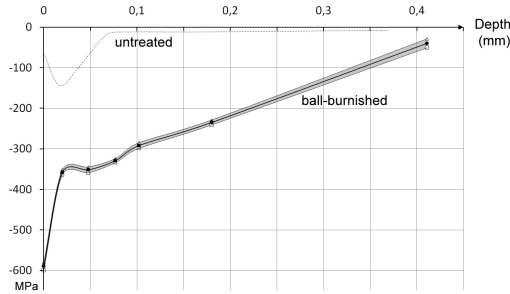
Fig. 4 Residual stresses in axial direction

In summary, with the parameters used in this work, LPB of AISI 1045 steel specimens produces four main effects in the surface zone: reduction of the roughness, a 50% reduction in the grain size, compressive residual stresses in the surface layer, and a 20–25% increase in the *HBN* material hardness. These effects are beneficial from a fatigue point of view, resulting in a significant enhancement of the fatigue behaviour of the ball-burnished specimens.

The fatigue tests were done in a Zwick-Roell UBM 200tc rotating bending fatigue machine. Fig. 5 shows the results, where the fatigue limit obtained for the untreated material is 352 *MPa*. According to the roughness measurements the surface finish modifying factor c_s of the fatigue limit is 0.96 in this case [1], then the bending fatigue limit of the material is σ_n' =352/0.96=367 *MPa*. The equation of the mirror polished specimens (untreated) is:

$$\sigma_N = 1960 \, N^{-0.12} \tag{1}$$

being σ_N the fatigue strength at N cycles. The equation of the ball-burnished specimens is:

$$\sigma_N^{bb} = 1100 \, N^{-0.066} \tag{2}$$

where σ_N^{bb} is the fatigue strength of the ball-burnished specimens at N cycles.

The scatter of the results is slightly higher for the ball-burnished specimens in comparison with the untreated ones. However, this scatter is still low, being a clue of the regularity of the burnishing process applied. The fatigue fractures of the ball-burnished specimens were examined in order to have a qualitative understanding of the effects of ball-burnishing in the nucleation and propagation of the fatigue cracks. Fig. 6 shows the fracture sections of two specimens: specimen-1 (Fig. 6, left side) and specimen-2 (Fig. 6, right side). The specimen-1 broke after 19,000 cycles at 560 *MPa*; the specimen-2 broke after 2,400,000 cycles at 440 *MPa*. The fracture surface of specimen-1 shows a crenelated shape caused by several fronts of cracks nucleated along the surface (Fig. 6.a) and also it is observed the presence of secondary cracks in the zone close to the fracture surface. No secondary cracking have been observed in the specimen-2 and the fatigue fracture is caused by a single crack nucleated in the surface.
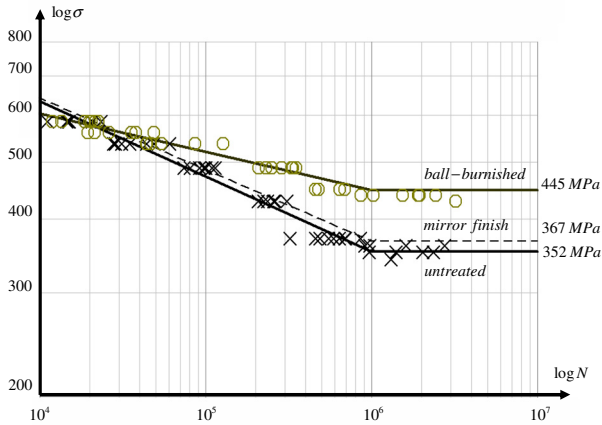
Fig. 5 Rotating bending fatigue tests results

Microscopic analysis shows that fatigue cracks are prone to nucleate in the boundaries between the surface patches produced by LPB (caused by the non-uniform plastic flow of the material). These boundaries behave as stress concentrators, favouring fatigue crack nucleation.
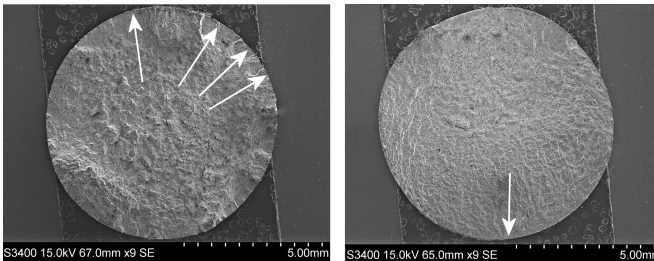
Fig. 6 Points of crack nucleation in specimens 1 and 2

3   Data for Fatigue Calculations

According to Eqs (1) and (2), the relation between the fatigue strengths of the ball-burnished and the untreated specimens from 30,000 to 10^6 cycles is:

$$\sigma_N^{bb} = 18 \, (\sigma_N)^{0.54} \tag{3}$$

the coefficient c_{bb} (Fig. 7) is:

$$c_{bb}(N) = \frac{\sigma_N^{bb}}{\sigma_N} = 0.56 \, N^{0.56} \tag{4}$$

As an alternative to the use of the Marin equation, an equivalent mean stress can be found that causes the same improvement in the fatigue behaviour as the ball-burnishing. This uniaxial "effective mean stress" σ_m^{ef} is compressive and constant in time (no relaxation), and uniform along the specimen section (no gradient). The criterion of Dietmann [3] is assumed a good one to take into account the effect of moderate compressive mean stresses in the fatigue behaviour of ductile steels:

$$\left(\frac{\sigma_n^{bb}}{\sigma_n'}\right)^2 + \frac{\sigma_m^{ef}}{\sigma_{ut}} = 1 \tag{5}$$

where σ_n' is the fatigue limit of the untreated material and σ_n^{bb} the fatigue limit of the ball-burnished specimens; the effective mean stress is in this case:

$$\sigma_m^{ef} = \sigma_{ut}\left(1 - \left(\frac{\sigma_n^{bb}}{\sigma_n'}\right)^2\right) = \sigma_{ut}(1 - c_{bb}^2) \approx -400 \; MPa \tag{6}$$
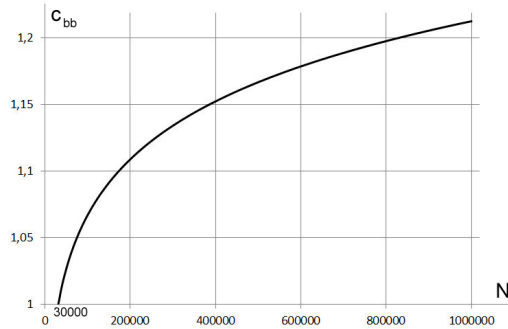
Fig. 7 LPB modifying coefficient

Cyclic stress relaxation causes a reduction in the beneficial effects of LPB. As Fig. 5 shows, the effect of LPB, mainly the compressive residual stresses σ_{res} (macro-stresses) vanishes quickly for stress amplitudes σ_a over 550 *MPa*, but remains for millions of cycles in the fatigue limit zone ~450 *MPa*. To collect experimental data on the rate of stress relaxation for intermediate stress levels, two ball-burnished specimens (3 and 4) were tested at 490 *MPa* (the estimated life is N=246,000 cycles) by measuring the surface axial and tangential residual stresses using X-Ray diffraction at 0, 25,000, 50,000, 100,000, and 150,000 cycles. Specimen-3 finally broke in 300,000 cycles and specimen-4 in 260,000 cycles; Fig.8 shows the time evolution of the residual stresses.
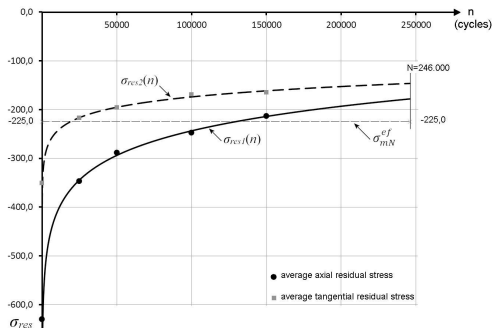
Fig. 8 Relaxation of the biaxial residual stresses (logarithmic equation)

The effective mean stress depends on the life N (see Fig. 9):

$$\sigma_{mN}^{ef} = \sigma_{ut}\left(1 - \left(\frac{\sigma_N^{bb}}{\sigma_N}\right)^2\right) = \sigma_{ut}\left(1 - c_{bb}^2(N)\right) \tag{7}$$

making use of Eqs (1), (2) and (7) it results:

$$\sigma_{mN}^{ef} = 870 - 275 \, N^{0,11} \tag{8}$$
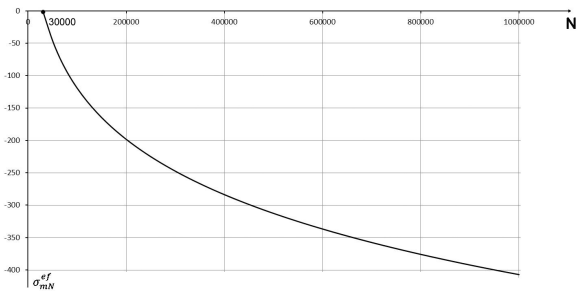
Fig. 9 Effective mean stress versus number of cycles

Multiaxial fatigue calculations based on the actual stresses, the sums of the applied stresses plus the biaxial residual stresses, in ball-burnished components are difficult because the relaxation makes it necessary to use complex multiaxial cumulative damage methods [6,7]. Additionally, the residual stress relaxation had to be experimentally obtained for every stress level in axial and tangential directions, which is burdensome and expensive. Because of these problems, two alternatives have been proposed here: effective mean stress and modifying coefficients. Design and analysis engineers most commonly use the second method. However, the first method (similar to the use of stabilized residual stresses [2]) is useful

for instance when a component is only partially ball-burnished. The comparisons of LPB with other alternative finishing processes as SP and LSP are strongly dependent on the process parameters and the material, but assuming conventional values for SP and LSP and medium carbon steels as AISI 1045 Table 1 summarizes the comparison of several mechanical properties based in bibliography data [8] and the results presented in this work.

Table 1 A comparison among LPB, SP and LSP finishing processes

	high	medium	low
reduction of surface roughness	LPB	SP & LSP	
cold-work	SP	LPB	LSP
depth of compressive residual stresses	LSP	LPB	SP
stress relaxation rate	SP	LPB	LSP
fatigue strength	**LSP**	**LPB**	**SP**

4   Conclusions

Low-plasticity burnishing causes four main effects in the specimens: surface biaxial compressive residual stresses of about 630 MPa in the axial direction and 350 MPa in the tangential direction, a high-quality surface finish, a 50% reduction of the grain size in the surface zone, and a 20–25% increase in the HBN surface hardness. These effects enhance the fatigue behaviour, mainly the residual stresses; the rotating bending tests show a progressive improvement of the fatigue strength in the range of 30,000 to 10^6 cycles. It was found that the fatigue limit increased by 20%, which corresponds to a modifying coefficient c_{bb} equal to 1.21 at 10^6 cycles for the Marin equation. The residual stresses in the surface are biaxial and non-isotropic, decreasing in time due to cyclic relaxation. However, for every stress amplitude σ_a, it is possible to find an effective uniaxial and constant mean stress σ_{mN}^{ef}, equivalent to the actual residual stresses from a fatigue point of view; the law of variation of this effective mean stress with life N was also presented. Calculations based on the effective mean stress are useful at times, for instance when a component is only partially ball-burnished, because the same Basquin curve is valid for any point in the component, which avoids the need to consider different curves as is the case with the modifying coefficient option.

References

1. Avilés, R.: Análisis de Fatiga en Máquinas. Editorial Paraninfo, Madrid, Spain (2005)
2. Benedetti, M., Fontanari, V., Scardi, P., Ricardo, C.L.A., Bandini, M.: Reverse bending fatigue of shot peened 7075-T651 aluminium alloy: The role of residual stress relaxation. International Journal of Fatigue 31, 1225–1236 (2009)
3. Dietmann, H.: Festigkeitsberechnung bei Mehrachsiger Schwingbeansoruchung. Z. Konstruktion 25, 181–189 (1973)
4. Prévey, P.S., Cammett, J.T.: The influence of surface enhancement by low plasticity burnishing on the corrosion fatigue performance of AA7075-T6. International Journal of Fatigue 20(9), 975–982 (2004)
5. Rodríguez, A., López de Lacalle, L.N., Celaya, A., Lamikiz, A., Albizuri, J.: Surface improvement of shafts by the deep ball-burnishing technique. Surface and Coatings Technology 206, 2817–2824 (2012)
6. Socie, D.F., Marquis, G.B.: Multiaxial Fatigue. SAE International (2000)
7. Wang, C.H., Brown, M.W.: Life prediction techniques for variable amplitude multiaxial fatigue – Part 1: Theories. Journal of Engineering Materials and Technology 118, 367–370 (1996)
8. McClung, R.C.: A literature survey on the stability and significance of residual stresses during fatigue. Fatigue and Fracture of Engineering Materials and Structures 30, 173–205 (2007)

Models for Determining the Static Stiffness of Collet Sleeves

E. Soriano, H. Rubio, and J.C. García-Prada

University Carlos III of Madrid, Spain
{esoriano,hrubio,jcgprada}@ing.uc3m.es

Abstract. The most versatile general purpose clamping device is collet chuck. Most of collet chucks use solid thin slotted clamping sleeves made of a hardened steel and ground to a high degree of accuracy on both internal and external surfaces. This paper first presents a straightforward analytical model to determinate the static stiffness of collet sleeves. Second, it presents the Finite Element Method (FEM) analyses that were conducted to check the proposed analytical model. Third, it describes an automatic (wedge-actuated) prototype, which was designed and built for determining the static stiffness of collet sleeves. The proposed analytical model was verified by means of Finite Element Analyses (FEA) and experimental investigations. The results will confirm the linear behavior of the models with excellent levels of correlation. The work results provide reliable theoretical and technical supports for the optimization of the design and application of collet sleeves.

Keywords: Collet stiffness, Clamping force, Wedge hook chuck, Finite Element Analysis (FEA).

1   Introduction

Some of the most important devices in machine tools are collet chucks, which are often used in turning, milling, grinding and inspection. Collet chucks must achieve high rotational speeds while maintaining good rotational accuracy. Majority of collet chucks use solid thin slotted clamping sleeves made of hardened steel and ground to a high degree of accuracy on internal cylindrical\tapered and external cylindrical\tapered surfaces.

It was found that static stiffness of a collet chuck can be quite high, only $\approx 5\%$ less than a monolithic or shrink-fit connection [5]. It has to be noted, however, that relatively minor design and fabrication specifics may result in significant changes of the stiffness parameters. Jeong-Du Kim and Kyung-Duk Kim [2], proposed a novel method to eliminate burrs in spring collets made of chrome-molybdenum by abrasive flow machining. Obviously, burrs affect to the stiffness behavior of collets.

M. Tsutsumi [7] developed a detector, based on strain gages, to measure the clamping force of manual collet chuck holders, in its static state. However, it was

shown that spring collets, with thin slotted clamping sleeves, have poor repeatability of the clamping force distribution. For this reason collet chucks for high speed or high precision operation have a wedge-actuated axial tightening system preventing distortions and thus improving concentricity and balancing conditions [4].

Since a collet chuck is, essentially, a wedge mechanism. Thus, the clamping force depends, for a given driving force to the mechanism, on efficiency of the wedges, on friction coefficient at the clamping surfaces, on clearance between collet and workpiece or tool and on collet stiffness [6]. Thus, the exact computation of collet stiffness ensures a safe high-speed cutting process, and makes it possible to fully utilize the potential of modern machine tools.

In the field of automatic collet chucks, two alternatives of clamping mechanisms are proposed, collet chucks can be driven by pushing and by pulling, Fig. 1.

The basic principle of collet chuck holders is the wedge effect, Fig. 1. The axial movement of the collet (2) or the cone (4) will make the jaws of the collet expand or contract, moreover the applied axial force will increase the normal force on the collet and thus the friction force and the transmitted torque will be also increased, such that the collet can expand and contract thus creating the clamping movement. Automatic collet chuck holders can be designed for external or internal clamping, collet chuck holders for internal clamping are called expanding mandrels.

In this paper, the analytical model used to explain the collet deflections mechanisms is based on a conventional elasticity problem. It also presents the Finite Element Method (FEM) analyses that are conducted to check the analytically obtained results. Finally, a prototype is designed and built, which confirms the obtained results. Besides, the prototype can be used as collets manufacturer fixture. Dead-length collets [1] for automatic chuck holders are tested.

The 3D FEM analysis was conducted using the commercial package ANSYS. The proposed analytical model was implemented in Matlab.
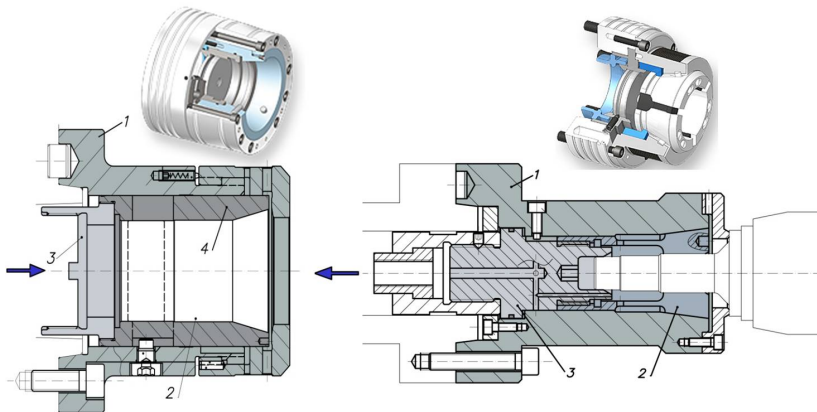
Fig. 1 Automatic collet chuck driven by pushing and by pulling.

2   Analysis of the Clamping Mechanisms

The operating principle of automatic collet chuck holders can be described mathematically through a two dimensional model, as shown in Fig. 2. Considering an uniform distribution of contact pressure p, only satisfied when both tapered contact surfaces has the same length, the normal force F_n, generated by the contact pressure p, can be expressed as the integral between the maximum and the minimum radius of the collet tapered surface, Eq. (1). Where r_s is the maximum radius, r_i is the minimum radius and r is the radius for the area element, dA. It is assumed that normal wear, δ_n, is uniform for all points of the tapered surface. Therefore, the maximum pressure occurs for the minimum value of the radius, r_i, Eq. (2).
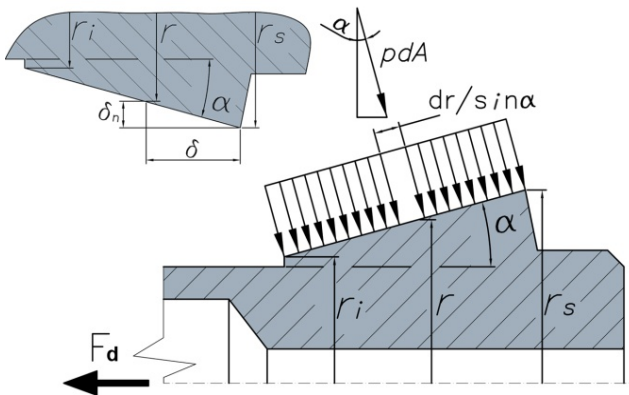
Fig. 2 Cone-collet contact pressure

$$F_n = \int_{r_i}^{r_s} p\,dA = \int \frac{p_{max} r_i}{r} \frac{2\pi r}{\sin \alpha} dr = \frac{2\pi p_{max} r_i}{\sin \alpha}(r_s - r_i) \qquad (1)$$

$$p = p_{max} \frac{r_i}{r} \qquad (2)$$

$$F_d = F_n \sin \alpha = 2\pi p_{max} r_i (r_s - r_i) \qquad (3)$$

Thus, as shown in Fig. 2, the driving force F_d is given by Eq. (3).

The friction coefficient between the cone and collet surfaces is μ. When $tan\alpha \approx \mu$, in order to unclamping the joint will be required an opposite force equal to the driving force F_d.

Since the magnitude of the driven radial displacement of the spring collet jaws is very small and can be compared to the tolerances of collets and workpieces, it is necessary to exactly determinate the tolerances to predict the clamping force.

The maximal and the minimal clearances are determined by the tolerances of the collet and the workpiece, Fig. 3. These relationships are expressed in Eq. (4) and Eq. (5). On the other hand, the diameter of the internal surface of the collet must be equal to the diameter of the clamped diameter of the workpiece in its working state.
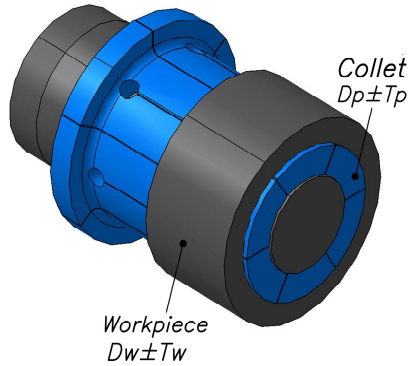
Fig. 3 Dimensions of the collet and the workpiece

$$C_{max} = \frac{\left(D_p + T_{p,max}\right) - \left(D_w + T_{w,min}\right)}{2} \tag{4}$$

$$C_{min} = \frac{\left(D_p + T_{p,min}\right) - \left(D_w + T_{w,max}\right)}{2} \tag{5}$$

Each collet jaw can be considered as a cantilever, Fig. 4. Using the elementary classical model Eq. (6) it is possible to analytically estimate the maximal deflection ε, produced by the clamping force F_s. The radial stiffness of the collet jaw k_R, is given by Eq. (7) and moreover the amount of the clamping force used for deforming the collet ΔF_s, Eq. (8). So it is possible to calculate the needed increasing in the driving force.

$$\varepsilon = \frac{F_s L^4}{8EI} \tag{6}$$

$$k_R = \frac{8EI}{L^4} \tag{7}$$

$$\Delta F_s = \frac{\Delta F_d}{\tan \alpha} = n C_i k_R \tag{8}$$
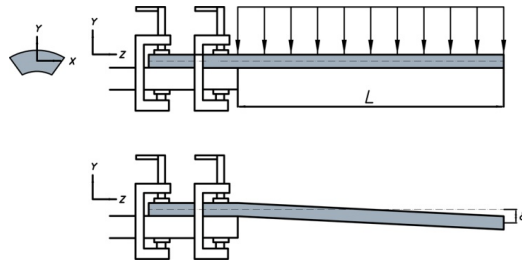
Fig. 4 Equivalent representation of a collet jaw

3   FEM-Analysis

This section presents the FEM analyses that were conducted to check the proposed straightforward analytical model. For performing the simulations by means of FEM, a commercial code was used (ANSYS). For all simulations the geometry of study corresponds to a basic expanding mandrel driven by pulling with collets according to the DIN 6343 standard [1]. Geometry and dimensions of analyzed mandrel and collet are summarized in Fig. 5 and table 1. Mandrel parts were chosen of steel, for sake of simplicity the mechanical behavior of materials were considered to be elastic perfectly plastic materials and the von Mises criterion was used as well, table 2.
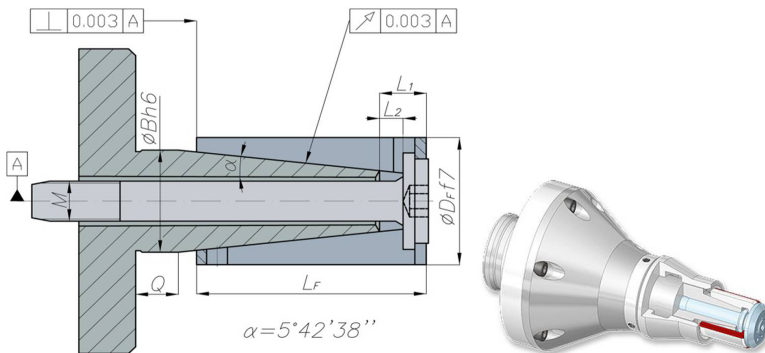
Fig. 5 Mandrel and collet geometry

Table 1 Mandrel and collet dimensions in mm

$D_F f7$	$Bh6$	L_F	L_1	L_2	Q	M
19.70	14	35	11	6	5	5

Table 2 Components materials

Component	Material	Elastic Modulus (GPa)	Poisson ratio	Yield Strength (MPa)
Cone	18CrMo4	210	0.28	685
Collet	50CrV4	210	0.28	950
Piston	C45E	210	0.2	430

In order to check the proposed analytical model, during the collet expansion and thus, the amount of clamping force required to reach the workpiece or the cutting tool and its static radial stiffness, a 3D model was adopted and implemented in ANSYS software. The model consisted of two parts, collet and driving cone. The model was homogeneously meshed with a total of 23145 ten-nodes tetrahedral elements. Diverse meshes were considered until required convergence in results was achieved. A Cartesian coordinate system has been used (X, Y, Z), Fig. 6, fixed on the collet which origin is placed at the front of the model.

The nonlinear simulations were carried out considering friction between both bodies, $\mu = 0.09$ [3]. As shown in Fig. 6, driving forces F_d, applied in the longitudinal direction of the collet, were varying between 25 N to 250 N, the end of the driving cone was fixed.
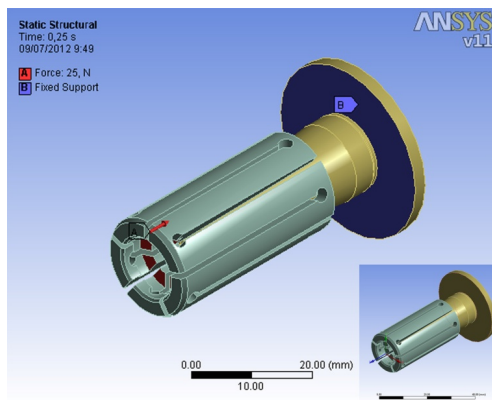
Fig. 6 Coordinate system and applied loads

4   Experimental Bench Device and Test

Fig. 7a shows the automatic device developed for the collet experimental test.
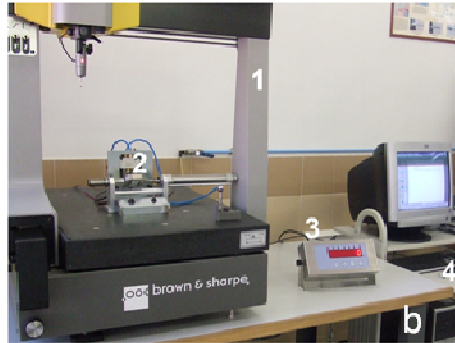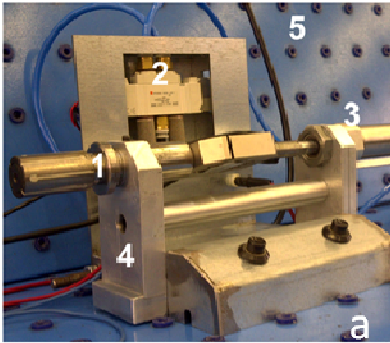
Fig. 7a Experimental device: 1. Automatic expanding mandrels, consisting of collet, driving cone and piston, 2. Electro-Pneumatic circuit, 3. Double acting air cylinder, 4. Bed device, 5. Electrical and air supplier.

Fig. 7b Experimental setup for measuring the collet radial deflection

In order to validate the proposed analytical and numerical models the next test was run:

- Determination test for measuring the collet deflections and the subsequent determination of the required amount of driving force (clamping force) and static radial stiffness of the collet sleeve.

The radial displacement of the collet with changes in driving force, and thus in clamping force, was measured. Fig. 7b shows the experimental setup. The variance in the radial displacement of the collet was measured using a coordinate measuring machine (1) and computer (4), driving forces were simultaneously measured by the load cell (2) and a load cell indicator (3).

5   Results Analysis

For a better understanding of results analysis, we define a dimensionless parameter, τ, Eq. (9), where L_a is the cone length which is contacting the collet for any time and L_b is given by Eq. (10), see Fig. 5. Obviously, $0 \leq \tau \leq 1$.

$$\tau = \frac{L_a}{L_b} \tag{9}$$

$$L_b = L_F - L_1 \tag{10}$$

The contact pressure p_{max}, between the cone and the collet for a driving force of 250 N, was analytically determined by Eq. (3), its value was 834.445 kPa. Fig. 8a shows the contact pressure distribution (cone-collet) when the driving force is 250 N obtained by means of Finite Element Analysis (FEA). The contact pressure remains nearly constant as assumed.
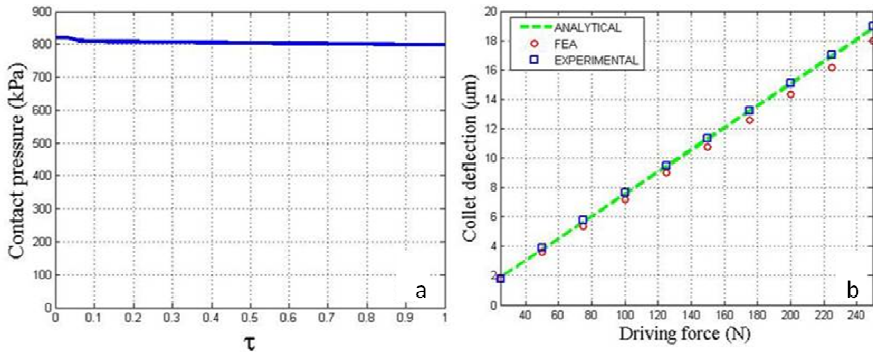
Fig. 8 a Contact-pressure distribution cone-collet, $F_d = 250N$

Fig. 8b Collet deflections: analytical model, FEA, experimental test

The amount of the driving force used for deforming the collet obtained from the analytical model, FEM model and experimental test are shown in Fig. 8b. Also it is possible to obtain the collet radial stiffness, k_R, from the value of the slope of the resulting line or Eq.(7).

6   Conclusions

From the proposed models obtained results is possible to conclude that reducing the taper angle will improve mechanical advantage and thus further reducing driving forces, however this will result, attending to the Von Misses criterion, in greater stresses. The transmitted clamping force depends strongly on the clearances determinate by the tolerances of the collet and the workpiece and also on the collet radial stiffness. Generally speaking, lower clearances and collet radial stiffness contribute to leave more effective clamping force. Machining accuracy and productivity can be increased by means of reducing the preset static clamping force.

References

1. DIN 6343, Druck-Spannzangen, Deutsches Institut für Normung, Berlin (1993)
2. Kim, J.D., Kim, K.D.: Deburring of burrs in spring collets by abrasive flow machining. Int. J. Adv. Manuf. Tech. 24, 469–473 (2004)

3. Meriam, J.L., Kraige, L.G.: Engineering Mechanics. John Wiley and Sons, New York (2002)
4. Rivin, E.I.: Tooling structure: interface between cutting edge and machine tool. Annals of the CIRP 49, 591–634 (2000)
5. Rotberg, J., Lenz, E., Levin, M.: Drill and Clamping Interface in High-Performance Drilling. Int. J. Adv. Manuf. Tech. 14, 229–238 (1998)
6. Soriano, E., Rubio, H., García-Prada, J.C.: Analysis of the Clamping Mechanisms of Collet-Chucks Holders for Turning. In: New Trends in Mechanism and Machine Science, Mechanisms and Machine Science, vol. 7, pp. 393–400. Springer Science (2012)
7. Tsutsumi, M.: Chucking force distribution of collet chuck holders for machining centers. J. Mech. Work. Technology 20, 491–501 (1989)

Measuring How Well a Structure Supports Varying External Wrenches

François Guay[1], Philippe Cardou[1], Ana Lucia Cruz-Ruiz[2], and Stéphane Caro[3]

[1] Laboratoire de robotique, Département de génie mécanique, Université Laval,
Quebec City, QC, Canada
`francois.guay.2@ulaval.ca, pcardou@gmc.ulaval.ca`
[2] IRCCyN, École Centrale de Nantes, 1 rue de la Noë, 44321, Nantes, France
`ana-lucia.cruz-ruiz@eleves.ec-nantes.fr`
[3] CNRS/IRCCyN, 1 rue de la Noë, 44321, Nantes, France
`stephane.caro@irccyn.ec-nantes.fr`

Abstract. An index is introduced, the minimum degree of constraint satisfaction, which quantifies the robustness of the equilibrium of an object with a single scalar. This index is defined under the assumptions that the object is supported by forces of known lines of action and bounded amplitudes, and that the external perturbation forces and moments vary within a known set of possibilities. A method is proposed to compute the minimum degree of constraint satisfaction by resorting to the quick-hull algorithm. The method is then applied to two examples chosen for their simplicity and diversity, as evidence of the broad spectrum of applications that can benefit from the index. The first example tackles the issue of fastening a workpiece, and the second, the workspace of a cable-driven parallel robot. From these numerical experiments, the minimum degree of constraint satisfaction proves useful in grasping, cable-driven parallel robots, Gough-Stewart platforms and other applications.

1 Introduction

In mechanism and structure design, the definition of a sound and meaningful performance index that would apply to a wide variety of situations would be of tremendous help. Such a concept would allow the automation of a part of the design process, enabling a systematic scan of the possible solutions. With this objective in mind, several researchers have proposed indices—see the excellent review by Merlet [5].

Among the most popular indices, we find the *manipulability*, originally proposed by Yoshikawa [9]. This index represents the volume of the ellipsoid obtained by mapping the unit-sphere through the Jacobian matrix of a robotic manipulator. Hence, the manipulability represents a geometric average of the kinematic sensitivity of the robot. If the kinematic sensitivity is null in one direction of motion, then the ellipsoid becomes flat, and its volume zero. This implies that the robot cannot support an object in this direction of motion. The drawback of this approach is that

a manipulator may be very close to instability while retaining a large manipulability if its associated ellipsoid is thin along one dimension and thick along the others.

Another widely used index is the *dexterity*, as defined by Salisbury and Craig [7]. Geometrically, this index measures the distortion of the ellipsoid associated with the Jacobian matrix of a manipulator by taking the ratio of its largest semi-axis to its smallest. The problem with this approach is that it does not account for the size of the ellipsoid. Thus, the concept of capacity is occluded by that of evenness.

Another drawback of dexterity is that it is ill-defined when the Jacobian matrix is not dimensionally-homogeneous, a problem that has been noted by several authors. Workarounds have been proposed [1, 8, 4], but all of them entail some arbitrariness, and, perhaps for this reason, have not generally received acceptance from the robotics community. In this paper, we propose a normalisation that is no less arbitrary than those proposed previously, but that has the merit of being simple and straightforward. In any case, as was pointed out by Park and Kim [6], "arbitrariness is an unavoidable consequence of the geometry of $SE(3)$."

Most importantly, the dexterity and the manipulability do not account for the varying force and moment capabilities of the actuators, nor for the external forces and moments that the object has to support. In general, the designer can and must evaluate these constraints during the design process.

In this paper, we take into account the actuator capacities, as well as the set of expected external forces and moments, and incorporate them into the definition of our performance index. These assumptions are formally explained in section 2. In section 3, we define the proposed index, various examples of increasing complexities are presented in sections 4 and 5, and a summary is given in section 6.

2   Mechanical Model of a Structure Supporting an Object

We start from a rigid body in space, whose free-body diagram is shown in Fig. 1. This object is subjected to a system of external forces (e.g., gravity or air friction), which we represent by their resulting force at E and moment, $\mathbf{f}_e$ and $\mathbf{n}_e$. The location of point E generally depends on the application considered, and experience shows that the choice of E is usually straightforward. The external wrench is to be balanced by the forces $\mathbf{f}_i$, $i = 1, \ldots, m$, applied by the supporting structure on the object at the corresponding points C_i, $i = 1, \ldots, m$. We assume that the directions of these forces are known and given by unit vectors $\mathbf{u}_i$, $i = 1, \ldots, m$. When the supporting forces come from physical contacts between the object and the structure, this implies the absence of friction, and vectors $\mathbf{u}_i$ pointing towards the object. When the object is suspended by a cable, then $\mathbf{u}_i$ points in the direction opposite to the object.

From Fig. 1, the equations of static equilibrium are

$$\mathbf{W}\mathbf{f} + \mathbf{w}_e = \mathbf{0}_6, \tag{1}$$
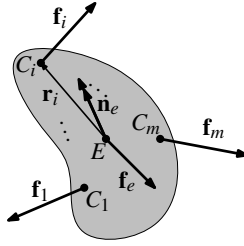
Fig. 1 Free-body diagram of an object in space

where

$$\mathbf{W} \equiv \begin{bmatrix} \mathbf{u}_1 & \cdots & \mathbf{u}_m \\ \frac{1}{r}\mathbf{r}_1 \times \mathbf{u}_1 & \cdots & \frac{1}{r}\mathbf{r}_m \times \mathbf{u}_m \end{bmatrix}, \ \mathbf{f} \equiv \begin{bmatrix} f_1 \\ \vdots \\ f_m \end{bmatrix}, \ \mathbf{w}_e \equiv \begin{bmatrix} \mathbf{f}_e \\ (1/r)\mathbf{n}_e \end{bmatrix},$$

f_i is the amplitude of the ith force, $\mathbf{0}_3$ is the three-dimensional zero vector, and $r^2 = (1/m)\sum_{i=1}^{m} \|\mathbf{r}_i\|_2^2$ is used to render the equations dimensionally homogeneous. One may see a problem occuring when $r = 0$ m, that is when all points C_i, $i = 1,\ldots,m$, are located at E. In such a case, all forces are concurrent at E, so that the rigid body becomes a particle, and a sum of moments is no longer needed.

We assume that the external wrenches $\mathbf{w}_e$ that could be applied on the object by its environment form a known polytope, the set of task wrenches $\mathscr{T}$, or

$$\mathscr{T} = \{\mathbf{w}_e \in \mathbb{R}^6 : \ \mathbf{w}_e = \sum_{j=1}^{n} \alpha_j \mathbf{w}_{e,j}, \ \sum_{j=1}^{n} \alpha_j = 1, \ \alpha_j \geq 0, \ j = 1,\ldots,n\}. \quad (2)$$

The designer generally has an approximate idea of the wrenches that will be applied by the environment, which he or she can approximate with the polytope $\mathscr{T}$.

We also work under the assumption that the structure can only withstand forces f_i within given ranges, e.g., the limited resistance of the contact surface, the inability of cables to push, or the limited capacities of actuators. These ranges of forces form the set $\mathscr{F}$ of feasible forces, a box (a.k.a. orthotope) in m-dimensional space, namely,

$$\mathscr{F} = \{\mathbf{f} \in \mathbb{R}^m : \ \underline{\mathbf{f}} \leq \mathbf{f} \leq \bar{\mathbf{f}}\}, \quad (3)$$

where $\underline{\mathbf{f}}$ and $\bar{\mathbf{f}}$ are the lower and upper bounds on the force array $\mathbf{f}$.

3 A Measure of the Structure Capacity

For the object to remain in equilibrium, it must not only satisfy the static equilibrium equations (1), but also have supporting forces $\mathbf{f}$ within the allowed ranges for any of the task wrenches $\mathbf{w}_e$. These conditions can be symbolically expressed as

$$\forall \mathbf{w} \in \mathscr{T}, \ \exists \mathbf{f} \in \mathscr{F} : \ \mathbf{w}_e = -\mathbf{W}\mathbf{f}. \quad (4)$$

This condition can also be understood graphically. The two sets $\mathscr{F}$ and $\mathscr{T}$ are defined in different spaces, which are connected through the linear relationship of the equation of static equilibrium. In Fig. 2, the box $\mathscr{F}$ of allowed forces is mapped onto the wrench space through the linear transformation $\mathbf{w} = -\mathbf{W}\mathbf{f}$. The resulting set is labelled $\mathscr{W}$, and is a special type of polytope called a zonotope [2]. From the feasibility condition (4), we conclude that the system is in equilibrium if and only if

$$\mathscr{T} \subseteq \mathscr{W}. \tag{5}$$
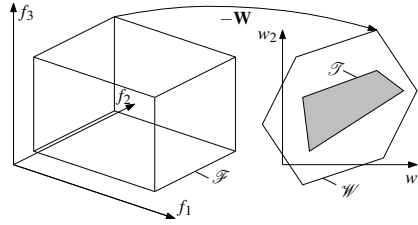
Fig. 2 An analog representation of the mapping of $\mathscr{F}$ onto the wrench space

Our measure should be a function indicating how far set $\mathscr{T}$ is from being partly outside of $\mathscr{W}$. It should be positive when the structure can support the task wrenches, and negative otherwise. It should be as smooth as possible to ease its optimisation.

As an indicator of the *degree of inclusion* of $\mathscr{T}$ within $\mathscr{W}$, we propose an index that we call the *minimum degree of constraint satisfaction*, and which we define as

$$s = \min_{j=1,\dots,n} \left(\min_{l=1,\dots,p} s_{j,l} \right), \tag{6}$$

where the degree of constraint satisfaction $s_{j,l}$ is the signed distance from vertex $\mathbf{w}_{e,j}$ of $\mathscr{T}$ to the lth face of $\mathscr{W}$. We take $s_{j,l}$ to be positive when the constraint is satisfied, and negative otherwise. With this definition, the minimum degree of constraint satisfaction s remains negative as long as at least one of the vertices of $\mathscr{T}$ remains outside of $\mathscr{W}$; becomes zero whenever $\mathscr{T} \subseteq \mathscr{W}$ and a vertex of $\mathscr{T}$ lies on the boundary of $\mathscr{W}$; and is positive when $\mathscr{T}$ is in the interior of $\mathscr{W}$.

The computation of the proposed indicator function is performed in five steps:

(*i*) Compute the vertices of $\mathscr{F}$, $\mathbf{f}_k$, $k = 1,\dots,q$, $q = 2^m$, through the formula $\mathbf{f}_k = (\mathbf{1}_{m \times m} - \text{diag}(\beta_k))\underline{\mathbf{f}} + \text{diag}(\beta_k)\overline{\mathbf{f}}$, where β_k is the array of m bits giving the binary representation of k.

(*ii*) Map the vertices onto the wrench space as $\mathbf{w}_k = -\mathbf{W}\mathbf{f}_k$, $k = 1,\dots,q$.

(*iii*) Compute the convex hull of $\mathscr{W}$ from $\mathbf{w}_k$, $k = 1,\dots,q$. Fortunately, several routines are readily-available for this purpose. Here, we use the quickhull algorithm implemented in the `qhull` package for Matlab. This returns the polytope $\mathscr{W}$ in the form $\mathscr{W} = \{\mathbf{w} \in \mathbb{R}^6 : \mathbf{a}_l^T \mathbf{w} \leq b_l, \, l = 1,\dots,p\}$.

(*iv*) Compute the degree of constraint satisfaction $s_{j,l}$ associated with the jth vertex of $\mathcal{T}$, $\mathbf{w}_{e,j}$, and the lth face of $\mathcal{W}$, $\mathbf{a}_l^T \mathbf{w} = b_l$. This is done by projecting a vector from $\mathbf{w}_{e,j}$ to the hyperplane of the lth face of $\mathcal{W}$ onto its normal $\mathbf{a}_l/\|\mathbf{a}_l\|_2$, which gives $s_{j,l} = (b_l - \mathbf{w}_{e,j}^T \mathbf{a}_l)/\|\mathbf{a}_l\|_2$.

(*v*) Compute the *closeness* of $\mathcal{T}$ to being completely included in $\mathcal{W}$ as the minimum s of the degrees of constraint satisfaction, as per eq. (6).

4 Example: Holding a Workpiece

In this example, we consider the problem of clamping a metal block having dimensions 150 mm $\times$ 100 mm for a polishing run. The polisher consists of a rotating circular brush following a strip pattern, applying a moment of 500 N·mm, and a force of 100 N in the direction of the brush motion. We are to determine the optimal four-contact-point pattern that provides the most robust equilibrium.

A free-body diagram of our metal block is shown in Fig. 3. We assume that each contact point is on a distinct edge of the rectangle and that friction is negligible. We parameterise the positions of the forces f_1 and f_2 with x and y and assume that the remaining forces are symmetric to f_1 and f_2 with respect to the origin.

The weight of the metal block is ignored, so that the task wrench set $\mathcal{T}$ is solely determined by the forces and moments applied by the tool. The force-moment system $(\mathbf{f}_e, n_e)$ equivalent to each possible position and direction of motion of the brush is computed as $\mathcal{T} = \{\mathbf{f}_e \in \mathbb{R}^2, n_e \in \mathbb{R} : \|\mathbf{f}_e\|_\infty \leq 100 \text{ N}, |n_e| \leq 15 \text{ N m}\}$.
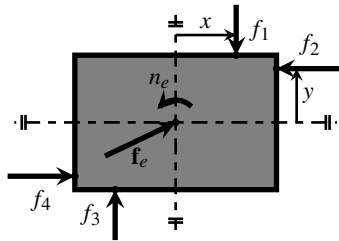

Fig. 3 Free-body diagram of the workpiece

The minimum degree of constraint satisfaction s is computed for all possible positions of f_1 and f_2, which results in the graph of Fig. 4. In this figure, recall that the x-axis represents the positions of f_1 on the upper edge, while the y-axis represents that of f_2 on the right edge. Figure 4 shows that the metal block is best held in place by choosing the contact points at $x = 100$ mm and $y = 95$ mm. Interestingly, the contour $s = 0$ N corresponds to the stability frontier, so that we must have $|x| \geq 40$ mm and $|y| \geq 40$ mm for the workpiece to be stable.
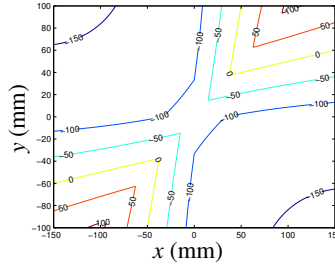
Fig. 4 Isocontours of the proposed index *s* in Newtons as a function of the contact-point positions

5 Example: The Wrench-Feasible Workspace (WFW) of a Planar Cable-Driven Parallel Robot (CDPR)

Let us use the index *s* to trace the WFW of a cable-driven parallel robot CDPR. A cable-driven parallel robot is a parallel robot that utilizes cables instead of rigid links. This particular characteristic provides CDPRs with advantages such as high dynamics and a large workspace, however their workspace is greatly reduced by the fact that eq. (4) can only be satisfied with non-negative forces or feasible cable tensions (the cables can pull but not push).

For such robots, the set of feasible forces $\mathscr{F}$ defined in eq. (3) becomes the set of feasible cable tensions. The sets $\mathscr{W}$ and $\mathscr{T}$ in Fig. 2 define the available and required wrench sets of the robot. The available wrench set represents the ability of the cables to generate forces and moments on the moving platform, while the required wrench set represents the forces and moments that are applied by the environment on the platform for a specific task.

The WFW is the set of mobile platform poses for which the required wrench set is contained in the available wrench set. This implies that a pose belonging to the WFW must satisfy eq. (5) and that the tensions along each cable should be non-negative and respect a tension range subject to the capabilities of the actuators.
This workspace can be traced along a given area by using the minimum degree of constraint satisfaction to measure the degree of inclusion of the required wrench set polytope in the available wrench set polytope for each pose. The condition $s = 0$ defines the stability frontier, that is, the boundary of the WFW of the CDPR, and the positive values of *s* correspond to poses inside the WFW.

We used this observation to revisit the example of Fig. 5 of Gouttefarde et al. [3]. In this example, the geometry of the CDPR is as illustrated in Fig. 5, $\mathscr{F} = \{\mathbf{f} \in \mathbb{R}^4 : \|\mathbf{f}\|_\infty \leq 50 \text{ N}\}$, and $\mathscr{T} = \{\mathbf{f}_e \in \mathbb{R}^2, n_e \in \mathbb{R} : \|\mathbf{f}_e\|_\infty \leq 10 \text{ N}, |n_e| \leq 0.5 \text{ N m}\}$.
We compute the minimum degree of constraint satisfaction *s* for each pose along a three dimensional grid. The robot is displaced along the XY plane and rotated through a range of orientations from $-36°$ to $36°$. The top and 3D views of the resulting WFW are shown in Fig. 5, and correspond to those obtained in [3]. The computed surface defines the stability frontier, therefore the platform must be kept within this boundary in order to remain stable.
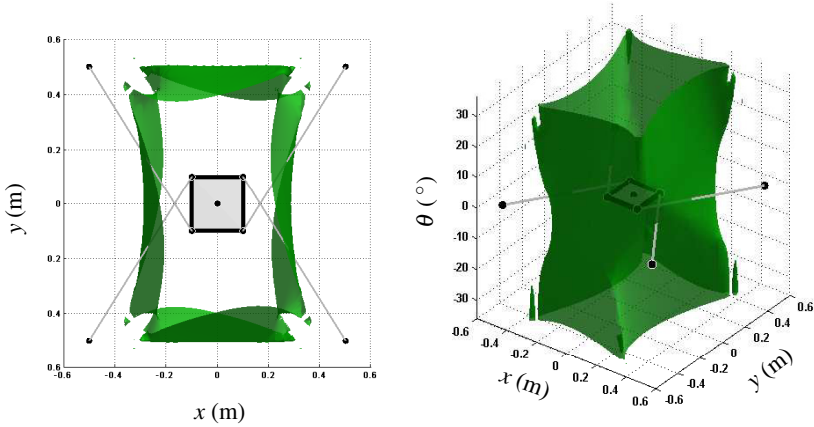
Fig. 5 Boundary of the total-orientation WFW for the example proposed by Gouttefarde et al. [3]

In order to obtain a more quantitative view of the capacity of the robot to withstand the required wrench set, the minimum degree of constraint satisfaction was also used to compute the constant orientation WFW. Figure 6 shows the resulting workspaces for fixed orientations of 0° and 45°, which also correspond to those obtained in [3]. The contour where $s = 0$ defines the stability frontier. We note that the workspace is contained inside the convex hull formed by the base anchor points and that its shape and size are altered by the 45° rotation of the platform. We also note that in both cases the CDPR has a higher capacity to balance the required wrench set at the center of the workspace, and that this capacity is gradually reduced as the platform is shifted away from the center.
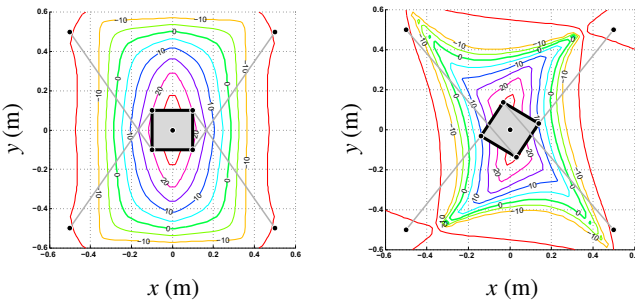
Fig. 6 Isocontours of the proposed index s in Newtons as a function of the pose

6 Conclusions

In summary, we have defined a new kinetostatic index that is quite general, as demonstrated by the variety of the presented examples. In short, this index informs the designer of the closeness to instability, in Newtons. A negative value of the index indicates an unstable design, and a positive value, a stable one. We believe the index to be an interesting alternative to the manipulability and the dexterity, as it takes into account not only the geometry of the device, but also the forces and moments required by the task or allowed by the actuators or support members. Moreover, the minimum degree of constraint satisfaction represents the worst-case scenario, unlike manipulability and dexterity, which is thought more useful to the designer. The index is not flawless, however, and we are currently exploring alternative solutions to the dimensional homogeneity problem and to the associated computational burden.

References

1. Angeles, J.: The design of isotropic manipulator architectures in the presence of redundancies. The International Journal of Robotics Research 11(3), 196–201 (1992)
2. Bouchard, S., Gosselin, C., Moore, B.: On the ability of a cable-driven robot to generate a prescribed set of wrenches. ASME Journal of Mechanisms and Robotics 2(1), 011,010 (2010)
3. Gouttefarde, M., Daney, D., Merlet, J.P.: Interval-analysis-based determination of the wrench-feasible workspace of parallel cable-driven robots. IEEE Transactions on Robotics 27(1), 1–13 (2011)
4. Khan, W.A., Angeles, J.: The kinetostatic optimization of robotic manipulators: The inverse and the direct problems. ASME Journal of Mechanical Design 128(1), 168–178 (2006)
5. Merlet, J.P.: Jacobian, manipulability, condition number, and accuracy of parallel robots. ASME Journal of Mechanical Design 128(1), 199–206 (2006)
6. Park, M.K., Kim, J.W.: Kinematic manipulability of closed chains. In: Advances in Robot Kinematics, pp. 99–108. Portoroz-Bernadin (1996)
7. Salisbury, J.K., Craig, J.J.: Articulated hands: Force control and kinematic issues. The International Journal of Robotics Research 1(4), 4–17 (1982)
8. Tandirci, M., Angeles, J., Farzam, R.: Characteristic point and the characteristic length of robotic manipulators. In: ASME Design Engineering Conferences, 22nd Biennial Mechanisms Conference (1992)
9. Yoshikawa, T.: Analysis and control of robot manipulators with redundancy. In: Proceedings of the First International Symposium on Robotics Research, Bretton Woods, NH, USA, pp. 735–747 (1983)

Effects of Plasticity Induced by Assembly Process on Contact Pressure of Shrink Fits with Grooved Hubs

J.C. Pérez-Cerdán, M. Lorenzo, and C. Blanco

University of Salamanca, Spain
{juha,mlorenzo,cbh}@usal.es

Abstract. Plastic strains states generated after assembly process in shrinks fits are not desirable since could limit the good conditions performance of joined parts. So design methods leading to reduce those states are strongly welcomed. In this paper, the effects of one of those methods, a grooved hub, on the plastic strain distribution at the interface are analyzed from the results of diverse numerical simulations of the thermal assembly process by means of FEM. According to results, the proposed geometry is revealed as an effective method for notably reducing the plastic strain state with loss of the maximum transmitted torque lower than 6%. This way, the working conditions are closer to the ones established in the theoretical design of the shrink fit.

Keywords: Interference fit, shrink fit, contact pressure, plastic strains, stress concentration.

1   Introduction

Nowadays an interference fit can be assembled by two different procedures. On one hand by axial insertion of the shaft into the hub, resulting a press fit. On the other hand by a thermal process consisting in applying a thermal cycle in which either the hub is heated or the shaft is cooled. At the end of the assembly process, the inner diameter of the hub (d_h) increases and the outer diameter of the shaft decreases (d_s) until a final diameter d is achieved verifying $d_h < d < d_s$. As results a contact pressure appears at shaft-hub interface which allows the transmission of a torque between the assembled parts [10].

Diverse methods both numerically and experimentally were developed for obtaining the distribution of contact pressure. However, experimental methods, such as ultrasonic techniques [4], face a very complex problem which actually is hard to be solved. So, numerical simulation of the assembly processes seems to be an adequate way of estimating the contact pressure [5, 8, 12] and from it, the efficiency of the torque transmission of the joint.

During the assembly process important changes can be produced in stress distributions throughout the joint interface such as stress concentrations [11] or undesirable residual stress or plastic strains [2] which could compromise the efficiency of the joint. Diverse studies [1, 9] have analyzed the elastic-plastic stress distributions in shaft-hub joints thermally fitted.

The addition of the stress concentrations at the edges of the hub, which are not considered in the pressure cylinder theory, and the residual stresses produced by plastic strains induced by assembly process could limit the life in service of the joined components. So, many methods for reducing the stress concentrations in interference fits where developed, for example, by machining a groove in the hub [3, 6] or by modifying the hub geometry with chamfers [7].

In this paper we carried out the analysis of the stress and strain states in different interference fits generated during the assembly process by thermal dilatation of different hubs (considering conventional and grooved hubs) in which occur: no plasticity, localized plasticity, and generalized plasticity. From the obtained results, the analysis of the effect of the groove on the stress and strain state of the shrink fit is performed. To achieve this goal, diverse numerical simulations by means of finite elements method (FEM) of the thermal assembly process were carried out. This way, the consequences produced by the thermal procedure on the working conditions of the assembled elements are revealed.

2   Numerical Modeling

The thermal assembly of three different hub geometries was numerically simulated by FEM: (i) a conventional hub (Fig. 1a), (ii) a hub with a circumferential groove (Fig. 1b) which verifies the optimal design conditions and (iii) a grooved hub outside of the design zone proposed in a previous work [6]. For each one of them, three different types of fits according to ISO standard for fits and tolerances were considered: a soft fit, 200H7/s6 with a maximum radial interference of $\delta = 75$ μm, a medium fit, 200H7/v6 with a radial interference of $\delta = 140$ μm, and a severe fit, 200H7/x6 with an interference $\delta = 152$ μm. Thus, considering a conventional steel (AISI 1085) for both parts with Young modulus, $E= 210$ GPa, Poisson coefficient, $\nu = 0.3$ and yield strength, $S_Y=276$ MPa, no plasticity related phenomena will be expected for the soft fit, while a localized plasticity will be found in the medium fit and, finally, a full plasticity will be expected in the heavy fit. The plasticity behaviour was considered to be elastic perfectly plastic.

For all the cases analyzed, both cylinders are coaxial, so the assembly exhibits revolute symmetry. This axisymmetry let to simplify the modeling stage in FEM analysis, reducing the initial 3D geometry to a bidimensional one with the corresponding computing time saving. Such rectangles are initially superposed due to radial interference, δ. A cylindrical coordinate system (r, θ, z) for each part is used as Fig. 1 shows. Considering l as the hub length, the symmetry plane $z = l/2$ includes the medium cross section of both cylinders and $r = R$ represents the interface, being R the transition radius. FEM simulations were carried out by means of a commercial code (MSC. Marc) and the geometry was meshed with quadrilateral

elements of 4 nodes per element. Several meshes were tried until the required convergence in results was achieved. The hub length l is 100 mm with a shaft-hub lengths ratio L/l=4, and the hub thickness is $e = 40$ mm.

Briefly, the thermal case was simulated considering the coupled thermo-mechanical analysis with the same material for both components (thermal conductivity, $K = 60.5$ w/m K, thermal dilatation coefficient, $\alpha = 1.2 \ 10^{-5} \ K^{-1}$). The simulation was developed into two phases. Firstly, the shaft is moved into the hub once this one has been heated to a temperature $T = 450K$ enough for ensuring a minimum clearance $h = 1$ mm. Later, the hub is slowly cooled down to room temperature (T_r =298K) causing a reduction of hub diameter and, consequently, a contact pressure over the shaft.

<div align="center">(a)   (b)</div>
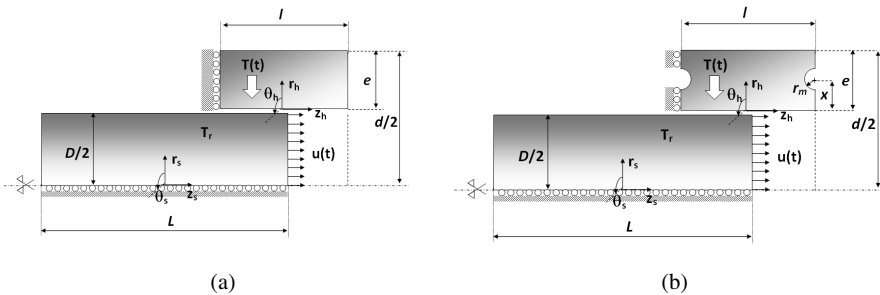
Fig. 1 Shrink fit geometrical model for the cases analyzed: (a) conventional hub and (b) grooved hub

The design equations given by the pressure cylinder theory [10] can be used without committing a significant underestimation of the stress state on the edges of the hub if two geometrical conditions in a grooved hub are fulfilled [6]. The groove geometry can be described with two parameters: the notch radius r_m and the distance from the notch center to the contact zone, x. Thus, a parameter $\lambda = r_m/x$ must be included within the range, $0.52< \lambda <0.55$, and a second parameter $\xi = r_m/(e/2)$ must be within the range $0.40< \xi <0.56$. So, taking into account such restrictions, two different kinds of grooved hubs were considered: (i) type *IN*, whose design parameters are included within the established range ($\lambda = 0.54$ and ξ=0.50) and (ii) type *OUT*, whose design parameters are outside of such design zone ($\lambda = 0.50$ and ξ=0.30).

3   Stress Distributions throughout Interface

According to the pressure cylinder theory, the contact pressure p is uniformly distributed and it can be obtained as the opposite of the radial stress at interface. Thus, Fig. 2, 3 and 4 shows the contact pressure distributions for each one of the three hubs analyzed considering the soft, medium and severe interference fits. Results obtained by the numerical simulation of the thermal assembly are compared with the ones given by the theory (dashed line).
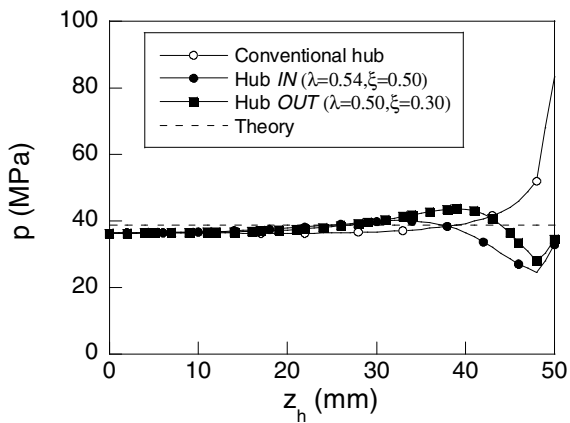
Fig. 2 Distribution of the contact pressure at the 200H7s6 fit interface
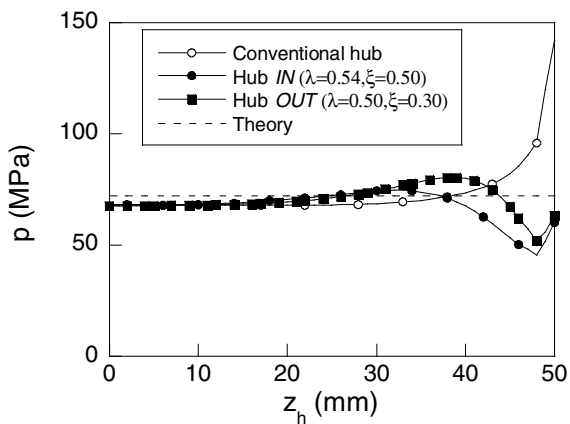
Fig. 3 Distribution of the contact pressure at the 200H7v6 fit interface
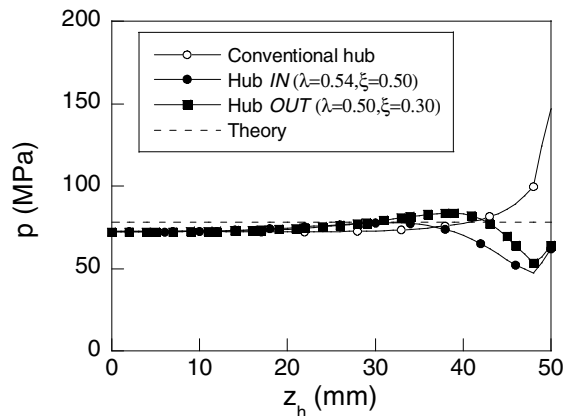
Fig. 4 Distribution of the contact pressure at the 200H7x6 fit interface

As Figs. 2-4 reflects, the circumferential groove clearly modifies the contact pressure in the shrink fits, notably reducing the stress concentration at the vicinity of the hub extremity (40 mm $< z_h <$ 50 mm), being this effect more accused in the grooved hub type *IN*. Thus, over such zone the grooved hubs present a little bit lower contact pressure than the one predicted by the theory. These changes in the distributions of contact pressure can affect the interference fit performance during the life in service. The maximum transmitted torque is easily obtained from the pressure cylinders theory equations as follows:

$$M_{th} = \mu p 2\pi R^2 l \tag{1}$$

From the obtained distribution of the contact pressure p (Fig. 2-4), the maximum transmitted torque can be calculated for each case according to the expression:

$$M = 2\pi\mu R^2 \int_0^l p \, dz_h \tag{2}$$

So, considering a common friction coefficient μ=0.3, the loss of the maximum transmitted torque, caused by the reduction of the contact pressure, is never higher than 6% of the M_{th} (Eq. 1), except for the case 200H7x6 type *IN* (Table 1).

Table 1 Maximum transmitted torque

	M(kN m)			
	Theoretical	**Conv. Hub**	**Hub *IN***	**Hub *OUT***
200H7/s6	72.70	73.72	68.64	71.70
200H7/v6	135.71	137.04	127.54	133.08
200H7/x6	147.35	144.98	134.06	140.20

Consequently, the use of hubs with a groove milled allows a huge reduction of the stress concentration at the edges of the hub without a significant loss of transmitted torque.

In order to go deeper in the analysis, the effects of the circumferential groove on the plasticity induced by assembly process are analyzed for each one of the interference fits in the following way. Thus, for the soft interference fit where no plastic strains are expected for the value of the steel yield strength given, the von Mises distribution is presented in Fig. 5 for both groove types. However, for a better understanding in the cases of the medium and severe fits, the analysis is focused directly on the plastic strain distributions shown in Figs. 6 and 7, respectively.

Fig. 5 shows, in the same way as was previously observed in the contact pressure distributions, a heavy reduction of the stress concentration at the edges of the hub. The values of the von Mises stress are always lower than the material yield strength and, consequently, no plastic strains appear at the interface.

However, in the case of the medium fit (Fig. 6), plastic strains appear in a conventional hub over the zone 38 mm < z_h < 50 mm, where approximately the contact pressure distributions exceeds the theoretical value as shown in Fig. 3. In this case, the stress decreases caused by the presence of the circumferential groove and, in particular, on the contact pressure, causes a notable loss of the plastic strains nearby the edges of the hub. This reduction is higher for inner points in the case of the grooved hub *type IN* than the ones obtained for grooved hub *type OUT*.
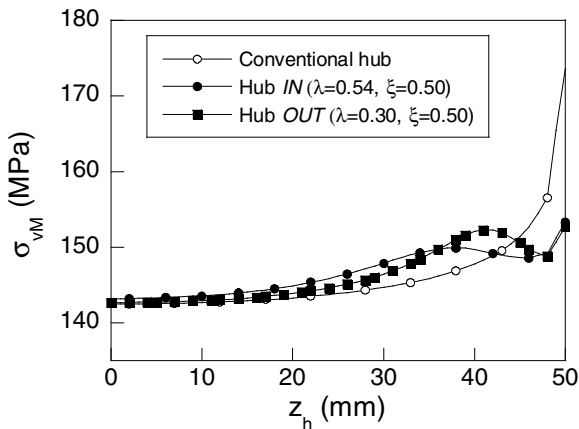
Fig. 5 Distribution of the von Mises stress at the 200H7s6 fit interface
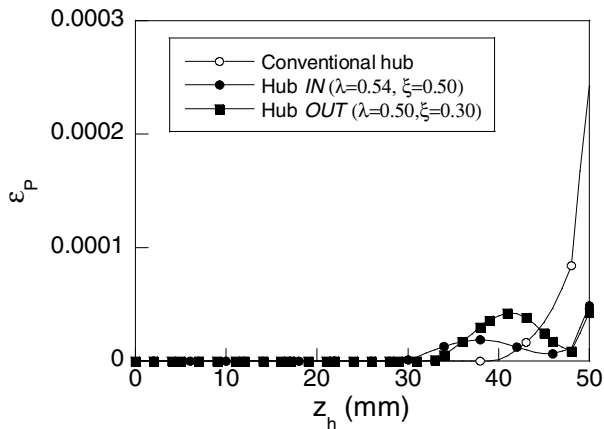
Fig. 6 Distribution of the equivalent plastic strain stress at the 200H7v6 fit interface
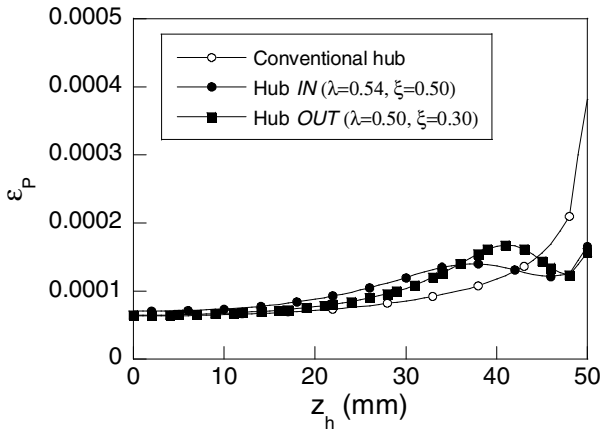
Fig. 7 Distribution of the equivalent plastic strain stress at the 200H7x6 fit interface

Finally, in the case of the severe interference fit (Fig. 7) plastic strains appear throughout the whole interface exhibiting the same effects previously commented with regard to Fig. 6, but, obviously, the values of the plastic strains are higher as results of the increment of the value of stresses caused by radial interference. Far from the groove, the effects on the stress distributions, and hence on strains, are vanished and consequently, the values of the obtained plastic strains are the same for all the cases.

So, results show a way of reducing the magnitude of both the stress and plastic strains state in shrink fits with severe radial interferences without reducing the maximum transmitted torque: to mill a circumferential groove on the edges of the hub. Thus, the groove sensible decreases the plastic strains on the hub. This effect is even more accused when the groove geometry verifies the design conditions deduced in [6]. This supposes a better coupling, avoiding undesirable effects which reduce the efficiency of the torque transmission and could produce harmful and undesirable effects during the life in service.

4   Conclusions

After the thermal process for assembly a shrink fit, a huge stress concentration appears at the extremities of the hub causing, in commonly used steels, plastic strains when the radial interference is severe. Obviously, the occurrence of yielding can reduce the life in service of this type of joints. A simple way of notably reducing this harmful effect without significant reductions of the transmitted torque is to mill a circumferential groove in the hub. This reduction is optimized when the values of the groove parameters verify the design conditions proposed in [6].

References

1. Bengeri, M., Mack, W.: The influence of the temperature dependence of the yield stress on the stress distribution in a thermally assembled elastic-plastic shrink fit. Acta Mechanica 103, 243–257 (1994)
2. Gamer, U., Lance, R.H.: Residual stress in shrink fits. International Journal of Mechanical Sciences 25(7), 465–470 (1983)
3. Grimm, T.R., Chiu, A.C.: Design of hubs to minimize interference stresses–a finite element study. In: Proceedings of the Computers in Engineering, ASME, pp. 85–91 (1988)
4. Lewis, R., Marshall, M.B., Dwyer-Joyce, R.S.: Measurement of interface pressure in interference fits. Journal of Mechanical Engineering Sciences Part C 219(2), 127–139 (2005)
5. Özel, A., Temiz, Ş., Aydin, M.D., Şen, S.: Stress analysis of shrink-fitted joints for various fit forms via finite element method. Materials & Design 26(4), 281–289 (2005)
6. Pérez Cerdán, J.C., Lorenzo, M., Blanco, C., Moreno, P.: Analysis of Contact Stresses in Interference Fit Joints with Circumferential Round Notch on the Hub. In: Proceedings of the 13th World Congress in Mechanism and Machine Science, Guanajuato, México, vol. A23 (2011)
7. Pérez Cerdán, J.C., Lorenzo, M., Blanco, C.: Stress concentrations in interference fits joints with chamfered hubs. Applied Mechanics and Materials 184-185, 489–492 (2012)
8. Prasad, N.S., Sashikanth, P., Ramamurti, V.: Stress distribution in interference joints. Computers and Structures 51(5), 535–540 (1994)
9. Sen, S., Aksakal, B.: Stress analysis of interference fitted shaft-hub system under transient heat transfer conditions. Materials and Design 25, 407–417 (2004)
10. Shigley, J.E., Mischke, C.R.: Standard handbook of machine design. McGraw-Hill (1988)
11. Strozzi, A., et al.: Normalization of the stress concentrations at the rounded edges of a shaft-hub interface fit. The Journal of Strain Analysis for Engineering Design 46(6), 478–491 (2011)
12. Zhang, Y., McClain, B., Fang, X.D.: Design of interference fits via finite element method. International Journal of Mechanical Sciences 42(9), 1835–1850 (2000)

Study of the Stress Intensity Factor of an Unbalanced Rotating Cracked Shaft

B. Muñoz-Abella, L. Rubio, and P. Rubio

University Carlos III of Madrid, Spain
mmunoz@ing.uc3m.es

Abstract. The components of machines very often present defects that can grow to fatigue cracks when they are submitted to the working solicitations. In the case of shaft,this is particularly important because the catastrophic failures can lead to personal injuries or economic problems. When a cracked shaft rotates, the breathing mechanism appears. The crack opens and closes passing from the open state to the close state with a transition that produces a partial opening. The shafts present additionally misalignments or/and unbalances that alter their normal function. In this paper, we present a Finite Element Method (FEM) study of the influence of the eccentricity in the breathing mechanism of a rotating cracked shaft. The classical Jeffcott rotor model has been chosen for this study. To simulate the rotation of the shaft, different angular positions have been considered. The Stress Intensity Factor (SIF) along the crack front during the rotation has been studied considering different angles of eccentricity. The work allows to know the influence of the unbalance of rotating shafts in the crack breathing mechanism, in the values of the Stress Intensity Factor and in the propagation of cracks.

Keywords: Rotating shaft, crack, unbalance, Stress Intensity Factor.

1 Introduction

The increasing importance of safety and costs derived from failure in machinery has pushed the researchers in the field of damage detection to analyze the behavior of mechanical components with defects. The failures of machines are produced quite often by the presence and propagation of fatigue cracks due to the loads and solicitations they carry. Those failures sometimes are catastrophic and produce personal injuries or economic problems.

Among the machine parts, shafts are one of the main components of machines. They work in rotation, usually carrying bending and torsion efforts. All of them together, can produce the shaft failure by generation and propagation of fatigue cracks.

When a cracked shaft rotates, the crack can open and close once per revolution depending on the loads, the stiffness of the shaft at the cracked section. The opening and closing of the crack has been modeled in different ways. The simplest one, very much used because of that, is the switch model. It considers that the crack is open or closed, so that the crack is half the rotation in the open state and the other half in the closed one. However, the breathing behavior is the most feasible behavior of the crack, although it is more complex. In this case, the crack passes from the closed state to the open state gradually in a rotation. As in the switch model, the crack is closed when it is situated in the compression zone of the shaft and it is open when situated in the tensile zone. The transition between both situations produces partial opening (or closing) of the crack when the static deflection dominates the behavior of the rotating shaft. The partial opening/closing of the crack has been studied, numerically or analytically, by different authors [1, 2, 3] always considering an aligned and balanced shaft. The opening and closing of the crack is very much connected with the the values taken by the the Stress Intensity Factor (SIF) at the crack front as the shaft rotates. The SIF is a parameter of fracture mechanics that allows to predict the stress state in the proximity of the crack front due to remote loads. The crack is open while the SIF remains positive, otherwise the crack will be closed.

Unfortunately, in the real work of large shafts, it is very usual that the shafts present unbalances or misalignments that modify the normal behavior of the component. The presence of eccentric masses [4, 2, 5, 6, 12, 7] can be considered as a very common unbalance case in rotors. The unbalance, as mention before, modifies the dynamic behavior of the rotating shafts and may hide the presence of the cracks or, on the other hand, can increase their effects.

In this paper we present the numerical study of the influence of the eccentricity in a rotating cracked shaft using a finite element model of a cracked Jeffcott rotor. The analysis has been made using the commercial finite element code ABAQUS. We have analyse the SIF along the crack front, for each angle of rotation and for different positions of the eccentricity. We can identify, through the study of the SIF, when and where the opening takes place.

2   The Cracked Shaft Model

As mentioned before, the model chosen for this study is the classical Jeffcott rotor widely used in rotordynamics [11, 8, 9, 10, 5, 6, 7]. This simple but useful model consists in a massless shaft simply supported at the ends, with a concentrated mass (a disc). The crack is situated at the mid span of the shaft having a straight front, for sake of simplicity, oriented on a plane normal to the axis of the shaft. The eccentric mass has been placed on the disc of the Jeffcott rotor as an additional mass as can be seen in Figure 1.The round bar

total length is equal to 900mm, whereas the diameter is 20mm. The material of the shaft is aluminium with the following mechanical properties: Youngs Modulus $E=72GPa$, Poisson ratio $\mu=0.33$ and density $\rho=2800Kg/m^3$.

The rotation of the shaft has been simulated considering eight different angular positions, one for every eighth of a rotation, called angle of rotation ϕ, see Figure 2. At each angular position given, we analyze the static behavior of the shaft (considering the gravity effect), variables such as displacements, open portion of open crack and SIF, among others. On the other hand, the influence of the mass eccentricity on the opening of the crack has been studied considering different positions of the eccentric mass on the disc, given by different angles measured from the position of the crack, called angle of eccentricity θ, as shown in Figure 3. The effect of the eccentric mass, has been included as an inertial force, F_e calculated as a mass m located at a distance e from the center of the Jeffcott rotor rotating with the angular rotating velocity Ω, see Figure 3. Values taken for this analysis are $m=0.2$ Kg, $e=80mm$ and $\Omega=1000\ rpm$.
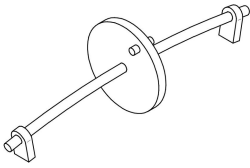
Fig. 1 Jeffcott rotor with an eccentric mass
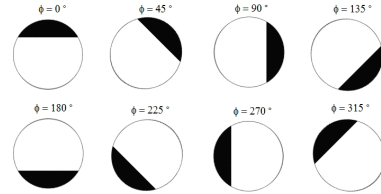
Fig. 2 Angular positions of the crack during one rotation

In order to know how much other variables are involved in the problem, like the size of the crack, three crack lengths, $\alpha = a/D=0.1;\ 0.25$ and 0.5, have been considered.

The numerical simulation of the problem has been carried out using the Finite Element commercial code ABAQUS. As there is no symmetry in the problem, the analysis has been developed for a complete 3D model of the shaft. The mesh of the three dimensional model is made employing 8 node linear brick elements. To avoid the interpenetration between the crack faces when the crack is in the compression zone (closed), a surface-to-surface contact interaction has been defined.

The analyzed cases has been done accordingly with the following:

- crack length $\alpha=0.1;\ 0.25;\ 0.5$
- eccentricity angle $\theta= 0^o;\ 45^o;\ 90^o;\ 135^o;\ 180^o$
- rotation angle $\phi= 0^o;\ 45^o;\ 90^o;\ 135^o;\ 180^o;\ 225^o;\ 270^o;\ 315^o;\ 360^o$

To simulate the balanced shaft, the cases corresponding to the same three crack lengths and eight rotation angles have been also modeled in order to compare with the corresponding unbalanced cases.
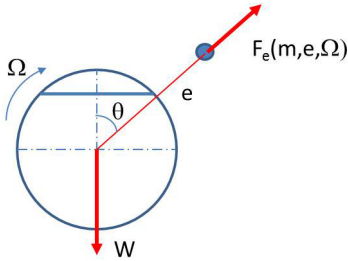
Fig. 3 Resume of the applied forces on the shaft
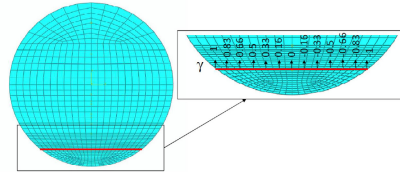
Fig. 4 Positions on the crack front, γ

Although the behavior of a rotating cracked shaft is a nonlinear problem due to the vibrations produced and also to the breathing mechanism of the crack, we have evaluated the SIF treating the problem as a succession of static ones in which the nonlinearity is reduced to the contacts in the crack. The commercial code ABAQUS linearizes internally this problem, so that our study can be considered lineal.

3 Stress Intensity Factor at the Crack Front

The model developed using commercial code ABAQUS, allows to obtain the SIF along the crack front in a total of 13 locations, given by variable γ, as indicated in Figure 4.

The non-dimensional values of the SIF versus non-dimensional location on the front, γ, have been plotted in Figure 5 cases (a,b,c,d,e). In this case, we have chosen the crack length $\alpha=0.25$. Each figure shows, for a given eccentricity (θ) the SIF values for five angles of rotation ($\phi=0^0$, 45^0, 90^0, 135^0, 180^0) (only half the rotation has been considered in the plots). Looking to those figures we can see that when the crack and the eccentricity are at the same location, ($\theta=0^0$), Figure 5 (a), the SIF is always positive which means that the crack is always open. It is true for the whole front and the whole rotation. On the other hand, when the crack is just opposite to the eccentric mass ($\theta=180^0$) Figure 5 (e), the values of the SIF are always null which means that the crack is completely closed (at any moment of the rotation and at any location in the front). The cases corresponding to the other three (b,c,d), represent intermediate cases where the crack is partially open with positive and negative values of the SIF along the front. The figures show clearly the influence of the eccentricity and the angle of rotation on the breathing mechanism of the crack.

For the sake of clarity, the results in terms of stress and open area of the crack corresponding to the case $\alpha = 0.25$ and $\theta = 90^0$ for the whole rotation, have been plotted in Figures 6 and 7. In Figure 6 the tensile stress at the
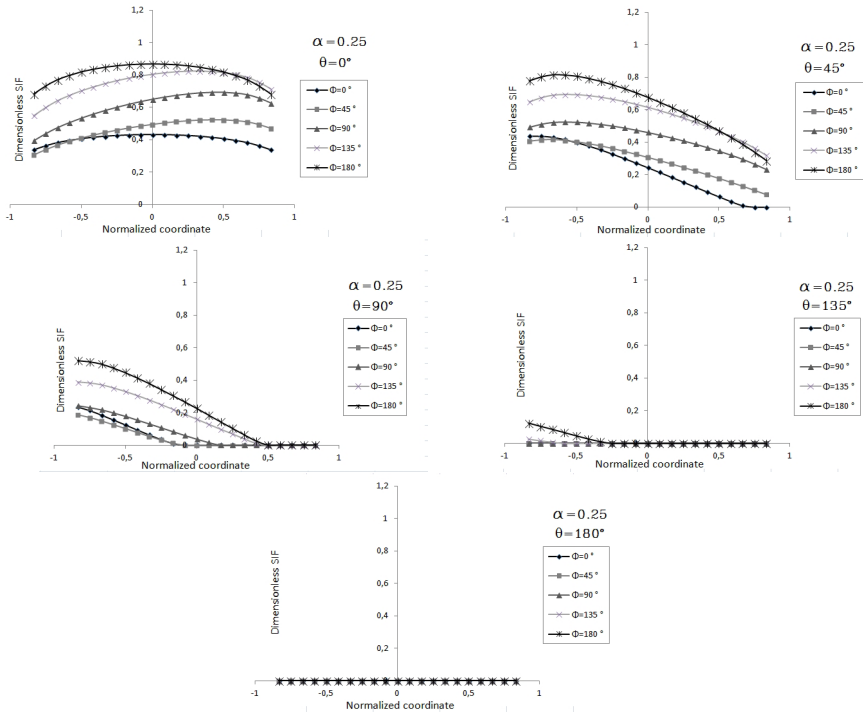
Fig. 5 Non-dimensional SIF vs location in the front, γ. Case α=0.25.

front of the crack is plotted. The white colour corresponds to the open part of the crack (tensile stress). Note the agreement with the plotted results of SIF in Figure 5 c). More clear is the plot of the open part of the crack for the same case that can be observed in Figure 7.
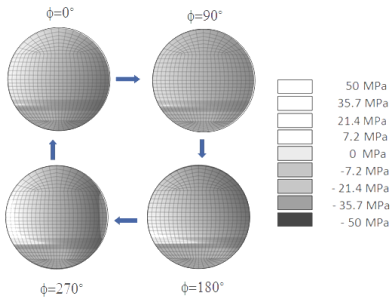
Fig. 6 Stress map at the cracked section. Case $\alpha = 0.25$ and $\theta = 90^0$
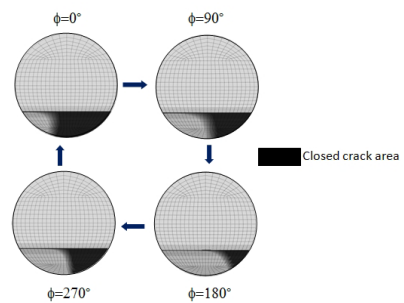
Fig. 7 Opening map at the cracked section. Case $\alpha = 0.25$ and $\theta = 90^0$

In order to know the influence of the crack length, the values of the SIF have been plotted versus the crack front. In this case, we have selected a specific eccentricity $\theta = 45^0$, so we have plotted a figure for each crack length for different angles of rotation. In Figure 8 we can observe that as the crack is larger the values of the SIF are greater. On the other hand, the behavior of the front in terms of opening and closing is nearly the same for the different values of length, being more similar the cases of medium and large cracks.

4   Analysis of the Breathing Mechanism Using the SIF

To have a better interpretation of the data obtained for the SIF, we have calculated for each location on the front, a new variable, ΔK, given by the following expression:

$$\Delta K(\gamma) = K_{max}(\gamma) - K_{min}(\gamma) \qquad (1)$$

where $K_{max}(\gamma)$ and $K_{min}(\gamma)$ corresponds to the maximum value of the SIF and the minimum value of the SIF, respectively, both in a rotation for each location γ on the front of the crack.

ΔK is a good indicator of the opening of the crack. If a point of the crack front is open at least once in a rotation, ΔK for this point will be positive. If ΔK takes value 0, that means that the point will be always closed during the rotation. That indicator shows the feasibility of the crack to grow. In Figure 9, we have plotted the value of ΔK in each location of the front, for each angle of rotation, θ. The figures corresponds to the three values of α considered
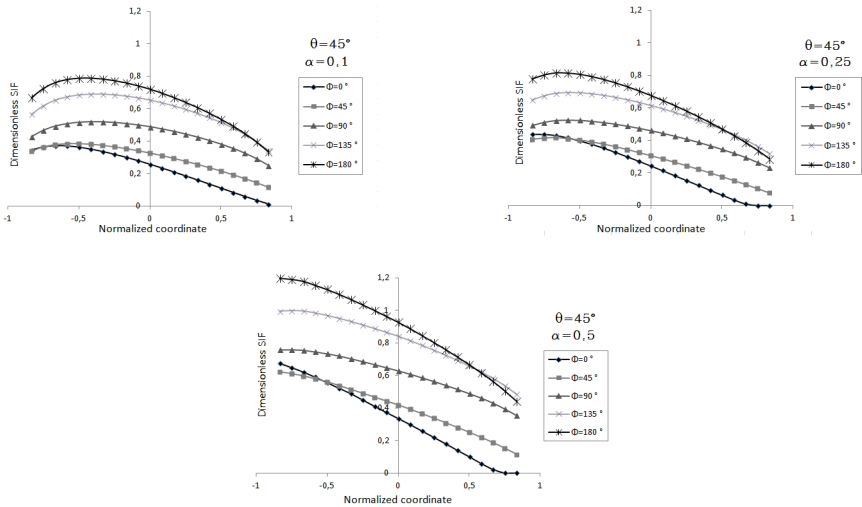
Fig. 8 Non-dimensional SIF vs location in the front, γ. Case $\theta = 45^0$.

Fig. 9 ΔK vs location in the front. Case $\theta = 45^0$.

in this study. The figures include, just for comparison, the behavior of the balanced cracked shaft.

5 Conclusions

In this paper a numerical study of the evolution of the Stress Intensity Factor of an unbalanced cracked shaft during a rotation has been developed. The influence of some variables involved in the problem have also been analyzed. The conclusions of the paper can be summarized in the following:

- Regarding the angle of eccentricity, data show that the position of the eccentric mass with respect to the crack (angle of eccentricity) influences very much the opening and closing of the crack. When both crack and eccentric mass are at the same position, the crack is always open along the rotation. However, if the eccentric mass is opposite to the crack, then the crack never opens. With other relative positions of eccentric mass and crack, data show the partial opening of the crack during the rotation.
- With respect to the crack length, data show that the SIF grows with the length of the crack. The pattern is the same independently of the crack length.
- For a better interpretation of the data, a new variable is proposed, ΔK, calculated at each location on the front. This variable allows to know if the crack would probably grow or not depending on its value. For a positive value, the crack very probably will grow.

References

1. Dimarogonas, A.D., Papadopoulos, C.A.: Vibration of cracked shafts in bending. Journal of Sound and Vibration 91, 583–593 (1983)
2. Darpe, A.K., Gupta, K., Chawla, A.: Transient response and breathing behaviour of a cracked Jeffcott rotor. Journal of Sound and Vibration 272, 207–243 (2004)
3. Bachschmid, N., Pennacchi, P., Tanzi, E.: Some remarks on breathing mechanism, on non-linear effects and on slant and helicoidal cracks. Mechanical Systems and Signal Processing 22, 879–904 (2008)
4. Sekhar, A.S., Prabhu, B.S.: Condition monitoring of crecked rotors throeugh transient response. Mechanism and Machine Theory 33(8), 1167–1275 (1998)
5. Patel, T.H., Darpe, A.K.: Influence of crack breathing model on nonlinear dynamics of a cracked rotor. Journal of Sound and Vibration 311, 1953–1972 (2008)
6. Cheng, L., Li, N., Chen, X.F., He, Z.J.: The influence of crack breathing and imbalance orientation angle on the characteristics of the critical speed of a cracked rotor. Journal of Sound and Vibration 330, 2031–2048 (2011)
7. Rubio, L., Fernández-Sáez, J.: A new efficient procedure to solve the nonlinear dynamics of a cracked rotor. Nonlinear Dynamics 70, 1731–1745 (2012)
8. Darpe, A.K., Gupta, K., Chawla, A.: Dynamics of a bowed rotor with a transverse surface crack. Journal of Sound and Vibration 296, 888–907 (2006)
9. Darpe, A.K.: A novel way to detect trasnverse surface crack in a rotating shaft. Journal of Sound and Vibration 305, 151–171 (2007)
10. Jun, O.S., Gadala, M.S.: Dynamic behavior analysis of cracked rotor. Journal of Sound and Vibration 309, 210–245 (2008)
11. Penny, J.E.T., Friswell, M.I.: Simplified modelling of rotor cracks. In: Proceedings of ISMA: International Conference on Noise and Vibration Engineering, vol. 2, pp. 607–615 (2002)
12. Rubio, L., Muñoz-Abella, B., Rubio, P., Montero, L.: Influence of the eccentricity in the crack breathing in a rotating shaft. In: Proceedings of ECT 2012: International Conference on Engineering Computational Technology (2012)

Automatic Identification of the Inertia and Friction of an Electromechanical Actuator

C. Roldán, F.J. Campa, O. Altuzarra, and E. Amezua

University of the Basque Country, Spain
`constantino.roldan@ehu.es`

Abstract. The aim of the present work is to present a fast identification method to estimate the inertial and friction parameters of a rigid body dynamic model of an electromechanical actuator. These are the dominant effects that determine the dynamics of machines and although the inertia is easily predictable, the friction can only be accurately known performing experimental measurements. The work provides the mathematical aspects of the identification method as well as several practical aspects for its implementation. The procedure is applied to an actuator based on a motor and a gearbox, and a comparison of the torque estimated and the real one are provided.

Keywords: Identification, Mechatronics, Actuators, Dynamics Modeling, Friction.

1   Introduction

At present, the market demand for higher precision, stiffness and speed calls for an optimal mechatronic design of machines. To do so, the modeling of the dynamics of actuators, manipulators, robots, and machine tools is of great relevance. With the use of these models, designers can improve the dynamic behavior of the machine modifying actuators, redesigning lighter or stiffer mechanical components, or improving the control architecture. The mechatronic analysis starts with the dynamic modeling of the transmission mechanism of the machine, leading to a multibody model or a lumped parameters model [4]. After the modal analysis and the calculation of the transfer functions is done, the mechatronic modeling of the transmission dynamics and the control dynamics allow the estimation of the bandwidth of the system, which characterizes its global dynamic behaviour [1].

One of the main problems of the dynamics modeling is the lack of accurate data that can be relevant for the analysis. Inertial terms, as well as stiffness can be accurately predicted by means of analytical methods, or finite element modeling. However, very little estimations can be done about friction and damping, whose influence is usually underestimated due to the absence of data. System identification methods can be used to overcome this problem [3,5]. They are based on the

use of experimental data from the machine, several inputs and outputs, to mathematically build a model that fits them.

The present work presents a method for automatic parameter identification of a rigid body with friction dynamic model of an electromechanical actuator. First, the rigid body model is presented. Second, the system identification method selected is presented. Third, the experimental procedure is presented, as well as the results obtained for an actuator based on a motor and a gearbox. The article ends with some conclusions and future works.

2   Rigid Body Model of the Actuator with Friction

The actuator studied in the present work is based on an asynchronous motor and a gearbox. The dynamic behavior is represented by a rigid body model with friction. The model, shown in Fig. 1, considered is purely inertial, with 1 degree of freedom θ that represents the rotation measured on the motor encoder. There are two lumped inertias, from the motor J_m and from the gearbox J_g, whose total is considered as J. The motor makes a torque τ. Also, friction torque is considered as τ_f.
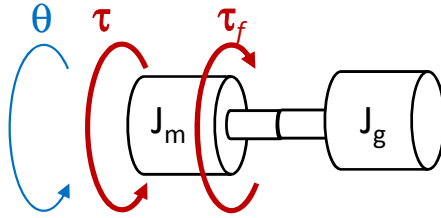
Fig. 1 Rigid body with friction model

Hence, the equation of motion of the system can be written as

$$\tau - \tau_f = J\ddot{\theta} \tag{1}$$

The modeling of the friction torque is based on a nonlinear model [2]. Two approaches have been compared, one considering the Coulomb friction and the viscous friction, and another one that also takes into account the Striebeck effect, see Fig. 2, where also both a discontinuous and a continuous model of only Coulomb friction are shown.

The first model is shown in Eq. (2), where c is the torsional viscous friction coefficient, and F_c is the Coulomb friction torque, which has been represented with a hyperbolic tangent dependent on β and the motor speed.

$$\tau_f = c\dot{\theta} + F_c \cdot tanh\left(\beta\dot{\theta}\right) \tag{2}$$

On the other hand, the second friction model considers also the Striebeck effect as a torque F_{cs} modeled as a function of the product of a hyperbolic secant dependent on α.

$$\tau_f = c\dot{\theta} + \left(F_c + F_{cs}\, sec\, h\left(\alpha\dot{\theta}\right)\right) \cdot tanh\left(\beta\dot{\theta}\right) \tag{3}$$
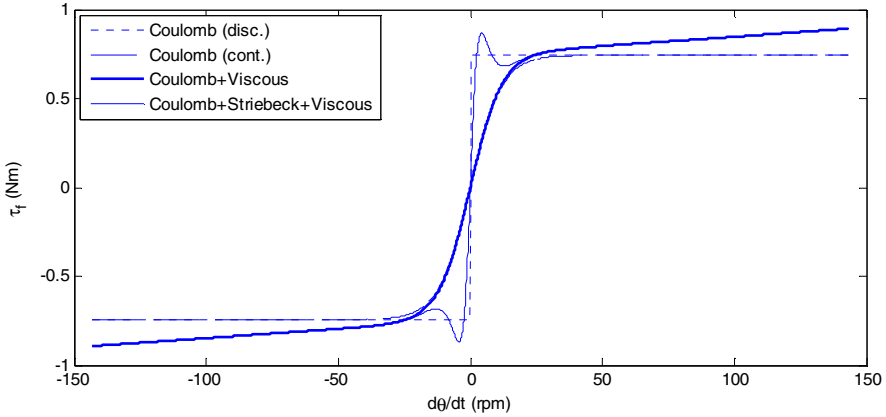
Fig. 2 Comparison of the friction models considered

3   Grey-Box Identification Method

The so-called grey-box identification methods are used to quantify the value of the parameters that characterize the dynamic of a given system from the measurement of several of its variables [5]. They differ from the black-box identification methods in that the parameters identification is based on a previously developed model of the system dynamics. Once the model is developed and the variables measured, the identification of the unknown parameters is based on the minimization of a criterion that compares the measurement with the model prediction.

The first step to apply this method consists on rearranging the equation of motion of Eq. (1) as a pseudo-linear regression.

$$\hat{\tau}\left(t\mid\rho,\eta\right) = \boldsymbol{\rho}^T \boldsymbol{\varphi}\left(t,\eta\right) \tag{4}$$

In Eq. (4) $\boldsymbol{\rho}$ is the unknown parameters vector, which is dependent on the also unknown parameter vector $\boldsymbol{\eta}$ and the vector $\boldsymbol{\varphi}$, which contains several measurable variables. For example, when only the Coulomb friction and the viscous friction are considered, these terms are as follows in Eq. (5).

$$\boldsymbol{\rho} = \left\{ \begin{array}{c} J \\ c \\ F \end{array} \right\} \qquad \boldsymbol{\varphi}(t,\boldsymbol{\eta}) = \left\{ \begin{array}{c} \ddot{\theta}(t) \\ \dot{\theta}(t) \\ tanh\left(\beta\dot{\theta}(t)\right) \end{array} \right\} \qquad \boldsymbol{\eta} = \{\beta\} \tag{5}$$

Once the model is arranged, the identification problem consists on minimizing the following functional V_N.

$$V_N(\boldsymbol{\rho},\boldsymbol{\eta}) = \sum_{t=1}^{N} \left| \tau(t_i) - \boldsymbol{\rho}^T \boldsymbol{\varphi}(t_i,\boldsymbol{\eta}) \right|^2 = \left\| \boldsymbol{\tau} - \boldsymbol{\Phi}(\boldsymbol{\eta})\boldsymbol{\rho} \right\|^2 \tag{6}$$

The columns of the matrix $\boldsymbol{\Phi}(\boldsymbol{\eta})$ contain each of the terms of the vector $\boldsymbol{\varphi}$, where N is the size of the measured sample.

$$\boldsymbol{\Phi}(\boldsymbol{\eta}) = \begin{bmatrix} \ddot{q}(t_1) & \dot{q}(t_1) & tanh\left(\beta\dot{q}(t_1)\right) \\ \ddot{q}(t_2) & \dot{q}(t_2) & tanh\left(\beta\dot{q}(t_2)\right) \\ \vdots & \vdots & \vdots \\ \ddot{q}(t_N) & \dot{q}(t_N) & tanh\left(\beta\dot{q}(t_N)\right) \end{bmatrix} \tag{7}$$

Indeed, the functional constitutes a separable least squares problem where the estimation of the unknown parameter vector $\boldsymbol{\rho}$ can be calculated approximating it as Eq. (8).

$$\hat{\boldsymbol{\rho}} \equiv \boldsymbol{\Phi}^+(\boldsymbol{\eta})\boldsymbol{\tau} \tag{8}$$

Where $\boldsymbol{\Phi}^+(\boldsymbol{\eta})$ is the Moore-Penrose pseudo-inverse of the matrix $\boldsymbol{\Phi}(\boldsymbol{\eta})$. Substituting Eq. (8) into Eq. (6), the identification problem is simplified as the functional that must be minimized, hence becoming dependent only on the parameter vector $\boldsymbol{\eta}$. In this way, the estimation of $\boldsymbol{\rho}$ is somewhat postponed.

$$V_N(\hat{\boldsymbol{\rho}},\boldsymbol{\eta}) \equiv \left\| \boldsymbol{\tau} - \boldsymbol{\Phi}(\boldsymbol{\eta})\boldsymbol{\Phi}^+(\boldsymbol{\eta})\boldsymbol{\tau} \right\|^2 = \left\| \left[\mathbf{I} - \boldsymbol{\Phi}(\boldsymbol{\eta})\boldsymbol{\Phi}^+(\boldsymbol{\eta}) \right]\boldsymbol{\tau} \right\|^2 \tag{9}$$

Once the functional is minimized for an estimated value of $\hat{\boldsymbol{\eta}}$, the unknown parameters vector $\hat{\boldsymbol{\rho}}$ is finally estimated as Eq. (10).

$$\hat{\boldsymbol{\rho}}(\hat{\boldsymbol{\eta}}) \equiv \boldsymbol{\Phi}^+(\hat{\boldsymbol{\eta}})\boldsymbol{\tau} \tag{10}$$

4   Experiments

Several experimental tests have been done on an actuator based on an asynchronous motor Schneider BSH1401P with encoder and a gearbox Neugart PLE-160

with a reduction of 1:40. The control of the actuator is based on a PID servo control. It has been programmed in Labview using a National Instruments PXIe.

The velocity of the motor has been measured from the motor encoder and then the acceleration was calculated by numeric differentiation. Finally, the torque was obtained from the current signal of the motor. The sampling frequency was set on 72 Hz.

4.1 Motion Planning

In order to be representative of the dynamic behaviour of the actuator, the motion programmed must excite as much as possible the frequencies inside the bandwidth. However, under the rigid body assumption, the identification must be oriented to identify the actuator response at 0 Hz and the friction.

In [5], several recommendations are made: first, the execution of several multisine velocity profiles with fixed frequencies and amplitudes, second, execution of a multisine with flat amplitude in the frequency domain up to 40 Hz, third, parameter identification with each signal, and finally, calculation of the average and deviation of all the parameters. The problem of this approach is that the identifications are made with a small sample of all the motions that the actuator can perform, so the parameters estimated are not representative enough.

Here, the execution of the multiprofile velocity signal of Fig. 3 is proposed. The motion is divided in four profiles: first, a sum of sinusoids with frequencies 0.1, 0.3, 0.5 Hz and increasing amplitude from 10 rpm to 3100 rpm, second, two stages of ascending and descending velocity steps from 10 rpm to 3700 rpm, third, two stages with constant acceleration and deceleration, and, four, two stages of exponentially increasing and decreasing velocity. This profile represents better in a single signal the diversity of motions that the actuator can perform in the whole range of velocities and, as a consequence, the estimation should be more robust.
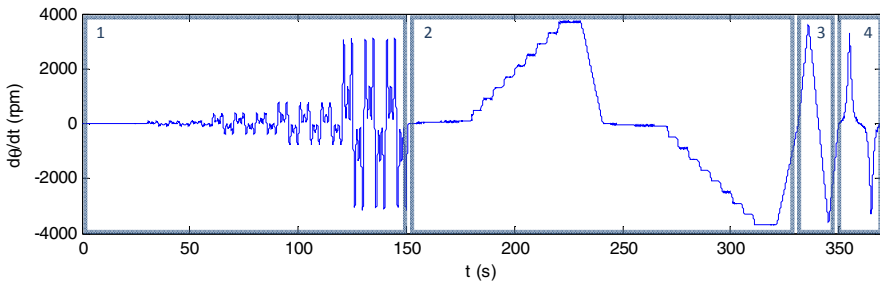
Fig. 3 Velocity multiprofile test

4.2   Results

In Table 1, all the parameters estimated with the different methods and models are compared with the available data from the manufacturers. There, test GBI-CV-MP indicates the parameters estimated with the grey-box method using the Coulomb+viscous friction model and a multiprofile signal. Test GBI-CSV-MP is the same but adding the Striebeck effect to the friction model. Experiments GBI-CV-MS and GBI-CSV-MS test the two friction models and are made with the same identification method applied to several multisine signals, and then averaging the parameters as suggested by [5].

Table 1 Estimated parameters

Test	J ($\cdot10^{-4}kg\cdot m^2$)	c ($\cdot10^{-3}N\cdot m\cdot s/rad$)	Fc ($N\cdot m$)	β	Fcs ($N\cdot m$)	α
Manufacturer datasheet	14	-	-	-	-	-
GBI-CV-MP	13	1,7	0,478	10,78	-	-
GBI-CSV-MP	13	1,7	0,477	9,21	0,069	9,648
GBI-CV-MS	10,6 ± 4,6	-4,1±18	0,46±0,09	18,89± 33,37		
GBI-CSV-MS	10,4±4,4	-5,1±17	0,54±0,14	124± 273	1,11±2,02	222± 489
VS-CVdisc	-	1,5	0,341	-	-	-

The resulting parameters have been compared with the manufacturer data and with a manual identification method based on performing several steps of constant velocity from 10 rpm to 3700 rpm. At constant velocity, the friction parameters of a discontinuous model with Coulomb and viscous friction can be estimated as a linear function of the motor velocity. The resulting parameters are shown in Table 1 as VS-CVdisc.

Regarding the results from the multiprofile signal, the inertia is similar to the one provided by the manufacturers, and the friction parameters are close to the ones obtained with the VS-CVdisc test, as it can be seen in Fig. 4. Furthermore, it can be seen that the Striebeck effect is neglectable. Therefore, the simple friction could be used for the simulation of the dynamics of the system.

On the other hand, in Table 1 when the multisine signal has been used for the identification, a large standard deviation is observed. Also the mean values do not fit to experimental ones as much as the multiprofile results.
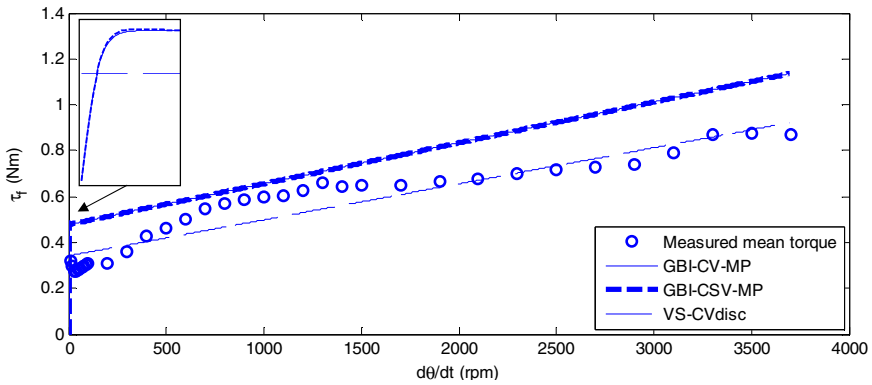
Fig. 4 Measured mean torque vs. Friction models

Figure 5 shows a simulation of the dynamics of the systems with the parameters obtained using the simple friction model. The simulations shows that the parameters obtained represent quite well the dynamics.
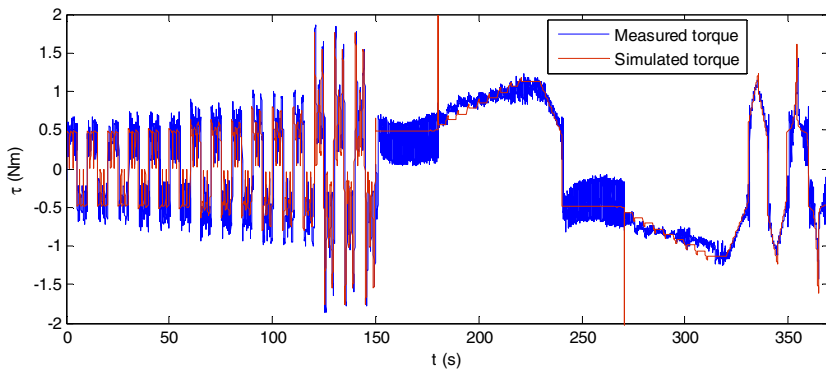
Fig. 5 Measured torque vs. Simulated torque

5   Conclusions

A fast method for rigid body dynamics with nonlinear friction identification has been presented. It has been demonstrated that the identification of the parameters is highly dependent of the signal measured, which has to be representative enough of the different movements that the actuator can perform. The tests carried out with an electromechanical actuator show that the identification on a single multi-profile velocity signal provides more consistent parameters than the averaged parameters of several identifications based on multisine signals.

References

1. Altintas, et al.: Machine tool feed drives. CIRP Annals-Manufacturing Technology 60, 779–796 (2011)
2. Armstrong-Helouvry, B., Dupont, P., Canudas de Wit, C.: A survey of models, analysis tools and compensation methods for the control of machines wit friction. Automatica, Survey Paper 30(7), 1083–1138 (1994)
3. Berglud, E., Hovland, G.E.: Automatic elasticity tuning of industrial robot manipulators. In: Proceedings of the 39th IEEE, Conference on Decision and Control, Sydney, Australia (2000)
4. Magnani, G., Rocco, P.: Mechatronic analysis of a complex transmission chain for performance optimization in a machine tool. Mechatronics 20, 85–101 (2010)
5. Wernholt, E., Gunnarsson, S.: Nonlinear identification of a physically parameterized robot model. In: SYSID 2006, Newcastle, Australia (2006)

Author Index